

# Phonons and crystal-field excitations in highly correlated materials probed by optical spectroscopy

Inaugural - Dissertation

zur

Erlangung des Doktorgrades  
der Mathematisch-Naturwissenschaftlichen Fakultät  
der Universität zu Köln

vorgelegt von

Thomas André David Möller

aus Köln

Köln, im Februar 2009

Berichterstatter: Prof. Dr. M. Grüninger  
Priv.-Doz. Dr. R. Bulla

Vorsitzender  
der Prüfungskommission: Prof. Dr. L. Bohatý

Tag der mündlichen Prüfung: 28. April 2009

Für meine Frau Melanie,  
meine Eltern,  
meine Familie.



# Contents

<b>1</b>	<b>Introduction</b>	<b>1</b>
<b>2</b>	<b>Calculating the Electronic Structure of a Crystal</b>	<b>5</b>
2.1	The Hartree-Fock Calculation . . . . .	8
2.1.1	Hartree-Fock Theory and Slater Determinants . . . . .	8
2.1.2	Self-Consistent Field Technique . . . . .	9
2.1.3	Radial Schrödinger Equation . . . . .	11
2.2	Configuration-Interaction Method . . . . .	15
2.2.1	Configuration Interaction . . . . .	15
2.2.2	Correlation Energy . . . . .	16
2.2.3	Truncated Configuration Interaction . . . . .	16
2.3	Coupled Antisymmetrized Basis Functions . . . . .	18
2.3.1	Coefficients of Fractional Parentage . . . . .	18
2.3.2	Basis Functions within the Russell-Saunders-coupling scheme . .	19
2.3.3	One- and Two-Electron Operators . . . . .	20
2.4	Racah-Wigner Algebra . . . . .	26
2.4.1	Irreducible Tensor Operator . . . . .	26
2.4.2	Wigner-Eckart Theorem . . . . .	27
2.4.3	Matrix Elements of Tensor Operators . . . . .	28
2.4.4	Unit Double Tensor Operator . . . . .	29
2.5	Coulomb Interaction . . . . .	31
2.5.1	Coulomb Operator . . . . .	31
2.5.2	Slater Integrals . . . . .	32
2.5.3	Direct Interaction between Equivalent Electrons . . . . .	33
2.5.4	Direct Interaction between Non-Equivalent Electrons . . . . .	34
2.5.5	Exchange Interaction between Non-Equivalent Electrons . . . . .	36
2.5.6	Direct and Exchange Interaction between Non-Equivalent Elec- trons . . . . .	37
2.6	Crystal Field Splitting . . . . .	39
2.6.1	Crystal-Field Theory and Ewald Sum Formulation . . . . .	39
2.6.2	Matrix Elements of the Crystal-Field Operator . . . . .	40
2.7	Spin-Orbit Interaction . . . . .	42
2.8	Hybridization and Tight-Binding Approximation . . . . .	45
2.8.1	Linear Combination of Atomic Orbitals (LCAO) . . . . .	45
2.8.2	Hopping Integrals . . . . .	46
2.8.3	Slater-Koster Approximation . . . . .	47
2.8.4	Sharma's Method . . . . .	48
2.8.5	Harrison's Rules . . . . .	49

2.8.6	Sobel'man's Parentage-Scheme Approximation . . . . .	50
2.8.7	Racah-Wigner expression for the tight-binding operator . . . . .	52
2.9	Exchange Interactions . . . . .	56
2.10	External Fields . . . . .	58
2.10.1	Stark Effect . . . . .	58
2.10.2	Zeeman Splitting . . . . .	60
2.11	Observable . . . . .	63
2.11.1	Response Functions and Optical Conductivity . . . . .	63
2.11.2	Magnetic Susceptibility . . . . .	66
2.11.3	Phonons . . . . .	67
2.12	Numerical calculation . . . . .	70
2.12.1	Lanczos algorithm . . . . .	70
2.12.2	LAPACK and BLAS . . . . .	72
<b>3</b>	<b>Fourier-Transform spectroscopy</b>	<b>73</b>
3.1	Determination of the response functions . . . . .	79
3.1.1	Drude-Lorentz model . . . . .	79
3.1.2	Kramers-Kronig analysis . . . . .	80
<b>4</b>	<b>Measurements</b>	<b>85</b>
4.1	Crystal-Field Excitations in VOCl . . . . .	85
4.1.1	Group-Theoretical Considerations . . . . .	88
4.1.2	Cluster-Model Calculations . . . . .	101
4.2	Phonons in hexagonal YMnO <sub>3</sub> and YMn <sub>0.7</sub> Ga <sub>0.3</sub> O <sub>3</sub> . . . . .	124
4.2.1	Ga Substitution . . . . .	126
4.2.2	Phonon Analysis . . . . .	127
4.2.3	Phonon Analysis of YMn <sub>0.7</sub> Ga <sub>0.3</sub> O <sub>3</sub> . . . . .	144
4.3	Spin-lattice interactions in multiferroic MnWO <sub>4</sub> . . . . .	160
4.3.1	Phonon Analysis . . . . .	163
4.3.2	Cluster-Model Calculations . . . . .	183
4.4	Phonon modes of monoclinic BiB <sub>3</sub> O <sub>6</sub> . . . . .	196
4.5	CaCrO <sub>3</sub> , an antiferromagnetic metallic oxide . . . . .	207
4.5.1	Introduction . . . . .	207
4.5.2	Crystal Growth . . . . .	208
4.5.3	Crystal and Magnetic Structure . . . . .	208
4.5.4	LSDA and LDA+U Calculations . . . . .	211
4.5.5	Resistivity . . . . .	212
4.5.6	Optics on CaCrO <sub>3</sub> . . . . .	212
<b>5</b>	<b>Conclusion</b>	<b>233</b>
<b>A</b>	<b>Wigner n-j symbols</b>	<b>237</b>
A.1	3-j symbol . . . . .	237
A.2	6-j symbol . . . . .	238
A.3	9-j symbol . . . . .	239

<b>B Expansion coefficients for tight-binding operator</b>	<b>241</b>
<b>List of Publications</b>	<b>303</b>
<b>Danksagung</b>	<b>305</b>
<b>Abstract</b>	<b>307</b>
<b>Zusammenfassung</b>	<b>309</b>
<b>Bibliography</b>	<b>311</b>
<b>Reference</b>	<b>311</b>
<b>Supplement</b>	<b>329</b>
Offizielle Erklärung . . . . .	329



# 1 Introduction

Within the wide class of transition-metal oxides the strong correlation between electrons leads to unusual (often technologically useful) electronic and magnetic properties such as high-temperature superconductivity and colossal magnetoresistance. These materials are denoted as *correlated* electron systems, because one electron strongly influences the other ones. Since we are dealing with transition-metal oxides, these compounds have incompletely filled  $d$  or  $f$  electron shells with narrow bands and the electrons tend to localize. But in case of half-filled bands, these compounds are expected to be metals, but found experimentally to be insulators. It is often not possible to use band-structure calculations to describe the electronic structure of correlated materials. The application of optical spectroscopy allows the investigation of the electronic structure and the low-energetic excitations in transition-metal compounds. Furthermore, optical spectroscopy can be used to probe the coupling of the electronic structure to the different degrees of freedom.

In this thesis we combined the usage of optical spectroscopy with the application of cluster-model configuration-interaction calculations. We begin with a detailed description of a new program for doing cluster-model configuration-interaction calculations, which was developed in the framework of this thesis. In many cases configuration-interaction cluster-model calculations with full ionic multiplet structure, including crystal-field effects and covalency within a local cluster model, provide a reasonable description of the experimental results. This cluster-model configuration-interaction calculation neglects the translational symmetry and treats the local on-site electron-electron interactions explicitly. Due to the limited size of the cluster only materials with no long-range interaction can be analyzed. Metallic or half-metallic behavior cannot be described well. Typically, a cluster calculation starts with the Slater determinants of the ground configuration and the application of the creation/annihilation algebra. But the number of Slater determinants scales drastically with increasing cluster size. Using the Racah-Wigner algebra [1–6] and the related Wigner-Eckart theorem we can reduce the computational effort compared with the creation/annihilation algebra. This becomes important, if the size of the calculated cluster is more and more increased, e.g. for double-cluster calculations. The Wigner-Eckart theorem reduces the calculation of the matrix elements of a certain operator to the calculation of a reduced matrix element and the multiplication with a Clebsch-Gordan coefficient. The knowledge of Slater determinants is no longer necessary and the calculation effort scales with the number of angular momenta being involved. In order to use the Racah-Wigner algebra we have to represent the contributions to the Hamiltonian as spherical tensor operators. Expressions for the matrix elements of the on-site Coulomb and the spin-orbit interactions within the Racah-Wigner algebra are given by Cowan [7]. In contrast to

previous publications [8, 9] we present a general expression for the matrix elements of the crystal-field operator within the Racah-Wigner algebra, which is valid for arbitrary configurations. The application of this algebra offers an elegant and accurate description of the electronic structure whereas the dependence of results of the cluster-model calculation on the ionic multiplets is obvious. The crystal-field operator is treated within the point-charge model, where the electrostatic field is described by the Ewald sum formulation [10]. In addition to the crystal-field operator we give an expression for the matrix elements of the covalency operator within the widely-used Slater-Koster tight-binding approximation [11] using Sobel'man's parentage scheme [12]. The application of the Racah-Wigner algebra was not possible, because we were not able to express the tight-binding operator as a spherical tensor operator. Although Sobel'man's parentage scheme is not as fast and elegant as the Racah-Wigner algebra, we still do not need to know the Slater determinants and conserve the dependence of the results of the cluster-model calculation on the ionic multiplet as well.

In the second part of the thesis, we begin with the analysis of the crystal-field excitations of the transition-metal oxyhalide VOCl by using group theoretical as well as cluster-model calculations.

The group of transition-metal oxyhalides consists of (at room-temperature) crystallographically iso-structural compounds and shows rather strong electron localization, resulting in (electrically) Mott-insulating properties. Within this system several electronic configurations and their interactions with the crystal lattice can be probed systematically.

In the following, we investigate the spin-lattice interaction in the multiferroic compounds h-YMnO<sub>3</sub> and MnWO<sub>4</sub>. We start with hexagonal YMnO<sub>3</sub> and analyze the phonon spectra and their dependence on Ga doping by using a Drude-Lorentz model. Replacing Mn by Ga changes the orbital occupation (from  $d^4$  to  $d^{10}$ ) and the ionic radius. Additionally, we can achieve a better understanding of the origin of ferroelectricity in these hexagonal systems. Substituting Ga for Mn lowers also the Néel temperature from  $T_N = 72$  K for YMnO<sub>3</sub> to  $T_N = 35$  K for YMn<sub>0.7</sub>Ga<sub>0.3</sub>O<sub>3</sub> [168].

In addition, we study the temperature dependence of the phonon spectra of the monoclinic compound MnWO<sub>4</sub> by using a generalized Drude-Lorentz model. The spin-lattice interaction in this compound plays an important role in the coupling between antiferromagnetic and ferroelectric orders. Furthermore, we analyze the crystal-field excitations, which are strongly suppressed due to the spin-selection rule.

The understanding of the exceptional optical nonlinearities of BiB<sub>3</sub>O<sub>6</sub> requires a quantitative description of the lattice dynamics. We present a detailed investigation of the linear optical response of BiB<sub>3</sub>O<sub>6</sub> in the phonon range for different polarizations at  $T = 20$  K and 300 K. We analyze the data by using a generalized Drude-Lorentz model, which allows us to obtain the frequency, the damping, the strength and the orientation of the dipole moment of each phonon mode.

We end up with a detailed investigation of the antiferromagnetic metal CaCrO<sub>3</sub>. Transition-metal oxides exhibit a quite general relation between magnetic order and electrical conductivity: insulators usually exhibit antiferromagnetism, whereas ferromagnetism typically coexists with metallic conductivity. So observations of antifer-

---

romagnetic order in transition-metal oxides with metallic conductivity are of great interest. Early electrical conductivity measurements [254, 256] show a metallic behavior, whereas more recently measurements [252] indicate an insulating behavior. These controversies are connected with the difficulty to prepare high-quality stoichiometric materials and with the lack of large single crystals. In contrast to electrical resistivity measurements, optical data can reveal the metallic properties of a polycrystalline metal with insulating grain boundaries if the wavelengths are smaller than the typical grain size.



## 2 Calculating the Electronic Structure of a Crystal

The strong electronic correlations in many transition-metal compounds with a partially filled  $3d$  shell cause the insulating behavior of these materials. Within the Zaanen-Sawatzky-Allen scheme [13], these correlated systems are categorized into Mott-Hubbard (MH) and charge-transfer (CT) insulators.

The Mott-Hubbard theory [14] involves the  $d-d$  Coulomb and exchange interactions and can be written as

$$H = -t \sum_{\langle i,j \rangle, \sigma} \left( c_{i\sigma}^\dagger c_{j\sigma} + h.c. \right) + U \sum_i n_{i,\uparrow} n_{i,\downarrow}, \quad (2.0.1)$$

where  $n_{i,\uparrow} \equiv c_{i\sigma}^\dagger c_{i\sigma}$  represents the number operator and  $c_{i\sigma}^\dagger$  creates (annihilates) an electron on lattice site  $i$  with spin  $\sigma = \uparrow, \downarrow$ . The first term describes the reduction of the kinetic energy of an electron by changing its position with an energy gain  $t$ . The second term represents the energy of double occupancy. The characteristic energy  $U$  is hereby defined as the repulsive Coulomb energy of two electrons on the same lattice site. The singly occupied sites will form the so-called *lower Hubbard band (LHB)*, the doubly occupied sites form the *upper Hubbard band (UHB)*. The size of the hopping  $t$  and the coordination number  $z$  determine the band width  $W$ . In case of a cubic system the band width is given by  $W = 2zt$ . In the limit  $U/t \rightarrow 0$ , the system is metallic, because the LHB and UHB overlap and are half filled. In the other limit  $U/t \rightarrow \infty$  the system is an insulator (for half filled bands). The LHB and UHB are far away from each other and the electrons are immobile because the energy for double occupancy is very high. Within the insulating state and depending on the configuration (bond angles, orbitals, ...) an antiferromagnetic arrangement of neighboring spins is favored, while in the ferromagnetic case the virtual hopping is blocked by Pauli's exclusion principle.<sup>1</sup> Since the Mott-Hubbard model can be solved analytically only in one dimension, numerical investigations in two and more dimensions contain several approximations: The Coulomb interaction between the transition metal and its neighbored anions is neglected. Here the charge-transfer energy  $\Delta = \epsilon_p - \epsilon_d$ , where  $\epsilon_d$  denotes the energy of the transition-metal  $d$  orbital and  $\epsilon_p$  the energy of the ligand  $p$  orbital, has to be taken into account. This energy does not depend on  $U$  but is related to the electronegativity of the anion and the Madelung potential. Considering the charge-transfer energy, two kinds of excitations are now possible: one electron can be transferred between two transition metals, or one electron can be transferred from the ligand to a transition

---

<sup>1</sup>The antiferromagnetic arrangement is described by the Goodenough-Kanamori-Anderson rule [274–276] for  $180^\circ$  superexchange.

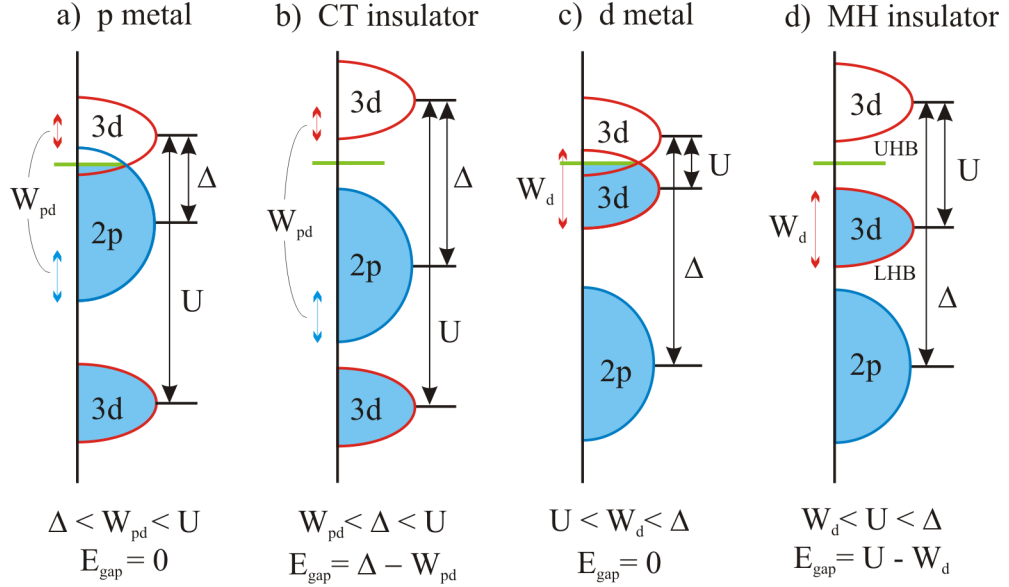


Figure 2.1: Zaanen-Sawatzky-Allen scheme. Depending on the Coulomb repulsion  $U$ , the charge-transfer energy  $\Delta$ , and the bandwidth  $W$  we get different kinds of metallic and insulating states, where  $W_{pd} = \frac{1}{2}(W_p + W_d)$ . In order to be more illustrative, the hybridization in this picture is neglected. The green line indicate the Fermi energy  $E_F$ .

metal. Depending on which excitation is lower in energy, i.e. if  $U$  or  $\Delta$  is smaller, the insulator is called *Mott-Hubbard insulator* or *charge-transfer insulator*.

The Zaanen-Sawatzky-Allen scheme, shown in Fig. 2.1, depends on the Hubbard  $U$ , the charge-transfer energy  $\Delta$  and a finite band width of the  $d$  and  $p$  bands. For  $\Delta < U$  the electronic structure is dominated by the ligand band (charge-transfer type) and for  $\Delta > U$  by the  $3d$  Hubbard band.

But even the Mott-Hubbard model, which includes the charge-transfer energy, is often inadequate in describing the full behavior of the insulating transition-metal compounds. It is important to take the charge, lattice, orbital and spin degrees of freedom into account.

Thus, we have to consider a full multi-band theory, which includes not only the electron-electron Coulomb repulsion. An often used calculation technique starts with a central transition-metal cation surrounded by nearest-neighbor anions forming a cluster with a purely ionic configuration. By using a configuration-interaction approach considering configurations of the type  $d^n, d^{n+1}\underline{L}, d^{n+2}\underline{L}\underline{L}$  we take hybridization and covalency as well as the  $d-d$  Coulomb interactions into account. Here  $\underline{L}$  denotes a hole in the ligand band. The on-site energies are parameterized with  $U$  and  $\Delta$  in the same way as done in the Zaanen-Sawatzky-Allen scheme. Within this so-called *cluster-model calculation* the cluster can be expressed by a matrix consisting of several configurations of the cluster and their mixing with each other. Diagonalising the so-called ‘‘Hamilton

---

matrix”, we get the energies and the corresponding eigenstates of the cluster. Using the eigenstates, we can calculate the optical conductivity within the Kubo-Greenwood model and compare the results with the optical data.

In the following sections we give a detailed description of the cluster-model calculation. We start with an introduction of the Hartree-Fock theory including some basic assumptions which are valid for the cluster model as well. In the following, we describe the principles of a configuration-interaction calculation and the determination of the matrix elements of one- and two-particle operators. Before we describe the determination of the different parts of the Hamiltonian, we give a brief introduction to the Racah-Wigner algebra. In addition, we present some useful expressions for the calculation of the matrix elements of tensor operators. The model Hamiltonian consists of four parts: The Coulomb interaction, the crystal-field splitting, the spin-orbit coupling and the covalency contribution. Furthermore, we present expressions for the matrix elements of the Stark and the Zeeman operator. We end up with the determination of the optical conductivity, the magnetic susceptibility and the phonon frequencies.

All expressions of this chapter are given in atomic units. So all energies are in rydbergs ( $e^2/2a_0 \cong 13.6058$  eV) and all lengths are measured in terms of the Bohr radius.

## 2.1 The Hartree-Fock Calculation

The calculation of the electronic structure of a crystal starts with the Hartree-Fock calculation, which is an often used approximation for solving the Schrödinger equation of a many-electron system. This section contains some fundamental principles, which are valid not only for the pure Hartree-Fock calculation, but also for the cluster-model calculation, which we use for the analysis of the optical spectra. The section, which is adapted from [7], starts with a general introduction in the Hartree-Fock method and its basic assumptions. In the following we present the self-consistent field procedure, which is required for solving the Hartree-Fock equations. At the end of the section, we describe the determination of the radial wave functions by solving the radial Schrödinger equation numerically, which become important for the determination of several cluster-model calculation parameters such as the Slater integrals  $F^k$ ,  $G^k$  and the spin-orbit coupling constant  $\zeta$ .

The Schrödinger equation can be solved analytically only for pure two-body systems like the hydrogen atom. For more general many-electron systems this is not possible. But for the majority of the elements in the periodic table the motion of every electron is coupled to the motion of all other electrons as well as to the nucleus. In particular, we are interested in transition-metal compounds with strong electronic correlations within the open  $3d$  shell. The electronic structure of such systems can be calculated only approximately.

### 2.1.1 Hartree-Fock Theory and Slater Determinants

The Hartree-Fock method [15] is a widely used approximation for non-correlated compounds. By assuming that every electron moves in the potential created both by the nucleus and by the average potential of all the other electrons, we reduce the many-electron problem to the problem of solving a number of coupled single-electron equations. The single-particle functions (orbitals, or spin orbitals) being involved in this assumption describe the motion of the electron and do not depend explicitly on the instantaneous motions of the other electrons. Only for one-electron systems the single-particle functions are exact eigenfunctions of the full electronic Hamiltonian. However, as long as we consider systems near their equilibrium, the Hartree-Fock theory provides a good description of the electronic structure of these systems.

The Hartree-Fock theory was developed in order to solve a new variant of the electronic Schrödinger equation which was developed from the time-independent Schrödinger equation by making use of the Born-Oppenheimer approximation [16]. In the Born-Oppenheimer approximation the motions of the electrons are regarded as uncoupled from those of the nuclei because of the big difference in mass. Thus the “electronic” Schrödinger equation is solved for fixed nuclear positions

$$\left[ \hat{T}_e(\mathbf{r}) + \hat{V}_{eN}(\mathbf{r}, \mathbf{R}) + \hat{V}_{NN}(\mathbf{R}) + \hat{V}_{ee}(\mathbf{r}) \right] \Psi(\mathbf{r}, \mathbf{R}) = E\Psi(\mathbf{r}, \mathbf{R}). \quad (2.1.1)$$

Here the symbol  $\mathbf{r}$  denotes the electronic and the symbol  $\mathbf{R}$  the nuclear degrees of free-

dom.  $\hat{T}_e$  represents the electronic kinetic energy,  $\hat{V}_{eN}$  the electron-nucleus interaction,  $\hat{V}_{NN}$  the nuclei-nuclei interaction, and  $\hat{V}_{ee}(\mathbf{r})$  the electron-electron interaction. The electronic energy eigenvalue  $E$  is a function of the chosen positions  $\mathbf{R}$  of the nuclei. Determine the energy for different nuclear positions we obtain the potential energy surface:  $E(\mathbf{R})$ .

If we assume that the electrons in a  $N$ -electron system do not interact with each other ( $\hat{V}_{ee} = 0$ ), then the Hamiltonian is separable, and the total electronic wave function  $\Psi(r_1, r_2, \dots, r_N)$  describing the motions of the electrons is the product of hydrogen wave functions  $\chi$ ,

$$\Psi_{HP}(\mathbf{x}_1, \mathbf{x}_2, \dots, \mathbf{x}_N) = \chi_1(\mathbf{x}_1)\chi_2(\mathbf{x}_2) \cdots \chi_N(\mathbf{x}_N). \quad (2.1.2)$$

which is known as a *Hartree Product*. Here, we introduced the so-called space-spin coordinates  $\mathbf{x} = \{\mathbf{r}, \sigma\}$ , with  $\sigma$  representing the spin coordinate. Note, that this functional form does not satisfy the antisymmetry principle, which states that a wave function describing fermions should be antisymmetric with respect to the interchange of any set of space-spin coordinates. The wave function  $\Psi_{HP}$  does not fulfill the antisymmetry principle yet. To achieve this, the wave function can be rewritten as a so-called Slater determinant [26]:

$$\Psi = \frac{1}{\sqrt{N!}} \begin{vmatrix} \chi_1(\mathbf{x}_1) & \chi_2(\mathbf{x}_1) & \cdots & \chi_N(\mathbf{x}_1) \\ \chi_1(\mathbf{x}_2) & \chi_2(\mathbf{x}_2) & \cdots & \chi_N(\mathbf{x}_2) \\ \vdots & \vdots & \ddots & \vdots \\ \chi_1(\mathbf{x}_N) & \chi_2(\mathbf{x}_N) & \cdots & \chi_N(\mathbf{x}_N) \end{vmatrix}. \quad (2.1.3)$$

The use of Slater determinants guarantees the adherence to the Pauli principle: the determinant will vanish if any of the two orbitals are identical. A consequence of this functional form is that the electrons cannot be distinguished because each electron is associated with every orbital. Describing the electrons by a Slater determinant includes the assumption that each electron moves independently of all the others except that it feels the Coulomb repulsion due to the average positions of all electrons (and it also experiences an “exchange” interaction due to anti-symmetrization).

### 2.1.2 Self-Consistent Field Technique

The electronic Hamiltonian contains one- and two-electron operators and the nuclear repulsion term, which is constant for fixed nuclei:

$$\mathcal{H} = - \sum_{i=1}^n \left( \frac{1}{2} \nabla_i^2 - \sum_{k=1}^N \frac{Z_k}{r_{ik}} \right) + \sum_{j=1}^n \sum_{i < j} \frac{1}{r_{ij}} + \sum_{l=1}^N \sum_{k < l} \frac{Z_k Z_l}{R_{kl}}. \quad (2.1.4)$$

Here  $n$  represents the number of electrons,  $N$  the number of nuclei and  $Z_i$  the nuclear charges of nucleus  $i$ . In this decomposition, the two-electron operators are critical because they prevent a product ansatz for  $n > 1$ . To circumvent this problem, Hartree has established an approximation technique that is known as the so-called *self-consistent*

*field (SCF) technique:* The basic idea starts with the assumption that all orbitals are known and that we can determine the interaction of a single electron with all the other electrons as a mean value from their potential field. In the next step we add these mean values to the one-electron operators to obtain effective one-electron Hamiltonians

$$\mathcal{H}_{\text{eff}}(i) = -\frac{1}{2}\nabla_i^2 - \sum_{k=1}^N \frac{Z_k}{r_{ik}} + \frac{1}{2} \sum_{\substack{j=1 \\ j \neq i}}^n \int \chi_j^* \frac{1}{r_{ij}} \chi_j dV_j. \quad (2.1.5)$$

These Hamiltonians represents the sum of all effective one-electron Hamiltonian plus the constant nuclear repulsion term:

$$\mathcal{H}_{el} = \sum_{i=1}^n \mathcal{H}_{\text{eff}}(i) + \sum_{l=1}^n \sum_{k<l} \frac{Z_k Z_l}{R_{kl}}. \quad (2.1.6)$$

We can start the self-consistent field technique if we use a product of orbitals as an ansatz for the wave function. But the orbitals and the effective Hamiltonians depend on each other: We need to know the orbitals to determine the effective Hamiltonians, but we have to know the effective Hamiltonians to construct the orbitals. We can avoid this problem by using an iterative solution: We need start-orbitals  $\varphi(0)$  to form effective Hamiltonians  $\mathcal{H}_{\text{eff}}(1)$ , whose eigenfunctions form the orbitals  $\varphi(1)$ . These imply new effective Hamiltonians  $\mathcal{H}_{\text{eff}}(2)$ , etc. We continue this process until the potential and the orbitals become self-consistent, which represents a good approximation for the electronic wave function  $\Psi_{el}$ :

$$\Psi_{el} \approx \prod_{i=1}^n \varphi(i). \quad (2.1.7)$$

The expectation value of the electronic energy is

$$E = \int \Psi_{el}^* \mathcal{H}_{el} \Psi_{el} = 2 \sum_{i=1}^{n/2} H_i + \sum_{j=1}^{n/2} \sum_{i<j} (2 J_{ij} - K_{ij}) \sum_{l=1}^{N/2} \sum_{k<l} \frac{Z_k Z_l}{R_{kl}}, \quad (2.1.8)$$

in which  $H_i$ ,  $J_{ij}$ , and  $K_{ij}$  are defined as

$$\begin{aligned} H_i &= \int \varphi_i^* \left[ -\frac{1}{2}\nabla_i^2 - \sum_{k=1}^M \frac{Z_k}{r_{ik}} \right] \varphi_i dV, \\ J_{ij} &= \iint \varphi_i^*(1) \varphi_j^*(2) \frac{1}{r_{ij}} \varphi_i(1) \varphi_j(2) dV_1 dV_2, \\ K_{ij} &= \iint \varphi_i^*(1) \varphi_j^*(2) \frac{1}{r_{ij}} \varphi_j(1) \varphi_i(2) dV_1 dV_2. \end{aligned} \quad (2.1.9)$$

Note, that the self-consistent field procedure may converge to an electronically excited state, depending on the choice of the initial orbitals.

By using the variation theorem we can avoid this problem [17]: “*The expectation value of the energy is always higher than or equal to the lowest energy eigenvalue.*” Due to the

dependence of the energy expectation value on the orbitals, we use only those values which do not change with minimal alterations of orbital values because these energy values describe the electronic ground state. This extension of the Hartree technique is known as the Hartree-Fock method.

The usage of molecular orbitals, which are defined as a linear combination of atomic orbitals:

$$\phi_i = \sum_{j=1}^m C_{ji} \cdot \chi_j, \quad (2.1.10)$$

leads to a reformulation of the Hartree-Fock method [20]. Here, the atomic orbitals  $\chi_j$  define a  $m$ -dimensional basis of functions which are defined at the beginning and remain unchanged thereafter. The molecular orbitals' coefficients are collected in a matrix  $C$ . Roothaan's ansatz limits the number of atomic orbitals and allows the application of all tools of matrix algebra due to the usage of matrices and vectors. The so-called Roothaan-Hall equations [20, 21] can be written in the form of a generalized eigenvalue problem

$$\mathbf{FC} = \mathbf{SC}\epsilon, \quad (2.1.11)$$

where  $F$  is the so-called Fock matrix,  $C$  is a matrix of coefficients,  $S$  is the overlap matrix of the basis functions, and  $\epsilon$  is the (diagonal, by convention) matrix of orbital energies. In the case of an orthonormalized basis set, the overlap matrix  $S$  is reduced to the identity matrix.

### 2.1.3 Radial Schrödinger Equation

Within the so-called *central field approximation* the effective ionic potential is spherically symmetric and depends only on the magnitude of  $r$  and not on the angles  $\theta$  and  $\phi$ . Here the angular momentum  $L$  is classically a constant of motion. The orbital wave function  $\chi(\mathbf{x})$  then is an eigenfunction of  $L^2$  and  $L_z$ . Thus  $\chi(\mathbf{x})$  is a function of  $r$  times a spherical harmonics  $Y_{lm}$  (times a spin function). It is convenient to write the radial wave function with an explicit factor  $r^{-1}$ , so that the total wave function  $\chi(\mathbf{x})$  gets the form

$$\chi_i(\mathbf{x}) = \frac{1}{r} P_{n_i l_i}(r) Y_{l_i, m_{l_i}}(\theta, \phi) \sigma_{m_{s_i}}(s_z) \equiv |n_i l_i m_{l_i} m_{s_i}\rangle. \quad (2.1.12)$$

The radial wave function  $P_{n_i l_i}(r) \equiv P_i(r)$  is normalized to one ( $\int_0^\infty P_i^*(r) P_i(r) dr = 1$ ) and fulfills the boundary condition  $P_i(r=0) = P_i(r=\infty) = 0$ . The spherical harmonics  $Y_{l_i, m_{l_i}}$  and the spin function  $\sigma_{m_{s_i}}(s_z)$  in (2.1.12) can be exactly determined and the remaining part of the Hartree-Fock calculation is the determination of the radial wave functions  $P_i(r)$ . Thus the radial Schrödinger equation has to be solved

$$\begin{aligned} & \left[ -\frac{d^2}{dr^2} + \frac{l_i(l_i+1)}{r^2} - \frac{2Z}{r} + \sum_{j=1}^q (w_j - \delta_{i,j}) \int_0^\infty \frac{2}{r_>} P_j^2(r_2) dr_2 - (w_i - 1) A_i(r) \right] P_i(r) \\ & = \varepsilon_i P_i(r) + \sum_{\substack{j=1 \\ j \neq i}}^q w_j [\delta_{l_i l_j} \epsilon_{ij} + B_{ij}(r)] P_j(r), \end{aligned} \quad (2.1.13)$$

in which

$$A_i(r) = \frac{2l_i + 1}{4l_i + 1} \sum_{k>0} \begin{pmatrix} l_i & k & l_i \\ 0 & 0 & 0 \end{pmatrix}^2 \int_0^\infty \frac{2r_{<}^k}{r_{>}^{k+1}} P_i^2(r_2) dr_2, \quad (2.1.14)$$

and

$$B_{ij}(r) = \frac{1}{2} \sum_k \begin{pmatrix} l_i & k & l_j \\ 0 & 0 & 0 \end{pmatrix}^2 \int_0^\infty \frac{2r_{<}^k}{r_{>}^{k+1}} P_j(r_2) P_i(r_2) dr_2. \quad (2.1.15)$$

Here,  $Z$  is the charge of the nucleus,  $w_i$  represents the number of electrons and  $\varepsilon_i$  the binding energy of an electron in the subshell  $n_i l_i$ <sup>2</sup>. In all these integrals, the terms  $r_{<}$  and  $r_{>}$  represent the smaller and the greater value of  $r$  and  $r_2$ . The set of  $q$  equations – one for each subshell  $n_i l_i$  – are the Hartree-Fock equations [17–19] (HF) for the spherically averaged atom. The first two terms in (2.1.13),  $-d^2/dr^2 + l_i(l_i + 1)/r^2$ , result from the variation of the kinetic energy and the third term refers to the nuclear potential energy. The next term refers to the direct portion of the electron-electron interactions; the terms involving  $A_i$  and  $B_{ij}$  refer to the exchange portions. The terms involving the Lagrangian multipliers  $\epsilon_{ij}$  express the orthogonality requirement. (In the case of closed shells,  $i$  and  $j$ ,  $P_i$  and  $P_j$  are automatically orthogonal and  $\epsilon_{ij}$  and  $\epsilon_{ji}$  can be set to zero.) Solutions of the  $i$ th HF equation are gained by trial-and-error adjustment of  $\varepsilon_i$  in order to find that value which results in a normalized solution  $P_i$ .

This leads to Koopmans' theorem [22]: “*The negative form of the eigenvalue  $\varepsilon_i$  of the HF equation is equal to the configuration-averaged ionization energy of an electron in subshell  $n_i l_i$ ; in this case the orbitals of the ion are considered to be the same as those of the atom.*”

Since the  $i$ th HF equation involves the radial wave functions  $P_j$  of all other orbitals, a set of  $N$  coupled integro-differential equations can be solved only by an iterative procedure (if  $N > 1$ ). Each iterative cycle consists of three steps:

1. We assume a set of trial functions  $P_j(r)$ ,  $1 \leq j \leq N$ .
2. For each equation  $i$ ,  $V_H$ ,  $A_i$  and  $B_{ij}$  are computed, which results in an estimate of  $\epsilon_{ij}$ . Here  $V_H$  represents the Hartree energy [23] and is defined as

$$V_H = \sum_{j=1}^q (w_j - \delta_{i,j}) \int_0^\infty \frac{2}{r_{>}} P_j^2(r_2) dr_2. \quad (2.1.16)$$

3. We can solve the  $i$ th HF equation to obtain a new  $P_i(r)$ .

Repeating these three steps we use a new set of trial functions each time, until the output functions obtained in step (3) are identical with the functions assumed in step (1), and all functions with a given  $l$  are mutually orthogonal, within the desired tolerances. The output functions are then self-consistent with the trial input functions used in

---

<sup>2</sup>With the sign convention,  $\varepsilon_i$  is negative for bound electrons and positive for free electrons.

computing the central field in step (2), and so this procedure is called a self-consistent-field (SCF) method. *Appropriate trial input functions for the  $(m + 1)$ th iteration cycle can usually be obtained by using (normalized) linear combinations of the input and the output functions from the preceding cycle:*

$$P_i^{(m+1)}(\text{input}) = cP_i^{(m)}(\text{output}) + (1 - c)P_i^{(m)}(\text{input}). \quad (2.1.17)$$

*The value of  $c$  is chosen by trial and error procedure in order to reach the maximum speed of convergence; usually this value is around 0.5, but it may be anywhere from 0.05 to 1.1.*

The most straightforward method of finding a new output function  $P_i(r)$  in step (3) cf. (2.1.13) is the following: As a result of steps (1) and (2) everything in (2.1.13) is known with the exception of the desired function  $P_i(r)$  and the unknown parameter  $\varepsilon_i$ . We start with the boundary condition

$$P_i(0) = 0, \quad (2.1.18)$$

which is required to keep the electron density finite at  $r = 0$ . For small values of  $r$ , all electron-electron terms in (2.1.13) are negligible compared with the kinetic and nuclear terms. The differential equation is reduced to that of a hydrogenic atom, for which  $P_i \propto r^{l_i+1}$  for small values of  $r$ . Therefore we assume an arbitrary value  $a_0^{(0)}$  of the initial slope

$$a_0 \equiv \left[ \frac{P_i(r)}{r^{l_i+1}} \right]_{r \rightarrow 0}. \quad (2.1.19)$$

If we begin with (2.1.18) and (2.1.19) and assume some value of  $\varepsilon_i$ , the numerical integrations<sup>3</sup> of the differential equation (2.1.13) up to a suitably large value of  $r$  results in a particular integral  $P^I(r)$  of the inhomogeneous differential equation. If we start with the same starting conditions, the numerical integration of the homogenous differential equation, obtained from (2.1.13) by setting all  $\varepsilon_{ij}$  and  $B_{ij}$  to zero, results

---

<sup>3</sup>A commonly used method for the numerical integration of differential equations was developed by Numerov [24]: If the differential equation is written as  $y'' = f(r)y + g(r)$  and if  $y$  is already known at the points  $r_j$  and  $r_{j-1}$  on a mesh in which  $h = r_i - r_{i-1}$  (all  $i$ ), then the value of  $y$  at  $r_{j+1}$  can be expressed as follows

$$Y_{j+1} = 2Y_j - Y_{j-1} + h^2 \left[ f_j y_j + \frac{1}{12} (g_{j+1} + 10g_j + g_{j-1}) \right],$$

in which

$$Y = y \left( 1 - \frac{1}{12} h^2 f \right).$$

Because of numerical instabilities the integration process starts from the two boundaries of the wave function. The integration process starting at  $r = 0$  with  $P(r) \propto r^{(l+1)}$  is called “outward” integration. The other, starting at  $r = r_{max}$  with  $P(r) \propto \exp[-r(\varepsilon_i)^{1/2}]$ , is called “inward” integration. Theses two forms of integration are carried out only to a matching radius depending on  $\varepsilon_i$  where the outward and inward integrations produce functions with both equal values and equal slopes.

in the function  $P^H(r)$ . Any integral of (2.1.13) which satisfies the above mentioned equation (2.1.18) can be written as

$$P_i(r) = P^I(r) + \alpha P^H(r). \quad (2.1.20)$$

In this equation  $\alpha$  is an appropriate constant, so that  $P_i$  satisfies the boundary condition

$$\lim_{r \rightarrow \infty} [P_i(r)] = 0 \quad (2.1.21)$$

required for the wave function of any bound electron; the value of the “initial slope” of  $P_i$  is

$$a_0 = (1 + \alpha)a_0^{(0)}. \quad (2.1.22)$$

The value of  $a_0$  and the norm of  $P_i(r)$  depend on the assumed value of  $\varepsilon_i$ . The parameter  $\varepsilon_i$  was originally introduced as Lagrangian multiplier associated with the normalization condition on  $P_i(r)$ . It must be guaranteed that  $\|P_i(r)\| = 1$ . The additional requirements that  $a_0$  must be positive and that all  $P_i(r)$  have  $(n - l - 1)$  nodes lead to a unique integral  $P_i(r)$  of the HF equation (2.1.13), by analogy with the hydrogenic result. The pure Hartree-Fock method shows several disadvantages which can be avoided by using the Hartree-plus-statistical exchange approximation (HX) introduced by Cowan [25]. The HX method is an approximation to the exact HF equations and uses Hartree’s method for the self-interaction correction. The method is computationally much simpler and completely free of iteration-instability problems. It requires no starting parameter except an universal starting potential function. In order to approximate the remainder of the HF exchange terms a modification of Slater’s  $\rho^{1/3}$  term is used. The HX method gives results in rather good agreement with HF except for the radial wave functions  $P_i(r)$  of the inner shells, which are unimportant for all purposes except for the interaction with the nucleus.

One widely used program to do the Hartree-Fock calculation is the Cowan package [7] based on the original Herman-Skillman program [27]. Determining the single-configuration radial wave function for spherical symmetrized atoms can be done via several homogeneous differential-equation approximations to the HF method with relativistic corrections included.

## 2.2 Configuration-Interaction Method

The following section gives an introduction to the configuration interaction method, which is an essential element in the cluster-model configuration interaction calculation used in this thesis. This section is partly taken from [28].

### 2.2.1 Configuration Interaction

Configuration Interaction (CI) is a method for solving the time-independent Schrödinger equation by using matrix mechanics. The usage of the matrix formalism simplifies the solution of the Schrödinger equation  $H\psi = E\psi$  by means of a computer.

In order to apply the matrix mechanics we have to define a vector space for the description of the problem. Within the Born-Oppenheimer approximation, we can neglect the nuclei. In case of an arbitrary  $N$ -electron system, we can express the wave function as a linear combination of all possible  $N$ -electron Slater determinants formed from a complete set of orbitals (single-particle functions). By solving the Schrödinger equation by using the matrix formalism on a complete basis of  $N$ -electron functions, we obtain all electronic eigenstates of the system. In case of a complete basis the electron correlation function is exactly described in contrast to the density-functional theory where only approximations are used. Within the configuration interaction method, we write a  $N$ -electron basis function  $|\Psi\rangle$ , which is an eigenvector of the Hamiltonian  $H$ , as substitutions or “excitations” of the Hartree-Fock “reference” determinant  $|\Phi_0\rangle$ , i.e.

$$|\Psi\rangle = c_0|\Phi_0\rangle + \sum_{ra} c_a^r |\Phi_a^r\rangle + \sum_{a<b,r<s} c_{ab}^{rs} |\Phi_{ab}^{rs}\rangle + \sum_{a<b<c,r<s<t} c_{abc}^{rst} |\Phi_{abc}^{rst}\rangle + \dots, \quad (2.2.1)$$

in which  $|\Phi_a^r\rangle$  represents the Slater determinant formed by replacing orbital  $a$  in  $|\Phi_0\rangle$  with orbital  $r$ , etc. We can express every  $N$ -electron Slater determinant by the set of  $N$  orbitals from which it is formed. This set of orbital occupancies is often referred to as a CONFIGURATION. The configuration interaction method may fail if the reference configuration is not dominant.

If we solve the Schrödinger equation and use a given set of one-particle functions and all possible  $N$ -electron basis functions, the configuration interaction procedure is called “full CI” which corresponds to solving Schrödinger’s equation exactly within the space spanned by the specified one-electron basis. If the one-electron basis is complete the procedure is called a “complete CI” [35]. Caused by the vast number of  $N$ -electron basis functions, a full CI can not be performed even with an incomplete one-electron basis. Therefore, the configuration interaction space must be reduced whereas the approximate CI wave function and its energy should be as close as possible to the exact value. This reduction of the CI space is a central problem in the configuration interaction theory: The most common approximation is the truncation of the CI space expansion, “truncated CI”, according to the excitation level relative to the reference state  $|\Phi_0\rangle$  in (2.2.1). Wave functions including only those  $N$ -electron basis functions which represent single ( $\Phi_a^r$ ) or double ( $\Phi_{ab}^{rs}$ ) excitations relative to the reference state

in (2.2.1). As long as the Hamilton operator includes only one- and two-electron operators, only configurations singly and doubly excited can interact directly with the reference configuration.

## 2.2.2 Correlation Energy

In order to estimate the quality of the configuration interaction method we can use the fraction of the correlation energy which is recovered by the truncated CI. The correlation energy is defined as

$$E_{corr} = E_0 - E_{HF}, \quad (2.2.2)$$

where  $E_{HF}$  represents the Hartree-Fock limit and  $E_0$  the exact (non-relativistic) energy of the system. The energy  $E_{corr}$  will always be negative because the Hartree-Fock energy is, due to the variational theorem, an upper bound to the exact energy. The energy  $E_0$  can be calculated by performing a full CI within a complete one-electron basis set. In case of an incomplete one-electron basis set, the correlation energy represents the correlation energy of the given one-electron basis. Within the Hartree-Fock theory the inter-electron repulsion is treated only in an averaged way.

The correlation energy consists of two parts: The “dynamical” correlation energy is the energy recovered by fully allowing the electrons to avoid each other. The second part, called the “non-dynamical”, or “static” correlation energy, reflects the inadequacy of a single reference in describing a given (molecular) state, and is due to nearly degenerate states or rearrangement of electrons within partially filled shells.

## 2.2.3 Truncated Configuration Interaction

The CI expansion is typically truncated according to its excitation level. The structure of the CI matrix with respect to its excitation level is given below [34].  $|S\rangle$ ,  $|D\rangle$ ,  $|T\rangle$  and  $|Q\rangle$  represent blocks of singly, doubly, triply, and quadruply excited determinants, respectively. The Hamiltonian  $\mathcal{H}$  is Hermitian; in case of exclusively real orbitals, the Hamiltonian is also symmetric. Thus only the lower triangle of  $\mathcal{H}$  is shown below

$$\mathcal{H} = \begin{array}{l} \langle \Phi_0 | \\ \langle S | \\ \langle D | \\ \langle T | \\ \langle Q | \\ \vdots \end{array} \left[ \begin{array}{cccccc} \langle \Phi_0 | H | \Phi_0 \rangle & & & & & \dots \\ 0 & \langle S | H | S \rangle & & & & \dots \\ \langle D | H | \Phi_0 \rangle & \langle D | H | S \rangle & \langle D | H | D \rangle & & & \dots \\ 0 & \langle T | H | S \rangle & \langle T | H | D \rangle & \langle T | H | T \rangle & & \dots \\ 0 & 0 & \langle Q | H | D \rangle & \langle Q | H | T \rangle & \langle Q | H | Q \rangle & \dots \\ \vdots & \vdots & \vdots & \vdots & \vdots & \ddots \end{array} \right]. \quad (2.2.3)$$

Due to Brillouin’s theorem [39] the matrix elements  $\langle S | \mathcal{H} | \Phi_0 \rangle$  are zero, which is valid when the reference function  $|\Phi_0\rangle$  is obtained by the Hartree-Fock method<sup>4</sup>. Furthermore, the blocks  $\langle X | H | Y \rangle$  which are not necessarily zero may still be sparse; for example, the matrix element  $\langle \Phi_{ab}^{rs} | H | \Phi_{cdef}^{tuvw} \rangle$  which belongs to the block  $\langle D | H | Q \rangle$ , will

<sup>4</sup>“Hartree-Fock guarantees that off-diagonal elements of the Fock matrix are zero. It turns out that the matrix element between two Slater determinants which differ by one spin orbital is equal to an off-diagonal element of the Fock matrix.”, see [30].

be non-zero only if  $a$  and  $b$  are contained in the set  $\{c, d, e, f\}$  and if  $r$  and  $s$  are contained in the set  $\{t, u, v, w\}$ . Double excitations make the largest contributions to the CI wave function besides the reference state, since they interact directly with the Hartree-Fock reference. Although singles, triples, etc. do not interact directly with the reference state, they can still become part of the CI wave function (i.e. they have non-zero coefficients) because they mix with the doubles, directly or indirectly.

The number of  $N$ -electron basis functions increases dramatically if the excitation level is increased. So the CISDTQ method is limited to systems containing very few heavy atoms. Full CI calculations are of course even more difficult to perform, so that in spite of their importance as benchmarks, only few full CI energies using flexible one-electron basis sets have been obtained. If spatial symmetry is ignored the dimension of the full CI space with total spin  $S$  is computed by

$$D_{nNS} = \binom{n}{N/2+S} \binom{n}{N/2-S}, \quad (2.2.4)$$

in which  $n$  denotes the number of orbitals and  $N$  the number of electrons.

In the often used frozen-core approximation the lowest-lying ionic orbitals (occupied by the inner-shell electrons) are constrained to remain doubly-occupied in all configurations. For the atoms ranging from Lithium to Neon the frozen core typically consists of the  $1s$  atomic orbital, while the frozen-core for those atoms ranging from Sodium to Argon consists of the atomic orbitals  $1s$ ,  $2s$ ,  $2p_x$ ,  $2p_y$  and  $2p_z$ . The inner-shell electrons of an atom are less sensitive to their environment than the valence electrons. Thus the error introduced by freezing the core orbitals is generally small. Applying the frozen core approximation, we can decrease the number of configurations within the configuration interaction method and reduce the computational effort to construct the Hamiltonian. Truncating the CI space will introduce an error in the wave functions, in the related energies and all other properties. Furthermore the CI energies are no longer *size extensive*<sup>5</sup> or *size consistent*<sup>6</sup>. The truncated configuration interaction method is neither size extensive nor size consistent. Due to the lack of the property of size extensivity, the accuracy of a truncated configuration interaction calculation decrease with increasing system size. In order to correct the CI energies Davidson suggests the following correction [41]

$$\Delta E_{DC} = E_{SD}(1 - c_0), \quad (2.2.5)$$

where  $E_{SD}$  is the basis set correlation energy recovered by a CISD procedure and  $c_0$  is the coefficient of the Hartree-Fock wave function in (2.2.1). This correction approximately accounts for the effects of “unlinked quadruple” excitations (i.e. simultaneous pairs of double excitations).

<sup>5</sup>A calculation method is *size extensive* if the energy calculated thereby scales linearly with the number of particles  $N$ .

<sup>6</sup>A method is called *size consistent* if there exists an energy  $\varepsilon = E_A + E_B$  which consists of two well separated subsystems  $A$  and  $B$ . In contrast to the definition of size extensivity, which applies at any geometry, the definition of size consistency applies only in the case of infinite separation. Furthermore, size consistency usually implies correct dissociation into fragments, too.

## 2.3 Coupled Antisymmetrized Basis Functions

This section, which follows the explanations of Cowan [7], introduces several expressions which are valid for the cluster-model calculation. We begin with the construction of the wave functions used in the configuration interaction calculation and end up with the principle determination of matrix elements of one- and two-electron operators. This is important, because the usage of one- and two-electron operators avoids the complete antisymmetrization of the wave functions. Without these fundamental considerations we cannot calculate the Hamiltonian within the configuration interaction method. In addition, the so-called “coefficients of fractional parentage”, which are defined in this section, are an essential component of Sobel’man’s parentage scheme approximation used in the determination of the tight-binding operator (see section “2.8 Hybridization and Tight-Binding Approximation”).

### 2.3.1 Coefficients of Fractional Parentage

Basis wave functions for a  $N$ -electron atom are constructed from linear combinations of products of  $N$  one-electron orbitals (2.1.12). If we do not couple the angular momenta together, we can achieve antisymmetrized wave functions by forming determinantal functions:

$$\psi = \frac{1}{\sqrt{N!}} \sum_P (-1)^p \prod_{i=1}^N |n_i l_i m_{l_i} m_{s_i}(r_j)\rangle, \quad (2.3.1)$$

in which the summation runs over all  $N!$  permutations of the coordinate subscripts  $j$ , and  $p$  is the parity of the permutation  $P$ . To guarantee a properly normalized function the factor  $(N!)^{-1/2}$  is required.

To construct multiplet wave functions of a subshell  $nl^w$

$$|l^w, \alpha, L, S, M_L, M_S\rangle, \quad (2.3.2)$$

with  $w$  denoting the number of electrons in the subshell  $nl$ , we have to couple the angular momenta of the different orbitals according to some coupling scheme. Here  $\alpha$  distinguishes between multiplets with the same  $L$  and  $S$  quantum numbers, which could be found for example within a  $3d^3$  subshell, in which two multiplets with  $L = 2$  and  $S = \frac{1}{2}$  exist. The quantum numbers  $M_L$  and  $M_S$  in (2.3.2) represents the magnetic quantum numbers corresponding to  $L$  and  $S$  respectively. The coupling of the angular momenta is done with the aid of the Clebsch-Gordan (CG) coefficients. The application of Clebsch-Gordan expansions to antisymmetrized product functions may lead to normalization difficulties if two or more electrons are equivalent ( $n_i l_i = n_k l_k$ ). We can avoid these difficulties by using appropriate linear combinations of coupled simple-product functions which are not antisymmetrized. These combinations are independent of  $M_L$  and  $M_S$ , which are therefore dropped from notation. If  $|l^{w-1} \bar{\alpha} \bar{L} \bar{S}\rangle$  is an antisymmetric basis function for a subshell  $nl^{w-1}$  with  $w - 1$  equivalent electrons

and  $\bar{\alpha} \bar{L} \bar{S}$  indicating a multiplet within this subshell, and if<sup>7</sup>

$$|(l^{w-1} \bar{\alpha} \bar{L} \bar{S}, l) LS\rangle = \sum_{\bar{M}_L m_l} CG(\bar{L} \bar{M}_L m_l; LM_L) \sum_{\bar{S}_L m_s} CG(\bar{S}_L \bar{M}_S m_s; SM_S) \times |l^{w-1} \bar{\alpha} \bar{L} \bar{S}\rangle |l\rangle \quad (2.3.3)$$

is a coupled but not antisymmetrized function, then a completely antisymmetric function  $|l^w \alpha LS\rangle$  for subshell  $nl^w$  can be written in terms of the *coefficients of fractional parentage*<sup>8</sup> (cfp) denoted by “ $(l^{w-1} \bar{\alpha} \bar{L} \bar{S} \} l^w \alpha LS)$ ”, which were introduced by Racah [5]

$$|l^w \alpha LS\rangle = \sum_{\bar{\alpha} \bar{L} \bar{S}} |(l^{w-1} \bar{\alpha} \bar{L} \bar{S}, l) LS\rangle (l^{w-1} \bar{\alpha} \bar{L} \bar{S} \} l^w \alpha LS). \quad (2.3.4)$$

The coefficients of fractional parentage describe how the antisymmetric multiplet wave function  $|l^w \alpha LS\rangle$  of subshell  $nl^w$  is constructed by the multiplet wave functions of subshell  $nl^{w-1}$  by adding a further electron via angular momentum coupling.

Antisymmetric functions for an arbitrary subshell with  $w$  electrons are in principle constructed by repeated application of (2.3.4), starting with  $w = 2$ . The terms  $\bar{\alpha} \bar{L} \bar{S}$  are called *parent terms* for the terms  $\alpha LS$ .

The coefficients of fractional parentage satisfy the relations [7]

$$\sum_{\bar{\alpha} \bar{L} \bar{S}} (l^w \alpha LS \} l^{w-1} \bar{\alpha} \bar{L} \bar{S}) (l^{w-1} \bar{\alpha} \bar{L} \bar{S} \} l^w \alpha' LS) = \delta_{\alpha, \alpha'}, \quad (2.3.5)$$

due to orthonormalization, and

$$\sum_{\alpha LS} [L, S] (l^{w-1} \bar{\alpha} \bar{L} \bar{S} \} l^w \alpha LS) (l^w \alpha LS \} l^{w-1} \bar{\alpha}' \bar{L} \bar{S}) = \frac{1}{w} (4l + 3 - w) [\bar{L}, \bar{S}] \delta_{\bar{\alpha}, \bar{\alpha}'}, \quad (2.3.6)$$

which is useful for checking the correctness of the calculated values of the cfp. A complete set of tables is given by Nielson and Koster [45].

### 2.3.2 Basis Functions within the Russell-Saunders-coupling scheme

The above presented procedure gives completely antisymmetrized wave functions for a subshell with  $w$  equivalent electrons. But within the configuration-interaction calculation, we have to deal with configurations which contain different subshells. For an

<sup>7</sup>The expression  $|(l^{w-1} \bar{\alpha} \bar{L} \bar{S}, l) LS\rangle$  represents a multiplet wave function of subshell  $nl^w$  with multiplet  $LS$ , which is constructed from the multiplet wave function of subshell  $nl^{w-1}$ , with multiplet indicated by  $\bar{\alpha} \bar{L} \bar{S}$ , by adding a further electron with angular momentum  $l$  to this wave function. The sums run on the one hand over the corresponding magnetic quantum number  $\bar{M}_L$  and  $\bar{M}_S$  of the multiplet  $\bar{\alpha} \bar{L} \bar{S}$  and on the other hand over the magnetic quantum numbers  $m_l$  and  $m_s$  of the added electron. The CG expressions represent the Clebsch-Gordan coefficients, which describe the adding of  $l$  to  $L$  and  $s$  to  $S$  respectively. Finally, the expression  $|l\rangle$  is the single-electron wave function of the added electron.

<sup>8</sup>Racah's notation  $([l^{w-1} \bar{\alpha} \bar{L} \bar{S}, l] \alpha LS \} l^w \alpha LS)$  is redundant.

arbitrary electron configuration of  $q$  different subshells

$$n_1 l_1^{w_1} n_2 l_2^{w_2} \cdots n_q l_q^{w_q}, \quad \sum_{j=1}^q w_j = N, \quad (2.3.7)$$

completely coupled basis functions  $\psi$  can be constructed by multiple Clebsch-Gordan expansions, using products of  $q$  multiplet functions (2.3.4), one function for each subshell. For numerical calculations the  $LS$  (Russell-Saunders)-coupling scheme is often used [43]

$$|\psi\rangle = \{[(l_1^{w_1} \alpha_1 L_1 S_1, l_2^{w_2} \alpha_2 L_2 S_2) \mathfrak{L}_2 \mathfrak{S}_2, l_3^{w_3} \alpha_3 L_3 S_3] \mathfrak{L}_3 \mathfrak{S}_3, \dots\} \mathfrak{L}_q \mathfrak{S}_q \mathfrak{J}_q \mathfrak{M}_q. \quad (2.3.8)$$

The  $J\mathfrak{J}$  coupling scheme or other coupling schemes may be sometimes physically more appropriate. Transformation matrices describing the transition from one coupling scheme to another can be found in [46]. The coupled function  $|\psi\rangle$  in (2.3.8) is antisymmetric with respect to interchange of electron coordinates within any subshell  $n_i l_i^{w_i}$ , but not with respect to the interchange of coordinates between two different subshells. The latter type of antisymmetrization is added, similarly to (2.3.1) by summing limited types of permutations. The completely antisymmetrized basis functions are of the form

$$\psi = \left[ \frac{\prod_j (w_j!)}{N!} \right]^{1/2} \sum_P (-1)^P \varphi^{(P)}, \quad (2.3.9)$$

in which the permutations  $P$  involve coordinate exchanges between two different subshells only. Here  $\varphi$  is an antisymmetrized function of the type (2.3.1) or (2.3.4). The prefactor  $[(\prod_j (w_j!))/(N!)]^{1/2}$  is required for normalization. Another more complicated method for antisymmetrization is based on the aid of mixed-shell coefficients of fractional parentage introduced by Armstrong [44], which must be seen as a generalization of Racah's coefficients of fractional parentage.

### 2.3.3 One- and Two-Electron Operators

For the evaluation of the Hamilton operator we do not need to know the basis wave functions (2.3.9) themselves, but only the matrix elements  $\langle \phi | \hat{O} | \phi' \rangle$  of operators  $\hat{O}$  that are symmetric with regard to all electron coordinates. For matrix elements between two basis functions  $|\phi\rangle$  and  $|\phi'\rangle$  which belong to the same configuration, complications due to the antisymmetrization permutations shown in (2.3.9) are reduced.

There are two types of operators which are relevant in the electronic structure calculation. The first type can be written as a sum of one-electron operators  $\hat{f}(i)$

$$O_{One} = \sum_{i=1}^N \hat{f}(i), \quad (2.3.10)$$

where  $\hat{f}(i)$  acts only on the  $i$ th electron. These operators depend only on e.g. the position or momentum of the  $i$ th electron, independent of the position or the momentum of

the other electrons. Examples for this kind of operator are the operator of the crystal field or the operator of the dipole moment. The second type of operator is a sum of two-electron operators

$$O_{Two} = \sum_{i=1}^N \sum_{j>i}^N \hat{g}(i, j) \equiv \sum_{i<j} \hat{g}(i, j), \quad (2.3.11)$$

in which  $\hat{g}(i, j)$  is an operator that involves the  $i$ th and  $j$ th electron only. The sum in (2.3.11) runs over all unique pairs of electrons. An example of a two-electron operator is the Coulomb interaction between two electrons.

The Slater-Condon rules [47, 48] allow the expression of matrix elements of these two types of operators in terms of one- and two-electron integrals. The derivation of these rules can be found in [34]. The results are expressed in terms of orbitals: The one-electron integrals are written as

$$\langle i | \hat{f} | j \rangle = \int \phi_i^*(\mathbf{r}_1) \hat{f}(\mathbf{r}_1) \phi_j(\mathbf{r}_1) d\mathbf{r}_1 \quad (2.3.12)$$

and the two-electron integrals as

$$\langle ij | g_{i,j} | kl \rangle = \langle ij | kl \rangle - \langle ij | lk \rangle, \quad (2.3.13)$$

in which – assuming  $g_{i,j} \equiv \frac{1}{r_{12}}$  –

$$\langle ij | kl \rangle = \int \phi_i^*(\mathbf{r}_1) \phi_j^*(\mathbf{r}_2) \frac{1}{r_{12}} \phi_k(\mathbf{r}_1) \phi_l(\mathbf{r}_2) d\mathbf{r}_1 d\mathbf{r}_2. \quad (2.3.14)$$

Before we can apply Slater's rules, we have to arrange the two Slater determinants in maximum coincidence. Due to the antisymmetry of the wave function, the switching of two columns in a determinant introduces a minus sign. If we want to calculate  $\langle \Phi_1 | \hat{H} | \Phi_2 \rangle$  with

$$\begin{aligned} |\Phi_1\rangle &= |abcd\rangle \\ |\Phi_2\rangle &= |crds\rangle \end{aligned} \quad (2.3.15)$$

we first have to interchange columns of  $|\Phi_1\rangle$  or  $|\Phi_2\rangle$  to make the two determinants look as much alike as possible. Here, we rearrange  $|\Phi_2\rangle$  as

$$|\Phi_2\rangle = |crds\rangle = -|crsd\rangle = |srcd\rangle. \quad (2.3.16)$$

After we have got the determinants in maximum coincidence, we can use the following rules, taken from [34]:

1. Identical determinants:

$$\begin{aligned} |\Phi_1\rangle &\equiv |\Phi_2\rangle \\ \langle \Phi_1 | O_{One} | \Phi_2 \rangle &= \sum_m \langle m | \hat{f} | m \rangle \\ \langle \Phi_1 | O_{Two} | \Phi_2 \rangle &= \frac{1}{2} \sum_m \sum_n \langle mn || mn \rangle. \end{aligned} \quad (2.3.17)$$

2. Determinants that differ by one spin orbital:

$$\begin{aligned}
 |\Phi_1\rangle &= |\cdots mn \cdots\rangle \\
 |\Phi_2\rangle &= |\cdots pn \cdots\rangle \\
 \langle\Phi_1|O_{One}|\Phi_2\rangle &= \langle m|\hat{f}|p\rangle \\
 \langle\Phi_1|O_{Two}|\Phi_2\rangle &= \sum_n \langle mn||pn\rangle.
 \end{aligned} \tag{2.3.18}$$

3. Determinants that differ by two spin orbitals:

$$\begin{aligned}
 |\Phi_1\rangle &= |\cdots mn \cdots\rangle \\
 |\Phi_2\rangle &= |\cdots pq \cdots\rangle \\
 \langle\Phi_1|O_{One}|\Phi_2\rangle &= 0 \\
 \langle\Phi_1|O_{Two}|\Phi_2\rangle &= \langle mn||pq\rangle.
 \end{aligned} \tag{2.3.19}$$

4. Determinants that differ by more than two spin orbitals:

$$\begin{aligned}
 |\Phi_1\rangle &= |\cdots mno \cdots\rangle \\
 |\Phi_2\rangle &= |\cdots pqr \cdots\rangle \\
 \langle\Phi_1|O_{One}|\Phi_2\rangle &= 0 \\
 \langle\Phi_1|O_{Two}|\Phi_2\rangle &= 0.
 \end{aligned} \tag{2.3.20}$$

Because of the antisymmetry of the basis functions  $\psi$ , the value of the matrix element

$$\langle\psi|f_i|\psi'\rangle \tag{2.3.21}$$

is independent of any electron coordinate  $r_i$ . The value of the matrix element of  $f_i$  is the same as that of  $f_j$ : In (2.3.21) the coordinates appear only as integration variables. Changing the names of these variables does not affect the value of the integral. Thus changing the name of the integration variable  $r_i$  to  $r_j$  and simultaneously changing the name of the variable  $r_j$  to  $r_i$  we obtain

$$\langle\psi|f_i|\psi\rangle = \langle\psi'|f_j|\psi'\rangle, \tag{2.3.22}$$

in which  $\psi'$  is identical with  $\psi$  except that the names of the variables  $r_i$  and  $r_j$  have been interchanged. But because of the antisymmetry of  $\psi$ ,  $\psi'$  is just the negative of  $\psi$ . It follows that

$$\langle\psi|f_i|\psi\rangle = (-1)^2 \langle\psi|f_j|\psi\rangle = \langle\psi|f_j|\psi\rangle, \tag{2.3.23}$$

and therefore, by using the equation (2.3.9), that

$$\langle\psi|\sum_i f_i|\psi\rangle = N \langle\psi|f_i|\psi\rangle = \frac{\prod_k w_k!}{(N-1)!} \sum_P \sum_{P'} (-1)^{p+p'} \langle\psi^{(P)}|f_N|\psi'^{(P')}\rangle. \tag{2.3.24}$$

For deriving the final expression we follow Cowan [7] and consider a fixed permutation  $P$ . In the evaluation of the matrix element on the right-hand side of (2.3.24), integration over any coordinate  $r_i$  other than  $r_N$  will involve simple overlap integrals of one-electron orbitals

$$\langle n_j l_j m_{l_j} m_{s_j}(i) | n'_j l'_j m'_{l_j} m'_{s_j}(i) \rangle. \quad (2.3.25)$$

Because of the orthonormality of these spin orbitals, (2.3.25) will be zero unless

$$n_j l_j m_{l_j} m_{s_j} = n'_j l'_j m'_{l_j} m'_{s_j}. \quad (2.3.26)$$

The matrix element in (2.3.24) will be zero unless the permutation  $P'$  is such that

$$n_j l_j = n'_j l'_j, \quad (2.3.27)$$

i.e., unless  $r_i$  occurs in the same subshell  $l_j^{w_j}$  in both  $\psi^{(P)}$  and  $\psi'^{(P')}$ . Since such a correspondence of subshells must hold for every coordinate  $i \neq N$ , it must be valid as seen by a process of elimination also for  $i = N$ . But this means that the matrix element in (2.3.24) will be zero unless  $P' \equiv P$ , because the permutations involved do not include coordinate permutations within a subshell. Therefore

$$\langle \psi | \sum_i f_i | \psi' \rangle = \frac{\prod_k w_k!}{(N-1)!} \sum_P \langle \psi^{(P)} | f_N | \psi'^{(P)} \rangle. \quad (2.3.28)$$

Now those permutations will be considered for which the coordinate  $N$  occurs in the subshell  $l_j^{w_j}$  for some specific  $j$ ; because of the nature of the permutation  $P$ , the coordinate  $r_N$  will always be the coordinate of the last ( $w_j$ th) electron of the subshell. With the position of this coordinate thus fixed the number of permutations in question will be the number of permutations  $(N-1)!$  of all coordinates other than  $r_N$ , divided by the numbers of unallowed permutations within each subshell:

$$\frac{(N-1)!}{w_1! w_2! \cdots (w_j - 1)! \cdots w_q!}. \quad (2.3.29)$$

Since all such permutations are of the same numerical value referring to the matrix element in (2.3.28), the partial sum comprising these permutations can be expressed by the following equation

$$\frac{\prod_k w_k!}{(N-1)!} \cdot \frac{(N-1)!}{w_1! w_2! \cdots (w_j - 1)! \cdots w_q!} \langle \psi^{(P_j)} | f_N | \psi'^{(P_j)} \rangle = w_j \langle \psi^{(P_j)} | f_N | \psi'^{(P_j)} \rangle, \quad (2.3.30)$$

in which  $P_j$  is any of these permutations, for which the coordinate  $r_N$  is the last coordinate of  $l_j^{w_j}$ . Summing up the results contributed by each of these subshells we get the following equation

$$\langle \psi | \sum_{k=1}^N f_k | \psi' \rangle = \sum_{j=1}^q w_j \langle \psi^{(P_j)} | f_N | \psi'^{(P_j)} \rangle = \sum_{j=1}^q w_j \langle \psi | f_{(j)} | \psi' \rangle, \quad (2.3.31)$$

in which in the final expression  $\psi$  and  $\psi'$  are coupled product functions with basic unpermuted coordinate ordering, antisymmetric only with regard to coordinate interchanges within each subshell.  $f_{(j)}$  operates on the last electron coordinate of the  $j$ th subshell. Similar expressions can be found for matrix elements of symmetric operators between wave functions  $|\psi\rangle$  and  $|\psi'\rangle$  belonging to two different configurations:

$$\langle\psi|\sum_{k=1}^N f_k|\psi'\rangle = (w_\sigma w'_{\sigma'})^{1/2} (-1)^{\Delta p} \langle\psi^{(P_\sigma)}|f_N|\psi'^{(P_{\sigma'})}\rangle. \quad (2.3.32)$$

Here  $\sigma$  and  $\sigma'$  are subshell indices expressed by the following equation

$$w_k - \delta_{k\sigma} = w'_k - \delta_{k\sigma'}, \quad 1 \leq k \leq q. \quad (2.3.33)$$

If no such  $\sigma$  and  $\sigma'$  exist, then the matrix element is zero; integration over at least one electron coordinate  $r_i$  ( $i < N$ ) involves an overlap integral  $\langle nl|n'l'\rangle$  for which  $nl \neq n'l'$  thus the integral is zero, due to the orthonormalization of the spin orbitals. The factor  $\Delta p$  is the difference in parity of  $P$  and  $P'$  with

$$\Delta p = p - p' = \sum_{j=\sigma+1}^q w_j - \sum_{j=\sigma'+1}^q w'_j. \quad (2.3.34)$$

In (2.3.32)  $P_\sigma$  is any permutation for which  $r_N$  is the last coordinate of  $l_\sigma^{w_\sigma}$ , and  $P_{\sigma'}$  is identical with  $P_\sigma$  except that  $r_N$  is the final coordinate of  $l_{\sigma'}^{w'_{\sigma'}}$ . (The single-configuration result (2.3.31) applies if the special case  $\sigma = \sigma' = j$  and  $w_\sigma = w'_{\sigma'}$ , except for the summation over  $j$ .)

For the two electron operator the final result for the single-configuration matrix element is [7]

$$\langle\psi|\sum_{i<j} g_{ij}|\psi'\rangle = \sum_{j=1}^q \frac{w_j(w_j-1)}{2} \langle\psi|g_{(jj)}|\psi'\rangle + \sum_{i<j} w_i w_j [\langle\psi|g_{(ij)}|\psi'\rangle - \langle\psi|g_{(ij)}|\psi'^{(ex)}\rangle], \quad (2.3.35)$$

in which  $\psi$  and  $\psi'$  are partially antisymmetrized, coupled functions with a basic unpermuted coordinate ordering. Thus  $\psi'^{(ex)}$  is the same as  $\psi'$  with the exception that the final electron coordinates of the  $i$ th and  $j$ th subshells are exchanged.  $g_{(jj)}$  operates on the last two electron coordinates of the  $j$ th subshell and  $g_{(ij)}$  operates on the final coordinates of the  $i$ th and  $j$ th subshells. The expression for the two-configuration cases is [7]

$$\begin{aligned} \langle\psi|\sum_{i<j} g_{ij}|\psi'\rangle &= \sum_{\rho\sigma\rho'\sigma'} (-1)^{\Delta p} \frac{[w_\rho(w_\sigma - \delta_{\rho\sigma}) w'_{\rho'}(w'_{\sigma'} - \delta_{\rho'\sigma'})]^{1/2}}{(1 + \delta_{\rho\sigma}\delta_{\rho'\sigma'})} \\ &\times [\langle\psi^{(P_{\rho\sigma})}|g_{N-1,N}|\psi'^{(P_{\rho'\sigma'})}\rangle - (1 - \delta_{\rho\sigma})(1 - \delta_{\rho'\sigma'}) \langle\psi^{(P_{\rho\sigma})}|g_{N-1,N}|\psi'^{(P_{\sigma'\rho'})}\rangle], \end{aligned} \quad (2.3.36)$$

in which  $\Delta p$  is obtained by (2.3.34). The summation must consider all the indices of the subshells  $\rho\sigma\rho'\sigma'$  which agree with the following equation

$$w_k - \delta_{k\rho} - \delta_{k\sigma} = w'_k - \delta_{k\rho'} - \delta_{k\sigma'}, \quad 1 \leq k \leq q. \quad (2.3.37)$$

The expression (2.3.36) is equivalent to that given by Fano [49]. He uses a different phase convention and includes an additional factor  $i^l$  in each spin orbital. So his expression of the matrix elements differ by the factor  $(-1)^{(l_{\rho'}+l_{\sigma'}-l_{\rho}-l_{\sigma})/2}$  from the above equation (2.3.36). For  $\rho = \rho'$  and  $\sigma = \sigma'$  (2.3.36) reduces to the single-configuration expression (2.3.35).

With the expressions (2.3.31), (2.3.32), (2.3.35) and (2.3.36) the matrix elements of symmetric operators can be determined between not fully antisymmetrized wave functions which are antisymmetric only with respect to the interchange of electron coordinates within a given subshell.

## 2.4 Racah-Wigner Algebra

In this section, which based on Cowan [7], we give an introduction to the Racah-Wigner algebra, which is used in the cluster-model calculation. The section starts with a definition of a spherical tensor operator and the Wigner-Eckart theorem, which is an essential element of the calculation technique used in this thesis. In the following, we describe relations, which are required in the calculation of matrix elements of spherical tensor operators.

The Racah-Wigner algebra [3–6, 52–54] provides notational and calculational simplifications of great elegance, which are practically indispensable for the evaluation of matrix elements between complex configurations. This algebra is concerned with the evaluation of the angular part of a matrix element. It is particularly concerned with the complications that arise from coupling the various angular momentum quantum numbers. Determining the radial integrals is unaffected by angular momenta coupling. Racah's methods are strictly concerned with basis functions that have been antisymmetrized (with respect to the electron-coordinate interchange) only within a subshell of equivalent electrons, and this antisymmetrization is assumed to have been accomplished via the method of the coefficients of fractional parentage. Thus the Racah formalism is to be applied only with matrix elements between functions  $\psi$  that are simple products of single subshell functions like

$$\prod_{i=1}^q |l^{w_i} \alpha_i L_i S_i\rangle. \quad (2.4.1)$$

These are of the type (2.3.4), except that the angular momenta  $L_i S_i$  have been coupled together according to some coupling scheme. In the calculations discussed in this thesis, the above mentioned conditions have always been met.

### 2.4.1 Irreducible Tensor Operator

An irreducible tensor operator of rank  $k$  is defined by Racah [4] as an operator  $T^{(k)}$  whose  $2k + 1$  components  $T_q^{(k)}$  ( $q = -k, \dots, k$ ) satisfy the same commutation rule with respect to the angular momentum  $J$  as the spherical harmonic operators  $Y_{kq}$ . This means that the tensor is transformed under a rotation of the coordinate axes in the same way as one of the spherical harmonics  $Y_{lm}(\theta, \phi)$ :

$$\begin{aligned} [(J_x \pm i J_y), T_q^{(k)}] &= [(k \mp q)(k \pm q + 1)]^{1/2} T_{q\pm 1}^{(k)} \\ [J_z, T_q^{(k)}] &= q T_q^{(k)}. \end{aligned} \quad (2.4.2)$$

For  $k = 1$  we get the following relation

$$T_{\pm 1}^{(1)} = \frac{\mp 1}{\sqrt{2}} (T_x \pm i T_y), \quad T_0^{(1)} = T_z. \quad (2.4.3)$$

So  $J$  is a tensor operator of rank 1 with the components  $\frac{\pm 1}{\sqrt{2}}J_{\mp}, J_z$ . For an operator that does not have an effect on spins but only involves the spatial coordinates  $(r, \theta, \phi)$ ,  $T_q^{(k)}$  must have the same angular form as  $Y_k^q$ ; i.e. that

$$T_q^{(k)} = A_k Y_k^q, \quad (2.4.4)$$

in which  $A_k$  may be a function of  $r = |\mathbf{r}|$  but it must be independent of  $\theta, \phi$  and  $q$ .

An example are the renormalized spherical harmonics

$$C_q^{(k)}(\theta, \phi) = \sqrt{\frac{4\pi}{2k+1}} Y_k^q(\theta, \phi). \quad (2.4.5)$$

### 2.4.2 Wigner-Eckart Theorem

If a tensor operator  $T_q^{(k)}$  has an effect on a space that is spanned by a set of basis function  $|\alpha j m\rangle$  which are eigenfunctions of the operators  $J^2$  and  $J_z$ , with  $\alpha$  representing any quantities that are required to completely specify the basis function, then the matrix elements of an irreducible tensor operator show the same dependence on  $(m, q, m')$  as the Clebsch-Gordan coefficients (CG) for the angular momentum coupling. This result is known as the Wigner-Eckart theorem [1, 2]:

$$\begin{aligned} t_{jj'} &:= \langle \alpha j m | T_q^{(k)} | \alpha' j' m' \rangle = \frac{1}{\sqrt{j}} CG(j' k m' q; j m) \langle \alpha j || T_q^{(k)} || \alpha' j' \rangle \\ &= (-1)^{-j'+k-m} \begin{pmatrix} j' & k & j \\ m' & q & -m \end{pmatrix} \langle \alpha j || T_q^{(k)} || \alpha' j' \rangle \\ &= (-1)^{j-m} \begin{pmatrix} j & k & j' \\ -m & q & m' \end{pmatrix} \langle \alpha j || T_q^{(k)} || \alpha' j' \rangle. \end{aligned} \quad (2.4.6)$$

Here, the round brackets indicate the 3-j symbol, which is related to the Clebsch-Gordan coefficients by (A.1.1). The expression “ $\langle \dots || \dots \rangle$ ” represents the reduced matrix element. In the last step in this equation the symmetry relation of the 3j symbol [7] has been used, together with the fact that  $k$  is integer. The matrix element  $t_{jj'}$  is zero, unless

$$m = q + m' \quad (2.4.7)$$

and unless  $j, q$  and  $j'$  satisfy the triangle conditions ( $|j - j'| \leq q \leq j + j'$ ). These two conditions together constitute the matrix-element *selection rules*. The 3j symbol in (2.4.6) only involves purely geometrical properties of the tensor operator. The physical nature of the operator is contained in the reduced matrix element<sup>9</sup>  $\langle \alpha j || T_q^{(k)} || \alpha' j' \rangle$ . The reduced matrix element for the angular momentum operator  $J$  is given by

$$\langle \alpha j || J^{(1)} || \alpha' j' \rangle = \delta_{\alpha j, \alpha' j'} \sqrt{j(j+1)(2j+1)}. \quad (2.4.8)$$

<sup>9</sup>Racah's original phase conventions [3–6], used here, differ from those employed by Fano and Racah [52]. Their conventions employ an additional factor  $i^l$  in the definition of  $Y_{lm}$  and a corresponding additional factor  $i^k$  in the definition of  $C^{(k)}$ .

### 2.4.3 Matrix Elements of Tensor Operators

The calculation of the tensor matrix element is reduced to the determination of the reduced matrix element. In the following some important identities for the calculation of the reduced matrix element [4, 7] will be given.

The reduced matrix element of a tensor product  $V_Q^{(K)}$  consisting of two commuting tensor operators  $T^{(k_1)}$  and  $W^{(k_2)}$ ,

$$V_Q^{(K)} \equiv [T^{(k_1)} \times W^{(k_2)}]_Q^{(K)} \equiv \sum_{q_1 q_2} CG(k_1 k_2 q_1 q_2; K Q) T_{q_1}^{(k_1)} W_{q_2}^{(k_2)}, \quad (2.4.9)$$

with  $K = k_1 + k_2$  and  $Q = q_1 + q_2$ , operating on different parts of a system, is defined by

$$\begin{aligned} & \langle \alpha_1 j_1 \alpha_2 j_2 \| [T^{(k_1)} \times W^{(k_2)}]^{(K)} \| \alpha'_1 j'_1 \alpha'_2 j'_2 \rangle \\ &= [j, j', K]^{1/2} \langle \alpha_1 j_1 \| T^{(k_1)} \| \alpha'_1 j'_1 \rangle \langle \alpha_2 j_2 \| W^{(k_2)} \| \alpha'_2 j'_2 \rangle \left\{ \begin{array}{ccc} j_1 & j_2 & j \\ j'_1 & j'_2 & j' \\ k_1 & k_2 & K \end{array} \right\}, \end{aligned} \quad (2.4.10)$$

in which  $[l_1, l_2, \dots] \equiv (2l_1 + 1)(2l_2 + 1) \dots$ . The expression in braces represents the 6-j symbol (A.2.3).

If  $W^{(k_2)}$  is equal to the identity operator  $C_0^{(0)} \equiv 1$ , we get the reduced matrix element for a tensor operator  $T_q^{(k)}$ , which only has an effect on  $|\alpha_1 j_1 m_1\rangle$ ,

$$\begin{aligned} \langle \alpha_1 j_1 \alpha_2 j_2 \| T^{(k)} \| \alpha'_1 j'_1 \alpha'_2 j'_2 \rangle &= \delta_{\alpha_2 j_2, \alpha'_2 j'_2} (-1)^{j_1 + j_2 + j' + k} [j, j']^{1/2} \left\{ \begin{array}{ccc} j_1 & j_2 & j \\ j' & k & j'_1 \end{array} \right\} \\ &\times \langle \alpha_1 j_1 \| T^{(k)} \| \alpha'_1 j'_1 \rangle. \end{aligned} \quad (2.4.11)$$

If  $W^{(k)}$  has only an effect on  $|\alpha_2 j_2 m_2\rangle$ , we obtain a similar expression for the reduced matrix element

$$\begin{aligned} \langle \alpha_1 j_1 \alpha_2 j_2 \| W^{(k)} \| \alpha'_1 j'_1 \alpha'_2 j'_2 \rangle &= \delta_{\alpha_1 j_1, \alpha'_1 j'_1} (-1)^{j_1 + j'_2 + j + k} [j, j']^{1/2} \left\{ \begin{array}{ccc} j_1 & j_2 & j \\ k & j' & j'_2 \end{array} \right\} \\ &\times \langle \alpha_2 j_2 \| W^{(k)} \| \alpha'_2 j'_2 \rangle. \end{aligned} \quad (2.4.12)$$

These two expressions simplify the evaluation of reduced matrix elements for coupled basis functions in terms of reduced matrix elements for subspace functions.

Of particular importance is the following tensor product with  $k_1 = k_2$  and  $K = 0$ . The tensor product than is equivalent to a scalar product. As a consequence the matrix element has the form

$$\begin{aligned} \langle \alpha_1 j_1 \alpha_2 j_2 j m \| T^{(k)} \cdot W^{(k)} \| \alpha'_1 j'_1 \alpha'_2 j'_2 j' m' \rangle &= \delta_{j m, j' m'} (-1)^{j_1 + j_2 + j} \left\{ \begin{array}{ccc} j_1 & j_2 & j \\ j'_2 & j'_1 & k \end{array} \right\} \\ &\times \langle \alpha_1 j_1 \| T^{(k)} \| \alpha'_1 j'_1 \rangle \langle \alpha_2 j_2 \| W^{(k)} \| \alpha'_2 j'_2 \rangle. \end{aligned} \quad (2.4.13)$$

It is convenient to define a unit irreducible tensor operator  $u^k$ , which has an effect on the spatial coordinates and is normalized with regard to<sup>10</sup>

$$\langle l \| u^{(k)} \| l' \rangle = 1 \quad (2.4.14)$$

with  $l$ ,  $k$  and,  $l'$  satisfying the triangle relations. An example valid for  $l + k + l'$  even is

$$u_q^{(k)} = \frac{C_q^{(k)}}{\langle l \| C^{(k)} \| l' \rangle}. \quad (2.4.15)$$

Another example for  $k = 1$  is

$$u_q^{(1)} = \frac{J_q^{(1)}}{\langle l \| J^{(1)} \| l' \rangle}. \quad (2.4.16)$$

For a subshell  $l^w$  of equivalent electrons, we define a symmetric unit tensor operator

$$U^{(k)} \equiv \sum_{i=1}^w u_i^{(k)}. \quad (2.4.17)$$

The reduced matrix element of this operator  $U^{(k)}$  can be calculated from

$$\begin{aligned} \langle l^w \alpha LS \| U^{(k)} \| l^w \alpha' L' S' \rangle &= \delta_{S, S'} w (-1)^{l+L+k} [L, L']^{1/2} \sum_{\bar{\alpha} \bar{L} \bar{S}} (-1)^{\bar{L}} \left\{ \begin{array}{ccc} l & k & l \\ L & \bar{L} & L' \end{array} \right\} \\ &\times (l^w \alpha LS \{ l^{w-1} \bar{\alpha} \bar{L} \bar{S} \} (l^{w-1} \bar{\alpha} \bar{L} \bar{S}) \{ l^w \alpha' L' S' \}), \end{aligned} \quad (2.4.18)$$

with “ $\{ \dots \} \dots$ ” denoting the cfp. This matrix element is zero, unless  $0 \leq k \leq 2l$  and unless  $L$ ,  $k$ , and,  $L'$  satisfy the triangle relations. The matrix element is also symmetric

$$\langle l^w \alpha' L' S' \| U^{(k)} \| l^w \alpha LS \rangle = (-1)^{L'-L} \langle l^w \alpha LS \| U^{(k)} \| l^w \alpha' L' S' \rangle. \quad (2.4.19)$$

#### 2.4.4 Unit Double Tensor Operator

If we want to evaluate matrix elements of the spin-orbit operator  $l^{(1)} \cdot s^{(1)}$  for functions  $|l^w \alpha LS\rangle$  it is rather unsatisfactory to separate  $L$  from  $S$  when  $\alpha$ ,  $L$ , and  $S$  are inherently linked together. In order to be able to consider mathematically distinct reduced matrix elements, it is convenient to define a double tensor operator of rank  $(k, \kappa)$ , which behaves as an irreducible tensor operator of rank  $k$  with respect to  $L$  and as tensor of rank  $\kappa$  with respect to  $S$ . For the spin-orbit operator the unit double tensor

$$v^{(k1)} \equiv u^{(k)} \cdot s^{(1)} \quad (2.4.20)$$

is important. In analogy to (2.4.17) we can define a symmetric unit double tensor for a subshell  $l^w$  of  $w$  equivalent electrons as follows:

$$V^{(k1)} \equiv \sum_{i=1}^w v_i^{(k1)} = \sum_{i=1}^w u_i^{(k)} s_i^{(1)}. \quad (2.4.21)$$

<sup>10</sup>This is a generalization of the  $u^{(k)}$  defined by Racah [4], eq. (58), which he defined only for  $l = l'$ .

The reduced matrix element of this tensor is given by the equation

$$\begin{aligned}
 \langle l^w \alpha LS \| V^{(k1)} \| l^w \alpha' L' S' \rangle &= \sqrt{\frac{3}{2}} w (-1)^{l+L+k} [L, L', S, S']^{1/2} \sum_{\bar{\alpha} \bar{L} \bar{S}} (-1)^{\bar{L} + \bar{S} + S + 3/2} \\
 &\times \left\{ \begin{matrix} l & l & k \\ L & L' & \bar{L} \end{matrix} \right\} \left\{ \begin{matrix} s & s & 1 \\ S & S' & \bar{S} \end{matrix} \right\} \\
 &\times (l^w \alpha LS \{ l^{w-1} \bar{\alpha} \bar{L} \bar{S} \}) (l^{w-1} \bar{\alpha} \bar{L} \bar{S} \{ l^w \alpha' L' S' \}) .
 \end{aligned} \tag{2.4.22}$$

The matrix element is non-zero only for  $0 \leq k \leq 2l$ ;  $L$ ,  $k$  and,  $L'$  as well as  $S$ , 1 and,  $S'$  must satisfy the triangle relations.

## 2.5 Coulomb Interaction

In this section, we will apply the knowledge of the previous sections and calculate the first part of the Hamiltonian. The Coulomb interaction describe the electrostatic interaction between the electrons. We present Cowan's expressions [7] for the various parts of the Coulomb interaction within the Racah-Wigner algebra, which makes it easier to derive closed algebraic expressions for the Coulomb interaction between basis functions of the general configurations. Here, all expressions are formulated within the Russell-Saunders coupling scheme.

### 2.5.1 Coulomb Operator

The description of the Coulomb operator begins with the interaction between two electrons: The evaluation of the matrix element of the Coulomb interaction starts with a multipole expansion of  $e^2/r_{12}$ , which reduces the calculation of  $(2l+1)^4$  matrix elements (these are 625 for  $d$  electrons) to  $(l+1)$  parameters. Using the spherical harmonic addition theorem we find the equation

$$\frac{e^2}{r_{12}} = e^2 \sum_{k=0}^{\infty} \frac{r_{<}^k}{r_{>}^{k+1}} P_k(\cos \omega) = e^2 \sum_{k=0}^{\infty} \frac{r_{<}^k}{r_{>}^{k+1}} \sum_{q=-k}^k (-1)^q C_{-q}^{(k)}(\theta_1, \phi_1) C_q^{(k)}(\theta_2, \phi_2), \quad (2.5.1)$$

in which  $r_{<}$  and  $r_{>}$  are respectively the lesser and greater value of the distances  $r_1$  and  $r_2$ , i.e., the distance which the electrons have from the nucleus. Here  $C_q^{(k)}$  are the renormalized spherical harmonics (2.4.5).

This kind of expansion can be done only in the case of electrons which are located at the same ion. The expression for electrons located on two different ions is given in section "2.9 Exchange Interactions". The matrix element of (2.5.1) between two two-electron product functions can be expressed as

$$\begin{aligned} \langle ij | \frac{e^2}{r_{12}} | tu \rangle &= \delta_{m_{s_i}, m_{s_t}} \delta_{m_{s_j}, m_{s_u}} \sum_{k=0}^{\infty} R^k(ij, tu) \\ &\times \sum_{q=-k}^k \delta_{q, m_{i_t} - m_{i_i}} \delta_{q, m_{j_t} - m_{j_u}} (-1)^q c^k(l_i m_i, l_t m_t) c^k(l_j m_j, l_u m_u), \end{aligned} \quad (2.5.2)$$

in which the first two  $\delta$ -factors result from the summation over spin variables, and

$$R^k(ij, tu) = \int_0^{\infty} \int_0^{\infty} \frac{e^2 r_{<}^k}{r_{>}^{k+1}} P_i^*(r_1) P_j^*(r_2) P_t(r_1) P_u(r_2) dr_1 dr_2 \quad (2.5.3)$$

are the radial integrals, with "ij" and "tu" representing the corresponding quantum numbers  $n_i l_i, n_j l_j \dots$ . The expression  $c^k$  marks the Gaunt coefficients [55]. In some special cases this matrix element expression (2.5.2) can be simplified as follows:

## 2.5.2 Slater Integrals

The direct contribution ( $i \equiv t, j \equiv u$ ) (2.5.2) can be rewritten as

$$\langle ij | \frac{e^2}{r_{12}} | ij \rangle = \sum_{k=0}^{\infty} F^k(ij) c^k(l_i m_i, l_i m_i) c^k(l_j m_j, l_j m_j), \quad (2.5.4)$$

with

$$F^k(ij) \equiv R^k(ij, ij) = \int_0^{\infty} \int_0^{\infty} \frac{e^2 r^k}{r_{>}^{k+1}} |P_i(r_1)|^2 |P_j(r_2)|^2 dr_1 dr_2. \quad (2.5.5)$$

The Gaunt coefficients  $c^k$  are non-zero only for  $0 \leq k \leq \min(2l_i, 2l_j)$ . So the summation in (2.5.4) can be restricted to these values of  $k$ .

The exchange contributions ( $i \equiv u, j \equiv t$ ) can be expressed by

$$- \langle ij | \frac{e^2}{r_{12}} | ji \rangle = -\delta_{m_{s_i}, m_{s_j}} \sum_{k=0}^{\infty} G^k(ij) |c^k(l_j m_j, l_j m_j)|^2, \quad (2.5.6)$$

in which

$$G^k(ij) \equiv R^k(ij, ji) = \int_0^{\infty} \int_0^{\infty} \frac{e^2 r^k}{r_{>}^{k+1}} P_i^*(r_1) P_j^*(r_2) P_j(r_1) P_i(r_2) dr_1 dr_2. \quad (2.5.7)$$

The Gaunt selection rules restrict the values of  $k$  to  $k = |l_i - l_j|, \dots, (l_i + l_j)$ .

The radial integrals  $F^k$  and  $G^k$  (generally called  $R^k$ ) are also referred to as Slater integrals [47]. These integrals<sup>11</sup> are always positive and fulfill the following relations

$$\begin{aligned} F^0 &> F^1 > F^2 > \dots > 0, \\ G^0 &> G^1 > G^2 > \dots > 0. \end{aligned} \quad (2.5.10)$$

The numerical calculation of these integrals is difficult, because only a few of the most important configuration-interactions can be included explicitly, and it is impractical to include more than a very limited number. Thus it is useful to estimate the effect

---

<sup>11</sup>In order to avoid large denominators, which appear in the calculations of the matrix elements, Condon and Shortley [50] have established the reduced radial integrals  $F_k$  and  $G_k$  which are related to the radial  $F^k$  and  $G^k$  integrals by the expression

$$F_k \equiv \frac{F^k}{D_k} \quad \text{and} \quad G_k \equiv \frac{G^k}{D_k}, \quad (2.5.8)$$

in which  $D_k$  are the least common denominators (for different  $m_{l_i} m_{l_j}$ ) of the coefficients of the corresponding  $F^k, G^k$ . For  $d$  electrons:  $D_k = 441$ . Another definition of the Slater integrals is given by Racah [4], the so-called Racah parameters, which (for  $d$  electrons) are related by the expressions

$$A \equiv F^0 - \frac{49}{441} F^4, \quad B \equiv \frac{9}{441} F^2 - \frac{5}{441} F^4, \quad C \equiv \frac{35}{441} F^4 \quad (2.5.9)$$

in order to simplify the appearance of the expressions for the matrix elements of the energy.

of infinitely many small perturbations by using scaled-down theoretical values of the single-configuration Coulomb integrals  $F^k$  and  $G^k$ . This semiempirical correction has qualitatively been justified by the theoretical investigations of Rajnak and Wybourne [56–60]. Appropriate scaling factors range from about 0.7 or 0.8 for neutral atoms to about 0.9 or 0.95 for highly ionized atoms.

The general calculation of the matrix elements of the Coulomb interaction is quite complex because we have to distinguish between several cases:

1. Direct interaction between equivalent electrons<sup>12</sup> in a subshell of an ion in a given configuration.
2. Direct interaction between non-equivalent electrons in two subshells of an ion in a given configuration.
3. Exchange interaction between non-equivalent electrons in two subshells of an ion in a given configuration.
4. Direct and exchange interaction between non-equivalent electrons in two subshells of an ion in two different configurations.

In all cases the Coulomb energy can be expressed with the aid of the radial Slater integrals  $F_k(R_d^k)$  and  $G_k(R_e^k)$  as is shown by the relation:

$$\langle \psi | \sum_{i < j} \frac{e^2}{r_{ij}} | \psi' \rangle = \sum_{i < j} \left[ \sum_k f_k F^k + \sum_k g_k G^k \right], \quad (2.5.11)$$

with  $f_k$  and  $g_k$  representing the angular momenta parts. ( $R_d^k$  and  $R_e^k$  are needed in case 4 and represent the generalization of the Slater integrals).

### 2.5.3 Direct Interaction between Equivalent Electrons

CASE 1: In the Russell-Saunders coupling scheme, the Coulomb interaction is diagonal in  $\mathfrak{J}_q$  and  $\mathfrak{M}_q$  and independent of  $\mathfrak{M}_q$ . Due to the invariance of the spin under the Coulomb operator, the Coulomb operator has an effect only on  $\mathfrak{L}$  and not on  $\mathfrak{S}$ , and the coupling  $(\mathfrak{L}_q \mathfrak{S}_q)\mathfrak{J}_q$  can be ignored by the determination of the matrix elements which are independent of  $\mathfrak{J}_q$  and diagonal in  $\mathfrak{L}_q$  and  $\mathfrak{S}_q$ .

The calculation of the direct Coulomb interaction within a subshell  $n_j l_j$  of a given configuration can be accomplished by using the first term of the right-hand side of (2.3.35). The resulting expression is

$$\sum_k f_k^d(l_j l_j) F^k(l_j l_j) = \sum_k \delta_j \frac{1}{2} w_j (w_j - 1) \langle l_j^{w_j} \alpha_j L_j S_j | C_m^{(k)} \cdot C_n^{(k)} | l_j^{w_j} \alpha'_j L'_j S'_j \rangle F^k(l_j l_j), \quad (2.5.12)$$

<sup>12</sup>One-electron orbitals having the same value of  $nl$  are called *equivalent orbitals*. Correspondingly, electrons having the same values of  $nl$  are called *equivalent electrons*.

in which  $C_m^{(k)} \cdot C_n^{(k)}$  is a scalar product of two tensor operators which can be evaluated with the help of (2.4.13) and with  $\delta_j$  defined as

$$\delta_j \equiv \delta_{\mathfrak{J}_q \mathfrak{M}_q, \mathfrak{J}'_q \mathfrak{M}'_q} \prod_{i=1}^q (\delta_{L_i S_i \mathfrak{L}_i \mathfrak{S}_i, L'_i S'_i \mathfrak{L}'_i \mathfrak{S}'_i}) \times \prod_{\substack{i=1 \\ i \neq j}}^q (\delta_{\alpha_i, \alpha'_i}). \quad (2.5.13)$$

Rewriting (2.5.12) with (2.4.15) we finally achieve the expression for the angular momentum prefactor  $f_k(l_j l_j)$  with  $k > 0$

$$f_k(l_j l_j) = \delta_j \frac{1}{2} \langle l_j \| C^{(k)} \| l_j \rangle^2 \left\{ [L_j]^{-1} \sum_{\alpha'' L''} \langle l_j^{w_j} \alpha'' L'' S_j \| U^{(k)} \| l_j^{w_j} \alpha_j L_j S_j \rangle \right. \\ \left. \times \langle l_j^{w_j} \alpha'' L'' S_j \| U^{(k)} \| l_j^{w_j} \alpha'_j L_j S_j \rangle - \delta_{\alpha_j, \alpha'_j} \frac{w_j(4l_j + 2 - w_j)}{(2l_j + 1)(4l_j + 1)} \right\}, \quad (2.5.14)$$

relative to the multiplet average. In the case of  $k = 0$  we achieve for the angular momentum prefactor the following expression:

$$f_0(l_j l_j) = \delta_j \frac{1}{2} [l_j] \left\{ w_j^2 [l_j]^{-1} \delta_{\alpha_j, \alpha'_j} - \delta_{\alpha_j, \alpha'_j} w_j [l_j]^{-1} \right\}. \quad (2.5.15)$$

Within a set of equivalent electrons  $l^{w_j}$  the Coulomb interaction does not contribute to the level structure if there are less than two electrons or less than two holes in the subshell.

## 2.5.4 Direct Interaction between Non-Equivalent Electrons

CASE 2: The direct Coulomb operator for non-equivalent electrons originates in the second term of (2.3.35) and can be expressed as

$$\sum_{i < j} w_i w_j \langle \psi | \sum_k \frac{e^2 r_{<}^k}{r_{>}^{k+1}} C_m^{(k)} \cdot C_n^{(k)} | \psi' \rangle = \sum_{i < j} \sum_k f_k(l_i, l_j) F^k(l_i, l_j). \quad (2.5.16)$$

The coefficient of the Slater integral  $F^k$  is the angular matrix element

$$f_k(l_i, l_j) = \langle l_i \| C^{(k)} \| l_i \rangle \langle l_j \| C^{(k)} \| l_j \rangle I_{ij}^{(k)}, \quad (2.5.17)$$

in which  $I_{ij}^{(k)}$  is defined as:

$$I_{ij}^{(k)} \equiv w_i w_j \langle \psi \| u_{(m)}^{(k)} \cdot u_{(n)}^{(k)} \| \psi' \rangle = \langle \psi \| U_{(i)}^{(k)} \cdot U_{(j)}^{(k)} \| \psi' \rangle. \quad (2.5.18)$$

In the last step of (2.5.18) the relation (2.4.17) is used. This operator only has an effect on the angular momentum and therefore is diagonal in all spins, denoted by  $\delta$ -factors

$$\delta_{\mathfrak{J}_q \mathfrak{M}_q, \mathfrak{J}'_q \mathfrak{M}'_q} \prod_{m=1}^q \delta_{S_m \mathfrak{S}_m, S'_m \mathfrak{S}'_m}. \quad (2.5.19)$$

The operator describes the interaction between the  $i$ th and the  $j$ th subshell. All other subshells should have the same quantum numbers denoted by  $\delta$ -factors

$$\delta_{\mathfrak{L}_j, \mathfrak{L}'_j} \prod_{m=j+1}^q \delta_{\alpha_m L_m, \alpha'_m L'_m} \delta_{\mathfrak{L}_m, \mathfrak{L}'_m}. \quad (2.5.20)$$

The remaining matrix element

$$\langle (\dots \mathfrak{L}_{j-1}, L_j) \mathfrak{L}_j | U_{(i)}^{(k)} \cdot U_{(j)}^{(k)} | (\dots \mathfrak{L}'_{j-1}, L'_j) \mathfrak{L}'_j \rangle \quad (2.5.21)$$

can be determined by using the uncoupling formulae (2.4.11) and (2.4.12). We start with uncoupling  $L_j$  from  $\mathfrak{L}_{j-1}$  by using (2.4.13). Then, if  $i < j - 1$ , we use (2.4.11)  $(j - i - 1)$  times to successively uncouple  $L_{j-1}, L_{j-2}, \dots, L_{i+1}$ . If  $i > 1$ , we use (2.4.12) to uncouple  $L_i$  from  $\mathfrak{L}_{i-1}$ .

Finally we achieve [46]

$$\begin{aligned} I_{ij}^{(k)} &= (-1)^{\mathfrak{L}'_{j-1} + L_j + \mathfrak{L}_j} \left\{ \begin{array}{ccc} \mathfrak{L}_{j-1} & L_j & \mathfrak{L}_j \\ L'_j & \mathfrak{L}'_{j-1} & k \end{array} \right\} \\ &\quad \times \langle \dots \mathfrak{L}_{j-1} \| U_{(i)}^{(k)} \| \dots \mathfrak{L}'_{j-1} \rangle \langle l_j^{w_j} \alpha_j L_j S_j \| U^{(k)} \| l_j^{w_j} \alpha'_j L'_j S'_j \rangle \\ &= (-1)^{\mathfrak{L}'_{j-1} + L_j + \mathfrak{L}_j} \left\{ \begin{array}{ccc} \mathfrak{L}_{j-1} & L_j & \mathfrak{L}_j \\ L'_j & \mathfrak{L}'_{j-1} & k \end{array} \right\} \\ &\quad \times \left[ \prod_{m=i+1}^{j-1} (-1)^{\mathfrak{L}_{m-1} + L_m + \mathfrak{L}'_m + k} [\mathfrak{L}_m, \mathfrak{L}'_m]^{1/2} \left\{ \begin{array}{ccc} \mathfrak{L}_{m-1} & L_m & \mathfrak{L}_m \\ \mathfrak{L}'_m & k & \mathfrak{L}'_{m-1} \end{array} \right\} \right] \\ &\quad \times \langle \dots \mathfrak{L}_i \| U_{(i)}^{(k)} \| \dots \mathfrak{L}'_i \rangle \langle l_j^{w_j} \alpha_j L_j S_j \| U^{(k)} \| l_j^{w_j} \alpha'_j L'_j S'_j \rangle \\ &= (-1)^{\mathfrak{L}'_{j-1} + L_j + \mathfrak{L}_j} \left\{ \begin{array}{ccc} \mathfrak{L}_{j-1} & L_j & \mathfrak{L}_j \\ L'_j & \mathfrak{L}'_{j-1} & k \end{array} \right\} \\ &\quad \times \left[ \prod_{m=i+1}^{j-1} (-1)^{\mathfrak{L}_{m-1} + L_m + \mathfrak{L}'_m + k} [\mathfrak{L}_m, \mathfrak{L}'_m]^{1/2} \left\{ \begin{array}{ccc} \mathfrak{L}_{m-1} & L_m & \mathfrak{L}_m \\ \mathfrak{L}'_m & k & \mathfrak{L}'_{m-1} \end{array} \right\} \right] \\ &\quad \times \left[ \delta_{i,1} + (1 - \delta_{i,1}) (-1)^{\mathfrak{L}_{i-1} + L'_i + \mathfrak{L}_i + k} [\mathfrak{L}_i, \mathfrak{L}'_i]^{1/2} \left\{ \begin{array}{ccc} \mathfrak{L}_{i-1} & L_i & \mathfrak{L}_i \\ k & \mathfrak{L}'_i & L'_i \end{array} \right\} \right] \\ &\quad \times \langle l_i^{w_i} \alpha_i L_i S_i \| U^{(k)} \| l_i^{w_i} \alpha'_i L'_i S'_i \rangle \langle l_j^{w_j} \alpha_j L_j S_j \| U^{(k)} \| l_j^{w_j} \alpha'_j L'_j S'_j \rangle. \end{aligned} \quad (2.5.22)$$

For  $k = 0$  this expression can be reduced to

$$I_{ij}^{(0)} = \delta_{c,c'} w_i w_j [l_i, l_j]^{1/2}, \quad (2.5.23)$$

in which  $c$  and  $c'$  represent the configurations between which  $I_{ij}^{(k)}$  is calculated. Inserting this expression in (2.5.17) we get the equation

$$f_k(l_i l_j) = \delta_{c,c'} w_i w_j. \quad (2.5.24)$$

Thus the  $k = 0$  terms in (2.5.17) contribute only to the averaged energy of all states of the configuration  $E_{av}$ ; they do not make any other contribution to the Hamiltonian matrix elements, neither on nor off the diagonal. If either the subshell  $l_i^{w_i}$  or the subshell  $l_j^{w_j}$  is actually filled, then  $f_k$  is zero for  $k > 0$ .

### 2.5.5 Exchange Interaction between Non-Equivalent Electrons

CASE 3: Similar to (2.5.17) the exchange part for non-equivalent electrons has the form

$$\sum_{i < j} \sum_k g'_k(l_i l_j) G^k(l_i l_j). \quad (2.5.25)$$

In order to determine the angular coefficient  $g'_k$  analogous to (2.5.17) we use the following formula

$$\begin{aligned} g'_k(l_i l_j) &= -\frac{1}{2} \langle l_i \| C^{(k)} \| l_j \rangle^2 \sum_r (-1)^r [r] \left\{ \begin{matrix} l_i & l_i & r \\ l_j & l_j & k \end{matrix} \right\} \langle \psi | U_{(i)}^{(k)} \cdot U_{(j)}^{(k)} + 4V_{(i)}^{(r1)} \cdot V_{(j)}^{(r1)} | \psi' \rangle \\ &= -\frac{1}{2} \langle l_i \| C^{(k)} \| l_j \rangle^2 \sum_r (-1)^r [r] \left\{ \begin{matrix} l_i & l_i & r \\ l_j & l_j & k \end{matrix} \right\} [I_{ij}^{(r)} + 4I_{ij}^{(r1)}]. \end{aligned} \quad (2.5.26)$$

A detailed derivation of the above expression is given by Cowan [7].

In (2.5.26)  $I_{ij}^{(r)}$  is identical with the quantity (2.5.22) except that  $k$  is replaced by  $r$ . This expression is still diagonal in all spins and in all other quantum numbers but not for  $\alpha_i L_i, \alpha_j L_j$ , and  $\mathfrak{L}_m$  ( $i \leq m \leq j$ ). The operator  $V_{(i)}^{(r1)} \cdot V_{(j)}^{(r1)}$  is applied to spins as well as to orbital momenta, and therefore  $I_{ij}^{(r1)}$  is diagonal only in quantum numbers other than  $\alpha_i L_i S_i, \alpha_j L_j S_j$ , and  $\mathfrak{L}_m \mathfrak{S}_m$  ( $i \leq m \leq j$ ). The determination of  $I_{ij}^{(r1)}$  is analogous to  $I_{ij}^{(r)}$  but the uncoupling of spins as well as orbital momenta must be taken into account. The final expression of  $I_{ij}^{(r1)}$  has the same form as (2.5.22). But for every factor involving the orbital momenta a similar factor for the corresponding spins has to be added and the reduced matrix elements are those of  $V^{(r1)}$  instead of  $U^{(r)}$ . Thus

the values of  $I_{ij}^{(r1)}$  can be formed by making use of the following formula:

$$\begin{aligned}
 I_{ij}^{(r1)} = & (-1)^{\mathfrak{L}'_{j-1} + \mathfrak{S}'_{j-1} + L_j + S_j + \mathfrak{L}_j + \mathfrak{S}_j} \left\{ \begin{array}{ccc} \mathfrak{L}_{j-1} & L_j & \mathfrak{L}_j \\ L'_j & \mathfrak{L}'_{j-1} & r \end{array} \right\} \left\{ \begin{array}{ccc} \mathfrak{S}_{j-1} & S_j & \mathfrak{S}_j \\ S'_j & \mathfrak{S}'_{j-1} & 1 \end{array} \right\} \\
 & \times \left[ \prod_{m=i+1}^{j-1} (-1)^{\mathfrak{L}_{m-1} + L_m + \mathfrak{L}'_m + r} [\mathfrak{L}_m, \mathfrak{L}'_m]^{1/2} \left\{ \begin{array}{ccc} \mathfrak{L}_{m-1} & L_m & \mathfrak{L}_m \\ \mathfrak{L}'_m & r & \mathfrak{L}'_{m-1} \end{array} \right\} \right. \\
 & \quad \left. (-1)^{\mathfrak{S}_{m-1} + S_m + \mathfrak{S}'_{m+1}} [\mathfrak{S}_m, \mathfrak{S}'_m]^{1/2} \left\{ \begin{array}{ccc} \mathfrak{S}_{m-1} & S_m & \mathfrak{S}_m \\ \mathfrak{S}'_m & 1 & \mathfrak{S}'_{m-1} \end{array} \right\} \right] \\
 & \times \left[ \delta_{i,1} + (1 - \delta_{i,1}) (-1)^{\mathfrak{L}_{i-1} + L'_i + \mathfrak{L}_i + r} [\mathfrak{L}_i, \mathfrak{L}'_i]^{1/2} \left\{ \begin{array}{ccc} \mathfrak{L}_{i-1} & L_i & \mathfrak{L}_i \\ r & \mathfrak{L}'_i & L'_i \end{array} \right\} \right. \\
 & \times (-1)^{\mathfrak{S}_{i-1} + S'_i + \mathfrak{S}_i + 1} [\mathfrak{S}_i, \mathfrak{S}'_i]^{1/2} \left\{ \begin{array}{ccc} \mathfrak{S}_{i-1} & S_i & \mathfrak{S}_i \\ 1 & \mathfrak{S}'_i & S'_i \end{array} \right\} \left. \right] \\
 & \times \langle l_i^{w_i} \alpha_i L_i S_i \| V^{(r1)} \| l_i^{w_i} \alpha'_i L'_i S'_i \rangle \langle l_j^{w_j} \alpha_j L_j S_j \| V^{(r1)} \| l_j^{w_j} \alpha'_j L'_j S'_j \rangle.
 \end{aligned} \tag{2.5.27}$$

If either the subshell  $l_i^{w_i}$  or the subshell  $l_j^{w_j}$  is filled,  $I^{(r)}$  for  $r > 0$  and  $I^{(r1)}$  for all  $r$  will become zero and (2.5.26) will be reduced to

$$g'_k(l_i l_j) = -\delta_{c,c'} \langle l_i \| C^{(k)} \| l_j \rangle^2 w_i w_j [l_i, l_j]^{-1}. \tag{2.5.28}$$

In order to find the contribution of the exchange interaction to the Hamiltonian matrix elements over and above  $E_{av}$  we have to subtract this value from (2.5.26). Because of the disappearance of  $g_k$  in the case of a filled subshell, the  $ij$  summation in (2.5.25) need only run over unfilled shells.

## 2.5.6 Direct and Exchange Interaction between Non-Equivalent Electrons

CASE 4: The electron-electron Coulomb matrix elements are of the form

$$\langle \psi | \sum_{i < j} \sum_k \frac{e^2 r^k}{r^{k+1}} C_{(m)}^{(k)} \cdot C_{(n)}^{(k)} | \psi' \rangle = \sum_{\rho \sigma \rho' \sigma'} \sum_k [r_d^k R_d^k(l_\rho l_\sigma, l_{\rho'} l_{\sigma'}) + r_e^k R_e^k(l_\rho l_\sigma, l_{\rho'} l_{\sigma'})] \tag{2.5.29}$$

in which the radial integrals are defined as

$$R_d^k(l_i l_j, l'_i l'_j) = \int_0^\infty \int_0^\infty \frac{e^2 r^k}{r^{k+1}} P_i^*(r_1) P_j^*(r_2) P_{i'}(r_1) P_{j'}(r_2) dr_1 dr_2, \tag{2.5.30}$$

and

$$R_e^k(l_i l_j, l'_i l'_j) \equiv R_d^k(l_i l_j, l'_i l'_j) = \int_0^\infty \int_0^\infty \frac{e^2 r^k}{r^{k+1}} P_i^*(r_1) P_j^*(r_2) P_{j'}(r_1) P_{i'}(r_2) dr_1 dr_2. \tag{2.5.31}$$

Here  $P_i$  and  $P_j$  are radial functions for the bra configuration and  $P_{i'}$  and  $P_{j'}$  correspond to the ket configuration. In contrast to the Slater integrals  $F^k$  and  $G^k$ , the  $R^k$  integrals are not necessarily positive. Analogous to the single configuration the factors  $r_d^k$  and  $r_e^k$  denote the angular coefficients of these radial integrals for the direct and exchange part.

The expressions for the  $r_d^k$  and  $r_e^k$  coefficients can be found in Cowan's textbook [7]. This kind of interactions is very small in most cases and therefore is neglected in this thesis.

The CI energy perturbations and the configuration mixing are largest when the magnitude of the CI matrix elements is large compared with the energy difference between the unperturbed levels. Consequently CI effects tend to be largest between configurations whose differences in the center-of-gravity energies  $E_{av}$  are small, and/or with cases in which the Coulomb matrix elements  $r^k R^k(ij, i'j')$  are large in magnitude. Large values of  $R^k$  tend to occur particularly when  $n_i n_j = n_{i'} n_{j'}$ , because the various radial wave functions then tend to have maximum overlap.

In order to keep the basis set manageable and small it is important that the Hamilton operator has even parity, and so the CI matrix elements are zero, unless the bra and ket functions have a common parity. Further, the Hamilton operator involves only one- and two-electron operators and thus the interactions can occur only between two configurations that differ at most in two orbitals. Furthermore, the matrix of the Coulomb operator in the  $LS$  representation is diagonal in the quantum numbers  $LS$ . Therefore non-zero Coulomb CI matrix elements exist only if both configuration have some basis states indicated with  $LS$  in common. Thus the two configurations  $sp$  and  $sf$  do not interact.

## 2.6 Crystal Field Splitting

In this section we describe the calculation of one of the most important part in the Hamiltonian: The crystal-field operator describe the influence of the surrounding ions on the energy levels of a given ion. We start with a general formulation of the electrostatic potential and give a brief overview of the Ewald sum formulation, which is essential in order to determine the crystal-field parameters  $A_{k,m}$ . In addition, we derive an expression for the matrix elements of the crystal-field operator, which is valid for a general configuration and not only for special cases [8].

### 2.6.1 Crystal-Field Theory and Ewald Sum Formulation

Crystal-field theory assumes that the ligands surrounding a given ion are fixed, non overlapping and have a hard spherical charge distributions with a definite arrangement (crystal structure). For the calculation of the electrostatic potential  $V(\vec{r})$ , the ions can be replaced by point charges, located at  $R_j = (r_j, \theta_j, \phi_j)$ , and  $V(\vec{r})$  can be expressed as a series of spherical harmonics [61]  $C_m^{(k)}(\theta, \phi)$ , where  $C_m^{(k)}(\theta, \phi)$  denotes the renormalized spherical harmonics (2.4.5)

$$V(\vec{r}) = \sum_{j=1}^N \sum_{k=0}^{\infty} \sum_{m=-k}^k A_{k,m} r_j^k C_m^{(k)}(\theta, \phi), \quad (2.6.1)$$

where,  $r_j^k$  denotes the expectation value of the  $k$ th power of the radius of ion  $j$ . Due to the parity of the spherical harmonics, we can restrict the sum over  $k$  to  $k \leq 2l_j$ , where  $l_j$  represents the angular momentum of the  $j$ th subshell. The crystal-field parameters  $A_{k,m}$  are given by the Taylor expansion [62] in  $r$  of the Ewald sum [10] around  $r = 0$ , with

$$A_{k,m} = \frac{q_j}{R_j^{k+1}} \sqrt{\frac{4\pi}{2k+1}} Y_k^{-m}(\theta_j, \phi_j), \quad (2.6.2)$$

Before the matrix elements of the crystal field can be determined with the help of the Racah-Wigner algebra, the crystal field-parameters  $A_{k,m}$  have to be known, which contain all characteristics of the crystal. The calculation of the electrostatic potential  $V$  is difficult because the sum in (2.6.1) does not converge. Therefore, the determination of these parameters is done by means of the Ewald summation method. If the sum of all charges in the unit cell is zero, then the potential can be rewritten as the sum of two terms:

$$V(\mathbf{r}) \equiv V_{RS}(\mathbf{r}) + V_{FS}(\mathbf{r}), \quad (2.6.3)$$

in which  $V_{RS}(\mathbf{r})$  represents the short-range term calculated in real space and  $V_{FS}(\mathbf{r})$  represents the long-range term calculated in Fourier space.  $V_{FS}(\mathbf{r})$  should be finite for all arguments (most notably  $r = 0$ ). The difficulty of the problem is reduced to the determination of the long-range part if we assume that the short-range part can be

done easily. Using the Fourier sum, we implicitly assume that the system under study is periodic. The electrostatic potential (2.6.1) is then given by the equation [63]

$$V(\mathbf{r}) = \sum_{g \neq 0} \frac{4\pi}{V_e g^2} e^{-g^2/4G^2 + i\mathbf{g}\mathbf{r}} \sum_n q_n e^{-i\mathbf{g}\mathbf{a}_n} + \sum_{\mathbf{l}, n} \frac{q_n}{|\mathbf{l} + \mathbf{a}_n - \mathbf{r}|} \operatorname{erfc}(G|\mathbf{l} + \mathbf{a}_n - \mathbf{r}|) - \frac{q_1}{r} \operatorname{erf}(Gr), \quad (2.6.4)$$

$\mathbf{l} \in \mathcal{T}$  are lattice vectors of a translation lattice  $\mathcal{T}$ , the expressions  $\mathbf{a}_n$  represent the lattice vectors of the unit cell,  $G$  is a parameter that determines the cut-off range of the real space sum, and the so-called error function are given by

$$\operatorname{erf}(z) \doteq \frac{2}{\sqrt{\pi}} \int_0^z e^{-t^2} dt, \quad \text{and} \quad \operatorname{erfc}(z) \doteq \frac{2}{\sqrt{\pi}} \int_z^\infty e^{-t^2} dt = 1 - \operatorname{erf}(z), \quad (2.6.5)$$

The two sums in (2.6.4) are absolutely convergent due to a Gaussian cut-off. Here only the Ewald sum expansion around  $r = 0$  is important. Thus we can use a Taylor expansion of the last term in (2.6.4)

$$\frac{1}{r} \operatorname{erf}(Gr) = \frac{2G}{\sqrt{\pi}} \left( 1 - \frac{(Gr)^2}{3} + \frac{(Gr)^4}{10} - \frac{(Gr)^6}{42} + \dots \right). \quad (2.6.6)$$

The prefactors  $A_{k,m}$  are the results of the Taylor expansion of the Ewald sum [62, 64] around  $r = 0$ , with

$$A_{k,m} = \frac{1}{\sqrt{k+m!}\sqrt{k-m!}} (\partial_z^{k-|m|} (-\operatorname{Sign}[m] \partial_x + i \partial_y)^{|m|}) V(r, \theta, \phi) \Big|_{r=0} \quad (2.6.7)$$

if  $k \leq 6$ . An alternative calculation of the  $A_{k,m}$  parameters has been developed by Huang [65].

## 2.6.2 Matrix Elements of the Crystal-Field Operator

The crystal-field operator acts only within a subshell  $j$  of a single configuration. The matrix elements of the crystal-field operator can be calculated by applying the Wigner-Eckart theorem

$$\begin{aligned} \langle \psi | V_j(r) | \psi' \rangle &= \langle \psi | \sum_{k=0}^{2l_j} \sum_{m=-k}^k A_{k,m}^j r_j^k C_m^{(k)}(\theta\phi) | \psi' \rangle \\ &= \sum_{k=0}^{2l_j} \sum_{m=-k}^k A_{k,m}^j (-1)^{\mathfrak{J}-\mathfrak{M}} \begin{pmatrix} \mathfrak{J} & k & \mathfrak{J}' \\ -\mathfrak{M} & m & \mathfrak{M}' \end{pmatrix} \langle \beta \mathfrak{J} \| r_j^k C_j^{(k)} \| \beta' \mathfrak{J}' \rangle, \end{aligned} \quad (2.6.8)$$

where “ $\langle \dots \| r_j^k C_j^{(k)} \| \dots \rangle$ ” represents the reduced matrix element and the expression in big brackets the Wigner-3j symbol. The term  $\beta \mathfrak{J}$  indicates the wave function (2.3.8) without the magnetic quantum number  $\mathfrak{M}$ . For calculating the reduced matrix element in (2.6.8), we can rewrite the reduced matrix element with Racah’s unit tensor:

$$\begin{aligned} \langle \beta \mathfrak{J} \| r_j^k C_j^{(k)} \| \beta' \mathfrak{J}' \rangle &= \langle \beta \mathfrak{J} \| U_j^{(k)} \| \beta' \mathfrak{J}' \rangle \langle n_j l_j \| r_j^k C_j^{(k)} \| n'_j l'_j \rangle \\ &\equiv \langle \beta \mathfrak{J} \| U_j^{(k)} \| \beta' \mathfrak{J}' \rangle P_{j,j'}^{(k)}. \end{aligned} \quad (2.6.9)$$

Applying the identity (2.4.11) to the unit-tensor matrix element we get the expression:

$$\begin{aligned} \langle \dots \mathfrak{L}_N \mathfrak{S}_N \mathfrak{J} \| U_j^{(k)} \| \dots \mathfrak{L}'_N \mathfrak{S}'_N \mathfrak{J}' \rangle &= \delta_{all\ spins} (-1)^{\mathfrak{L}_N + \mathfrak{S}_N + \mathfrak{J}' + k} [\mathfrak{J}, \mathfrak{J}']^{1/2} \left\{ \begin{array}{ccc} \mathfrak{L}_N & \mathfrak{S}_N & \mathfrak{J} \\ \mathfrak{J}' & k & \mathfrak{L}'_N \end{array} \right\} \\ &\times \langle \dots \mathfrak{L}_N \| U_j^{(k)} \| \dots \mathfrak{L}'_N \rangle, \end{aligned} \quad (2.6.10)$$

which describes the uncoupling of  $\mathfrak{L}_N$  from  $\mathfrak{J}$ . As the operator has an effect only on the orbital momentum, the matrix will be diagonal in all spins (denoted by the  $\delta$ -factor). For the calculation of the matrix elements we can ignore all spin couplings. In order to calculate the unit-tensor matrix element we have to apply (2.4.11) to (2.6.10) in order to uncouple  $L_N$  from  $\mathfrak{L}_N$ . This has to be done ( $N - j$ ) times if we successively want to uncouple  $L_i$  from  $\mathfrak{L}_i$  ( $i = \{j + 1, \dots, N\}$ ). And then finally (if  $j > 1$ ) using (2.4.12) to uncouple  $L_j$  from  $\mathfrak{L}_{j-1}$ . The result are  $\delta$ -factors in all quantum numbers,  $\alpha_j L_j$  and  $\mathfrak{L}_j$  excepted. The remaining matrix element in (2.6.10) then is:

$$\begin{aligned} \langle \dots \mathfrak{L}_N \| U_j^{(k)} \| \dots \mathfrak{L}'_N \rangle &= \left[ \prod_{m=j+1}^N \delta_{\alpha_m L_m, \alpha'_m L'_m} (-1)^{\mathfrak{L}_{m-1} + L_m + \mathfrak{L}'_m + k} \right. \\ &\quad \left. \times [\mathfrak{L}_m, \mathfrak{L}'_m]^{1/2} \left\{ \begin{array}{ccc} \mathfrak{L}_{m-1} & L_m & \mathfrak{L}_m \\ \mathfrak{L}'_m & k & \mathfrak{L}'_{m-1} \end{array} \right\} \right] \\ &\times \left[ \delta_{j1} + (1 - \delta_{j1}) \left( \prod_{m=1}^{j-1} \delta_{\alpha_m L_m, \alpha'_m L'_m} \right) \right. \\ &\quad \left. \times (-1)^{\mathfrak{L}_{j-1} + L'_j + \mathfrak{L}_j + k} [\mathfrak{L}_j, \mathfrak{L}'_j]^{\frac{1}{2}} \left\{ \begin{array}{ccc} \mathfrak{L}_{j-1} & L_j & \mathfrak{L}_j \\ k & \mathfrak{L}'_j & L'_j \end{array} \right\} \right] \\ &\times \langle l_j^{w_j} \alpha_j L_j S_j \| U^{(k)} \| l_j^{w_j} \alpha'_j L'_j S'_j \rangle, \end{aligned} \quad (2.6.11)$$

with  $w$  denoting the number of electrons in the  $j$ th subshell. Using (2.4.18), we can calculate the matrix element of the unit tensor  $U^{(k)}$ .

The reduced matrix element  $P_{j,j'}^{(k)}$  thus gets the form

$$\begin{aligned} P_{j,j'}^{(k)} &\equiv \langle n_j l_j \| r^k C^{(k)} \| n'_j l'_j \rangle = \langle l_j \| C^{(k)} \| l'_j \rangle \int_0^\infty R_{n_j, l_j}(r) r^k R_{n'_j, l'_j}(r) dr \\ &= (-1)^{l_j} [l_j, l'_j]^{1/2} \left( \begin{array}{ccc} l_j & k & l'_j \\ 0 & 0 & 0 \end{array} \right) \\ &\quad \times \int_0^\infty R_{n_j, l_j}(r) r^k R_{n'_j, l'_j}(r) dr. \end{aligned} \quad (2.6.12)$$

Here,  $R_{n_j, l_j}(r)$  is the radial wave function of the  $j$ th atom with quantum numbers  $n_j$  and  $l_j$ . The integral in (2.6.12) represents the expectation value of the  $k$ th power of the ionic radius.

## 2.7 Spin-Orbit Interaction

In solid-state physics the non-relativistic Schrödinger equation is only a first approximation. Neglecting relativistic corrections would lead to doubly degenerate bands, spin up and spin down, which can be split by a spin-dependent term in the Hamiltonian. The spin-orbit interaction describes the coupling between the angular momentum and the electron spin and represents a relativistic correction to the Schrödinger equation. The description of compounds including rare earth elements with open  $d$  and  $f$  shells requires the consideration of the spin-orbit interaction, because this interaction is stronger than the crystal field splitting. In this section we describe the derivation of the spin-orbit interaction and present Cowan's expressions [7] for the matrix element of the spin-orbit coupling for general configurations.

The energy of a magnetic dipole generated by the spin of an electron in a magnetic field is

$$V_{ls} = \mu_B \boldsymbol{\sigma} \mathbf{B}. \quad (2.7.1)$$

Here the magnetic field  $\mathbf{B}$  is excited by the moving nucleus. The problem for calculating this energy is the determination of the magnetic field  $\mathbf{B}$ . The intrinsic magnetic moment of the electron is  $\mu_B \boldsymbol{\sigma}$ , if the electron is motionless. In this picture, the electron sees nuclear charge the moving around the electron itself. Following Biot-Savart's law the magnetic field of the nucleus moving around the electron at the position of the electron is expressed by:

$$\mathbf{B} = -\frac{e \mathbf{v} \times \mathbf{r}}{c r^3}. \quad (2.7.2)$$

The electric field strength at a position  $\mathbf{r}$  is  $\mathbf{E} = e(\mathbf{r}/r^3)$ . Thus the magnetic field can be written as

$$\mathbf{B} = -\frac{1}{c} \mathbf{v} \times \mathbf{E}. \quad (2.7.3)$$

Replacing  $\mathbf{E}$  in (2.7.3) by the force  $\mathbf{F}$ , which is proportional to the gradient of the potential  $V(r)$ , the above equation (2.7.3) can be written as

$$\mathbf{B} = -\frac{1}{ec} (\mathbf{v} \times \mathbf{r}) \frac{1}{r} \frac{dV(r)}{dr}. \quad (2.7.4)$$

Introducing the angular momentum  $-\mathbf{l} = m\mathbf{v} \times \mathbf{r}$  we obtain the final equation for the magnetic field

$$\mathbf{B} = -\frac{1}{mecr} \frac{dV(r)}{dr} \mathbf{l}. \quad (2.7.5)$$

But in this picture the nucleus moves. The transformation to the nuclear frame is Lorentz invariant, because the moving particle is accelerated. This transformation was done by Thomas [67] and adds a factor of  $1/2$ , the so-called Thomas precession factor<sup>13</sup>.

<sup>13</sup>“An electric field with a component perpendicular to the electron velocity causes an additional acceleration of the electron perpendicular to its instantaneous velocity, leading to a curved electron trajectory. In essence, the electron moves in a rotating frame of reference, implying an additional precession of the electron, called the Thomas precession.”, see [68]

Thus the final formula for the energy of the electron is

$$V_{ls} = \mu_B \boldsymbol{\sigma} \mathbf{B}_l = \frac{\mu_B}{2m_e c r} \frac{dV(r)}{dr} (\boldsymbol{\sigma} \cdot \mathbf{l}) = \xi(r) (\mathbf{s} \cdot \mathbf{l}), \quad (2.7.6)$$

with

$$\xi(r) = \frac{1}{2m^2 c^2 r} \frac{dV(r)}{dr}. \quad (2.7.7)$$

Like the crystal-field operator, the spin-orbit operator acts only within a subshell of a given configuration and the matrix element of this operator can be calculated within the Racah-Wigner algebra. Here the tensor operator consists of the scalar product of the two irreducible tensor operators  $l^{(1)}$  and  $s^{(1)}$ . The reduced matrix element can be written as follows

$$\langle \psi | \sum_{j=1}^N \xi_j(r) \mathbf{l}_j^{(1)} \cdot \mathbf{s}_j^{(1)} | \psi' \rangle = \sum_{j=1}^q d_j \xi_j. \quad (2.7.8)$$

The radial integral  $\xi_j$  determines the size of the spin-orbit splitting:

$$\xi_j = \xi_{n_j l_j} = \frac{\alpha^2}{2} \int_0^\infty \frac{1}{r} \left( \frac{dV^j}{dr} \right) |P_{n_j l_j}(r)|^2 dr. \quad (2.7.9)$$

The coefficient  $d_j$  of the  $j$ th ion in the configuration can be expressed in terms of the unit operator (2.4.16) and we get the equation

$$d_j = w_j \langle l_j | \mathbf{l}^{(1)} | l_j \rangle \langle \psi | \mathbf{u}_j^{(1)} \cdot \mathbf{s}_j^{(1)} | \psi' \rangle. \quad (2.7.10)$$

In the Russell-Saunders coupling scheme, the matrix element (2.7.10) can be found by applying the uncoupling relation (2.4.13) for scalar products. In addition to the factor  $\delta_{\mathfrak{J}_q, \mathfrak{M}_q, \mathfrak{J}'_q, \mathfrak{M}'_q}$  the second matrix element in (2.7.10) is obtained by the procedure described above. It has the form:

$$\begin{aligned} & w_j \langle \dots (\mathfrak{L}_q \mathfrak{S}_q) \mathfrak{J}_q | \mathbf{u}_j^{(1)} \cdot \mathbf{s}_j^{(1)} | \dots (\mathfrak{L}'_q \mathfrak{S}'_q) \mathfrak{J}'_q \rangle \\ &= w_j (-1)^{\mathfrak{L}'_q + \mathfrak{S}_q + \mathfrak{J}_q} \left\{ \begin{array}{ccc} \mathfrak{L}_q & \mathfrak{S}_q & \mathfrak{J}_q \\ \mathfrak{S}'_q & \mathfrak{L}'_q & 1 \end{array} \right\} \langle \dots \mathfrak{L}_q | \mathbf{u}_j^{(1)} | \dots \mathfrak{L}'_q \rangle \langle \dots \mathfrak{S}_q | \mathbf{s}_j^{(1)} | \dots \mathfrak{S}'_q \rangle \\ &= (-1)^{\mathfrak{L}'_q + \mathfrak{S}_q + \mathfrak{J}_q} \left\{ \begin{array}{ccc} \mathfrak{L}_q & \mathfrak{S}_q & \mathfrak{J}_q \\ \mathfrak{S}'_q & \mathfrak{L}'_q & 1 \end{array} \right\} \langle \dots \mathfrak{L}_q \mathfrak{S}_q | V_j^{(11)} | \dots \mathfrak{L}'_q \mathfrak{S}'_q \rangle, \end{aligned} \quad (2.7.11)$$

in which the symmetric double tensor (2.4.21) has been introduced to make the notation more compact. If  $j < q$  we successively uncouple  $L_q S_q, L_{q-1} S_{q-1}, \dots$  and, finally

$L_{j+1}S_{j+1}$ . If  $j > 1$  we uncouple  $L_jS_j$  from  $\mathfrak{L}_{j-1}\mathfrak{S}_{j-1}$ . The final result then is

$$\begin{aligned}
 d_j = & \delta_{\mathfrak{J}_q, \mathfrak{M}_q, \mathfrak{J}'_q, \mathfrak{M}'_q} \left( \prod_{m \neq j} \delta_{\alpha_m L_m S_m, \alpha'_m L'_m S'_m} \right) \left( \prod_{m < j} \delta_{\mathfrak{L}_m, \mathfrak{S}_m, \mathfrak{L}'_m, \mathfrak{S}'_m} \right) \\
 & \times (-1)^{\mathfrak{L}'_q + \mathfrak{S}_q + \mathfrak{J}_q} \begin{Bmatrix} \mathfrak{L}_q & \mathfrak{S}_q & \mathfrak{J}_q \\ \mathfrak{S}'_q & \mathfrak{L}'_q & 1 \end{Bmatrix} \\
 & \times \left[ \prod_{m=j+1}^q (-1)^{\mathfrak{L}_{m-1} + L_m + \mathfrak{L}'_m + 1} [\mathfrak{L}_m, \mathfrak{L}'_m]^{1/2} \begin{Bmatrix} \mathfrak{L}_{m-1} & L_m & \mathfrak{L}_m \\ \mathfrak{L}'_m & 1 & \mathfrak{L}'_{m-1} \end{Bmatrix} \right. \\
 & \quad \left. \times (-1)^{\mathfrak{S}_{m-1} + S_m + \mathfrak{S}'_m + 1} [\mathfrak{S}_m, \mathfrak{S}'_m]^{1/2} \begin{Bmatrix} \mathfrak{S}_{m-1} & S_m & \mathfrak{S}_m \\ \mathfrak{S}'_m & 1 & \mathfrak{S}'_{m-1} \end{Bmatrix} \right] \\
 & \times \left[ \delta_{j1} + (1 - \delta_{j1}) (-1)^{\mathfrak{L}_{j-1} + L'_j + \mathfrak{L}_j + 1} [\mathfrak{L}_j, \mathfrak{L}'_j]^{1/2} \begin{Bmatrix} \mathfrak{L}_{j-1} & L_j & \mathfrak{L}_j \\ 1 & \mathfrak{L}'_j & L'_j \end{Bmatrix} \right. \\
 & \quad \left. \times (-1)^{\mathfrak{S}_{j-1} + S'_j + \mathfrak{S}_j + 1} [\mathfrak{S}_j, \mathfrak{S}'_j]^{1/2} \begin{Bmatrix} \mathfrak{S}_{j-1} & S_j & \mathfrak{S}_j \\ 1 & \mathfrak{S}'_j & S'_j \end{Bmatrix} \right] \\
 & \times \sqrt{l_j(l_j + 1)(2l_j + 1)} \langle l_j^{w_j} \alpha_j L_j S_j \| V^{(11)} \| l_j^{w_j} \alpha'_j L'_j S'_j \rangle.
 \end{aligned} \tag{2.7.12}$$

The reduced matrix element of  $V^{(11)}$  is zero for a closed subshell, so that  $d_j$  is also zero. The summation over  $j$  in (2.7.8) therefore needs to be carried out only with regard to partially filled subshells,  $1 \leq w_j \leq 4l_j + 1$ .

## 2.8 Hybridization and Tight-Binding Approximation

In this section we consider the hybridization within the Slater-Koster tight-binding approximation [11]. The hybridization describes the hopping of electrons between the ions being involved in the cluster-model calculation and mixes the eigenstates of these ions. This contribution describes also the interaction between two different configurations within the configuration interaction calculation. Without this contribution, the Hamilton matrix would be block diagonal. For the most transition-metal compounds, the hybridization is only a small but often important contribution to the Hamiltonian. We derived a new expression for the matrix elements of the tight-binding operator within the Sobel'man's parentage scheme approximation [12] valid for general configurations. We begin with a general introduction in the tight-binding formalism and the Slater-Koster approximation. In the following, we present Sharma's method of calculating the so-called *Slater-Koster coefficients* and Harrison's rules for determine the hopping integrals. We end up with an introduction of Sobel'man's parentage scheme approximation and the derivation of the expression for the matrix elements of the tight-binding operator.

### 2.8.1 Linear Combination of Atomic Orbitals (LCAO)

The contribution of hybridization is considered within the Slater-Koster tight-binding approximation [11]. The tight-binding formalism is an extension of Bloch's original LCAO<sup>14</sup> method [69], and can be directly derived from the density-functional theory [70]. Let us consider a periodic lattice, in which the lattice vectors are denoted as  $\mathbf{R}_m$ , with a set of atoms  $i$  located at positions  $\mathbf{b}_i$  in each unit cell. Associated with each atom is a set of atomic-like orbitals  $\phi_{i\alpha}$ , in which  $\alpha$  denotes both the orbital and the angular quantum numbers of the atomic state. In general, orbitals which are located on different atoms are not orthogonal. In this case, we use Löwdin's method [71] to construct a set of orthogonal wave functions  $\Psi_{i\alpha}$ ,

$$\int \Psi_{i\alpha}^*(\mathbf{r} - \mathbf{R}_m - \mathbf{b}_i) \Psi_{j\beta}(\mathbf{r} - \mathbf{R}_n - \mathbf{b}_j) d^3r = \delta_{i,j} \delta_{m,n}, \quad (2.8.2)$$

which have symmetry properties similar to those of the corresponding  $\phi_{i\alpha}$ .

We can describe the system by a set of non-interacting single-particle wave functions, which obey Fermi statistics, analogous to standard LCAO calculations and the Hohenberg-Kohn-Sham density-functional theory (DFT) formalism [72, 73]. Following

---

<sup>14</sup> Using the linear combination of atomic orbitals or LCAO method we can construct crystal wave functions  $\phi$  as a superposition of atomic orbitals  $\chi_r$

$$\phi = \sum_r c_r \chi_r, \quad (2.8.1)$$

each multiplied by a corresponding coefficient  $c_r$ . By minimizing the total energy of the system, we can determine an appropriate set of coefficients  $c_r$ .

Bloch's theorem we can write these wave functions as

$$\tilde{\Psi}_{\mathbf{k}i\alpha} = N^{-1/2} \sum_n e^{i\mathbf{k}\cdot\mathbf{R}_n} \Psi_{i\alpha}(\mathbf{r} - \mathbf{R}_n - \mathbf{b}_i), \quad (2.8.3)$$

in which  $\mathbf{k}$  is the Bloch wavevector and  $N$  is the number of unit cells in the sum. Diagonalizing the Hamiltonian  $\mathcal{H}$  and using the basis functions (2.8.3) we obtain the solution of Schrödinger's equation for wavevector  $\mathbf{k}$ . Within one of these blocks the matrix elements can be written in the form

$$\mathcal{H}_{i\alpha,j\beta}(\mathbf{k}) = \sum_n e^{i\mathbf{k}\cdot\mathbf{R}_n} \int \Psi_{i\alpha}^*(\mathbf{r} - \mathbf{R}_n - \mathbf{b}_i) \mathcal{H} \Psi_{j\beta}(\mathbf{r} - \mathbf{b}_j) d^3r, \quad (2.8.4)$$

in which the translation symmetry of the lattice is used to remove one of the sums over the lattice vectors  $\mathbf{R}_n$ . Given the Hamilton operator as a function of the wave vector  $\mathbf{k}$ , the band energy  $\varepsilon_n(\mathbf{k})$  is obtained by solving the single-particle Schrödinger equation

$$\sum_{nj} \mathcal{H}_{i\alpha,j\beta}(\mathbf{k}) c_{nj\beta}(\mathbf{k}) = \varepsilon_n(\mathbf{k}) c_{ni\alpha}(\mathbf{k}), \quad (2.8.5)$$

in which the  $c_{ni\alpha}(\mathbf{k})$  are the expansion coefficients of the Löwdin functions, and  $n$  is the band index.

## 2.8.2 Hopping Integrals

The Hamiltonian  $\mathcal{H}$  in (2.8.4) includes a single-particle potential, which may be written, without any approximation, as

$$V(\mathbf{r}) = \sum_{nk} V_k(\mathbf{r} - \mathbf{R}_n - \mathbf{b}_k), \quad (2.8.6)$$

in which the potential  $V_k$  is centered on the  $k$ th atom and vanishes at a certain distance from that atom. If we insert this expression and the wave function expansion (2.8.3) into (2.8.4), then each term of the integral results from either the regions centered around the two atomic-like wave functions  $\Psi_{i\alpha}$  and  $\Psi_{j\beta}$ , or from the regions centered around the potential at  $\mathbf{b}_k$ . So these integrals can be classified into four categories:

1. If all regions are located on the same atom, we speak of an *on-site* integral.
2. If the potential is located at the same position as one of the wave functions, while the other wave function is located at a different position, we speak of a *two-center* integral.
3. If both the wave functions and the potential are all located at different sites, we speak of a *three-center* integral.
4. If both wave functions come from the same site but the potential is on a different site. This category represents a crystal-field correction to the on-site terms. This category was not considered by Slater and Koster, but the formalism was developed by Mercer and Chou [75] and Cohen [76].

### 2.8.3 Slater-Koster Approximation

Following Slater and Koster [11], we regard the potentials  $V_k(r)$  as spherically symmetric. Therefore the wave functions  $\Psi$  and  $\phi$  can be specified by the usual angular-momentum quantum numbers. The on-site integrals only contribute to the diagonal elements of the Hamiltonian. In the two-center approximation the integrals in (2.8.4) depend only on the distance  $u$  between the two atoms, and the Hamiltonian has the form

$$\mathcal{H}_{\alpha\beta}^{ij}(\mathbf{u}) = \int \Psi_{i\alpha}^*(\mathbf{r} - \mathbf{u}) \mathcal{H}_{2c} \Psi_{j\beta}(\mathbf{r}) d^3r, \quad (2.8.7)$$

in which  $\mathcal{H}_{2c}$  is the two-center part of the Hamiltonian, i.e., the kinetic energy operator and a spherically symmetric potential centered on atom  $i$  or on atom  $j$ . These terms depend on the orientation of  $\mathbf{u}$ , on the distance between atoms ( $u = |\mathbf{u}|$ ), and on the angular momenta contained in the quantum numbers  $\alpha$  and  $\beta$ . If we restrict the atomic orbitals  $\phi_i$  to  $s$ ,  $p$ , and  $d$  angular momenta, then each term of equation (2.8.7) can be written in terms of 14 Slater-Koster parameters. Here these parameters will be expressed by the form  $H_{ab\gamma}(\mathbf{u})$ , in which  $a$  and  $b$  specify the angular momenta of the orbitals ( $s$ ,  $p$ ,  $d$ ,  $\dots$ ); and  $\gamma = \sigma, \pi, \delta$  specifies the component of the angular momentum relative to the direction  $\mathbf{u}$ . In the case of two identical atoms, four pairs of Slater-Koster parameters are related by symmetry resulting in ten independent parameters. Note, that the matrix elements are short range, i.e. the integral (2.8.7) will vanish if the wave functions  $\Psi_{i\alpha}(\mathbf{r} - \mathbf{u})$  and  $\Psi_{j\beta}(\mathbf{r})$  do not overlap. The on-site and two-center integrals  $\mathcal{H}_{ab\gamma}(\mathbf{u})$  are chosen to reproduce the first-principles single-particle band structure of the given crystal.

Mattheiss [77] modified this two-center tight-binding method in order to omit the Löwdin transformation and used non-orthogonal orbitals. As a consequence the basis functions (2.8.3) are replaced by the functions

$$\tilde{\phi}_{\mathbf{k}i\alpha}(\mathbf{r}) = N^{-1/2} \sum_n e^{i\mathbf{k}\cdot\mathbf{R}_n} \phi_{i\alpha}(\mathbf{r} - \mathbf{R}_n - \mathbf{b}_i). \quad (2.8.8)$$

Since these are no longer orthogonal, the problem of diagonalizing the Schrödinger equation is solved by transforming it into a generalized eigenvalue equation

$$\mathcal{H}\psi = \varepsilon S\psi. \quad (2.8.9)$$

This equation involves the equation of the Hamiltonian matrix elements (2.8.4) with  $\Psi_{i\alpha}$  replaced by the corresponding  $\phi_{i\alpha}$ , and an overlap matrix

$$S_{i\alpha,j\beta}(\mathbf{k}) = \sum_n e^{i\mathbf{k}\cdot\mathbf{R}_n} \int \phi_{i\alpha}^*(\mathbf{r} - \mathbf{R}_n - \mathbf{b}_i) \phi_{j\beta}(\mathbf{r} - \mathbf{b}_j) d^3r. \quad (2.8.10)$$

Since the matrix (2.8.10) does not include a Hamiltonian term, it can be exactly split up into on-site terms and two-center terms, as can be shown by the following definition:

$$S_{\alpha\beta}^{ij}(\mathbf{k}) = \int \phi_{i\alpha}^*(\mathbf{r} - \mathbf{u}) \phi_{j\beta}(\mathbf{r}) d^3r, \quad (2.8.11)$$

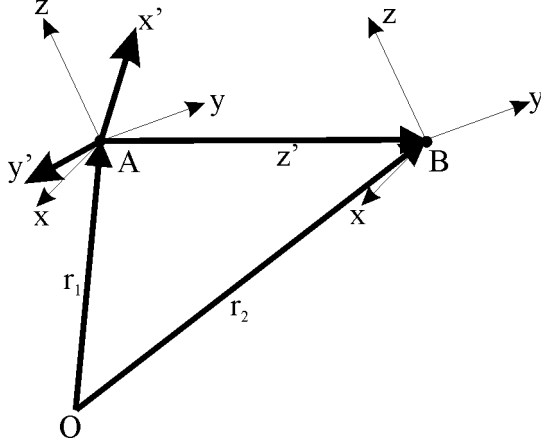


Figure 2.2: The coordinate systems  $x, y, z$  at  $A$  and  $B$  (in which the ions are located) are oriented parallel.

These terms show the same symmetry as the corresponding two-center Hamiltonian matrix elements (2.8.7). These two-center terms can be parameterized into terms denoted as  $S_{ab\gamma}$  in the same way as the corresponding Hamiltonian. This introduces another 14 Slater-Koster parameters (ten if the atoms are identical) for systems described in terms of  $s, p$ , and  $d$  orbitals. The use of this formalism with non-orthogonal wave functions has two advantages: The most obvious advantage is that we obtain additional parameters facilitate fitting band structures. The other advantage is connected with the usage of atomic wave functions: The two-center Slater-Koster parameters in equations (2.8.7) and (2.8.11) have a shorter range than the orthogonal wave functions  $\Psi$ , usually only a few nearest-neighbor shells and the non-orthogonal matrix elements depend only on the local environment of each atom.

### 2.8.4 Sharma's Method

Determining the Slater-Koster prefactors of the  $H_{ab\gamma}(\mathbf{u})$  can be done for any angular momentum number  $l_a, l_b$ , and  $\gamma$  by using Sharma's method [78]: The single-particle matrix element of the Hamilton operator (2.8.7) – with quantum numbers  $l_i, m_i$ , and ion positions  $\mathbf{r}_i$  – can be expressed as

$$\mathcal{H}_{l_1, m_1, l_2, m_2}(\mathbf{r}_1, \mathbf{r}_2) = \langle l_1 m_1 | \mathcal{H} | l_2 m_2 \rangle, \quad (2.8.12)$$

in which

$$|l_i m_i\rangle = u_i(\mathbf{r}) Y_{l_i}^{m_i}(\theta, \phi) \quad (2.8.13)$$

is the single-particle wave function of ion  $i$ . Here the  $u_i(\mathbf{r})$  represent the radial part of orbital  $|l_i m_i\rangle$ , which is measured with respect to the coordinate system  $(xyz)$  which has its origin at the ionic position  $\mathbf{r}_i$ . The orientation of the  $(xyz)$  system has been assumed to be the same as that of the two ions  $A$  and  $B$  (see Fig. 2.2). In order to orient the quantization axes of ion  $A$  and ion  $B$  antiparallel to each other and parallel

to the distance vector pointing from the origin  $A$  at  $\mathbf{r}_1$  to the origin  $B$  at  $\mathbf{r}_2$  we make use of the rotation groups and express the orbital  $|l_1 m_1\rangle$  at ion  $A$  as

$$|l_1 m_1\rangle = \sum_{m'_1} D_{m'_1, m_1}^{(l_1)}(\alpha, \beta, \gamma) |l_1 m'_1\rangle, \quad (2.8.14)$$

in which  $D_{m'_1, m_1}^{(l_1)}(\alpha, \beta, \gamma)$  denotes the rotation-group element. The Euler angles  $(\alpha, \beta, \gamma)$  define the rotation of the old coordinate system  $(xyz)$  into the new system  $(x'y'z')$  where the  $z'$  axis is parallel to the distance vector pointing from the origin  $A$  at  $\mathbf{r}_1$  to the origin  $B$  at  $\mathbf{r}_2$ . Analogous to the relation shown above we find the following relation for the orbitals located at ion  $B$

$$|l_2 m_2\rangle = \sum_{m'_2} D_{m'_2, m_2}^{(l_2)}(\alpha, \beta, \gamma) |l_2 m'_2\rangle. \quad (2.8.15)$$

Substitution of (2.8.14) and (2.8.15) in (2.8.12) provides the equation

$$\mathcal{H}_{l_1, m_1, l_2, m_2}(\mathbf{r}_1, \mathbf{r}_2) = \sum_{m'_1, m'_2} D_{m'_1, m_1}^{(l_1)*}(\alpha, \beta, \gamma) D_{m'_2, m_2}^{(l_2)}(\alpha, \beta, \gamma)' \langle l_1 m'_1 | \mathcal{H} | l_2 m'_2 \rangle'. \quad (2.8.16)$$

In the two-center approximation the following condition holds:

$$\langle l_1 m'_1 | \mathcal{H} | l_2 m'_2 \rangle = \langle l_1 m'_1 | \mathcal{H} | l_2 m'_1 \rangle \delta_{m'_1, m'_2}. \quad (2.8.17)$$

Rewriting (2.8.16) with (2.8.17) we get the relation

$$\mathcal{H}_{l_1, m_1, l_2, m_2}^{single} = \sum_{m'_1=0}^{\min(l_1, l_2)} (2 - \delta_{0, m'_1}) J(l_1, m_1, l_2, m_2; m'_1) \langle l_1 m'_1 | \mathcal{H} | l_2 m'_1 \rangle. \quad (2.8.18)$$

Here “ $J(l_1, m_1, l_2, m_2; m'_1)$ ” denotes the Slater-Koster coefficients and “ $\langle l_1 m'_1 | \mathcal{H} | l_2 m'_1 \rangle$ ” represents the two-center hopping integrals which can be determined by Harrison’s rules or by fitting the two-center hopping integrals to first-principle band structure calculations. For example, the expression “ $\langle 11 | \mathcal{H} | 21 \rangle$ ” represents the  $V_{pd\pi}$  hopping integral.

### 2.8.5 Harrison’s Rules

For transition-metals and for transition-metal compounds the hopping integrals  $V_{l_i, l_j, m}$  can be calculated by the general formula

$$V_{l_i, l_j, m} = \eta_{l_i, l_j, m} \frac{\hbar^2 \sqrt{r_{l_i}^{2l_i-1} r_{l_j}^{2l_j-1}}}{m d^{l_i+l_j+1}} \quad (2.8.19)$$

with

$$\eta_{l_i, l_j, m} = \frac{(-1)^{l_j+m+1}}{6\pi} \frac{(l_i + l_j)! (2l_i)! (2l_j)!}{2^{l_i+l_j} l_i! l_j!} \sqrt{\frac{(2l_i + 1)! (2l_j + 1)!}{(l_i + m)! (l_i - m)! (l_j + m)! (l_j - m)!}}. \quad (2.8.20)$$

The equations are derived by Harrison and Willis [80]. They are valid for arbitrary angular momenta  $l_i$  and  $l_j$ . In (2.8.19) the expression  $d$  represents the distance between the two ions  $A$  and  $B$ . The ionic radii of the ions are denoted by  $r_{l_i}$  and  $r_{l_j}$ , respectively. In order to determine the hopping integrals we can use one of the following formulae [79]:

$$V_{ss\sigma} = -1.32 \frac{\hbar^2}{md^2}, \quad (2.8.21)$$

$$V_{sp\sigma} = 1.42 \frac{\hbar^2}{md^2}, \quad (2.8.22)$$

$$V_{pp\sigma} = 2.22 \frac{\hbar^2}{md^2}, \quad (2.8.23)$$

$$V_{pp\pi} = -0.63 \frac{\hbar^2}{md^2}. \quad (2.8.24)$$

### 2.8.6 Sobel'man's Parentage-Scheme Approximation

The application of the Racah-Wigner algebra was not possible, because we were not able to express the tight-binding operator as a spherical tensor operator. Although Sobel'man's parentage scheme [12] is not as fast and elegant as the Racah-Wigner algebra we do not need to know the Slater determinants and conserve the ionic multiplet dependence as well. The tight-binding operator describes transitions of the following form

$$l^m [\alpha_1 L_1 S_1] l^p [\alpha_2 L_2 S_2] L S M_L M_S \rightarrow l^{m-1} [\alpha'_1 L'_1 S'_1] l^{p+1} [\alpha'_2 L'_2 S'_2] L' S' M'_L M'_S. \quad (2.8.25)$$

Here,  $m$  and  $p$  are the number of electrons in subshell 1 and 2,  $\alpha_k L_k S_k$  indicate the multiplet of subshell  $k = \{1, 2\}$ ,  $L = L_1 + L_2$  the total angular momentum,  $S = S_1 + S_2$  the total spin and,  $M_L$  and  $M_S$  their corresponding magnetic quantum number. The calculation of matrix elements for this transition is based on the reformulation of the multiplet wave functions for the  $n l^m$  and  $n' l'^{p+1}$  subshells in terms of (2.3.4). Following Sobel'man [12] the matrix element of a symmetric single-particle operator  $F = \sum_{i=1}^m f_i$  which describes the transition (2.8.25) may be written as

$$\begin{aligned} & \langle l^m [\alpha_1 L_1 S_1] l^p [\alpha_2 L_2 S_2] L S M_L M_S | F | l^{m-1} [\alpha'_1 L'_1 S'_1] l^{p+1} [\alpha'_2 L'_2 S'_2] L' S' M'_L M'_S \rangle \\ &= \sqrt{m(p+1)} (-1)^{\Delta p} \\ & \times (l^{m-1} \alpha'_1 L'_1 S'_1 \} l^m \alpha_1 L_1 S_1) \times (l^p \alpha_2 L_2 S_2 \} l^{p+1} \alpha'_2 L'_2 S'_2) \\ & \times \langle l^{m-1} [\alpha'_1 L'_1 S'_1] l [\alpha_1 L_1 S_1], l^p [\alpha_2 L_2 S_2] L S M_L M_S | f_N | \\ & \quad l^{m-1} [\alpha'_1 L'_1 S'_1], l^p [\alpha_2 L_2 S_2] l' [\alpha'_2 L'_2 S'_2] L' S' M'_L M'_S \rangle. \end{aligned} \quad (2.8.26)$$

In Sobel'man's expression (2.8.26),  $f_m$  describes the application of the single particle operator on the last ( $m$ th) coordinate. The matrix element in the last line of this equation includes the expression " $l^{m-1} [\alpha'_1 L'_1 S'_1] l [\alpha_1 L_1 S_1]$ ", which describes the coupling of a single electron, with angular momentum  $l$ , to the multiplet of subshell  $l^{m-1}$  indicated

by  $\alpha'_1 L'_1 S'_1$ , which built up the multiplet  $\alpha_1 L_1 S_1$  of the subshell  $l^m$ . The expression “ $l^p [\alpha_2 L_2 S_2] l' [\alpha'_2 L'_2 S'_2]$ ” represents the same procedure for the multiplet of subshell  $l^{p+1}$ . The factor  $\sqrt{m(p+1)} (-1)^{\Delta p}$  arises from coordinate permutations. The factor “ $\Delta p$ ” is equal to  $p$  if we consider a system, consisting of only two subshells. But, in the general case of  $q$  subshells

$$l_1^{w_1}, \dots, l_i^m, \dots, l_j^p, \dots, l_q^{w_q} \rightarrow l_1^{w'_1}, \dots, l_i^{m-1}, \dots, l_j^{p+1}, \dots, l_q^{w'_q}, \quad (2.8.27)$$

where  $w'_k = w_k$  for all subshells except  $k = i$  and  $k = j$ , we have to use Cowan’s expression [7] for  $\Delta p$

$$\Delta p \equiv p + \sum_{k=i+1}^{j-1} w_k. \quad (2.8.28)$$

Determining the tight-binding operator we rewrite (2.8.26) in terms of the single-particle operator (2.8.18).

For the matrix element of the tight-binding operator we obtain

$$\begin{aligned} \langle \psi | \mathcal{H}_{tb} | \psi' \rangle &= \langle \dots l_i^m \alpha_i L_i S_i \mathfrak{L}_i \mathfrak{S}_i \dots l_j^p \alpha_j L_j S_j \mathfrak{L}_j \mathfrak{S}_j \dots | \mathcal{H}_{tb} | \\ &\quad \dots l_i^{m-1} \alpha'_i L'_i S'_i \mathfrak{L}'_i \mathfrak{S}'_i \dots l_j^{p+1} \alpha'_j L'_j S'_j \mathfrak{L}'_j \mathfrak{S}'_j \dots \rangle \\ &= \sum_{M_{L_1}=-L_1}^{L_1} \sum_{M_{S_1}=-S_1}^{S_1} \dots \sum_{M_{L_k}=-L_k}^{L_k} \sum_{\mathfrak{M}_{\mathfrak{L}_k}=-\mathfrak{L}_k}^{\mathfrak{L}_k} \sum_{M_{S_k}=-S_k}^{S_k} \sum_{\mathfrak{M}_{\mathfrak{S}_k}=-\mathfrak{S}_k}^{\mathfrak{S}_k} \dots \\ &\quad \sum_{M'_{L'_1}=-L'_1}^{L'_1} \sum_{M'_{S'_1}=-S'_1}^{S'_1} \dots \sum_{M'_{L'_t}=-L'_t}^{L'_t} \sum_{\mathfrak{M}'_{\mathfrak{L}'_t}=-\mathfrak{L}'_t}^{\mathfrak{L}'_t} \sum_{M'_{S'_t}=-S'_t}^{S'_t} \sum_{\mathfrak{M}'_{\mathfrak{S}'_t}=-\mathfrak{S}'_t}^{\mathfrak{S}'_t} \dots \\ &\quad \sqrt{m(p+1)} (-1)^{\Delta p} (l^{m-1} \alpha'_i L'_i S'_i) \{l^m \alpha_i L_i S_i\} (l^p \alpha_j L_j S_j) \{l^{p+1} \alpha'_j L'_j S'_j\} \\ &\quad \times CG_{Total} \\ &\quad \times CG(L'_i, M'_{L_i}, l_i, m_{l_i}, L_i, M_{L_i}) CG(S'_i, M'_{S_i}, 0.5, m_{s_i}, S_i, M_{S_i}) \\ &\quad \times CG(L_j, M_{L_j}, l_j, m_{l_j}, L'_j, M'_{L_j}) CG(S_j, M_{S_j}, 0.5, m_{s_j}, S'_j, M'_{S_j}) \\ &\quad \times \delta_{m_{s_i}, m_{s_j}} \\ &\quad \times \mathcal{H}_{l_i m_{l_i}, l_j m_{l_j}}^{single}, \end{aligned} \quad (2.8.29)$$

in which

$$\begin{aligned} m_{l_i} &\equiv (M_{L_i} - M'_{L_i}), & m_{l_j} &\equiv (M'_{L_j} - M_{L_j}), \\ m_{s_i} &\equiv (M_{S_i} - M'_{S_i}), & m_{s_j} &\equiv (M'_{S_j} - M_{S_j}). \end{aligned} \quad (2.8.30)$$

The definition of these quantum numbers is justified by the Clebsch-Gordan coefficients ( $CG$ ), which are zero otherwise. The parameters  $k$  and  $t$  indicate that all summations

for  $2 \leq k \leq q$  and  $2 \leq t \leq q$  have to be inserted in (2.8.29). The appearance of the  $\delta$ -factor is caused by the fact that the tight-binding operator has no effect on the spin quantum numbers.

The term  $CG_{Total}$  represents the total Clebsch-Gordan coefficient which couples all angular momenta in the wave functions  $\psi$  and  $\psi'$ . It is defined as

$$\begin{aligned}
 CG_{Total} \equiv & CG(\mathfrak{L}_q, \mathfrak{M}_{\mathfrak{L}_q}, \mathfrak{S}_q, \mathfrak{M}_{\mathfrak{S}_q}, \mathfrak{J}_q, \mathfrak{M}_{\mathfrak{J}_q}) CG(\mathfrak{L}'_q, \mathfrak{M}'_{\mathfrak{L}'_q}, \mathfrak{S}'_q, \mathfrak{M}'_{\mathfrak{S}'_q}, \mathfrak{J}'_q, \mathfrak{M}'_{\mathfrak{J}'_q}) \\
 & \times \prod_{i=2}^q \left[ CG(\mathfrak{L}_{i-1}, \mathfrak{M}_{\mathfrak{L}_{i-1}}, L_i, M_{L_i}, \mathfrak{L}_i, \mathfrak{M}_{\mathfrak{L}_i}) \right. \\
 & \quad \times CG(\mathfrak{S}_{i-1}, \mathfrak{M}_{\mathfrak{S}_{i-1}}, S_i, M_{S_i}, \mathfrak{S}_i, \mathfrak{M}_{\mathfrak{S}_i}) \\
 & \quad \times CG(\mathfrak{L}'_{i-1}, \mathfrak{M}'_{\mathfrak{L}'_{i-1}}, L'_i, M'_{L'_i}, \mathfrak{L}'_i, \mathfrak{M}'_{\mathfrak{L}'_i}) \\
 & \quad \left. \times CG(\mathfrak{S}'_{i-1}, \mathfrak{M}'_{\mathfrak{S}'_{i-1}}, S'_i, M'_{S'_i}, \mathfrak{S}'_i, \mathfrak{M}'_{\mathfrak{S}'_i}) \right],
 \end{aligned} \tag{2.8.31}$$

in which

$$\begin{aligned}
 \mathfrak{L}_1 & \equiv L_1, & \mathfrak{L}'_1 & \equiv L'_1, \\
 \mathfrak{S}_1 & \equiv S_1, & \mathfrak{S}'_1 & \equiv S'_1.
 \end{aligned} \tag{2.8.32}$$

In order to save computation time we rewrite the matrix element (2.8.29) as follows:

$$\langle \psi | \mathcal{H}_{tb} | \psi' \rangle = \sum_{m_i=-l_i}^{l_i} \sum_{m_j=-l_j}^{l_j} \mathcal{M}(l_i, m_i, l_j, m_j) \times \mathcal{H}_{l_i m_i, l_j m_j}^{single}. \tag{2.8.33}$$

Here  $\mathcal{M}(l_i, m_i, l_j, m_j)$  represents the matrix element in (2.8.29) with the last line  $\mathcal{H}_{l_i m_i, l_j m_j}^{single}$  omitted. The matrix  $\mathcal{M}(l_i, m_i, l_j, m_j)$  depends on the quantum numbers  $(l_i, m_i, l_j, m_j)$  and the two configurations  $\psi$  and  $\psi'$  involved. By calculating  $\mathcal{M}$  only once depending on the two configurations  $\psi$  and  $\psi'$  we can reduce the time for the calculation.

### 2.8.7 Racah-Wigner expression for the tight-binding operator

In contrast to the statements written above we find finally an expression for the tight-binding operator within the Racah-Wigner algebra. We start with a formula similar to those given by Arrio *et al.* [82]

$$\mathcal{H}_{tb}(l_i, l_j) = \sum_{m'_1=0}^{\min(l_i, l_j)} \sum_{t=0}^{\infty} \sum_{q=-t}^t b_q^t(l_i, l_j, m'_1) C_q^{(t)}. \tag{2.8.34}$$

In order to express the tight-binding operator within the Slater-Koster approximation we have to determine the  $b_q^t$  coefficients by setting Sharma's expression for the Slater-

Koster prefactors [78]

$$J(l_1, m_1, l_2, m_2, m'_1) = (-1)^{m'_1 - m_2} \sum_{l=|l_1 - l_2|}^{l_1 + l_2} \left[ \sqrt{(4\pi) \cdot (2l + 1)} \begin{pmatrix} l_1 & l_2 & l \\ -m'_1 & m'_1 & 0 \end{pmatrix} \right. \\ \left. \times \begin{pmatrix} l_1 & l_2 & l \\ -m_1 & m_2 & m_1 - m_2 \end{pmatrix} Y_{m_2 - m_1}^t(\beta, \alpha) \right], \quad (2.8.35)$$

equal to an expansion over spherical harmonics

$$J(l_1, m_1, l_2, m_2, m'_1) = \sum_{t=|l_1 - l_2|}^{l_1 + l_2} \sum_{q=-t}^t \left[ b_q^t(l_i, l_j, m'_1) \cdot c^t(l_1 m_1 l_2 m_2) \right]. \quad (2.8.36)$$

Here, the expression

$$c^t(l_1 m_1 l_2 m_2) \equiv \langle l_1 m_1 | C_{m_1 - m_2}^{(t)} | l_2 m_2 \rangle \\ = \left( \frac{4\pi}{\sqrt{(2k + 1)}} \right)^{1/2} \int_0^{2\pi} \int_0^\pi Y_{m_1}^{*l_1}(\theta, \phi) Y_{m_1 - m_2}^k(\theta, \phi) Y_{m_2}^{l_2}(\theta, \phi) \sin \theta d\theta d\phi \\ = (-1)^{m_1} \sqrt{(2l_1 + 1)(2l_2 + 1)} \cdot \begin{pmatrix} l_1 & t & l_2 \\ 0 & 0 & 0 \end{pmatrix} \begin{pmatrix} l_1 & t & l_2 \\ -m_1 & m_1 - m_2 & m_2 \end{pmatrix}, \quad (2.8.37)$$

denotes the Gaunt coefficients [55], which include strong selection rules due to the 3j-symbols being involved in (2.8.37). Thus, we can restrict the summation over  $t$  in (2.8.34) to the range from  $|l_i - l_j|$  to  $(l_i + l_j)$ . Solving (2.8.34) for the different values of  $l_i$ ,  $l_j$ , and  $m'_1$  we get the  $b_q^t$  coefficients which are tabulated in Appendix B.

In order to derive an expression for the matrix elements of the tight-binding operator, which is valid for arbitrary configurations, we modify the formula for the dipole operator

$$\langle \psi | r^t C_q^{(t)} | \psi' \rangle \rightarrow \langle \psi | b_q^t C_q^{(t)} | \psi' \rangle, \quad (2.8.38)$$

and get the following expression for the matrix elements of the tight-binding operator<sup>15</sup>

$$\langle \psi | \mathcal{H}_{tb} | \psi' \rangle = \langle \dots l_i^n \alpha_i L_i S_i \mathfrak{L}_i \mathfrak{S}_i \dots l_j^k \alpha_j L_j S_j \mathfrak{L}_j \mathfrak{S}_j \dots | \mathcal{H}_{tb} | \\ \dots l_i^{n-1} \alpha'_i L'_i S'_i \mathfrak{L}'_i \mathfrak{S}'_i \dots l_j^{k+1} \alpha'_j L'_j S'_j \mathfrak{L}'_j \mathfrak{S}'_j \dots \rangle \\ = \sum_{m'_1=0}^{\min(l_i, l_j)} \sum_{t=|l_1 - l_2|}^{l_1 + l_2} \sum_{q=-t}^t (-1)^{\mathfrak{J}_q - \mathfrak{M}_q} \begin{pmatrix} \mathfrak{J}_q & t & \mathfrak{J}'_q \\ -\mathfrak{M}_q & q & \mathfrak{M}'_q \end{pmatrix} b_q^t(l_i, l_j, m'_1) \cdot D_{\mathfrak{L}\mathfrak{S}} \quad (2.8.39)$$

Here, we use Cowan's expressions [7] for the reduced matrix elements of the dipole operator

$$D_{\mathfrak{L}\mathfrak{S}} \equiv D_1 \cdot D_2 \cdot D_3 \cdot D_4 \cdot D_5 \cdot D_6 \cdot D_7 \cdot P_{l_i l_j}^{(t)}, \quad (2.8.40)$$

<sup>15</sup>Due to the strong selection rules of the 3j-symbol, the matrix elements vanish for  $q \neq \mathfrak{M}_q - \mathfrak{M}'_q$ .

and replace the factor  $P_{l_i l_j}^{(t)} \equiv \langle n_i l_i | r^{(t)} | n_j l_j \rangle$  by 1. The factor  $D_{\mathfrak{E}\mathfrak{S}}$  consists of seven factors, which describe cfp expansions, recouplings, and uncouplings. In the following we will give a brief discussion of each factor.

The first factor  $D_1$  arises from coordinate permutations and is given by

$$D_1 = (-1)^{\Delta p} \sqrt{n \cdot k}, \quad (2.8.41)$$

with

$$\Delta p = k - 1 + \sum_{m=i+1}^{j-1} w_m. \quad (2.8.42)$$

The factor  $D_2$  describes an expansion over coefficient-of-fractional-parentage and is defined by

$$D_2 = (l_i^n \alpha_i L_i S_i \{ | l_i^{n-1} \alpha'_i L'_i S'_i \} (l_j^{k-1} \alpha_j L_j S_j | \} l_j^k \alpha'_j L'_j S'_j). \quad (2.8.43)$$

Note, the factor is unequal to 1 only for  $n > 2$  and/or  $k > 2$ .

Additionally, we have to uncouple  $\mathfrak{S}$  from  $\mathfrak{L}$  and  $\mathfrak{L}'$  and get a further factor

$$D_3 = \delta_{\mathfrak{S}_q, \mathfrak{S}'_q} (-1)^{\mathfrak{L}_q + \mathfrak{S}_q + \mathfrak{J}'_q + t} [\mathfrak{J}_q, \mathfrak{J}'_q]^{1/2} \left\{ \begin{array}{ccc} \mathfrak{L}_q & \mathfrak{S}_q & \mathfrak{J}_q \\ \mathfrak{J}'_q & t & \mathfrak{L}'_q \end{array} \right\}. \quad (2.8.44)$$

If  $q > j$  we have to repeatedly uncouple  $L_q, L_{q-1}, \dots, L_{j+1}$  and obtain the following factor

$$D_4 = \prod_{m=j+1}^q \delta_{\alpha_m L_m S_m, \alpha'_m L'_m S'_m} \delta_{\mathfrak{S}_m \mathfrak{S}'_m} (-1)^{\mathfrak{L}_{m-1} + L_m + \mathfrak{L}'_m + t} [\mathfrak{L}_m, \mathfrak{L}'_m]^{1/2} \\ \times \left\{ \begin{array}{ccc} \mathfrak{L}_{m-1} & L_m & \mathfrak{L}_m \\ \mathfrak{L}'_m & t & \mathfrak{L}'_{m-1} \end{array} \right\}. \quad (2.8.45)$$

If  $i > 1$  we have to recouple from  $l_{i-1}^{w_i-1} (l_i^{n-1} l_i)$  to  $(l_{i-1}^{w_i-1} l_i^{n-1}) l_i$  and get the following factor

$$D_5 = \left( \prod_{m=1}^{i-1} \delta_{\alpha_m L_m S_m, \alpha'_m L'_m S'_m} \delta_{\mathfrak{L}_m \mathfrak{S}_m, \mathfrak{L}'_m \mathfrak{S}'_m} \right) \\ \times (-1)^{\mathfrak{L}_{i-1} + L'_i + l_i + \mathfrak{L}_i} [\mathfrak{L}'_i, L_i]^{1/2} \left\{ \begin{array}{ccc} \mathfrak{L}_{i-1} & L'_i & \mathfrak{L}'_i \\ l_i & \mathfrak{L}_i & L_i \end{array} \right\} \\ \times (-1)^{\mathfrak{S}_{i-1} + S'_i + s_i + \mathfrak{S}_i} [\mathfrak{S}'_i, S_i]^{1/2} \left\{ \begin{array}{ccc} \mathfrak{S}_{i-1} & S'_i & \mathfrak{S}'_i \\ s_i & \mathfrak{S}_i & S_i \end{array} \right\}. \quad (2.8.46)$$

If  $i < (j-1)$ , we get an additional factor of the following form, which describes the jump of  $l_i$  over each of the intervening subshells  $i < m < j$

$$D_6 = \left( \prod_{m=i+1}^{j-1} \delta_{\alpha_m L_m S_m, \alpha'_m L'_m S'_m} (-1)^{l_i + L_m + \mathfrak{L}_{m-1} + \mathfrak{L}'_m} [\mathfrak{L}_{m-1}, \mathfrak{L}'_m]^{1/2} \left\{ \begin{array}{ccc} l_i & \mathfrak{L}'_{m-1} & \mathfrak{L}_{m-1} \\ L_m & \mathfrak{L}_m & \mathfrak{L}'_m \end{array} \right\} \right. \\ \left. \times (-1)^{s_i + S_m + \mathfrak{S}_{m-1} + \mathfrak{S}'_m} [\mathfrak{S}_{m-1}, \mathfrak{S}'_m]^{1/2} \left\{ \begin{array}{ccc} s_i & \mathfrak{S}'_{m-1} & \mathfrak{S}_{m-1} \\ S_m & \mathfrak{S}_m & \mathfrak{S}'_m \end{array} \right\} \right). \quad (2.8.47)$$

Finally, we have to recouple  $l_i$  once more and obtain

$$\begin{aligned}
 D_7 = & \delta_{\mathfrak{S}_j, \mathfrak{S}'_j} (-1)^{\mathfrak{S}'_{j-1} + S'_j + \mathfrak{S}_j} [\mathfrak{S}_{j-1}, S'_j]^{1/2} \begin{Bmatrix} \mathfrak{S}'_{j-1} & S'_j & \mathfrak{S}_j \\ S_j & \mathfrak{S}_{j-1} & s \end{Bmatrix} \\
 & \times (-1)^{L_j + l_j + L'_j} [\mathfrak{L}_{j-1}, L'_j, \mathfrak{L}_j, \mathfrak{L}'_j]^{1/2} \begin{Bmatrix} \mathfrak{L}_{j-1} & \mathfrak{L}'_{j-1} & l_i \\ L_j & L'_j & l_j \\ \mathfrak{L}_j & \mathfrak{L}'_j & t \end{Bmatrix}. \tag{2.8.48}
 \end{aligned}$$

Although Cowan's result is rather complex, it provides a general, closed-form expression which can be perfectly used by the computer program.

## 2.9 Exchange Interactions

In this section we treat the “direct” Coulomb and exchange interaction between two atomic shells at different sites. The usage of this mechanism offers the description of magnetic ion systems with unquenched orbital momenta. Although this contribution to the Hamiltonian is not considered in the analysis of the optical spectra, it continues the explanation in section “2.5 Coulomb interaction”.

Following Levy [83], we can express the matrix element as

$$\langle \phi'_a(1)\phi'_b(2) | -\frac{e^2}{r_{ij}} | \phi_a(1)\phi_b(2) \rangle. \quad (2.9.1)$$

Although the operator  $e^2/r_{ij}$  is a two-electron operator, it operates on two different antisymmetrized sets of states. Therefore, with respect to each ion, the interatomic exchange operator is a one-electron operator.

In order to evaluate the matrix elements we have to expand the orbitals about another center; therefore we refer all wave functions to a common center and use the one-center expansion

$$\frac{1}{r_{12}} = \sum_{k=0}^{\infty} \frac{r_{<}^k}{r_{>}^{k+1}} C^{(k)}(1) \cdot C^{(k)}(2), \quad (2.9.2)$$

where

$$C_q^{(k)}(i) = \sqrt{\frac{4\pi}{(2k+1)}} Y_{kq}(\Omega_i) \quad (2.9.3)$$

and  $r_{<}$  is the lesser and  $r_{>}$  the greater of  $r_1$  and  $r_2$ .

If we assume that the expansion of  $1/r_{12}$  is given in terms of operators referred to center  $A$ , we have to reexpress the wave functions about center  $B$ , in terms of harmonics referred to center  $A$  using the expression [84]

$$\begin{aligned} \psi(r_{ib}) = R_{nL}(r_{ib})Y_{LM}(\Omega_{ib}) &= \sum_{l=0}^{\infty} \sum_{\lambda=|L-l|}^{L+l} \nu'_{l\lambda nL}(r_{ia}, R_{ab}) ([l] [\lambda] / 4\pi)^{1/2} \\ &\times \bar{V}(l L \lambda; 0 0 0) [Y^{[l]}(\Omega_{ab}) \times Y^{[l]}(\Omega_{ia})]_M^{[L]} \end{aligned} \quad (2.9.4)$$

where

$$\begin{aligned} r_{ib} &= r_{ia} - R_{ab}, \\ \nu'_{l\lambda nL}(r_{ia}, R_{ab}) &\equiv \frac{1}{\pi} \int_{-\infty}^{\infty} j_{\lambda}(kR_{ab}) j_l(kr_{ia}) \bar{\psi}(k) k^2 dk, \end{aligned} \quad (2.9.5)$$

and

$$\bar{\psi}(k) \equiv 4\pi \int_0^{\infty} R_{nL}(r_{ib}) j_L(kr_{ib}) r_{ib}^2 dr_{ib}. \quad (2.9.6)$$

The  $j_\lambda(kR)$  represent spherical Bessel functions, the spherical harmonics follow the convention of Fano and Racah [52]. The  $\bar{V}$  symbols are related to the Wigner 3-j symbols:

$$\bar{V}(j_1 j_2 j_3; m_1 m_2 m_3) = (-1)^{j_1+j_2+j_3} \begin{pmatrix} j_1 & j_2 & j_3 \\ m_1 & m_2 & m_3 \end{pmatrix}. \quad (2.9.7)$$

By using a rather lengthy recoupling [83], we can write the matrix element (2.9.1) as follow:

$$\begin{aligned} \langle \phi'_a(1) \phi'_b(2) | & \sum_{k_1=|l'_a-l_a|}^{l'_a+l_a} \sum_{k_2=|l'_b-l_b|}^{l'_b+l_b} \sum_{\Lambda=|k_1-k_2|}^{k_1+k_2} -\Gamma_{k_1 k_2 \Lambda}(n'_a l'_a n'_b l'_b, n_a l_a n_b l_b) \\ & \times [u^{[k_1]}(1) \times u^{[k_2]}(2) \times C^{[\Lambda]}(\Omega_{ab})]^{[0]} \left( \frac{1}{2} + 2s_1 \cdot s_2 \right) | \phi_a(1) \phi_b(2) \rangle \end{aligned} \quad (2.9.8)$$

where  $\phi_a(i) \equiv |l_a m_a\rangle | \frac{1}{2} m_{s\alpha} \rangle$ , and

$$\begin{aligned} \Gamma_{k_1 k_2 \Lambda} & \equiv (-1)^{l_a+l'_b+\frac{1}{2}(k_1+k_2+\Lambda)} (e/4\pi)^2 [k_1][k_2][\Lambda] ([l'_a][l_a][l'_b][l_b])^{1/2} \\ & \times \sum_{k,l,l'=0}^{\infty} \sum_{\lambda=|l_b-l|}^{l_b+l} \sum_{\lambda'=|l'_b-l'|}^{l'_b+l'} (-1)^k [l][l'][\lambda][\lambda'] \bar{V}(l'_a l k; 000) \bar{V}(l' l_a k; 000) \\ & \times \bar{V}(l_b l \lambda; 000) \bar{V}(l' l'_b \lambda'; 000) \bar{V}(\lambda \lambda' \Lambda; 000) \left\{ \begin{matrix} l_a & l'_a & k_1 \\ l & l' & k \end{matrix} \right\} \left\{ \begin{matrix} \Lambda & k_2 & k_1 \\ \lambda & l_b & l \\ \lambda' & l'_b & l' \end{matrix} \right\} \\ & \times \int_0^\infty \int_0^\infty \frac{r^k}{r^{k+1}} R_{n'_a l'_a}(r_1) \nu'_{l \lambda n_b l_b}(r_1, R_{ab}) R_{n_a l_a}(r_2) \nu'_{l' \lambda' n'_b l'_b}(r_2, R_{ab}) r_1^2 r_2^2 dr_1 dr_2. \end{aligned} \quad (2.9.9)$$

Comparing this expression with Racah's result for one center, we find that in contrast to the one-center problem, where angular momentum is conserved and the product of the two operators is a scalar invariant, the spherical harmonic in the triple product of the two-center expansion requires that the irreducible products of these operators be nonscalar. The radial integrals in the coefficient  $\Gamma_{k_1 k_2 \Lambda}$  correspond to the Slater  $G^k$  integrals for one center.

## 2.10 External Fields

Up to now all contributions to the Hamiltonian  $\mathcal{H}$  were considered without static external fields, i.e., without a static external magnetic field or a static external electric field. The external fields, especially the magnetic field, become relevant, if we calculate observable like the magnetic susceptibility, and compare these with experimental data. Starting from Cowan's expressions [7] for the Stark and the Zeeman effect we derive generalized equations for the matrix elements of the Stark and the magnetic-moment operator, valid for arbitrary configurations.

### 2.10.1 Stark Effect

A uniform, static, external electric field  $\mathfrak{E}$  exerts forces on the nuclei and on the electrons in the crystal that are mostly parallel and antiparallel to  $\mathfrak{E}$ , respectively. These polarize the ions and produce non-zero electric dipole moments with magnitudes, which are proportional in first order to the field strength. The degeneracy of the atomic levels with respect to  $M_L$  but not to the spin quantum number  $M_S$  is removed. This effect was first observed by Stark [85]. It is caused by the interaction between the ions and the external field: Applying an external electric field  $\mathfrak{E}$  to the crystal adds a further term – the so-called Stark term – to the Hamilton operator:

$$\mathcal{H}_{Stark} = \mathfrak{E} \sum_i e \mathbf{r}_i. \quad (2.10.1)$$

In order to get the eigenvalues of this operator in rydbergs ( $e^2/2a_0$ ), the strength of the electric field  $\mathfrak{E}$  is measured in units of

$$\frac{e^2}{a_0^2} = 5.1423 \cdot 10^{-9} \text{ volts/cm}. \quad (2.10.2)$$

An additional factor 2 is thereby introduced on the right-hand side of (2.10.1).

To determine the matrix elements of this operator

$$\langle \psi | \mathcal{H}_{Stark} | \psi' \rangle = 2 \mathfrak{E} \langle \psi | \sum_i e \mathbf{r}_i | \psi' \rangle \quad (2.10.3)$$

we have to express the position vector  $\mathbf{r}$ , which is a vector operator, as a tensor operator: A vector operator  $\mathbf{V}$  with vector components  $V_x$ ,  $V_y$ , and  $V_z$  can be written as an irreducible tensor operator  $\mathbf{T}$  of rank one. The components are given by

$$\begin{aligned} T_1^{(1)} &= -\frac{1}{\sqrt{2}} (V_x + i V_y), \\ T_{-1}^{(1)} &= \frac{1}{\sqrt{2}} (V_x - i V_y), \\ T_0^{(1)} &= V_z. \end{aligned} \quad (2.10.4)$$

These three functions are proportional to the three spherical harmonics  $Y_{11}$ ,  $Y_{10}$  and  $Y_{1-1}$ . The normalization prefactors  $(-1/\sqrt{2}, 1/\sqrt{2}, 1)$  are chosen such that  $T_0^{(1)}$  is identical with  $V_z$ . So we can write the position vector  $\mathbf{r}$  as an irreducible tensor operator of rank one by using the renormalized spherical harmonics (2.4.5)

$$\mathbf{r}^{(1)} = rC^{(1)}. \quad (2.10.5)$$

Thus we can apply the Wigner-Eckart theorem to calculate the matrix elements of the Stark operator (2.10.3):

$$h_{\psi, \psi'}^q \equiv \langle \psi | \mathcal{H}_{Stark}^q | \psi' \rangle = -2 \mathfrak{E}_q e \sum_{j=1}^N (-1)^{\mathfrak{J}-\mathfrak{M}} \begin{pmatrix} \mathfrak{J} & 1 & \mathfrak{J}' \\ -\mathfrak{M} & q & \mathfrak{M}' \end{pmatrix} \langle \beta \mathfrak{J} \| r_j C_j^{(1)} \| \beta' \mathfrak{J}' \rangle, \quad (2.10.6)$$

with  $\beta = (\alpha_1 L_1 S_1 \mathfrak{L}_1 \mathfrak{S}_1 \dots \alpha_N L_N S_N \mathfrak{L}_N \mathfrak{S}_N)$ .

Here the expression  $q = \{-1, 0, 1\}$  represents one of the components of the tensor operator  $\mathbf{r}^{(1)}$ . The matrix elements of the vector operator components can be determined by using linear combinations of these tensor operator components  $h_{\psi, \psi'}^{(q)}$ :

$$\begin{aligned} \langle \psi | V_x | \psi' \rangle &= -\frac{1}{\sqrt{2}} \left( h_{\psi, \psi'}^{(q=1)} - h_{\psi, \psi'}^{(q=-1)} \right), \\ \langle \psi | V_y | \psi' \rangle &= \frac{i}{\sqrt{2}} \left( h_{\psi, \psi'}^{(q=1)} + h_{\psi, \psi'}^{(q=-1)} \right), \\ \langle \psi | V_z | \psi' \rangle &= h_{\psi, \psi'}^{(q=0)}. \end{aligned} \quad (2.10.7)$$

Due to the fact that an electric field has no effect on the spin quantum numbers, the reduced matrix elements (2.10.6) can be determined analogously to the crystal-field operator (2.6.8). We can rewrite the reduced matrix element (2.10.6) with Racah's unit tensor:

$$\begin{aligned} \langle \beta \mathfrak{J} \| r_j C_j^{(1)} \| \beta' \mathfrak{J}' \rangle &= \langle \beta \mathfrak{J} \| U_j^{(1)} \| \beta' \mathfrak{J}' \rangle \langle n_j l_j \| r_j C_j^{(1)} \| n_j' l_j' \rangle \\ &\equiv \langle \beta \mathfrak{J} \| U_j^{(1)} \| \beta' \mathfrak{J}' \rangle P_{j, j'}^{(1)}. \end{aligned} \quad (2.10.8)$$

Applying the identity (2.4.11) to the matrix element of the unit tensor and using the well known uncoupling procedure we get the following expression:

$$\begin{aligned}
 \langle \dots \mathfrak{L} \mathfrak{S} \mathfrak{J} \| U_j^{(1)} \| \dots \mathfrak{L}' \mathfrak{S}' \mathfrak{J}' \rangle &= \delta_{all\ spins} (-1)^{\mathfrak{L} + \mathfrak{S} + \mathfrak{J}' + 1} [\mathfrak{J}, \mathfrak{J}']^{1/2} \left\{ \begin{array}{ccc} \mathfrak{L} & \mathfrak{S} & \mathfrak{J} \\ \mathfrak{J}' & 1 & \mathfrak{L}' \end{array} \right\} \\
 &\times \left[ \prod_{m=j+1}^N \delta_{\alpha_m L_m, \alpha'_m L'_m} (-1)^{\mathfrak{L}_{m-1} + L_m + \mathfrak{L}'_m + 1} \right. \\
 &\times \left. [\mathfrak{L}_m, \mathfrak{L}'_m]^{1/2} \left\{ \begin{array}{ccc} \mathfrak{L}_{m-1} & L_m & \mathfrak{L}_m \\ \mathfrak{L}'_m & 1 & \mathfrak{L}'_{m-1} \end{array} \right\} \right] \\
 &\times \left[ \delta_{j1} + (1 - \delta_{j1}) \left( \prod_{m=1}^{j-1} \delta_{\alpha_m L_m, \alpha'_m L'_m} \right) \right. \\
 &\times \left. (-1)^{\mathfrak{L}_{j-1} + L'_j + \mathfrak{L}_j + 1} [\mathfrak{L}_j, \mathfrak{L}'_j]^{\frac{1}{2}} \left\{ \begin{array}{ccc} \mathfrak{L}_{j-1} & L_j & \mathfrak{L}_j \\ 1 & \mathfrak{L}'_j & L'_j \end{array} \right\} \right] \\
 &\times \langle l_j^{w_j} \alpha_j L_j S_j \| U^{(1)} \| l_j^{w_j} \alpha'_j L'_j S'_j \rangle.
 \end{aligned} \tag{2.10.9}$$

This expression is identical to the crystal-field expression for  $k = 1$ . The values of  $P_{j,j'}^{(1)}$  are given by (2.6.12).

### 2.10.2 Zeeman Splitting

A uniform, static, external magnetic field interacts with the magnetic dipole moments associated with the orbital angular momenta. In contrast to an electric field, the magnetic field completely removes the degeneracy of the atomic levels with respect to  $M_L$  and  $M_S$ . This effect was first observed by Zeeman [86]. The energy of interaction of an ion with an external magnetic field  $\mathbf{B}$  is

$$\mathcal{H}_{mag} = -\mathbf{M} \cdot \mathbf{B}. \tag{2.10.10}$$

Here the intrinsic magnetic moment  $\mathbf{M}$  of an ion is given by

$$\mathbf{M} = \mu_B (L + g_s S) \tag{2.10.11}$$

with the anomalous gyromagnetic ratio  $g_s = 2.0023192$  for the electron spin  $S$  and the Bohr magneton

$$\mu_B = \frac{e^2 \hbar}{2mc} = 9.2741 \cdot 10^{-21} \text{ erg/gauss} = 4.2543 \cdot 10^{-10} \text{ Ry/gauss}. \tag{2.10.12}$$

Due to the anomalous gyromagnetic ratio the magnetic moment  $\mathbf{M}$  is not proportional to the total angular momentum  $J = L + S$ . Thus the magnetic moment  $\mathbf{M}$  – in contrast to the total angular momentum  $J$  – is not a conserved property and does not commute with the zero-field Hamilton operator  $\mathcal{H}_0$ .

The operator of the magnetic-moment (2.10.10) has to be added to the zero-field Hamiltonian  $\mathcal{H}_0$ . Here we consider only weak static magnetic fields with flux densities of  $10^4$  to  $10^5$  gauss. For stronger fields it is necessary to consider a quadratic Zeeman effect [87], corresponding to diamagnetic effects<sup>16</sup> proportional to  $B^2$ .

The matrix elements of the magnetic-moment operator (2.10.10) can be determined similarly to the case of the Stark operator. The magnetic-moment operator  $\mathbf{M}$  consists of two vector operators  $L$  and  $S$  of rank one. Thus we can write the matrix element of (2.10.10) as

$$\begin{aligned} h_{\psi,\psi'}^q &\equiv \langle \psi | \mathcal{H}_{mag}^q | \psi' \rangle = -\mathbf{B}_q \sum_{j=1}^N (-1)^{\mathfrak{J}-\mathfrak{M}} \begin{pmatrix} \mathfrak{J} & 1 & \mathfrak{J}' \\ -\mathfrak{M} & q & \mathfrak{M}' \end{pmatrix} \langle \beta \mathfrak{J} \| L_j^{(1)} + g_s S_j^{(1)} \| \beta' \mathfrak{J}' \rangle \\ &= -\mathbf{B}_q \sum_{j=1}^N (-1)^{\mathfrak{J}-\mathfrak{M}} \begin{pmatrix} \mathfrak{J} & 1 & \mathfrak{J}' \\ -\mathfrak{M} & q & \mathfrak{M}' \end{pmatrix} \\ &\quad \times \left( \langle \beta \mathfrak{J} \| L_j^{(1)} \| \beta' \mathfrak{J}' \rangle + g_s \langle \beta \mathfrak{J} \| S_j^{(1)} \| \beta' \mathfrak{J}' \rangle \right) \end{aligned} \quad (2.10.14)$$

with  $\beta = (\alpha_1 L_1 S_1 \mathfrak{L}_1 \mathfrak{S}_1 \dots \alpha_N L_N S_N \mathfrak{L}_N \mathfrak{S}_N)$ .

Here the expression  $q = \{-1, 0, 1\}$  represents again one of the components of the tensor operators  $L^{(1)}$  and  $S^{(1)}$ . The matrix elements of the vector operator components can be determined analogous to (2.10.7).

The reduced matrix element of the angular-momentum operator  $L^{(1)}$  can be determined by the well known uncoupling procedure similar to (2.10.9). Here Racah's unit-tensor operator is replaced by the angular-momentum operator  $L^{(1)}$ .

<sup>16</sup>The diamagnetic contribution can be written as

$$\chi_{Larmor} = -\frac{\alpha^2}{8\pi} \cdot \sum_j \frac{\langle r_j^2 \rangle}{a_0^2} \cdot \frac{4\pi a_0^3/3}{v}, \quad (2.10.13)$$

which is mostly a small correction and is therefore neglected in the thesis. Here  $\alpha = e^2/\hbar c$  is the fine-structure constant,  $a_0$  the Bohr radius, and  $v$  the specific volume of the ion. The summation is over all electrons of the ion.

Using (2.4.8) we get the following expression for the reduced matrix element

$$\begin{aligned}
 \langle \dots \mathfrak{L} \mathfrak{S} \mathfrak{J} \| L_j^{(1)} \| \dots \mathfrak{L}' \mathfrak{S}' \mathfrak{J}' \rangle &= \delta_{all\ spins} (-1)^{\mathfrak{L} + \mathfrak{S} + \mathfrak{J}' + 1} [\mathfrak{J}, \mathfrak{J}']^{1/2} \left\{ \begin{array}{ccc} \mathfrak{L} & \mathfrak{S} & \mathfrak{J} \\ \mathfrak{J}' & 1 & \mathfrak{L}' \end{array} \right\} \\
 &\times \left[ \prod_{m=j+1}^N \delta_{\alpha_m L_m, \alpha'_m L'_m} (-1)^{\mathfrak{L}_{m-1} + L_m + \mathfrak{L}'_m + 1} \right. \\
 &\times [\mathfrak{L}_m, \mathfrak{L}'_m]^{1/2} \left\{ \begin{array}{ccc} \mathfrak{L}_{m-1} & L_m & \mathfrak{L}_m \\ \mathfrak{L}'_m & 1 & \mathfrak{L}'_{m-1} \end{array} \right\} \Big] \\
 &\times \left[ \delta_{j1} + (1 - \delta_{j1}) \left( \prod_{m=1}^{j-1} \delta_{\alpha_m L_m, \alpha'_m L'_m} \right) \right. \\
 &\times (-1)^{\mathfrak{L}_{j-1} + L'_j + \mathfrak{L}_j + 1} [\mathfrak{L}_j, \mathfrak{L}'_j]^{\frac{1}{2}} \left\{ \begin{array}{ccc} \mathfrak{L}_{j-1} & L_j & \mathfrak{L}_j \\ 1 & \mathfrak{L}'_j & L'_j \end{array} \right\} \Big] \\
 &\times \delta_{L_j, L'_j} \sqrt{L_j(L_j + 1)(2L_j + 1)}.
 \end{aligned} \tag{2.10.15}$$

The reduced matrix element of the spin operator  $S^{(1)}$  can be written as

$$\begin{aligned}
 \langle \dots \mathfrak{L} \mathfrak{S} \mathfrak{J} \| S_j^{(1)} \| \dots \mathfrak{L}' \mathfrak{S}' \mathfrak{J}' \rangle &= \delta_{all\ L} (-1)^{\mathfrak{L} + \mathfrak{S} + \mathfrak{J}' + 1} [\mathfrak{J}, \mathfrak{J}']^{1/2} \left\{ \begin{array}{ccc} \mathfrak{L} & \mathfrak{S} & \mathfrak{J} \\ 1 & \mathfrak{J}' & \mathfrak{S}' \end{array} \right\} \\
 &\times \left[ \prod_{m=j+1}^N \delta_{\alpha_m S_m, \alpha'_m S'_m} (-1)^{\mathfrak{S}_{m-1} + S_m + \mathfrak{S}'_m + 1} \right. \\
 &\times [\mathfrak{S}_m, \mathfrak{S}'_m]^{1/2} \left\{ \begin{array}{ccc} \mathfrak{S}_{m-1} & S_m & \mathfrak{S}_m \\ \mathfrak{S}'_m & 1 & \mathfrak{S}'_{m-1} \end{array} \right\} \Big] \\
 &\times \left[ \delta_{j1} + (1 - \delta_{j1}) \left( \prod_{m=1}^{j-1} \delta_{\alpha_m S_m, \alpha'_m S'_m} \right) \right. \\
 &\times (-1)^{\mathfrak{S}_{j-1} + S'_j + \mathfrak{S}_j + 1} [\mathfrak{S}_j, \mathfrak{S}'_j]^{\frac{1}{2}} \left\{ \begin{array}{ccc} \mathfrak{S}_{j-1} & S_j & \mathfrak{S}_j \\ 1 & \mathfrak{S}'_j & S'_j \end{array} \right\} \Big] \\
 &\times \delta_{S_j, S'_j} \sqrt{S_j(S_j + 1)(2S_j + 1)}.
 \end{aligned} \tag{2.10.16}$$

## 2.11 Observable

In contrast to the previous sections, which describe exclusively the contributions to the Hamilton operator  $\mathcal{H}$ , this section illustrates the determination of the magnetic susceptibility and the optical conductivity. By comparing these observables with measured data, we can estimate the quality of the calculation and optimize the calculation parameters in order to get the best agreement. In the first part of this section, we begin with a derivation of the response functions from the Maxwell equations and end up with an expression for the optical conductivity within the Kubo-Greenwood theory. In the second part, we derive expressions for the magnetic susceptibility. Subsequently, we present expressions for the phonon frequencies using the dynamical matrix method. This calculation technique is very sensitive to errors introduced by the uncertainties of the calculation parameters. In addition, the determination of the phonon frequencies requires a great computational effort which scales unpropitious with the size of the cluster.

### 2.11.1 Response Functions and Optical Conductivity

The optical properties of solids are given by the response of the electrons and the nuclei to a time-dependent electromagnetic perturbation caused by the incoming light. So the calculation of these properties is reduced to the determination of a response function which is either the complex dielectric function or the optical conductivity.

The propagation of electromagnetic waves within the crystal is described by Maxwell's equations in the presence of matter:

$$\begin{aligned}\nabla \times \mathbf{E} + \frac{1}{c} \frac{\partial \mathbf{B}}{\partial t} &= 0, \\ \nabla \cdot \mathbf{B} &= 0, \\ \nabla \times \mathbf{H} - \frac{1}{c} \frac{\partial \mathbf{D}}{\partial t} &= \frac{4\pi}{c} \mathbf{j}_{cond}, \\ \nabla \cdot \mathbf{D} &= 4\pi \rho_{ext}.\end{aligned}\tag{2.11.1}$$

Here the crystal properties are considered by introducing the electric displacement  $\mathbf{D}$  and the magnetic induction<sup>17</sup>  $\mathbf{B}$ .

Within the linear approximation, which is valid for small electric and magnetic fields but not for ferromagnets, the electric displacement  $\mathbf{D}$  is connected to the electric field  $\mathbf{E}$  by the frequency-dependent dielectric constant  $\epsilon_1$ :

$$\mathbf{D} = \epsilon_1(\mathbf{q}, \omega) \mathbf{E} = (1 + 4\pi \chi_e) \mathbf{E} = \mathbf{E} + 4\pi \mathbf{P},\tag{2.11.3}$$

<sup>17</sup>The total current density  $\mathbf{j}$  occurring in Maxwell's equations (2.11.1) consists of two contributions:  $\mathbf{j}_{cond}$  arise from the motion of free electrons within an electric field.  $\mathbf{j}_{bound}$  emerges from the redistribution of bound charges:

$$\mathbf{j} = \mathbf{j}_{cond} + \mathbf{j}_{bound}.\tag{2.11.2}$$

Here we assume that there is no external current  $\mathbf{j}_{ext}$ . The total charge density  $\rho$  has also two components: An external charge  $\rho_{ext}$  added from outside of the crystal (here  $\rho_{ext} \equiv 0$ ) and a contribution  $\rho_{pol}$  due to the polarization.

in which  $\chi_e$  represents the dielectric susceptibility and  $\mathbf{P} = \chi_e \mathbf{E}$  the dipole moment density (polarization)<sup>18</sup>. Similarly the permeability  $\mu_1$  connects the magnetic field  $\mathbf{H}$  to the magnetic induction  $\mathbf{B}$ :

$$\mathbf{B} = \mu_1 \mathbf{H} = (1 + 4\pi \chi_m) \mathbf{H} = \mathbf{H} + 4\pi \mathbf{M}, \quad (2.11.4)$$

with  $\chi_m$  representing the magnetic susceptibility  $\chi_m$  and  $\mathbf{M} = \chi_m \mathbf{H}$  the magnetic moment density (magnetization)<sup>19</sup>. The magnetic susceptibility is typically four to five orders of magnitude smaller (except for ferromagnetic materials) than the dielectric susceptibility  $\chi_e$ , which is of the order of unity. Hence the dia- and paramagnetic properties can in general be neglected in comparison to the dielectric properties when electromagnetic waves pass through the crystal. Therefore the assumptions of  $\mu_1 = 1$  ( $\chi_m = 0$ ) and of the absence of magnetic losses in the crystal are justified.

In order to describe  $\epsilon_1$  and  $\sigma_1$  by one complex function we start with the Maxwell equations:

$$\begin{aligned} c \cdot \nabla \times \mathbf{H} &= \frac{\partial \mathbf{D}}{\partial t} + 4\pi \mathbf{j}_{cond}, \quad \mathbf{j}_{cond} = \sigma_1 \mathbf{E}, \quad \mathbf{D} = \epsilon_1 \mathbf{E} \\ \Rightarrow c \cdot \nabla \times \mathbf{H} &= \left( \epsilon_1 \frac{\partial}{\partial t} + 4\pi \sigma_1 \right) \mathbf{E}, \quad \text{ansatz: } \mathbf{E} = \mathbf{E}_0 e^{i(\mathbf{q}\mathbf{r} - \omega t)}, \quad \mathbf{H} = \mathbf{H}_0 e^{i(\mathbf{q}\mathbf{r} - \omega t)} \\ \Rightarrow i c \cdot \mathbf{q} \times \mathbf{H}(\mathbf{q}, \omega) &= (-i\omega \epsilon_1 + 4\pi \sigma_1) \mathbf{E}(\mathbf{q}, \omega) = -i\omega \hat{\epsilon} \mathbf{E}. \end{aligned} \quad (2.11.5)$$

In the last line we introduce the definition of the complex dielectric function  $\hat{\epsilon}$ :

$$\hat{\epsilon}(\mathbf{q}, \omega) \equiv \epsilon_1(\mathbf{q}, \omega) + i \frac{4\pi \sigma_1(\mathbf{q}, \omega)}{\omega} \equiv \epsilon_1(\mathbf{q}, \omega) + i \epsilon_2(\mathbf{q}, \omega). \quad (2.11.6)$$

The dielectric function can also be expressed by the complex index of refraction  $\hat{N}(\mathbf{q}, \omega) = \sqrt{\hat{\epsilon}(\mathbf{q}, \omega)} = n(\mathbf{q}, \omega) + i\kappa(\mathbf{q}, \omega)$ .

$$\epsilon_1(\mathbf{q}, \omega) = n^2(\mathbf{q}, \omega) - \kappa^2(\mathbf{q}, \omega), \quad \epsilon_2(\mathbf{q}, \omega) = 2n(\mathbf{q}, \omega) \kappa(\mathbf{q}, \omega). \quad (2.11.7)$$

Here,  $n(\mathbf{q}, \omega)$  represents the index of refraction and  $\kappa(\mathbf{q}, \omega)$  the extinction coefficient. Equivalent to the complex dielectric function we can define a complex optical conductivity  $\hat{\sigma}(\mathbf{q}, \omega) \equiv \sigma_1(\mathbf{q}, \omega) + i\sigma_2(\mathbf{q}, \omega)$ . These two complex functions are related by

$$\hat{\epsilon}(\mathbf{q}, \omega) = 1 + i \frac{4\pi}{\omega} \hat{\sigma}(\mathbf{q}, \omega). \quad (2.11.8)$$

In the general case of an anisotropic medium, the dielectric function depends on the direction of the electric field and has to be represented as a  $(3 \times 3)$  tensor of rank 2

<sup>18</sup>For a positive dielectric susceptibility ( $\chi_e > 0$ ),  $\mathbf{E}$  is reduced within matter ( $\mathbf{E} = \mathbf{D} - 4\pi \mathbf{P}$ ), because the external electric field is screened by the polarization ( $\nabla \mathbf{E} \neq 0$ ).

<sup>19</sup>For a positive magnetic susceptibility ( $\chi_m > 0$ ),  $\mathbf{B}$  is enhanced, because the magnetic moments are aligned parallel to the magnetic field.

which is in case of non-magnetic materials ( $\mu_1 \equiv 0$ ) symmetric). For a strong electric field, the dielectric function depends also on the field strength. Therefore the calculation of the dielectric function discussed here is restricted to small electric fields.

We can neglect the  $\mathbf{q}$ -dependence of the response functions because the wavelength is much larger than the unit cell and the wave-vector dependence of the Fourier-transformed fields is negligible:  $|\mathbf{q}| \propto 1/\lambda \approx 0$ . Thus the  $\mathbf{q}$ -dependence of the response function can be dropped from notation.

As a consequence of the law of causality, the real and the imaginary part of a complex response function  $G(\omega) = G_1(\omega) + iG_2(\omega)$  are not independent of each other. The relationship is called Kramers-Kronig relation [89, 90]:

$$\begin{aligned} G_1(\omega) &= \frac{1}{\pi} \mathcal{P} \int_{-\infty}^{\infty} \frac{G_2(\omega')}{\omega' - \omega} d\omega' \\ G_2(\omega) &= -\frac{1}{\pi} \mathcal{P} \int_{-\infty}^{\infty} \frac{G_1(\omega')}{\omega' - \omega} d\omega' \end{aligned} \quad (2.11.9)$$

with  $\mathcal{P}$  representing the Cauchy principle value. For the details of the Kramers-Kronig relations see section “3.1.2 Kramers-Kronig analysis”.

The optical conductivity can be described by the Kubo-Greenwood formula [91, 92]<sup>20</sup>:

$$\sigma_1(\omega) = \frac{2\pi}{\hbar V \omega} \sum_{mn} \frac{|\langle \psi_n | \hat{j} | \psi_m \rangle|^2}{E_n - E_m}. \quad (2.11.10)$$

Here  $V$  represents the volume of the unit cell and  $\hat{j}$  the current operator in the tight-binding model which can be written as [94]

$$\hat{j} = -ie \sum_{\alpha\beta} (\mathbf{R}_\beta - \mathbf{R}_\alpha) \langle \psi_m | \mathcal{H}_{tb} | \psi_n \rangle + e^2 \sum_{\alpha\beta} (\mathbf{R}_\beta - \mathbf{R}_\alpha) [(\mathbf{R}_\beta - \mathbf{R}_\alpha) \cdot \mathbf{A}] \langle \psi_m | \mathcal{H}_{tb} | \psi_n \rangle. \quad (2.11.11)$$

The second term is the approximate diamagnetic contribution [93] with constant external vector potential  $\mathbf{A}$ . This contribution is only a small correction and will be neglected. The determination of the current operator involves the tight-binding Hamiltonian which reduces the computational effort, because this Hamiltonian is in general calculated before.

Another often used representation of the Kubo-Greenwood formula applies to the electron Green's function [95]:

$$\sigma_1(\omega) = \frac{2\pi}{\hbar V \omega} \text{Im} \left[ \langle \psi_0 | \hat{j}^\dagger \frac{1}{\omega + E_0 + i\gamma - \mathcal{H}} \hat{j} | \psi_0 \rangle \right]. \quad (2.11.12)$$

<sup>20</sup>Here the optical conductivity is given in SI units, i.e.,  $[\sigma(\omega)] = \Omega^{-1} m^{-1}$ .

Here  $|\psi_0\rangle$  is the ground state of the Hamiltonian  $\mathcal{H}$  with energy  $E_0$ . The expression  $\gamma$  is a small (real) number (damping) introduced in the calculation to shift the poles of the Green's function into the complex plane. Introducing a complete basis,  $\sum_n |\psi_n\rangle\langle\psi_n| = 1$  and using the well-known (Dirac) identity

$$\lim_{\gamma \rightarrow 0} \left[ \frac{1}{x + i\gamma} \right] = \mathcal{P} \left[ \frac{1}{x} \right] - i\pi\delta(x), \quad (2.11.13)$$

where  $\mathcal{P}$  denotes the principle part and  $x$  a real number, we can rewrite (2.11.12) as

$$\sigma_1(\omega) = \frac{2\pi}{\hbar V \omega^2} \sum_n |\langle\psi_n|\hat{j}|\psi_0\rangle|^2 \delta(\omega - (E_n - E_0)), \quad (2.11.14)$$

in which  $|\psi_n\rangle$  denotes the eigenvectors of the Hamiltonian  $\mathcal{H}$  with eigenvalues  $E_n$ . In practise, the  $\delta$ -functions are smeared out by a finite damping  $\gamma$ . This can be described by Lorentzians according to

$$\delta(x) \rightarrow \frac{1}{\pi} \frac{\gamma}{x^2 + \gamma^2}. \quad (2.11.15)$$

Note, that for compounds with broken inversion symmetry at the transition-metal ion site, we have to consider energetically higher lying configurations containing excited p-states at the transition-metal ion site. But due to the enormous computational effort, we neglect these contributions and consider only the contributions from d-states, the spin-orbit coupling and the charge-transfer excitations to the optical conductivity.

### 2.11.2 Magnetic Susceptibility

The (volume) magnetic susceptibility  $\chi_m$  is the degree of magnetization of a material in response to an applied magnetic field and is related to the real part of the magnetic permeability  $\hat{\mu}$  by the following equation:

$$\mu_1 = \mu_0 (1 + \chi_m). \quad (2.11.16)$$

The magnetic susceptibility also is represented by a  $(3 \times 3)$  tensor. The derivation of the expression for the magnetic susceptibility starts with the free energy of an ion which is given by

$$f = -\frac{1}{\beta} \ln [Tr (e^{-\beta(\mathcal{H} - \mathbf{M} \cdot \mathbf{B})})], \quad (2.11.17)$$

in which  $\beta = 1/k_B T$ . In the following the component of the magnetization operator  $\mathbf{M}$  parallel to the magnetic field  $\mathbf{B}$  is denoted by  $M$ . Differentiating the free energy  $f$  with respect to the magnetic field  $\mathbf{B}$  we get the following expression for the magnetization  $m$

$$m \doteq \langle M \rangle_{\mathcal{H} - M \cdot B} = -\frac{\partial f}{\partial B} = Tr (M e^{-\beta(\mathcal{H} - M \cdot B)}) / Tr (e^{-\beta(\mathcal{H} - M \cdot B)}). \quad (2.11.18)$$

Differentiating again we achieve the expression for the initial magnetic susceptibility

$$\chi_m = \left. \frac{\partial m}{\partial B} \right|_{B=0} = \int_0^\beta d\tau \langle M(\tau) M \rangle_{\mathcal{H}}, \quad M(\tau) = e^{\tau \mathcal{H}} M e^{-\tau \mathcal{H}}. \quad (2.11.19)$$

Here we have to consider the non-commutativity of  $M$  and  $\mathcal{H}$ . In order to calculate the magnetic susceptibility  $\chi_m$  in (2.11.19), we use the complete eigenbasis  $\{|n\rangle\}$  of  $\mathcal{H}$  with  $\mathcal{H}|n\rangle = E_n|n\rangle$ . Here  $Z = \text{Tr}(e^{-\beta\mathcal{H}}) = \sum_n e^{-\beta E_n}$  denotes the partition function. Inserting the completeness relation  $\sum_n |n\rangle\langle n| = 1$  between the two magnetization operators in (2.11.19), we get the spectral representation of the susceptibility [96]

$$\chi_m = \frac{1}{Z} \sum_{m,n} |\langle m|M|n\rangle|^2 \frac{e^{-\beta E_m} - e^{-\beta E_n}}{E_n - E_m}. \quad (2.11.20)$$

Because of their different behavior we divide this expression for low temperatures into two parts: In case of  $E_m = E_n$  the expression (2.11.20) represents the **Curie** susceptibility and can be expressed as [96]

$$\chi_C = \frac{\beta}{Z} \sum_{m,n}^{E_m=E_n} |\langle m|M|n\rangle|^2 e^{-\beta E_n}. \quad (2.11.21)$$

If  $E_m \neq E_n$  the **van Vleck** susceptibility is given by the following formula [96]

$$\chi_{vV} = \frac{1}{Z} \sum_{m,n}^{E_m \neq E_n} |\langle m|M|n\rangle|^2 \frac{e^{-\beta E_m} - e^{-\beta E_n}}{E_n - E_m}. \quad (2.11.22)$$

The van Vleck susceptibility only exists, because  $M$  does not commute with  $\mathcal{H}$ .

In order to calculate the molar magnetic susceptibility, measured in “emu/mol”, all energies have to be measured in “erg” and the Bohr magneton in “emu G”

$$[\chi] = \frac{\mu_B^2}{E} = \frac{emu^2 G^2}{erg} = \frac{emu^2 (erg/cm^3)}{erg} = emu. \quad (2.11.23)$$

We get the final expression by multiplying this ionic susceptibility with the Avogadro number  $N_A \approx 6.022 \cdot 10^{23} \text{ mol}^{-1}$ .

### 2.11.3 Phonons

A phonon is a quantized mode of vibration with frequency  $\omega$ . The possible phonon frequencies in the crystal can be determined by the dynamical matrix method. Here the phonons are represented by harmonic oscillators: The equations of motion for the nuclei are determined by the total energy  $E_{total}(\mathbf{R})$  of the system. The nuclear coordinates  $\mathbf{R}$  are regarded as parameters, where  $\mathbf{R}_i$  represents the coordinate and  $M_i$  the mass of nucleus  $i$ .

If the nuclei are treated classically, the problem reduces to the (coupled) classical equations of motion for each nuclear position  $\mathbf{R}_i$

$$M_i \frac{\partial^2 \mathbf{R}_i}{\partial t^2} = \mathbf{F}_i(\mathbf{R}) = -\frac{\partial}{\partial \mathbf{R}_i} E_{total}(\mathbf{R}), \quad (2.11.24)$$

in which  $\mathbf{F}_i$  indicates the force on the nucleus  $i$ . At low temperature, it is useful to write the expressions in terms of an expansion of the total energy  $E_{total}(\mathbf{R})$  of the crystal. Equilibrium positions  $\{\mathbf{R}_i^0\} = \mathbf{R}^0$  are determined by the zero-force condition on each nucleus,

$$\mathbf{F}_i(\mathbf{R}^0) = 0. \quad (2.11.25)$$

Lattice dynamics are described by higher powers of displacements, the so-called dynamical matrix,

$$C_{i,\alpha;j,\beta} = \frac{\partial^2 E_{total}(\mathbf{R})}{\partial \mathbf{R}_{i,\alpha} \partial \mathbf{R}_{j,\beta}}, \quad (2.11.26)$$

in which  $\alpha, \beta$  indicate cartesian components. Within the harmonic approximation [97] the vibrational modes at frequency  $\omega$  are described by displacements

$$\mathbf{u}_j(t) = \mathbf{R}_j(t) - \mathbf{R}_j^0 \equiv \mathbf{u}_j e^{i\omega t} \quad (2.11.27)$$

so that (2.11.24) can be rewritten as

$$-\omega^2 M_i u_{i,\alpha} = - \sum_{j,\beta} C_{i,\alpha;j,\beta} u_{j,\beta}. \quad (2.11.28)$$

The full solution for all vibrational states is the set of independent oscillators. Solving the classical equation

$$\det \left| \frac{1}{\sqrt{M_i M_j}} C_{i,\alpha;j,\beta} - \omega^2 \right| = 0 \quad (2.11.29)$$

we can determine the vibrational frequency  $\omega$  of each oscillator. For a crystal, the atomic displacement eigenvectors obey the Bloch theorem, i.e., the vibration of atom  $s$  is classified by  $\mathbf{k}$  and the translation vector  $\mathbf{T}_n$ , and the displacements can be written as

$$\mathbf{u}_{s,\mathbf{T}_n} = \mathbf{u}_s(\mathbf{k}) e^{i\mathbf{k} \cdot \mathbf{T}_n}. \quad (2.11.30)$$

Analogous to the electrons, inserting this expression into (2.11.29) decouples the equations at different  $\mathbf{k}$  values with frequencies  $\omega_{i,\mathbf{k}}$  which are solutions of the  $3N \times 3N$  determinant equation<sup>21</sup>

$$\det \left| \frac{1}{\sqrt{M_s M_{s'}}} C_{s,\alpha;s',\alpha'}(\mathbf{k}) - \omega_{i,\mathbf{k}}^2 \right| = 0, \quad (2.11.31)$$

in which the reduced force constant for wave vector  $\mathbf{k}$  is given by

$$C_{s,\alpha;s',\alpha'}(\mathbf{k}) = \sum_{\mathbf{T}_n} e^{i\mathbf{k} \cdot \mathbf{T}_n} \frac{\partial^2 E_{total}(\mathbf{R})}{\partial \mathbf{R}_{s,\alpha}(0) \partial \mathbf{R}_{s',\alpha'}(\mathbf{T}_n)}, = \frac{\partial^2 E_{total}(\mathbf{R})}{\partial \mathbf{u}_{s,\alpha}(\mathbf{k}) \partial \mathbf{u}_{s',\alpha'}(\mathbf{k})}. \quad (2.11.32)$$

The solutions of (2.11.31) form the so-called dispersion curves. These dispersion curves are divided into three acoustic modes, with  $\omega \rightarrow 0$  for  $\mathbf{k} \rightarrow 0$ , and  $(3N - 3)$  optic modes.

---

<sup>21</sup> $N$  represents the total number of ions in the unit cell.

The determination of the reduced force constant (2.11.32) requires the calculation of the total energy as a function of the position of the nuclei, i.e., “frozen phonons”. The numerical computation of the second derivative of a function  $f(\mathbf{x})$  depending on a set of variables  $\mathbf{x} = \{x_1, x_2, \dots, x_n\}$  can be done by the following relation [99]:

$$\frac{\partial^2 f(\mathbf{x})}{\partial x_i \partial x_j} = \lim_{h \rightarrow 0} \left[ \frac{f(x_i + h, x_j + h) - f(x_i + h, x_j - h)}{4h^2} - \frac{f(x_i - h, x_j + h) - f(x_i - h, x_j - h)}{4h^2} \right]. \quad (2.11.33)$$

Therefore the determination of the dynamical matrix requires  $(6N \times 6N)$  calculations of the total energy at each  $\mathbf{k}$  point. This calculation effort can be reduced by making use of the fact that the dynamical matrix is Hermitian. So only  $\frac{6N}{2}(1+6N)$  calculations are necessary. The squares of the phonon frequencies are then given by the eigenvalues of this dynamical matrix.

In case of negative eigenvalues the corresponding vibrational frequencies will be imaginary. This implies that the system is unstable with respect to a distortion which corresponds with this eigenvalue. Note, that the first three vibrational frequencies at the  $\Gamma$  point should be equal to zero because they correspond to the translation of the lattice.

## 2.12 Numerical calculation

This section describes some details which are important in the numerical calculation of the Hamilton operator and the above mentioned observables.

In the framework of this thesis a computer program has been written for the calculation of the electronic structure. The program “e-structure” is predominantly written in Fortran90 following [100] and contains the following programs/subroutines written by other authors:

- The self-consistent Hartree-Fock program “Rcn36k” written by Cowan and coworkers [7] is included in the program [101] and partially modified in order to fix some bugs.
- The determination of the coefficients of the expansion of the Ewald sum is done by the subroutine written by M. Haverkoort [62].
- Some “numerical recipes” routines [99].

The program was successfully compiled with the Pathscale<sup>TM</sup> Fortran Compiler 2.4 and the Intel Fortran Compiler (8.1 and 9.1) for Linux.

### 2.12.1 Lanczos algorithm

The Hamilton matrix in the configuration-interaction calculation has typically the size of a few million matrix elements<sup>22</sup>. The diagonalization of this large matrix cannot be done analytically. In optical spectroscopy we are interested in low-lying excitations. These excitations are predominantly described by the lowest eigenstates. So we need only the smallest eigenvalues and their corresponding eigenvectors. The determination of these eigenvalues and eigenvectors of the Hamilton matrix can be done by the Lanczos method [102]: The basic idea of the Lanczos method is that the Hamiltonian can be transferred to a tridiagonal representation by using an appropriate basis transformation. The algorithm is carried out iteratively: First it is necessary to select an arbitrary vector  $|\phi_0\rangle$  in the Hilbert space of the model being studied. In order to determine the ground-state energy of the model, the overlap between the actual ground state  $|\psi_0\rangle$  and the initial state  $|\phi_0\rangle$  has to be nonzero. If we know nothing about the ground state, this requirement is usually easily satisfied by selecting an initial state with randomly chosen coefficients in the basis. By applying the Hamiltonian  $\mathcal{H}$  to the initial state we can define a new vector. Subtracting the projection over  $|\phi_0\rangle$ , we obtain

$$|\phi_1\rangle = \mathcal{H}|\phi_0\rangle - \frac{\langle\phi_0|\mathcal{H}|\phi_0\rangle}{\langle\phi_0|\phi_0\rangle}|\phi_0\rangle, \quad (2.12.1)$$

---

<sup>22</sup>For example, the calculation of a  $TiO_6$  cluster with one  $d$  electron on the Ti-site, requires the diagonalization of matrix with a dimension of 77230.

which satisfies  $\langle \phi_0 | \phi_1 \rangle = 0$ . Now it is possible to construct a new state that is orthogonal to the previous two as

$$|\phi_2\rangle = \mathcal{H}|\phi_1\rangle - \frac{\langle \phi_1 | \mathcal{H} | \phi_1 \rangle}{\langle \phi_1 | \phi_1 \rangle} |\phi_1\rangle - \frac{\langle \phi_1 | \phi_1 \rangle}{\langle \phi_0 | \phi_0 \rangle} |\phi_0\rangle. \quad (2.12.2)$$

It can be shown that  $\langle \phi_0 | \phi_2 \rangle = \langle \phi_0 | \phi_1 \rangle = 0$ . This procedure can be generalized by defining an orthogonal basis recursively as

$$|\phi_{n+1}\rangle = \mathcal{H}|\phi_n\rangle - a_n|\phi_n\rangle - b_n^2|\phi_{n-1}\rangle, \quad (2.12.3)$$

where  $n = 0, 1, 2, \dots$ , and the coefficients are given by

$$a_n = \frac{\langle \phi_n | \mathcal{H} | \phi_n \rangle}{\langle \phi_n | \phi_n \rangle}, \quad b_n^2 = \frac{\langle \phi_n | \phi_n \rangle}{\langle \phi_{n-1} | \phi_{n-1} \rangle}, \quad (2.12.4)$$

supplemented by  $b_0 = 0, |\phi_{-1}\rangle = 0$ . In this basis the Hamilton matrix has the tridiagonal form

$$\mathcal{H} = \begin{pmatrix} a_0 & b_1 & 0 & 0 & \dots \\ b_1 & a_1 & b_2 & 0 & \dots \\ 0 & b_2 & a_2 & b_3 & \dots \\ 0 & 0 & b_3 & a_3 & \dots \\ \vdots & \vdots & \vdots & \vdots & \ddots \end{pmatrix}, \quad (2.12.5)$$

as expected above. The matrix in this form can be diagonalized easily using standard library subroutines. To diagonalize the matrix completely, a number of iterations equal to the size of the Hilbert space is necessary. It can be proved that the eigenvalues are approximate eigenvalues of the original Hamilton matrix  $\mathcal{H}$ .

Note, that the information about the ground state of the problem can be obtained already by a small number of iterations (typically of the order of 100 or less).

The Lanczos algorithm can be described as a systematic way to improve a given variational state that is used to represent the ground state of the system. The Hermitian Lanczos algorithm is a simplified Arnoldi's algorithm which is applied to the Hermitian matrix. It transforms the original matrix into a tridiagonal matrix which is real and symmetric. The dependency of the Lanczos algorithm on small numerical errors define the stability of the algorithm. For the Lanczos algorithm, the calculated eigenvalues/vectors are good approximations to those of the original matrix. But the orthogonality of the eigenvectors is quickly lost due to round-off errors. In some cases this leads to eigenvalues of the resultant tridiagonal matrix which may not be approximations to the original matrix. Therefore, the Lanczos algorithm is not very stable and we require a modification of the Lanczos algorithm which find and remove those "spurious" eigenvalues. Many implementations of the Lanczos algorithm restart after a certain number of iterations. The implicitly restarted Lanczos method [105], which is implemented in the ARPACK library [104, 106], is one of the most popular restarted variations: The ARPACK library computes a few eigenvalues and the corresponding

eigenvectors of a general (complex)  $n \times n$  matrix  $A$ . (Depending on the properties of the matrix  $A$ , the algorithm is called an “Implicitly Restarted Arnoldi Method” or “Implicitly Restarted Lanczos Method”). For many standard problems, only the action of the matrix on a vector is needed. Because of the Hermitian nature of the Hamilton matrix only the upper tridiagonal part of the matrix has to be saved. The ARPACK library requires only the action of the matrix on an arbitrary vector. So only the non-zero matrix elements are relevant. The Hamilton matrix in the program is stored as a list containing the  $x$  and the  $y$  position of the non-zero matrix element and the element itself. This reduces the memory requirement to a few GB RAM.

### 2.12.2 LAPACK and BLAS

“The LAPACK (*Linear Algebra Package*) library is a collection of Fortran77 subroutines for solving systems of simultaneous linear equations, least-squares solutions of linear systems of equations, eigenvalue problems, and singular value problems.”, see [107]. Routines for the associated matrix factorizations (LU, Cholesky, QR, SVD, Schur, generalized Schur) are also included. All calculations can be done for real and complex matrices, both in single and double precision.

“The BLAS (*Basic Linear Algebra Subprograms*) library is a collection of routines that provide standard building blocks for performing basic vector and matrix operations. The Level 1 BLAS perform scalar, vector, and vector-vector operations, the Level 2 BLAS perform matrix-vector operations, and the Level 3 BLAS perform matrix-matrix operations.”, see [108].

### 3 Fourier-Transform spectroscopy

In this section, we give a detailed description of the Fourier-Transform spectrometer, which is used for the measurement of the reflectance and the transmittance of the samples presented in this thesis.

The measurement of the infrared excitations described in this thesis, i.e. the measurement of the reflectance and the transmittance of a sample, was done by using the Fourier-transform spectrometer. In the following, we will divide the frequency range we are interested in, into the far-infrared (FIR, 50 - 500  $\text{cm}^{-1}$ ), mid-infrared (MIR, 500 - 5000  $\text{cm}^{-1}$ ), near-infrared (NIR, 5000 - 12000  $\text{cm}^{-1}$ ), visible-light (VIS, 12000 - 25000  $\text{cm}^{-1}$ ) and ultraviolet-light (UV) region. The Fourier-transform spectroscopy offers several advantages in comparison with a dispersive measurement. In this standard setup consisting out of a white-light source and a monochromator the reflectance  $R(\omega)$  and the transmittance  $T(\omega)$  are determined frequency-wise. In contrast to this technique, the Fourier-transform spectrometer collects the whole spectrum at once and we can perform  $N$  independent measurements in the same time that the dispersive technique needs to measure a whole spectrum consisting of  $N$  frequency intervals. This Fellgett [109] or multiplex advantage will produce a gain of the order of  $\sqrt{N}$  in the signal-to-noise ratio of the resulting spectrum. This is one of the most important advantages of Fourier-transform spectroscopy, because a serious problem of infrared spectroscopy, particularly at low frequencies, is intensity. The emission of the infrared light sources, for example a black body source, decreases rapidly towards low frequencies. In addition, the Fourier-transform spectroscopy allows the application of large circular apertures, whereas the dispersive technique requires narrow slit apertures to reach a given frequency resolution. This is the Jacquinot or throughput advantage. In addition, the Fourier-transform spectrometer includes a HeNe laser as an internal wavelength calibration standard (referred to as the Connes advantage).

A sketch of the the Fourier-transform spectrometer used in this thesis is shown in Fig. 3.1. The light of a broad-band lamp<sup>1</sup> is focused on an aperture wheel, which controls the size of the light spot on the sample. Reflected by a parabolic mirror, a parallel beam enters the Michelson interferometer [110]. Here the so-called beam splitter divides the light into two beams, one is reflected on a fixed mirror and the other one on a moving mirror which introduces a time delay. This leads to constructive or destructive interference when the two back-reflected parts of the beam interfere with each other depending on the ratio of the lengths of both beams: Let  $L$  be the length of the optical path between the fixed mirror and the beam splitter. At the begin of

---

<sup>1</sup>For the FIR range, we use the heat radiation from a quartz enclosure. A global, typically a heated piece of silicon carbide, is used for the MIR range. For the NIR range we use a tungsten lamp.

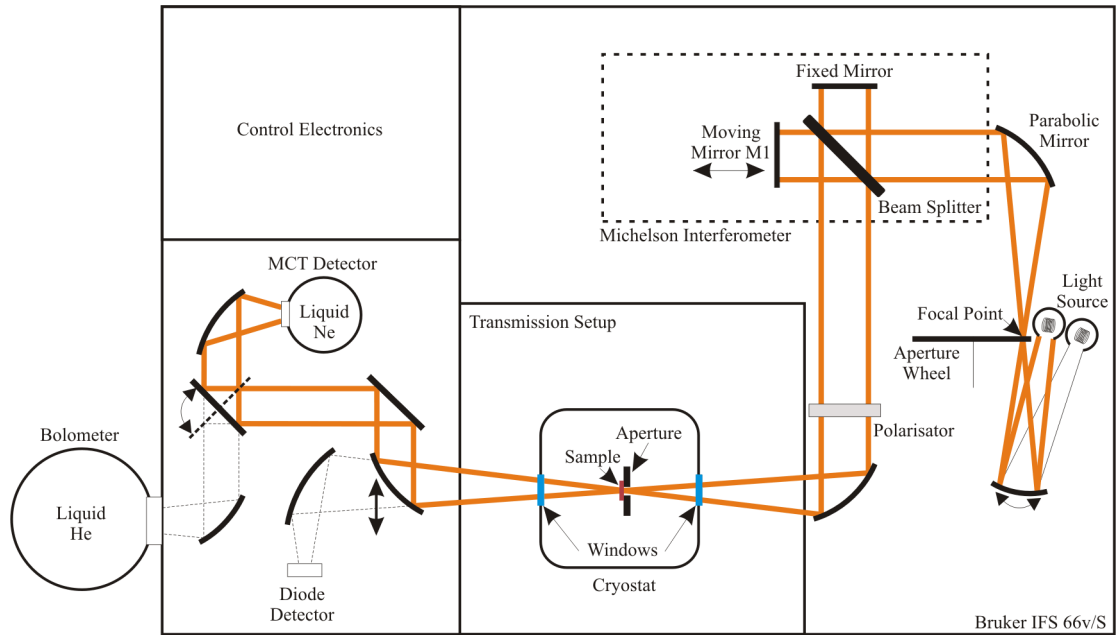


Figure 3.1: A sketch of the Bruker IFS 66v/S Fourier-transform spectrometer.

the measurement process, the length of the optical path between the moving mirror  $M1$  and the beam splitter is equal to  $L$ . By moving mirror  $M1$  we achieve an optical retardation  $x$ , which leads to constructive interference for  $x = n\lambda$  ( $n \in \mathbb{N}$ ) constructive and to destructive interference for  $x = n + \frac{1}{2}\lambda$ . Measuring the intensity of the signal at many discrete positions of the moving mirror, we get the so-called “interferogram”, see Fig. 3.2 and Fig. 3.3.

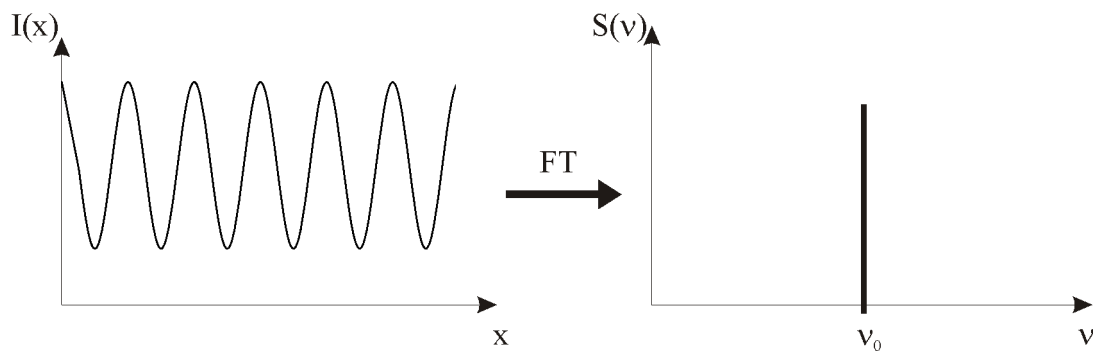


Figure 3.2: The interferogram of a monochromatic light source.

For a monochromatic light source (see Fig. 3.2) the intensity as a function of the mirror position can be written as

$$I(x) = S(\nu_0) \cos(2\pi\nu_0 x), \quad (3.0.1)$$

in which  $\nu_0 = 1/\lambda$  represents the wave number and  $S(\nu_0)$  the intensity of the monochromatic spectral line at wave number  $\nu_0$ . For a polychromatic light source, the intensity can be expressed as an integral over all possible wavelengths:

$$I(x) = \int_0^\infty S(\nu) \cos(2\pi\nu x) d\nu. \quad (3.0.2)$$

The interferogram of a broad-band lamp is shown in Fig. 3.3. Here the interferogram has only one position of maximum height, the so-called “white-light position”. At this point the retardation  $x$  between the two beams in the interferometer is zero. Only constructive interference takes place.

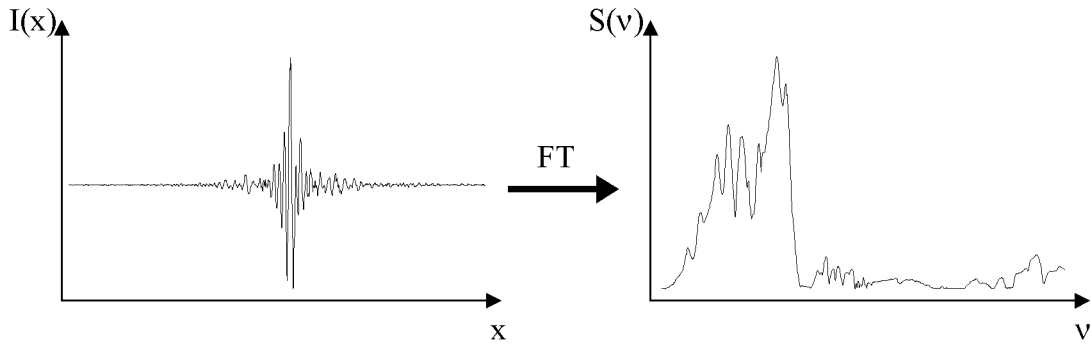


Figure 3.3: Interferogram of a polychromatic light source.

The frequency spectrum can be calculated by applying a Fourier transformation to the interferogram:

$$f(x) = \lim_{p \rightarrow \infty} \sum_{n=-p}^p c_n e^{in\omega x}, \quad c_n = \frac{1}{p} \int_{-p}^p f(x) e^{\frac{2\pi}{p} nx} dx. \quad (3.0.3)$$

The measured interferogram is a discrete function because only a finite number of mirror positions can be saved. So the variables  $x$  and  $\nu$  are replaced by discrete nodes  $n\Delta x$  and  $k\Delta\nu$ . Here the distances between two nodes on the  $x$  and the  $\nu$  axis are related by the following expression:

$$\Delta\nu = \frac{1}{N \cdot \Delta x}. \quad (3.0.4)$$

This relation, the so-called “Rayleigh criterion”, defines the resolution of the spectrometer: If we want to distinguish to frequencies with distance  $\Delta\nu$  we have to measure the interferogram up to  $\frac{1}{N \cdot \Delta x}$ . For example, to achieve a resolution of  $\Delta\nu = 0.1 \text{ cm}^{-1}$  the mirror has to move  $6 \text{ cm}$ .

Now, the frequency spectra can be calculated by the following equation:

$$S(k \cdot \Delta\nu) = \sum_{k=0}^{N-1} I(n \cdot \Delta x) e^{i2\pi nk/N}. \quad (3.0.5)$$

The position of the mirror is determined by measuring the interferogram of a laser with well-known wavelength. The laser signal is detected by a diode after passing the interferometer (Connes advantage). The diode measures only the laser signal because its intensity is several orders of magnitudes stronger than the intensity of the white light source<sup>2</sup>.

The sampling theorem<sup>3</sup> states that unambiguous interpretation of the signal is possible only when the spectrum outside the Nyquist bandwidth is zero. Otherwise frequencies higher than the cut-off frequency are folded back, falsifying the resulting spectrum (“aliasing”).

After leaving the interferometer the light passes through the polarizer (consisting of polyethylene or BaF<sub>2</sub>) and is focused on the sample, which is located in a He-cooled cryostat<sup>4</sup>. In contrast to transmittance measurements, we have to place for reflectivity measurements an additional unit containing four mirrors into the spectrometer, which enables measurements under quasi-normal incidence (11°). At last, several mirrors focus the light coming from the sample onto the detector.

Depending on the frequency range we are interested in, we have to use different detectors: We use semiconductor diodes for the near-infrared regime, the nitrogen-cooled HgCdTe (“MCT”) semiconductor diode for the mid-infrared regime and a He-cooled Bolometer for the far-infrared regime.

Besides the advantages of the Fourier-transform spectrometer we have to keep some things in mind: As mentioned above, the resolution of the spectrometer is inversely proportional to the length of the interferogram ( $N \cdot \Delta x$ ). This implies, that we cannot reach an infinite resolution, because we cannot measure an interferogram of infinite

---

<sup>2</sup>In between two minima of the diode signal the detector is triggered electronically, giving a higher density of data points. This is needed to measure a broader range of frequencies.

<sup>3</sup>“*The Nyquist-Shannon sampling theorem*”

$$f_s \geq 2(f_{\max} - f_{\min}) \quad (3.0.6)$$

*states that perfect reconstruction of a signal is possible when the sampling frequency  $f_s$  is greater than twice the maximum frequency of the signal being sampled, or equivalently, that the Nyquist frequency ( $\nu_N = \frac{N}{2} \Delta\nu = \frac{1}{2\Delta x}$ ) exceeds the bandwidth of the signal being sampled. If lower sampling rates are used, the original signal’s information may not be completely recoverable from the sampled signal.”, see [112].*

<sup>4</sup>Temperatures between 8.5 and 780 K can be achieved. In order to avoid the formation of ice layers at low temperatures, the pressure within the cryostat has to be less than 10<sup>-5</sup> mbar. Because the pressure within the spectrometer is roughly 10 mbar, the cryostat is separated from the rest of the spectrometer by transparent windows made of polyethylene and potassium bromide (KBr) for the FIR and MIR/NIR regime, respectively.

---

length. Thus, we have to truncate the interferogram at a certain point, which introduces the so-called “leakage effect”, described mathematically by multiplying the interferogram with a so-called boxcar function. This function is equal to one for all  $x$  positions of the measured interferogram and zero otherwise. The Fourier transform of this product function can be calculated by using the convolution theorem [111]: The Fourier transform of a product of two functions  $f_1$  and  $f_2$  is equal to the convolution of the two Fourier transformed functions  $\tilde{f}_1$  and  $\tilde{f}_2$ . The Fourier transform of the boxcar function is the sinc function which leads to broad artifacts (side bands) in the spectrum. We can partly remove this problem by multiplying the interferogram with a function, which has a more favorable Fourier transform, which strongly fades out the side bands of the interferogram. One of this so-called “apodization”<sup>5</sup> or window functions is the Blackman-Harris 3-term function:

$$w(n) = 0.42 - 0.5 \cdot \cos\left(\frac{2n\pi}{M}\right) + 0.08 \cdot \cos\left(\frac{4n\pi}{M}\right), \quad n = 0, \dots, M \quad (3.0.7)$$

which is used in all measurements. Here  $M$  represents the length of the interferogram. The application of an apodization function leads to a broadening and a reduction of the erroneous side peaks in the frequency spectrum. This effect is important only for very sharp lines (compared to the frequency resolution), which can be found in spectra of molecules. But the results presented in this work are not notably influenced by this effect.

The digitalization of the interferogram leads to other problems: The spectrum is only known at discrete frequency points, namely multiples of the fundamental frequency given by the finite length of the interferogram and the discrete nature of the data acquisition. This so-called “picket-fence effect” can be corrected by enlarging the erroneous by adding zeros at the end of the interferogram, i.e., we increase  $N$  in (3.0.4). In contrast to other interpolation methods, this method has no effect on the line shape of the frequency spectrum.

The Fourier transformation gives generally a complex spectrum  $S(\nu)$  if the interferogram is not symmetric around the white-light position. This asymmetry results from the discrete structure that is in general not centered exactly at the white-light position and the usage of electronic filters, which are necessary to avoid the aliasing effect. In order to get a real frequency spectrum  $R(\nu)$  we have to determine the phase  $\phi$  of the complex spectrum:

$$R(\nu) = \operatorname{Re} [S(\nu)e^{i\phi}], \quad \phi = \arctan \left[ \frac{\operatorname{Im}[S(\nu)]}{\operatorname{Re}[S(\nu)]} \right]. \quad (3.0.8)$$

A fast determination of the phase factor is achieved by using the Mertz [113] method.

---

<sup>5</sup>Apodization literally means “removing the feet”.

To achieve finally the reflectance (transmittance) spectrum of the sample we have to measure a reference spectrum  $S_R(\nu)$  ( $S_0(\nu)$ ):

$$R(\nu) = \frac{S_R(\nu)}{S_{Au}(\nu)}, \quad T(\nu) = \frac{S_T(\nu)}{S_0(\nu)}. \quad (3.0.9)$$

In case of a reflectance measurement  $R(\nu)$ ,  $S_{Au}(\nu)$  represents a single-channel spectrum where the sample is replaced by a gold mirror. In case of a transmittance measurement  $T(\nu)$ , a reference spectrum  $S_0(\nu)$  is needed, whereas the sample is removed.

In conclusion, Fourier spectroscopy is an excellent tool for the investigation of optical properties of matter. It is fast and provides a very high accuracy.

## 3.1 Determination of the response functions

In most cases the interaction of a solid with an electromagnetic wave can be described within the linear-response theory [114]. In order to determine the included response functions from the measured reflectance we use two different methods in this thesis which are described in the following.

### 3.1.1 Drude-Lorentz model

We start with the so-called *normal Drude-Lorentz model* [114] and fit the included parameters to the experimental data: Within this model the charge carriers are treated as quantum mechanical, damped, independent, harmonic oscillators which are excited by the electric field<sup>6</sup>. In case of hexagonal and orthorhombic compounds, we can find a set of axes (here, the crystallographic axes  $\{a, b, c\}$ ) such that the real as well as the imaginary part of the  $3 \times 3$  tensor of the dielectric function  $\hat{\epsilon}$  have diagonal form. For this crystal symmetries, we can express the matrix elements  $\epsilon_i(\omega)$  with  $i = \{a, b, c\}$  of the dielectric function as

$$\epsilon_i(\omega) = \epsilon_i^\infty + \sum_j \frac{\omega_{p,j}^2}{\omega_{0,j}^2 - \omega^2 - i\gamma_j\omega}. \quad (3.1.1)$$

The expression depends on a set of parameters  $(\epsilon^\infty, \omega_{0,j}, \omega_{p,j}, \gamma_j)$ , which can be fitted to experimental data. Here  $\omega_{0,j}$ ,  $\gamma_j$ , and  $\omega_{p,j}$  denote the transverse eigenfrequency, damping, and the “plasma frequency” of the  $j$ th oscillator. The sum in (3.1.1) runs over all contributions to  $\epsilon(\omega)$ . Due to the fact that it is not possible to include all excitations we have to truncate the summation at a certain frequency and summarize all higher frequency terms in a constant  $\epsilon^\infty$ , which also contains the vacuum contribution equal to 1. The plasma frequency  $\omega_{p,j}$  represents the maximum frequency which the charge carriers in the crystal can follow and is given by the following expression:

$$\omega_{p,j} \equiv \sqrt{\frac{4\pi N e^2}{m}}. \quad (3.1.2)$$

Here  $e$  designates the electronic charge,  $m$  the effective band mass, and  $N$  the density of electrons. Using the Fresnel formula for (quasi) normal incidence

$$R = |\tilde{r}(\omega)|^2 = \left| \frac{1 - \sqrt{\hat{\epsilon}(\omega)}}{1 + \sqrt{\hat{\epsilon}(\omega)}} \right|^2, \quad (3.1.3)$$

in which  $\tilde{r} = (1 - \hat{N}(\omega))/(1 + \hat{N}(\omega))$  denotes the complex reflection coefficient and  $\hat{N}$  the complex index of refraction, we can determine the reflectance and fit<sup>7</sup> the parameter  $(\epsilon^\infty, \omega_{0,j}, \omega_{p,j}, \gamma_j)$  to the experimental data. In addition, we can determine the

<sup>6</sup>The Drude response which describes metals as a classical gas of electrons can be derived from the Kubo formula [91].

<sup>7</sup>All fits in this thesis using the normal Drude-Lorentz model have been performed using the program ReFFIT 1.2.56 by A. Kuz'menko (Département de Physique de la Matière Condensée, Université de Genève, Switzerland).

optical conductivity directly by using the relation (2.11.8). In sections “4.3 Spin-lattice interactions in multiferroic  $\text{MnWO}_4$ ” and “4.4 Phonon modes of monoclinic  $\text{BiB}_3\text{O}_6$ ” we consider monoclinic compounds, where the tensor of the dielectric function includes two non-diagonal matrix elements unequal to zero. In order to describe these compounds as well, we use the procedure described by Kuz’menko et al. [188] and extend the normal Drude-Lorentz to a *generalized* Drude-Lorentz model.

The Drude-Lorentz model can also be used to describe the magnetic permeability  $\hat{\mu}$  which is represented by a complex tensor analogous to the dielectric function  $\hat{\epsilon}$ .

### 3.1.2 Kramers-Kronig analysis

In addition to the Drude-Lorentz model, we use the Kramers-Kronig relation (see section “2.11.1 Response Functions and Optical Conductivity”) to determine the complex response functions directly from the measured reflectance. In contrast to the Drude-Lorentz model, the Kramers-Kronig analysis consider every detail of the experimental data. We start with the polar form of the complex reflection coefficient  $\tilde{r}(\omega)$ :

$$\tilde{r}(\omega) = |r(\omega)| \cdot e^{i\phi_r(\omega)} = \frac{n-1+ik}{n+1+ik}, \quad \ln[\tilde{r}(\omega)] = \ln|r(\omega)| + i\phi_r(\omega), \quad |r(\omega)| = \sqrt{R(\omega)}. \quad (3.1.4)$$

For normal incidence the real  $\ln|r(\omega)|$  and the imaginary part  $\phi_r(\omega)$  of  $\ln[\tilde{r}(\omega)]$  are connected by the Kramers-Kronig relation (2.11.9) and we can calculate the phase  $\phi_r(\omega)$ :

$$\phi_r(\omega_0) = -\frac{1}{\pi} \mathcal{P} \int_{-\infty}^{\infty} \frac{\ln|r(\omega)|}{\omega^2 - \omega_0^2} d\omega = -\frac{2\omega_0}{\pi} \mathcal{P} \int_0^{\infty} \frac{\ln|r(\omega)|}{\omega^2 - \omega_0^2} d\omega. \quad (3.1.5)$$

Here, the problem is that we do not know  $\ln|r(\omega)|$  for all frequencies between 0 and  $\infty$ . So we have to extrapolate  $R$  for example with a Drude-Lorentz fit. This has to be done very carefully, because the Kramers-Kronig transformation (3.1.5) is very sensitive to the extrapolation procedure. Especially, the Kramers-Kronig transformation requires a smooth transition between the experimental data and the extrapolation function at the first  $\omega_f$  and the last  $\omega_l$  measured data point. In addition, the numerical integration in (3.1.5) is nontrivial. The problem with the singularity at  $\omega = \omega_0$  is removed by subtracting

$$\int_0^{\infty} \frac{\ln|r(\omega_0)|}{\omega'^2 - \omega_0^2} d\omega' = 0, \quad (3.1.6)$$

from (3.1.5). This leads to the following expression:

$$\phi_r(\omega_0) = -\frac{2\omega_0}{\pi} \mathcal{P} \int_0^{\infty} \frac{\ln|r(\omega)|}{\omega^2 - \omega_0^2} d\omega = -\frac{2\omega_0}{\pi} \mathcal{P} \int_0^{\infty} \frac{\ln|r(\omega)| - \ln|r(\omega_0)|}{\omega^2 - \omega_0^2} d\omega. \quad (3.1.7)$$

The integral in (3.1.7) can be divided into three parts:

$$\begin{aligned} \phi_r(\omega_0) &= -\frac{2\omega_0}{\pi} \mathcal{P} \int_0^{\infty} \frac{\ln|r(\omega)| - \ln|r(\omega_0)|}{\omega^2 - \omega_0^2} d\omega \\ &= -\frac{2\omega_0}{\pi} \mathcal{P} \left[ \int_0^{\omega_0-\epsilon} \dots d\omega + \int_{\omega_0+\epsilon}^{\omega_0+\epsilon} \dots d\omega + \int_{\omega_0+\epsilon}^{\infty} \dots d\omega \right]. \end{aligned} \quad (3.1.8)$$

The first integral can be calculated by the Simpson or the trapez rule. The second integral can be evaluated by the usage of the l'Hospital rule

$$\begin{aligned}
 -\frac{2\omega_0}{\pi} \lim_{\epsilon \rightarrow 0} \int_{\omega_0-\epsilon}^{\omega_0+\epsilon} \frac{\ln|r(\omega)| - \ln|r(\omega_0)|}{(\omega - \omega_0)(\omega + \omega_0)} d\omega &= -\frac{2\omega_0}{\pi} \int_{\omega_0-\epsilon}^{\omega_0+\epsilon} \frac{\left. \frac{d \ln|r(\omega)|}{d\omega} \right|_0}{\omega + \omega_0} d\omega \\
 &\approx -\frac{1}{\pi} \left. \frac{d \ln|r(\omega)|}{d\omega} \right|_0 \cdot 2\epsilon,
 \end{aligned} \tag{3.1.9}$$

which causes the dependence of the Kramers-Kronig transformation on the slope of the extrapolation function at  $\omega_f$  and  $\omega_l$ . The determination of the third integral in (3.1.8) is difficult because the numerical integration cannot be performed up to infinity. So we have to truncate the integral at a certain value  $\omega_1$  (cutoff frequency) and estimate the remaining part. For  $\omega \rightarrow \infty$  the reflectance  $R$  behaves like  $R(\omega) = R(\omega_1) \left(\frac{\omega_1}{\omega}\right)^4$ . So we have to determine the following integral [114]

$$-\frac{2\omega_0}{\pi} \int_{\omega_1}^{\infty} \frac{\ln \left| \sqrt{R(\omega_1) \left(\frac{\omega_1}{\omega}\right)^4} \right|}{\omega^2 - \omega_0^2} d\omega = \frac{1}{2} \cdot \frac{2}{\pi} \cdot \frac{\omega_0}{\omega_1} \cdot \Phi \left( (\omega_0/\omega_1)^2, 2, \frac{1}{2} \right). \tag{3.1.10}$$

Here  $\Phi$  represents the Lerch transcendent. As shown in Fig. 3.4 the cutoff frequency has to be set at a sufficient high frequency to achieve a smooth transition to the  $\omega^4$  behavior. The subtraction of (3.1.6) introduces an error since we integrate only up to the cutoff frequency  $\omega_1$ . We can annihilate this error by simply adding this term again to (3.1.7)

$$\int_0^{\infty} \frac{\ln|r(\omega_0)|}{\omega'^2 - \omega_0'^2} d\omega' = \frac{1}{\pi} \cdot (\ln|r(\omega_0)| - \ln|r(\omega_1)|) \cdot \ln \left( \frac{\omega_1 + \omega_0}{\omega_1 - \omega_0} \right). \tag{3.1.11}$$

The phase angle  $\phi_r$  is known modulo  $\pi$ . This is due to the fact that the sign of  $\sqrt{R}$  is not fixed experimentally. However, the way the transform is made guarantees that  $\phi_r = 0$  for  $\omega = \infty$ . This implies that we have to use  $\tilde{r} = (\hat{N} - 1)/(\hat{N} + 1)$  instead of  $\tilde{r} = (1 - \hat{N})/(1 + \hat{N})$ , because this has a phase angle zero (not  $\pi$ ) for  $\text{Re}(\hat{N}) > 1$ ,  $\text{Im}(\hat{N}) = 0$ . The latter condition is automatically satisfied in the high-frequency limit of a physical response function.

We use the complex reflection coefficient to determine the complex index of refraction:

$$\tilde{r} = \frac{\hat{N} - 1}{\hat{N} + 1} \Rightarrow \hat{N} = \frac{1 + \tilde{r}}{1 - \tilde{r}}. \tag{3.1.12}$$

The response functions can be determined in the following way:

$$\hat{N}^2 = \mu_1 \hat{\epsilon}, \quad \mu_1 \equiv 1 \tag{3.1.13}$$

$$\Rightarrow \hat{\sigma} = -\frac{i\omega}{4\pi} (\hat{\epsilon} - 1). \tag{3.1.14}$$

In order to calculate the optical conductivity in “practical units”, we have to multiply  $\hat{\sigma}$  by  $\frac{\pi}{15}$  [115]: In cgs units the conductivity is expressed in [ $s^{-1}$ ].

$\omega_0$ [ $cm^{-1}$ ]	$\omega_p$ [ $cm^{-1}$ ]	$\gamma$ [ $cm^{-1}$ ]	S
0	300	1	-
100	200	5	4.000
280	200	20	0.510
300	400	5	1.778
600	700	1	1.361
650	30	3	0.002
11000	10000	1500	0.826
13000	10000	1500	0.592
15000	7000	1500	0.218

Table 3.1: Drude-Lorentz model parameter, where,  $S$  denotes the oscillator strength  $S = \omega_p^2/\omega_0^2$ .

If we write the standard formula for the optical conductivity  $\sigma_1$  in  $s^{-1}$ , using frequencies expressed in  $cm^{-1}$ , we have to multiply the conductivity by a factor of  $(2\pi c) \cdot 10^2$ , where  $c$  is the speed of light in  $m/s$ . In order to get the conductivity in SI units we have to multiply the cgs conductivity by  $(10^{-2} 4\pi \epsilon_0)$ , where  $\epsilon_0$  is the permittivity of free space and the  $10^{-2}$  prefactor is used to have the final conductivity in  $\Omega^{-1} cm^{-1}$ . In the end the conductivity is written with frequencies in  $cm^{-1}$  and has to be multiplied by  $(8\pi^2 \epsilon_0 c) = 0.209585 \Omega^{-1}$ . Since  $(\pi/15) = 0.209439$ , this is a good approximation to the exact value.

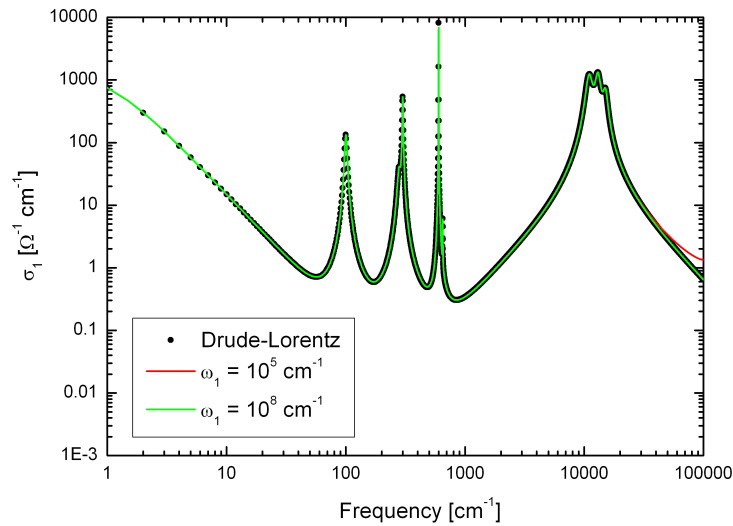


Figure 3.4: Comparison of Drude-Lorentz result and Kramers-Kronig transformation and the dependence of the Kramers-Kronig transformation on the cutoff frequency  $\omega_1$ .

In order to compare the results of the Kramers-Kronig analysis with the Drude-Lorentz model we construct a reflectance using the normal Drude-Lorentz model with nine oscillators. The model parameters are shown in Tab. 3.1. Using (2.11.8) we can easily calculate the optical conductivity. Applying the Kramers-Kronig transformation to the reflectance between  $\omega_f = 30 \text{ cm}^{-1}$  and  $\omega_l = 2000 \text{ cm}^{-1}$  we determine the optical conductivity as well. In contrast to real experimental data, we have no problems with the transition between the reflectance data and the extrapolation function. As shown in Fig. 3.4 we see an perfect description of the Drude-Lorentz results, for a sufficient high cutoff frequency  $\omega_1 = 10^8 \text{ cm}^{-1}$ .



## 4 Measurements

In the following chapter we present the results of our optical measurements. The chapter is divided into four parts. The first section reports about the crystal-field excitations in the transition-metal oxyhalide VOCl. We investigate VOCl as a reference compound for the local crystal-field excitations of  $3d^2$   $V^{3+}$  ions. The final aim is to distinguish between local crystal-field excitations and propagating orbital waves in compounds where the exchange interactions are important. In the next section we describe the analysis of the lattice dynamics and their dependence on Ga doping in the hexagonal multiferroic compounds  $YMnO_3$  and  $YMn_{0.7}Ga_{0.3}O_3$ , which provides a better understanding of the origin of ferroelectricity in these hexagonal systems. In the following we present the investigation of the spin-lattice interaction in the multiferroic, monoclinic compound  $MnWO_4$ , which plays an important role in the coupling between the antiferromagnetic and the ferroelectric orders. The analysis of the lattice dynamics provides a better understanding of this coupling. Furthermore we present a detailed study of the lattice dynamics of the monoclinic compound  $BiB_3O_6$ , which is required for a quantitative understanding of the nonlinear optical properties of this sample. In the last section we investigate the anomalous antiferromagnetic metallic oxide  $CaCrO_3$ , which shows an exception of a quite general relation between magnetic order and electrical conductivity in transition-metal oxides: insulators usually exhibit antiferromagnetism, whereas ferromagnetism typically coexists with metallic conductivity. So observations of antiferromagnetic order in transition-metal oxides with metallic conductivity are of great interest.

### 4.1 Crystal-Field Excitations in VOCl

In this section we analyze the crystal-field excitations in the orthorhombic transition-metal oxyhalide VOCl by using group-theoretical considerations as well as cluster-model calculations presented in the last sections. VOCl is used as a reference system for  $YVO_3$  where orbital excitations were observed [116]. In  $YVO_3$ , the collective Jahn-Teller effect, i.e. the coupling to the lattice, as well as exchange interactions lead to an interaction of orbitals on different sites [117, 118], which can result in coupled long-range spin and orbital order. If the coupling to the lattice is dominant, the excitations are well described by local crystal-field excitations [61, 119, 120]. These excitations change the orbital occupation on a single site, i.e. the dispersion is negligible. In the opposite case of dominant exchange interactions, one expects orbital waves (orbitons) with a significant dispersion [121], which represents novel collective elementary excitations. These orbitons are analogous to spin waves in a magnetically ordered state and are expected to reveal the fundamental orbital interactions responsible for the interesting physical properties. In order to distinguish between orbitons and local crystal-field

excitations, it is necessary to compare the optical data of  $\text{YVO}_3$  with the expectations for local crystal-field excitations of  $3d^2 \text{V}^{3+}$  ions. Motivated by the results of the analysis of the sister compound  $\text{TiOCl}$ , where the orbital excitations are very well described in terms of local crystal-field excitations [120, 122], we probe the absorption spectrum of  $\text{VOCl}$ .

After a short overview of the transition-metal oxyhalides  $\text{MOX}$  we describe some group-theoretical principles and the different selection rules caused by the dipole operator. In the following, we present a detailed group theoretical analysis of the crystal-field excitations of  $\text{VOCl}$  and compare the prediction with the experimental observations. In the second part, we supplement the cluster-model calculations presented by Benckiser [124] and give a detailed analysis of the eigenstates which are essential for the description of the experimental data.

The observation of challenging low-dimensional phenomena in  $\text{TiOCl}$  [120, 122] has reattracted interest in the transition-metal oxyhalides  $\text{MOX}$  with  $\text{M} = \{\text{Sc}, \text{Ti}, \text{V}, \text{Cr}, \text{Fe}\}$  and  $\text{X} = \{\text{Cl}, \text{Br}\}$ . The group of transition-metal oxyhalides consists of (at room-temperature) crystallographically iso-structural compounds, which allows the systematic investigation of the interactions between the crystal lattice and the several electronic configurations of the transition-metal. All oxyhalides show (electrically) Mott-insulating properties caused by strong electron localization. Like all transition-metal oxyhalides,  $\text{VOCl}$  crystallizes in an orthorhombic structure with space group  $Pmmn$  ( $D_{2h}^{13}$ ) at 150 K [123], with one crystallographic V site.  $\text{VOCl}$  consists of strongly distorted  $[\text{VO}_4\text{Cl}_2]$  octahedral units where the  $\text{V}^{3+}$  ions are coordinated by four oxygen and two chlorine ions. The octahedral units are linked via edges along the crystallographic **b** axis and via corners along the **a** axis, forming quasi-two-dimensional bilayers in the **ab** plane. These planes are well separated from each other by two layers of Cl ions [125, 126]. Recent neutron as well as synchrotron measurements show a structural phase transition at  $T_N \approx 80$  K [123], where the site symmetry on the V site changes from  $C_{2v}$  (295 K) to  $C_2$  (20 K).

$\text{VOCl}$  is believed to exhibit (quasi) two-dimensional antiferromagnetic order below  $T_N$  (80 K) [127]. Fausti *et al.* [127] expect that the occupation of the  $d_{xy}$  orbital leads to a substantial direct exchange interaction between ions in different chains in  $\text{VOCl}$ , which favors a two-dimensional antiferromagnetic order. (In  $\text{TiOCl}$ , the occupation of the  $d_{y^2-z^2}$  orbital in the ground state forms quasi-1D  $S = 1/2$  chains, which causes strong direct exchange between neighboring Ti sites along the **b** axis and negligible coupling in the other directions. By using a one-dimensional  $S = 1/2$  Heisenberg model the magnetic susceptibility of  $\text{TiOCl}$  can be well described at high temperatures.) In contrast to  $\text{TiOCl}$ , the magnetic susceptibility of  $\text{VOCl}$  is isotropic at high temperatures and well described by a two-dimensional Heisenberg model for a square lattice. Wiedenmann *et al.* [128] report of a phase transition to a two-dimensional antiferromagnet at  $T_N = 80$  K ( $T_N = 150 \pm 5$  K [129]). Previous optical and electrical measurements have shown that  $\text{VOCl}$  is a semiconductor with a gap of  $\sim 2$  eV [129]. The resistivity at room temperature is  $5 \cdot 10^7 \Omega\text{cm}$  [129].

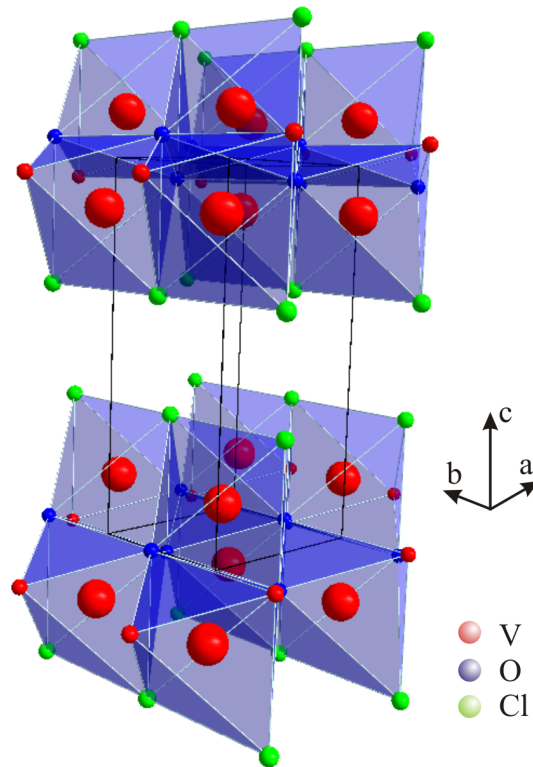


Figure 4.1: Crystal structure of VOCl.

Single crystals of VOCl have been grown by the chemical-vapor transport technique by T. Taetz and A. Möller.<sup>1</sup> The purity of the crystals was checked by x-ray powder diffraction.

Measuring the transmittance  $T(\omega)$  we can determine weakly infrared-active excitations below the gap of Mott-Hubbard insulators, where the reflectance is nearly constant and featureless. Therefore, the transmittance can be approximate by [136]

$$T(\omega) \approx (1 - R(\omega))^2 \exp(-\alpha(\omega)d). \quad (4.1.1)$$

Using the linear absorption coefficient  $\alpha = 2\omega\kappa/c$  we get a qualitative description of the absorption

$$\alpha(\omega) \approx -\ln T(\omega)/d + 2 \ln(1 - R(\omega))/d \approx -\ln T(\omega)/d + \text{const.} \quad (4.1.2)$$

Neglecting the almost constant second term we can use  $-\ln(T(\omega))/d$  or also  $-\ln(T(\omega))$  equivalently to  $\alpha(\omega)$  for the determination of weak orbital excitations.

The measured transmittance of VOCl at  $T = 20$  K and  $T = 300$  K for  $\mathbf{E} \parallel \mathbf{a}$  and  $\mathbf{E} \parallel \mathbf{b}$  is shown in Fig. 4.2. The features below 0.20 eV represent the upper part of the

<sup>1</sup>Institute of Inorganic Chemistry, University of Cologne, Greinstr. 6, 50939 Cologne, Germany.

phonon spectra whereas excitations above  $\sim 1.5$  eV indicate the beginning of the Mott-Hubbard gap. The excitations between 0.95 eV and 1.2 eV correspond to spin-forbidden transitions, which become weakly allowed by spin-orbit coupling or by the simultaneous excitation of a magnon. In case of such spin-flip bands the coupling to the lattice is only weak (the large width of spin-allowed excitations is attributed to vibronic Franck-Condon sidebands, see below). Additionally, these spin-flip bands often are very sharp because the orbital occupation is unchanged. The room-temperature behavior above 1.4 eV agrees very well with the optical absorption measurements at 300 K reported by Venien *et al.* [129].

Comparing the room-temperature ( $T = 300$  K) with the low temperature spectra ( $T = 20$  K), we find remarkable differences. The positions of the excitations at 0.32 eV ( $\mathbf{E} \parallel \mathbf{a}$ ) and 0.38 eV ( $\mathbf{E} \parallel \mathbf{b}$ ) stay nearly unchanged for both temperatures. But, at  $T = 20$  K, the spectra show a step at 0.21 eV in both directions. The step is caused probably by the structural transition, mentioned above. We will analyze this feature later on. Furthermore, we find a similar behavior at 1.48 eV in the low temperature regime, but the step is less pronounced. The different crystal-field excitations will be analyzed in the following.

### 4.1.1 Group-Theoretical Considerations

In order to analyze the crystal-field excitations in this compound we make use of the group theory, which plays a major role in the determination of the degeneracy and the symmetry types of the electronic levels in the crystalline field. The full rotational symmetry of the free atom includes an infinite number of symmetry operations,<sup>2</sup> which commute with the Hamiltonian. All rotations about any axis are symmetry operations of the full rotation  $O(3)$  group. But the lower symmetry of the crystal field includes only a finite number of rotations about finite angles, inversions and reflections. Within the unit cell there are sets of points in which each member of the set has an identical environment. These points are designated as SITES and the symmetry operations associated with one of these points define a group (SITE GROUP or POINT GROUP<sup>3</sup>), which is a sub-group<sup>4</sup> of the full rotational  $O(3)$  group and is isomorphic to one of the 32 point groups permitted in crystal structures. Each member of the set shows the complete symmetry of the appropriate site group.

<sup>2</sup>Improper rotations, inversion operations, mirror planes, and rotations build up the symmetry operations which create the 32 crystal classes corresponding to the 32 point groups [130].

<sup>3</sup>The symmetry operations in the point groups leave at least one point in space unchanged justifying the name “point group”. The operations included in space groups leave lines, planes, or polyhedra unchanged [132].

<sup>4</sup>If all elements of a group  $\mathcal{H}$  are also elements of a group  $\mathcal{G}$ , the group  $\mathcal{H}$  is called a SUB-GROUP of  $\mathcal{G}$  ( $\mathcal{H} \subseteq \mathcal{G}$ ). The ORDER of a group  $\mathcal{G}$  is defined by the number  $g$  of elements of  $\mathcal{G}$ . If  $g$  exists,  $\mathcal{G}$  is called a FINITE group. If there is no (finite) number  $g$ ,  $\mathcal{G}$  is called an INFINITE group. Crystallographic site-symmetry groups are always finite [131].

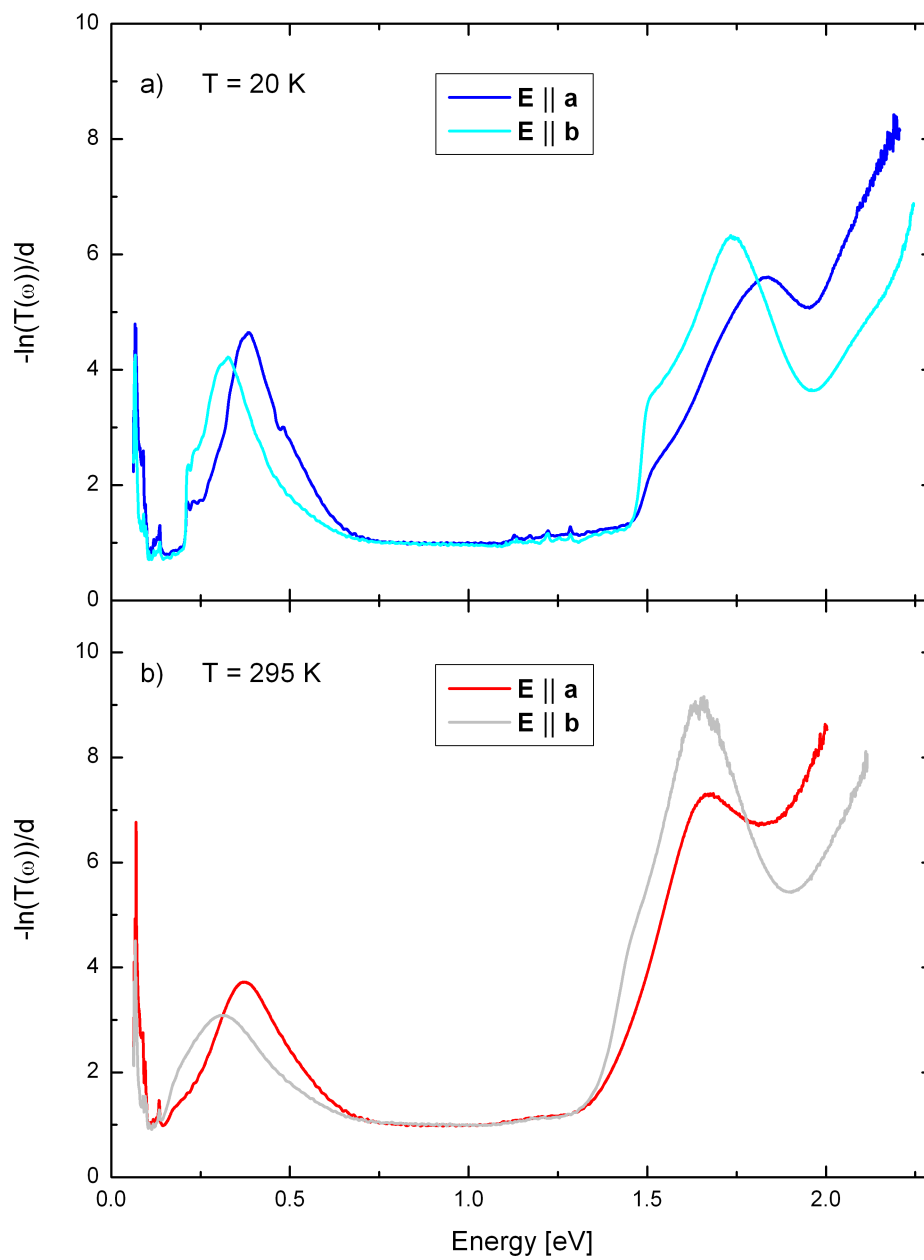


Figure 4.2:  $-\ln(T(\omega))/d$  of VOCl at a) 20 K and b) 295 K for  $\mathbf{E} \parallel \mathbf{a}$  and  $\mathbf{E} \parallel \mathbf{b}$ .

In the following we will present the definitions of several expressions, which we use in the group-theoretical analysis. The following definitions are taken from [132]: A REPRESENTATION of a group is defined by a set of non-zero square matrices which multiply in the same way as the elements of the group. Furthermore, the order of the matrices is called the DIMENSION of the representation. If the symmetry operation  $\hat{\mathbf{R}}$  is represented by the matrix  $\mathcal{D}(\hat{\mathbf{R}})$  then the trace of  $\mathcal{D}(\hat{\mathbf{R}})$  is called the CHARACTER of  $\hat{\mathbf{R}}$  for that representation. The so-called CHARACTER TABLES contain the characters of the various representations for a group. The definition of the character is motivated by the fact that the full matrices of a representation are often not needed, because the character alone can provide sufficient information. The matrices which describe the symmetry operation of a group can often be transformed to block matrices. A block matrix is called a IRREDUCIBLE representation, if there exists no similarity transformation, which reduces the representation further. Note, that the number of irreducible representations of a group is always equal to the number of classes. Additionally we can write every reducible representation  $\Gamma_r$  of a group as a sum of irreducible ones  $\Gamma_i$  of the same group:

$$\Gamma_r = \sum_i N_i \Gamma_i. \quad (4.1.3)$$

Here  $N_i$  represents the number of times  $\Gamma_i$  appears in  $\Gamma_r$  and can be determined by using the following expression:

$$N_i = \frac{1}{h} \sum_X n(X) \chi_r(X) \chi_i(X), \quad (4.1.4)$$

where  $h$  indicates the order of the group,  $\chi_r(X)$  and  $\chi_i(X)$  represent the character of the reducible  $\Gamma_r$  and irreducible representation  $\Gamma_i$ , respectively. The number of symmetry operations in the class is determined by  $n(X)$ .<sup>5</sup> If we lower the symmetry of a point group to one of its subgroups we may find that the irreducible representations of the point group are reducible representations of the subgroup. This has an important consequence for the analysis of crystal-field excitations: If the eigenstates of a crystal field are reducible representations of a crystal field of lower symmetry, a splitting of these eigenstates occurs if we lower the symmetry.

In addition, we present five theorems which are useful in analyzing crystal-field excitations, where the theorems are cited from [132]:

1. The number of non-equivalent irreducible representations of a group is equal to the number of classes in that group.
2. The sum of the squares of the dimensions of all the non-equivalent irreducible representations of a group is equal to the order of the group.

---

<sup>5</sup>The element  $P$  of a site-symmetry group is CONJUGATED to the element  $Q$  of the same group, if there exists another element  $X$  of the group such that  $P = X^{-1}QX$ . The elements of a group which are conjugated to each other form a so-called CLASS, [131].

3. The sum of the squares of the absolute values of the characters in any irreducible representation is equal to the order of the group.
4. The characters of two non-equivalent irreducible representations  $i$  and  $j$  satisfy

$$\sum_{\hat{\mathbf{R}}} \chi_i^*(\hat{\mathbf{R}}) \chi_j(\hat{\mathbf{R}}) = 0, \quad (4.1.5)$$

where  $\chi_i(\hat{\mathbf{R}})$  and  $\chi_j(\hat{\mathbf{R}})$  are the characters of the symmetry operation  $\hat{\mathbf{R}}$  in the representations  $i$  and  $j$ , and where the sum runs over the  $h$  symmetry operations of the group.

5. If the characters for some particular representation  $i$  satisfy

$$\sum_{\hat{\mathbf{R}}} \left| \chi_i(\hat{\mathbf{R}}) \right|^2 = h, \quad (4.1.6)$$

then  $i$  is irreducible.

Combining theorem (3) and (4) we get the so-called GREAT ORTHOGONALITY THEOREM

$$\sum_{\hat{\mathbf{R}}} \chi_i^*(\hat{\mathbf{R}}) \chi_j(\hat{\mathbf{R}}) = h \delta_{ij}, \quad (4.1.7)$$

which is very useful in generating character tables. The different irreducible representations are labelled after Bethe ( $\Gamma_1, \Gamma_2, \dots$ ) and Mulliken ( $A_1, A_2, B_1, \dots$ ). In Mulliken's nomenclature the one-dimensional irreducible representations are denoted with  $A$  if they are symmetric with respect to the principle symmetry axis  $C_n$  and  $B$  otherwise. The subscripts 1 or 2 indicate the behavior under the symmetry operations  $\sigma_v$ . The representation  $A$  is called the "totally symmetric" representation, which must always be present. Furthermore, we indicate two-fold degenerated irreducible representations with the letter  $E$  while three-, four-, and five-dimensional irreducible representations are labeled with  $T, G, H$ , respectively. The subscripts  $g$  (for gerade) and  $u$  (for ungerade) indicate the behavior under inversion. By convention, the number within the first column of the character table represents the dimensionality of the irreducible representation.

In addition to these group theoretical considerations we have to take some limiting factors of optical spectroscopy into account: We approximate the measured optical transitions by electric dipole transitions, because other multipole transitions are much weaker. The electric quadrupole transitions for example are eight orders of magnitude less probable than electric dipole transitions. An electric dipole transition is forbidden if the matrix element  $\langle i | \epsilon \cdot \hat{\mathbf{p}} | f \rangle$  of the dipole operator  $\hat{\mathbf{p}}$  is zero. (Here,  $i$  indicates the *initial* and  $f$  the *final* eigenstate). In order to determine the forbidden electric dipole transitions, we can use group-theory: The transition between two eigenstates  $i$  and  $f$  is forbidden, if the product of the irreducible representations describing the eigenstates  $i$  and  $f$  do not contain the irreducible representation of the dipole operator.

Furthermore, the dipole operator acts only on the angular momentum part of the wave function. Thus, an optical transition with linearly polarized light cannot change the spin (SPIN SELECTION RULE,  $\Delta S = 0$ ). This selection rule can be relaxed by taking into account spin-orbit coupling, which can be responsible for the admixing of terms of different spin multiplicity. Additionally, if we excite two spin-carrying modes simultaneously with total spin equal to zero, we can avoid the spin selection rule. For instance a spin-forbidden orbital excitation may gain a finite spectral weight by the simultaneous excitation of a magnon, giving rise to a so-called MAGNON-EXCITON SIDEBAND [138–140]. In case of a spin-forbidden excitation which energy is comparable with that of a spin-allowed transition we find an increased strength [141] due to the so-called “intensity stealing” where a spin-forbidden transition acquires intensity by “stealing” from e.g. a spin-allowed or a charge-transfer band, if both excitation mix with each other.

Within the Russel-Saunders coupling scheme, the matrix element of the dipole operator

$$p_{J,J'} = \langle \alpha L S J M | \hat{\mathbf{p}} | \alpha' L' S' J' M' \rangle \quad (4.1.8)$$

is non-zero, if

$$\Delta J = J - J' = 0, \pm 1, \quad (4.1.9)$$

and

$$J = J' = 0 \quad \text{is not allowed,} \quad (4.1.10)$$

and

$$\Delta M = M - M' = 0, \pm 1, \quad (4.1.11)$$

is fulfilled. Here,  $\Delta M = 0$  indicates linear polarized and  $\Delta M = \pm 1$  circular (clockwise (+1), counterclockwise (-1)) polarized light. The  $\Delta J$  selection rule can be extended to  $\Delta L = 0, \pm 1$ , except for transitions from initial states with  $L = 0$  to final states with  $L = 0$ .

The dipole operator  $\hat{\mathbf{p}}$  is a vector operator of the form  $\hat{\mathbf{p}} = r C^{(1)}$ , where  $C^{(1)}$  denotes the renormalized spherical harmonic tensor operator (2.4.5) of rank 1. Thus, the parity of the dipole operator is given by the parity of the spherical harmonics  $(-1)^k$ . Here,  $k \equiv 1$ , due to the dipole approximation. Hence, the dipole operator has odd parity, and transitions occur only between states of opposite parity: If we consider a transition-metal site with inversion symmetry, a  $d - d$  transition is forbidden within the dipole approximation, because the matrix element of the dipole operator between the two  $d$  wave functions vanishes due to the even parity of the  $3d$  wave functions

$$\langle \text{even} | \text{odd} | \text{even} \rangle = 0. \quad (4.1.12)$$

Hence, a  $d - d$  transitions do not contribute to the optical conductivity  $\sigma(\omega)$ . One possibility to gain finite spectral weight is the simultaneous excitation of a phonon that removes the center of inversion, in which case the parity selection rule does not apply anymore. The absence of inversion symmetry allows a mixture of e.g.  $d$  and  $p$

wave functions. In this case spin-allowed transitions are observed with intensities 100 times larger than spin-forbidden ones, but still a few orders of magnitude less intense than fully allowed transitions, because the  $p-d$  mixing is smaller in the dynamic environment than in the static one. In order to determine the orbital excitation energy, the phonon energy, which in transition-metal compounds is of the order of 50 - 80 meV, has to be subtracted from the experimentally observed peak position. In real samples, inversion symmetry may additionally be broken by impurities or other lattice imperfections, e.g. oxygen non-stoichiometry. But the contribution is expected to be still much smaller than the phonon-assisted one in the case of low impurity concentrations. In addition, the parity selection rule may be violated by an external electric field which mixes states of opposite parity via the Stark effect [142].

In case of a broken inversion symmetry at the transition-metal ion site, we have to take energetically higher lying configurations at the transition-metal ion into account. Here, the ground state  $|\psi_0\rangle$  can be written as

$$|\psi_0\rangle = \alpha|\psi_d\rangle + \beta|\psi_p\rangle, \quad (4.1.13)$$

where  $|\psi_d\rangle$  and  $|\psi_p\rangle$  represent wave functions with  $d$ - and  $p$ -character, respectively. Although, the contributions of  $p$ -states to the ground state are small, i.e.  $\beta \ll \alpha$ , these  $p$ -states contribute decisively to the optical conductivity. For compounds with broken inversion symmetry at the transition-metal ion site we have strong contributions from transitions between  $p$ - and  $d$ -states at the transition-metal ion to the optical conductivity. In the following, we neglect the contributions of  $p$ -states at the transition-metal site due to the enormous computational effort, and consider only the contributions from the  $d$ -states, the spin-orbit coupling and the charge-transfer excitations to the optical conductivity.

The dipole approximation implies a further selection rule: The dipole operator vanishes if  $\Delta l = l' - l \neq \pm 1$ , where  $l$  and  $l'$  denote the angular momenta of the initial and the final eigenstate, respectively. This means that e.g. transitions from  $s$  to  $p$  are allowed, but  $s$  to  $f$  are forbidden. But there exist several violations of this selection rule, e.g. transitions between  $p^2 - pg$  observed in PbI [142]. The violations arise as a result of configuration interaction between  $pd$  and  $pg$  configurations. Furthermore, there is another type of  $\Delta l$  violations: The electric dipole operator is an one-electron operator, and as a result transitions can theoretically occur only between two configurations that differ in only one electron. Nevertheless, transitions such as  $s^2 - dp$  are observed that have the appearance of involving two-electron jumps – one jump with  $\Delta l = \pm 1$  and another one with  $\Delta l = \pm 2$ . The explanation lies again in configuration interaction effects [48].

In VOCl all  $d-d$  excitations are allowed without the additional excitation of a phonon because there is no inversion symmetry on the V sites. The lowest crystal-field  $d-d$  excitations are located below the charge gap and above the phononic regime. In order to investigate these excitations, we have to distinguish between  $d-d$  and other

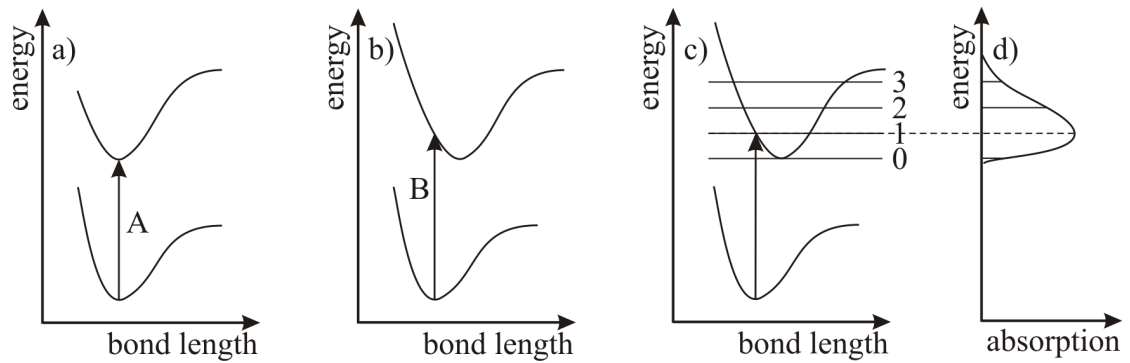


Figure 4.3: The Franck-Condon principle: a) The diagram shows a transition between two states with the same nuclear separation. The horizontal position of a parabola (potential) indicates the distance to the ligands after the lattice has been allowed to relax in the particular orbital state. b) The vertical transition B involves no nuclear movement and is allowed. c) + d) The vibrational states of the upper electronic state have been added. The lines within a parabola denote phonon excitations. The strongest overlap is obtained for the level which is closest to where the vertical arrow cuts through a parabola. Due to the dispersion of the phonons and due to the contribution of phonons with different energies, the sharp subbands of individual excited states are usually not resolved in a solid, yielding a single broad band. The width and the line shape of an absorption band in  $\sigma(\omega)$  depends on the difference in bond length of the different orbital states.

excitations such as e.g. excitons which are measured simultaneously. In the case of a sizable electron-phonon coupling the orbital excitations are dressed by vibrational excitations. The combined vibrational-electronic excitation is called “vibron”. The coupling to phonons give rise to a pronounced broadening. The underlying principle is the Franck-Condon principle [143–146].

Due the uncertainty principle of quantum mechanics, high-energy transitions in solids are very fast, i.e. crystal-field transitions take place in about  $10^{-15}$  sec, which is much faster than the time scale of nuclear motions of about  $10^{-13}$  sec. Thus, the transition is vertical in the corresponding energy diagram Fig. 4.3, reflecting that the lattice cannot change during the transition. Therefore the positions of the nuclei can be assumed to be unchanged during an electronic transitions. This has significant effects upon the appearance of band spectra. As shown in Fig. 4.3 c) the transition from the relaxed ground state to the second vibronic excited state (1) is the strongest. But also the transitions to the (0), (2), (3) states may exhibit a finite probability, which is determined by the overlap of the phonon wave functions at the initial and final state (known as Franck-Condon factors). This results in several absorption lines for the corresponding  $d-d$  transition, namely phononic side bands, in addition to the pure electronic transition. In crystals several phonons (each with dispersion) may contribute to the Franck-Condon process, which makes the absorption band rather structureless.

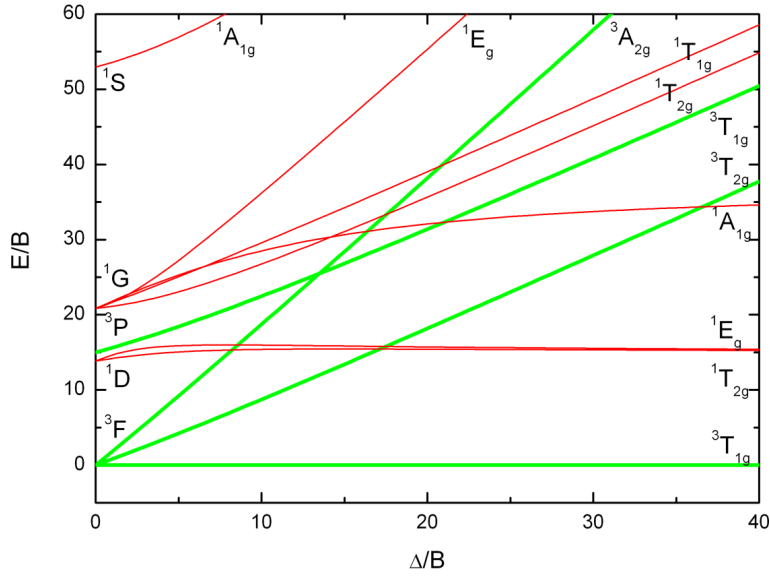


Figure 4.4: Tanabe-Sugano diagram for a  $d^2$  configuration in a cubic environment [148] with Racah parameters  $B = \frac{9}{441} F^2 - \frac{5}{441} F^4 = 886 \text{ cm}^{-1}$ , and  $C = \frac{35}{441} F^4 = 3916 \text{ cm}^{-1}$ . The parameter  $\Delta$  indicates the strength of the crystal field in units of the Racah parameter  $B$ . The colors indicate the degree of spin degeneracy: red (1-fold) and green (3-fold).

We are interested in the low-energetic excitations, which are determined by the lowest eigenstates. In the following, we use a point-charge model picture where we neglect spin-orbit coupling as well as the hybridization between the V ion and the surrounding ligands. In addition, we assume that  $\mathbf{x} \parallel \mathbf{a}$ ,  $\mathbf{y} \parallel \mathbf{b}$ , and  $\mathbf{z} \parallel \mathbf{c}$ . The analysis of the crystal-field excitations shown in Fig. 4.2 starts with the free  $V^{3+}$  ion, which has a  $3d^2$  electronic configuration. Without crystal field, the ground state is formed by the  ${}^3F$  multiplet according to Hund's rules. The  ${}^1D$  multiplet lies below the  ${}^3P$  and  ${}^1G$  terms. This can be explained by the fact that the electrons in the  ${}^1G$  multiplet ( $L = 4$ ) occupy the same orbital and cannot avoid each other. Within the  ${}^3P$  multiplet the electrons have to run more in the opposite direction around each other than in the  ${}^1D$  multiplet giving rise to an increased potential energy. In order to identify the different absorption lines shown in Fig. 4.2 with crystal-field excitations, i.e. transitions between crystal-field eigenstates provided by the dipole operator, we have to distinguish between two site symmetries on the V site: Within the room-temperature phase ( $T > 80 \text{ K}$ ) the site symmetry is  $C_{2v}$  [133], and  $C_2$  for the low-temperature phase ( $T < 80 \text{ K}$ ) [123]. The ground state in a crystal field with cubic symmetry is the nine-fold degenerate  ${}^3T_1$  level, see Fig.4.4. We start with the analysis of the crystal-field excitations in the room-temperature regime: Lowering the site-symmetry from  $O_h$  to  $C_{2v}$ , the cubic  ${}^3T_{1g}$  level splits into three distinct orbitals ( ${}^3A_2 + {}^3B_1 + {}^3B_2$ ) [184], each showing three-fold spin degeneracy,<sup>6</sup> see Fig. 4.5.

<sup>6</sup>The crystal-field operator acts only on the angular momentum part of the wave function and cannot remove the spin degeneracy.

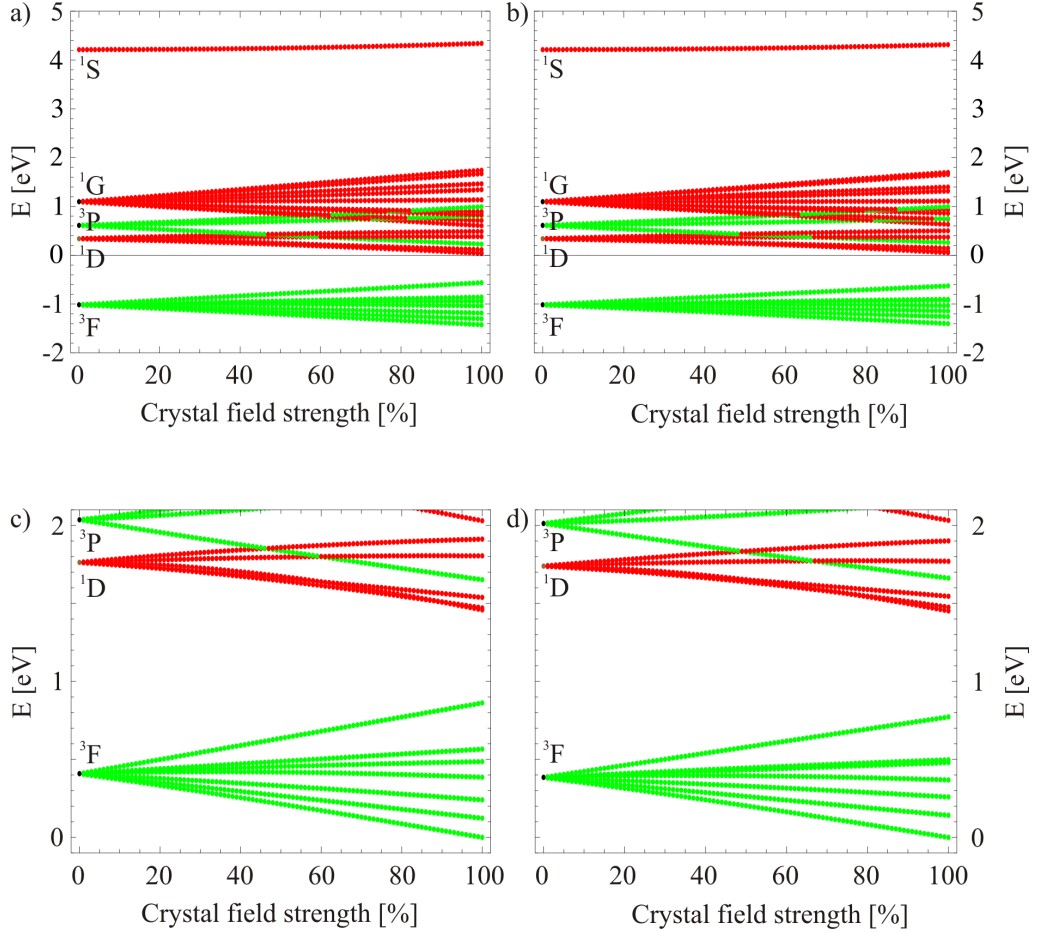


Figure 4.5: The splitting of the terms with increasing crystal-field strength for a) + c)  $C_2$  (relevant for  $T < 80$  K) and b) + d)  $C_{2v}$  site symmetry (relevant for  $T > 80$  K). In c) and d) the energies are scaled to the crystal-field ground states. The degree of degeneracy is indicated by the red (1-fold) and green (3-fold) color. The calculation parameters used in this point-charge model are  $F_V^2 = 8.157$  eV,  $F_V^4 = 5.114$  eV,  $\langle r^2 \rangle_V = 0.467$  Å<sup>2</sup>, and  $\langle r^4 \rangle_V = 0.448$  Å<sup>4</sup>.

As shown in Fig. 4.5 b) the crystal-field splitting is not strong enough to break Hund's first rule. But the crystal field mixes multiplets with the same spin. So the ground state in VOCl at 300 K is given by the following linear combination of multiplet wave functions with  $S = 1$ :

$$|\psi_{\text{crystal field}}^{\text{gs}}\rangle = 0.9769 \cdot |^3F\rangle + 0.0232 \cdot |^3P\rangle, \quad (4.1.14)$$

in which  $|^3F\rangle$  and  $|^3P\rangle$  represent the  $^3F$  and  $^3P$  multiplet wave functions of the free ion, respectively.

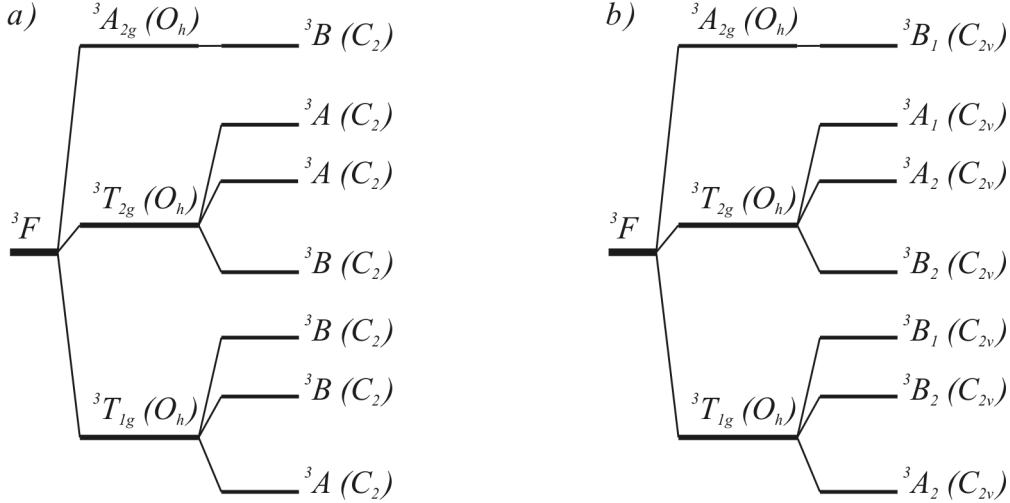


Figure 4.6: The splitting of the cubic ground state  ${}^3T_1$  by lowering the symmetry from  $O_h$  to a)  $C_2$  ( $T < 80$  K) and b)  $C_{2v}$  ( $T > 80$  K).

The contribution of the  ${}^3P$  multiplet to the ground state is quite small and so we will neglect this multiplet in the further analysis. The other multiplets are irrelevant for describing the ground state.

In order to identify the irreducible representations with the crystal-field eigenstates shown on the right hand side of Fig. 4.5 a), we have to apply the symmetry operations of the  $C_{2v}$  point group, which are given in the character table Tab. 4.1, to the crystal-field eigenstates  $|\psi\rangle$ .

Here, the  $C_2(z)$  symmetry operation represents a  $180^\circ$  rotation around the  $z$  axis, which is described by the rotation operator [149]  $\mathcal{D}(\alpha, \beta, \gamma)$  (with Euler angles  $\alpha = 0, \beta = 0, \gamma = \pi$ ):

$$C_2|\psi\rangle = \mathcal{D}(\alpha, \beta, \gamma)|\psi\rangle = \pm|\psi\rangle. \quad (4.1.15)$$

If  $C_2|\psi\rangle = +|\psi\rangle$ , the crystal-field eigenstate  $|\psi\rangle$  corresponds to one of the  $A$  irreducible representations. The opposite algebraic sign indicates the  $B_1$  or  $B_2$  irreducible representation.

The other symmetry operations  $\sigma_v(xz)$  and  $\sigma_v(yz)$  represent reflections at the  $xz$  and  $yz$  plane, respectively. The crystal-field eigenstates  $|\psi\rangle = |\mathfrak{J}\mathfrak{M}\rangle$ , which are characterized

	$E$	$C_2(z)$	$\sigma_v(xz)$	$\sigma_v(yz)$	basis
$A_1$	1	1	1	1	$z, x^2, y^2, z^2$
$A_2$	1	1	-1	-1	$xy$
$B_1$	1	-1	1	-1	$x, xz$
$B_2$	1	-1	-1	1	$y, yz$

Table 4.1: Character table for  $C_{2v}$  point group.

	$A_1$	$A_2$	$B_1$	$B_2$
$A_1$	$A_1$	$A_2$	$B_1$	$B_2$
$A_2$	$A_2$	$A_1$	$B_2$	$B_1$
$B_1$	$B_1$	$B_2$	$A_1$	$A_2$
$B_2$	$B_2$	$B_1$	$A_2$	$A_1$

Table 4.2: Multiplication table for the  $C_{2v}$  point group.

by the total angular momentum  $\mathfrak{J}$  and the corresponding quantum magnetic number  $\mathfrak{M}$ , transform under the symmetry operation  $\sigma_v(xz)$  as follows

$$\sigma_v|\mathfrak{J} \mathfrak{M}\rangle = (-1)^{\mathfrak{J}-\mathfrak{M}}|\mathfrak{J} - \mathfrak{M}\rangle. \quad (4.1.16)$$

Applying the symmetry operations to the crystal-field eigenstates, we can identify the irreducible representations as shown in Fig. 4.6, where the ground-state has predominantly  $xy$  character, i.e.  ${}^3A_2$ .

In case of the low-temperature regime, the identification of the crystal-field eigenstates with the irreducible representations can be done analogously. The  $C_2$  point group is a sub-group of  $C_{2v}$  and we can use the  $C_{2v}$  character table Tab. 4.1 for the  $C_2$  group if we omit the  $\sigma_v(xz)$  and  $\sigma_v(yz)$  reflections. Furthermore, the irreducible representations  $A_1$ ,  $A_2$ ,  $B_1$  and  $B_2$  lose their indices 1 and 2. As shown in Fig. 4.5 a), the strength of the crystal-field splitting is comparable to the room-temperature regime and the contribution of the  ${}^3P$  multiplet to the crystal-field ground state changes from 2.317 % (295 K) to 2.143 % (20 K). Applying the  $C_2$  rotation to the crystal-field eigenstates, we can identify the irreducible representations as shown in Fig. 4.6 a).

In order to find the forbidden dipole transitions, we have to determine the product of the irreducible representations of the eigenstates which are involved in the transitions. As mentioned above, these products must include the irreducible representation of the dipole operator. The products of all irreducible representations in the  $C_{2v}$  point group are given in the multiplication table Tab. 4.2. The cartesian components of the dipole operator are represented by the irreducible representations  $B_1(x)$ ,  $B_2(y)$ , and  $A_1(z)$  as shown in Tab. 4.1. In the low-temperature regime, the  $z$  component of the dipole operator is described by the  $A$  and the other components by the  $B$  irreducible representation. The result of the group-theoretical analysis is shown in Tab. 4.3.

Comparing the theoretically predicted excitation energies with the experimental values, see Fig. 4.2, we find a good agreement for the low-lying transitions, but the differences between theory and experiment increase with increasing energy. This is caused on the one hand by inaccuracies in the determination of the crystal structure, see below, and on the other hand by the simple point-charge picture, where we neglect the hybridization, which is important in the description of the higher-lying excitations. Thus, we find a strong polarization dependence of the transitions, i.e. we should find several excitations only in one polarization direction, within the room-temperature regime. But

transitions	irreducible representations	excitation energies [eV]	dipole components	experimental values [eV]
room-temperature regime ( $C_{2v}$ site symmetry)				
$gs \rightarrow 1^{st}$	$A_2 \rightarrow B_2$	0.142	$x$	-
$gs \rightarrow 2^{nd}$	$A_2 \rightarrow B_1$	0.259	$y$	0.317
$gs \rightarrow 3^{rd}$	$A_2 \rightarrow B_2$	0.368	$x$	0.379
$gs \rightarrow 4^{th}$	$A_2 \rightarrow A_2$	0.480	$z$	-
$gs \rightarrow 5^{th}$	$A_2 \rightarrow A_1$	0.498	<i>forbidden</i>	-
$gs \rightarrow 6^{th}$	$A_2 \rightarrow B_1$	0.772	$y$	-
$gs \rightarrow 7^{th}$	$A_2 \rightarrow A_1$	1.451	<i>forbidden</i>	-
$gs \rightarrow 8^{th}$	$A_2 \rightarrow A_2$	1.476	$z$	-
$gs \rightarrow 9^{th}$	$A_2 \rightarrow B_2$	1.546	$x$	-
$gs \rightarrow 10^{th}$	$A_2 \rightarrow B_1$	1.662	$y$	-
low-temperature regime ( $C_2$ site symmetry)				
$gs \rightarrow 1^{st}$	$A \rightarrow B$	0.123	$x, y$	-
$gs \rightarrow 2^{rd}$	$A \rightarrow B$	0.241	$x, y$	0.327
$gs \rightarrow 3^{nd}$	$A \rightarrow B$	0.386	$x, y$	0.387
$gs \rightarrow 4^{th}$	$A \rightarrow A$	0.486	$z$	-
$gs \rightarrow 5^{th}$	$A \rightarrow A$	0.566	$z$	-
$gs \rightarrow 6^{th}$	$A \rightarrow B$	0.862	$x, y$	-
$gs \rightarrow 7^{th}$	$A \rightarrow A$	1.458	$z$	-
$gs \rightarrow 8^{th}$	$A \rightarrow A$	1.471	$z$	-
$gs \rightarrow 9^{th}$	$A \rightarrow B$	1.538	$x, y$	-
$gs \rightarrow 10^{th}$	$A \rightarrow B$	1.652	$x, y$	-

Table 4.3: Comparison of the results of the group-theoretical analysis and the excitation energies of the point-charge model calculation. Here “gs” indicates the ground state and “1<sup>st</sup>” (“2<sup>nd</sup>”, etc.) the first, (second) excited state, respectively.

this is not observed in the optical data. For example, the transition at  $\sim 1.65$  eV is observed for  $\mathbf{E} \parallel \mathbf{a}$  ( $\mathbf{E} \parallel \mathbf{x}$ ) and, within a few meV, for  $\mathbf{E} \parallel \mathbf{b}$  ( $\mathbf{E} \parallel \mathbf{y}$ ), in contrast to the group-theoretical result, which predicts this transition only for  $\mathbf{E} \parallel \mathbf{b}$ .

In addition, the point-charge model predicts an excitation at 0.142 (0.123) eV, which is probably related to the step in the low temperature spectra at 0.21 eV. (The step vanishes at  $T = 300$  K due to the temperature broadening of the peaks.) A possible explanation for the line shape of this excitation starts with the Franck-Condon principle. (We restrict our explanation to  $\mathbf{E} \parallel \mathbf{b}$ .) We assume, that we have two different excitations: The first one is at 0.21 eV and the other one at 0.32 eV. Within the Franck-Condon picture, each parabola corresponds to a different orbital state and represents the harmonic potential of the lattice. In case of the excitation at 0.21 eV, we have a transition from one minimum of the harmonic potential to the other, which causes a sharp absorption band, see Fig. 4.7 a). For the other transition, we may find

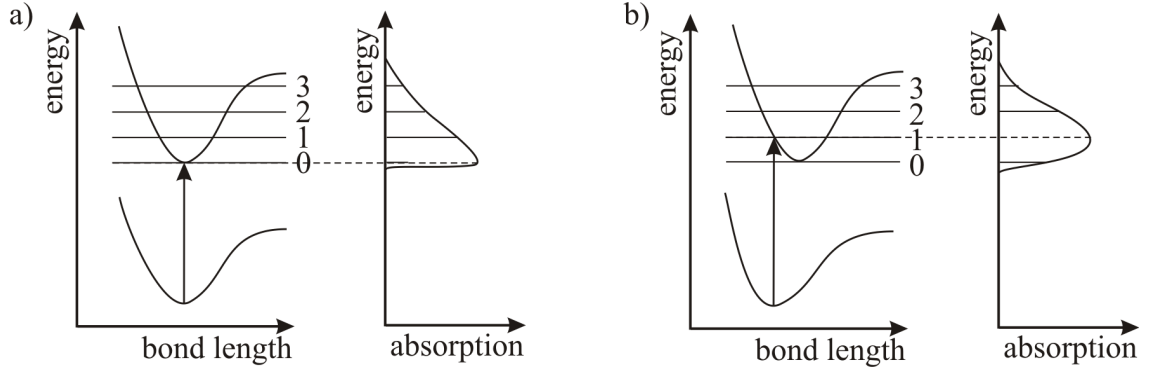


Figure 4.7: The width and the line shape of an absorption band depends on the difference in bond length of the different orbital states. Small differences cause a characteristic asymmetric line shape a), whereas large differences in the bond length give rise to symmetric absorption bands b).

a), in relation to the lower lying potential, shifted second potential with a symmetric form, see Fig. 4.7 b). Combining both peaks we may get the step line shape as found in the experimental data.

Finally, we perform a point-charge analysis of the isostructural compound  $\text{TiOCl}$ , which has the same space group as  $\text{VOCl}$  ( $Pm\bar{m}n$  at 300 K [134]), and the same point group symmetry at the Ti-site ( $C_{2v}$  at 300 K [134]). The results are in good agreement with the results reported by Rückamp [135]. As shown in Tab. 4.4, the results of the point-charge model for  $\text{TiOCl}$  differ by a factor of 2 from the optical data [122]. Additionally, we find, analogous to  $\text{VOCl}$ , a clear polarization dependence of the transitions and a spin-forbidden transition at 0.384 eV. Furthermore, in  $\text{TiOCl}$  the ground state is described by the  $A_1$  irreducible representation in contrast to  $\text{VOCl}$  where the ground state is described by  $A_2$ . In the end we find clear discrepancies between the results of the point-charge analysis for  $\text{TiOCl}$  and  $\text{VOCl}$  and the optical data indicating the important role of the hybridization in the description of the optical data of these compounds.

transitions	irreducible representations	excitation energies [eV]	dipole components	experimental values [eV] [122]
room-temperature regime ( $C_{2v}$ site symmetry)				
$gs \rightarrow 1^{st}$	$A_1 \rightarrow B_2$	0.328	$y$	1.510
$gs \rightarrow 2^{rd}$	$A_1 \rightarrow A_2$	0.384	<i>forbidden</i>	-
$gs \rightarrow 3^{nd}$	$A_1 \rightarrow B_1$	0.671	$x$	0.640
$gs \rightarrow 4^{th}$	$A_1 \rightarrow A_1$	1.263	$z$	-

Table 4.4: Results of the point-charge analysis for  $\text{TiOCl}$ . Here “gs” indicates the ground state and “1<sup>st</sup>” (“2<sup>nd</sup>”, etc.) the first, (second) excited state, respectively.

### 4.1.2 Cluster-Model Calculations

In order to achieve a better description of the experimental data we have to include further parts of the Hamiltonian, i.e. the spin-orbit coupling and the hybridization, and perform a cluster-model calculation as described in the second chapter. As mentioned in section “2.8 Hybridization and Tight-Binding Approximation”, the hybridization mixes the eigenstates of the transition-metal ion and the surrounding ligands.<sup>7</sup> The resulting wave functions contain ionic wave functions of different sites.

The cluster used in the cluster-model calculation consists of a V ion with  $3d^2$  electronic configuration and four oxygen ( $2p^6$ ) and two chlorine ( $3p^6$ ) ions around. The cluster with this electronic configuration represents the ground configuration. Configurations containing a V ion with  $3d^3$  electronic configuration and a hole on one of the ligands form the single-excited configurations.<sup>8</sup> Additionally, we denote configurations including a further electron on the V site ( $3d^4$ ) and a further hole on the ligand sites as “double-excited configurations”. Here, we have to distinguish between doubly occupied ligands with  $2p^4$  ( $3p^4$ ) electronic configuration and two singly occupied ligand sites  $\{2p^5, 2p^5\}$ ,  $\{2p^5, 3p^5\}$ , and  $\{3p^5, 3p^5\}$ . Altogether we have 28 configurations, and the size of the Hamilton matrix is  $136665 \times 136665$ . As mentioned in section “2.8 Hybridization and Tight-Binding Approximation”, the hybridization leads to an admixture of different configurations, which is described by the tight-binding operator. But we forbid the hopping of electrons between ions, when the hopping path passes through the central transition-metal ion because that has no physical meaning in the two-center tight-binding approximation.

The Slater integrals  $F^2$ ,  $F^4$  as well as the crystal-field parameters  $\langle r^2 \rangle$  and  $\langle r^4 \rangle$  and the spin-orbit coupling constant  $\zeta$  used in the cluster-model calculation are determined by a Hartree-Fock calculation as described in section “2.1 The Hartree-Fock Calculation”. The calculated values are shown in Tab. 4.5, where the Slater integrals are reduced to 80 % of the atomic values to include configuration-interaction as well as screening effects. (The value of this screening factor is given by Cowan [7], but its value is not unique. Therefore, we will analyze the dependence of the results of the cluster-model calculation on the value of this screening factor, see below). Furthermore, we set the ionic radius of the V-ion to  $r_V = 0.934 \text{ \AA}$  according to Harrison’s theory. In addition, we use  $r_O = 4.41 \text{ \AA}$  for the ionic radii of the O ion. Note, that in Harrison’s theory several effects are included which falsify the real value. The determination of the corresponding ionic radius  $r_{Cl}$  of the Cl ion is awkward because this value is not given in Harrison’s theory. Therefore, we estimate the value for the Cl ion by extrapolating Harrison’s values for Si, P, and S to Cl. We will analyze the dependence of the results of the cluster-model calculation on this value at the end of this section. Furthermore, the inclusion of the crystal-field as well as the spin-orbit splitting on the ligand site

<sup>7</sup>The ions surrounding the central transition-metal ion are called “ligands”.

<sup>8</sup>As mentioned in section “2.2.3 Truncated Configuration Interaction” we indicate with “single-excited” (“double-excited”) configurations, where the occupation number of the central transition-metal ion is increased by one (two) compared to the ground configuration.

parameter	$d^2$ configuration	$d^3$ configuration	$d^4$ configuration
$F_V^2$	8.157 eV	7.226 eV	6.142 eV
$F_V^4$	5.114 eV	4.493 eV	3.778 eV
$\langle r^2 \rangle_V$	0.467 Å <sup>2</sup>	0.589 Å <sup>2</sup>	0.815 Å <sup>2</sup>
$\langle r^4 \rangle_V$	0.448 Å <sup>4</sup>	0.772 Å <sup>4</sup>	1.699 Å <sup>4</sup>
$\zeta_V$	31.6 meV	26.5 meV	21.7 meV
$\langle r^2 \rangle_{Cl,3p^5}$	-	-	-
$\zeta_{Cl,3p^5}$	-	-	-
$F_{Cl,3p^4}^2$	5.858 eV	5.858 eV	5.858 eV
$\langle r^2 \rangle_{Cl,3p^4}$	-	-	-
$\zeta_{Cl,3p^4}$	-	-	-
$\langle r^2 \rangle_{O,2p^5}$	-	-	-
$\zeta_{O,2p^5}$	-	-	-
$F_{O,2p^4}^2$	7.321 eV	7.321 eV	7.321 eV
$\langle r^2 \rangle_{O,2p^4}$	-	-	-
$\zeta_{O,2p^4}$	-	-	-

Table 4.5: Parameters used in the cluster-model calculation for VOCl. The Slater integrals are already scaled to 80 % of the atomic values.

involves a difficulty: The application of a Hartree-Fock calculation to a negative ion ( $O^-$ ) is pretty awkward: The calculated radial wave functions of a negative ion include a large inaccuracy. Therefore, we cannot determine the parameters  $\langle r_{O^-}^2 \rangle$  and  $\zeta_{O^-}$ , and we will neglect the crystal-field as well as spin-orbit splitting on the ligand sites completely.

Another problem arises from the determination of the crystal structure [123]: By using neutron measurements the positions of the V ion cannot be determined exactly. This causes an inaccuracy in the crystal-field splitting as well as in the contribution of the hybridization, see “2.8 Hybridization and Tight-Binding Approximation”. The hopping integrals scale with the distance between the ligands and the transition-metal ion. Additionally, the Slater-Koster coefficients, which describe the relative orientation of the orbitals being involved in the hopping process, depend strongly on the crystal structure.

In contrast to the parameters described above, we cannot determine the values of the charge-transfer energies  $\Delta_{V-Cl}$  and  $\Delta_{V-O}$  exactly. In order to find the best description of the experimental data shown in Fig. 4.2 we analyze the dependencies of the results of the cluster-model calculation on the values of these charge-transfer energies as shown in Fig.4.8. Here, we set  $U_V = 4.5$  eV,  $U_{Cl} = U_O = 5.0$  eV, and  $r_{Cl} = 9.5$  Å,  $r_O = 4.41$  Å. In the following, the real part of the optical conductivity (denoted by  $\sigma_1(\omega)$ ) is calculated by using the Kubo-Greenwood formula (2.11.10), (2.11.14), (2.11.15) with damping  $\gamma$  (2.11.15) set to  $\sim 112$  meV (900 cm<sup>-1</sup>). The polarization dependence of the optical conductivity is determined by multiplying the matrix element of the current operator

$\hat{j}$ , see (2.11.11), by  $\cos(\phi)$ , where  $\phi$  represents the angle between the dipole moment vector and the cartesian unit vectors  $\mathbf{e}_x$ ,  $\mathbf{e}_y$ ,  $\mathbf{e}_z$ , respectively. Due to the Beer-Lambert law [194]

$$\alpha(\omega) = \frac{4\pi}{c \cdot n(\omega)} \sigma_1(\omega), \quad (4.1.17)$$

where  $c$  denotes the speed of light, the calculated optical conductivity  $\sigma_1(\omega)$  is proportional to the absorption  $\alpha(\omega)$ , if we assume a constant real part of the refraction index  $n(\omega) \equiv \text{const.}$

Note, that we do not include the admixture of energetically higher lying configurations containing excited p-states at the V site. But, due to the broken inversion symmetry in VOCl we have a relevant contribution of these p-states at the V site to the optical conductivity. Thus, we will consider only the contributions from the d-states, the spin-orbit coupling and the charge-transfer excitations to the optical conductivity.

As shown in Figs. 4.8 - 4.15 we find a strong dependence of the excitation energies on the charge-transfer energy  $\Delta_{V-O}$ : By increasing  $\Delta_{V-O}$  from 2 eV to 8 eV we observe a remarkable shift of the excitation energies between 0.5 eV and 1.0 eV towards smaller energies. In addition, the excitation energies located in the spin-forbidden area are pushed towards lower energies by increasing the charge-transfer energy  $\Delta_{V-Cl}$ . The strong dependencies of the excitation energies on the values of the charge-transfer energies are caused by the fact that  $\Delta_{V-Cl}$  and  $\Delta_{V-O}$  describe the energetical distances between the ground and the excited configurations. By reducing the values of these parameters we increase the admixture of the different configurations. Additionally, this shows the import role of hybridization in the description of the optical data.

We find the best description of the optical data for  $\Delta_{V-Cl} = 2$  eV, see Fig.4.8 and Fig. 4.9. Varying the charge-transfer energy  $\Delta_{V-O}$  from 2 eV to 8 eV we transfer spectral weight from higher to lower energies and shift the excitations around 0.5 eV and 1.5 eV to slightly lower frequencies. Nevertheless, the excitations around 1.5 eV carry to much spectral weight whereas the strengths of the excitations around 1.7 eV are to small.<sup>9</sup> Note, that the cluster-model calculation cannot describe the effect of intensity stealing mentioned above. Additionally, the line shapes of the optical conductivity depend on the value of the damping factor  $\gamma$  which is set to  $\sim 112$  meV ( $900 \text{ cm}^{-1}$ ) for all excitations and polarization directions. Using different values of the damping factor  $\gamma$  for each excitation would increase the quality of the description remarkably.

In order to achieve a better description of the optical data, we will optimize other calculation parameter such as the screening factor, the Hubbard  $U_V$ , and the value of the Cl-radius. In the following we set the charge-transfer energies to  $\Delta_{V-Cl} = 2$  eV and  $\Delta_{V-O} = 8$  eV.

---

<sup>9</sup>The enhancement of the absorption above 1.5 eV is caused by interband transitions which cannot be described by a cluster-model calculation including only one V-site.

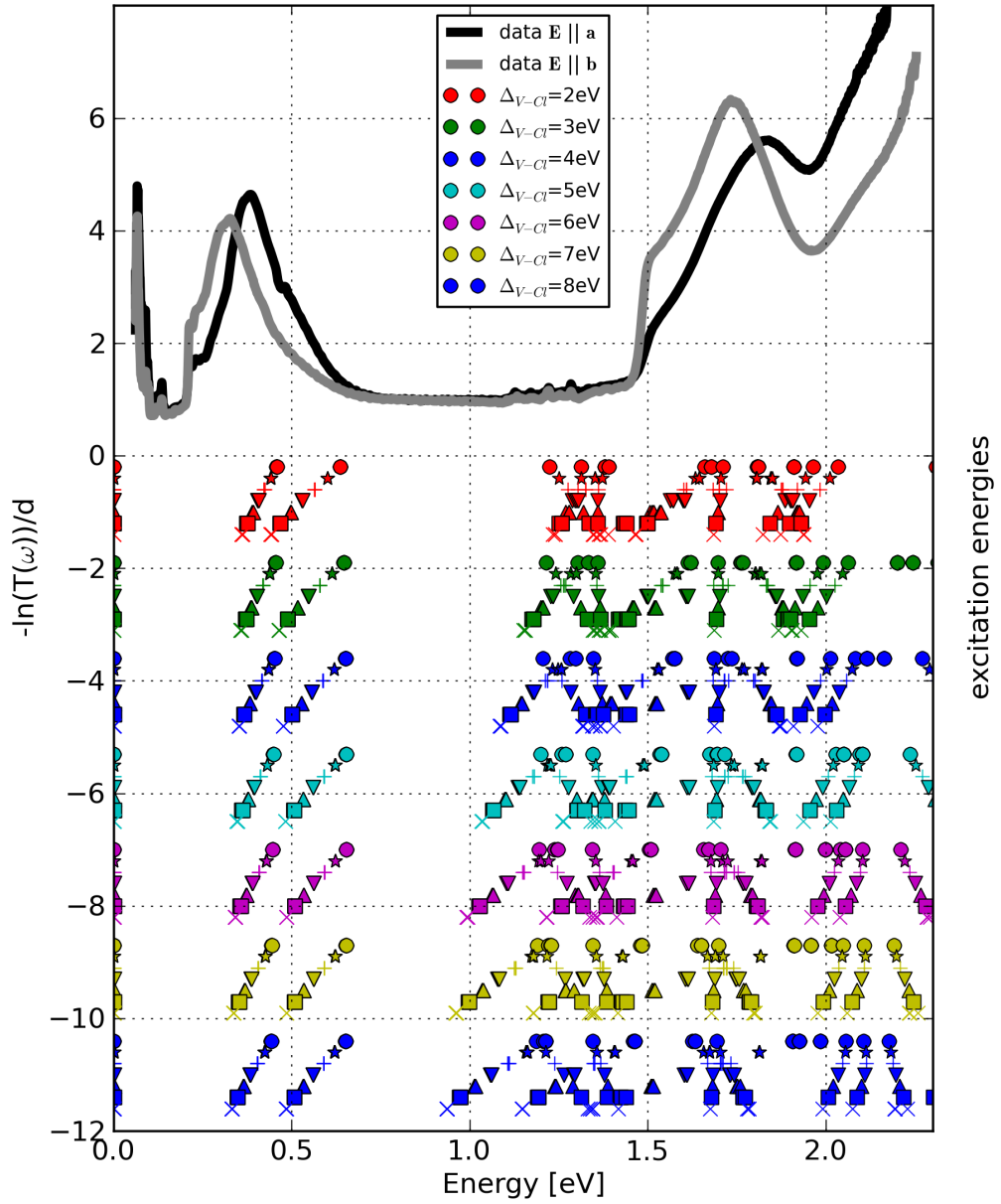


Figure 4.8: Dependence of the excitation energies on the charge-transfer energies  $\Delta_{V-Cl}$  and  $\Delta_{V-O}$  at  $T = 20$  K for  $\mathbf{E} \parallel \mathbf{a}$  and  $\mathbf{E} \parallel \mathbf{b}$ . Here, the color indicates the value of the charge-transfer energy  $\Delta_{V-Cl}$  whereas the values of the charge-transfer energy  $\Delta_{V-O}$  are indicated by the symbols “•” ( $\Delta_{V-O} = 2$  eV), “✱” ( $\Delta_{V-O} = 3$  eV), “+” ( $\Delta_{V-O} = 4$  eV), “▼” ( $\Delta_{V-O} = 5$  eV), “▲” ( $\Delta_{V-O} = 6$  eV), “□” ( $\Delta_{V-O} = 7$  eV), “×” ( $\Delta_{V-O} = 8$  eV). Calculation parameter:  $U_V = 4.5$  eV,  $U_{Cl} = U_O = 5.0$  eV,  $r_{Cl} = 9.5$  Å,  $r_O = 4.41$  Å,  $r_V = 0.934$  Å, screening factor = 80 %.

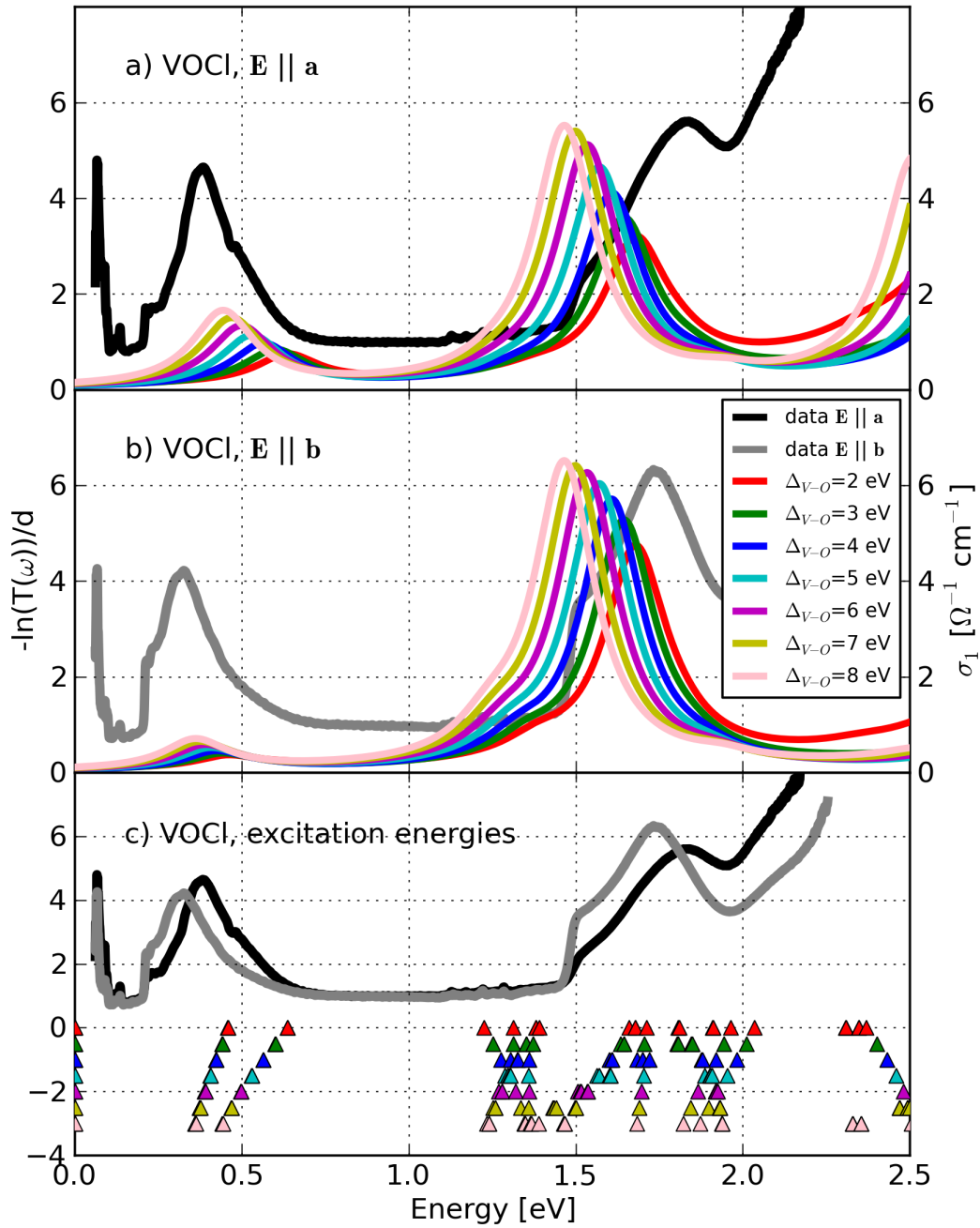


Figure 4.9: Dependence of the optical conductivity  $\sigma_1(\omega)$  and of the excitation energies on the charge-transfer energy  $\Delta_{V-O}$  for  $\Delta_{V-Cl} = 2$  eV at  $T = 20$  K for  $\mathbf{E} \parallel \mathbf{a}$  and  $\mathbf{E} \parallel \mathbf{b}$ . The optical conductivities are multiplied by a factor of  $2.7 \cdot 10^2$ . Calculation parameter:  $U_V = 4.5$  eV,  $U_{Cl} = U_O = 5.0$  eV,  $r_{Cl} = 9.5$  Å,  $r_O = 4.41$  Å,  $r_V = 0.934$  Å, screening factor = 80 %.

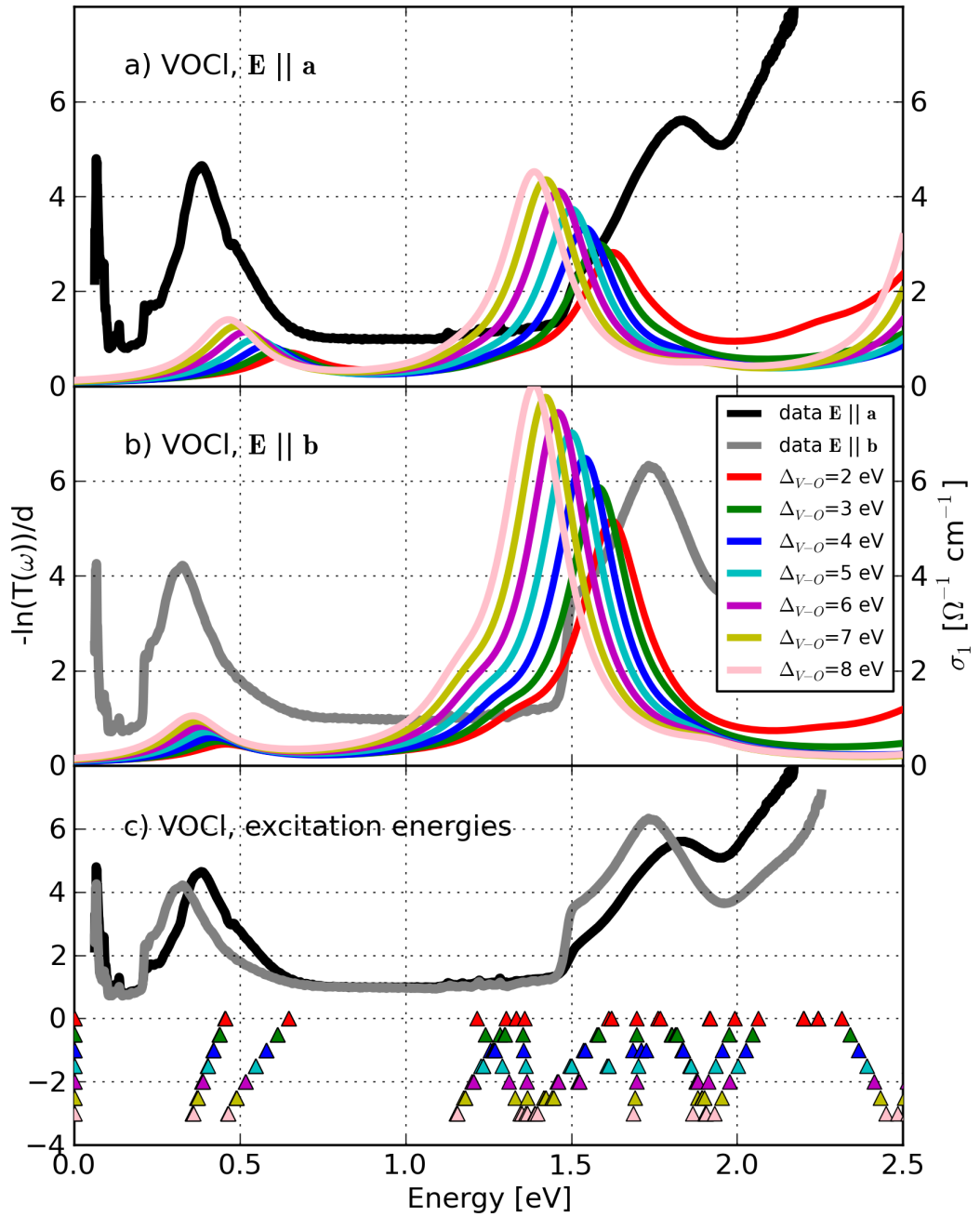


Figure 4.10: Dependence of the optical conductivity  $\sigma_1(\omega)$  and of the excitation energies on the charge-transfer energy  $\Delta_{V-O}$  for  $\Delta_{V-Cl} = 3$  eV at  $T = 20$  K for  $\mathbf{E} \parallel \mathbf{a}$  and  $\mathbf{E} \parallel \mathbf{b}$ . The optical conductivities are multiplied by a factor of  $2.7 \cdot 10^2$ . Calculation parameter:  $U_V = 4.5$  eV,  $U_{Cl} = U_O = 5.0$  eV,  $r_{Cl} = 9.5$  Å,  $r_O = 4.41$  Å,  $r_V = 0.934$  Å, screening factor = 80 %.

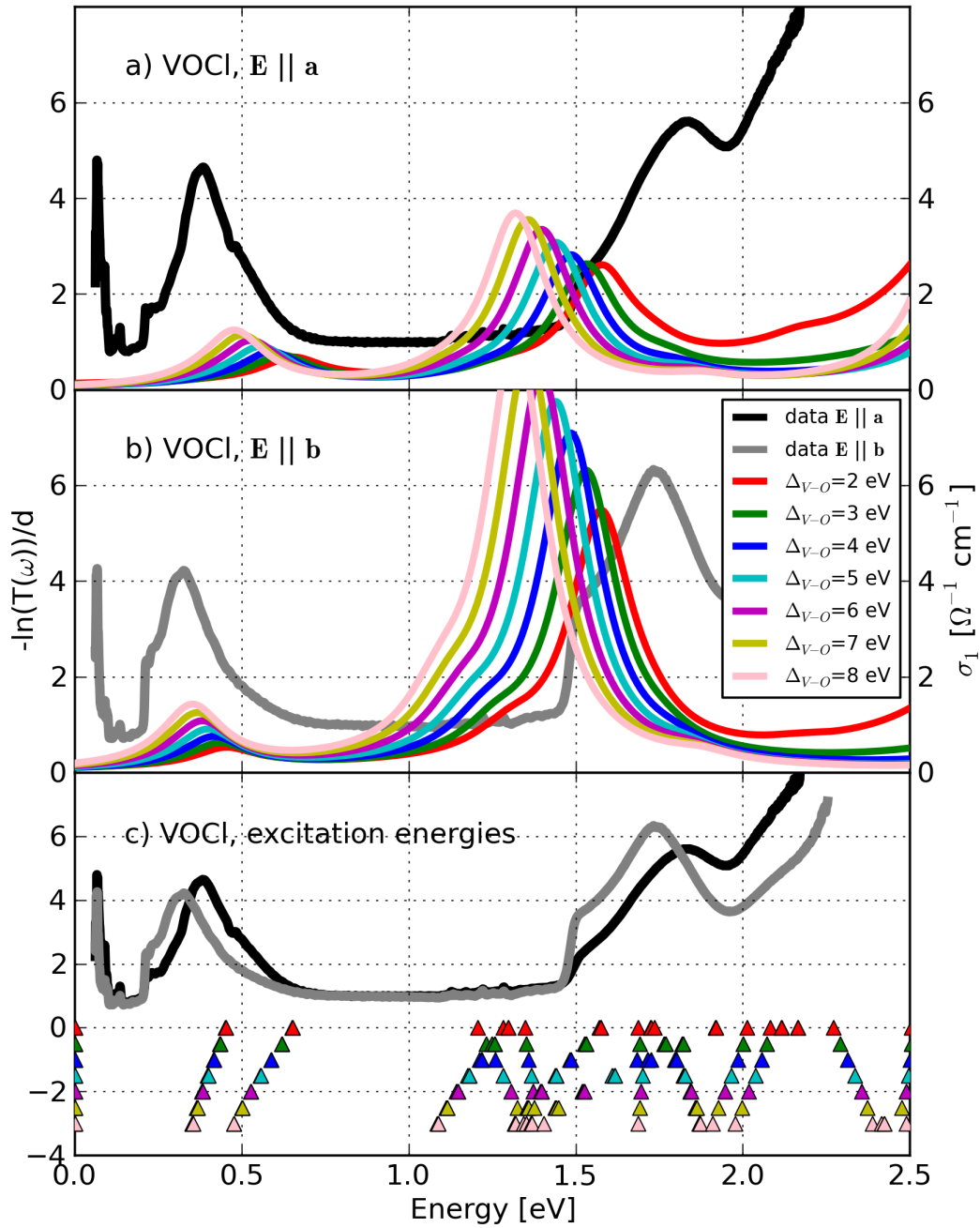


Figure 4.11: Dependence of the optical conductivity  $\sigma_1(\omega)$  and of the excitation energies on the charge-transfer energy  $\Delta_{V-O}$  for  $\Delta_{V-Cl} = 4$  eV at  $T = 20$  K for  $\mathbf{E} \parallel \mathbf{a}$  and  $\mathbf{E} \parallel \mathbf{b}$ . The optical conductivities are multiplied by a factor of  $2.7 \cdot 10^2$ . Calculation parameter:  $U_V = 4.5$  eV,  $U_{Cl} = U_O = 5.0$  eV,  $r_{Cl} = 9.5$  Å,  $r_O = 4.41$  Å,  $r_V = 0.934$  Å, screening factor = 80 %.

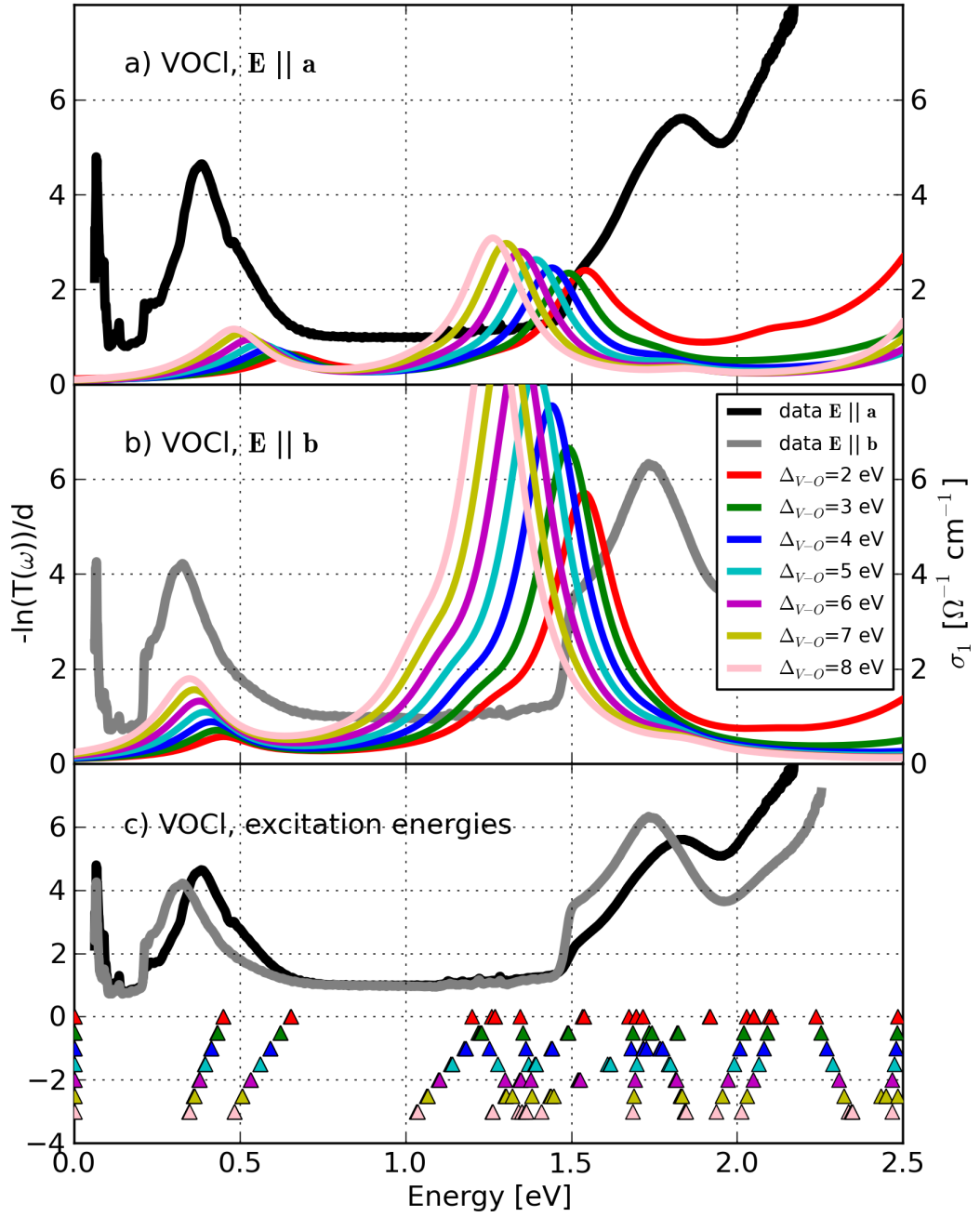


Figure 4.12: Dependence of the optical conductivity  $\sigma_1(\omega)$  and of the excitation energies on the charge-transfer energy  $\Delta_{V-O}$  for  $\Delta_{V-Cl} = 5$  eV at  $T = 20$  K for  $\mathbf{E} \parallel \mathbf{a}$  and  $\mathbf{E} \parallel \mathbf{b}$ . The optical conductivities are multiplied by a factor of  $2.7 \cdot 10^2$ . Calculation parameter:  $U_V = 4.5$  eV,  $U_{Cl} = U_O = 5.0$  eV,  $r_{Cl} = 9.5$  Å,  $r_O = 4.41$  Å,  $r_V = 0.934$  Å, screening factor = 80 %.

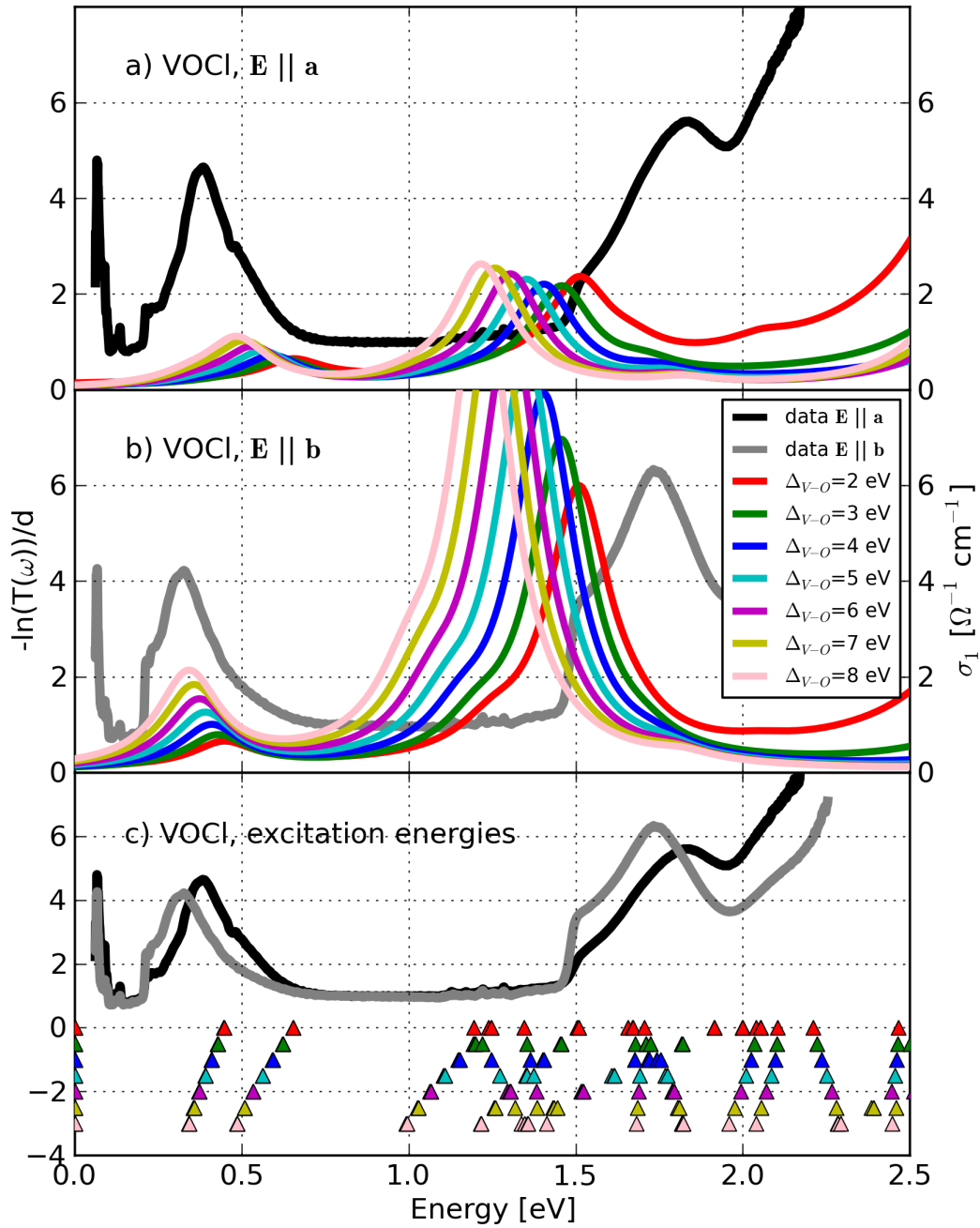


Figure 4.13: Dependence of the optical conductivity  $\sigma_1(\omega)$  and of the excitation energies on the charge-transfer energy  $\Delta_{V-O}$  for  $\Delta_{V-Cl} = 6$  eV at  $T = 20$  K for  $\mathbf{E} \parallel \mathbf{a}$  and  $\mathbf{E} \parallel \mathbf{b}$ . The optical conductivities are multiplied by a factor of  $2.7 \cdot 10^2$ . Calculation parameter:  $U_V = 4.5$  eV,  $U_{Cl} = U_O = 5.0$  eV,  $r_{Cl} = 9.5$  Å,  $r_O = 4.41$  Å,  $r_V = 0.934$  Å, screening factor = 80 %.

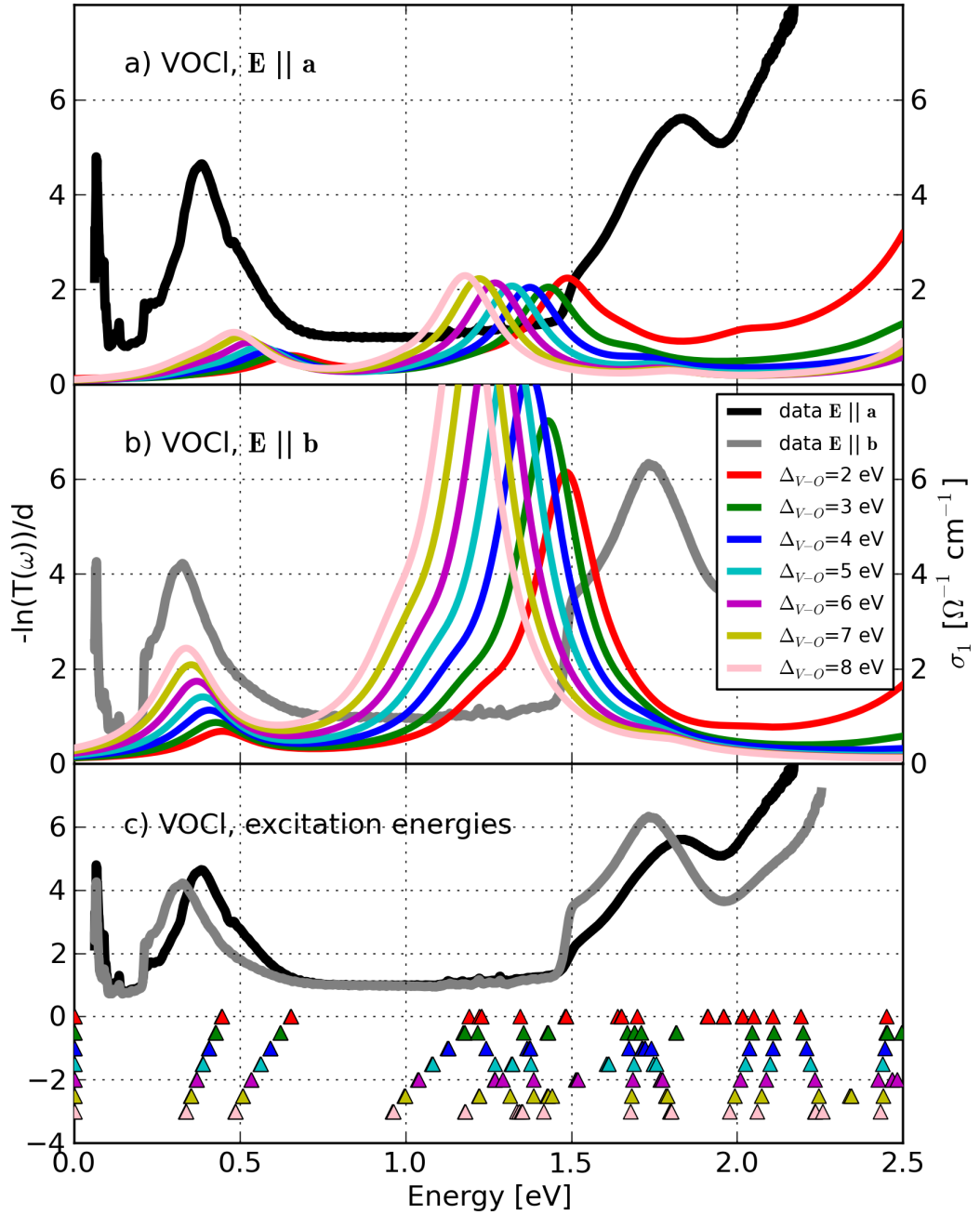


Figure 4.14: Dependence of the optical conductivity  $\sigma_1(\omega)$  and of the excitation energies on the charge-transfer energy  $\Delta_{V-O}$  for  $\Delta_{V-Cl} = 7$  eV at  $T = 20$  K for  $\mathbf{E} \parallel \mathbf{a}$  and  $\mathbf{E} \parallel \mathbf{b}$ . The optical conductivities are multiplied by a factor of  $2.7 \cdot 10^2$ . Calculation parameter:  $U_V = 4.5$  eV,  $U_{Cl} = U_O = 5.0$  eV,  $r_{Cl} = 9.5$  Å,  $r_O = 4.41$  Å,  $r_V = 0.934$  Å, screening factor = 80 %.

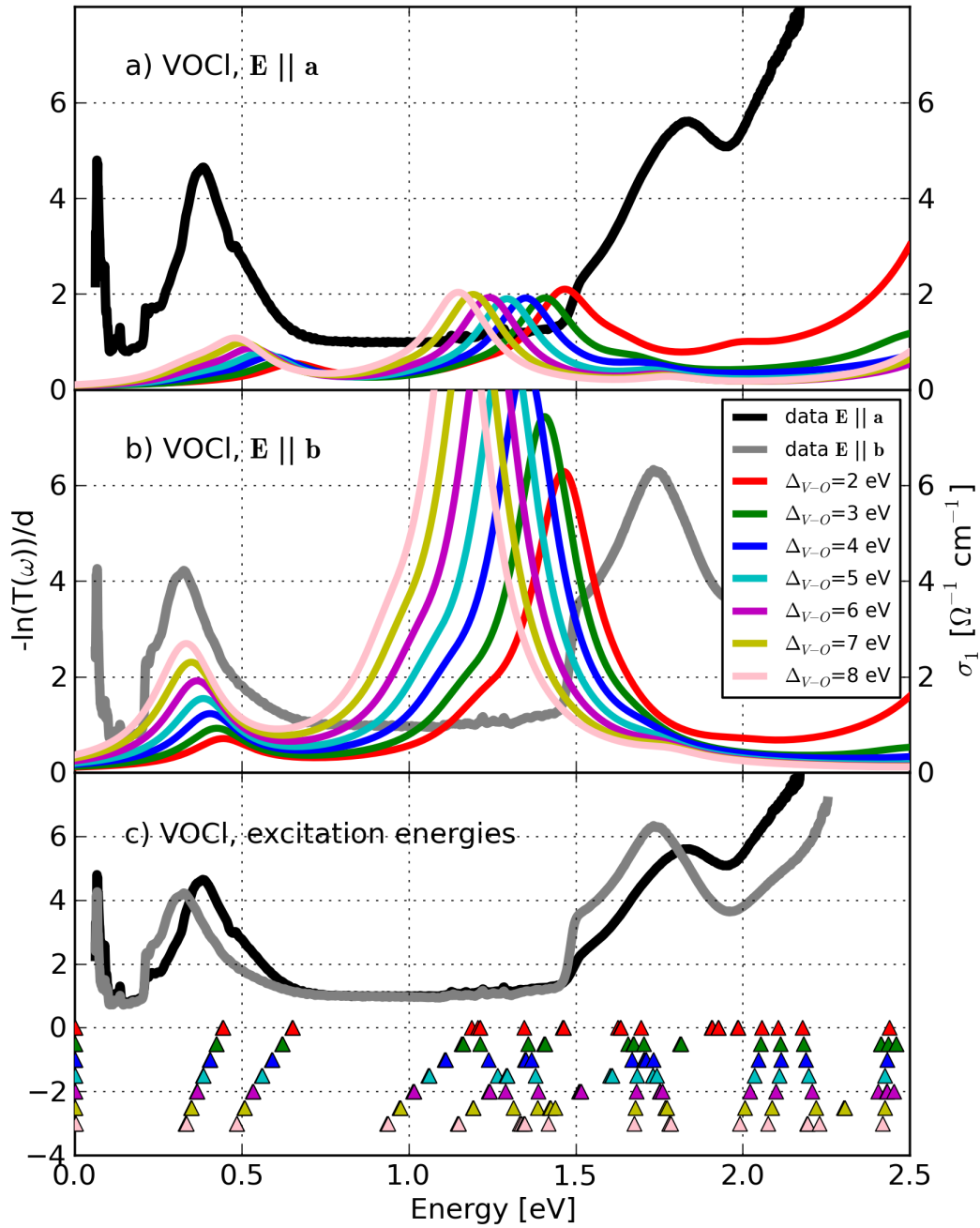


Figure 4.15: Dependence of the optical conductivity  $\sigma_1(\omega)$  and of the excitation energies on the charge-transfer energy  $\Delta_{V-O}$  for  $\Delta_{V-Cl} = 8$  eV at  $T = 20$  K for  $\mathbf{E} \parallel \mathbf{a}$  and  $\mathbf{E} \parallel \mathbf{b}$ . The optical conductivities are multiplied by a factor of  $2.7 \cdot 10^2$ . Calculation parameter:  $U_V = 4.5$  eV,  $U_{Cl} = U_O = 5.0$  eV,  $r_{Cl} = 9.5$  Å,  $r_O = 4.41$  Å,  $r_V = 0.934$  Å, screening factor = 80 %.

We start with analyzing the dependence of the results of the cluster-model calculation on the value of the Hubbard  $U_V$  at the V site, as shown in Fig. 4.16: The excitation energies below 2.0 eV are shifted towards lower energies with increasing  $U_V$  except for the excitation energies located at 1.35 eV, 1.7 eV, and 1.8 eV which are independent on the value of  $U_V$ . Additionally, by changing  $U_V$  from 2 eV to 8 eV the spectral weight of the optical conductivity for  $\mathbf{E} \parallel \mathbf{b}$  is slightly increased. Especially, the excitations around 1.5 eV show an enhancement of the spectral weight. For  $\mathbf{E} \parallel \mathbf{a}$  we find a similar behavior except for excitations located below 0.5 eV which stay nearly unchanged with increasing  $U_V$ . But, by varying  $U_V$  we cannot remove the strong direction dependence of the optical conductivity below 0.5 eV which is not observed by optical spectroscopy. We will set the value of  $U_V$  to 3 eV for the further analysis.

Now, we will analyze the dependence of the results of the cluster-model calculation on the value of the screening factor as shown in Fig. 4.17. By increasing the screening factor from 50 % to 90 % we find a remarkable shift of all excitation energies. The excitations below 0.5 eV are pushed to lower energies whereas the first excited state stay nearly unchanged. Additionally, by reducing the screening factor from 90 % to 50 %, we shift the excitation energies above 0.5 eV to lower energies. Only the excitations around 1.5 eV show a slightly contrary behavior. Furthermore, the optical conductivity show a remarkable dependence on the screening factor as well. By increasing the screening factor we transfer spectral weight from higher to lower energies. The strong dependence of the cluster-model calculation on the value of the screening factor is caused by the fact, that the screening factor reduces the values of all Slater integrals, which are relevant for all configurations. Finally, the variation of the screening factor does not remove the strong direction dependence of the optical conductivity above 1.0 eV. Thus, the variation of the screening factor does not lead to a appreciable better description of the optical data and we will set the screening factor to 70 % for the further analysis.

We continue the investigation by analyzing the dependence of the results of the cluster-model calculation on the value of the ionic radius  $r_{Cl}$  of the Cl ion. Harrison gives no value for this radius and we have to estimate the value by extrapolating Harrison's values for Si, P, and S to Cl as mentioned above. This procedure suggests a large value of  $r_{Cl} = 9.5 \text{ \AA}$ . As shown in Fig. 4.18 the excitation energies as well as the optical conductivity depend only slightly on the value of  $r_{Cl}$ . The excitation energies below 0.5 eV are nearly independent on this value, whereas the excitation energies above 1.0 eV show a more pronounced dependence on  $r_{Cl}$ . Most of these excitation energies are pushed to higher energies with increasing  $r_{Cl}$ . Additionally, the features in the optical conductivity at 1.5 eV are pushed to slightly lower energies with decreasing  $r_{Cl}$ . Furthermore, we transfer spectral weight from higher to lower energies by varying the radius of the Cl ion. But, we cannot remove the polarization dependence of the optical conductivity which is not observed by the optical conductivity. We achieve the best description of the optical data for  $r_{Cl} = 9.5 \text{ \AA}$ .

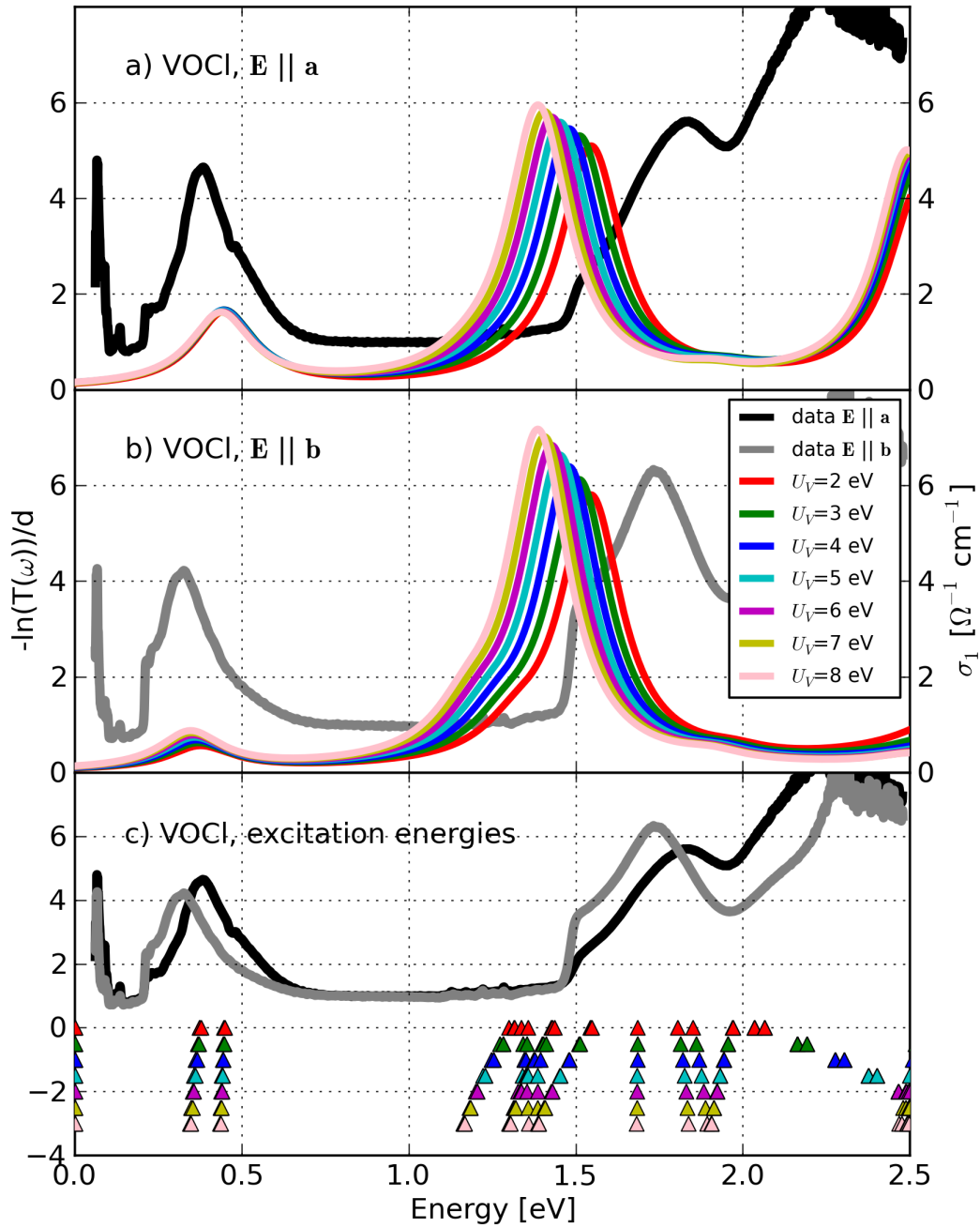


Figure 4.16: Dependence of the optical conductivity  $\sigma_1(\omega)$  and of the excitation energies on the value of the Hubbard  $U_V$  at  $T = 20$  K for  $\mathbf{E} \parallel \mathbf{a}$  and  $\mathbf{E} \parallel \mathbf{b}$ . The optical conductivities are multiplied by a factor of  $2.7 \cdot 10^2$ . Calculation parameter:  $\Delta_{V-Cl} = 2$  eV,  $\Delta_{V-O} = 8$  eV,  $U_{Cl} = U_O = 5.0$  eV,  $r_{Cl} = 9.5$  Å,  $r_O = 4.41$  Å,  $r_V = 0.934$  Å, screening factor = 80 %.

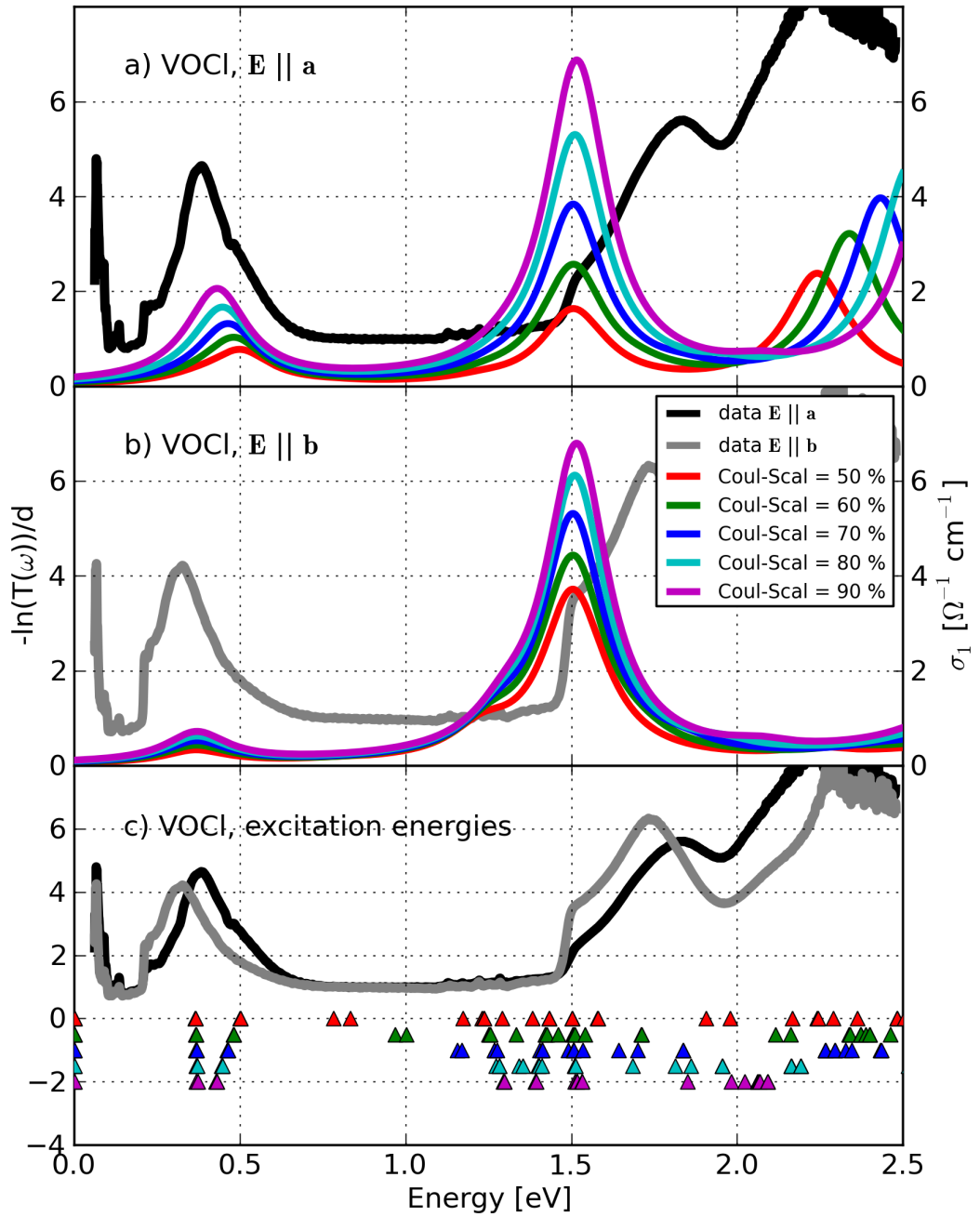


Figure 4.17: Dependence of the optical conductivity  $\sigma_1(\omega)$  and of the excitation energies on the screening factor at  $T = 20$  K for  $\mathbf{E} \parallel \mathbf{a}$  and  $\mathbf{E} \parallel \mathbf{b}$ . The optical conductivities are multiplied by a factor of  $2.7 \cdot 10^2$ . Calculation parameter:  $\Delta_{V-cl} = 2$  eV,  $\Delta_{V-O} = 8$  eV,  $U_V = 3.0$  eV,  $U_{Cl} = U_O = 5.0$  eV,  $r_{Cl} = 9.5$  Å,  $r_O = 4.41$  Å,  $r_V = 0.934$  Å.

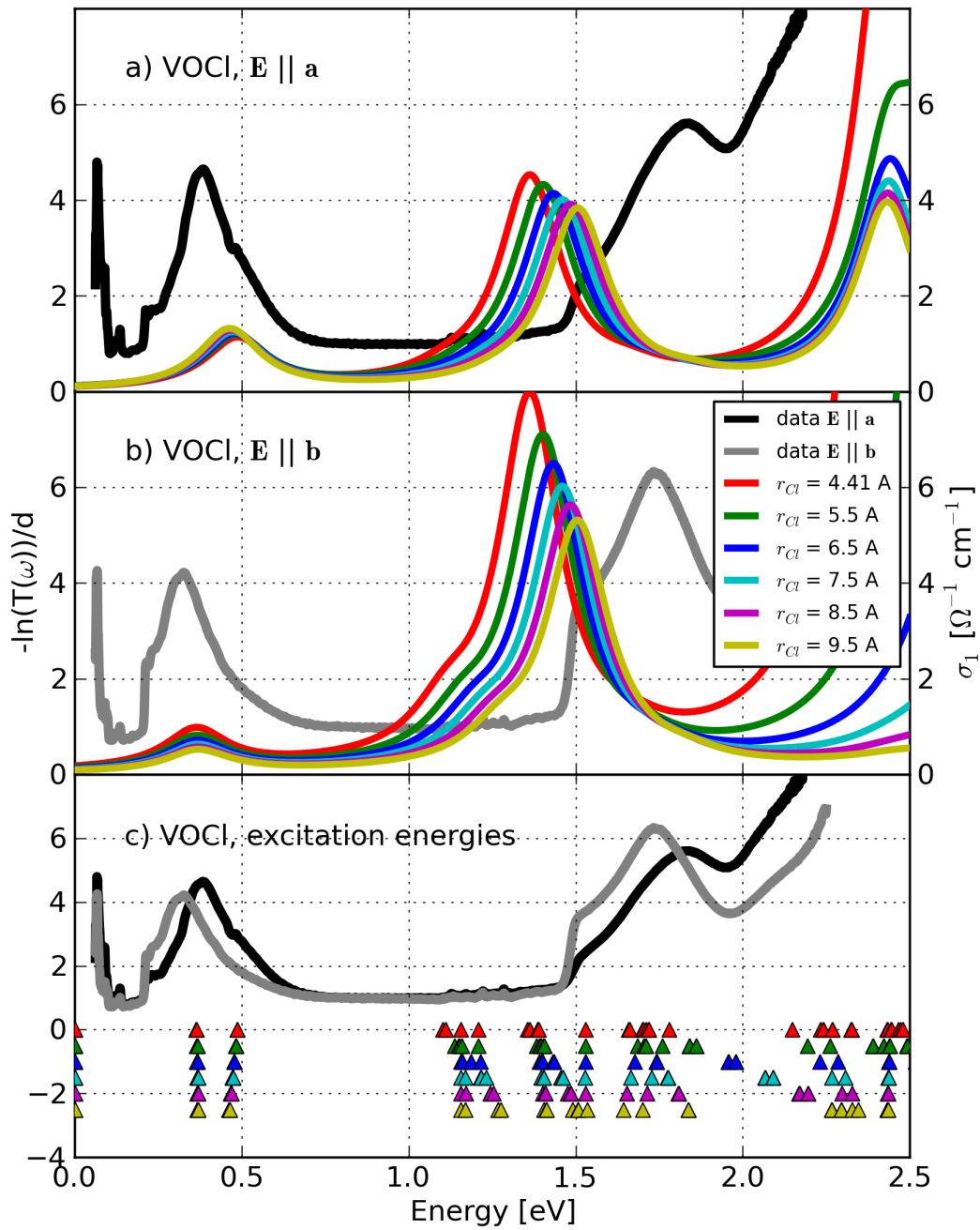


Figure 4.18: Dependence of the optical conductivity  $\sigma_1(\omega)$  and of the excitation energies on  $r_{Cl}$  at  $T = 20$  K for  $\mathbf{E} \parallel \mathbf{a}$  and  $\mathbf{E} \parallel \mathbf{b}$ . The optical conductivities are multiplied by a factor of  $2.7 \cdot 10^2$ . Calculation parameter:  $\Delta_{V-Cl} = 2$  eV,  $\Delta_{V-O} = 8$  eV,  $U_V = 3.0$  eV,  $U_{Cl} = U_O = 5.0$  eV,  $r_O = 4.41$  Å,  $r_V = 0.934$  Å, screening factor = 70 %.

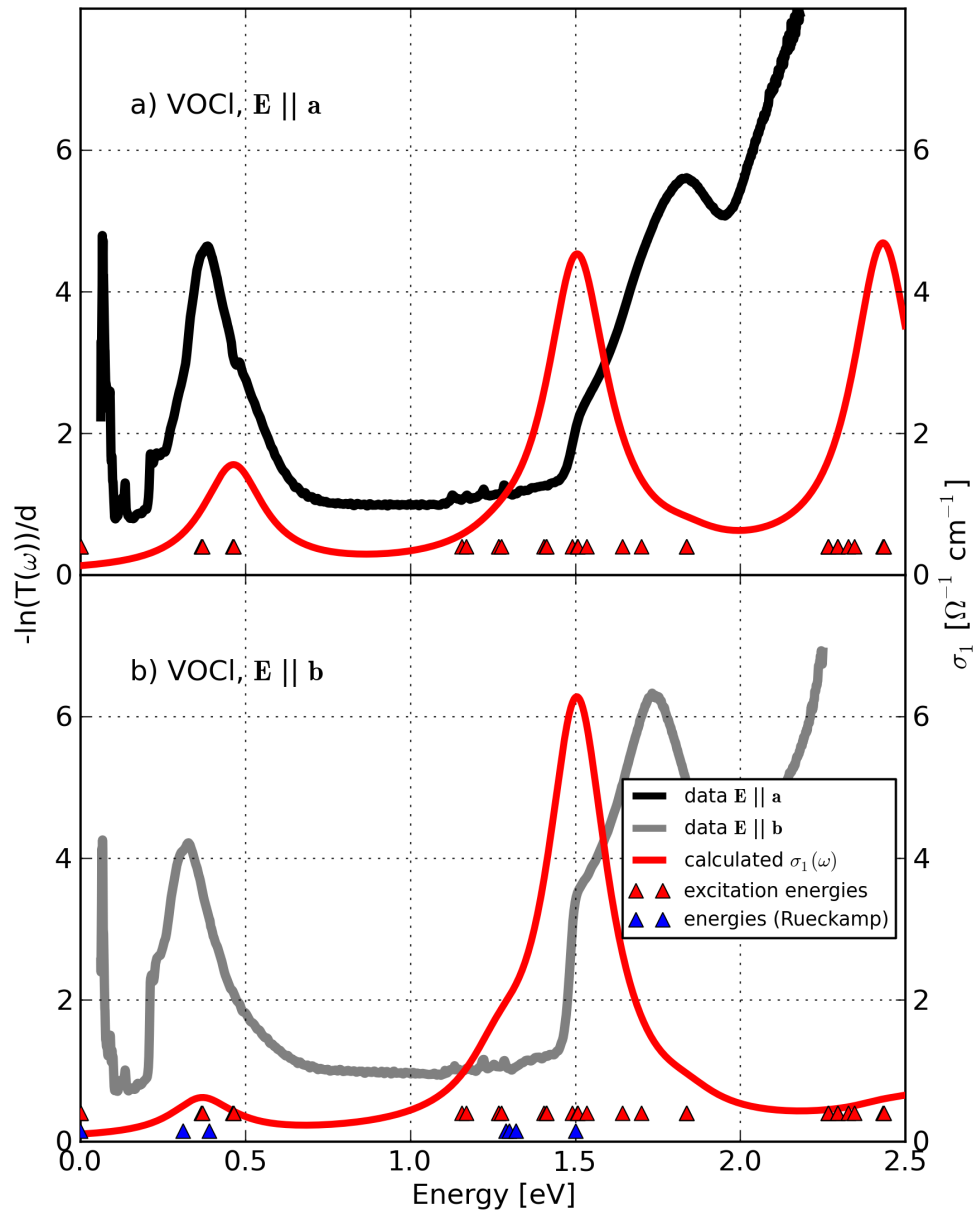


Figure 4.19: Comparison between the measured absorption (grey and light grey color) and the optical conductivity  $\sigma_1(\omega)$  (red color) of VOCl at  $T = 20$  K for  $\mathbf{E} \parallel \mathbf{a}$  and  $\mathbf{E} \parallel \mathbf{b}$ . The optical conductivity is multiplied by a factor of  $3.2 \cdot 10^2$ . The blue triangles represent the results of the cluster-model calculation for  $T = 295$  K done by Rückamp [124] by using the code XTLS 8 written by A. Tanaka (Hiroshima University, Japan). The red triangles indicate the excitation energies of our cluster-model calculation.

Summarizing the results of the analysis described above, we are not able to describe the optical data of VOCl properly, which may also be caused by the missing contributions of the p-states to the optical conductivity. Although we investigate the dependence of the cluster-model calculation on different calculation parameters we cannot identify the relevant parameter(s) which prevent the accurate description of the experimental data. As mentioned above, the optical conductivity depends strongly on the crystal structure.

In the following we continue the investigation of the crystal-field excitations in VOCl for the low-temperature phase by using  $\Delta_{V-Cl} = 2$  eV,  $\Delta_{V-O} = 8$  eV,  $U_V = 3.0$  eV,  $r_{Cl} = 9.5$  Å and setting the screening factor to 70 %. Using these parameters we describe the positions of the different excitations quite well and confirm roughly the results of the cluster-model calculation done by Rückamp [124] for the room-temperature phase, as shown in Fig. 4.19. In contrast to Rückamp we determine the positions of the excitations above 1.5 eV. But, we find a remarkable polarization dependence of the optical conductivity which is not observed by optical spectroscopy. Note, the enhancement of the optical conductivity above  $\sim 1.5$  eV for both polarization directions indicates the beginning of the charge-transfer band, which cannot be described by a single-cluster calculation. Additionally, the strength of a spin-forbidden excitation is increased if the energy of this excitation is comparable with that of a spin-allowed transition due to the so-called “intensity stealing”. But this effect can not be described by a single-site cluster-model calculations. Furthermore, we use only one value for the damping factor for all excitations for both polarization directions, which hinder an accurate description of the line shape of the excitations as well. Note, that we do not consider the admixture of energetically higher lying p-states at the V site to the optical conductivity.

In order to identify the different peaks we make use of the advantages of the calculation technique: By using the Racah-Wigner algebra we can determine the contribution of each configuration (multiplet) to the appropriate cluster-eigenstate by calculating the square of the normalized eigenvector and add up all entries of the squared eigenvector which belong to the corresponding configuration (multiplet). We will start the analysis by looking at the contributions of the different configurations used in the cluster-model calculation to the cluster-eigenstates. As shown in Tab. 4.6, the ground state contains a remarkable contribution of the single-excited configurations indicating the important role of the hybridization in this compound. Note, that the contribution of the ground configuration to the different eigenstates does not exceed 50 %. In addition, even the double-excited configurations are relevant for the description of this compound because the contributions of the double-excited configurations to the different eigenstates vary between 7.2 % and 22.4 %. Furthermore, all eigenstates below 3.0 eV belong to crystal-field excitations except the excitations between 2.20 eV and 2.30 eV which represent charge-transfer excitations.

Nr.:	absolute energies [eV]	excitation energies [eV]	ground configuration [%]	first order [%]	second order [%]
1	-7.2922	0.0000	40.9	48.8	10.3
2	-7.2918	0.0005	40.9	48.8	10.3
3	-7.2912	0.0010	40.9	48.8	10.3
4	-6.9255	0.3667	41.9	48.4	9.9
5	-6.9220	0.3702	41.9	48.2	9.8
6	-6.8307	0.4615	40.5	49.2	10.3
7	-6.8288	0.4634	40.6	49.4	10.3
8	-6.8285	0.4638	40.6	49.4	10.3
9	-6.1370	1.1552	40.4	48.8	10.9
10	-6.1229	1.1694	40.4	49.0	10.4
11	-6.0243	1.2679	49.6	43.0	7.2
12	-6.0167	1.2756	48.8	43.6	8.1
13	-5.8879	1.4043	45.0	47.2	7.9
14	-5.8810	1.4112	45.1	47.0	7.8
15	-5.8791	1.4131	45.1	47.2	7.8
16	-5.8022	1.4901	46.3	45.4	8.3
17	-5.7871	1.5051	49.5	43.4	7.6
18	-5.7842	1.5080	49.7	43.2	7.6
19	-5.7581	1.5342	44.3	46.8	9.3
20	-5.6491	1.6432	38.8	50.2	10.8
21	-5.5919	1.7003	38.0	50.8	11.3
22	-5.4554	1.8369	43.9	47.2	8.8
23	-5.4547	1.8375	43.9	47.2	8.8
24	-5.0259	2.2664	0.0	77.6	22.4
25	-5.0258	2.2664	0.0	77.6	22.4
26	-4.9975	2.2947	0.0	77.8	22.1
27	-4.9974	2.2948	0.0	77.8	22.1
28	-4.9652	2.3270	45.3	46.2	8.3
29	-4.9461	2.3462	43.5	47.6	9.0
30	-4.8598	2.4324	38.6	52.0	9.0
31	-4.8589	2.4334	38.6	52.0	9.0
32	-4.8574	2.4348	38.7	52.0	9.0

Table 4.6: Results of the cluster-model calculation for the low-temperature phase ( $T < 80$  K). Here, we assume that two energies belong to a degenerated eigenstate if they differ by less than 0.2 meV. The last two columns represent the sum of all configurations of the appropriate excitation order. The column “first order” represents the sum of all single-excited and the column “second order”, the sum of all double-excited configurations. Discrepancy from 100 % are caused by roundoff errors.

excitation energies	ground configuration		single-excited configurations	
	multiplet	contribution	multiplet	contribution
0.0000	$^3F$	38.31	$^4F, ^4P, ^2H, ^2G$	25.37, 9.76, 5.94, 4.01
0.0005	$^3F$	38.31	$^4F, ^4P, ^2H, ^2G$	25.39, 9.74, 5.93, 4.01
0.0010	$^3F$	38.29	$^4F, ^4P, ^2H, ^2G$	25.38, 9.76, 5.96, 4.02
0.3667	$^3F$	39.36	$^4F, ^4P, ^2H, ^2G$	24.86, 9.42, 6.08, 4.17
0.3702	$^3F$	39.34	$^4F, ^4P, ^2H, ^2G$	24.64, 9.61, 6.11, 4.09
0.4615	$^3F$	39.93	$^4F, ^4P, ^2H, ^2G$	31.58, 3.86, 5.16, 5.73
0.4634	$^3F$	39.92	$^4F, ^4P, ^2H, ^2G$	31.36, 4.05, 5.16, 5.67
0.4638	$^3F$	39.90	$^4F, ^4P, ^2H, ^2G$	31.28, 4.08, 5.22, 5.67
1.1552	$^1G, ^1D$	18.48, 21.26	$^2H, ^2G, ^2F, ^2D_2, ^2P$	10.46, 12.85, 10.40, 10.39, 3.02
1.1694	$^3F, ^1G, ^1D$	3.69, 3.90, 22.56	$^2H, ^2G, ^2F, ^2D_2, ^2P$	10.50, 11.30, 8.96, 8.12, 6.67
1.2679	$^3F, ^3P$	46.51, 3.08	$^4F, ^4P, ^2H, ^2G$	18.87, 3.93, 7.33, 6.85
1.2756	$^3F$	43.26	$^4F, ^4P, ^2H, ^2G$	17.56, 3.67, 7.62, 7.18
1.4043	$^3F$	42.81	$^4F, ^4P, ^2H, ^2G$	25.82, 3.76, 6.35, 6.14
1.4112	$^3F$	45.10	$^4F, ^4P, ^2H, ^2G$	27.36, 3.99, 6.20, 5.78
1.4131	$^3F$	44.67	$^4F, ^4P, ^2H, ^2G$	27.12, 3.95, 6.23, 5.84
1.4901	$^3F, ^1G, ^1D$	31.11, 4.58, 10.36	$^4F, ^2H, ^2G, ^2F, ^2D_2, ^2P$	13.24, 8.00, 8.98, 3.65, 4.20, 3.49
1.5051	$^3F$	48.43	$^4F, ^2H, ^2G$	19.99, 7.51, 7.50
1.5080	$^3F$	49.36	$^4F, ^2H, ^2G$	20.39, 7.50, 7.34
1.5342	$^3F, ^1G, ^1D$	20.59, 7.38, 16.08	$^4F, ^2H, ^2G, ^2F, ^2D_2, ^2P$	8.77, 8.61, 10.08, 5.42, 5.82, 4.84
1.6432	$^1G, ^1D, ^1D$	14.22, 22.35, 22.56	$^2H, ^2G, ^2F, ^2D_2, ^2P$	10.11, 16.66, 5.45, 5.09, 9.29
1.7003	$^1G, ^1D$	16.59, 21.26	$^2H, ^2G, ^2F, ^2D_2$	10.06, 21.83, 5.20, 10.46
1.8369	$^3P$	41.19	$^4F, ^4P, ^2F, ^2D_2$	20.36, 9.65, 7.40, 5.31
1.8375	$^3P$	40.96	$^4F, ^4P, ^2F, ^2D_2$	20.26, 9.59, 7.37, 5.29
2.2664	-	-	$^4F$	77.41
2.2664	-	-	$^4F$	77.44
2.2947	-	-	$^4F$	77.67
2.2948	-	-	$^4F$	77.68

Table 4.7: Part I: Contributions in [%] of the different multiplets to the ground and the excited state for the low-temperature phase ( $T < 80$  K) for the energetically low-lying eigenstates. Here, only those contributions are shown which are greater than 3 %. For the sake of simplicity, we neglect the contributions of multiplets in double-excited configurations. All multiplets of the single-excited configurations are coupled with the  $^2P$  multiplet of the ligand hole, which is dropped from notation.

excitation energies	ground configuration		single-excited configurations	
	multiplet	contribution	multiplet	contribution
2.3270	$^1G$	44.44	$^2H, ^2G, ^2F, ^2D_2$	19.66, 12.86, 7.70, 4.02
2.3461	$^1G, ^1D$	31.49, 11.39	$^2H, ^2G, ^2F, ^2P$	21.32, 10.87, 6.78, 3.27
2.4324	$^3F, ^3P$	3.19, 35.32	$^4F, ^4P, ^2F, ^2D_2,$ $^2P$	26.64, 11.23, 5.85, 3.26, 3.32
2.4334	$^3F, ^3P$	3.19, 35.35	$^4F, ^4P, ^2F, ^2D_2,$ $^2P$	26.69, 11.24, 5.86, 3.25, 3.33
2.4348	$^3F, ^3P$	3.15, 35.15	$^4F, ^4P, ^2F, ^2D_2,$ $^2P$	26.42, 11.21, 5.87, 3.27, 3.34

Table 4.8: Part II: Contributions in [%] of the different multiplets to the ground and the excited state for the low-temperature phase ( $T < 80$  K) for the energetically low-lying eigenstates. Here, only those contributions are shown which are greater than 3 %. For the sake of simplicity, we neglect the contributions of multiplets in double-excited configurations. All multiplets of the single-excited configurations are coupled with the  $^2P$  multiplet of the ligand hole, which is dropped from notation.

In order to deepen our investigation, we will look at the contributions of the different ionic multiplets to the energetically low-lying cluster eigenstates: As shown in Tab. 4.7, the ground state is predominantly formed by the  $^3F$  multiplet of the ground configuration but contains a remarkable portion of the  $^4F$  multiplet of the single-excited V ion with  $d^3$  electronic configuration as well.

For the energetically higher lying excitations below 1.0 eV the contributions of the different multiplets of the different configurations show only a marginal variation. In a simple one-particle picture, these crystal-field excitations represent intra  $t_{2g}$  transitions in good agreement with Ref. [116], see Fig. 4.4. The excitations at 1.1552 eV and 1.1694 eV are formed predominantly by the  $^1D$  multiplet as suggested by the Tanabe-Sugano diagram, see Fig. 4.4. The strong admixture of the  $^1G$  multiplet which is actually much higher in energy is caused by the crystal-field operator which mixes eigenstates with same spin. Additionally, these eigenstates have a different total spin than the ground state. Thus, transitions between the ground state and this two states are forbidden due to the spin selection rule. In principle, the spin-orbit coupling removes this selection rule but in VOCl the strength of the spin-orbit coupling is less than 31.6 meV leading to tiny features at roughly 1.2 eV in the optical data.

The eigenstates between 1.2 and 1.6 eV are formed predominantly by the  $^3F$  multiplet. In a simple one-particle picture, these excitations correspond to transitions between the  $t_{2g}$  and the  $e_g$  level. Note, that due to the reduced point-group symmetry on the V site, we find a reduced degree of degeneracy of the crystal-field eigenstates, see Fig. 4.6. The eigenstates above 1.6 eV correspond to energetically higher lying crystal-field eigenstates similar to those shown in the Tanabe-Sugano diagram Fig. 4.4.

But, the eigenstates located between 2.20 eV and 2.30 eV represent charge-transfer excitations which are formed predominantly by the  ${}^4F$  multiplet of the single-excited configurations.

Summarizing our investigation of the crystal-field excitations in VOCl, we find a good description of most of the positions of the different excitations in spite of inaccuracies in the crystal structure. However, we cannot describe the strength and the polarization dependence of the optical conductivity properly. But, we determine the contributions of the different ionic multiplets to the cluster-eigenstates and identify the peaks with charge-transfer and crystal-field excitations. Additionally, we describe several transitions within a simple one-particle picture in good agreement with [116]. Furthermore, we analyze the dependence of the results of the cluster-model calculation on the value of several calculation parameters such as the charge-transfer energies  $\Delta_{V-Cl}$  and  $\Delta_{V-O}$ , the screening factor, the Hubbard  $U_V$ , and the value of the Cl-radius. However, we cannot find a parameter-set describing the optical data correctly. Due to the limitation of the cluster-model calculation being used in the description of the optical data, we cannot describe the onset of the charge-transfer band. Additionally, the cluster-model calculation cannot describe the effect of intensity stealing. Furthermore, as shown in Tabs. 4.7 - 4.8, the hybridization in this compound play a dominant role. Therefore, we expect that the hopping between two different V sites is not negligible resulting in a remarkable contribution to the optical conductivity. Hence, we cannot ignore the hopping between two V ions in the description of the optical data. In addition, the cluster-model calculation does not consider the contributions of phonons or magnon-sidebands as well as p-states at the V ion.

Finally, we will conclude the investigation of VOCl by comparing the results of the cluster-model calculation presented above with crystal-field excitations in the isostructural compound TiOCl, which are investigated in great detail by Rückamp [135]. Therefore, we perform a cluster-model calculation for TiOCl where the cluster consists of a Ti ion with  $3d^1$  electronic configuration and four oxygen ( $2p^6$ ) and two chlorine ( $3p^6$ ) ions around. The calculation parameters used for the cluster-model calculation of TiOCl are shown in Tab. 4.9 where we scale the Slater integrals to 90 % of the atomic values.

parameter	$3d^1$ configuration	$3d^2$ configuration	$3d^3$ configuration
$F_{Ti}^2$	-	7.419 eV	6.102 eV
$F_{Ti}^4$	-	4.619 eV	3.750 eV
$\langle r^2 \rangle_{Ti}$	0.534 Å <sup>2</sup>	0.690 Å <sup>2</sup>	1.000 Å <sup>2</sup>
$\langle r^4 \rangle_{Ti}$	0.574 Å <sup>4</sup>	1.040 Å <sup>4</sup>	2.521 Å <sup>4</sup>
$\zeta_{Ti}$	24 meV	20 meV	15 meV
$F_{Cl,3p^4}^2$	6.590 eV	6.590 eV	6.590 eV
$F_{O,2p^4}^2$	8.236 eV	8.236 eV	8.236 eV

Table 4.9: Parameters used in the cluster-model calculation for TiOCl. The Slater integrals are already scaled to 90 % of the atomic values.

Additionally, we set the strength of the crystal-field splitting and the strength of the spin-orbit splitting on ligand-site equal to zero. In addition, we set the Hubbard  $U$  at the Ti site to  $U_{Ti} = 2$  eV ( $U_{Cl} = U_O = 5$  eV) and set the charge-transfer energies to  $\Delta_{Ti-Cl} = 2$  eV and  $\Delta_{Ti-O} = 8$  eV. Furthermore, we use  $r_O=4.41$  Å and  $r_{Cl}=9.5$  Å for the ionic radii of the O and the Cl ion, respectively. In order to describe the positions of the different excitations in the optical data of TiOCl properly, we use two different values for the hopping integral  $pd\sigma$  ( $pd\pi$ ) depending on the ions being involved in the hopping process. For hopping processes including the Ti as well as Cl ions we increase the hopping integral  $pd\sigma$  ( $pd\pi$ ) by a factor of 1.469 compared to those between Ti and O ions.

As shown in Fig. 4.20 we achieve a good description of the positions of the different excitations in the optical data of TiOCl. Especially, we can describe the position of the excitation at 1.5 eV for  $\mathbf{E} \parallel \mathbf{b}$  quite well. But, we find a strong disagreement between the calculated optical conductivity and the experimental data which is caused by several aspects. First of all, we include only one Ti ion in the cluster-model calculation and neglect the exchange processes between different Ti sites. Therefore, we cannot describe the onset of the charge-transfer band above 1.5 eV. Additionally, the cluster-model calculation cannot describe the effect of intensity stealing as well as the contributions of phonons or magnon-sidebands. Furthermore, we neglect the contribution of energetically higher lying p-states at the Ti ion to the optical conductivity which are relevant for the description of the experimental data due to the broken inversion symmetry at the Ti site.

By comparing the results of the cluster-model calculation with the results of the point-charge model for TiOCl shown in Tab. 4.4 we can identify the energetically low lying excited eigenstates with d-orbitals. In good agreement with Rückamp [135] we identify the excitation at 1.5 eV with a transition between the ground state and the  $yz$ -orbital. Additionally, we associate the excitation at 0.6 eV with a transition between the ground state and the  $xz$ -orbital. Although we cannot determine the position of the symmetry-forbidden transition in the optical data, we identify the first excited eigenstate with the  $xy$ -orbital. In order to estimate the contribution of the spin-orbit coupling to the optical conductivity we repeat the cluster-model calculation described above and turn off the spin-orbit coupling. As shown in Fig. 4.20, the spectral weight of the optical conductivity below 2.0 eV depends strongly on the spin-orbit coupling. Here, the spin-orbit coupling leads to an enhancement of the spectral weight of the symmetry-forbidden transition at 0.19 eV whereas the transitions at 0.6 eV and 1.5 eV do not contribute to the optical conductivity in strong disagreement to the experimental data.

Summarizing our investigation, we can describe the positions of all excitations in the optical data of TiOCl by using a cluster-model calculation as described in the second chapter. Nevertheless, we are not able to describe the strength of the different excitations in the optical conductivity.

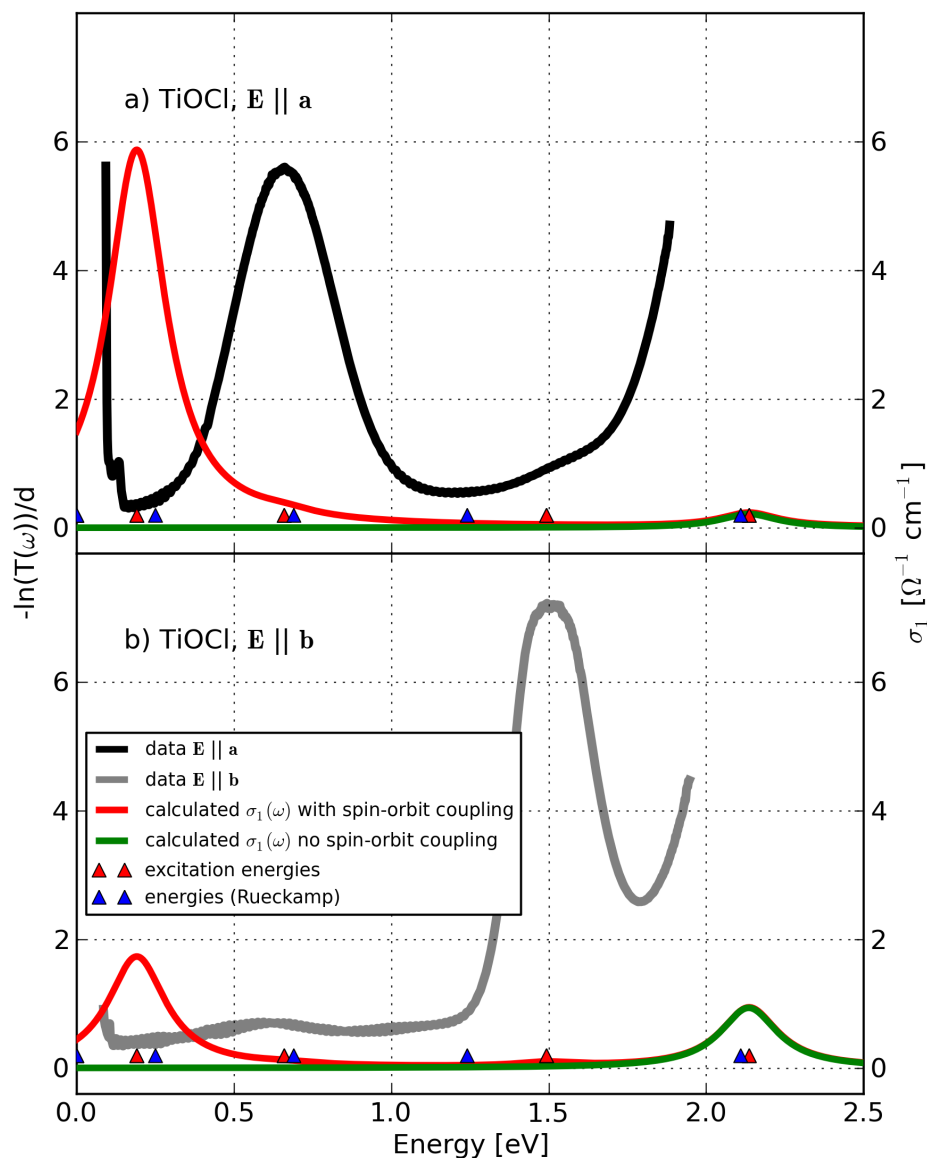


Figure 4.20: Comparison between the measured absorption  $-\ln(T(\omega))/d$  (grey and light grey lines) determined by Rückamp [135] and the calculated optical conductivity  $\sigma_1(\omega)$  (solid lines) of TiOCl for  $T = 295$  K for  $\mathbf{E}||\mathbf{a}$  (grey color) and  $\mathbf{E}||\mathbf{b}$  (light grey color). The optical conductivity is multiplied by a factor of  $1 \cdot 10^6$ . The blue triangles represent the results of the cluster-model calculation for  $T = 295$  K done by Rückamp [135] by using the code XTLS 8 written by A. Tanaka (Hiroshima University, Japan). The red triangles indicate the excitation energies of our cluster-model calculation.

## 4.2 Phonons in hexagonal $\text{YMnO}_3$ and $\text{YMn}_{0.7}\text{Ga}_{0.3}\text{O}_3$

In this section we describe the investigation of the spin-lattice interaction in the multiferroic, hexagonal compound  $\text{YMnO}_3$  and in the doped system  $\text{YMn}_{0.7}\text{Ga}_{0.3}\text{O}_3$ . In multiferroic compounds, there is a coupling between the static, electrical polarization and the magnetization. By analyzing the lattice dynamics and their dependence on Ga doping we investigate the influence of the magnetization on the dynamical polarization and achieve a better understanding of the origin of ferroelectricity in these hexagonal systems. Here, we present a detailed phonon analysis for several temperatures between 20 K and 295 K including a factor-group analysis. Furthermore, we compare our room-temperature infrared data with Raman and infrared data as well as lattice-dynamical calculations reported by Iliev *et al.* [152].

“Multiferroic” magnetoelectric manganites ( $\text{RMnO}_3$ ) shows fascinating novel phenomena such as the coexistence of ferroelectric and magnetic order and the control of polarization by external and internal magnetic fields. Additionally, multiferroic compounds shows phase diagram with cascades of magnetic and ferroelectric phase transitions upon changing temperature or magnetic fields [150, 151]. The coupling strength between electric polarization and magnetization can be controlled by an applied magnetic field and enables the control of dielectric properties. The observations of ferroelectric and antiferromagnetic domains [153, 154], anomalies of the dielectric constant at magnetic transitions [155], and the strong scattering of acoustic phonons off magnetic fluctuations found in thermal conductivity measurements [156] may be caused by the magnetoelectric coupling in  $\text{YMnO}_3$ .

The  $\text{RMnO}_3$  compounds crystallize with orthorhombic ( $o\text{-RMnO}_3$ ) or hexagonal ( $h\text{-RMnO}_3$ ) structure depending upon the ionic radius of the R ion.

- The *orthorhombic*  $o\text{-RMnO}_3$  with space group  $Pnma$  ( $C_{2h}^{16}$ ) [157, 158] contain rare-earth elements with large ionic radii ( $R = \text{La, Pr, Nd, Sm, Eu, Gd, Tb, and Dy}$ ) [159]. These compounds show the colossal magnetoresistance effect, i.e. a metal-insulator transition that changes the conductivity by many orders of magnitude at the Curie temperature [160]. The  $\text{Mn}^{3+}$  ion is octahedrally coordinated by O atoms. The octahedra form a corner-sharing three-dimensional network. The appearance of ferroelectricity is caused by the existence of a gradient of the magnetization (incommensurate helicoidal spin structure) leading to a transverse polarization [161, 162]. The coexistence and strong coupling between ferroelectricity and incommensurate magnetism in  $o\text{-RMnO}_3$  is related to Dzyaloshinskii-Moriya interactions [163]. In a traditional ferroelectric material such as  $\text{BaTiO}_3$ , the loss of inversion symmetry at  $T_{\text{FE}}$  causes electric polarization [164]. It is still a question whether such atomic displacements are relevant in this class of spin-driven ferroelectric materials [163].
- The *hexagonal* phase ( $h\text{-RMnO}_3$ ) with noncentrosymmetric space group  $P6_3cm$  ( $C_{6v}^3$ ) at room temperature is found for R ions with small ionic radii ( $R=\text{Ho}$ ,

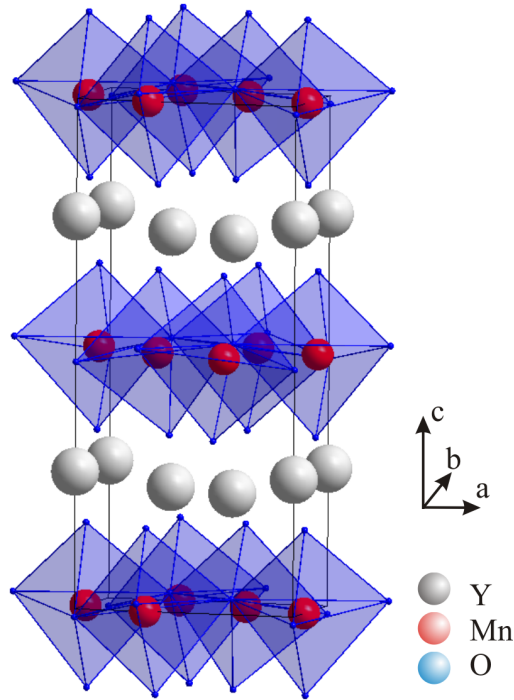
Er, Tm, Yb, Lu, Y, and Sc) [165]. The  $Mn^{3+}$  ions form a triangular lattice which has a  $\sqrt{3} \times \sqrt{3}$  superstructure (a trimerization of Mn ions). This leads to the absence of centrosymmetry, which allows off-center displacements along the polar ( $\mathbf{c}$ ) axis and thereby a spontaneous electric polarization<sup>10</sup> [166]. The hexagonal manganites form the class of “ferroelectromagnets” in which the ferroelectric and magnetic orders coexist at low temperatures. The investigation of ferroelectromagnets and the analysis of the coupling between the two orders may offer insights into the occurrence of ferroelectricity and magnetism in these materials. This coupling can result in the so-called “magnetoelectric effect”, where the dielectric (magnetic) properties of the ferroelectromagnets may be altered by the onset of the magnetic (electric) transition or by the application of a magnetic (electric) field. The hexagonal  $h$ - $RMnO_3$  present a high saturation polarization [167] of  $P \sim 5.5 \mu C/cm^2$ . Although exchange interactions between the magnetic  $Mn^{3+}$  ions are relatively strong with a Curie-Weiss temperature of around 700 K [155], magnetic ordering in these materials occurs at a much lower temperature, where the Néel temperature ranges from 70 K to 130 K [155] upon changing the R ion. This is partly a consequence of the quasi-two-dimensional magnetic structure of  $h$ - $RMnO_3$  where Mn spins form weakly coupled layers parallel to the  $\mathbf{ab}$  basal plane. Due to the large difference between the ferroelectric and spin ordering temperatures and the different origins of ferroelectricity and magnetism in hexagonal manganites, the interplay between electric and magnetic phenomena in these materials is not very strong.

Due to the intermediate ionic radius of Y,  $YMnO_3$  shows both crystal structures. The orthorhombic structure can be stabilized by either low-temperature or high-pressure synthesis or epitaxial thin film growth. Hexagonal  $h$ - $YMnO_3$  has an A-type antiferromagnetic order ( $T_N \sim 72$  K) [168] and reversible spontaneous electric polarization ( $T_{FE} \sim 1000$  K) [169, 170]. As shown in Fig. 4.21, the crystal structure of  $h$ - $YMnO_3$  consists of  $[MnO_5]$  trigonal bipyramids where each  $Mn^{3+}$  ion is surrounded by three in-plane and two apical oxygen ions. The  $[MnO_5]$  bipyramids are linked via corners to form a triangular lattice in the  $\mathbf{ab}$  plane, and adjacent layers are separated by layers of  $Y^{3+}$  ions. The apical oxygen ions of the  $[MnO_5]$  units also construct the antiprisms of  $[YO_6]$ , and the planar oxygen ions of  $[MnO_5]$  constitute the caps of the  $[YO_6]$  antiprisms as well.

The buckling and tilting of the  $[MnO_5]$  bipyramids are important for the stabilization of the ferroelectric state [171, 172]. The ferroelectric state is associated with displacements of the oxygen ions that coordinate  $Y^{3+}$ , which has formally a  $d^0$  state.<sup>11</sup>

<sup>10</sup>The linear magnetoelectric effect is forbidden by symmetry.

<sup>11</sup>The  $d^0$ -ness rule is generally accepted in ferroelectricity: A ferroelectric displacement of the B cation in  $ABO_3$  compounds is inhibited if the formal charge of the B ion does not correspond to a  $d^0$  electron configuration due to the strong on-site Coulomb interaction between  $d$  electrons. In contrast, the occupancy of transition-metal  $d$  electrons is crucial in the magnetic ordering. Thus the simultaneous magnetic and ferroelectric ordering in  $RMnO_3$  seems to break the  $d^0$ -ness rule. It was suggested that the multiferroic property in  $RMnO_3$  is a result of the effective  $d^0$ -ness along the  $\mathbf{c}$  axis [173, 174].

Figure 4.21: Crystal structure of  $\text{YMnO}_3$  [166].

In the ferroelectric phase, hexagonal  $h\text{-YMnO}_3$  has a noncentrosymmetric  $P6_3cm$  ( $C_{6v}$ ) structure at room temperature and the ferroelectric polarization appears along the  $\mathbf{c}$  axis. At  $T_{\text{FE}_2} \simeq 1350$  K [175]  $h\text{-YMnO}_3$  undergoes a transition to paraelectric  $P6_3/mmc$  ( $D_{6h}^4$ ) [175, 176]. Within the high-temperature hexagonal  $P6_3/mmc$  structure the  $\text{Mn}^{3+}$  ions in bipyramidal oxygen coordination form close-packed planes, which are separated by  $\text{Y}^{3+}$  ions. The symmetry changes to  $P6_3cm$  by a cooperative rotation of the bipyramidal axis from the  $\mathbf{c}$  axis below a temperature  $T_t$ . Additionally, the mirror planes perpendicular to the  $\mathbf{c}$  axis vanish. Using symmetry arguments, T. Lonkai *et al.* [177] pointed out that two separate phase transitions are expected in the transition from the high-temperature phase ( $P6_3/mmc$ ) to the room-temperature phase ( $P6_3cm$ ). (The two possible symmetries for the intermediate phase, which is stable between  $T_{\text{FE}_1} \simeq 1100$  K and  $T_{\text{FE}_2} \simeq 1350$  K [175], are  $P6_3cm$  (identical to the room temperature structure) and  $P6_3/mcm$ .)

### 4.2.1 Ga Substitution

The replacement of Mn by Ga changes the orbital occupation (from  $d^4$  for  $\text{Mn}^{3+}$  to  $d^{10}$  for  $\text{Ga}^{3+}$ ) and the ionic radius.  $\text{YGaO}_3$  is isostructural to  $\text{YMnO}_3$  [178] and by analyzing the evolution of the structural parameters from  $\text{YMnO}_3$  to  $\text{YGaO}_3$  we obtain a better understanding of the origin of ferroelectricity in these hexagonal systems. Substituting Ga for Mn in single crystals of  $\text{YMn}_{1-x}\text{Ga}_x\text{O}_3$  varies the different transition temperatures, and the spin-lattice interaction changes with increasing  $x$ . The

Néel temperature  $T_N$  decreases from 72 K for  $x = 0$  to 65 K for  $x = 0.1$  and to 35 K for  $x = 0.3$ . Also, the magnitude of the Curie-Weiss temperature  $T_{CW}$  decreases with increasing Ga concentration:  $T_{CW} = -567$  K for  $x = 0.0$ ,  $-531$  K for  $x = 0.3$ , and  $-501$  K for  $x = 0.5$ . The corresponding effective moments per Mn<sup>3+</sup> ion are  $4.93 \mu_B$  for  $x = 0.0$ ,  $4.38 \mu_B$  for  $x = 0.3$ , and  $3.62 \mu_B$  for  $x = 0.5$  [168]. The ratio of  $|T_{CW}|$  to  $T_N$ , an indication for the frustration in the magnetic structure, increases upon doping [168]. In contrast to theoretical analysis [180] recent experimental studies find an enhancement of the ferroelectric transition temperature  $T_{FE}$  and the Mn-spin reorientation temperature  $T_{SR}$  with increasing Ga substitution [179]. The substitution of nonmagnetic Ga for Mn suppresses antiferromagnetic ordering by diluting the magnetic system and leads to a strong enhancement of magnetocapacitance, which is caused by the increased magnetic coupling between layers [168]. In ferroelectric antiferromagnets, the coupling of the electric polarization  $P$  to the Néel order parameter  $L$ , which is not strongly affected by Ga substitution, gives rise to an anomaly of the dielectric susceptibility at the magnetic transition. Furthermore, the coupling of  $P$  to the uniform magnetic field  $H$  along the  $\mathbf{c}$  direction, which causes magnetocapacitance, increases by two orders of magnitude upon 30 % Ga substitution [168]. The smaller ionic radius of Ga and the filled  $d_{z^2}$  orbital were expected to have a larger effect on the local coordination around the Mn site. But a more pronounced alteration around the Y site was observed [169]. The lattice parameter  $\mathbf{a}$  decreases and  $\mathbf{c}$  increases upon Ga<sup>3+</sup> substitution, which results in an elongation of the [YO<sub>6</sub>] antiprisms, where the Y ions become more closely located near the barycenter. Due to the antiparallel displacements of the [Y1O<sub>6</sub>] and [Y2O<sub>6</sub>] local dipoles the total polarization does not decrease markedly. In contrast to smaller R ions, the substitution of Mn<sup>3+</sup> by Ga<sup>3+</sup> does not increase the tilting and buckling [169].

### 4.2.2 Phonon Analysis

In order to understand the interplay of structural, magnetic, and ferroelectric properties against Ga substitution we perform reflectivity measurements for  $T = 20 - 295$  K in the spectral range of  $100-8000 \text{ cm}^{-1}$  at quasnormal incidence. The spectra were measured for different polarization angles on polished surfaces of YMnO<sub>3</sub> and YMn<sub>0.7</sub>Ga<sub>0.3</sub>O<sub>3</sub>. The reference measurements were done with in-situ Au evaporation. The variation of the polarization angle was realized by rotating the polarizer.

YMnO<sub>3</sub> and YMn<sub>0.7</sub>Ga<sub>0.3</sub>O<sub>3</sub> crystals were grown by U. Adem and Th. Palstra<sup>12</sup> using a floating-zone furnace. The oxygen partial pressure was increased with increasing Ga concentration in order to stabilize the molten zone. The crystals have a diameter of 5 mm and are a few cm long.

Assuming that a primitive unit cell contains  $r$  atoms, we divide the vibrational degrees of freedom into  $3r$  branches throughout the first Brillouin zone. The individual vibra-

<sup>12</sup>Solid State Chemistry Laboratory, Materials Science Center, University of Groningen, 9747 AG Groningen, The Netherlands.

tions along the branches are labeled with a linear momentum vector  $k$ . As mentioned in section “2.11.3 Phonons” the dynamical matrix  $D(k)$  with dimension  $3r \times 3r$ , which is invariant under the primitive translations of the lattice, contains all information about the vibrational displacements of all atoms in the crystal. Within the infrared spectroscopy we can measure the branches only at the center of the Brillouin zone at  $k = 0$  — the so-called  $\Gamma$ -point, because the momenta of phonons excited by infrared spectroscopy is very small. The energy of three of the  $3r$  phonon branches, the so-called ACOUSTIC MODES, goes to zero as  $k \rightarrow 0$ . These vibrations correspond to pure translations of the crystal. The remaining  $3r - 3$  branches represent the optical modes. The observation of a phonon mode in infrared spectroscopy requires an inducible or alterable dipole moment, which changes under the influence of the electromagnetic wave. Such a mode is called “INFRARED ACTIVE”. In case of a vibrational mode which is symmetric with respect to an inversion center, we find no change in the dipole moment and the associated phonon mode is called “INFRARED INACTIVE”.

A phonon mode is “RAMAN ACTIVE”, if the mode is associated with a change in the polarizability tensor. The vibrational movement of the atoms in a crystal affects the ability of the nuclei to hold their electrons. This can result in a change in the polarizability of the ion. In case of centrosymmetric crystals the Raman active modes are IR inactive and *vice versa*, also called the rule of mutual exclusion.

The determination of the  $\Gamma$ -point phonon modes starts with the factor-group analysis [181–184], developed by Bhagavantum and Venkatarayudu, in which the symmetry properties of the crystal are determined by studying the effect of each symmetry operation in the factor group on each type of atom in the unit cell. The so-called FACTOR GROUP of a space group describes the symmetry of a unit cell by separating out the translations from the space group. The factor group is isomorphous with one of the 32 crystallographic point groups and assumes that all modes of a crystal can be determined by considering only one unit cell. The factor groups differ, however, from the point groups in several important ways [184]. (For example, within a factor group, the rotational axes and the symmetry planes do not need to meet at a common point, because there does not need to be a point within the unit cell that is left invariant by all the symmetry operations.) The factor groups are normally labelled either by the Schönflies symbol [185] in which the point group of the crystal class (e.g.  $C_{2v}$ ) is given a numerical right superscript to designate the factor-group (e.g.  $C_{2v}^2$ ); or they are labelled by the Hermann-Mauguin symbols [186] in which the crystal class symbol (e.g.  $Pmm2$ ) is modified to indicate explicitly the substitution of a screw axis or a glide plane (e.g.  $Pmm2_1$ ). The factor-group analysis is made by applying all of the symmetry operations of the factor group to each atom in the unit cell. The obtained representation can be reduced in order to determine the number of normal modes belonging to each irreducible representation. A detailed description of the factor-group analysis can be found in [184].

atom	Wyckhoff notation	Site symmetry	Irreducible representations
Y(1)	2(a)	$C_{3v}^v$	$A_1 + B_1 + E_1 + E_2$
Y(2)	4(b)	$C_3$	$A_1 + A_2 + B_1 + B_2 + 2 E_1 + 2 E_2$
Mn	6(c)	$C_s^v$	$2 A_1 + A_2 + 2 B_1 + B_2 + 3 E_1 + 3 E_2$
O(1)	6(c)	$C_s^v$	$2 A_1 + A_2 + 2 B_1 + B_2 + 3 E_1 + 3 E_2$
O(2)	6(c)	$C_s^v$	$2 A_1 + A_2 + 2 B_1 + B_2 + 3 E_1 + 3 E_2$
O(3)	2(a)	$C_s^v$	$A_1 + B_1 + E_1 + E_2$
O(4)	4(b)	$C_3$	$A_1 + A_2 + B_1 + B_2 + 2 E_1 + 2 E_2$

Table 4.10: Atomic site symmetries and irreducible representations for the atoms in hexagonal  $YMnO_3$  [152].

The factor-group analysis of the phonon modes in hexagonal  $YMnO_3$  starts with the determination of the irreducible representations of the symmetry-equivalent positions indicated by the Wyckoff symbols in the unit cell. The number of formula units per unit cell is  $Z = 6$  [152]. The site symmetries as well as the irreducible representation of each atomic site are shown in Tab. 4.10.

Combining the irreducible representations of the atomic sites we find the following reducible representation of the phonon modes of hexagonal  $YMnO_3$  at room temperature with space group  $P6_3cm$ :<sup>13</sup>

$$\Gamma_{\text{total}} = 10 A_1 + 5 A_2 + 10 B_1 + 5 B_2 + 15 E_1 + 15 E_2. \quad (4.2.1)$$

The group-theoretical analysis predicts that 9  $A_1$  and 14  $E_1$  are IR active,  $A_1$  for  $\mathbf{E} \parallel \mathbf{c}$ ,  $E_1$  for  $\mathbf{E} \perp \mathbf{c}$ . The Raman active modes are described by  $(9 A_1 + 14 E_1 + 15 E_2)$  and the acoustical modes by  $(A_1 + E_1)$ . Additionally, we have 20  $(5 A_2 + 10 B_1 + 5 B_2)$  silent phonon modes [152]. As mentioned in section “3.1.1 Drude-Lorentz model”, the tensor of the dielectric function is diagonal, and therefore the diagonal matrix elements represent the dielectric function in the  $\mathbf{a}$ ,  $\mathbf{b}$ , and  $\mathbf{c}$  direction, respectively

$$\hat{\epsilon}(\omega) = \begin{pmatrix} \epsilon_{\mathbf{a}}(\omega) & 0 & 0 \\ 0 & \epsilon_{\mathbf{b}}(\omega) & 0 \\ 0 & 0 & \epsilon_{\mathbf{c}}(\omega) \end{pmatrix}. \quad (4.2.2)$$

Due to the hexagonal symmetry, the phonon spectra for  $\mathbf{E} \parallel \mathbf{a}$  and  $\mathbf{E} \parallel \mathbf{b}$  are identical and it is sufficient to distinguish between  $\mathbf{E} \parallel \mathbf{c}$  and  $\mathbf{E} \perp \mathbf{c}$ . Thus, we can describe the linear dielectric response by two scalar functions  $\epsilon_{\mathbf{E} \parallel \mathbf{c}}(\omega)$  and  $\epsilon_{\mathbf{E} \perp \mathbf{c}}(\omega)$ . These scalar functions are determined by fitting the reflectivity  $R(\omega)$  for  $\mathbf{E} \parallel \mathbf{c}$  and  $\mathbf{E} \perp \mathbf{c}$ , respectively, using the Drude-Lorentz model.

As shown in Fig. 4.22 and Fig. 4.23 the fits yield a good description of the measured reflectivity  $R(\omega)$ . The optical conductivity was determined by applying the Kramers-Kronig transformation to  $R(\omega)$ , which was extrapolated using the Drude-Lorentz fit.

<sup>13</sup> $YMnO_3$  and  $YMn_{0.7}Ga_{0.3}O_3$  have the same space group, because  $YMnO_3$  is isostructural to  $YGaO_3$ .

The dotted lines indicate the eigenfrequencies of the phonon modes used in the fits. The fit parameters are listed in Tab. 4.12. In case of  $\mathbf{E} \parallel \mathbf{c}$ , where 9  $A_1$  modes are expected, we find 9 IR modes but require a further phonon mode at  $751 \text{ cm}^{-1}$  to describe the phonon spectrum properly. (In Fig. 4.22 and Fig. 4.23 the phonon spectra for  $\mathbf{E} \parallel \mathbf{c}$  are shown including fits consisting of 9 (red) and 10 (green) phonon modes, respectively.) This mode is probably caused by the multi-phonon background which is supported by its large width of  $\gamma=54.9 \text{ cm}^{-1}$  (20 K). Note that the reflectivity is sensitive to such weak contributions in particular in those frequency ranges where  $R(\omega)$  is large. In case of  $\mathbf{E} \perp \mathbf{c}$ , we find 14 phonon modes and one multi-phonon mode at  $\omega_0 = 770 \text{ cm}^{-1}$  with  $\gamma = 352 \text{ cm}^{-1}$  in good agreement with the number of phonon modes predicted by the factor-group analysis. The phonon mode at  $318 \text{ cm}^{-1}$  shows a large damping value ( $\gamma=32.6 \text{ cm}^{-1}$ ) at 20 K but a high oscillator strength of  $S=0.3$ . Probably, this might be a multi-phonon mode, too, and we have to take the tiny feature at  $361 \text{ cm}^{-1}$  into account.

In order to investigate the changes in the phonon spectra between  $T = 20 \text{ K}$  and  $T = 295 \text{ K}$ , we measured the spectra for both directions at several temperatures, as shown in Fig. 4.24. The fit parameters relative to the low-temperature fits at  $T = 20 \text{ K}$  for all measured temperatures are shown in Figs. 4.26 - 4.28.

We find a small change in the phonon spectra for  $\mathbf{E} \perp \mathbf{c}$  around the Néel temperature at  $T = 72 \text{ K}$ , see Fig. 4.29. We find an enhancement of the reflectance for  $\mathbf{E} \perp \mathbf{c}$  between  $420$  and  $480 \text{ cm}^{-1}$  with increasing temperature from  $60 \text{ K}$  to  $80 \text{ K}$  and a reduction from  $80 \text{ K}$  to  $100 \text{ K}$ . This might be caused by the scattering of O vibrations on magnetic excitations.

Additionally, we find a reduction of the phonon eigenfrequencies with increasing temperature, see Fig. 4.26.<sup>14</sup> Most modes decrease by about 1-2 % from  $20 \text{ K}$  to  $295 \text{ K}$ . However, the lowest peak at  $160$  ( $169$ )  $\text{cm}^{-1}$  for  $\mathbf{E} \parallel \mathbf{c}$  ( $\mathbf{E} \perp \mathbf{c}$ ) shows an anomalously large redshift of  $6.1$  ( $5.3$ ) %. This could be an indication of a so-called SOFT MODE, which becomes weaker with increasing temperature and indicates a phase transition for  $\omega_0(T) \rightarrow 0$ . In order to estimate the temperature of the phase transition roughly, we extrapolate the relative frequency of the  $160$  ( $169$ )  $\text{cm}^{-1}$  mode with a quadratic polynomial, as shown in Fig. 4.30. In case of  $\mathbf{E} \parallel \mathbf{c}$ , we find a phase transition temperature at  $T_{\text{trans}}^{\mathbf{E} \parallel \mathbf{c}} = 1012 \text{ K}$  which is very close to the ferroelectric transition temperature  $T_{\text{FE}} \sim 1000 \text{ K}$ . For  $\mathbf{E} \perp \mathbf{c}$ , the extrapolation predicts a phase transition at  $T_{\text{trans}}^{\mathbf{E} \perp \mathbf{c}} = 1648 \text{ K}$ . The large difference between both directions is likely to be caused by inaccuracies in the extrapolations. It is noteworthy that also the damping of the lowest modes show a very strong temperature dependence, e.g. an increase by factor of 5 for  $\mathbf{E} \parallel \mathbf{c}$  from  $20 \text{ K}$  to  $295 \text{ K}$ .

<sup>14</sup>The increase of less than 0.5 % of some eigenfrequencies with increasing temperature is caused probably by inaccuracies in the related fits.

Mode symmetry	our IR data [cm <sup>-1</sup> ]	Direction and sign of largest atomic displacements [152]	Calculated frequencies [cm <sup>-1</sup> ] [152]
$A_1$	149	+z(Y1); -z(Y2)	147 (147)
$A_1$	258	+z(Y1,Y2); -z(Mn)	222 (269)
$A_1$	300	+x(Mn); z(O3)	299 (301)
$A_1$	428	+z(O4,O3); -z(Mn)	423 (467)
$A_1$	481	+x,y(O1,O2); -x,y(Mn)	492 (496)
$E_1$	160	+x,y(Y2); -x,y(Y1)	158 (158)
$E_1$	207	+x,y(O1,O2); -x,y(Y1,Y2)	212 (231)
$E_1$	407	+x,y(O1); -x,y(O2)	410 (415)
$E_1$	463	+x,y(O4,O3); -x,y(O2,O1,Mn)	459 (477)
$E_1$	596	x,y(O3)	586 (589)

Table 4.11: Atomic displacements of several  $A_1$  and  $E_1$  phonon modes in  $h$ - $YMnO_3$  at  $T = 295$  K. The calculated frequencies in brackets represent the LO frequencies, the other frequencies the TO frequencies.

In hexagonal  $YMnO_3$  the space group changes at the ferroelectric transition temperature  $T_{FE} \sim 1000$  K [169] from  $P6_3cm$  to  $P6_3/mmc$ . Within the  $P6_3/mmc$  space group only 6 phonon modes are allowed (3 for  $\mathbf{E} \parallel \mathbf{c}$  and 3 for  $\mathbf{E} \perp \mathbf{c}$ ). Therefore, we expect crucial changes in the phonon spectra above  $T_{FE}$ .

In addition, we compare our room-temperature infrared data with Raman and infrared data as well as lattice-dynamical calculations<sup>15</sup> reported by Iliev *et al.* [152], see Tab. 4.13. The assignment of the modes of Iliev *et al.* [152] differs strongly from our results (see below). This is probably due to the fact that they analyzed data of a polycrystal, which does not provide any information on the polarization dependence.

In case of  $A_1$  modes, Iliev *et al.* found only four infrared-active and only seven Raman-active modes, instead of 9 modes in our data. The factor-group analysis predicts that all  $A_1$  phonon modes are both infrared and Raman active. The peaks at  $258 \text{ cm}^{-1}$ ,  $428 \text{ cm}^{-1}$ , and  $610 \text{ cm}^{-1}$  are found in all results. The excitations at  $149 \text{ cm}^{-1}$  and  $300 \text{ cm}^{-1}$  are found within a few wave numbers in our infrared data and in the Raman and calculation results of Iliev *et al.* but not in their infrared data. We find a peak at  $231 \text{ cm}^{-1}$  whereas their Raman data show a peak at  $190 \text{ cm}^{-1}$  and their calculation predicts a peak at  $204 \text{ cm}^{-1}$  (TO),  $216 \text{ cm}^{-1}$  (LO). But, they report an  $E_1$  mode in their infrared data at  $238 \text{ cm}^{-1}$  which is probably an  $A_1$  mode. Furthermore, they found a peak in their infrared data at  $398 \text{ cm}^{-1}$  and in their calculation results at  $388 \text{ cm}^{-1}$  (TO),  $398 \text{ cm}^{-1}$  (LO), which has no analogon in our infrared data. Further discrepancies can be found in Tab. 4.13.

<sup>15</sup>Iliev *et al.* [152] use a shell model, which describes the ionic interactions by sums of long-range Coulomb potentials and short-range potentials in the Born-Mayer form. Furthermore, the ions are replaced by point charges with charge  $Z$ . They are coupled with a force constant  $k$  to a massless shell with charge  $Q$  around it.

Iliev and collaborators found only six infrared-active and only four Raman-active  $E_1$  modes instead of 14 modes predicted by the factor-group analysis. The peaks at  $207\text{ cm}^{-1}$ ,  $243\text{ cm}^{-1}$ ,  $296\text{ cm}^{-1}$ ,  $377\text{ cm}^{-1}$ ,  $407\text{ cm}^{-1}$ , and  $596\text{ cm}^{-1}$  are found within a few wave numbers in all results. The excitation at  $160\text{ cm}^{-1}$  corresponds very well to the calculation result at  $158\text{ cm}^{-1}$ . The features at  $257\text{ cm}^{-1}$ ,  $311\text{ cm}^{-1}$ ,  $361\text{ cm}^{-1}$ ,  $416\text{ cm}^{-1}$ , and  $581\text{ cm}^{-1}$  in our measurements were not found by Iliev *et al.*, which might be caused by their large damping values at 295 K, see Tab. 4.12. They found peaks at  $632\text{ cm}^{-1}$  in their Raman and at  $457\text{ cm}^{-1}$  in their infrared data, which we do not find.

Although we find no overall agreement with the experimental results of Iliev *et al.*, we can use the calculation results to identify the direction and the sign of the largest atomic displacements of some phonon modes, see Tab. 4.11.

Additionally, the results of Iliev *et al.* suggest a classification of the different phonon modes: The lowest modes are connected with vibrations including the Y ions, which have the biggest mass of all ions in this compound. The next modes represent vibrations containing Y and Mn ions, followed by vibrations with Mn and O ions. The hardest modes include pure oxygen vibrations, due to their light mass.

Combining the results of Tab. 4.11 with the extrapolation of the soft mode for  $\mathbf{E} \parallel \mathbf{c}$ , we can clearly identify the soft mode with the displacement of the Y ions along the  $\mathbf{c}$  axis. This indicates a connection between ferroelectricity and the displacements of the Y ions along the  $\mathbf{c}$  axis.

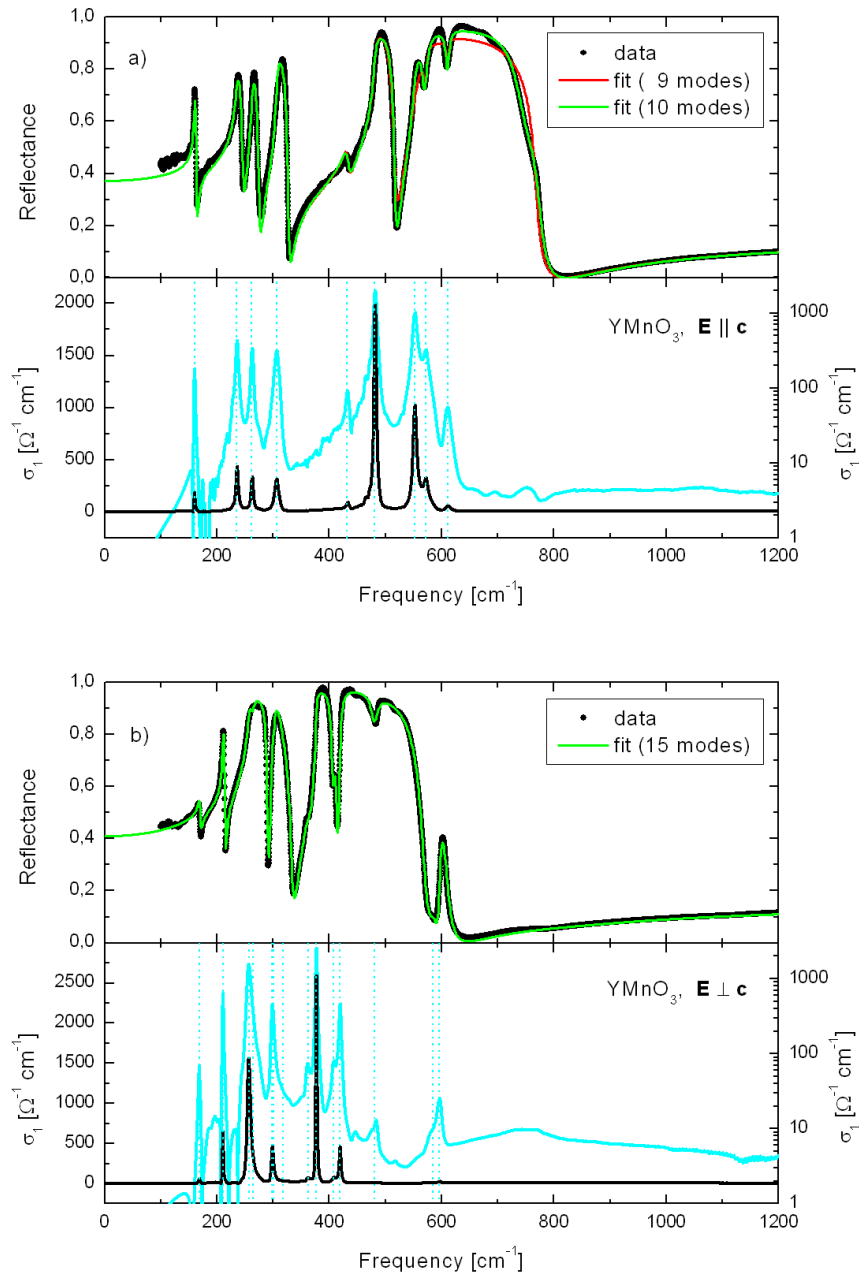


Figure 4.22: Reflectivity  $R(\omega)$ , fit and optical conductivity (cyan color indicates logarithmic scale) determined by the Kramers-Kronig analysis of  $YMnO_3$  at  $T = 20$  K for a)  $\mathbf{E} \parallel \mathbf{c}$  and b)  $\mathbf{E} \perp \mathbf{c}$ . The dotted lines indicate the eigenfrequencies of the phonon modes.

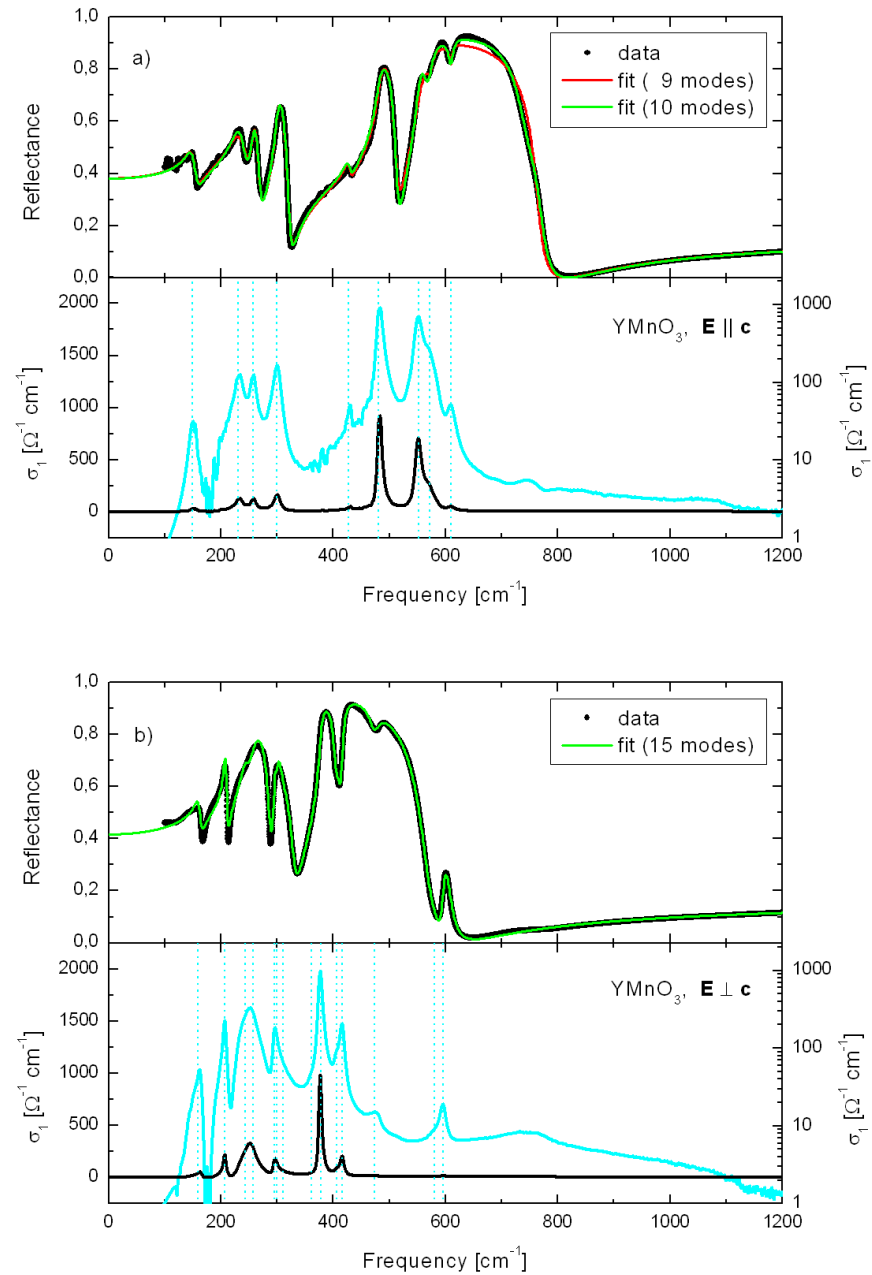
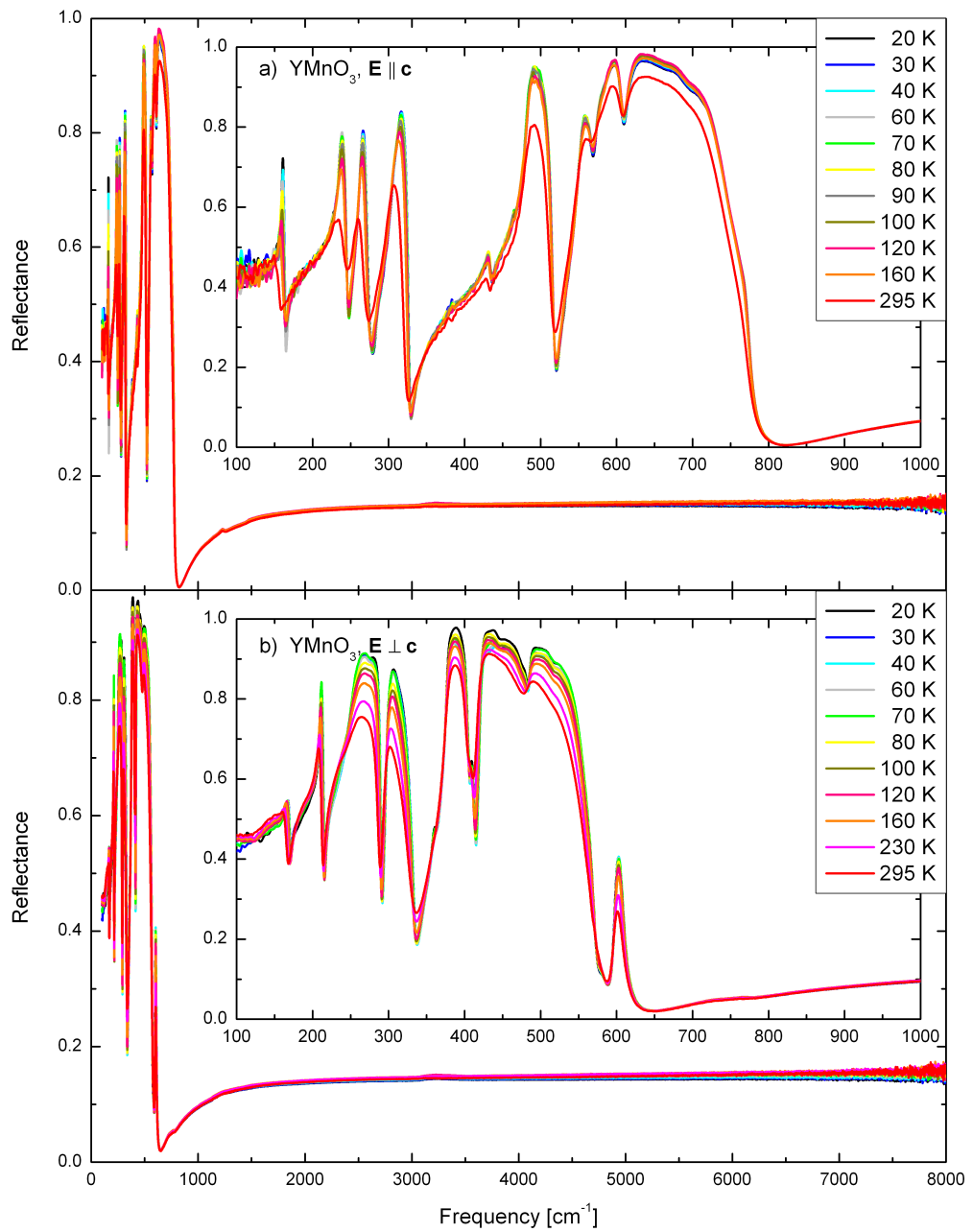


Figure 4.23: Reflectivity  $R(\omega)$ , fit and optical conductivity (cyan color indicates logarithmic scale) determined by the Kramers-Kronig analysis of YMnO<sub>3</sub> at  $T = 295$  K for a)  $\mathbf{E} \parallel \mathbf{c}$  and b)  $\mathbf{E} \perp \mathbf{c}$ . The dotted lines indicate the eigenfrequencies of the phonon modes.

$\mathbf{E} \parallel \mathbf{c}$				$\mathbf{E} \perp \mathbf{c}$			
$\omega_0 [cm^{-1}]$	$\omega_p [cm^{-1}]$	$\gamma [cm^{-1}]$	S	$\omega_0 [cm^{-1}]$	$\omega_p [cm^{-1}]$	$\gamma [cm^{-1}]$	S
T = 20 K							
160	159	2.5	0.982	169	115	3.8	0.463
235	387	6.7	2.710	211	264	2.0	1.570
262	301	5.9	1.320	257	716	5.4	7.810
306	362	5.1	1.400	264	268	7.1	1.040
431	271	13.0	0.394	298	241	2.4	0.651
481	826	5.6	2.950	301	196	4.3	0.424
552	707	10.2	1.640	318	174	32.6	0.300
572	361	9.9	0.399	363	255	16.7	0.493
611	128	7.0	0.044	377	547	2.2	2.110
*751	89	54.9	0.014	408	148	7.2	0.131
				419	289	4.1	0.476
				481	77	14.2	0.026
				584	78	21.8	0.018
				596	83	6.6	0.020
				*770	319	352.0	0.171
T = 295 K							
149	200	17.9	1.800	160	187	10.6	1.360
231	412	25.1	3.190	207	272	4.5	1.730
258	259	12.3	1.010	243	424	14.5	3.040
300	350	11.6	1.360	257	563	19.9	4.810
428	201	13.0	0.222	296	162	3.7	0.301
481	795	13.7	2.730	300	192	7.7	0.411
552	724	13.8	1.720	311	257	32.6	0.681
571	404	16.9	0.501	361	209	45.2	0.336
610	123	9.6	0.041	378	606	7.0	2.570
*748	87	58.4	0.014	407	193	13.4	0.224
				416	277	7.8	0.443
				474	95	22.7	0.040
				581	65	36.4	0.012
				596	88	10.3	0.022
				*737	425	676.7	0.333

Table 4.12: Fit parameters for the reflectivity of  $\text{YMnO}_3$  at T = 20 K and T = 295 K. Here,  $S = \omega_p^2/\omega_0^2$  represents the oscillator strength. The high-frequency dielectric constant at T = 20 K (295 K) is:  $\epsilon_\infty = 5.2$  (5.2) ( $\mathbf{E} \parallel \mathbf{c}$ ),  $\epsilon_\infty = 5.0$  (5.2) ( $\mathbf{E} \perp \mathbf{c}$ ). The “\*” indicates a multi-phonon mode.

Figure 4.24: Reflectance of  $\text{YMnO}_3$  for a)  $\mathbf{E} \parallel \mathbf{c}$  and b)  $\mathbf{E} \perp \mathbf{c}$ .

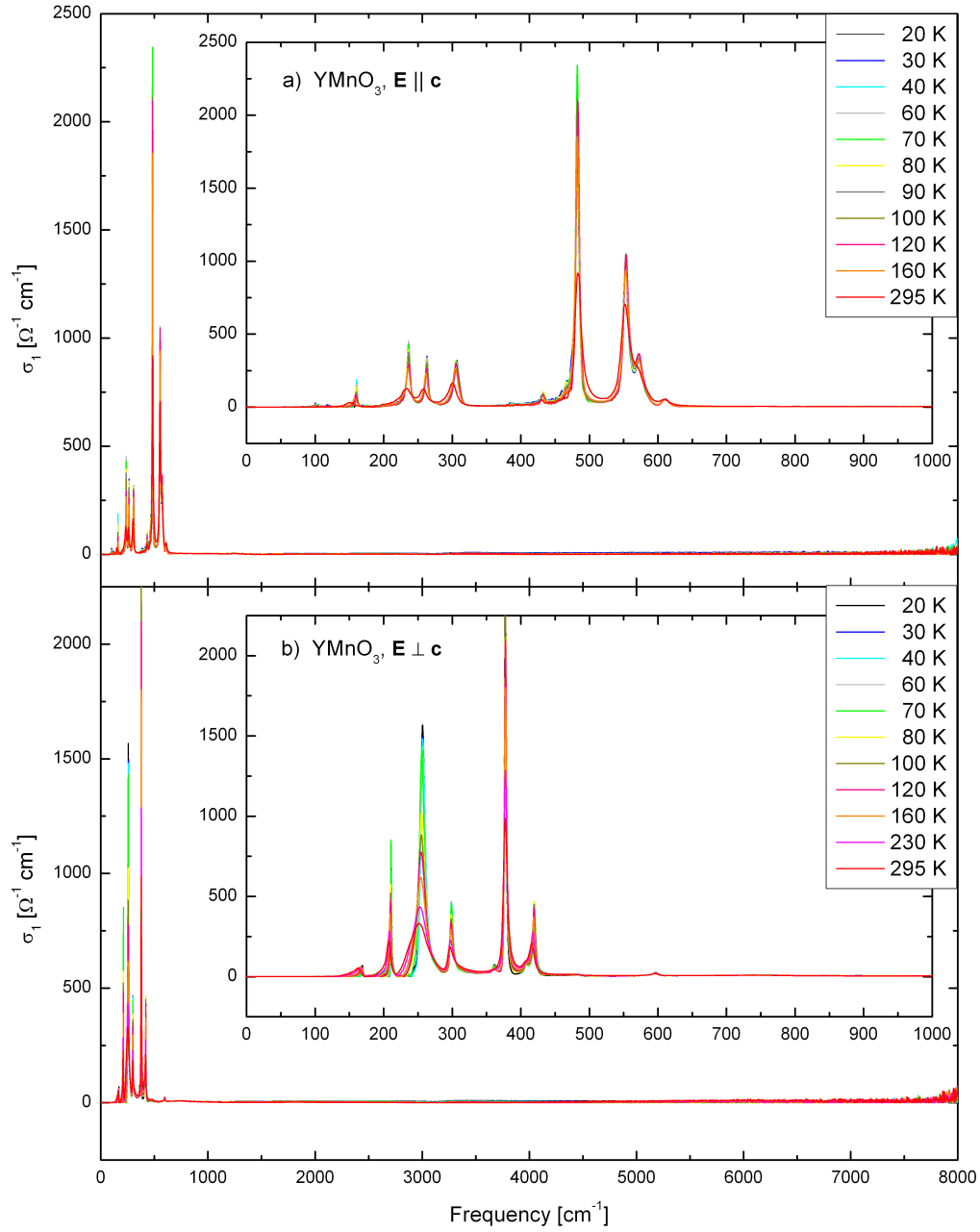


Figure 4.25: Optical conductivity  $\sigma_1(\omega)$  of  $\text{YMnO}_3$  for a)  $\mathbf{E} \parallel \mathbf{c}$  and b)  $\mathbf{E} \perp \mathbf{c}$ .

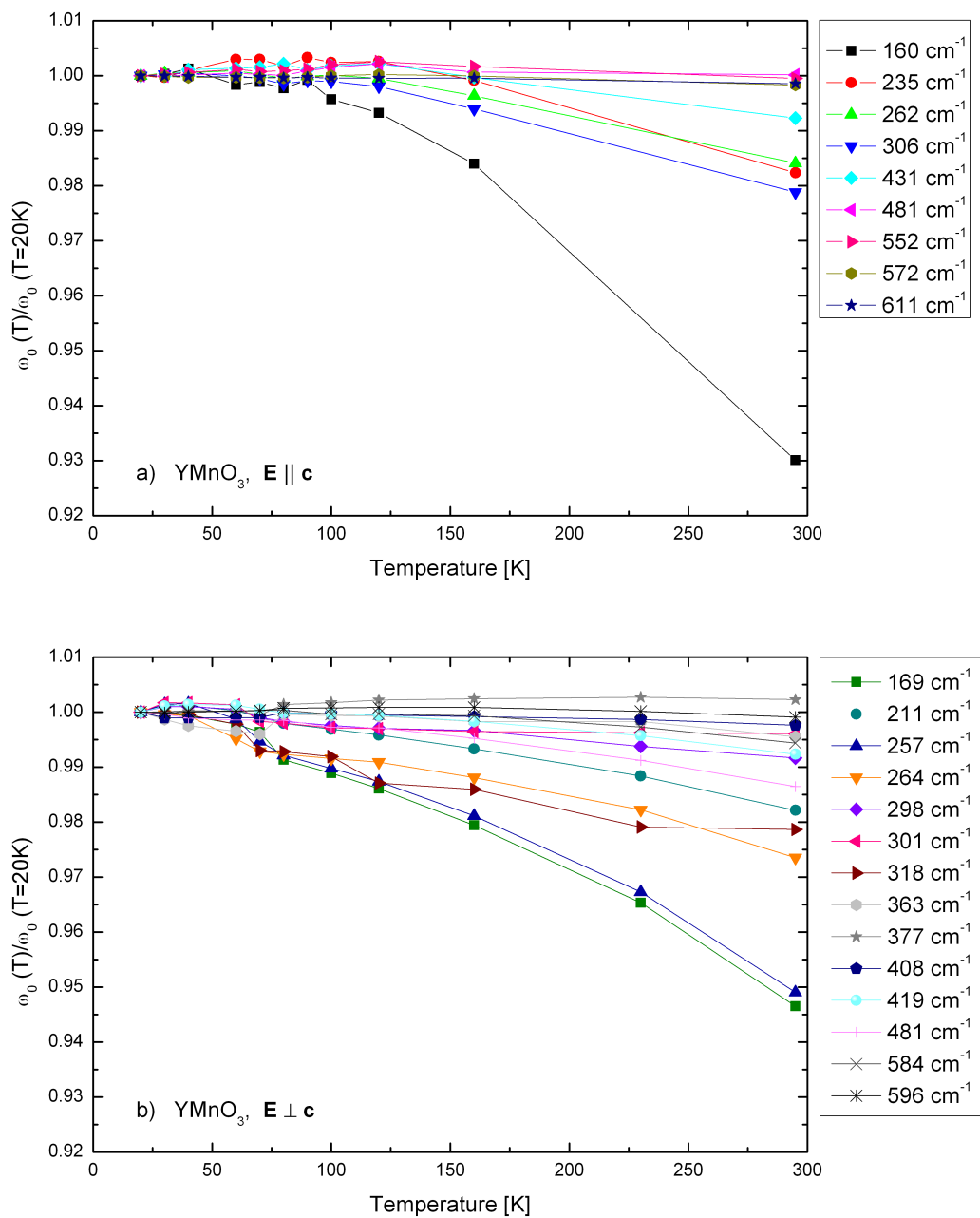


Figure 4.26: Relative eigenfrequency  $\omega_0(T)/\omega_0(T=20 \text{ K})$  of  $\text{YMnO}_3$  for a)  $\mathbf{E} \parallel \mathbf{c}$  and b)  $\mathbf{E} \perp \mathbf{c}$ .

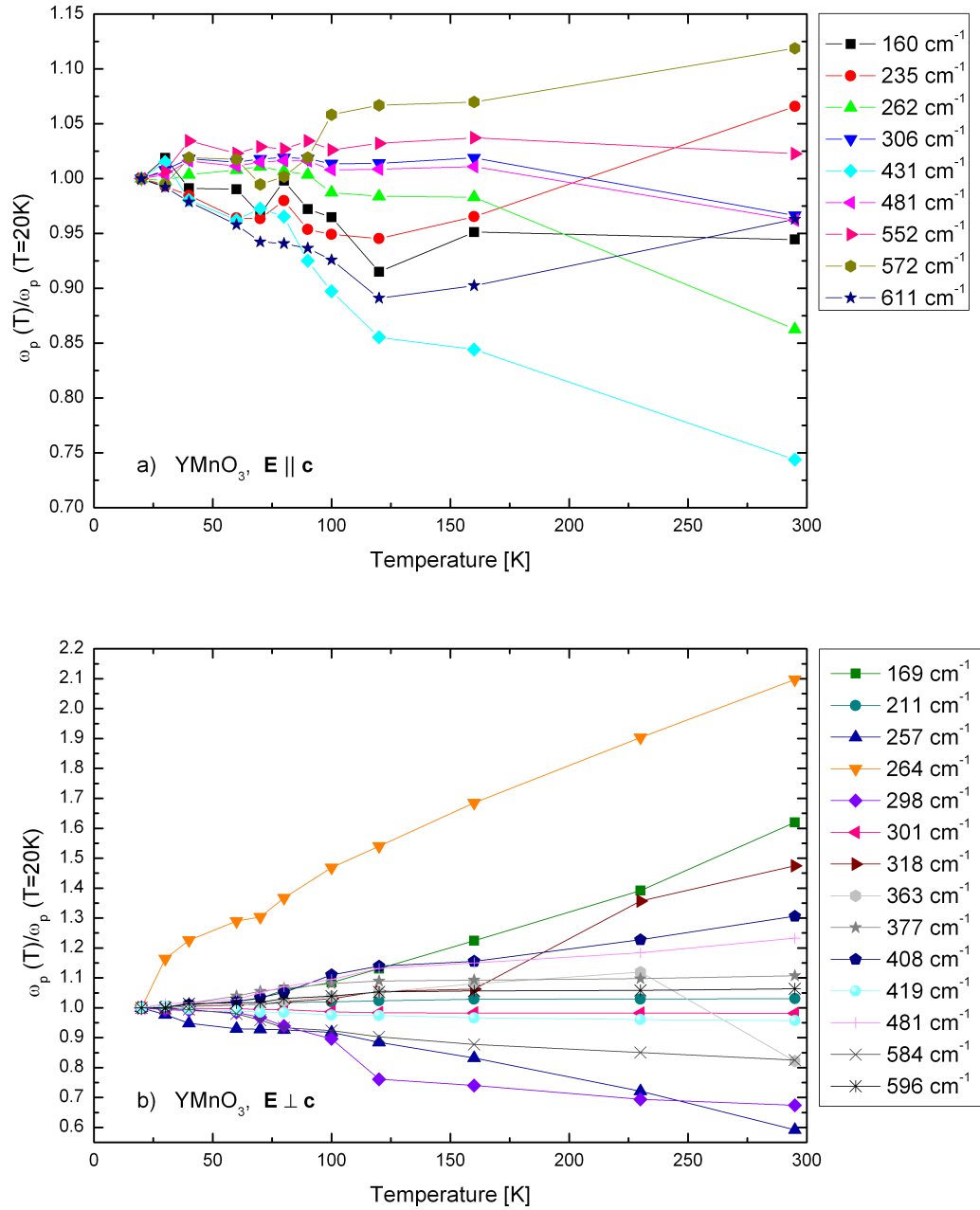


Figure 4.27: Relative plasma frequency  $\omega_p(T)/\omega_p(T=20 \text{ K})$  of  $YMnO_3$  for a)  $\mathbf{E} \parallel \mathbf{c}$  and b)  $\mathbf{E} \perp \mathbf{c}$ .

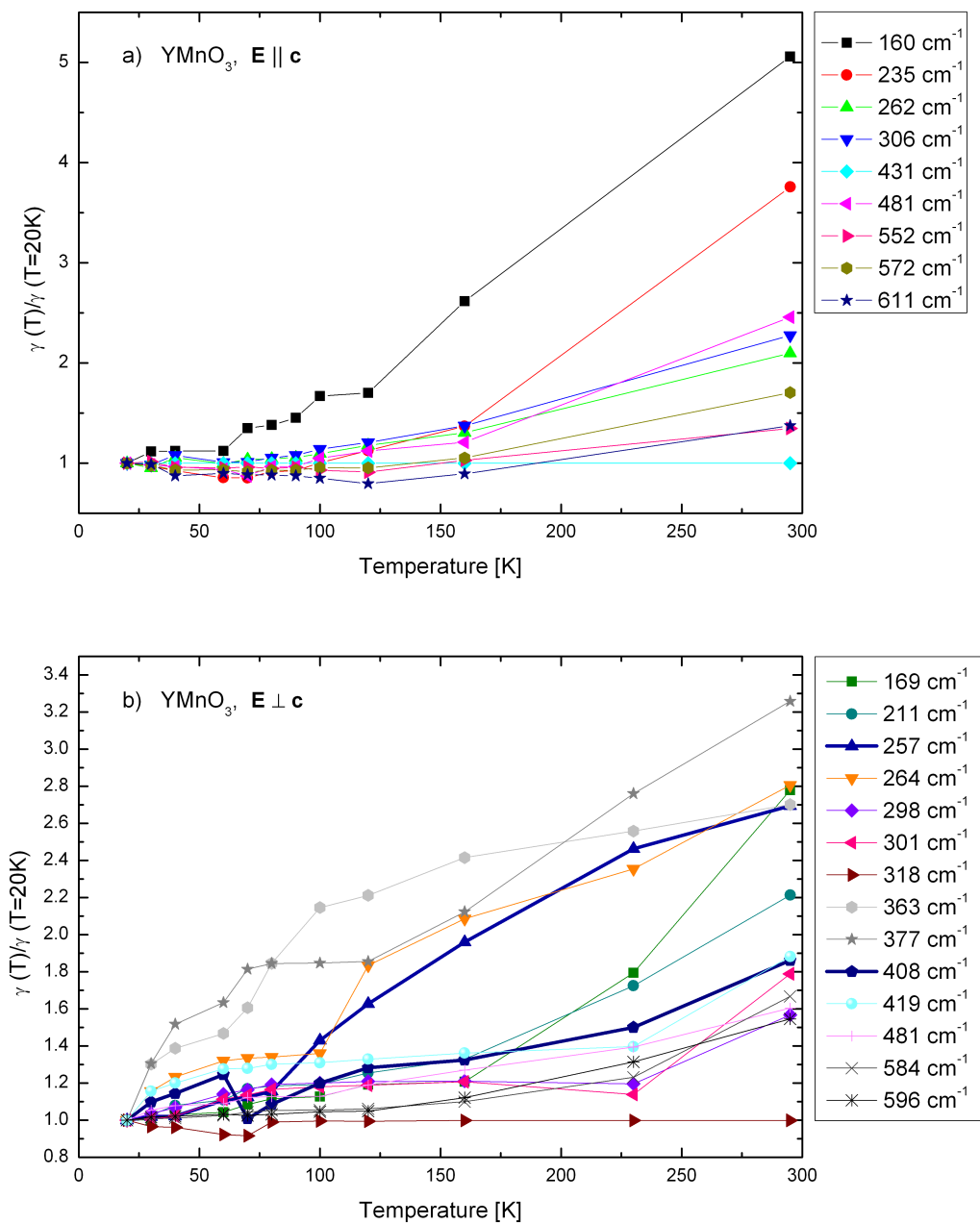


Figure 4.28: Relative damping  $\gamma(T)/\gamma(T=20\text{ K})$  of  $\text{YMnO}_3$  for a)  $\mathbf{E} \parallel \mathbf{c}$  and b)  $\mathbf{E} \perp \mathbf{c}$ .

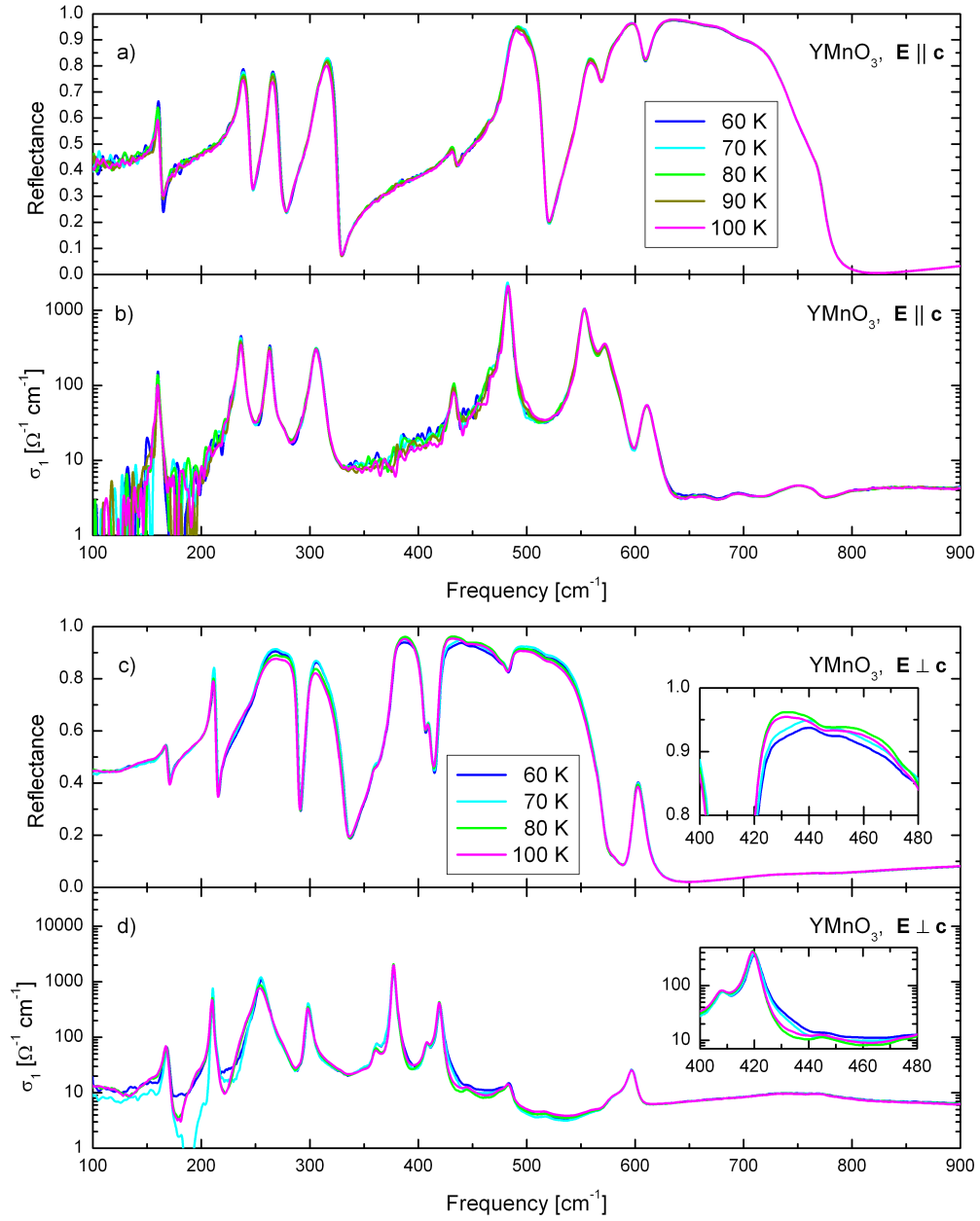


Figure 4.29: Reflectance  $R(\omega)$  and optical conductivity  $\sigma_1(\omega)$  of  $\text{YMnO}_3$  around the Néel temperature  $T_N = 72$  K [168] for a) - b)  $\mathbf{E} \parallel \mathbf{c}$  and c) - d)  $\mathbf{E} \perp \mathbf{c}$ .

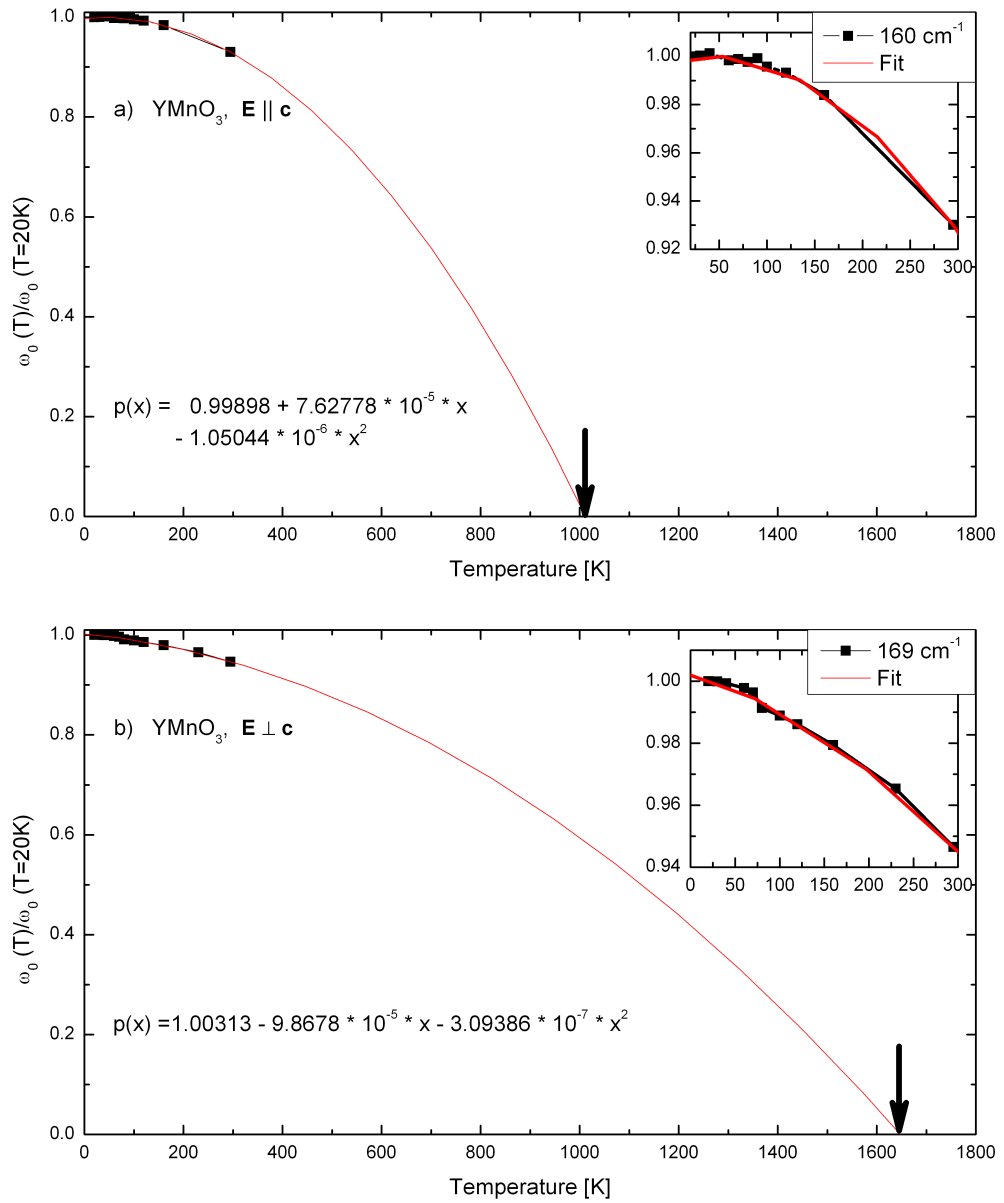


Figure 4.30: Relative eigenfrequency of the lowest phonon mode of  $\text{YMnO}_3$  extrapolated to higher temperatures for a)  $\mathbf{E} \parallel \mathbf{c}$  and b)  $\mathbf{E} \perp \mathbf{c}$ .

Infrared	Iliev [152] Infrared	Iliev [152] Raman	Calc. Iliev [152] TO LO
$A_1$ modes			
149	-	148	147 147
-	-	190	204 216
231	-	-	- -
258	265	257	222 269
300	-	297	299 301
-	398	-	388 398
428	428	433	423 467
481	-	459	492 496
552	-	-	- -
571	-	-	- -
610	612	-	588 601
-	-	681	662 662
*748	-	-	- -
$E_1$ modes			
-	-	-	117 118
-	-	-	147 149
160	-	-	158 158
207	211	-	212 231
243	238	-	233 245
257	-	-	- -
296	281	-	250 337
300	308	-	353 367
311	-	-	- -
361	-	-	- -
377	-	376	390 403
407	-	408	410 415
416	-	-	- -
-	457	-	459 477
474	491	-	492 527
-	-	-	559 559
581	-	-	- -
596	-	596	586 589
-	-	632	635 635
*745	-	-	- -

Table 4.13: Comparison of the experimental values of the infrared  $A_1$  and  $E_1$  mode frequencies in units of  $[cm^{-1}]$  in hexagonal  $YMnO_3$  at  $T = 295$  K with the results of Iliev *et al.* [152] at  $T = 300$  K.

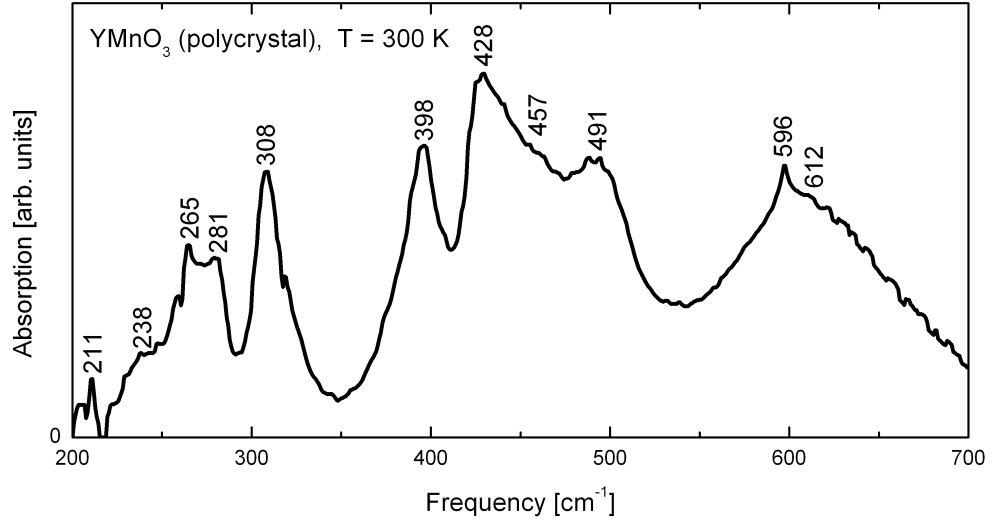


Figure 4.31: Infrared absorption spectrum of  $\text{YMnO}_3$  at  $T = 295 \text{ K}$  reported by Iliev *et al.* [152] between 200 and  $700 \text{ cm}^{-1}$ .

### 4.2.3 Phonon Analysis of $\text{YMn}_{0.7}\text{Ga}_{0.3}\text{O}_3$

The partial replacement of Mn by Ga leads to a shift of the eigenfrequencies of some phonon modes. As shown in Fig. 4.32 and Fig. 4.33 the reflectivity  $R(\omega)$  can be well described by the Drude-Lorentz model. The fit parameters are listed in Tab. 4.14. Applying the Kramers-Kronig transformation to  $R(\omega)$ , we get the optical conductivity. The dotted lines indicate the eigenfrequencies of the phonon modes used in the fits.

We can use the factor-group analysis to determine the number of phonon modes in the isostructural compounds  $\text{YMnO}_3$  and  $\text{YGaO}_3$ . The Ga-doped system represents a mixture of  $\text{YMnO}_3$  and  $\text{YGaO}_3$  and we find additional Mn-Ga vibrations. In contrast to pure Mn-Mn or Ga-Ga vibrations, the Mn-Ga vibrations have a dipole moment and are infrared active. Therefore, we expect an enhanced number of phonon modes than predicted by the factor-group analysis.

In case of  $\mathbf{E} \parallel \mathbf{c}$ , we find 11 phonon modes, see Fig. 4.32 and Fig. 4.33, but we require a further mode at  $707 \text{ cm}^{-1}$  to describe the spectra properly. (Fig. 4.32 includes a fit with 11 (red) and 12 (green) modes for  $\mathbf{E} \parallel \mathbf{c}$ .) This phonon mode is probably caused by the multi-phonon background which is supported by its large width of  $\gamma=212.3 \text{ cm}^{-1}$ . A very similar mode was necessary in case of  $\text{YMnO}_3$ . For  $\mathbf{E} \parallel \mathbf{c}$ , the Ga substitution in particular affects the distribution of spectral weight between 400 and  $600 \text{ cm}^{-1}$ ; at lower frequencies the data are hardly affected. The changes are much more drastic for  $\mathbf{E} \perp \mathbf{c}$ , see Fig. 4.39 and Fig. 4.40. At the same time, Ga substitution gives rise to an

increase of the peak widths, this effect is particularly pronounced for  $\mathbf{E} \perp \mathbf{c}$ . This can be seen clearly in Fig. 4.39 and Fig. 4.40.

In case of  $\mathbf{E} \perp \mathbf{c}$ , we find only 12 phonon modes and two multi-phonon modes, as shown in Tab. 4.14. Due to its extremely small oscillator strength ( $S = 0.001$ ) we can probably waive the multi-phonon mode at  $245 \text{ cm}^{-1}$ . (In order to find all phonon modes, we will compare the eigenfrequencies of the doped and the undoped system, see below.)

The phonon spectra of  $\text{YMn}_{0.7}\text{Ga}_{0.3}\text{O}_3$  as a function of temperature are shown in Fig. 4.34 for both directions. We find no overall change in the spectra around the Néel temperature  $T_N = 32 \text{ K}$  in both directions. As shown in Fig. 4.36 we find a reduction of the phonon eigenfrequencies with increasing temperature. The lowest peak at  $158 (163) \text{ cm}^{-1}$  for  $\mathbf{E} \parallel \mathbf{c}$  ( $\mathbf{E} \perp \mathbf{c}$ ) shows a strong shift of 5.2 (3.7) %, very similar to the observation in  $\text{YMnO}_3$ , although the effect is somewhat weaker here. Again, the lowest mode for  $\mathbf{E} \perp \mathbf{c}$  shows a strong increase in damping with increasing temperature, very similar to the case of  $\text{YMnO}_3$ . The relative fit parameters for  $\mathbf{E} \perp \mathbf{c}$  shown in Figs. 4.36 b) - 4.38 b) include a set of inaccuracies because several peaks cannot be determined exactly. For example, the phonon mode at  $322 \text{ cm}^{-1}$  is part of the large excitation between  $290 \text{ cm}^{-1} - 370 \text{ cm}^{-1}$  and cannot be located exactly. Additionally, as shown in Fig. 4.41, the peak at  $165 \text{ cm}^{-1}$  has only a very small spectral weight for all temperatures and cannot be determined exactly.

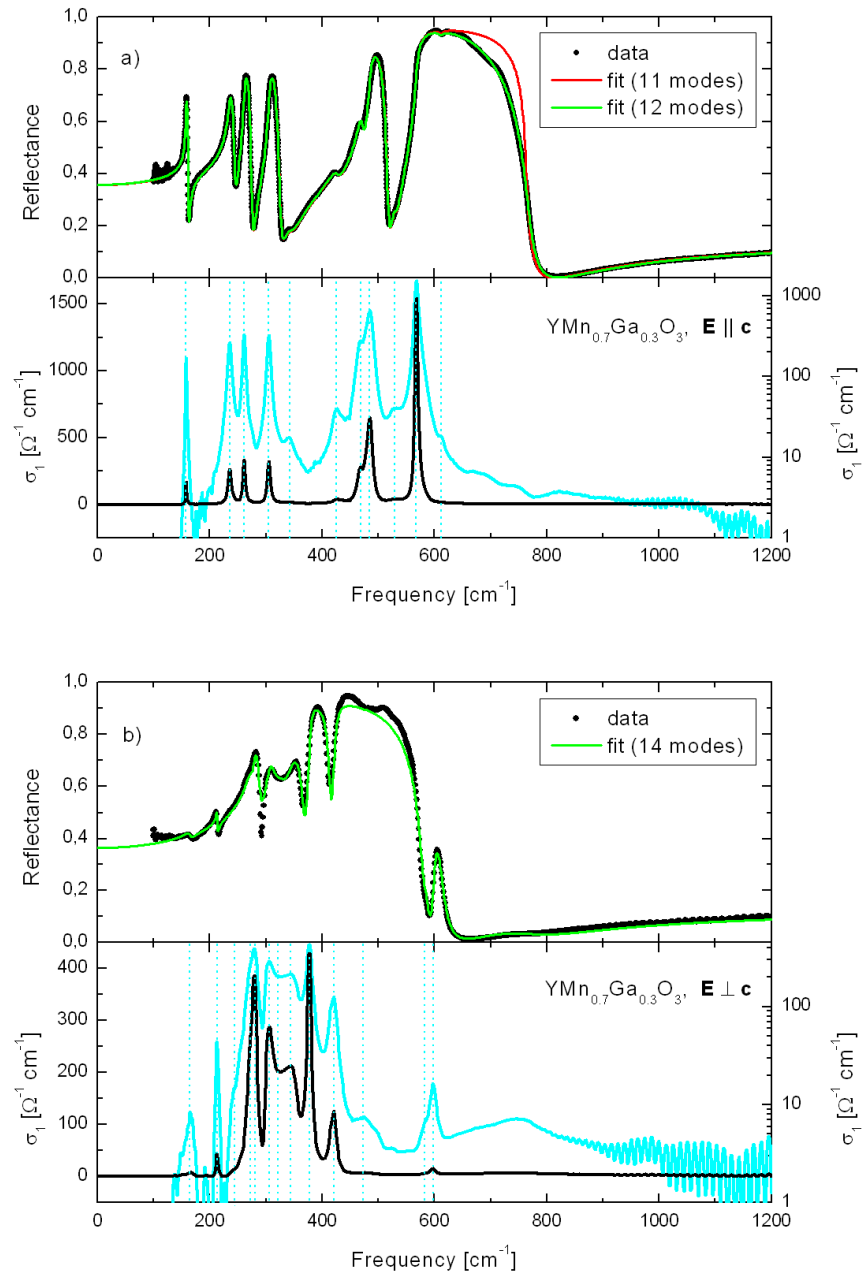


Figure 4.32: Reflectivity  $R(\omega)$ , fit and optical conductivity (cyan color indicates logarithmic scale) of YMn<sub>0.7</sub>Ga<sub>0.3</sub>O<sub>3</sub> at  $T = 20$  K for a)  $\mathbf{E} \parallel \mathbf{c}$  and b)  $\mathbf{E} \perp \mathbf{c}$ . The dotted lines indicate the eigenfrequencies of the phonon modes.

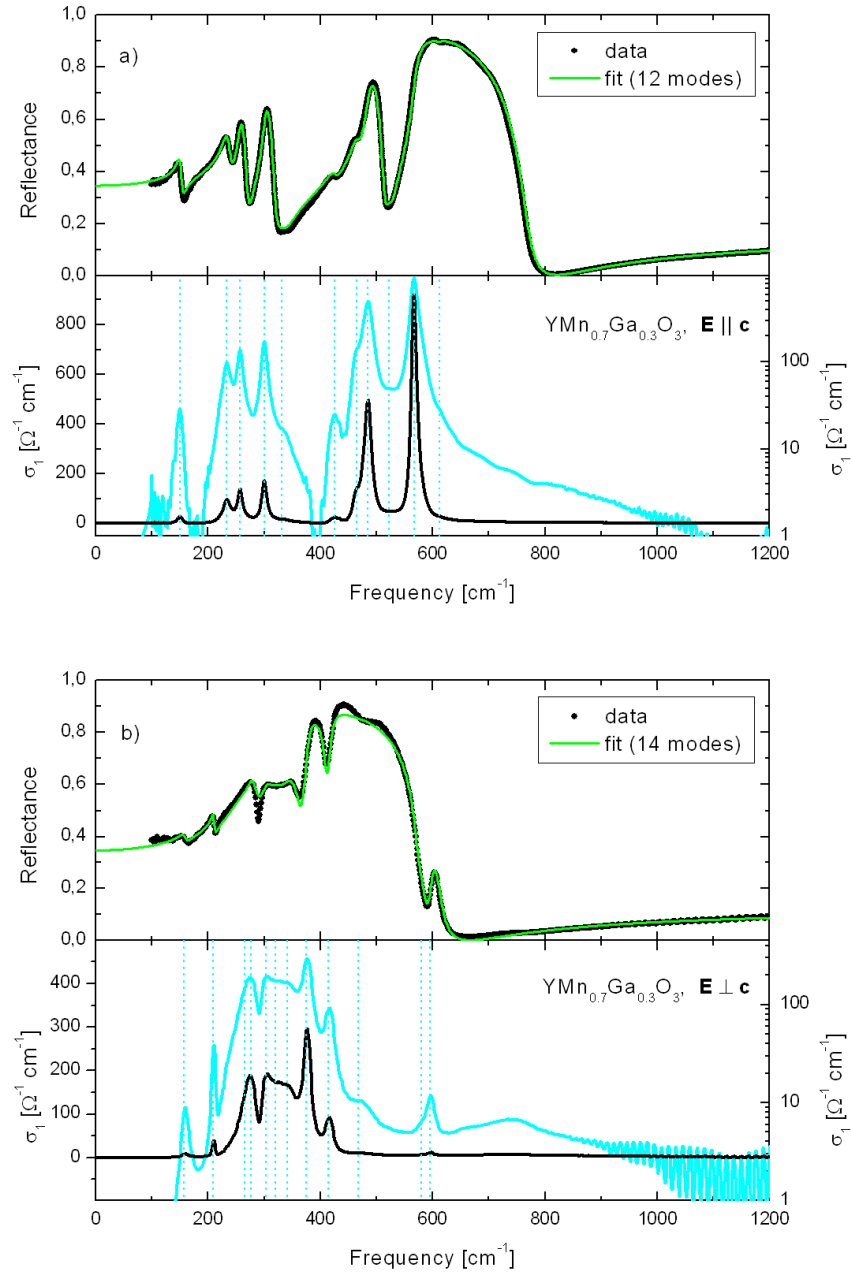


Figure 4.33: Reflectivity  $R(\omega)$ , fit and optical conductivity (cyan color indicates logarithmic scale) of  $\text{YMn}_{0.7}\text{Ga}_{0.3}\text{O}_3$  at  $T = 295$  K for a)  $\mathbf{E} \parallel \mathbf{c}$  and b)  $\mathbf{E} \perp \mathbf{c}$ . The dotted lines indicate the eigenfrequencies of the phonon modes.

$\mathbf{E} \parallel \mathbf{c}$				$\mathbf{E} \perp \mathbf{c}$			
$\omega_0 [cm^{-1}]$	$\omega_p [cm^{-1}]$	$\gamma [cm^{-1}]$	S	$\omega_0 [cm^{-1}]$	$\omega_p [cm^{-1}]$	$\gamma [cm^{-1}]$	S
T = 20 K							
158	146	2.3	0.856	165	64	10.4	0.151
236	342	7.5	2.100	213	78	2.4	0.129
261	316	5.6	1.470	*245	8	300.0	0.001
305	351	6.6	1.320	272	364	15.0	1.790
341	149	33.3	0.190	281	382	8.6	1.860
426	198	20.9	0.217	306	434	15.9	2.010
469	457	13.3	0.951	322	457	35.4	2.020
485	606	8.1	1.560	344	514	30.5	2.230
529	128	12.5	0.058	378	419	6.3	1.230
568	795	7.7	1.960	421	262	9.2	0.389
612	43	10.6	0.005	474	14	5.8	0.001
*707	185	212.3	0.068	583	31	11.7	0.003
				598	87	10.1	0.021
				*746	301	176.4	0.163
T = 295 K							
150	126	8.7	0.711	159	81	12.9	0.259
234	286	15.2	1.500	210	116	6.3	0.307
257	301	12.3	1.370	*241	7	313.1	0.001
301	338	11.5	1.260	265	383	36.2	2.090
331	139	36.4	0.177	277	369	19.5	1.770
425	170	19.2	0.161	303	370	25.3	1.490
465	337	18.4	0.523	320	390	39.4	1.490
485	630	14.7	1.690	342	479	43.6	1.960
523	121	17.5	0.053	375	408	12.5	1.180
568	850	13.2	2.240	415	214	12.6	0.265
612	42	13.8	0.005	468	12	12.6	0.001
*674	257	317.3	0.146	580	28	17.2	0.002
				595	76	16.0	0.016
				*775	103	60.2	0.018

Table 4.14: Fit parameters for the reflectivity of  $\text{YMn}_{0.7}\text{Ga}_{0.3}\text{O}_3$  at T = 20 K and T = 295 K. Here,  $S = \omega_p^2/\omega_0^2$  represents the oscillator strength. The high-frequency dielectric constant at T = 20 K (295 K) is:  $\epsilon_\infty = 5.0$  (5.0) ( $\mathbf{E} \parallel \mathbf{c}$ ),  $\epsilon_\infty = 4.4$  (4.2) ( $\mathbf{E} \perp \mathbf{c}$ ). The “\*” indicates a multi-phonon mode.

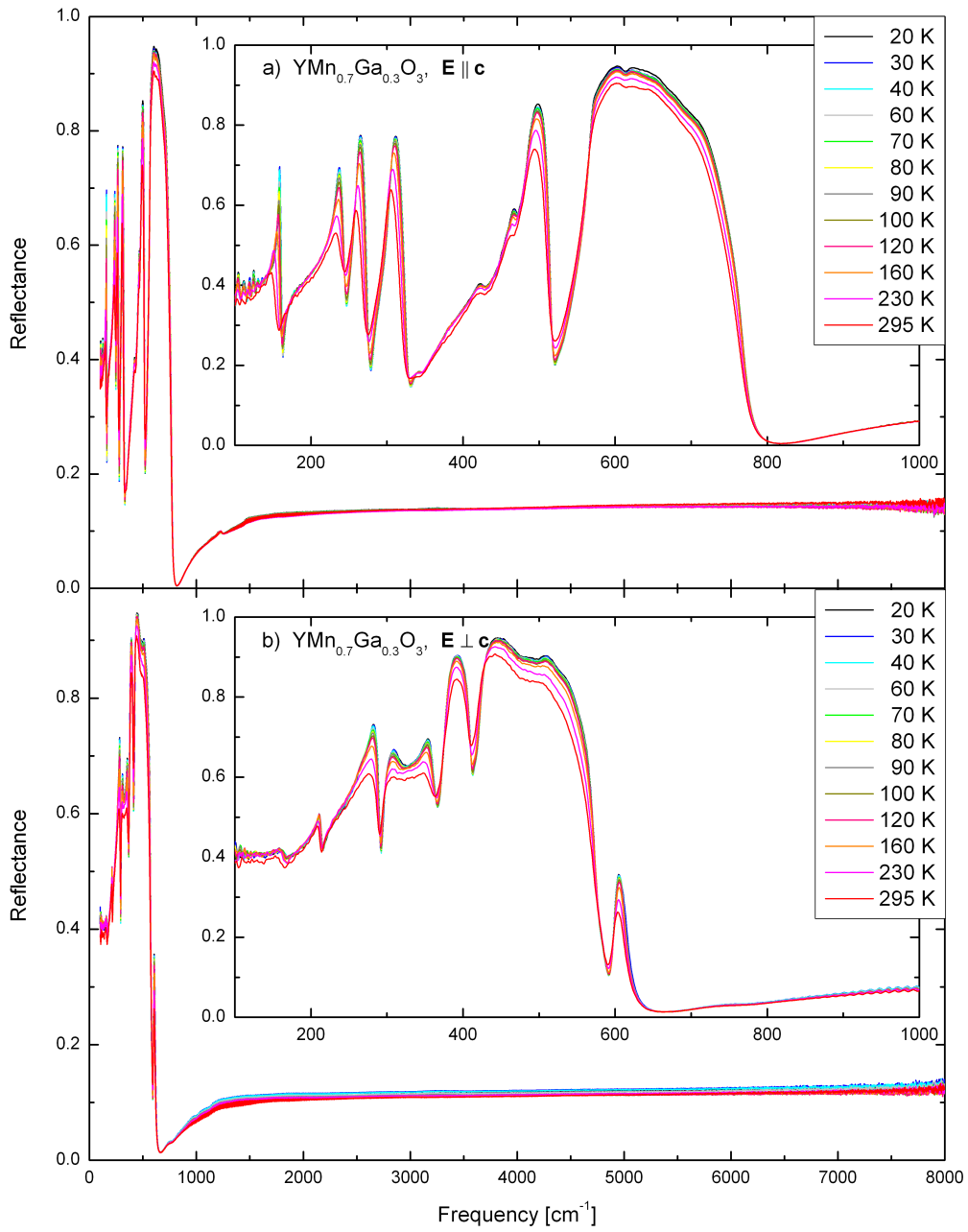


Figure 4.34: Reflectance of  $\text{YMn}_{0.7}\text{Ga}_{0.3}\text{O}_3$  for a)  $\mathbf{E} \parallel \mathbf{c}$  and b)  $\mathbf{E} \perp \mathbf{c}$ .

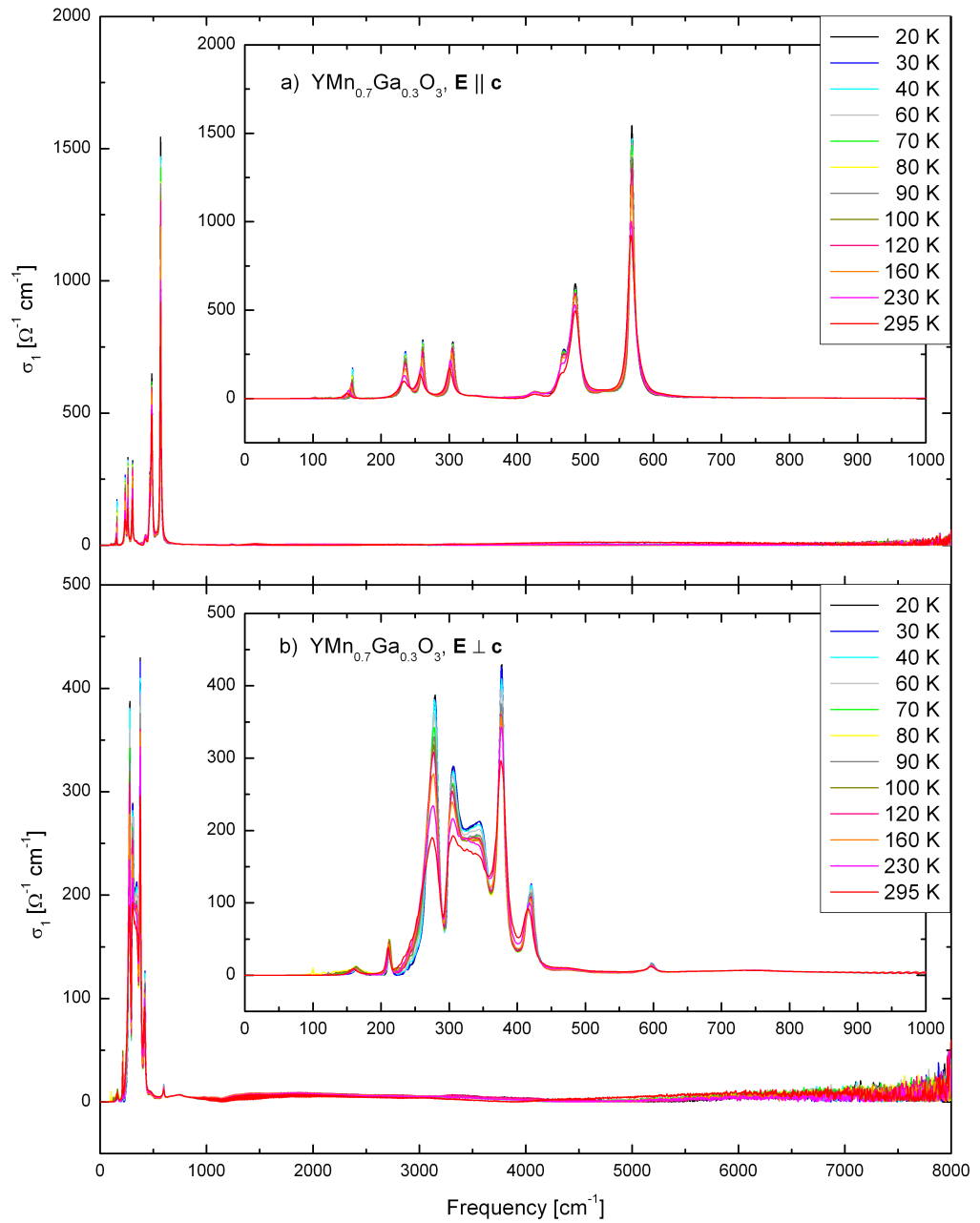


Figure 4.35: Optical conductivity  $\sigma_1(\omega)$  of  $\text{YMn}_{0.7}\text{Ga}_{0.3}\text{O}_3$  for a)  $\mathbf{E} \parallel \mathbf{c}$  and b)  $\mathbf{E} \perp \mathbf{c}$ .

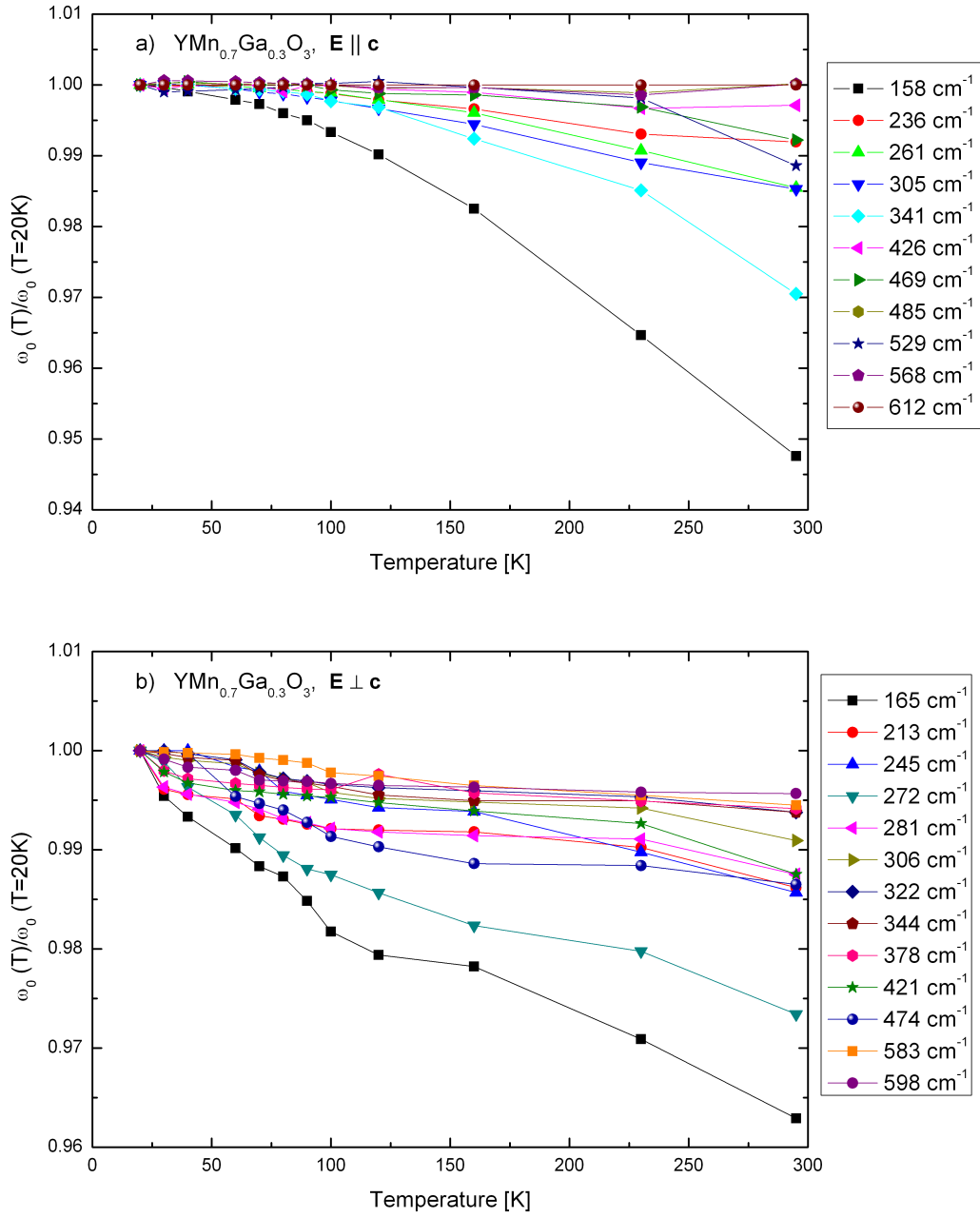


Figure 4.36: Relative eigenfrequency  $\omega_0(T)/\omega_0(T=20\text{ K})$  of  $YMn_{0.7}Ga_{0.3}O_3$  for a)  $\mathbf{E} \parallel \mathbf{c}$  and b)  $\mathbf{E} \perp \mathbf{c}$ .

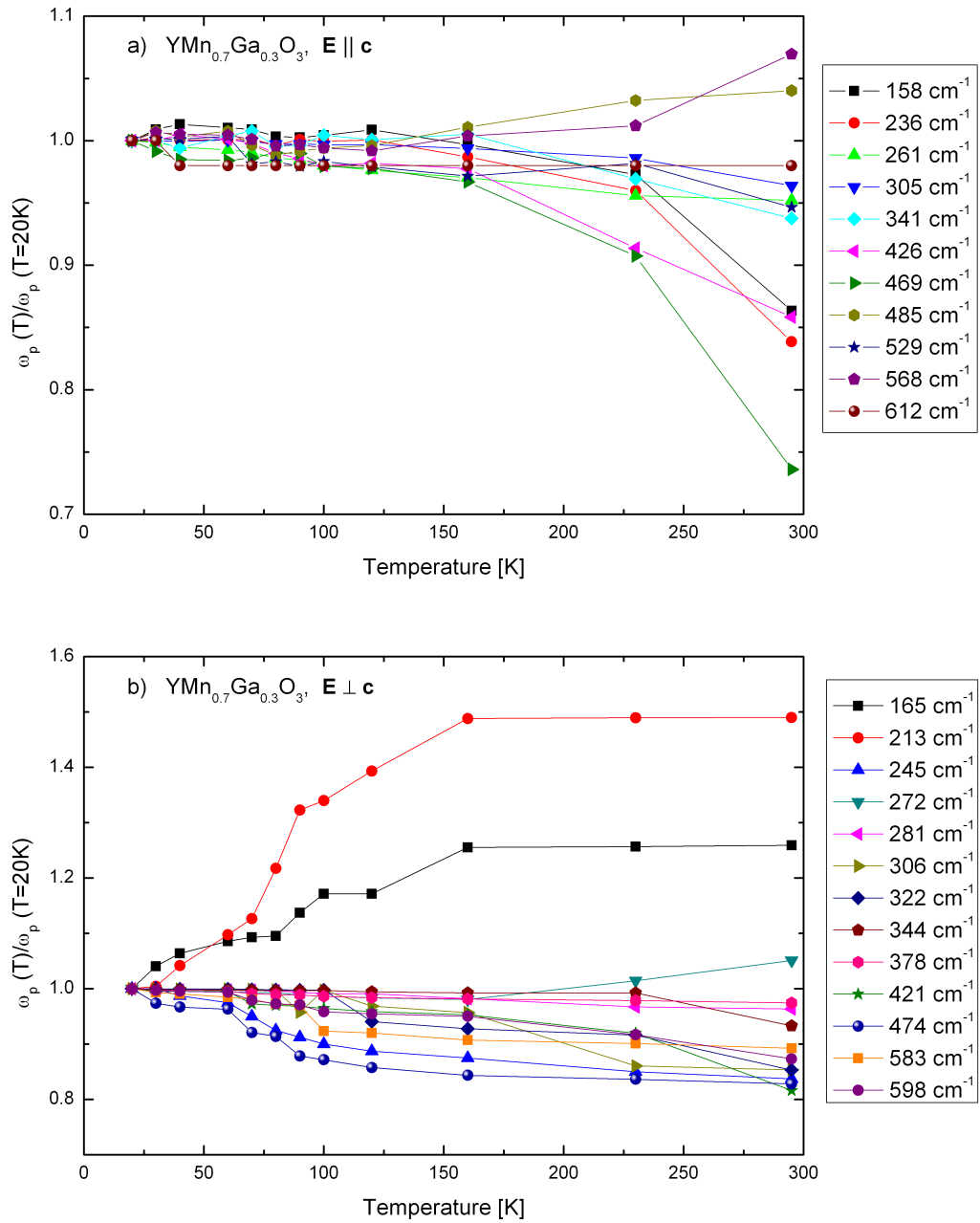


Figure 4.37: Relative plasma frequency  $\omega_p(T)/\omega_p(T=20\text{ K})$  of  $YMn_{0.7}Ga_{0.3}O_3$  for a)  $E \parallel c$  and b)  $E \perp c$ .

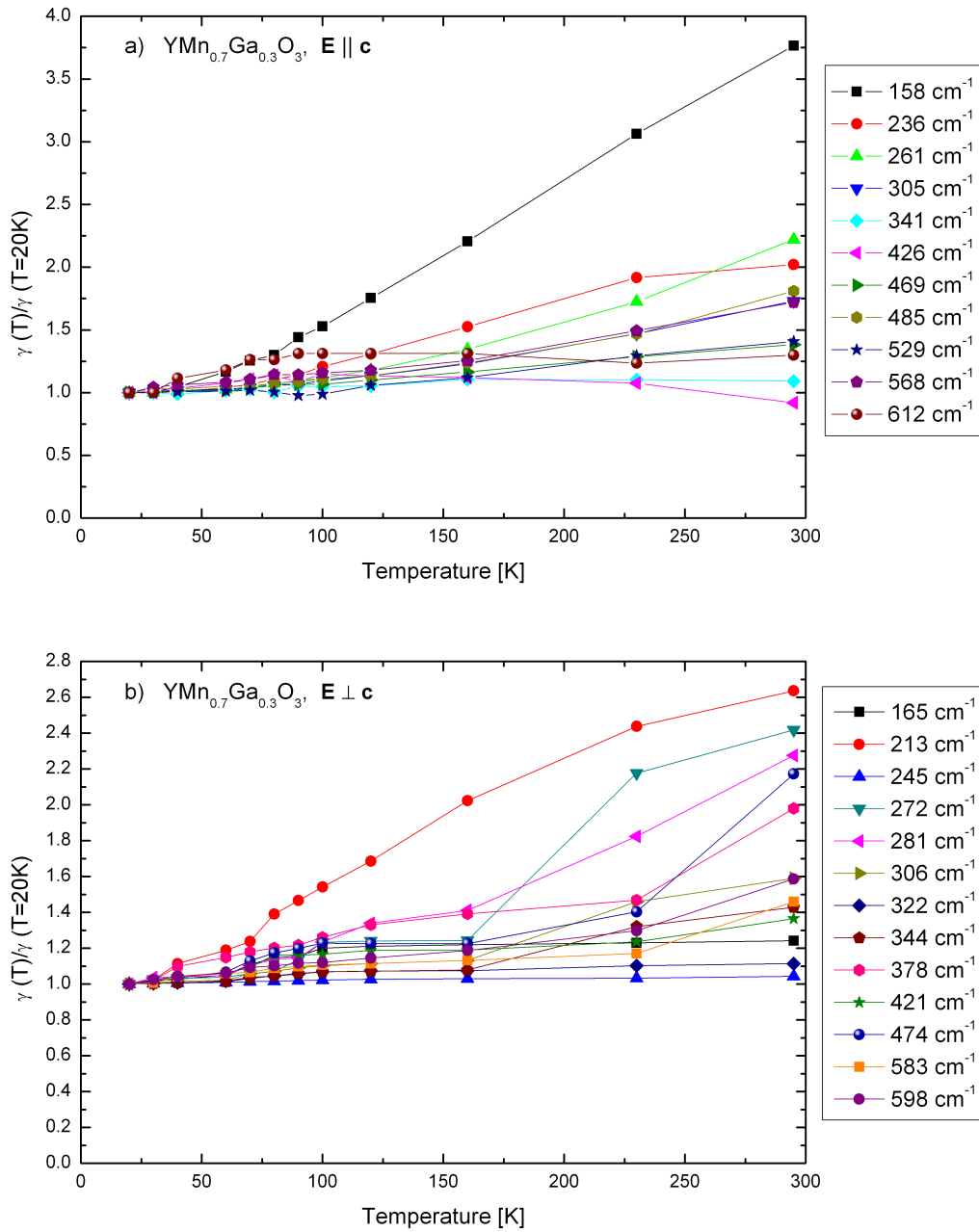


Figure 4.38: Relative damping  $\gamma(T)/\gamma(T=20 K)$  of  $YMn_{0.7}Ga_{0.3}O_3$  for a)  $\mathbf{E} \parallel \mathbf{c}$  and b)  $\mathbf{E} \perp \mathbf{c}$ .

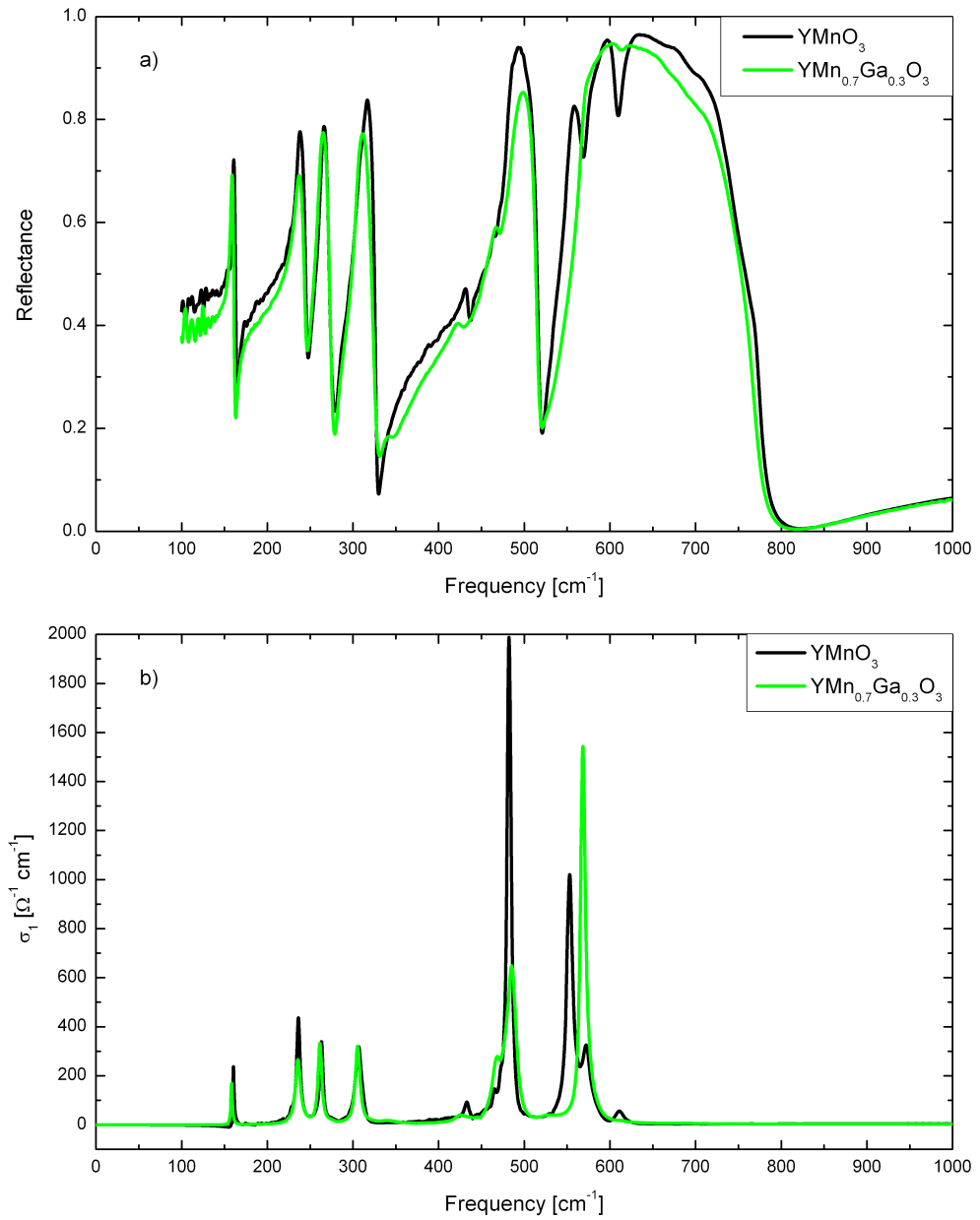


Figure 4.39: Comparison of the a) reflectance  $R(\omega)$  and b) optical conductivity  $\sigma(\omega)$  of  $\text{YMnO}_3$  and  $\text{YMn}_{0.7}\text{Ga}_{0.3}\text{O}_3$  for  $\mathbf{E} \parallel \mathbf{c}$  at  $T = 20$  K.

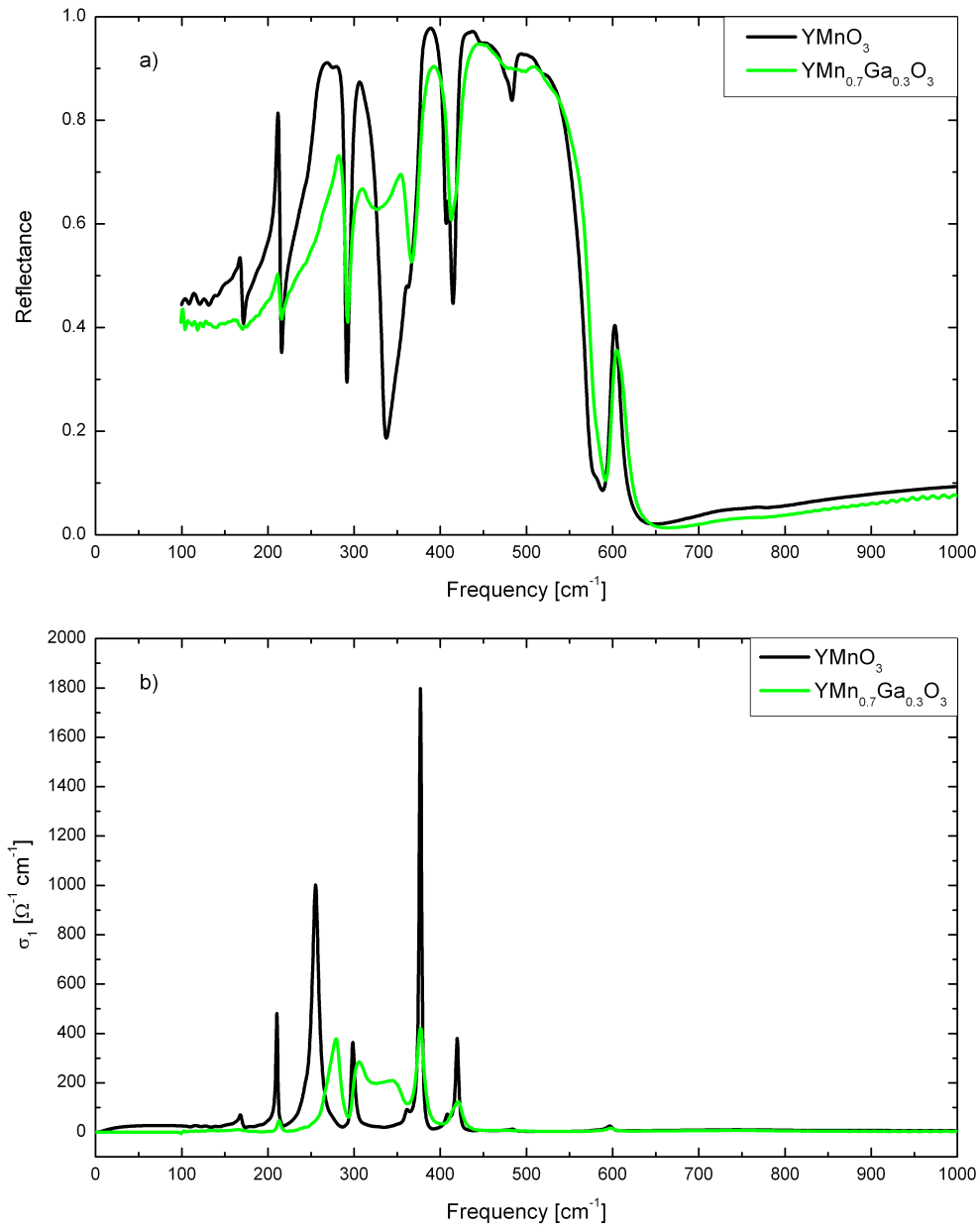


Figure 4.40: Comparison of the a) reflectance  $R(\omega)$  and b) optical conductivity  $\sigma(\omega)$  of  $\text{YMnO}_3$  and  $\text{YMn}_{0.7}\text{Ga}_{0.3}\text{O}_3$  for  $\mathbf{E} \perp \mathbf{c}$  at  $T = 20$  K.

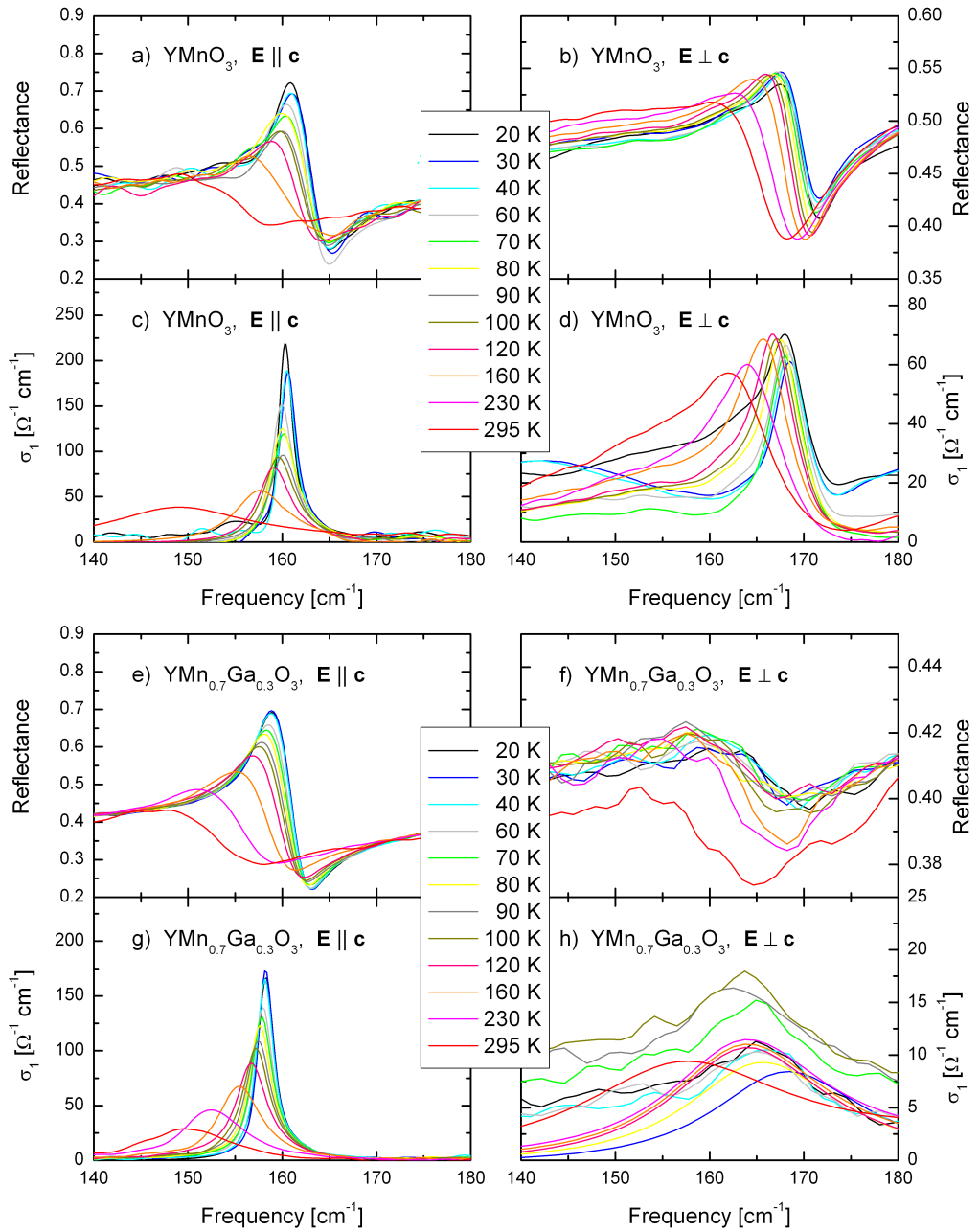


Figure 4.41: Reflectance  $R(\omega)$  and optical conductivity  $\sigma_1(\omega)$  of the lowest phonon mode of a) - d)  $\text{YMnO}_3$  and e) - h)  $\text{YMn}_{0.7}\text{Ga}_{0.3}\text{O}_3$  for  $\mathbf{E} \parallel \mathbf{c}$  and  $\mathbf{E} \perp \mathbf{c}$ .

$\mathbf{E} \parallel \mathbf{c}$		$\mathbf{E} \perp \mathbf{c}$	
phonon modes of $\text{YMnO}_3$	phonon modes of $\text{YMn}_{0.7}\text{Ga}_{0.3}\text{O}_3$	phonon modes of $\text{YMnO}_3$	phonon modes of $\text{YMn}_{0.7}\text{Ga}_{0.3}\text{O}_3$
160	158	169	165
235	236	211	213
262	261	257	*245
306	305	264	272
-	341	298	281
431	426	301	306
-	469	318	322
481	485	363	344
552	529	377	378
572	568	408	-
611	612	419	421
*751	*707	481	474
		584	583
		596	598
		*770	*746

Table 4.15: Comparison of the eigenfrequencies in units of  $[\text{cm}^{-1}]$  of the phonon modes used in the fits of  $\text{YMnO}_3$  and  $\text{YMn}_{0.7}\text{Ga}_{0.3}\text{O}_3$  at  $T = 20$  K. The “\*” indicates a multi-phonon mode.

As shown in Fig. 4.39 and Fig. 4.40, the substitution of 30 % Ga leads to several changes in the phonon spectra. A comparison of the eigenfrequencies of the relevant phonon modes is shown in Tab. 4.15.

In case of  $\mathbf{E} \parallel \mathbf{c}$ , the substitution of 30 % Ga causes only small changes in the phonon spectra, as shown in Fig. 4.39. The spectral weight as well as the eigenfrequencies of the phonon modes below  $400 \text{ cm}^{-1}$  are nearly unchanged. As shown in Tab. 4.15, two new phonon modes at  $341 \text{ cm}^{-1}$  and  $469 \text{ cm}^{-1}$  occur in  $\text{YMn}_{0.7}\text{Ga}_{0.3}\text{O}_3$ . As mentioned above, these modes are connected with Mn-Ga vibrations, which increase the total number of phonon modes, in comparison to the prediction of the factor-group analysis. The phonon mode at  $552 \text{ cm}^{-1}$  is probably shifted to  $529 \text{ cm}^{-1}$ , which could be caused by the larger mass of the Ga ion. All other eigenfrequencies agree within a few wave numbers. Comparing the lowest mode of the doped and the undoped system, we find a stronger shift in the undoped system with increasing temperature. As reported by Adem [169], the Ga substitution changes the Y coordination, i.e. the  $\text{YO}_6$  antiprisms elongate with Ga substitution because the  $\mathbf{c}$  axis elongates due to the filling of the  $d_{z^2}$  antibonding orbital. This suggests that the elongation of the  $\text{YO}_6$  antiprisms causes the greater shift of the soft mode in the undoped system.

In case of  $\mathbf{E} \perp \mathbf{c}$ , we find drastic changes in the phonon spectra between the doped and the undoped system, see Fig. 4.40. The phonon spectrum of the doped system above  $400 \text{ cm}^{-1}$  shows only small differences with respect to the spectrum of  $\text{YMnO}_3$ ,

whereas the eigenfrequencies as well as the spectral weight of the phonon modes below  $400 \text{ cm}^{-1}$  change remarkably. The peaks below  $300 \text{ cm}^{-1}$  lose spectral weight, which is transferred to the excitations between  $330 \text{ cm}^{-1}$  and  $370 \text{ cm}^{-1}$ .

The spectral weight of the lowest mode decreases drastically by a factor of 3 ( $S = 0.463 \rightarrow S = 0.151$ ) with doping, which is probably related to the elongation of the  $\text{YO}_6$  antiprisms. This suggests that the displacements of the Y ion perpendicular to the  $\mathbf{c}$  axis become less pronounced.

As mentioned above, we do not find the expected number of phonon modes in the doped system, which is caused probably by the tiny amplitude of some phonon modes. By comparing the eigenfrequencies of the doped and the undoped system, we assume that the analogon for the phonon mode at  $408 \text{ cm}^{-1}$  ( $\text{YMnO}_3$ ) is probably a part of the shoulder of the feature at  $421 \text{ cm}^{-1}$ . But we can neither estimate the eigenfrequency nor the oscillator strength of this phonon mode. Additionally, the comparison of the doped and the undoped system adumbrate, that the mode at  $245 \text{ cm}^{-1}$  in the doped system is probably a real phonon mode in spite of the large damping value of  $\gamma \approx 300 \text{ cm}^{-1}$ , see Tab. 4.15.

In order to check the shift of the eigenfrequencies of the phonon modes between the doped and the undoped system, we use the Teller-Redlich product rule [187]

$$\Omega = \frac{\prod_i \omega_i^{Mn}}{\prod_i \omega_i^{Ga}} = \left( \frac{m_{Mn}}{m_{Ga}} \right)^{\alpha/2}, \quad (4.2.3)$$

where  $m$  denotes the ionic mass in  $\text{YMnO}_3$  and  $\text{YMn}_{0.7}\text{Ga}_{0.3}\text{O}_3$ , respectively. The expression  $\omega_i$  designates the eigenfrequency of the  $i$ -th mode and  $\alpha$  gives the number of distinct sites that have been substituted. The number of formula units per unit cell is  $Z = 6$ , but we have only 30 % Ga. So, we use  $\alpha = (1/3)*6 = 2$ . Due to the right hand side of (4.2.3) we expect a shift of 2.3 % in the phonon eigenfrequencies. Experimentally, we find a shift in the eigenfrequencies of 4.5 % for  $\mathbf{E} \parallel \mathbf{c}$  (where we omit the modes of the doped system at  $341 \text{ cm}^{-1}$ ,  $469 \text{ cm}^{-1}$ , and  $707 \text{ cm}^{-1}$ ), and 7.1 % for  $\mathbf{E} \perp \mathbf{c}$ . In the last comparison, we omit the peaks at  $257 \text{ cm}^{-1}$ ,  $408 \text{ cm}^{-1}$ , and  $770 \text{ cm}^{-1}$  of the undoped system, because we do not find all phonon modes in the doped system for  $\mathbf{E} \perp \mathbf{c}$ . A better agreement between both sides of (4.2.3) is hindered by disorder, because the substitution of Ga is not complete.

The substitution of 30 % Ga should shift all phonon modes to lower frequencies, which corresponds to vibrations including Ga ions because of the bigger mass of Ga compared with Mn. But, the  $\text{Ga}^{3+}$  substitution decreases the lattice parameter  $\mathbf{a}$ , and increases  $\mathbf{c}$  [169] which leads to harder stretching vibrations (e.g.  $596 \text{ cm}^{-1} \rightarrow 598 \text{ cm}^{-1}$ ) for  $\mathbf{E} \perp \mathbf{c}$ , due to the reduced space around the oxygen ions which are involved in these vibrations.

In conclusion, we used optical spectroscopy to analyze the phonon spectra of the hexagonal ferroelectrics  $\text{YMnO}_3$  and  $\text{YMn}_{0.7}\text{Ga}_{0.3}\text{O}_3$  and achieve a good agreement with the prediction of the factor-group analysis. In addition, we compared our results with the

Raman scattering, infrared absorption and lattice-dynamical calculation results of Iliev *et al.* [152]. In contrast to their results, we find most of all phonon modes predicted by the factor-group analysis. Furthermore, we find a small change in the phonon spectra of  $YMnO_3$  for  $\mathbf{E} \perp \mathbf{c}$  between  $420 \text{ cm}^{-1}$  and  $480 \text{ cm}^{-1}$  around the Néel temperature  $T_N$ , which may be caused by the scattering of O vibrations on magnetic excitations. By comparing the behavior of the lowest phonon mode in the doped and the undoped system, we can confirm the results of Adem *et al.* [169] concerning the change in the coordination of the Y ion. Following Iliev *et al.* [152] we associate the lowest phonon mode with displacements of the Y ions along the  $\mathbf{c}$  axis, which indicate the important role of the Y ions for the occurrence of ferroelectricity in  $YMnO_3$ , whereas the  $Mn^{3+}$  ions have no influence due to the  $d^0$ -ness rule.

### 4.3 Spin-lattice interactions in multiferroic $\text{MnWO}_4$

In this section we describe the investigation of the spin-lattice interaction in the multiferroic, monoclinic compound  $\text{MnWO}_4$ , which plays an important role in the coupling between the antiferromagnetic and the ferroelectric order parameters. The analysis of the lattice dynamics provides a better understanding of this coupling. We present a detailed phonon analysis for several temperatures between 10 K and 295 K including a factor-group analysis. In contrast to the previous section, where we use the conventional Drude-Lorentz model, we apply here the so-called generalized Drude-Lorentz model [188] because the low symmetry of this compound requires a further fit parameter, which describes the orientation of the phonon mode within the  $\mathbf{ac}$  plane. Furthermore we analyze the crystal-field excitations in this compound by using group-theoretical as well as cluster-model calculations.

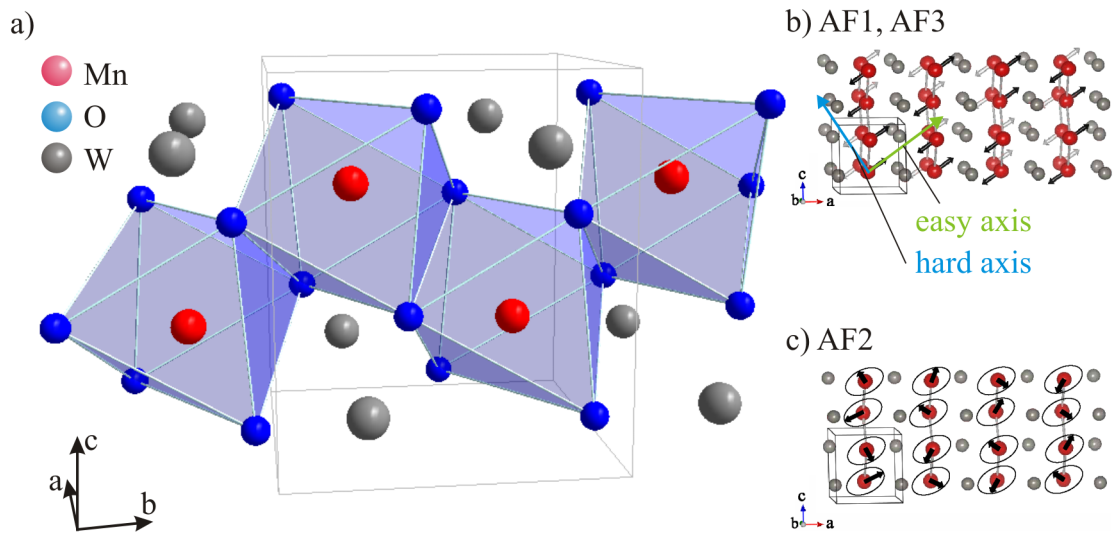


Figure 4.42: a) Crystal structure of  $\text{MnWO}_4$  [189]. b) Collinear magnetic structure in AF1 and AF3 taken from K. Taniguchi *et al.* [190, 191]: The magnetic moments lie in the  $\mathbf{ac}$  plane and are canted to the  $\mathbf{a}$  axis by about  $35^\circ$ . c) Elliptical spiral spin structure in AF2 taken from K. Taniguchi *et al.* [190]: The basal plane of spiral is inclined to the  $\mathbf{ab}$  plane.

$\text{MnWO}_4$  (also known as the mineral huebnerite) is one of the multiferroic materials in which the cycloidal spin structure induces ferroelectricity [190]. This material crystallizes in a wolframite structure [192], which is monoclinic with space group  $P2/c$  ( $C_{2h}^4$ ) ( $a = 4.830(1) \text{ \AA}$ ,  $b = 5.7603(9) \text{ \AA}$ ,  $c = 4.994(1) \text{ \AA}$ ,  $\beta = 91.14(2)^\circ$ ) [193]. Both  $\text{Mn}^{2+}$  and  $\text{W}^{6+}$  ions are coordinated by distorted octahedra of hexagonal close-packed oxygen ions. The  $[\text{MnO}_6]$  and  $[\text{WO}_6]$  octahedra are aligned in zigzag chains along the  $\mathbf{c}$  axis. The structure is composed of alternate stacks of the manganese and tungsten layers along the  $\mathbf{a}$  axis.

In this compound three-dimensional long-range antiferromagnetic order is realized, because the influence of the spins, which are further than the nearest neighbor one, cannot be neglected. The magnetic unit cell, with magnetic space group  $A_c2/a$  [197], consists of 16 crystallographic unit cells at 4.2 K [195].  $\text{MnWO}_4$  with magnetic  $\text{Mn}^{2+}$  ( $S=5/2$ ) is known to be a moderately frustrated antiferromagnetic system. Its Curie-Weiss constant  $\theta$  is  $\sim -75$  K while magnetic order appears only below  $T_{N_3} \sim 13.5$  K. Thus the frustration parameter  $f(= -\theta/T_{N_3})$  is  $\sim 5.6$  [190, 198].

$\text{MnWO}_4$  undergoes in contrast to other wolframites  $\text{MWO}_4$  ( $M = \text{Fe}, \text{Co}, \text{Ni}$ ), which show only one magnetic transition to a commensurate magnetic state with a propagation vector  $\mathbf{k} = (1/2, 0, 0)$ , several magnetic phase transitions at  $\sim 13.5$  K ( $T_{N_3}$ ),  $\sim 12.7$  K ( $T_{N_2}$ ), and  $\sim 7.5$  K ( $T_{N_1}$ ), related to three long-wavelength magnetic ordering states, AF3, AF2, and AF1 [195]. According to neutron diffraction results [195] the AF1 ( $T < T_{N_1}$ ) is a commensurate, collinear, antiferromagnetic phase with propagation vector  $\mathbf{k} = (\pm 1/4, 1/2, 1/2)$ . For  $T_{N_1} < T < T_{N_2}$ , Lautenschläger *et al.* [195] associate AF2 with an incommensurate, elliptical spiral phase with propagation vector  $\mathbf{k} = (-0.214, 1/2, 0.457)$ , whereas AF3 ( $T_{N_2} < T < T_{N_3}$ ) is an incommensurate-collinear antiferromagnetic phase [195], with the same propagation vector as AF2. Within AF1 and AF3, the magnetic moments are aligned collinearly in the  $\mathbf{ac}$  plane, forming an angle of about  $35^\circ$  with the  $\mathbf{a}$  axis, whereas in AF2, an additional component parallel to the  $\mathbf{b}$  axis exists [195]. The AF2 phase shows an elliptically modulated noncollinear spiral spin structure, see Fig. 4.43 a) [199] and Fig. 4.42 c). Here the basal plane of the elliptical spiral contains the easy axis (see Fig. 4.42 b)) of magnetization and the  $\mathbf{b}$  axis. The magnetic structure in the AF3 phase has a collinear sinusoidal structure (see Fig. 4.42 b) and Fig. 4.43 b) [199]), in which the magnetic moments lying along the easy axis. The AF1 phase has a magnetic structure which is characterized by an up-up-down-down ( $\uparrow\uparrow\downarrow\downarrow$ ) spin configuration along both the  $\mathbf{a}$  and the  $\mathbf{c}$  axes.

The phase transition from AF1 to AF2 is first order [199] which is suggested by the discontinuous change in the electric polarization and the shape of the anomalies in the dielectric constant and the specific heat at  $T_{N_1}$ . This can be explained by the discontinuous change in the propagation vector of the magnetic structures [195]. The propagation vector of the AF2 and AF3 is the same, because the magnetic structures differ only by the component of the magnetic moments in the direction of the  $\mathbf{b}$  axis. Therefore the  $T_{N_2}$  transition is expected to be of second order.

The helical magnetic order and a strong spin-lattice coupling [200] lead to the loss of inversion symmetry which explains qualitatively the appearance of ferroelectricity in the AF2 phase. Heyer *et al.* [201] report of a finite value of the ferroelectric polarization also in the low-temperature AF1 commensurate phase. A possible explanation for this observation is given by Arkenbout *et al.* [199]: Below  $T_{N_1}$  a small portion of the ferroelectric AF2 phase still remains and preserves the polarization direction. The coupling between antiferromagnetic and ferroelectric order parameters observed in  $\text{MnWO}_4$  must be mediated by strong spin-lattice interactions. Polarity alone does

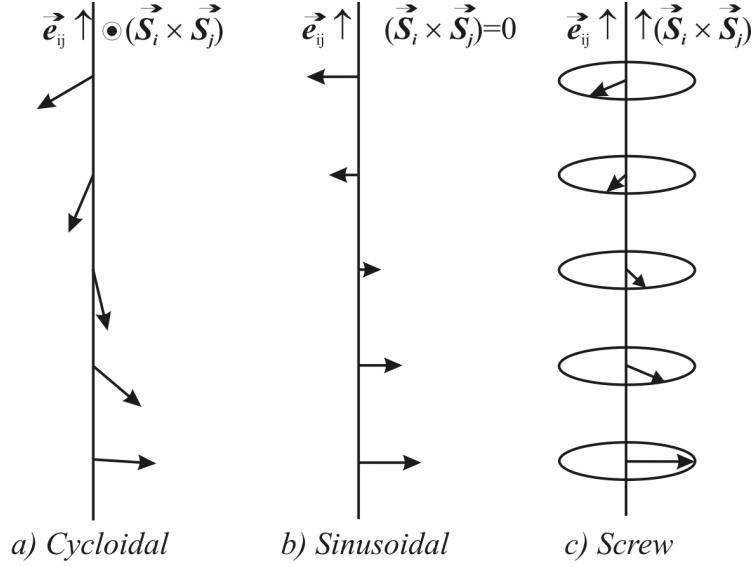


Figure 4.43: Schematic illustration of types of magnetic structure taken from [199] with a long wavelength.  $\vec{e}_{ij}$  represents the unit vector connecting neighboring sites  $i$  and  $j$ , and  $\vec{S}_i$  ( $\vec{S}_j$ ) denotes the magnetic moment at site  $i$  ( $j$ ).

not guarantee ferroelectricity. The loss of inversion symmetry within the AF2 phase is caused by the noncollinear spiral magnetic structure with a cycloidal component itself. Using symmetry considerations [199] we can express the relation between electric polarization  $P$  and magnetization  $M$  in systems with spiral magnetic structures by

$$\vec{P} \propto \gamma \vec{e}_{ij} \times (\vec{S}_i \times \vec{S}_j), \quad (4.3.1)$$

where  $\gamma$  represents a constant proportional to the spin-orbit coupling and to the superexchange interactions and  $\vec{S}$  is the magnetic moment. Furthermore,  $\vec{e}_{ij}$  indicates the unit vector connecting neighboring sites  $i$  and  $j$ . The vector is along the propagation vector of the spiral structure, and  $(\vec{S}_i \times \vec{S}_j)$  is parallel to the spin-rotation axis. Expression (4.3.1) indicates that a finite electric polarization can appear when the magnetic moments at sites  $i$  and  $j$  are coupled noncollinearly in a spiral manner, and the spin rotation axis is not parallel to the propagation vector. The direction of electric polarization is perpendicular to the spin rotation axis and to the propagation vector of the spiral (see Fig. 4.43). By a changing the chirality of the spiral we can reverse the direction of electric polarization. The net polarization is neither induced by the collinear sinusoidal structure  $[(\vec{S}_i \times \vec{S}_j) = 0; \text{Fig. 4.43 } b]$  nor by the screw spiral structure  $[\vec{e}_{ij} \parallel (\vec{S}_i \times \vec{S}_j); \text{Fig. 4.43 } c]$ . Following Katsura *et al.* [202] the ferroelectricity in spiral spin systems is caused by the Aharonov-Casher [203] effect or an inversed effect of Dzyloshinskii-Moriya interaction [204–206], which induces spin current (or spin chirality) between noncollinear spins.

atom	Wyckhoff notation	Site symmetry	Irreducible representations
Mn	2(f)	$C_2$	$A_g + A_u + 2 B_g + 2 B_u$
W	2(e)	$C_2$	$A_g + A_u + 2 B_g + 2 B_u$
O(1)	4(g)	$C_1$	$3 A_g + 3 A_u + 3 B_g + 3 B_u$
O(2)	4(g)	$C_1$	$3 A_g + 3 A_u + 3 B_g + 3 B_u$

Table 4.16: Atomic site symmetries [189] and irreducible representations for the atoms in monoclinic  $\text{MnWO}_4$  with space group  $P2/c$ .

By applying a magnetic field the ferroelectric phase expands or shrinks, see Fig. 4.44, where the shift of phase boundaries depends on the difference in the net magnetization between the ferroelectric phase and neighboring paraelectric phases [199]. With increasing difference, the phase boundary responds stronger to an applied magnetic field. The comparison of the electric and magnetic phase diagrams clearly demonstrates the strong interplay of the evolution of a cycloidal spiral phase and ferroelectric order in  $\text{MnWO}_4$ .

### 4.3.1 Phonon Analysis

In order to investigate the spin-lattice interaction, which plays an important role in the coupling between antiferromagnetic and ferroelectric order parameters, we perform reflectivity measurements at  $T = 10, 13, 20, 50, 100, 150, 200, 250,$  and  $295$  K in the spectral range of  $100\text{-}8000\text{ cm}^{-1}$  at quasinormal incidence. The spectra were measured for different polarization angles on polished (010) and (100) surfaces of  $\text{MnWO}_4$ . The reference measurements were done using Au evaporation. The variation of the polarization angle was realized by rotating the polarizer. The temperature of the sample was measured with a second thermometer glued on the sample with no thermal contact to the sample holder (cold finger). The crystal was grown by P. Becker and L. Bohatý.<sup>16</sup>

The determination of the phonon modes starts with the factor-group analysis [184], which begins with the determination of the irreducible representations of the symmetry-equivalent positions. These positions are indicated by the Wyckoff symbols in the unit cell and the number of formula units per unit cell is  $Z = 2$  [189]. The site symmetries as well as the irreducible representations of each atomic site are shown in Tab. 4.16 for  $T = 295$  K. In the phonon analysis, we assume no structural phase transition between 10 K and 295 K. The magnetic phase transitions at  $T_{N_1}$ ,  $T_{N_2}$ , and  $T_{N_3}$  are not connected with structural phase transitions [195].

<sup>16</sup>Institute of Crystallography, University of Cologne, Zùlpicher Str. 49b, 50674 Cologne, Germany

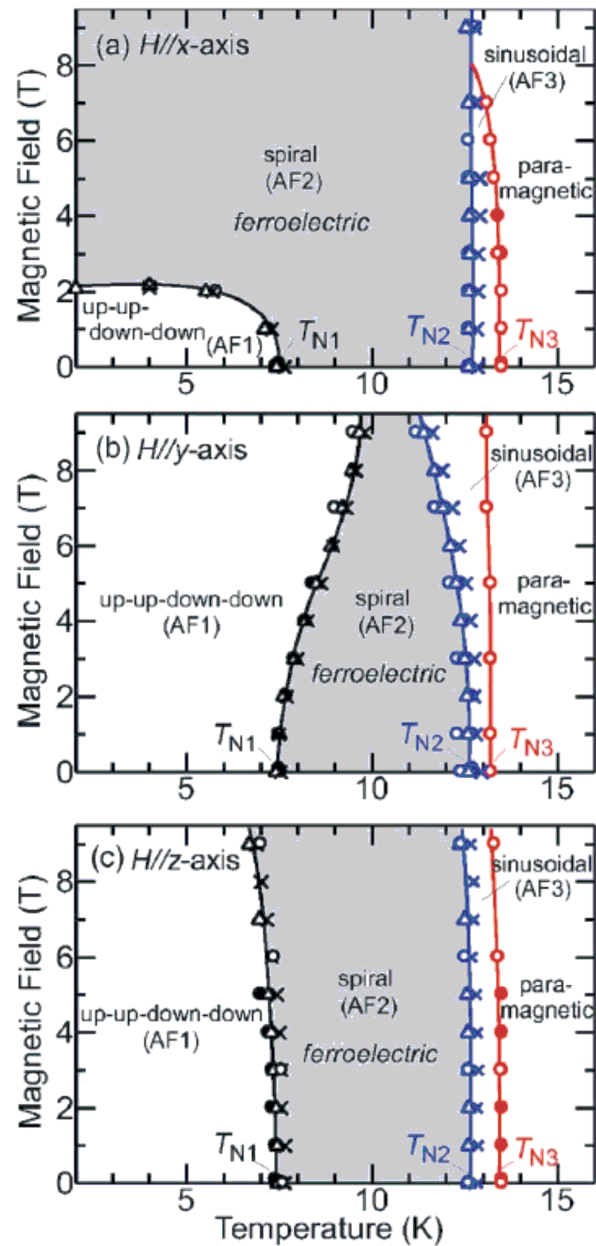


Figure 4.44: Magnetic and electric phase diagrams of  $\text{MnWO}_4$  taken from A. H. Arkenbout *et al.* [199] with magnetic fields applied along the a) easy, b)  $\mathbf{b}$ , and c) hard axes. Closed circles, open circles, open triangles, and crosses represent the data obtained by the measurements of magnetization, specific heat, dielectric constant, and pyroelectric current, respectively. Gray regions indicate ferroelectric phases [199].

Combining the irreducible representations we find the following reducible representation of the phonon modes for monoclinic  $MnWO_4$  at room temperature with space group  $P2/c$ :

$$\Gamma_{\text{total}} = 8 A_g + 8 A_u + 10 B_g + 10 B_u. \quad (4.3.2)$$

Thus, the total number of optical branches is 33, while the acoustic branches are  $A_u + 2 B_u$  [184]. As given by Rousseau [184], the  $A_g$  and  $B_g$  modes are Raman active, and the  $A_u$  and  $B_u$  modes are infrared active. Subtracting the acoustic modes, the factor-group analysis predicts 15 infrared-active phonon modes

$$\Gamma_{\text{IR}} = 7 A_u + 8 B_u. \quad (4.3.3)$$

This means that we expect seven infrared-active phonon modes for  $\mathbf{E} \parallel \mathbf{b}$ , if we assume  $\mathbf{y} \parallel \mathbf{b}$ ,  $\mathbf{z} \parallel \mathbf{c}$  and  $\mathbf{x} \perp \mathbf{c}$  lying in the  $\mathbf{ac}$  plane, where  $\mathbf{a}$ ,  $\mathbf{b}$  and  $\mathbf{c}$  are the crystallographic axes. In addition, we predict eight infrared-active modes for polarization in the  $\mathbf{ac}$  plane. Furthermore there are 18 Raman-active phonon modes

$$\Gamma_{\text{Raman}} = 8 A_g + 10 B_g. \quad (4.3.4)$$

Here we have no silent modes, because the sum of infrared, Raman, and acoustic modes is equal to the total number of all possible phonon modes in this compound.

In contrast to the previous section, we cannot use the conventional Drude-Lorentz model to describe phonon modes within the  $\mathbf{ac}$  plane, because the tensor of the dielectric function is no longer diagonal in this monoclinic compound. The off-diagonal matrix elements  $\epsilon_{xz}$  and  $\epsilon_{zx}$ , which should be identical for non-magnetic materials<sup>17</sup> ( $\mu_1 \equiv 0$ ), are not equal to zero. Thus, the tensor of the dielectric response has the following form:

$$\hat{\epsilon}(\omega) = \begin{pmatrix} \epsilon_{xx}(\omega) & 0 & \epsilon_{xz}(\omega) \\ 0 & \epsilon_{yy}(\omega) & 0 \\ \epsilon_{xz}(\omega) & 0 & \epsilon_{zz}(\omega) \end{pmatrix}. \quad (4.3.5)$$

The determination of the phonon modes in a monoclinic compound can be done analogously to the procedure described by Kuz'menko *et al.* [188]: We decompose the tensor (4.3.5) into a scalar  $\epsilon_b$  along the  $\mathbf{b}$  axis and a two-dimensional tensor  $\epsilon_{ac}$  within the  $\mathbf{ac}$  plane. Since the  $\mathbf{b}$  axis is perpendicular to the  $\mathbf{ac}$  plane, we can determine the  $A_u$  symmetry modes by measuring with the incident electric field  $\mathbf{E}$  parallel to the  $\mathbf{b}$  axis (see Fig. 4.48 e) and Fig. 4.49 e)).

In order to determine the modes with  $B_u$  symmetry, we have to measure at least three different polarization directions (with  $\mathbf{E} \parallel \mathbf{ac}$  plane, see Fig. 4.45), because the angle between the  $\mathbf{a}$  and the  $\mathbf{c}$  axis deviates from  $90^\circ$  (see Fig. 4.46). Additionally, we assume that the incident wave excites only TO vibrations inside the crystal [188].

<sup>17</sup>We will assume that the medium is nongyrotropic (it means, for example, that no magnetic field is applied) and there is no spatial dispersion.

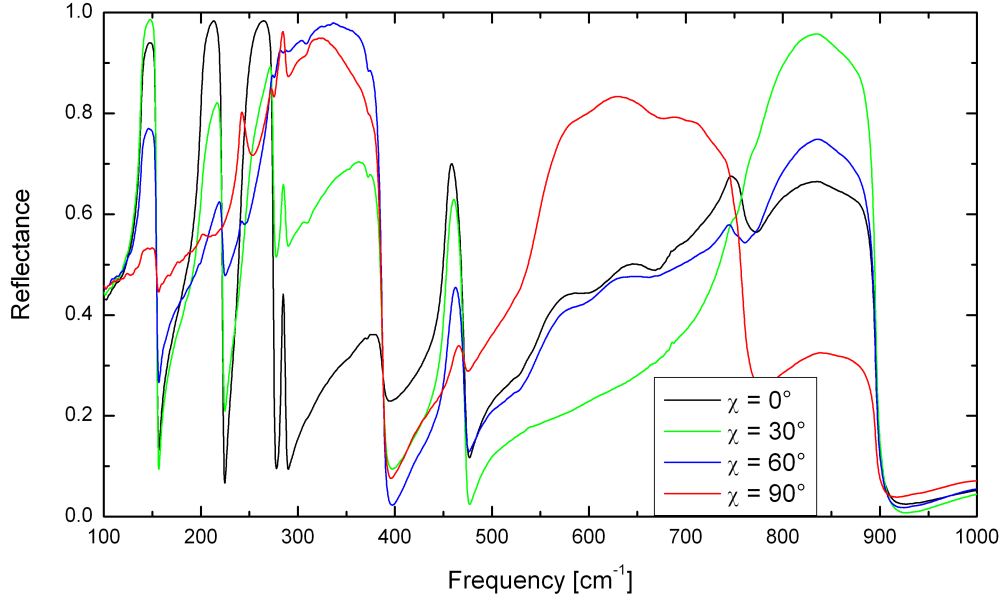


Figure 4.45: Reflectance of  $\text{MnWO}_4$  ( $\mathbf{E} \parallel \mathbf{ac}$ ) for four different polarization angles  $\chi$  at  $T = 10$  K.

Reflectivity spectra at  $T = 10$  K are shown for  $\mathbf{E} \parallel \mathbf{ac}$  in Figs. 4.48 a) - c) and for  $\mathbf{E} \parallel \mathbf{b}$  in Fig. 4.48 e). The phonon spectrum at  $T = 295$  K is plotted in Fig. 4.49. The scalar  $\epsilon_b$  is described by the conventional Drude-Lorentz model, whereas the tensor  $\hat{\epsilon}_{ac}$  requires a generalized Drude-Lorentz model:

$$\begin{aligned} \epsilon_b(\omega) = \epsilon_{yy} &= \epsilon_b^\infty + \sum_{i,A} \frac{\omega_{p,i}^2}{\omega_{0,i}^2 - \omega^2 - i\gamma_i\omega}, \\ \hat{\epsilon}_{ac}(\omega) &= \begin{pmatrix} \epsilon_{xx} & \epsilon_{xz} \\ \epsilon_{xz} & \epsilon_{zz} \end{pmatrix} = \hat{\epsilon}_{ac}^\infty + \sum_{i,B} \frac{\omega_{p,i}^2}{\omega_{0,i}^2 - \omega^2 - i\gamma_i\omega} \times \begin{pmatrix} \cos^2 \theta_i & \sin \theta_i \cos \theta_i \\ \sin \theta_i \cos \theta_i & \sin^2 \theta_i \end{pmatrix}. \end{aligned} \quad (4.3.6)$$

Here,  $\epsilon_b^\infty$  and  $\hat{\epsilon}_{ac}^\infty$  are the high-frequency dielectric constants,  $\omega_{0,i}$  is the transverse frequency,  $\omega_{p,i}$  the plasma frequency, and  $\gamma_i$  the damping of the  $i$ -th oscillator, and  $\theta_i$  (for the  $B_u$  modes) the angle between the dipole moment and the  $\mathbf{x}$  axis.

Due to the symmetry of the tensor  $\hat{\epsilon}$  of the dielectric function, we can always find a set of axes (a basis  $\{x, y, z\}$ ) such that the real or the imaginary part of  $\hat{\epsilon}$  have diagonal form. In case of an orthorhombic crystal, the two sets of axes coincide and the basis is related to the crystal structure, i.e. the crystallographic axes  $\mathbf{a}$ ,  $\mathbf{b}$ , and  $\mathbf{c}$ .<sup>18</sup>

<sup>18</sup>For an orthorhombic crystal, all optical constants (all matrix elements of  $\hat{\epsilon}$ ) can be determined experimentally using linearly polarized light parallel to the three crystallographic axes.

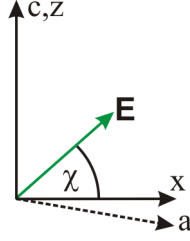


Figure 4.46: Orientation of the crystallographic axes  $\mathbf{a}$  and  $\mathbf{c}$  as well as the cartesian coordinate system and angle  $\chi$  between the polarization direction and the  $\mathbf{x}$  axis.

In monoclinic crystals, only one axis of the tensor  $\hat{\epsilon}$  is fixed with respect to the crystallographic system of coordinates; the two other axes rotate in the perpendicular plane. Due to the low symmetry, the orientation of the principal axes of  $\hat{\epsilon}_{ac}$  depends on  $\omega$  and is different for  $\text{Re}\{\hat{\epsilon}_{ac}\}$  and  $\text{Im}\{\hat{\epsilon}_{ac}\}$ . The calculation of the rotation angles  $\phi_{Re}$  and  $\phi_{Im}$  requires the diagonalization of  $\text{Re}\{\hat{\epsilon}_{ac}\}$  and  $\text{Im}\{\hat{\epsilon}_{ac}\}$  by two different rotation matrices.

An example for the relationship between  $\phi_{Im}$ ,  $\phi_{Re}$ , and  $\theta_i$  is shown in Fig. 4.47. In the case of some oscillators (e.g.  $\omega_0 = 753 \text{ cm}^{-1}$  and  $\omega_0 = 765 \text{ cm}^{-1}$ , see below),  $\phi_{Im}(\omega_0)$  and  $\theta_i$  are similar, but they may differ significantly for other modes.

Using the Fresnel equations [188] for normal incidence we obtain the reflectance for  $\mathbf{E} \parallel \mathbf{b}$  ( $R_b$ ) and  $\mathbf{E} \parallel \mathbf{ac}$  ( $R_{ac}$ ):

$$R_b(\omega) = \left| \left( 1 - \sqrt{\epsilon_b(\omega)} \right) \cdot \left( 1 + \sqrt{\epsilon_b(\omega)} \right)^{-1} \right|^2, \quad (4.3.7)$$

$$R_{ac}(\omega, \chi) = \left| \left( \left( \hat{1} - \sqrt{\hat{\epsilon}_{ac}(\omega)} \right) \cdot \left( \hat{1} + \sqrt{\hat{\epsilon}_{ac}(\omega)} \right)^{-1} \right) \cdot \begin{pmatrix} \cos \chi \\ \sin \chi \end{pmatrix} \right|^2,$$

in which  $\hat{1}$  denotes the unity tensor and  $\chi$  represents the angle between the polarization direction and the  $\mathbf{x}$  axis, as shown in Fig. 4.46. The “-1” exponent in the calculation of  $R_{ac}(\omega, \chi)$  implies calculation of the inverse matrix. Moreover, the calculation of  $R_{ac}(\omega, \chi)$  requires the determination of the square root of a tensor. Therefore, we rotate  $\hat{\epsilon}_{ac}(\omega)$  to a diagonal form, then we take the square root for each matrix element, and finally we rotate the resulting tensor back to its original basis.

The fit was carried out by the least-squares method. Minimization of  $\chi^2$  was performed by the Marquardt technique described in [99] with analytical calculation of the partial derivatives of  $\chi^2$  based on model parameters. All fits in this thesis using the generalized Drude-Lorentz model have been performed applying the program Optpal 2.8 by Dirk van der Marel and coworkers<sup>19</sup> with an extension for the generalized Drude-Lorentz model developed in collaboration with Alexander Gössling [207]. As shown

<sup>19</sup>Département de Physique de la Matière Condensée, Université de Genève, Switzerland

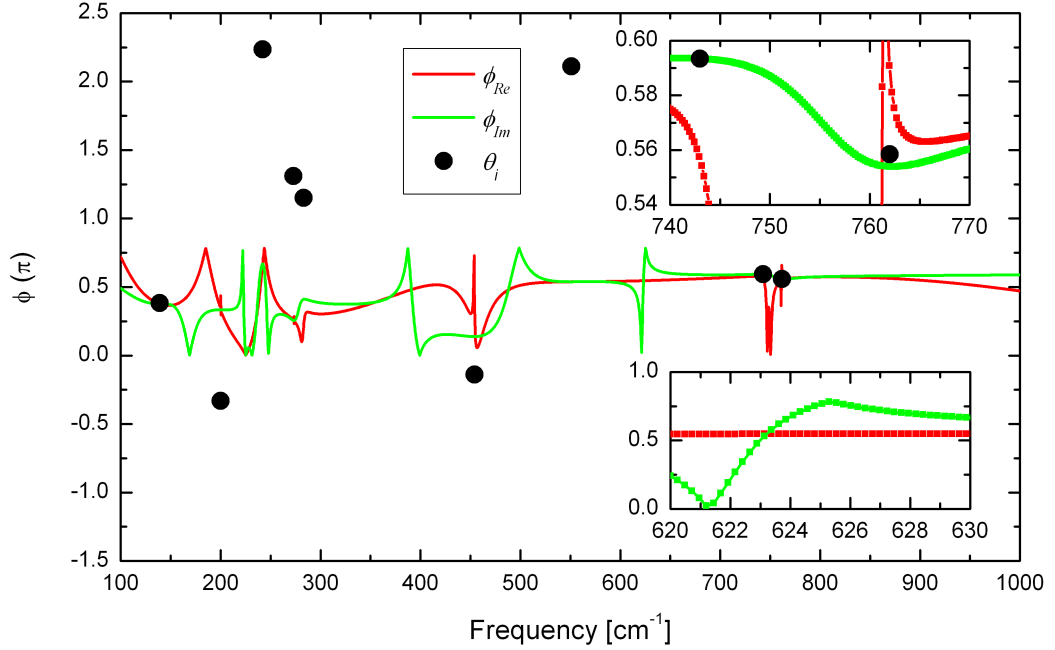


Figure 4.47: Rotation angles of the tensor of the dielectric function in  $\text{MnWO}_4$  at  $T = 10$  K. The rotation angles  $\phi_{Re}$  (red) and  $\phi_{Im}$  (green) are presented in combination with the angles  $\theta_i$  (black dots) for the different modes used in the fits for  $\mathbf{E} \parallel \mathbf{ac}$ .

in Fig. 4.48 e) and Fig. 4.49 e), the fits yield a good description of the measured reflectance for  $\mathbf{E} \parallel \mathbf{b}$ . For  $\mathbf{E} \parallel \mathbf{ac}$  we were not able to achieve a good description between 600 and 800  $\text{cm}^{-1}$ . The fit parameters are listed in Tab. 4.17.

In case of  $\mathbf{E} \parallel \mathbf{b}$ , where 7  $A_u$  modes are expected, we find 7 strong IR modes. The small feature at 231  $\text{cm}^{-1}$  corresponds probably to a polarizer leakage.

We find a remarkably high phonon mode at 858  $\text{cm}^{-1}$ , which is unusual for a transition-metal oxide including a heavy ion like W. In order to find an explanation for the occurrence of this high eigenfrequency, we compare the bond lengths of  $\text{MnWO}_4$  and  $\text{YMnO}_3$ : The Mn-O distances in  $\text{MnWO}_4$  range between 2.099 Å and 2.2272 Å [195], whereas the Mn-O distances in  $\text{YMnO}_3$  are shorter (1.8653 Å - 2.0971 Å [166]). Comparing the distances between the oxygen and the heavy ion (W for  $\text{MnWO}_4$  and Y for  $\text{YMnO}_3$ ), we find a remarkable difference: In contrast to  $\text{YMnO}_3$ , where the Y-O distances vary from 2.2102 Å to 2.4614 Å [166], we find shortened W-O distances in  $\text{MnWO}_4$ , which range between 1.794 Å and 2.1310 Å [195]. We think, that the short W-O distance, with a bond length of 1.794 Å, causes the high-energy phonon mode at 858  $\text{cm}^{-1}$ .

In case of  $\mathbf{E} \parallel \mathbf{ac}$ , where 8  $B_u$  modes are expected, we require a further mode to describe the phonon spectrum reasonably (see Figs. 4.48 a) - c), and Figs. 4.49 a) - c)). Still we cannot achieve a good description between 600 and 800  $\text{cm}^{-1}$ , which is caused probably by two-phonon contributions and a large multi-phonon background like in  $YMnO_3$ . Additionally, the reflectance is pretty high in this energy range and weak features may have a significant influence on the reflectivity. The peak at 273  $\text{cm}^{-1}$  is the strongest mode and we describe the phonon spectrum below 600  $\text{cm}^{-1}$  properly. Due to the low crystal symmetry, the directions of the two principal dielectric axes in the  $\mathbf{ac}$  plane depend on the frequency, which precludes the straightforward application of the Kramers-Kronig method to the  $\mathbf{ac}$  plane reflectance data. Therefore, the components of the tensor of the optical conductivity have been determined from (4.3.6) using (2.11.8) (see Figs. 4.53 a) - c)). The off-diagonal component  $\sigma_{xz}$  may have any sign, unlike the diagonal components  $\sigma_{xx}$  and  $\sigma_{zz}$ , which must be positive.

The temperature dependence of the phonon spectra for the different polarization directions is shown in Figs. 4.50 - 4.51. We find no qualitative change in the spectra between the AF2, AF3, and the paramagnetic phase. (The measurement of the phonon spectra within the AF1 could not be realized).

The temperature evolution of the eigenfrequencies of the  $A_u$  and  $B_u$  modes is shown in Fig. 4.55. There is no significant difference in the temperature dependence of the eigenfrequencies of the low- and high-frequency  $A_u$  as well as  $B_u$  modes. All modes are monotonically hardening upon cooling down. The  $A_u$  mode at 174  $\text{cm}^{-1}$  shows the strongest softening of all  $A_u$  modes, whereas the  $B_u$  mode at 200  $\text{cm}^{-1}$  shows a shift of roughly 3 % between 10 K and 295 K. Furthermore, we find no remarkable behavior in the other fit parameters (see Fig. 4.56 and Fig. 4.57<sup>20</sup>) and the reflectance (see Fig. 4.54) between the AF2 ( $T = 10$  K), AF3 ( $T = 13$  K), and the paramagnetic phase ( $T > 13$  K) for both directions  $\mathbf{E} \parallel \mathbf{ac}$  and  $\mathbf{E} \parallel \mathbf{b}$ .

In addition, in Fig. 4.58 the variation of the angle  $\theta_i$  of each phonon mode is shown. The phonon modes at 200  $\text{cm}^{-1}$  and 242  $\text{cm}^{-1}$  rotate clockwise with increasing temperature. The angle changes from  $-19^\circ$  ( $128^\circ$ ) at 10 K to  $-35^\circ$  ( $118^\circ$ ) at 295 K. The modes at 283  $\text{cm}^{-1}$  and 454  $\text{cm}^{-1}$  show the opposite behavior. The absolute change between 10 K and 295 K is  $6^\circ$  and  $11^\circ$ . We observe no irregularity in the variation of the angle  $\theta_i$  except for the mode at 242  $\text{cm}^{-1}$  between 13 K and 20 K, which is caused by the inaccuracy of the fit.

Hence, we conclude that the spin-lattice interaction is not strong enough to change the phonon spectra markedly at the magnetic phase transitions.

---

<sup>20</sup>The small enhancement of the damping of the phonon mode at 242  $\text{cm}^{-1}$  between 13 K and 20 K is caused by inaccuracies in the fit.

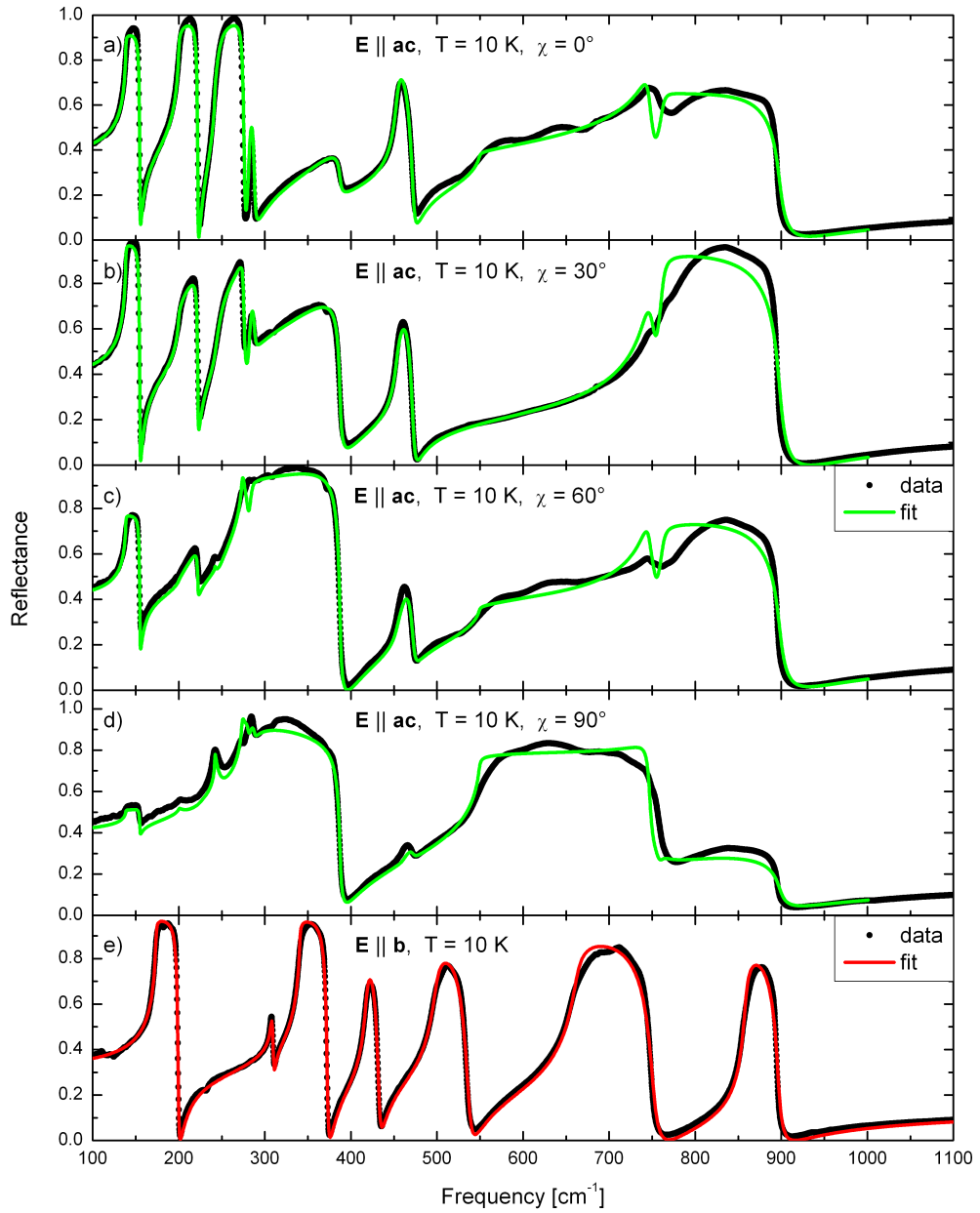


Figure 4.48: Reflectance of  $\text{MnWO}_4$  at  $T = 10 \text{ K}$  for a) - d)  $\mathbf{E} \parallel \mathbf{ac}$  plane at different polarization angles  $\chi$  (black) and fit using (4.3.7) with 9 phonon modes (green). e) Reflectivity at  $T = 10 \text{ K}$  for  $\mathbf{E} \parallel \mathbf{b}$  (black), fit using (4.3.7) (red).

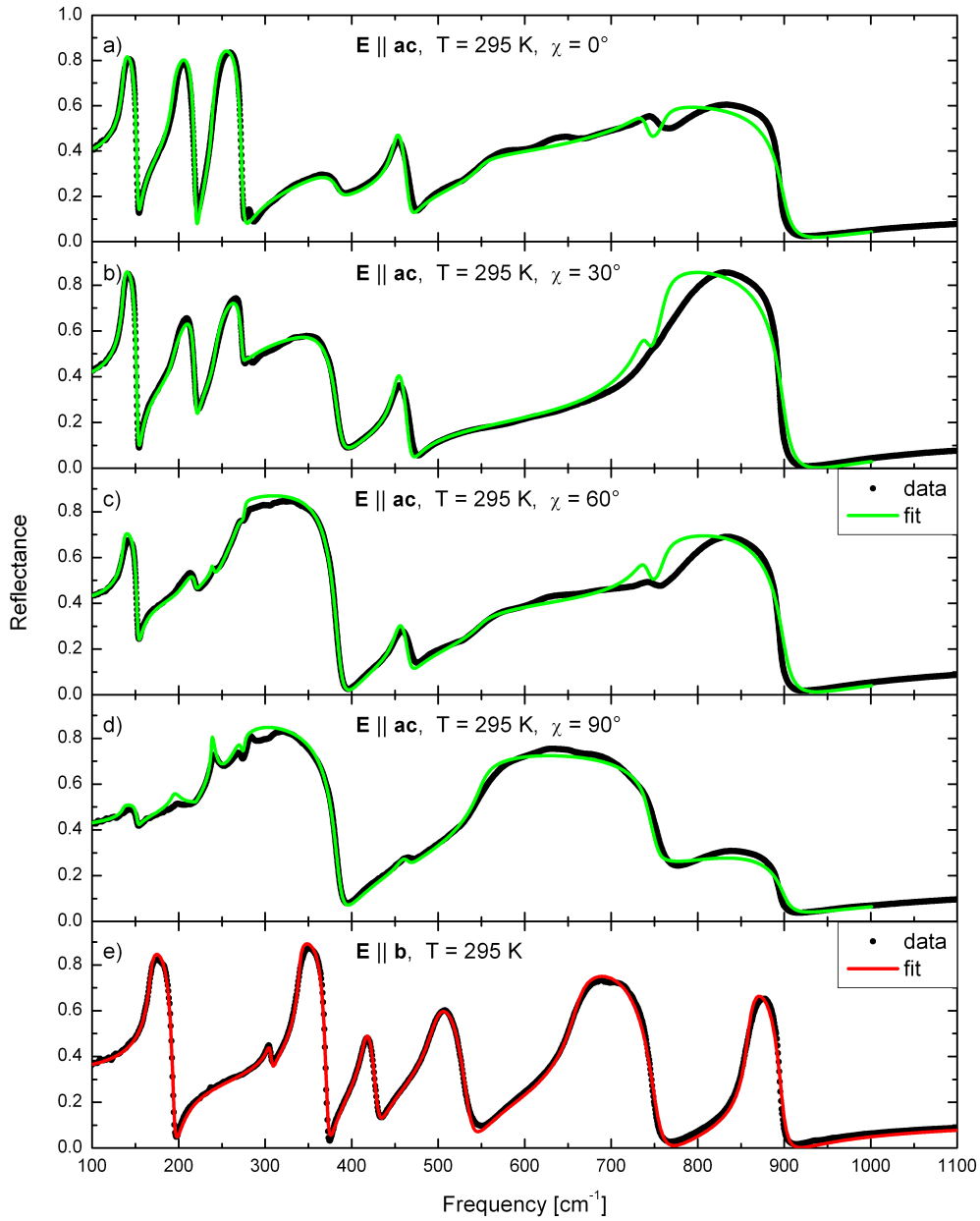


Figure 4.49: Reflectance of  $\text{MnWO}_4$  at  $T = 295 \text{ K}$  for a) - d)  $\mathbf{E} \parallel \mathbf{ac}$  plane at different polarization angles  $\chi$  (black) and fit using (4.3.7) with 9 phonon modes (green). e) Reflectivity at  $T = 295 \text{ K}$  for  $\mathbf{E} \parallel \mathbf{b}$  (black), fit using (4.3.7) (red).

<i>B modes</i>					<i>A modes</i>			
$\omega_0$	$\omega_p$	$\gamma$	$\theta$	S	$\omega_0$	$\omega_p$	$\gamma$	S
[ $cm^{-1}$ ]	[ $cm^{-1}$ ]	[ $cm^{-1}$ ]	[ $^\circ$ ]		[ $cm^{-1}$ ]	[ $cm^{-1}$ ]	[ $cm^{-1}$ ]	
139	299	0.6	22	4.659	174	338	1.1	3.790
200	393	1.1	-19	3.848	308	147	2.9	0.227
242	400	0.2	128	2.729	341	484	1.5	2.020
273	721	1.2	75	6.946	418	302	5.4	0.521
283	418	5.7	66	2.180	499	495	9.4	0.986
454	362	6.1	-8	0.638	662	720	11.7	1.180
551	1050	2.4	121	3.657	858	404	6.3	0.221
743	761	13.8	34	1.047				
762	686	6.7	32	0.811				

Table 4.17: Fit parameters for the reflectivity of  $MnWO_4$  at  $T = 10$  K using (4.3.7). Here,  $S = \omega_p^2/\omega_0^2$  denotes the oscillator strength. The high-frequency dielectric constants at  $T = 10$  K are:  $\epsilon_{xx}^\infty = 4.99$ ,  $\epsilon_{yy}^\infty = 4.93$ ,  $\epsilon_{zz}^\infty = 5.75$ , and  $\epsilon_{xz}^\infty = 0.009$ .

<i>B modes</i>					<i>A modes</i>			
$\omega_0$	$\omega_p$	$\gamma$	$\theta$	S	$\omega_0$	$\omega_p$	$\gamma$	S
[ $cm^{-1}$ ]	[ $cm^{-1}$ ]	[ $cm^{-1}$ ]	[ $^\circ$ ]		[ $cm^{-1}$ ]	[ $cm^{-1}$ ]	[ $cm^{-1}$ ]	
136	274	3.3	21	4.028	168	335	5.4	3.980
194	406	5.1	-35	4.389	306	135	6.0	0.195
238	374	1.1	118	2.469	340	481	4.2	2.000
270	733	14.9	72	7.316	415	288	12.0	0.482
276	336	4.5	72	1.483	496	505	21.6	1.040
451	284	11.7	3	0.397	660	722	21.9	1.200
550	1035	18.2	121	3.533	858	400	10.0	0.217
737	566	17.9	34	0.589				
760	825	16.2	33	1.180				

Table 4.18: Fit parameters for the reflectivity of  $MnWO_4$  at  $T = 295$  K using (4.3.7). Here,  $S = \omega_p^2/\omega_0^2$  denotes the oscillator strength. The high-frequency dielectric constants at  $T = 10$  K are:  $\epsilon_{xx}^\infty = 4.72$ ,  $\epsilon_{yy}^\infty = 4.82$ ,  $\epsilon_{zz}^\infty = 5.44$ , and  $\epsilon_{xz}^\infty = 0.049$ .

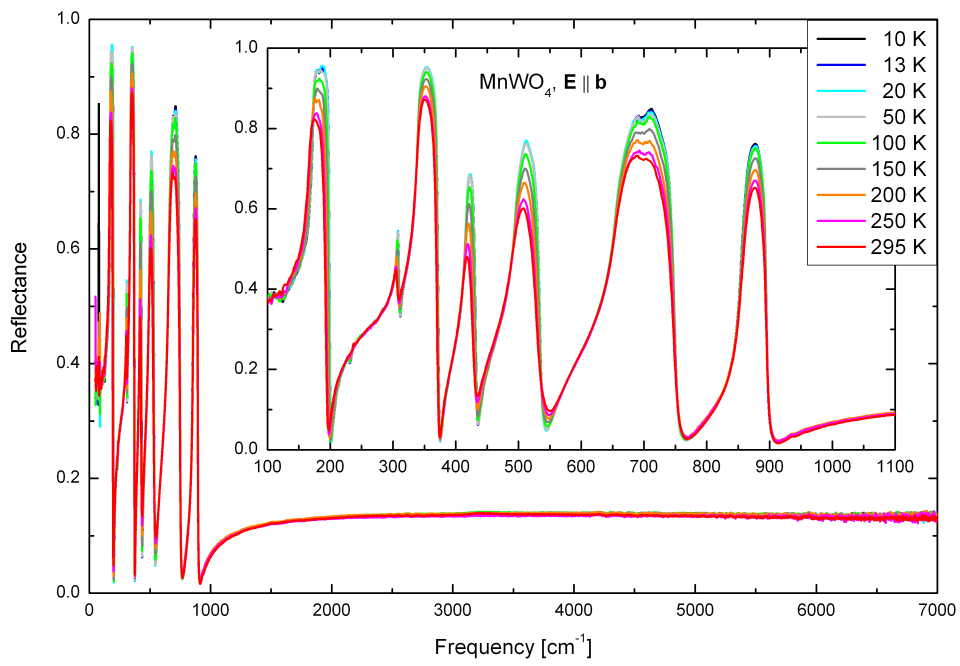


Figure 4.50: Temperature dependence of the reflectance of  $\text{MnWO}_4$  for  $\mathbf{E} \parallel \mathbf{b}$ .

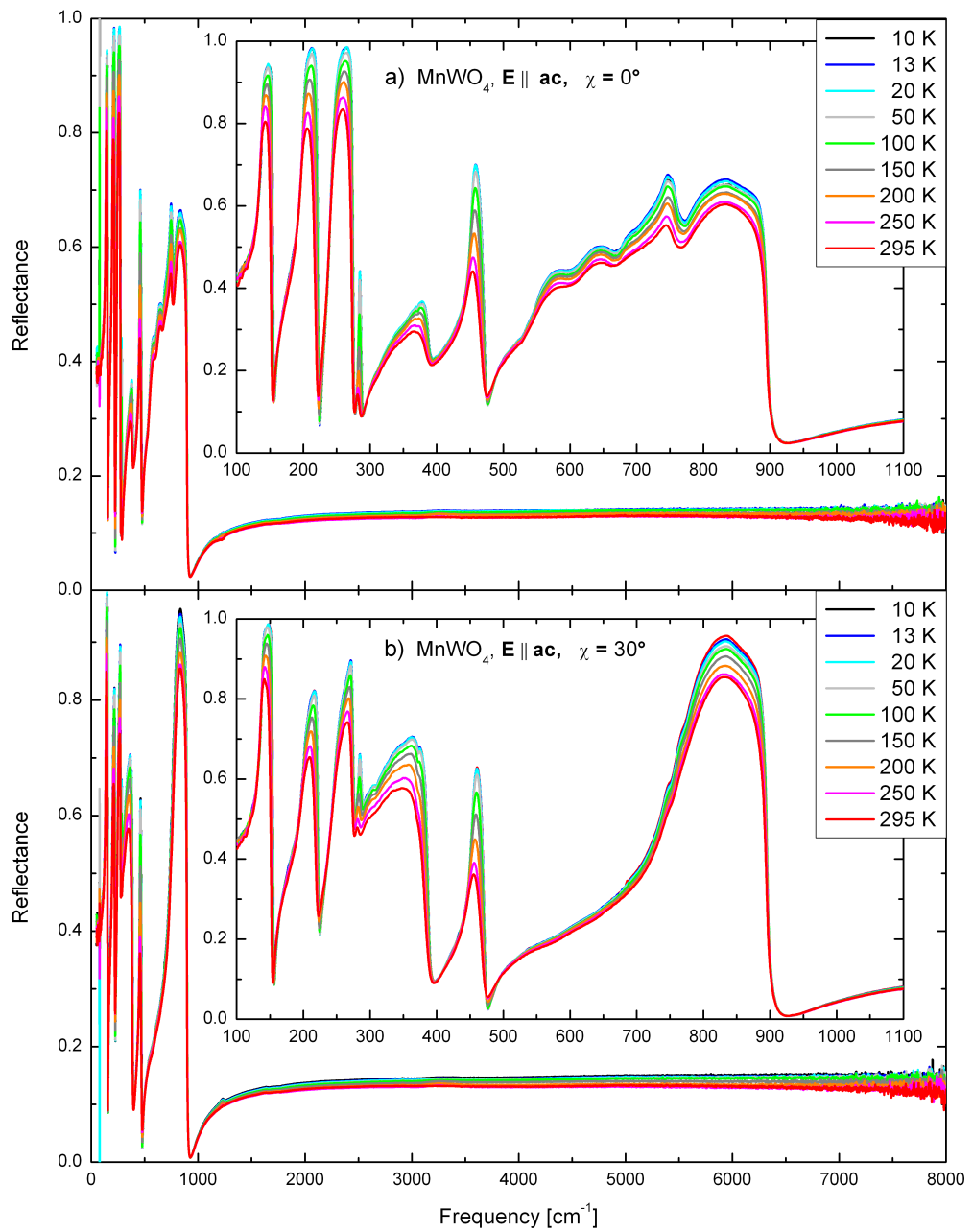


Figure 4.51: Temperature dependence of the reflectance of MnWO<sub>4</sub> ( $\mathbf{E} \parallel \mathbf{ac}$ ) at a)  $\chi = 0^\circ$  and b)  $\chi = 30^\circ$ .

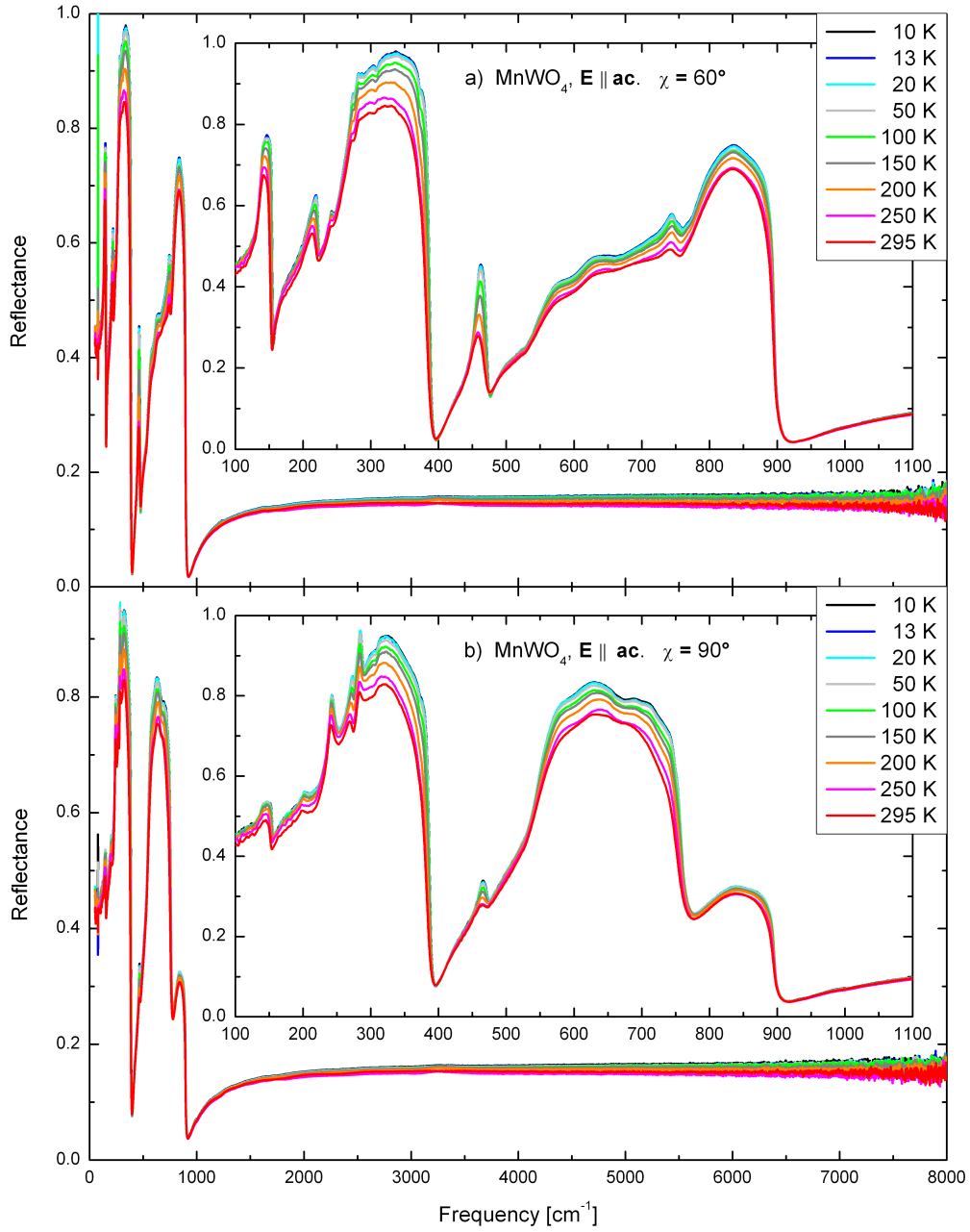


Figure 4.52: Temperature dependence of the reflectance of  $\text{MnWO}_4$  ( $\mathbf{E} \parallel \mathbf{ac}$ ) at a)  $\chi = 60^\circ$  and b)  $\chi = 90^\circ$ .

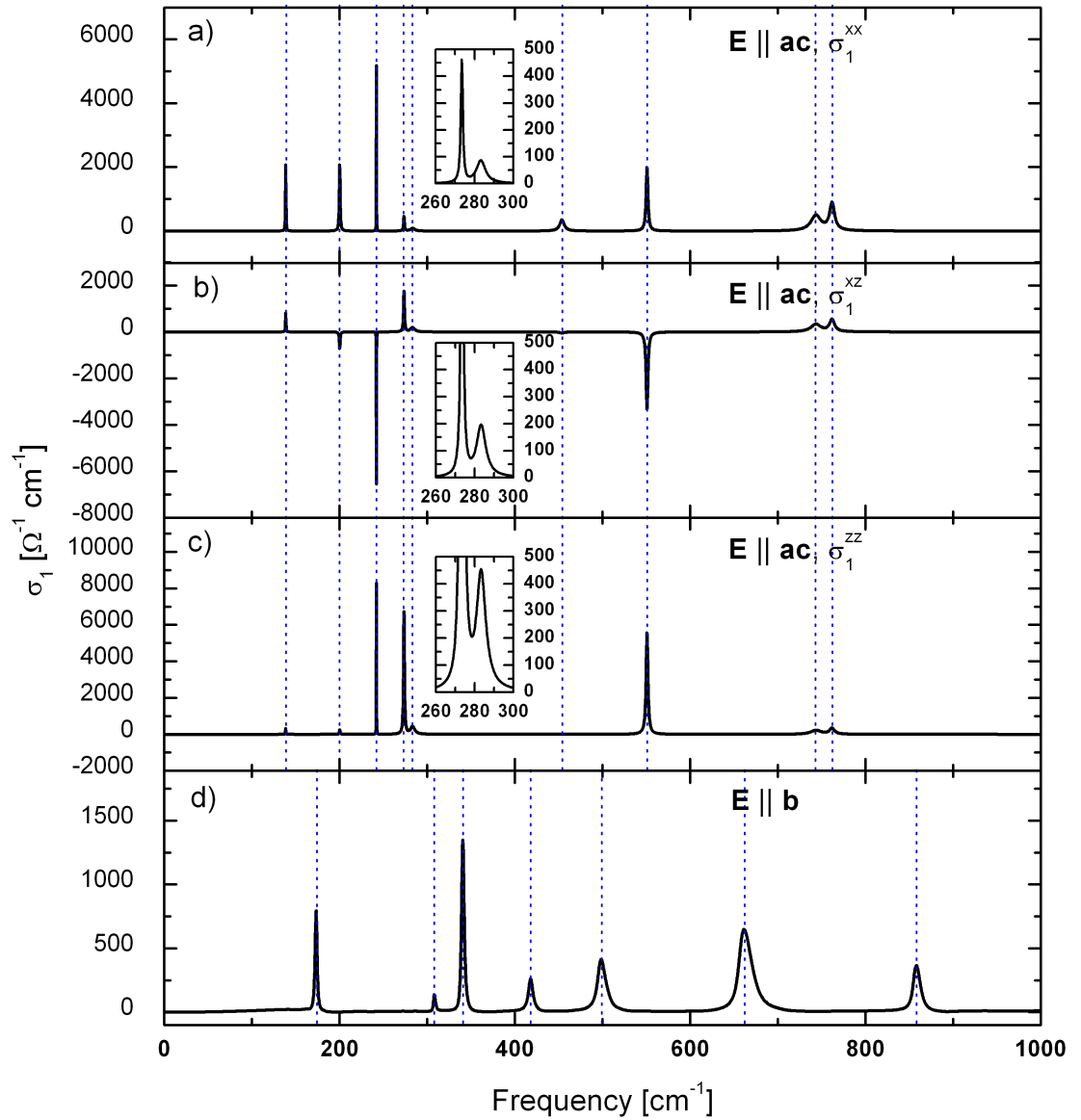


Figure 4.53: Optical conductivity of  $\text{MnWO}_4$  at  $T = 10$  K for a) - c)  $\mathbf{E} \parallel \mathbf{ac}$  and d)  $\mathbf{E} \parallel \mathbf{b}$ . The optical conductivity for  $\mathbf{E} \parallel \mathbf{b}$  was determined by applying the Kramers-Kronig transformation to the optical reflectance (black). The dotted lines indicate the eigenfrequencies of the phonon modes used in the fit. For  $\mathbf{E} \parallel \mathbf{ac}$  the components of the optical tensor  $\hat{\sigma}$  are shown, which are determined from (4.3.6) using (2.11.8).

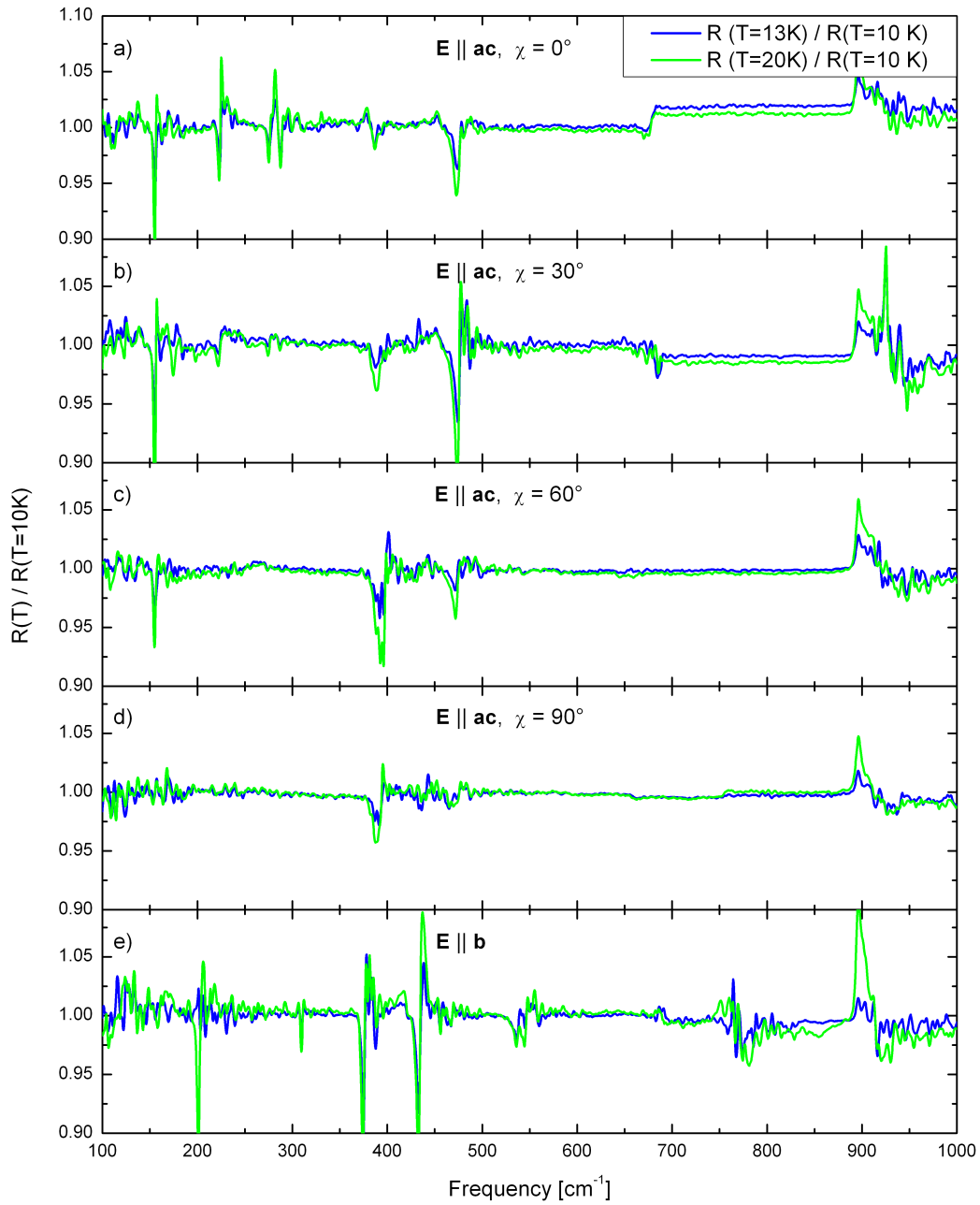


Figure 4.54: Temperature dependence of the relative reflectance below 50 K of  $\text{MnWO}_4$  for a)  $\mathbf{E} \parallel \mathbf{ac}$ ,  $\chi = 0^\circ$ , b)  $\mathbf{E} \parallel \mathbf{ac}$ ,  $\chi = 30^\circ$ , c)  $\mathbf{E} \parallel \mathbf{ac}$ ,  $\chi = 60^\circ$ , d)  $\mathbf{E} \parallel \mathbf{ac}$ ,  $\chi = 90^\circ$ , and e)  $\mathbf{E} \parallel \mathbf{b}$ . The sharp features in the graphs are caused by the large gradient of the reflectance at these frequencies, which leads to numerical inaccuracies.

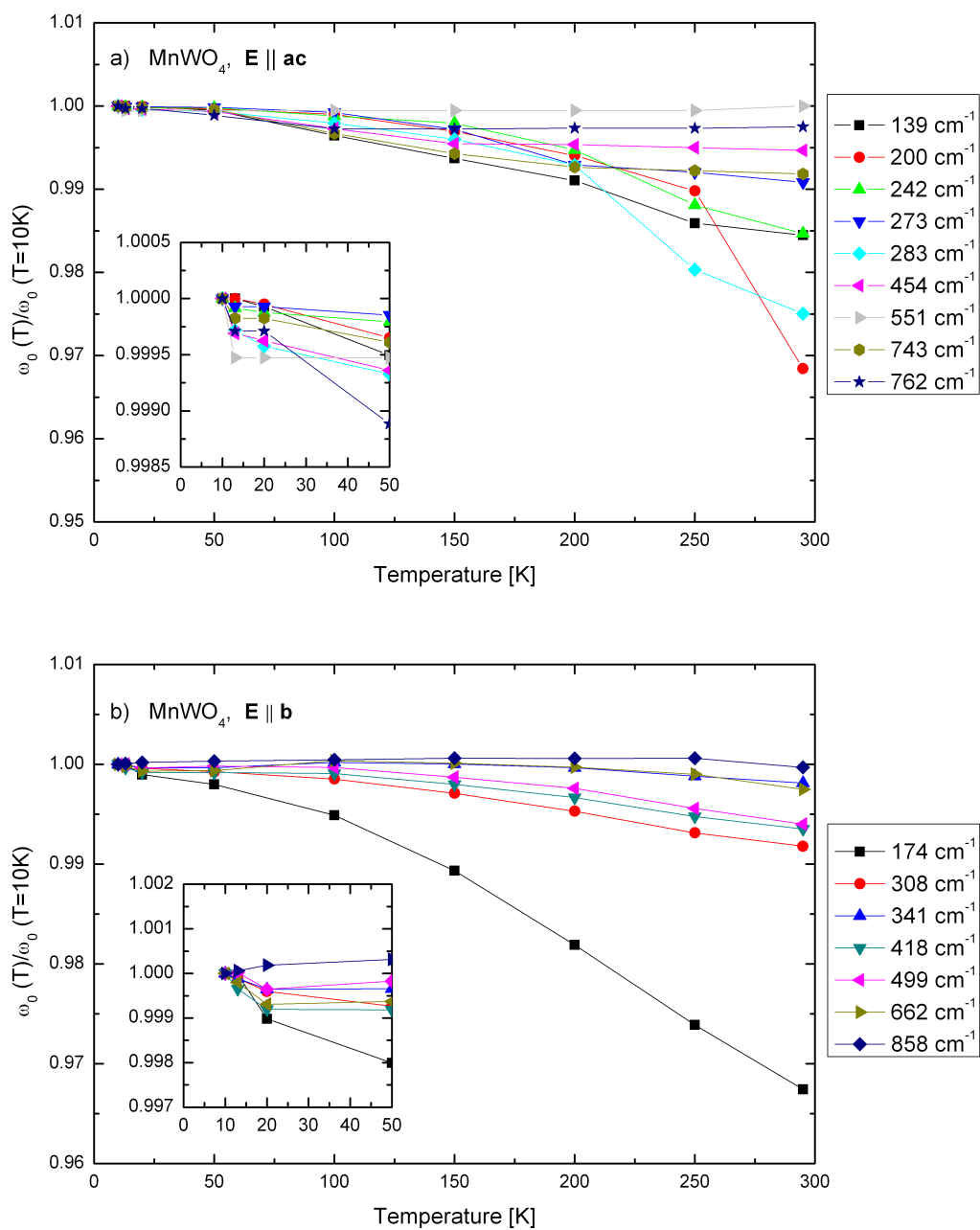


Figure 4.55: Relative eigenfrequencies  $\omega_0(T)/\omega_0(T=10\text{ K})$  of  $\text{MnWO}_4$  for a)  $\mathbf{E} \parallel \mathbf{ac}$  and b)  $\mathbf{E} \parallel \mathbf{b}$ . The insets show the temperature range below  $T = 50\text{ K}$ .

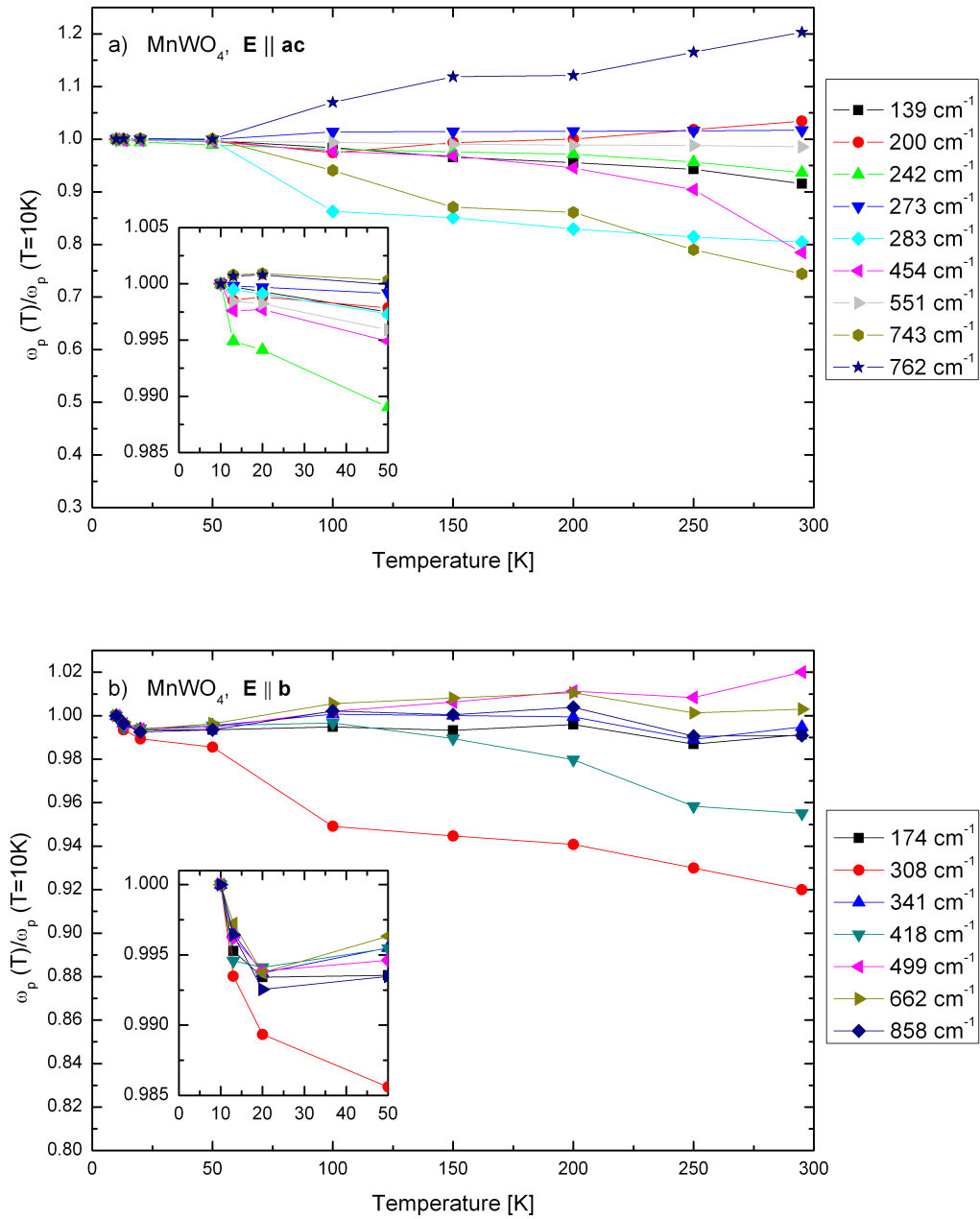


Figure 4.56: Relative plasma frequencies  $\omega_p(T)/\omega_p(T=10\text{K})$  of  $\text{MnWO}_4$  for a)  $\mathbf{E} \parallel \mathbf{ac}$  and b)  $\mathbf{E} \parallel \mathbf{b}$ . The insets show the temperature range below  $T = 50$  K.

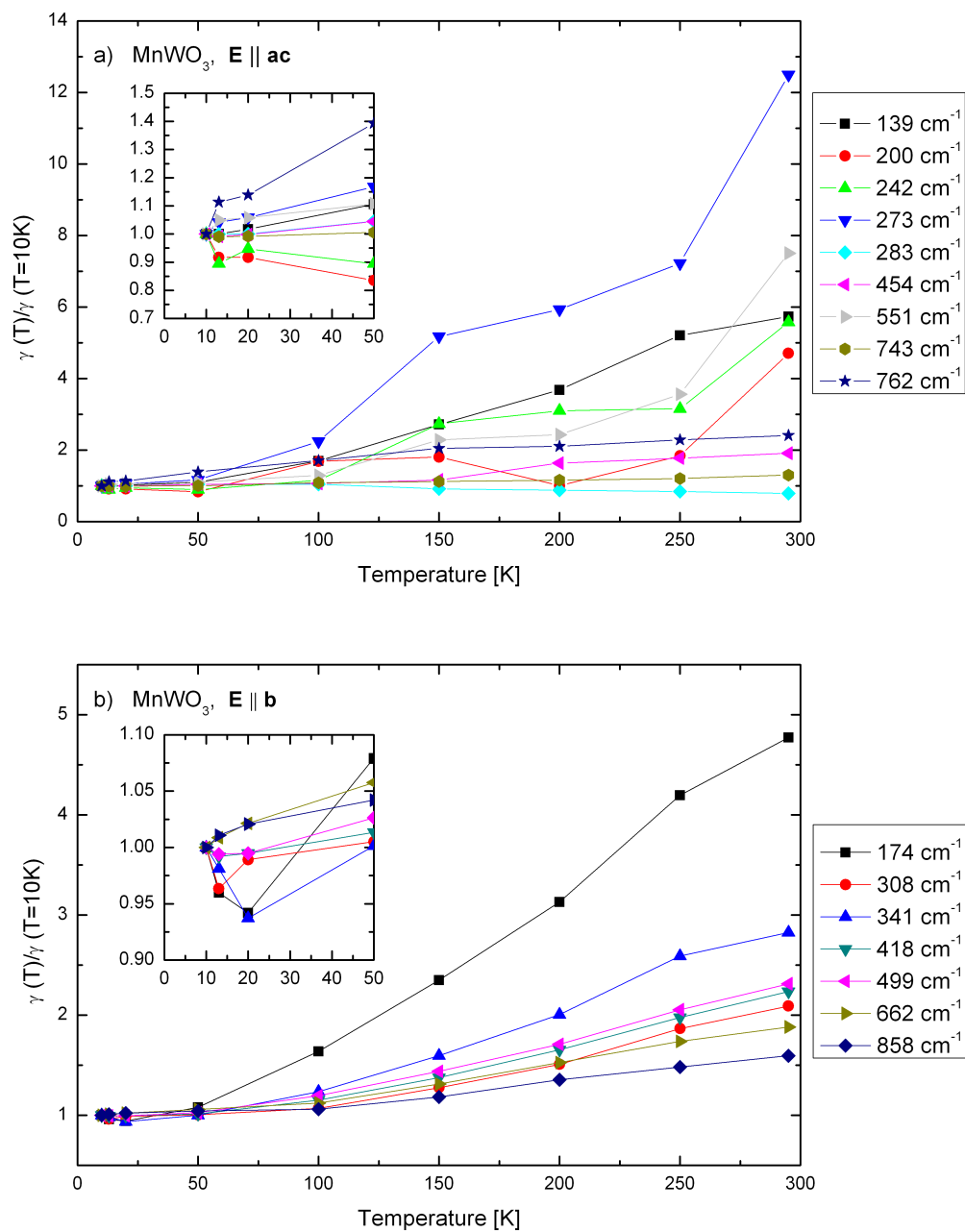


Figure 4.57: Relative damping  $\gamma(T)/\gamma(T=10\text{K})$  of  $\text{MnWO}_4$  for a)  $\text{E} \parallel \text{ac}$  and b)  $\text{E} \parallel \text{b}$ . The insets show the temperature range below  $T = 50\text{K}$ .

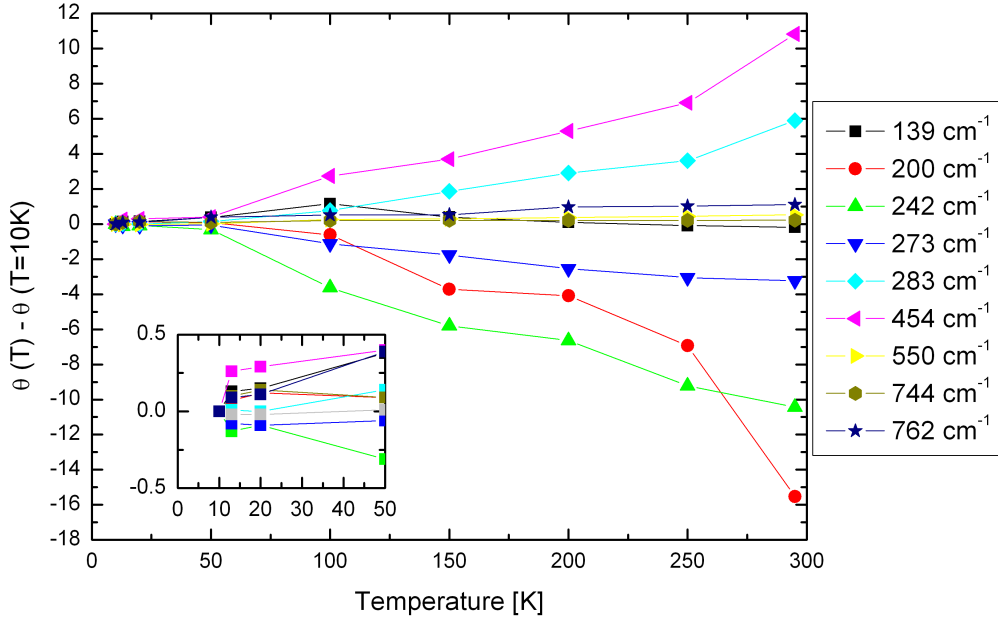


Figure 4.58: Absolute change of the angle  $\theta_i$  of  $\text{MnWO}_4$  for  $\mathbf{E} \parallel \mathbf{ac}$ . The inset shows the temperature range below  $T = 50$  K.

In Fig. 4.59 a) and b) the components of the complex dielectric function (4.3.5) along the  $\mathbf{b}$  axis,  $\epsilon_{yy}$ , and in the  $\mathbf{ac}$  plane,  $(1/2)(\epsilon_{xx} + \epsilon_{zz})$ , are shown. The form of the latter combination was chosen because the expression is invariant relative to the rotation of the system of coordinates within the  $\mathbf{ac}$  plane. Secondly, the form does not depend on the angles  $\theta_i$  and finally the expression would be equal to the dielectric function in case of a cubic crystal. The maxima of  $\text{Im}[\epsilon(\omega)]$  determine the frequencies of the TO modes. From a comparison of Fig. 4.59 a) and b) we come to the conclusion that on average the  $B_u$  modes for  $\mathbf{E} \parallel \mathbf{ac}$  are significantly more intensive (have greater effective charges) than the  $A_u$  modes for  $\mathbf{E} \parallel \mathbf{b}$ . Correspondingly, plasma frequencies and mode strengths of the  $B_u$  modes are on average greater than those of the  $A_u$  modes (see Tab. 4.17).

Concluding our investigations of the phonons, we find all infrared-active phonon modes predicted by the factor-group analysis. We describe the phonon spectra for  $\mathbf{E} \parallel \mathbf{ac}$  by a generalized Drude-Lorentz model developed by Kuz'menko *et al.* [188], and for  $\mathbf{E} \parallel \mathbf{b}$  by the conventional Drude-Lorentz model. We find no significant change in the phonon spectra between the AF2, AF3, and the paramagnetic phase.

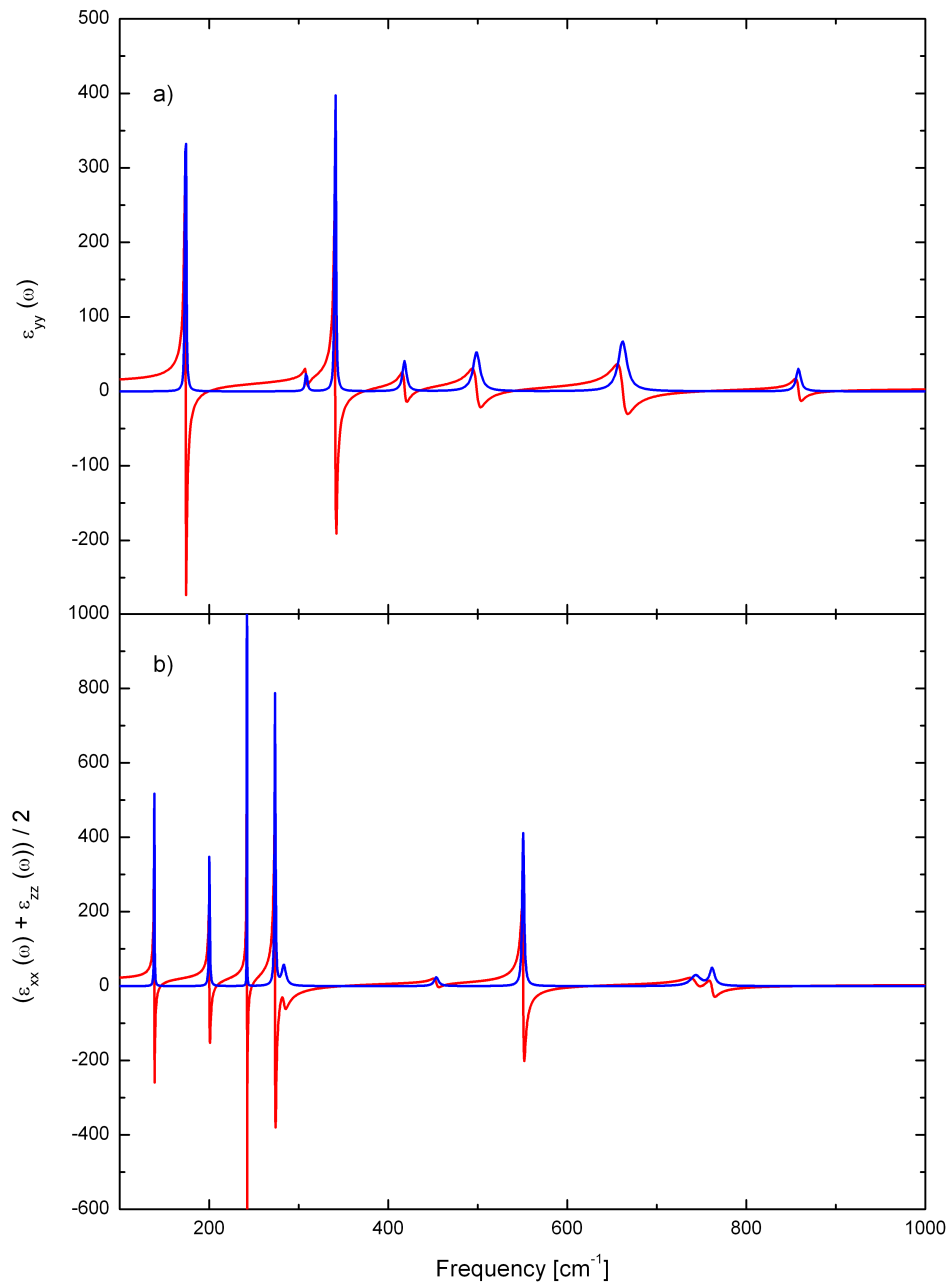


Figure 4.59: The frequency dependence of the real (red) and imaginary (blue) parts of a)  $\epsilon_{yy}$  and b)  $(1/2)(\epsilon_{xx} + \epsilon_{zz})$ .

### 4.3.2 Cluster-Model Calculations

In order to deepen our investigation of the infrared excitations below the band gap, we analyze the crystal-field excitations, similar to the procedure presented in section “4.1 Crystal-Field Excitations in  $\text{VOCl}_3$ ”.

We perform transmittance measurements at  $T = 30 \text{ K}$  and  $T = 295 \text{ K}$  in the spectral range of  $2000 - 23000 \text{ cm}^{-1}$  at normal incidence on two thin polished crystals. Note, that we measure within the paramagnetic regime far away from the highest magnetic ordering temperature  $13.5 \text{ K}$ . The spectra were measured for different polarization angles on polished (010) and (100) surfaces of  $\text{MnWO}_4$ . The variation of the polarization angle was realized by rotating the polarizer. All measurements were performed using linearly polarized light with the electric-field vector aligned parallel to the  $\mathbf{x}$ ,  $\mathbf{y}$ , and  $\mathbf{z}$  axis, where we assume  $\mathbf{x} \parallel \mathbf{a}$ ,  $\mathbf{y} \parallel \mathbf{b}$ , and  $\mathbf{z} \parallel \mathbf{c}$ .

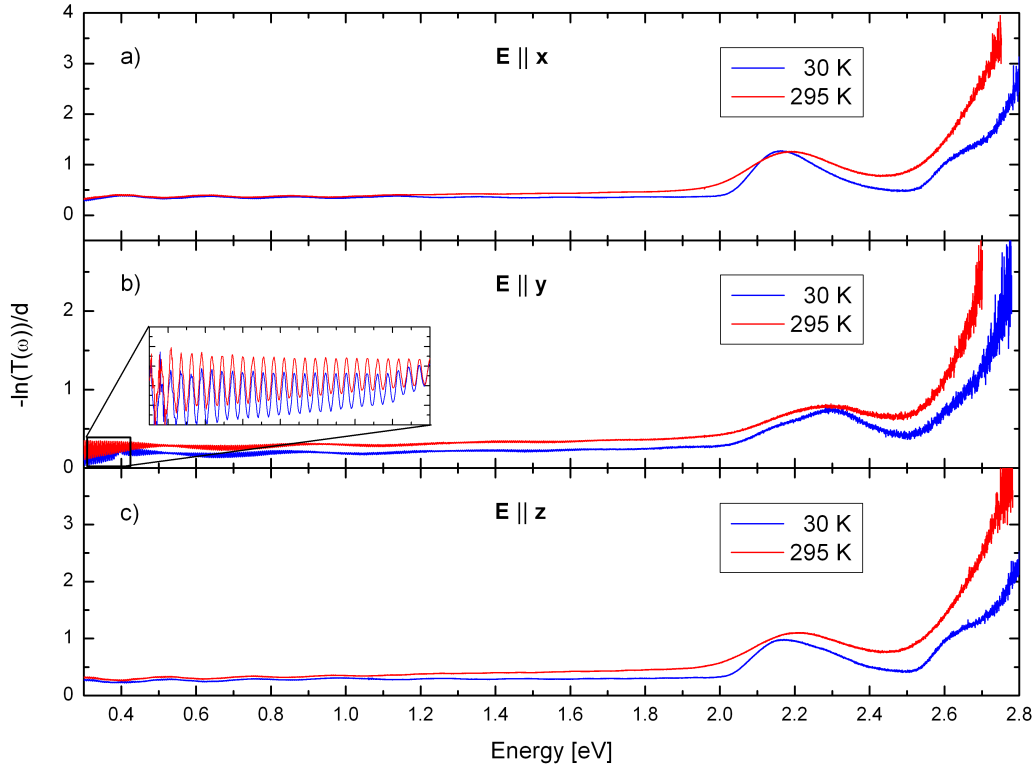


Figure 4.60:  $-\ln(T(\omega))/d$  of  $\text{MnWO}_4$  for  $\mathbf{E} \parallel \mathbf{x}$ ,  $\mathbf{E} \parallel \mathbf{y}$ , and  $\mathbf{E} \parallel \mathbf{z}$  for  $T = 30 \text{ K}$  (blue) and  $T = 295 \text{ K}$  (red).

The transmittance at  $T = 30$  K and  $T = 295$  K for  $\mathbf{E} \parallel \mathbf{x}$ ,  $\mathbf{E} \parallel \mathbf{y}$ , and  $\mathbf{E} \parallel \mathbf{z}$  is shown in Fig. 4.60 a) - c) in good agreement with the results of Ejima *et al.* [208] and Nogami *et al.* [209] who measured the absorption coefficient at room temperature. But, in contrast to them we determine the polarization dependence of the transmittance between 0.3 eV and 2.8 eV completely and measured the transmittance for two different temperatures. The values of the absorption coefficient given by Ejima *et al.* [208] were measured with unpolarized light, whereas Nogami *et al.* [209] determine the value of the absorption coefficient only for  $\mathbf{E} \perp \mathbf{b}$ .

The oscillations of the data below 1.0 eV shown in the inset of Fig. 4.60 b) correspond to so-called FABRY-PEROT FRINGES. These fringes result from multiple reflections at both coplanar faces of the sample. The behavior above 2.5 eV describes the onset of excitations across the gap. In the following, we are interested in the excitations around 2.25 eV.

In order to compare the results of the cluster-model calculation with the experimental data, we have to determine the optical conductivity from the transmittance measurements. Therefore, we extrapolate the reflectance from  $8000 \text{ cm}^{-1}$  ( $\sim 1$  eV) up to  $24000 \text{ cm}^{-1}$  ( $\sim 2.9$  eV) by using the conventional Drude-Lorentz fit of  $\text{MnWO}_4$  for  $\mathbf{E} \parallel \mathbf{b}$ , presented in the last section. Using the relation between  $R(\omega)$ ,  $T(\omega)$ ,  $\phi(\omega)$ ,  $n(\omega)$ , and  $k(\omega)$  in Ref. [207] we can derive the following expressions<sup>21</sup>

$$\begin{aligned} \phi(\omega) &= \frac{-1 + 2R(\omega) - R(\omega)^2 + \sqrt{(1 - 2R(\omega) + R(\omega)^2)^2 + 4R(\omega)^2T(\omega)^2}}{2R(\omega)^2T(\omega)}, \\ k(\omega) &= \frac{1}{4\pi d\omega} \ln \left( \frac{1}{\phi(\omega)} \right), \\ n(\omega) &= \frac{-1 - R(\omega) - \sqrt{-k(\omega)^2 + 4R(\omega) + 2k(\omega)^2R(\omega) - k(\omega)^2R(\omega)^2}}{-1 + R(\omega)}, \\ \sigma_1(\omega) &= 4\pi\epsilon_0\omega c \cdot 10^2 \cdot n(\omega) \cdot k(\omega), \end{aligned} \quad (4.3.8)$$

which determine the optical conductivity. ( $\epsilon_0$  indicates the vacuum permittivity). Here  $\phi(\omega)$  represents an abbreviation  $\phi(\omega) = \exp(-4\pi kd/\lambda) = \exp(-\alpha d)$ ,  $k(\omega)$  the extinction coefficient<sup>22</sup> and  $n(\omega)$  the real part of the complex refraction index. The calculation of the optical conductivity requires the determination of the thickness  $d$  of the sample. The observation of fringes with a frequency distance of  $\Delta\omega$  allows the calculation of the thickness by using the equation

$$d = \frac{1}{2 \cdot n \cdot \Delta\omega}, \quad [d] \text{ in cm, if } [\Delta\omega] \text{ in cm}^{-1}. \quad (4.3.9)$$

We obtain a thickness of  $d = 54 \text{ }\mu\text{m}$ , where we set  $n \equiv n(\omega = 2553 \text{ cm}^{-1})$ . Due to the absence of fringes for  $\mathbf{E} \parallel \mathbf{x}$  and  $\mathbf{E} \parallel \mathbf{z}$  we cannot determine the thickness of the crystal

---

<sup>21</sup>In order to get  $\sigma_1(\omega)$  in units of  $[\Omega^{-1} \text{ m}^{-1}]$  the frequency  $\omega$  has to be given in units of  $\text{cm}^{-1}$ .

<sup>22</sup>Here, the thickness  $d$  of the sample has to be given in cm.

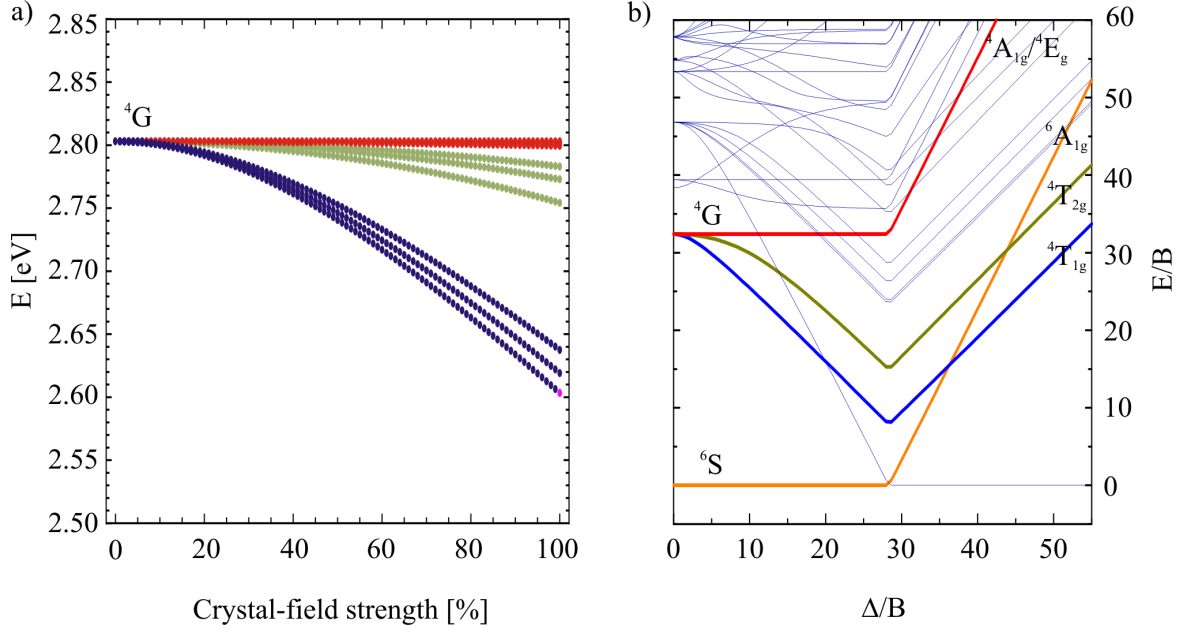


Figure 4.61: a) The splitting of the  ${}^4G$  multiplet of the free  $\text{Mn}^{2+}$  ion with increasing crystal-field strength within a point-charge model in  $\text{MnWO}_4$ . The energies are normalized to the ground state energy. Note, the crystal eigenstates are 4-fold degenerate. The calculation parameters are given as  $F_{\text{Mn}^{2+}}^2 = 8.308$  eV,  $F_{\text{Mn}^{2+}}^4 = 5.161$  eV,  $\langle r^2 \rangle_{\text{Mn}^{2+}} = 0.450$   $\text{\AA}^2$ ,  $\langle r^4 \rangle_{\text{Mn}^{2+}} = 0.466$   $\text{\AA}^4$ . b) Tanabe-Sugano diagram for a  $d^5$  configuration in a cubic environment [147] with Racah parameters  $B = 859$   $\text{cm}^{-1}$  and  $C = 3848$   $\text{cm}^{-1}$ . The parameter  $\Delta$  indicates the strength of the crystal field in units of the Racah parameter  $B$ .

used for the transmittance measurements for  $\mathbf{E} \parallel \mathbf{x}$  and  $\mathbf{E} \parallel \mathbf{z}$ . As shown in equation (4.3.8) the absolute value of the optical conductivity scales linear with the thickness of the sample. In the determination of the optical conductivity we set  $d = 54$   $\mu\text{m}$  for all polarization directions.

In order to identify the excitations at about 2.25 eV, we start with the free  $\text{Mn}^{2+}$  ion without crystal field. Here the five  $3d$  electrons occupy the  ${}^6S$  ground state. The higher lying multiplets are  ${}^4G$ ,  ${}^4F$ ,  ${}^4D$ ,  ${}^4P$ ,  ${}^2I$ ,  ${}^2H$ ,  ${}^2G_1$ ,  ${}^2G_2$ ,  ${}^2F_1$ ,  ${}^2F_2$ ,  ${}^2D_1$ ,  ${}^2D_2$ ,  ${}^2D_3$ ,  ${}^2P$ ,  ${}^2S$ . In the next step we include the effects of the crystal field within a point-charge model using the structural data reported by Lautenschläger *et al.* [195]. Furthermore we neglect the spin-orbit coupling as well as the hybridization. The  ${}^6S$  ground state, with  $L = 0$ , is not degenerate concerning the angular momentum and therefore no crystal-field splitting of this energy level occurs. In addition Hund's first rule is not broken and we have no mixing between different multiplets in the ground state, because there is only one  $S = 5/2$  multiplet. Therefore, all dipole transitions between the ground state and the excited states are forbidden. The site symmetry at the Mn site is  $C_2$

Nr. excited state	MnWO <sub>4</sub> point-charge model	MnO point-charge model
1	2.60 (4)	2.57 (12)
2	2.62 (4)	
3	2.64 (4)	
4	2.75 (4)	2.76 (12)
5	2.77 (4)	
6	2.78 (4)	
7	2.80 (12)	2.80 (12)

Table 4.19: Comparison of energies in eV of the lowest crystal-field transitions within a point-charge model below 3 eV in MnO and MnWO<sub>4</sub> between the ground state and the excited states. The values in brackets indicate the degree of degeneracy.

[196]. Lowering the symmetry from  $O_h$  to  $C_2$ , the  ${}^6A_{1g}$  level, which shows six-fold spin degeneracy, is not split. In addition, performing a group-theoretical analysis analogous to the procedure described in section “4.1 Crystal-Field Excitations in VOCl” we find no transition which is forbidden by symmetry arguments. As shown in Fig. 4.61 a) the three lowest excited eigenstates belong to the cubic  ${}^4T_{1g}$  state. Due to the reduced site-symmetry ( $C_2$ ) at the Mn site in MnWO<sub>4</sub> the cubic eigenstates show a further splitting. The energetic higher lying excited eigenstates belong to the cubic  ${}^4T_{2g}$  and  ${}^4A_{1g}/{}^4E_g$  states, respectively.

Furthermore, as shown in Fig. 4.61 a) and Tab. 4.19, the pure crystal-field splitting within a point-charge model without hybridization is very weak in MnWO<sub>4</sub>. In order to appraise these results we compare the strength of the crystal-field splitting with crystal-field transitions in MnO [210–217]. In the antiferromagnetic transition-metal monoxide MnO ( $T_N = 118$  K) the Mn<sup>2+</sup> ions are octahedrally coordinated by six O<sup>2-</sup> ions with point-group symmetry  $O_h$  at the Mn site. The crystal structure of MnO at 295 K is rocksalt (space group  $Fm\bar{3}m$ ) [218] with lattice parameter  $a = 4.4457(2)$  Å [219]. Within a single-particle picture, the  $e_g$  and the  $t_{2g}$  states in MnO are occupied with electrons whose spins are aligned parallel to each other. Thus, all dipole transitions between these crystal-field eigenstates are forbidden by the spin selection rule<sup>23</sup>. As mentioned in section “4.1.1. Group-Theoretical Considerations” this selection rule can be relaxed by taking into account spin-orbit coupling. Additionally, if we excite two spin-carrying modes simultaneously with total spin equal to zero, we can avoid the spin selection rule. For instance a spin-forbidden orbital excitation may gain a finite spectral weight by the simultaneous excitation of a magnon, giving rise to a so-called magnon-exciton sideband. We will discuss a possible contribution of this mechanism to the optical conductivity at the end of this section.

<sup>23</sup>The exchange splitting between the crystal-field eigenstates of different spin directions is 4.5 eV [220].

Nr. excited state	[210] calc.	[211] calc.	[212] EELS	[216] EELS	[217] EELS	[226] EELS	[213] optic	[214] optic	[215] optic
1	2.01	2.31	2.13	2.2	2.2	2.16	2.03	2.1	1.97
2	2.56	2.93	2.4	2.9	2.8	2.86	2.55	2.6	2.51
3	2.94		2.82				2.97	2.95	2.94
4	2.95								

Table 4.20: Comparison of energies in eV of the lowest crystal-field transitions below 3 eV in MnO between the ground state and the excited states.

As shown in Tab. 4.19, there are only small differences in the excitation energies between MnO and  $\text{MnWO}_4$ . Furthermore, in MnO the levels show a higher degeneracy (12 fold) than in  $\text{MnWO}_4$ . This is caused by the high point-group symmetry ( $O_h$ ) at the Mn site in MnO where all Mn-O bonds have the same length (2.2229 Å). In  $\text{MnWO}_4$ , the bond lengths between the  $\text{Mn}^{2+}$  ion and the surrounding ligands varies between 2.0988 Å and 2.2717 Å. Therefore, we expect only small differences between the strength of the crystal-field splitting in  $\text{MnWO}_4$  and MnO. Within the point-charge model we find a splitting of  $10Dq = 0.39$  eV for MnO in contrast to  $\text{MnWO}_4$  where we find a value of  $10Dq = 0.36$  eV if we assume a cubic point group symmetry around the  $\text{Mn}^{2+}$  ion. But, for MnO the strength of the crystal-field splitting between the  $e_g$  and the  $t_{2g}$  states has been determined to be between 0.7 and 1.25 eV [211, 213–215, 220–224]. This discrepancy<sup>24</sup> is caused by the inaccuracy of the point-charge model, which neglects the hybridization as well as the spin-orbit coupling.

Comparing the excitation energies for MnO calculated within a point-charge model with those determined by cluster calculations [210, 211], optical-absorption spectroscopy (optic) [213–215] and electron-energy-loss spectroscopy (EELS) [212, 216, 217], see Tab. 4.20, we find remarkable reductions of roughly 0.37 - 0.6 eV. The reduction may be caused by the hybridization, which increases the strength of the effective crystal-field and leads to a reduction of the energetic distance between the ground state and the higher lying excited states, as shown in Fig. 4.61 b). The values of the lowest crystal-field transitions in MnO are in good agreement with those reported for other compounds including a  $\text{Mn}^{2+}$  ion such as  $\text{Mn}_2\text{SiO}_4$  [227] (2.07 eV, 2.53 eV, 2.76 eV, 2.95 eV),  $\text{ZnGa}_2\text{S}_4:\text{Mn}^{2+}$  [228] (2.32 eV, 2.55 eV, 2.66 eV) and  $\text{MnF}_2$  [229] (2.38 eV, 2.95 eV, 3.10 eV). Therefore, we expect that the excitations around 2.2 eV observed in  $\text{MnWO}_4$  belong also to crystal-field transitions similar to MnO. But in order to describe these excitations, see Fig. 4.60, we have to take the spin-orbit coupling as well as the hybridization into account by using the cluster-model calculation described in the second chapter:

<sup>24</sup>Ghiringhelli *et al.* [225] report of a crystal-field splitting of only 0.5 eV and 1.0 eV depending on the theory which is being used for the determination of the crystal-field splitting.

parameter	$3d^5$ configuration	$3d^6$ configuration	$3d^7$ configuration
$F_{dd}^2$ (Mn)	8.750 eV	8.750 eV	8.750 eV
$F_{dd}^4$ (Mn)	5.166 eV	5.166 eV	5.166 eV
$\langle r^2 \rangle_{Mn}$	0.452 Å <sup>2</sup>	0.452 Å <sup>2</sup>	0.452 Å <sup>2</sup>
$\langle r^4 \rangle_{Mn}$	0.475 Å <sup>4</sup>	0.475 Å <sup>4</sup>	0.475 Å <sup>4</sup>
$\zeta_{Mn}$	40.0 meV	40.0 meV	40.0 meV
$\langle r^2 \rangle_{O,2p^5}$	0.000 Å <sup>2</sup>	0.000 Å <sup>2</sup>	0.000 Å <sup>2</sup>
$\zeta_{O,2p^5}$	0.0 meV	0.0 meV	0.0 meV
$F_{O,2p^4}^2$	0.000 eV	0.000 eV	0.000 eV
$\langle r^2 \rangle_{O,2p^4}$	0.000 Å <sup>2</sup>	0.000 Å <sup>2</sup>	0.000 Å <sup>2</sup>
$\zeta_{O,2p^4}$	0.0 meV	0.0 meV	0.0 meV

Table 4.21: Parameters used in the cluster-model calculation for MnWO<sub>4</sub>.

The cluster used in the cluster-model calculation for MnWO<sub>4</sub> consists of a Mn ion with  $3d^5$  electronic configuration and six oxygen ( $2p^6$ ) ions around forming a distorted octahedron. The single-excited configurations contain a Mn ion with ( $3d^6$ ) electronic configuration and a hole on one of the oxygen ligands. The double-excited configurations include a further electron on the Mn site ( $3d^7$ ) and a further hole on the ligand sites. Here, we have to distinguish between doubly-occupied ligands with  $2p^4$  configuration and two singly occupied sites  $\{2p^5, 2p^5\}$ . Altogether we have 28 configurations, and the size of the Hamilton matrix is  $177156 \times 177156$ . As mentioned in section “4.1 Crystal-Field Excitations in VOCl”, the interaction between two different configurations is described by the tight-binding operator. If the hopping of electrons between ions passes through the central transition-metal ion, we set the appropriate contribution of the tight-binding operator equal to zero and the involved configurations do not interact with each other. Due to the similarities between MnO and MnWO<sub>4</sub> mentioned above, we use for the cluster-model calculation of MnWO<sub>4</sub> the model parameters described by van Elp *et al.* [210] for MnO which are shown in Tab. 4.21. Additionally, we set the hopping integrals to  $pd\sigma = 1.3$  eV,  $pd\pi = -0.6$  eV,  $pp\sigma = -0.55$  eV, and  $pp\pi = 0.15$  eV. In contrast to van Elp *et al.* [210] we set the Hubbard U at the Mn site to  $U_{Mn} = 7.5$  eV ( $U_O = 0.0$  eV) and reduce the charge-transfer energy to  $\Delta_{Mn-O} = 3.5$  eV.

The results of the cluster-model calculation are shown in Fig. 4.62 where the real part of the optical conductivity  $\sigma(\omega)$  was calculated by using the Kubo-Greenwood formula (2.11.10), with damping set to  $\sim 112$  meV ( $900$  cm<sup>-1</sup>) for each excitation. The direction dependence of the optical conductivity was determined analogous to the procedure presented in section “4.1 Crystal-Field Excitations in VOCl”. As shown in Fig. 4.62, the green and dark yellow curves describe the positions of the transitions quite well although we use only one set of calculation parameters for all valid configurations, i.e. the parameters for the  $d^5$ , the  $d^6\bar{L}$ , and the  $d^7\bar{L}^2$  configurations<sup>25</sup> are the same, see Tab. 4.21.

<sup>25</sup>The expression  $\bar{L}$  represents a hole in the oxygen ligands.

As shown in Fig. 4.62, the absolute value of the optical conductivity for  $\mathbf{E} \parallel \mathbf{y}$  differ by a factor of 2 from the values determined for  $\mathbf{E} \parallel \mathbf{x}$  and  $\mathbf{E} \parallel \mathbf{z}$ . Note, that we do not know the thickness of the sample used for the transmittance measurements for  $\mathbf{E} \parallel \mathbf{x}$  and  $\mathbf{E} \parallel \mathbf{z}$  exactly. As mentioned above, we set the thickness to  $d = 54 \mu\text{m}$  for all polarization directions which may cause the difference in the absolute value of the optical conductivity. Furthermore, the small differences in the line shape of the optical conductivity are partially caused by using only one value for the damping for all excitations. However, we cannot describe the polarization dependence of the excitations between 2.1 eV and 2.5 eV which may be caused by neglecting the contribution of energetically higher lying p-states at the Mn site to the optical conductivity, see section “4.1.2 Cluster-Model Calculations”. But, as indicated by the black triangles in Fig. 4.62 c), we can describe the positions of all peaks.

We continue the analysis of the cluster-model calculation by making use of the advantages of the calculation technique: The usage of the Racah-Wigner algebra allows a detailed analysis of the ground and the excited states depending on the angular momenta. By determining the square of the normalized eigenvectors, we get the contribution of each angular momentum, i.e. each multiplet, to the appropriate eigenstate. We will start the analysis by looking at the contributions of the different configurations, used in the cluster-model calculation, to the cluster eigenstates: As shown in Tab. 4.22, the six-fold degenerate ground state is predominantly formed by the ground configuration  $\{3d^5, 2p^6, 2p^6, 2p^6, 2p^6, 2p^6, 2p^6\}$ . But, we find a remarkable contribution (23 %) of the single-excited configurations to the ground state. The contributions of the double-excited configurations to the low-lying eigenstates are small and we can neglect them in the further analysis.

As shown in Tab. 4.22 and Tab. 4.23 the ground state is predominantly formed by the  ${}^6S$  multiplet as suggested by the crystal-field analysis, mentioned above. As shown in Tab. 4.23, the energetically higher lying eigenstates represent crystal-field excitations. The excited states below 3 eV are formed predominantly by the  ${}^4G$  multiplet (in good agreement with the results of the point-charge analysis) and contain a large contribution ( $\approx 33$  %) of single-excited configurations. Additionally, the eigenstates below 2.5 eV show a remarkable admixture of the  ${}^4P$  multiplet which is caused by two facts: Within a point-charge model the  ${}^4P$  multiplet is next to the  ${}^4G$  multiplet and the crystal-field operator mixes multiplets which have the same spin. Comparing these eigenstates with the results of the point-charge model shown in Fig. 4.61, we associate the eigenstates below 2.5 eV with the cubic  ${}^4T_{1g}$  state which shows a further splitting due to the reduced point-group symmetry in  $MnWO_4$  at the Mn site. The excitations between 2.6 eV and 2.7 eV show an increased contribution of the  ${}^4G$  and of the energetically higher lying multiplets with spin (3/2) but no admixture of the  ${}^4P$  multiplet. This behavior is in good agreement with the results of the point-group analysis as well and represents the cubic  ${}^4T_{2g}$  state. Finally, the eigenstates between 2.7 eV and 3.0 eV belong to the cubic  ${}^4A_{1g}/{}^4E_g$ . This behavior is quite similar to the results reported for MnO [210–217].

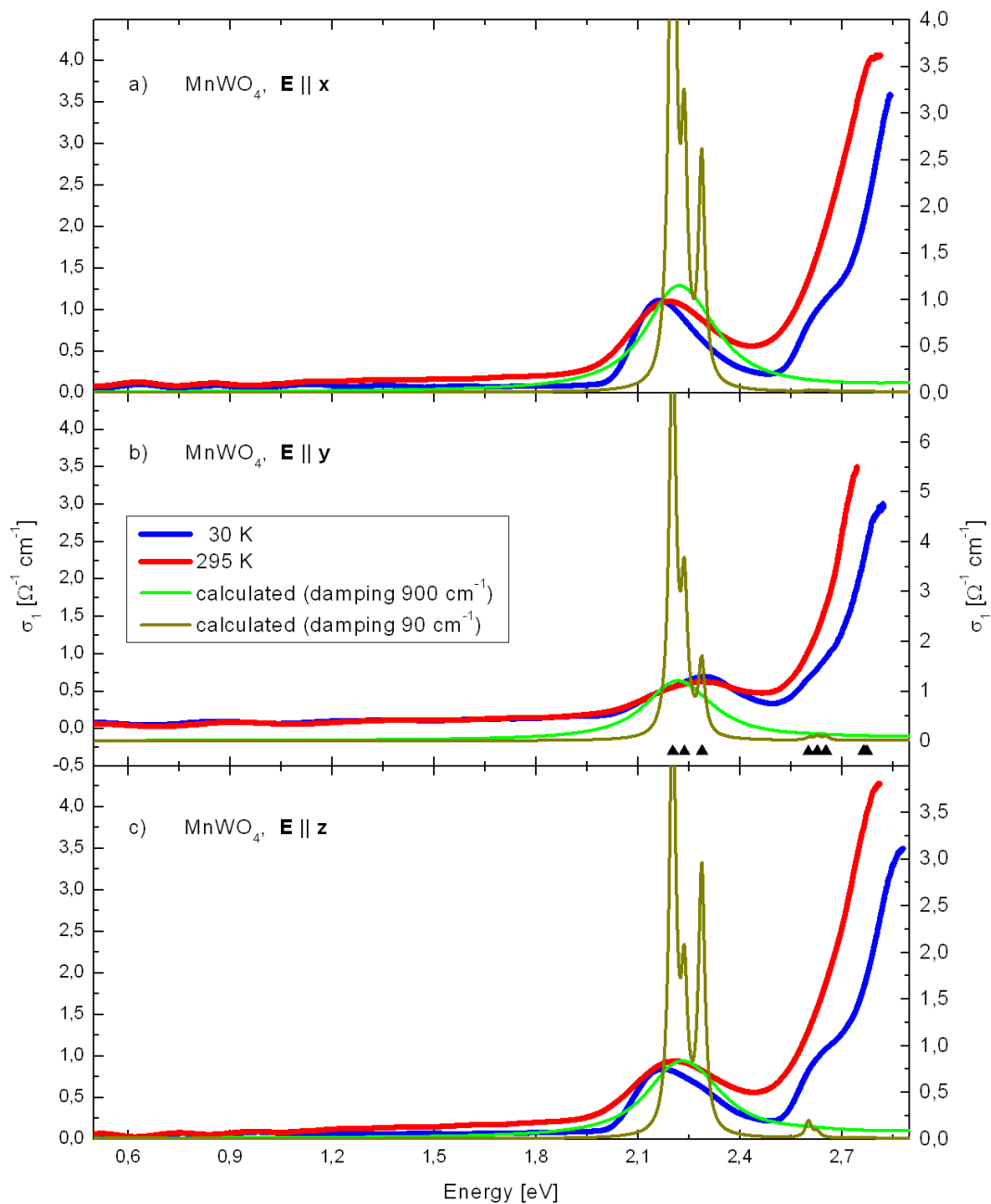


Figure 4.62: Optical conductivity of  $\text{MnWO}_4$  determined from transmittance and reflectance measurement for a)  $\mathbf{E} \parallel \mathbf{x}$ , b)  $\mathbf{E} \parallel \mathbf{y}$ , and c)  $\mathbf{E} \parallel \mathbf{z}$  for  $T = 30 \text{ K}$  (blue) and  $T = 295 \text{ K}$  (red). The calculated optical conductivity, multiplied by a factor of  $3.5 \cdot 10^4$ , is shown for two different values of the damping factor:  $900 \text{ cm}^{-1}$  (green line) and  $90 \text{ cm}^{-1}$  (dark yellow line). The black triangles indicate the calculated excitation energies shown in Tab. 4.22.

Nr.:	absolute energies [eV]	excitation energies [eV]	ground configuration [%]	first order [%]	second order [%]
1	-7.6023 (6)	0.0000	75.7	23.0	1.5
2	-5.3990 (2)	2.2033	64.3	33.4	2.1
3	-5.3988 (2)	2.2035	64.3	33.4	2.1
4	-5.3647 (2)	2.2375	64.3	33.4	2.0
5	-5.3645 (2)	2.2377	64.3	33.4	2.0
6	-5.3135 (2)	2.2888	64.5	33.2	2.0
7	-5.3132 (2)	2.2891	64.5	33.2	2.0
8	-5.0005 (2)	2.6018	64.3	33.4	2.1
9	-5.0000 (2)	2.6023	64.3	33.4	2.1
10	-4.9745 (2)	2.6277	64.2	33.6	2.0
11	-4.9736 (2)	2.6287	64.1	33.6	2.0
12	-4.9489 (2)	2.6534	64.4	33.4	2.0
13	-4.9484 (2)	2.6539	64.4	33.4	2.0
14	-4.8381 (2)	2.7641	65.8	32.2	1.7
15	-4.8378 (2)	2.7644	65.8	32.2	1.7
16	-4.8330 (2)	2.7693	65.8	32.0	1.7
17	-4.8327 (2)	2.7695	65.8	32.2	1.7
18	-4.8277 (4)	2.7746	65.8	32.0	1.7
19	-4.5040 (2)	3.0983	61.2	35.6	3.3

Table 4.22: Results of the cluster-model calculation for  $MnWO_4$  at  $T = 295$  K. The values in brackets indicate the degree of degeneracy. Here, we assume that two energies belong to a degenerate eigenstate if they differ by less than 0.2 meV. The last two columns represent the sum of all configurations of the appropriate excitation order. The column “first order” represents the sum of all single-excited and the column “second order” the sum of all double-excited configurations. Discrepancy from 100 % are caused by roundoff errors.

excitation energy [eV]	multiplet Mn-ion	contributions [%]
0.0000	${}^6S$	75.71
2.2033	${}^4G, {}^4P$	40.86, 22.41
2.2035	${}^4G, {}^4P$	40.87, 22.41
2.2375	${}^4G, {}^4P$	41.94, 21.09
2.2377	${}^4G, {}^4P$	41.95, 21.09
2.2888	${}^4G, {}^4P$	42.15, 21.43
2.2891	${}^4G, {}^4P$	42.15, 21.44
2.6018	${}^4G, {}^4F, {}^4D$	54.93, 6.03, 3.27
2.6023	${}^4G, {}^4F, {}^4D$	54.88, 6.02, 3.30
2.6277	${}^4G, {}^4F, {}^4D$	54.79, 5.56, 3.72
2.6287	${}^4G, {}^4F, {}^4D$	54.71, 5.56, 3.79
2.6534	${}^4G, {}^4F, {}^4D$	56.18, 4.78, 3.37
2.6539	${}^4G, {}^4F, {}^4D$	56.15, 4.78, 3.39
2.7641	${}^4G$	65.66
2.7644	${}^4G$	65.69
2.7693	${}^4G$	65.31
2.7695	${}^4G$	65.34
2.7746	${}^4G$	65.21
3.0983	${}^2I, {}^2H, {}^2F_1, {}^2D_1$	27.20, 13.86, 9.71, 3.06, 6.19

Table 4.23: Contributions of the different multiplets of the ground configuration of  $\text{MnWO}_4$  to the ground and the excited state for  $T = 295$  K. Here, only those contributions are shown which are greater than 2 %. Due to the sake of simplicity we do not show the different contributions of the several total angular momenta  $\mathfrak{J} = \mathfrak{L} + \mathfrak{S}$ , and the total spin  $\mathfrak{S}$ , see section “2.3.2 Basis Functions within the Russell- Saunders-coupling scheme”.

Nr.:	absolute energies [eV]	excitation energies [eV]	ground configuration [%]	first order [%]	second order [%]
1	-7.4540 (6)	0.0000	78.5	20.4	1.2
2	-5.2482 (2)	2.2058	68.0	30.0	1.5
3	-5.2477 (4)	2.2064	68.0	30.2	1.5
4	-5.2457 (4)	2.2083	67.9	30.2	1.5
5	-5.2442 (2)	2.2098	67.9	30.6	1.5
6	-4.8190 (2)	2.6350	68.0	30.0	1.5
7	-4.8151 (4)	2.6389	68.0	30.2	1.9
8	-4.8080 (6)	2.6460	67.9	30.4	1.7
9	-4.6319 (4)	2.8221	70.0	28.6	1.5
10	-4.6197 (8)	2.8344	69.9	28.8	1.5

Table 4.24: Results of the cluster-model calculation for MnO at  $T = 295$  K below 3 eV. The values in brackets indicate the degree of degeneracy. Here, we assume that two energies belong to a degenerate eigenstate if they differ by less than 0.2 meV. The last two columns represent the sum of all configurations of the appropriate excitation order. The column “first order” represents the sum of all single-excited and the column “second order” the sum of all double-excited configurations. Discrepancy from 100 % are caused by roundoff errors.

In order to classify the results of the cluster-model calculation for MnWO<sub>4</sub> we perform a cluster-model calculation for MnO as well. The results for MnO are shown in Tab. 4.24. Note, that in contrast to a previous cluster-model calculation done by van Elp *et al.* [210] we include the spin-orbit coupling resulting in a further splitting of the eigenstates see Tab. 4.25. Comparing the results for MnWO<sub>4</sub> with those for MnO, we find an enhanced degree of degeneracy for most of the eigenstates. This is caused by the fact, that the point-group symmetry on the Mn site in MnWO<sub>4</sub> is lower ( $C_2$ ) than in MnO ( $O_h$ ) resulting in a further splitting of the cubic  ${}^4T_{1g}$  and the  ${}^4T_{2g}$  eigenstates. Additionally, we find that the contributions of the different configurations to the eigenstates are similar to those for MnWO<sub>4</sub>, see Tab. 4.22. Especially, the admixture of the single-excited configurations to the ground state is comparable to the behavior in MnWO<sub>4</sub>.

In contrast to MnO we have no inversion symmetry in MnWO<sub>4</sub> on the Mn site, thus parity is not a good quantum number. Within a point-charge model all dipole-transitions between the ground state and the higher lying eigenstates are forbidden due to the spin selection rule, as mentioned above. But, the inclusion of spin-orbit coupling removes the spin selection rule and we gain a finite spectral weight for the electric dipole transitions.

Nr.:	with spin-orbit	without spin-orbit
1	0.0000 (6)	0.0000 (6)
2	2.2033 (2)	2.2033 (4)
3	2.2035 (2)	
4	2.2375 (2)	2.2375 (4)
5	2.2377 (2)	
6	2.2888 (2)	2.2888 (4)
7	2.2891 (2)	
8	2.6018 (2)	2.6023 (4)
9	2.6023 (2)	
10	2.6277 (2)	2.6279 (4)
11	2.6287 (2)	
12	2.6534 (2)	2.6528 (4)
13	2.6539 (2)	
14	2.7641 (2)	2.7641 (4)
15	2.7644 (2)	
16	2.7693 (2)	2.7692 (4)
17	2.7695 (2)	
18	2.7746 (4)	2.7743 (4)
19	3.0983 (2)	3.1030 (2)

Table 4.25: Results of the cluster-model calculation for  $\text{MnWO}_4$  at  $T = 295$  K depending on the spin-orbit coupling. The values in brackets indicate the degree of degeneracy. Here, we assume that two energies belong to a degenerate eigenstate if they differ by less than 0.2 meV.

In order to estimate the role of the spin-orbit coupling we repeat the cluster-model calculation described above and switch off the spin-orbit coupling. As shown in Tab. 4.25, we increase the degree of degeneracy by neglecting the spin-orbit coupling. But if we ignore the spin-orbit coupling the optical conductivity is equal to zero for all calculated frequencies. Thus, the spin-orbit coupling is essential for the description of the optical data. Additionally, we have no direct contribution of configuration-interaction effects to the optical conductivity.

Due to the fact, that we cannot describe strength and polarization dependence exactly, we cannot exclude contributions from simultaneous excitations of magnons. Tsuboi *et al.* [230] report of a very small contribution of the magnon sidebands in  $\text{MnF}_2$  to the absorption peak at roughly 520 nm representing the  ${}^6A_{1g} \rightarrow {}^4T_{1g}({}^4G)$  transition in  $\text{Mn}^{2+}$  ions. Sell *et al.* [231] determine the oscillator strength of these transitions to  $8.7 \cdot 10^{-12}$ - $7.1 \cdot 10^{-11}$ . Therefore, we think that the simultaneous excitations of magnons do not play an important role in the description of the optical conductivity in  $\text{MnWO}_4$ . Additionally, as mentioned in section “4.1 Crystal-Field Excitations in  $\text{VOCl}$ ”, spin-forbidden transitions can be quite strong if the energy of a spin-forbidden excitation is

comparable with that of spin-allowed transitions [141]. The spin-forbidden transition acquires intensity by “stealing” from e.g. a charge-transfer band (“intensity stealing”), if both excitations mix with each other. Here, the enhancement of the optical conductivity above  $\sim 2.5$  eV indicates the beginning of the charge-transfer band, which cannot be described by a single-cluster calculation. Furthermore, we neglect the contribution of energetically higher lying p-states at the Mn ion to the optical conductivity which are relevant for the description of the experimental data due to the broken inversion symmetry at the Mn site.

Summarizing our investigation, we can describe the positions of all excitations in the optical data by using a cluster-model calculation as described in the second chapter. By analyzing the dependence of the eigenstates on the ionic multiplets, we associate the features below 3 eV with crystal-field excitations similar to MnO,  $MnF_2$  [230, 231] and  $MnCl_2$  ( $MnBr_2$ ) [232]. Although we can not exclude a significant contribution of exchange processes between two  $Mn^{2+}$  ions to the measured optical conductivity because we consider only one  $Mn^{2+}$  ion in our cluster-model calculation, we think that we can neglect this mechanism due to the good agreement with other compounds including a  $Mn^{2+}$  ion [210–217, 220–224, 227–232].

## 4.4 Phonon modes of monoclinic $\text{BiB}_3\text{O}_6$

In this section we describe the phonon analysis of  $\text{BiB}_3\text{O}_6$  by using the generalized Drude-Lorentz model (4.3.6) presented in the previous section, and extend the results reported in our paper [237]. By comparing our data with room-temperature Raman and neutron data and first-principle calculations we can identify the fundamental phonon modes and achieve a good agreement with the results of the factor-group analysis.

Bismuth triborate,  $\text{BiB}_3\text{O}_6$ , is a polar, non-ferroelectric compound with outstanding nonlinear optical properties [233, 234]. The large optical nonlinearities open up a rich field of applications for frequency conversion of laser light via  $\chi^{(2)}$  and  $\chi^{(3)}$  processes, e.g. phase-matched second harmonic generation or optical parametric oscillation [235] and stimulated Raman scattering [236].

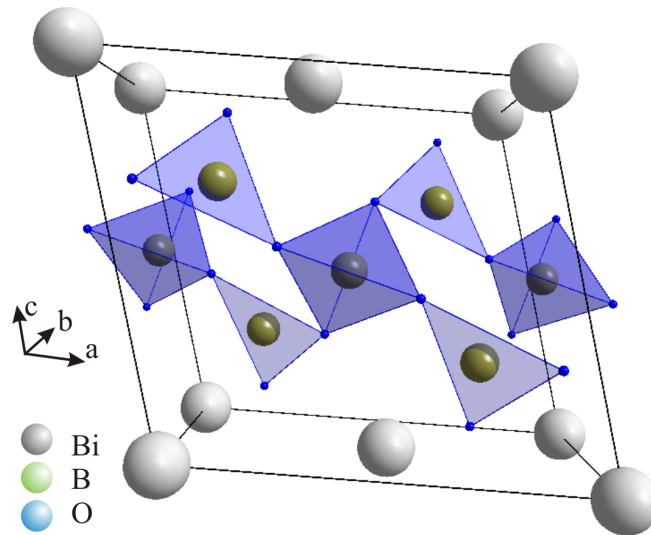


Figure 4.63: Crystal structure of  $\text{BiB}_3\text{O}_6$ .

The exceptional optical nonlinearities of  $\text{BiB}_3\text{O}_6$  have been attributed to the bonds of the  $[\text{BO}_3]$  units and to a lone-pair electron at the Bi ion [238]. Detailed studies of the lattice dynamics are required for a quantitative description of these bonds. Neither the bond-charge model<sup>26</sup> [238, 239], nor an ab-initio band structure calculation [240] yield a good description of these bonds. However, in both of these theories a strong influence of the bismuth-oxygen group, especially of the lone electron pair of the trivalent bismuth, is assumed to play a dominant role. Thus a detailed analysis of the lattice dynamics is required for a quantitative understanding of the nonlinear optical

<sup>26</sup>The bond-charge model regards a complex crystal as a combination of all constituent chemical bonds. A so-called multibond crystal can be decomposed into single bonds according to the chemical bonding structures of all involved atoms. Then, the physical properties of a crystal, i.e. the linear and nonlinear optical properties, can be ascribed to contributions from all contained chemical bonds.

properties. Infrared (IR) and Raman studies of the phonons are so far only available at room temperature [236, 241–244]. In particular, there is no polarization-dependent infrared study, but a polarization analysis is essential for an accurate determination of the phonon frequencies in monoclinic crystals [188].

Milky-colored, right-handed single crystals of  $\text{BiB}_3\text{O}_6$  were grown by P. Becker and L. Bohatý<sup>27</sup> using the top-seeded growth technique [244, 245]. The crystal structure with space group symmetry  $C2$  ( $C_2^3$ ) ( $a = 7.116(2) \text{ \AA}$ ,  $b = 4.993(2) \text{ \AA}$ ,  $c = 6.508(3) \text{ \AA}$ ,  $\beta = 105.62(3)^\circ$ ) consists of sheets of corner-sharing  $[\text{BO}_3]$  and  $[\text{BO}_4]$  units in a ratio of 2:1, see Fig. 4.63. These sheets are separated by sheets of six-fold coordinated Bi [246].

We performed reflectivity measurements [237] at  $T = 20 \text{ K}$  and  $300 \text{ K}$  in the spectral range of  $50\text{--}2500 \text{ cm}^{-1}$  at quasnormal incidence. The spectra were measured for different polarization angles on polished (010) and (100) surfaces of  $\text{BiB}_3\text{O}_6$ . As a reference we used an Au mirror. The variation of the polarization angle was realized by rotating the polarizer.

The investigation of the phonon spectra starts with the factor-group analysis [184], which yields the following irreducible representation for the space group  $C2$ ,

$$\Gamma_{\text{total}} = 14 A + 16 B, \quad (4.4.1)$$

with basis polynomials  $A = z$  and  $B = \{x, y\}$ . The three possible acoustic modes are represented by the following irreducible representation:

$$\Gamma_{\text{acoustic}} = 1 A + 2 B. \quad (4.4.2)$$

After subtraction of these three acoustic modes we obtain the IR-active modes:

$$\Gamma_{\text{IR}} = [14 A + 16 B] - [1 A + 2 B] = [13 A + 14 B]. \quad (4.4.3)$$

Due to the lack of a center of inversion,  $A$  and  $B$  modes are active both in Raman [242, 243] and in infrared spectroscopy

$$\Gamma_{\text{Raman}} = \Gamma_{\text{IR}} = [13 A + 14 B], \quad (4.4.4)$$

and we have no silent modes.

---

<sup>27</sup>Institute of Crystallography, University of Cologne, Zùlpicher Str. 49b, 50674 Cologne, Germany

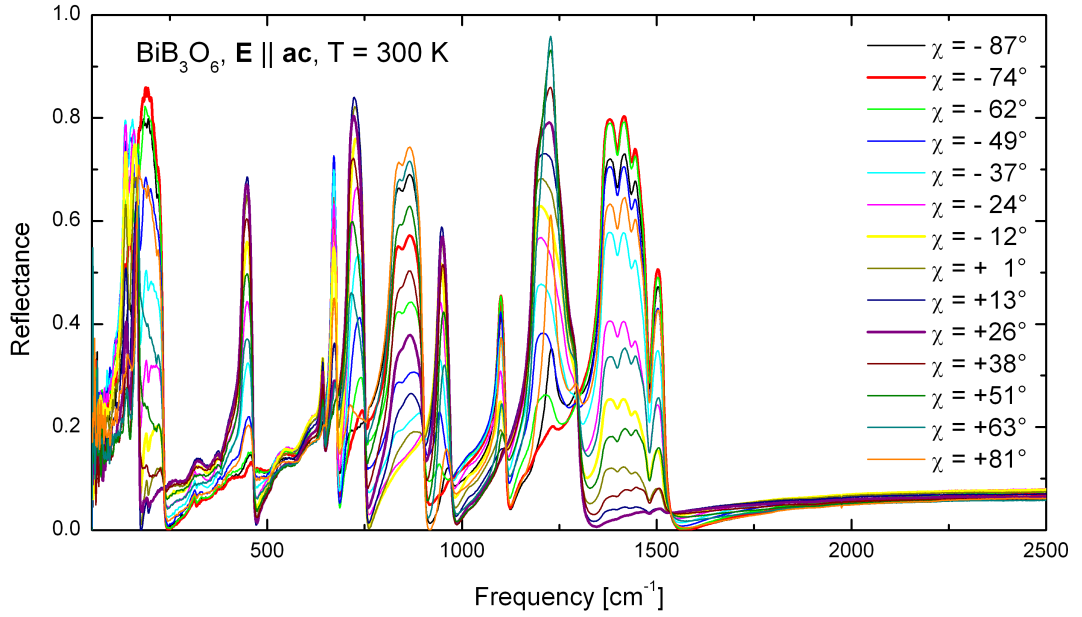


Figure 4.64: Reflectivity spectra of  $\text{BiB}_3\text{O}_6$  at  $T = 300$  K for 14 different angles.

Following the procedure described in the previous section, we decompose the tensor (4.3.5) of the linear dielectric response into a scalar  $\epsilon_b$  along the  $\mathbf{b}$  axis and a two-dimensional tensor  $\hat{\epsilon}_{ac}$  within the  $\mathbf{ac}$  plane. Note, that we assume  $\mathbf{y} \parallel \mathbf{b}$ ,  $\mathbf{z} \parallel \mathbf{c}$ , and  $\mathbf{x} \perp \mathbf{c}$  lying in the  $\mathbf{ac}$  plane, where  $\mathbf{a}$ ,  $\mathbf{b}$ , and  $\mathbf{c}$  are the crystallographic axes (see inset of Fig. 4.65 a). Since the  $\mathbf{b}$  axis is perpendicular to the  $\mathbf{ac}$  plane, the  $A$ -symmetry modes can be probed by measuring with the incident electric field  $\mathbf{E}$  parallel to the  $\mathbf{b}$  axis (e.g. on a (100) surface). Determining the  $B$ -symmetry modes requires the analysis of at least three polarization directions (with  $\mathbf{E} \parallel \mathbf{ac}$  plane on a (010) surface, see Fig. 4.64) because the angle between the  $\mathbf{a}$  and the  $\mathbf{c}$  axis deviates from  $90^\circ$ .

Using (4.3.7) we find an excellent description of the measured reflectivity, as shown in Fig. 4.65 and Fig. 4.66. In order to find phonon modes with smaller amplitude we measure additionally the FIR range ( $\omega < 700 \text{ cm}^{-1}$ ) at  $T = 20$  K. (The excitation below  $150 \text{ cm}^{-1}$  in the 20 K data are related to an artefact of the measurement.) The phonons extend up to almost  $1500 \text{ cm}^{-1}$  due to the small mass of the B ions. The fit parameters are listed in Tab. 4.26 and Tab. 4.27. In order to fit the 20 K reflectivity we use the fit parameters from the fit of the 300 K data above  $700 \text{ cm}^{-1}$ . In case of  $\mathbf{E} \parallel \mathbf{b}$ , where 13  $A$  modes are expected, we find 11 strong infrared modes and a series of weaker features. Most of the latter can be interpreted as multi-phonon excitations.

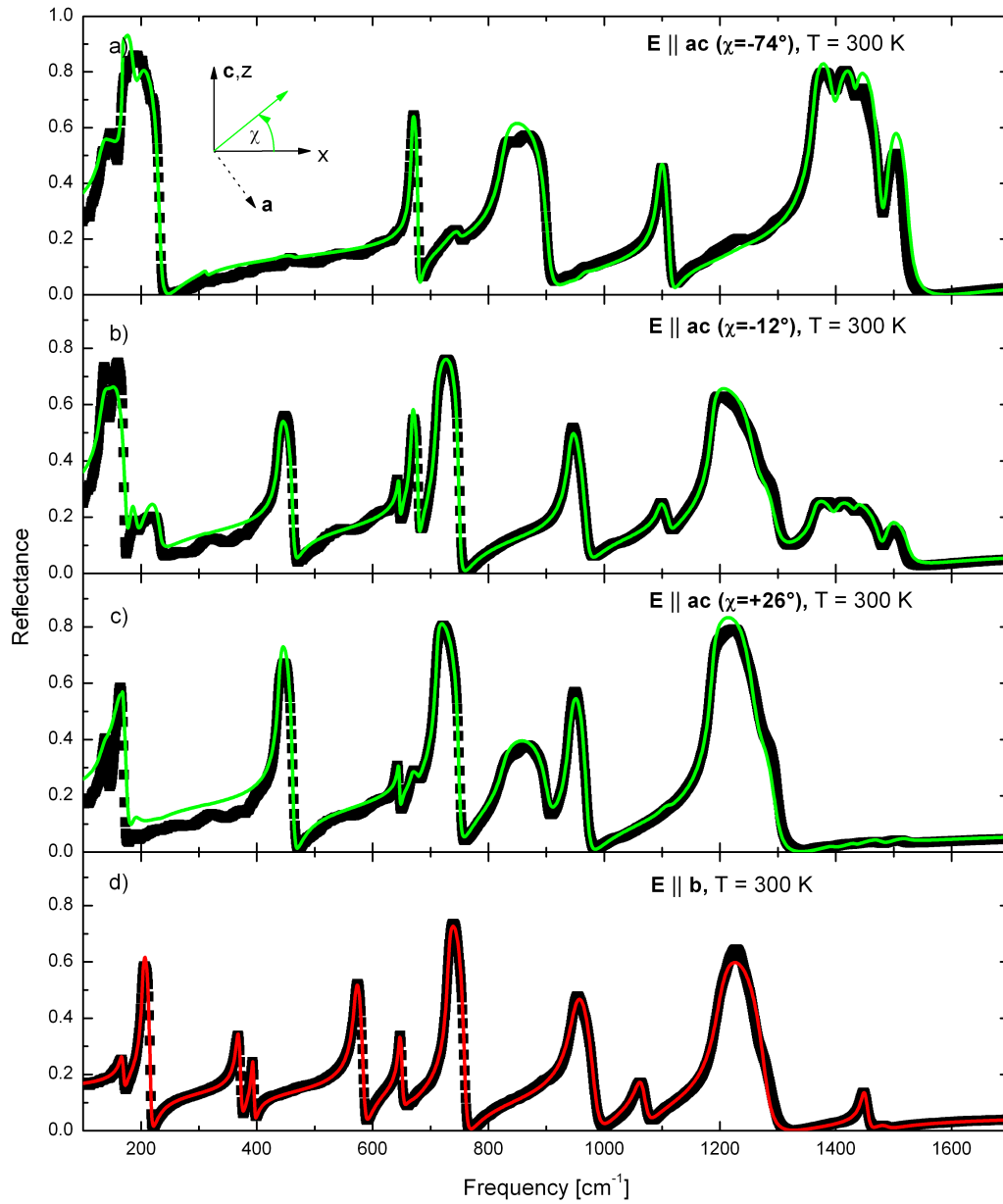


Figure 4.65: a) - c) Reflectivity spectra of  $\text{BiB}_3\text{O}_6$  at  $T = 300$  K for  $\mathbf{E} \parallel \mathbf{ac}$  plane at different polarization angles  $\chi$  (black) and fits using (4.3.7) (green). d) Reflectivity at  $T = 300$  K for  $\mathbf{E} \parallel \mathbf{b}$  (black), fit using (3.1.1) (red).

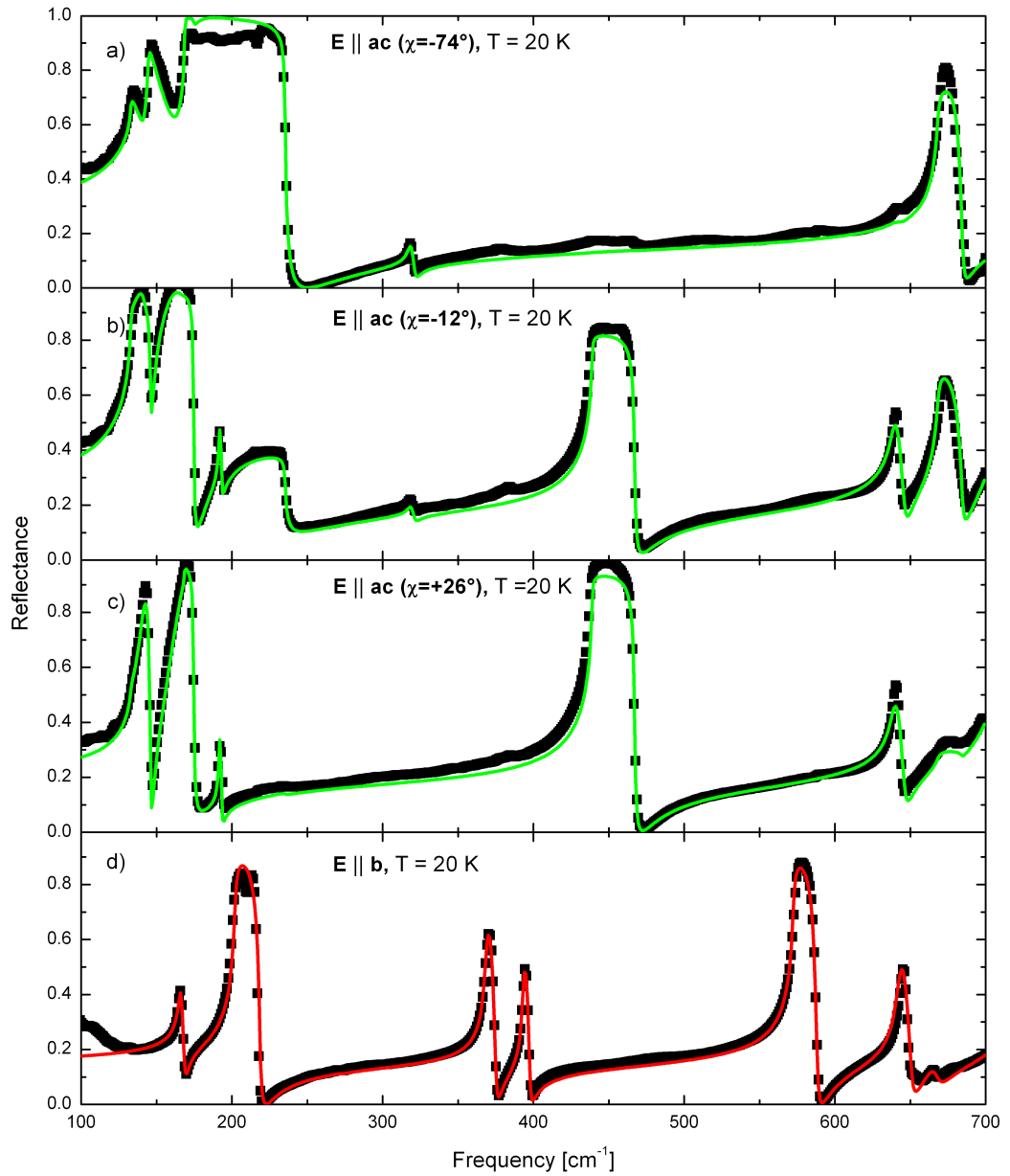


Figure 4.66: a) - c) Reflectivity spectra of BiB<sub>3</sub>O<sub>6</sub> at T = 20 K for  $\mathbf{E} \parallel \mathbf{ac}$  plane at different polarization angles  $\chi$  (black) and fits using (4.3.7) (green). d) Reflectivity at T = 20 K for  $\mathbf{E} \parallel \mathbf{b}$  (black), fit using (3.1.1) (red).

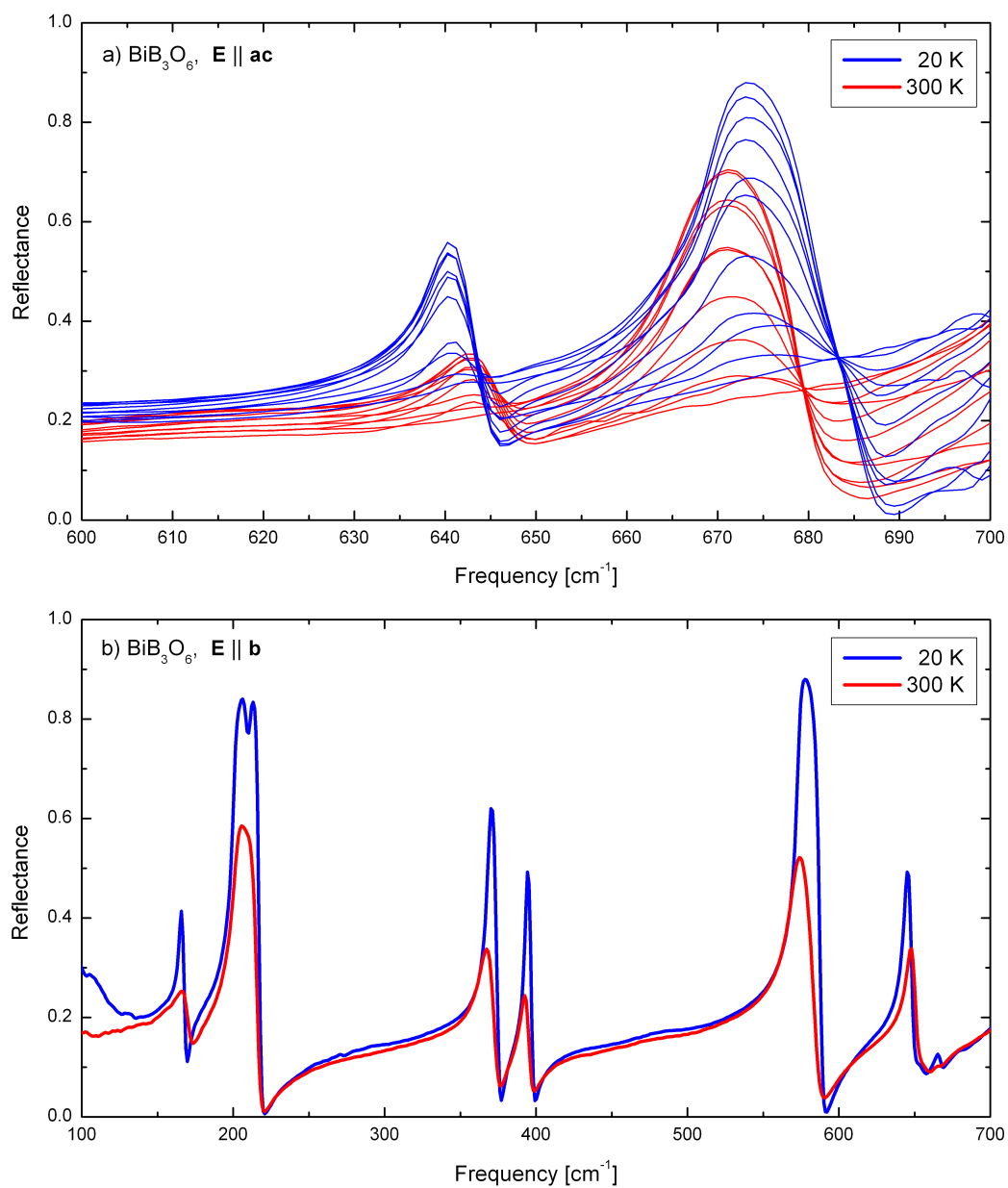


Figure 4.67: Part of the reflectivity spectra of  $\text{BiB}_3\text{O}_6$  at  $T = 20$  K and  $T = 300$  K for a)  $\mathbf{E} \parallel \mathbf{ac}$  (for different polarization angles  $\chi$ ) and b)  $\mathbf{E} \parallel \mathbf{b}$ .

<i>B modes</i>					<i>A modes</i>			
$\omega_0 [cm^{-1}]$	$\omega_p [cm^{-1}]$	$\gamma [cm^{-1}]$	$\theta [^\circ]$	S	$\omega_0 [cm^{-1}]$	$\omega_p [cm^{-1}]$	$\gamma [cm^{-1}]$	S
133	306	12.6	145	5.304	168	71	6.9	0.177
144	144	23.4	139	0.994	203	164	5.5	0.649
168	276	0.6	85	2.695	367	151	7.0	0.170
191	110	16.5	70	0.331	393	93	4.4	0.056
313	35	8.6	-84	0.013	570	304	9.2	0.285
439	346	6.5	22	0.622	647	174	6.0	0.072
645	138	4.1	187	0.046	662	151	41.1	0.052
667	319	3.2	134	0.228	731	396	6.6	0.294
711	514	4.8	15	0.523	947	522	23.1	0.304
826	753	15.6	77	0.830	1062	256	20.0	0.058
940	448	12.1	6	0.227	1199	668	25.6	0.310
1095	415	11.5	111	0.143	1448	208	12.3	0.021
1187	792	9.7	16	0.445	*1484	129	30.3	0.008
*1268	156	49.7	19	0.015				
1363	1028	10.5	112	0.569				
*1400	314	21.4	117	0.050				
*1434	101	12.9	127	0.005				
*1486	169	19.4	121	0.013				

Table 4.26: Fit parameters for the reflectivity of  $\text{BiB}_3\text{O}_6$  at  $T = 300$  K using (4.3.7).

Here,  $\omega_0$  represents the transverse frequency,  $\omega_p$  the plasma frequency,  $\gamma$  the damping,  $\theta$  the angle between the dipole moment and the  $\mathbf{x}$  axis (in case of the *B* modes), and  $S = \omega_p^2/\omega_0^2$  denotes the oscillator strength. The high-frequency dielectric constants at  $T = 300$  K are:  $\epsilon_{xx}^\infty = 3.6$ ,  $\epsilon_{yy}^\infty = 2.9$ ,  $\epsilon_{zz}^\infty = 3.2$ , and  $\epsilon_{xz}^\infty = -0.2$ . The four weak *B* modes at 1268, 1400, 1434, and 1486  $\text{cm}^{-1}$  probably correspond to multi-phonon excitations.

The *A* phonon mode at 272  $\text{cm}^{-1}$  is observed only in the 20 K data but not at 300 K, which is caused by its very small oscillator strength ( $S=0.001$ ). As shown in Fig. 4.67 b) the *A* phonon modes at 168  $\text{cm}^{-1}$  and 647  $\text{cm}^{-1}$  at 300 K are shifted to slightly lower frequencies with decreasing temperature, which is exceptionally, because the phonon modes should become harder at 20 K. In case of the mode at 647  $\text{cm}^{-1}$  we find a reduction of 8  $\text{cm}^{-1}$  after all. The other *A* modes show the expected reduction of the eigenfrequencies with increasing temperature.

Comparing the fit parameters of the *B* phonon modes at 20 K and 300 K, we see a small shift in the eigenfrequencies. All *B* phonon mode frequencies except the mode at 639  $\text{cm}^{-1}$  (20 K), see Fig. 4.67 a) become weaker at 300 K.

Before we will explain the remarkable negative shift in the phonon modes at 168  $\text{cm}^{-1}$ , 645  $\text{cm}^{-1}$ , and 647  $\text{cm}^{-1}$ , we have to distinguish between multi-phonon excitations and fundamental phonon modes. Therefore, we compare our data with recent room-

<i>B modes</i>					<i>A modes</i>			
$\omega_0$ [cm <sup>-1</sup> ]	$\omega_p$ [cm <sup>-1</sup> ]	$\gamma$ [cm <sup>-1</sup> ]	$\theta$ [°]	S	$\omega_0$ [cm <sup>-1</sup> ]	$\omega_p$ [cm <sup>-1</sup> ]	$\gamma$ [cm <sup>-1</sup> ]	S
133	325	0.4	148	5.973	166	78	2.9	0.221
144	210	1.5	110	2.124	202	177	1.8	0.764
169	264	0.1	87	2.443	272	8	3.6	0.001
192	40	1.2	19	0.044	369	159	2.7	0.186
319	61	4.0	122	0.037	393	107	2.2	0.074
439	382	0.7	13	0.758	573	308	1.9	0.288
639	279	6.0	183	0.191	643	222	5.1	0.120
668	364	2.2	134	0.297	666	100	9.9	0.023
711	514	4.8	15	0.523	731	396	6.6	0.294
826	753	15.6	77	0.830	947	522	23.0	0.304
940	448	12.1	6	0.227	1062	256	20.0	0.058
1095	415	11.5	111	0.143	1199	668	25.6	0.310
1187	792	9.7	16	0.445	1448	208	12.3	0.021
*1268	156	49.7	19	0.015	*1484	129	30.3	0.008
1363	1028	10.5	112	0.569				
*1400	314	21.4	117	0.050				
*1434	101	12.9	127	0.005				
*1486	169	19.4	121	0.013				

Table 4.27: Fit parameters for the reflectivity of BiB<sub>3</sub>O<sub>6</sub> at T = 20 K using (4.3.7).

Here,  $\omega_0$  represents the transverse frequency,  $\omega_p$  the plasma frequency,  $\gamma$  the damping,  $\theta$  the angle between the dipole moment and the  $\mathbf{x}$  axis (in case of the *B* modes), and  $S = \omega_p^2/\omega_0^2$  denotes the oscillator strength. The high-frequency dielectric constants at T = 20 K are:  $\epsilon_{xx}^\infty = 3.6$ ,  $\epsilon_{yy}^\infty = 2.9$ ,  $\epsilon_{zz}^\infty = 3.2$ , and  $\epsilon_{xz}^\infty = -0.2$ . The four weak *B* modes at 1268, 1400, 1434, and 1486 cm<sup>-1</sup> probably correspond to multi-phonon excitations.

temperature Raman data [236, 242, 243], neutron data [248], and first-principle calculations [248, 249] (see Tab. 4.28 and Tab. 4.29). In the latter, the determination of the phonon frequencies uses a numerical difference technique based on the calculation of the electronic structure [248]. Here, we use the results reported in [248], which show a better agreement with our results, whereas the values taken from [250] show discrepancies in the identification with *A* and *B* symmetry. For example, J. Yang [250] associates the mode at 563 cm<sup>-1</sup> (IR mode at 570 cm<sup>-1</sup>) with *B* symmetry, whereas we and D. Kasprovicz *et al.* [243] identify this mode with *A* symmetry.

In case of  $\mathbf{E} \parallel \mathbf{b}$  the peaks at 168 and 202 cm<sup>-1</sup> are found within a few wave numbers in all results. The tiny feature at 272 cm<sup>-1</sup> seems to be an overtone of the *B* mode<sup>28</sup> at 133 cm<sup>-1</sup>, but the first-principle results give evidence for a fundamental phonon mode. The excitation at 662 cm<sup>-1</sup> was found in the Raman and in the first-principle data at 688 cm<sup>-1</sup>. The Raman modes at 131 cm<sup>-1</sup> and 442 cm<sup>-1</sup> correspond to strongly

<sup>28</sup>Note that  $B \times B$  yields *A* symmetry.

Infrared	Kaminskii Raman [236]	Hu [242] Raman	Kasprowicz Raman [243]	Stein [248] Neutrons	Yang [248] Calculation
<i>A modes</i>					
-	131-135	-	135-148	-	-
168 (166)	168	169	169	173	190 {139}
202 (202)	215	203	210-216	235	236 {261}
- (272)	268-270	271	270	286	261 {264}
367 (369)	374	368	365	-	371 {374}
393 (393)	394	394	394	-	403 {452}
-	-	443	436-449	-	-
570 (573)	583	574	570	-	602 {625}
647 (643)	647	652	647-661	-	640 {652}
662 (666)	664-665	-	-	-	688 {675}
731 (731)	758-759	736	739	-	748 {768}
947 (947)	-	947	935	-	1020 {991}
-	988	-	-	-	-
1062 (1062)	1073-1074	-	1101	-	1109 {1090}
1199 (1199)	1178-1180	1200	1186	-	1274 {1266}
-	-	-	1227-1247	-	-
-	1285-1286	1294	1259-1265	-	-
1448 (1448)	1454-1456	1452	1446-1454	-	1557 {1520}
1484 (1484)	1483-1485	1488	1477-1481	-	-

Table 4.28: Comparison of the results for the *A*-symmetry phonon frequencies in units of  $[\text{cm}^{-1}]$  at  $T = 300$  K. The values in brackets indicate the eigenfrequencies at 20 K, whereas the values in curly brackets represent the calculated frequencies taken from [250].

IR-active *B* modes and can be attributed to a polarizer leakage. All other IR-active modes are found in Raman and first-principle data. Only the peak at  $1484 \text{ cm}^{-1}$  has no first-principle equivalent. All together we found 14 phonon modes in our infrared data, but the peak at  $272 \text{ cm}^{-1}$  is tiny. Therefore we interpret this feature as an overtone of the strong *B* mode at  $133 \text{ cm}^{-1}$ . If we neglect this excitation we end up with 13 *A* modes, as expected.

In case of  $\mathbf{E} \parallel \mathbf{ac}$ , each phonon mode shows a different orientation  $\theta$  of the dipole moment. This produces complex patterns in  $R_{ac}(\chi)$  which cannot be described by a conventional Drude-Lorentz model. We use 18 oscillators (see Table 4.26) to describe  $R_{ac}(\chi)$ , in contrast to the 14 *B* modes predicted. The use of four oscillators below  $250 \text{ cm}^{-1}$  is based on the 20 K data (see Fig. 4.66). We attribute the four modes at  $1268$ ,  $1400$ ,  $1434$ , and  $1486 \text{ cm}^{-1}$ , which are found both in the Raman and in the infrared data,<sup>29</sup> to multi-phonon excitations due to their large values of the damping

<sup>29</sup>The transverse frequencies agree within a few wave numbers.

Infrared	Kaminskii Raman [236]	Hu [242] Raman	Kasprowicz Raman [243]	Stein [248] Neutrons	Yang [248] Calculation
<i>B modes</i>					
133 (133)	133	141	134	-	137 {142}
144 (144)	147-148	159	145	149	172 {157}
168 (169)	163-166	187	169	175	177 {190}
191 (192)	198-200	225	184	198	216 {238}
313 (319)	314	317	316	338	311 {310}
-	365-366	-	370	-	-
-	391	-	394	-	-
439 (439)	438-440	444	448	-	477 {563}
-	569-570	572	573	-	-
645 (639)	645-646	-	643	-	641 {632}
667 (668)	664-665	684	668	-	675 {696}
711 (711)	712-720	733	740	-	741 {744}
826 (826)	-	840	856	-	872 {847}
940 (940)	940	967	937	-	1002 {979}
1095 (1095)	-	1100	1100	-	1157 {1139}
1187 (1187)	-	1207	1184	-	1267 {1251}
*1268 (1268)	-	1245	-	-	-
1363 (1363)	-	-	-	-	1470 {1433}
*1400 (1400)	-	1415	1416	-	-
*1434 (1434)	-	1472	1454	-	-
*1486 (1486)	-	1500	1484	-	-

Table 4.29: Comparison of the results for the  $B$ -symmetry phonon frequencies in units of  $[\text{cm}^{-1}]$  at  $T = 300$  K. The values in brackets indicate the eigenfrequencies at  $T = 20$  K, whereas the values in curly brackets are taken from [250].

$\gamma$ , their very weak amplitude, and their absence in the first-principle data.<sup>30</sup> Weak features may have a significant influence on the reflectivity if they are located on top of a *Reststrahlenband*.

The Raman modes at 370, 394, and 573  $\text{cm}^{-1}$  [243] correspond probably to IR-active  $A$  modes. All other IR-active modes were found in Raman and first-principle results. In case of the  $B$  modes the discrepancies between infrared and Raman data [242, 243] are much larger than for the  $A$  modes because the transverse and longitudinal modes mix for  $\mathbf{E} \parallel \mathbf{ac}$ . If we subtract the multi-phonon modes from our infrared data, we find 14  $B$  phonon modes, as expected.

In order to explain the remarkable negative shift in the phonon modes at 168  $\text{cm}^{-1}$ , 645  $\text{cm}^{-1}$  and 647  $\text{cm}^{-1}$ , we look at the change in the crystal structure between 20 K and 300 K. As reported by W.-D. Stein [248] the  $\mathbf{a}$  axis shrinks and the  $\mathbf{b}$  and  $\mathbf{c}$  axes

<sup>30</sup>The first-principle data predicts a peak at 1267  $\text{cm}^{-1}$  but we attribute this excitation to the strong peak 1187  $\text{cm}^{-1}$  in our infrared data.

elongate with increasing temperature. Here, the negative thermal expansion of the **a** axis is caused by the strong temperature dependence of the angle between adjacent Bi ions, whereas the distance between these ions is nearly constant [248]. Furthermore, W.-D. Stein reports of a small rotation of the  $[\text{BO}_4]$  tetrahedron around the **b** axis and a tilting of the  $[\text{BO}_3]$  triangles with increasing temperature. Additionally, the  $[\text{BiO}_4]$  units show a strong temperature dependence caused by a displacement of the Bi ions against their oxygen environment.

J. Yang [250] associates the *A* mode at  $139\text{ cm}^{-1}$ , which corresponds probably with our IR-active mode at  $168\text{ cm}^{-1}$ , with a translation of the borate units along the opposite translational direction of the central Bi cations. The temperature dependence of the displacement of the Bi ions may cause the unusual phonon shift. In addition, J. Yang predicts, that the other remarkable *A* mode at  $652\text{ cm}^{-1}$  (IR mode at  $647\text{ cm}^{-1}$ ) and the *B* mode at  $632\text{ cm}^{-1}$  (IR mode at  $645\text{ cm}^{-1}$ ), correspond to out-of-plane O-B-O bendings in the  $[\text{BO}_3]^{3-}$  unit linked with two O-B-O twistings in the  $[\text{BO}_4]^{5-}$  unit. (Due to the shared used oxygen atoms of the  $[\text{BiO}_4]^{5-}$ ,  $[\text{BO}_3]^{3-}$ , and  $[\text{BO}_4]^{5-}$  units, every vibrational mode of  $\text{BiB}_3\text{O}_6$  represents a combined motion of at least two different units.) Therefore, we assume, that the exceptional shift of these modes is caused probably by the complex interplay of the different units.

In conclusion, we find all phonon modes predicted by the factor-group analysis and distinguish between multi-phonon excitations and fundamental phonon by comparing our results with recent room-temperature Raman data [236, 242, 243], neutron data [248], and first-principle calculations. Furthermore, we give a possible explanation of the unusual phonon mode shift at  $168\text{ cm}^{-1}$  (*A* symmetry),  $645\text{ cm}^{-1}$  (*B* symmetry) and  $647\text{ cm}^{-1}$  (*A* symmetry) with increasing temperature.

## 4.5 $\text{CaCrO}_3$ , an antiferromagnetic metallic oxide

### 4.5.1 Introduction

Transition-metal oxides exhibit a quite general relation between magnetic order and electrical conductivity [251]: insulators usually exhibit antiferromagnetism, whereas ferromagnetism typically coexists with metallic conductivity. So observations of antiferromagnetic order in transition-metal oxides with metallic conductivity are of great interest. Here, we show that the perovskite  $\text{CaCrO}_3$  with orthorhombic space group  $Pbnm$  is a three-dimensional transition-metal oxide with metallic conductivity, antiferromagnetic exchange interactions, and C-type antiferromagnetic order. The metallic behavior has been established by means of optical spectroscopy, and the crystal structure, magnetic structure, and electronic structure have been studied in collaboration with the groups of M. Braden<sup>31</sup>, D.I. Khomskii, and V.I. Anisimov<sup>32</sup> [264]. The samples were grown by M. Isobe.<sup>33</sup>

In the following we first will discuss the results obtained within this collaboration on crystal growth, crystal and magnetic structure, and the electronic structure calculations. Then, we will focus on our optical study of  $\text{CaCrO}_3$ .

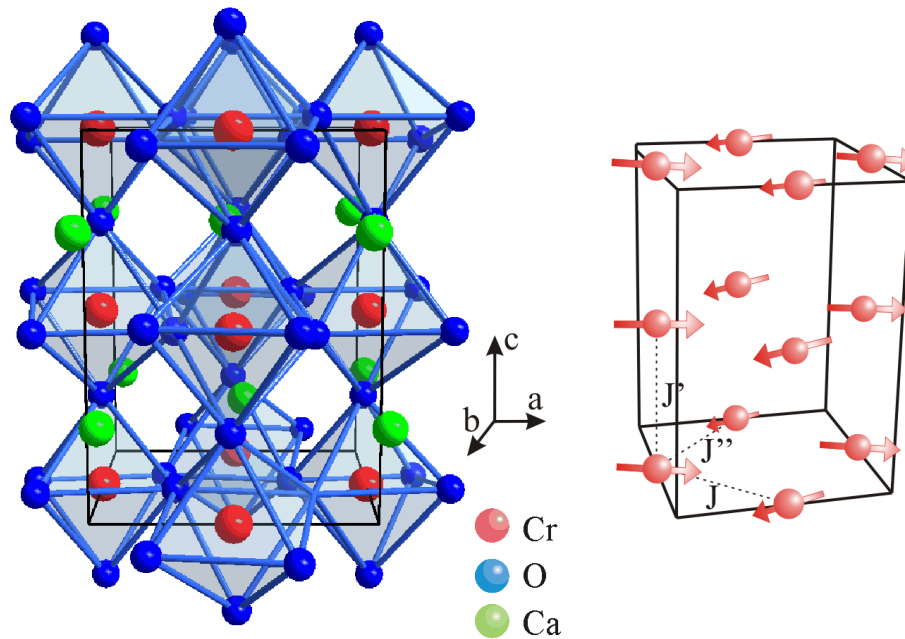


Figure 4.68: Crystal and magnetic structure of  $\text{CaCrO}_3$ .

<sup>31</sup>II. Physikalisches Institut, Universität zu Köln, Zùlpicher Str. 77, D-50937 Köln, Germany

<sup>32</sup>Institute of Metal Physics, 620041 Ekaterinburg GSP-170, Russia

<sup>33</sup>Institute for Solid State Physics, The University of Tokyo, 5-1-5 Kashiwanoha, Kashiwa, Chiba 277-8581, Japan.

Although other perovskites containing  $\text{Cr}^{4+}$  ions ( $\text{CaCrO}_3$ ,  $\text{SrCrO}_3$ , and  $\text{PbCrO}_3$ ) were already studied previously [252–257], the details of the crystal structure and the magnetic ordering are not known. Only very recently evidence for C-type antiferromagnetic order was reported in multi-phase samples of  $\text{SrCrO}_3$  [257].

Regarding the electrical conductivity, the existing data are controversial. The electrical conductivity reported in Refs. [254, 256] shows metallic behavior, whereas more recent measurements [252] indicate insulating behavior (see Fig. 4.71). A similar controversy exists also for  $\text{SrCrO}_3$ : Due to the less distorted crystal structure the electric conductivity [252] should show a more metallic behavior than in  $\text{CaCrO}_3$ . But metallic behavior was observed only under pressure [252]. These controversies are connected with the difficulty to prepare high-quality stoichiometric materials and with the lack of large single crystals.

Magnetization measurements [255] indicate a magnetic transition at 90 K (see Fig. 4.70) in  $\text{CaCrO}_3$ . Two electrons occupy the Cr  $3d$  shell ( $S=1$ ), rendering the material electronically similar to insulating  $\text{RVO}_3$  [258] (also  $3d^2$ ) and to metallic  $(\text{Ca}/\text{Sr})\text{RuO}_3$  [259].  $\text{CaCrO}_3$  shows an unusually high transition-metal valence  $\text{Cr}^{4+}$ , which may lead to a small or even negative charge-transfer gap [260, 261], i.e. holes in the O band. In  $\text{CrO}_2$  the negative charge-transfer gap leads to self-doping [262] and to the appearance of a ferromagnetic metallic state. In contrast, the layered perovskite  $\text{Sr}_2\text{CrO}_4$  is an antiferromagnetic Mott-Hubbard insulator with a gap of about 0.2 eV [263].

## 4.5.2 Crystal Growth

Polycrystalline  $\text{CaCrO}_3$  [264] was prepared by M. Isobe by a solid state reaction of  $\text{CaO}$  and  $\text{CrO}_2$  under 4 GPa at  $1000^\circ$  for 30 minutes. The obtained samples of stoichiometric reactions always include a varying amount of the impurities of  $\text{Cr}_2\text{O}_3$  and  $\text{CaCr}_2\text{O}_4$ . This impurity problem has also been reported by Goodenough *et al.* [255]. These impurities can be completely eliminated by a small excess of  $\text{CaO}$  (5–10%). Single-crystalline grains of up to 0.1 mm diameter were obtained by this procedure as well.

## 4.5.3 Crystal and Magnetic Structure

Powder neutron measurements were performed by A.C. Komarek [266] and confirm the close to perfect stoichiometry of the samples. The lattice parameters of  $\text{CaCrO}_3$  determined by synchrotron-radiation powder diffraction are shown in Fig. 4.69. For details see [264]. At the magnetic ordering temperature,  $T_N=90$  K, all three orthorhombic parameters show a step-like anomaly. In spite of the strong changes in the lattice constants of up to 0.5% for  $c$ , there is no visible effect in the lattice volume. The  $Pbnm$  structure is flattened, i.e.  $c$  shrinks and  $a$  and  $b$  elongate upon cooling. There is no evidence for phase mixture apart very close to  $T_N$ . Close inspection of the temperature dependence suggests that this lattice flattening already starts at much higher temperatures. As done in these experiments, all bond angles and distances can be

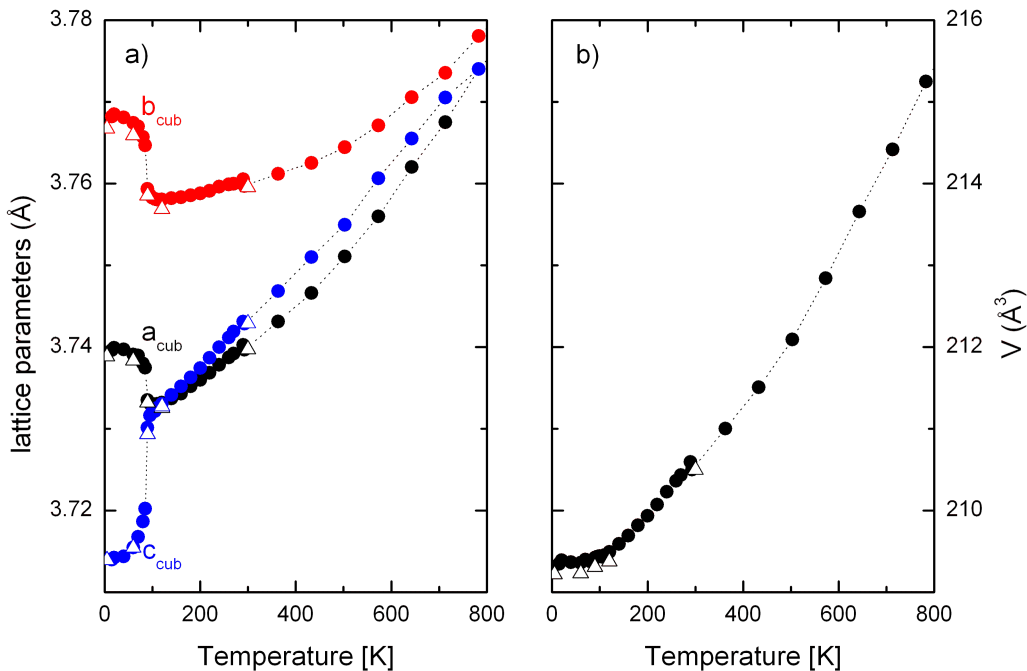


Figure 4.69: a) Orthorhombic lattice parameters  $\mathbf{a}$ ,  $\mathbf{b}$ , and  $\mathbf{c}$ , scaled to the parameter of a cubic perovskite:  $a_{cub} = a/\sqrt{2}$ ,  $b_{cub} = b/\sqrt{2}$ , and  $c_{cub} = c/2$  [264]. b) Lattice volume  $V$ . Circles refer to synchrotron and triangles to neutron diffraction results [264]. All measurements presented in this figure were done by A.C. Komarek [266].

calculated from the structural information given by neutron powder and x-ray single-crystal experiments. The results are given in Fig. 4.70. The  $\text{GdFeO}_3$ -type structure (space group  $Pbnm$ ) emerges from the ideal perovskite structure by rotating the  $\text{CrO}_6$  octahedra around angle  $\phi$ , and tilting around angle  $\Theta$  [265]. These angles are nearly constant between 3.5 and 300 K ( $\Theta = 10.5^\circ$  and  $\phi = 8.2^\circ$ ). The combination of tilt and rotation yields two distinct O positions: apical O1 out-of-plane and O2 in the  $\mathbf{ab}$  plane. Following the flattening of the lattice at  $T_N$ , we find an overall flattening of the octahedron: The Cr-O1 (Cr-O2) distance shrinks (elongates) upon cooling. The compression of the octahedron points to a temperature-driven redistribution amongst the  $t_{2g}$  orbitals, increasing the  $d_{xy}$  occupation upon cooling into the magnetically ordered state. In  $\text{Ca}_2\text{RuO}_4$ , which is electronically similar to  $\text{CaCrO}_3$ , a similar flattening of the octahedron has been observed. There, the flattening causes an orbital rearrangement [267–269]. But the effects are about an order of magnitude larger than in  $\text{CaCrO}_3$ .

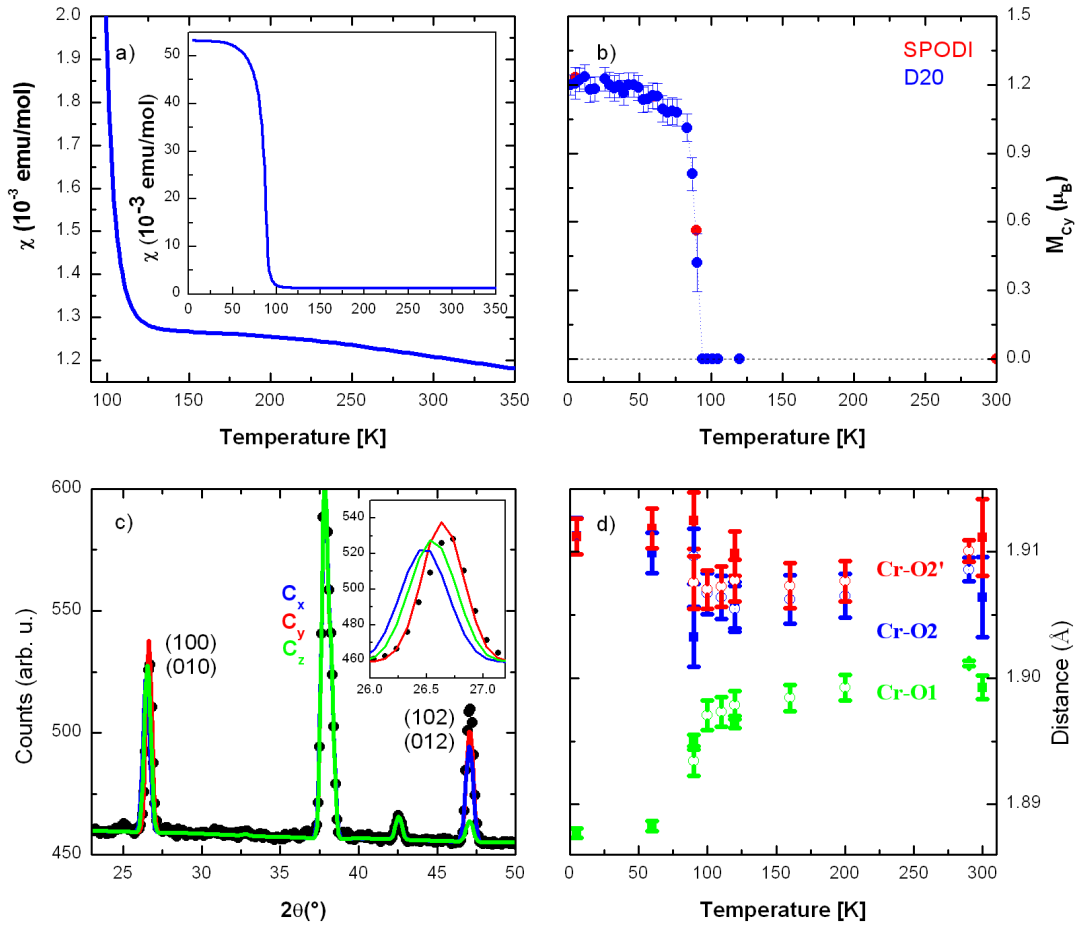


Figure 4.70: a) Magnetic susceptibility [264]. b)  $C_y$ -type ordered magnetic moment in  $\mu_B$  [264]. c) Magnetic (010)/(100) reflection at 3.5 K and calculated profiles for  $C_x$ -,  $C_y$ - and  $C_z$ -type magnetic order [264]. d) Cr-O1 and Cr-O2 bond lengths [264]. All data presented in this figure were obtained by A.C. Komarek [266].<sup>34</sup>

Below  $T_N=90$  K two strong magnetic peaks emerge at (100) and (102)/(012), which can be attributed to  $C_y$ -type antiferromagnetic order, see Fig. 4.70. In space group  $Pbnm$ , the  $C_y$ -type order may couple with  $F_x$  and  $G_z$  components according to the irreducible representation  $\Gamma_{2g}$  [270]. The  $F_x$  component perfectly agrees with the observation of weak ferromagnetism in the susceptibility, see Fig. 4.70 a). The observed ordered moment of  $1.2 \mu_B$  at low temperature is much below the expected value for a  $S=1$  moment.

<sup>34</sup>II. Physikalisches Institut, Universität zu Köln, Zùlpicher Str. 77, D-50937 Köln, Germany

#### 4.5.4 LSDA and LDA+U Calculations

The electronic band structure was analyzed by S.V. Streltsov<sup>35</sup> and V.I. Anisimov [264, 271] by performing *ab-initio* band structure calculations within the LSDA approximation using the linear muffin-tin orbitals method [272]. The total energies of different magnetic solutions were computed in order to determine the exchange constants. In LSDA,  $\text{CaCrO}_3$  is metallic in all studied magnetic structures: ferromagnetic, antiferromagnetic G-type (all nearest-neighbor (*nn*) spins antiparallel), antiferromagnetic A (antiferromagnetically coupled ferromagnetic **ab** planes) and two antiferromagnetic C-types with ferromagnetic chains running in different directions. The antiferromagnetic C-type structure exhibits the lowest energy, in good agreement with experiment. The calculated magnetic moment  $\mu = 1.52\mu_B/\text{Cr}$  overestimates the measured value ( $\mu = 1.2\mu_B$ ). The strong *pd* hybridization causes the reduction from the expected value of  $2\mu_B$  for a localized  $\text{Cr}^{4+}$  ( $S=1$ ) ion. The exchange parameters indicate a strong antiferromagnetic interaction between *nn* spins within the **ab** plane,  $J = 80$  K. The *nn* exchange along **c** is also antiferromagnetic with  $J' = 60$  K, in contrast to experiments which find a ferromagnetic arrangement in this direction. Its cause resides in a remarkably strong antiferromagnetic *nnn* interaction along the diagonal,  $J'' = 33$  K. Since  $J' < 4J''$ , the antiferromagnetic  $J'$  is overruled, yielding the C-type structure. Thus, the anisotropic magnetic structure develops due to strong and anisotropic next-nearest-neighbor (*nnn*) interactions despite nearly isotropic *nn* interactions. The structural anomalies at  $T_N$  can be explained by the strong magnetoelastic coupling caused by the subtle balance of the different interactions. The flattening of the octahedron enhances the  $d_{xy}$  occupation, thereby increasing  $J$  and decreasing  $J'$ . Within the LSDA approximation magnetic interactions are caused by the band magnetism of itinerant electrons. So the strong *pd* hybridization causes the large diagonal coupling parameters. In order to analyze the electronic correlations S.V. Streltsov and V.I. Anisimov also performed a LSDA+U calculation [264, 273] with on-site Coulomb interaction  $U = 3$  eV and Hund's rule coupling  $J_H = 0.87$  eV [262]. Here the ground state is also C-type antiferromagnetic, but within this analysis  $\text{CaCrO}_3$  is an insulator with a gap of  $E_g \sim 0.5$  eV. (In LSDA+U,  $E_g$  is often overestimated due to the static approximation of the Coulomb correlations.) Here, one electron localizes in the *xy* orbital at each Cr site and provides the in-plane antiferromagnetic interaction, the second electron occupies alternating  $1/\sqrt{2}(xz + yz)$  and  $1/\sqrt{2}(xz - yz)$  orbitals. This causes a ferromagnetic interaction along **c** according to the Goodenough-Kanamori-Anderson rules [274–276]. A similar state with G-type orbital order causing C-type magnetism was reported in insulating  $\text{YVO}_3$  [258, 277]. The high-flux powder neutron diffraction and SPODI<sup>36</sup> data do not yield any evidence for orbital ordering.

<sup>35</sup>Institute of Metal Physics, S.Kovalevskoy St. 18, 620041 Ekaterinburg GSP-170, Russia.

<sup>36</sup>Powder neutron measurements were performed on the SPODI diffractometer at the FRM-II ( $\lambda = 1.548\text{\AA}$ ).

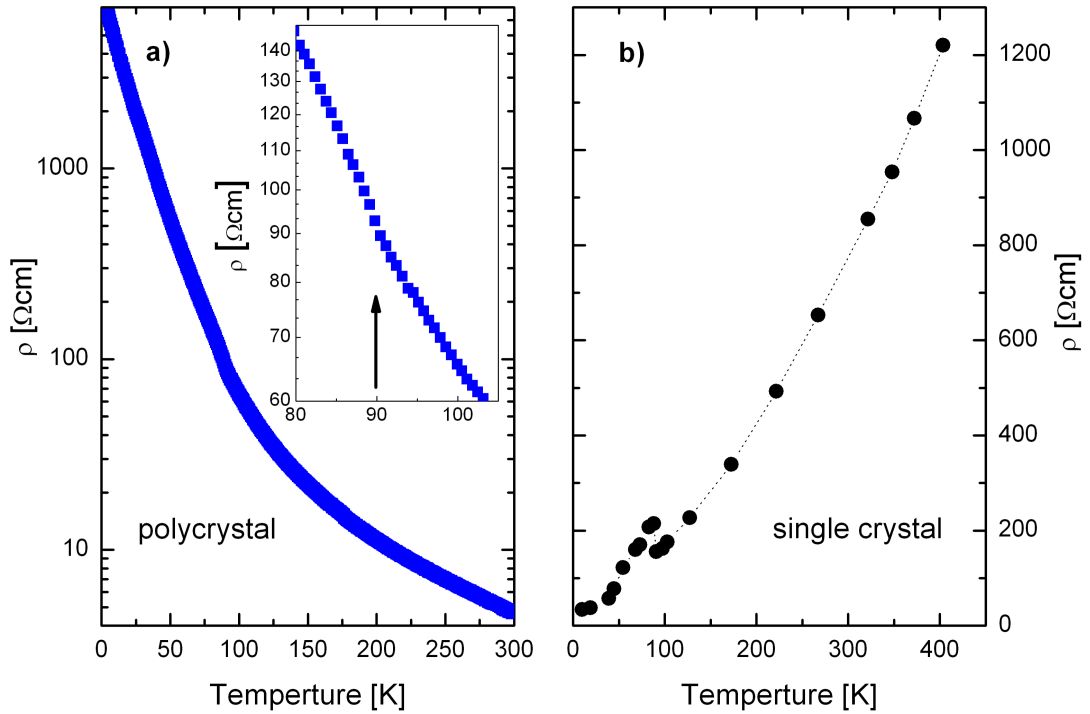


Figure 4.71: Electrical resistivity  $\rho(T)$  of  $\text{CaCrO}_3$ : a) Polycrystal [264], b) single crystal [256].

#### 4.5.5 Resistivity

The electrical resistivity  $\rho(T)$  was measured by an AC four-point method on a pellet of polycrystalline  $\text{CaCrO}_3$  powder which was cold-pressed at 12.5 kbar. The resistivity  $\rho(T)$  has negative slope and a small value at 300 K ( $\rho(T = 300\text{K}) = 5 \text{ } \Omega\text{cm}$ , see Fig. 4.71). In contrast to a semiconducting behavior  $\rho(T)$  does not diverge towards low temperature but tends to a finite value. The structural anomalies produce cracks which cause the clear jump in the resistivity at  $T_N$ . Weiher *et al.* [256] found a similar jump close to 90 K in their metallic single crystals. Thus we suggest that the sample exhibits a fully comparable magnetic transition and represents stoichiometric  $\text{CaCrO}_3$ . But  $\rho(T)$  of polycrystalline  $\text{CaCrO}_3$  appears to be dominated by grain boundaries causing the completely different resistivity behavior. Presumably, the high valence of  $\text{Cr}^{4+}$  is not stable at the surface of a grain.

#### 4.5.6 Optics on $\text{CaCrO}_3$

In contrast to DC electrical resistivity measurements, optical data can reveal the metallic properties of a polycrystalline sample with insulating grain boundaries. The light excites free charge carriers which respond to the external perturbation. For infrared frequencies with wavelengths smaller than the typical grain size, no conducting path through the entire sample is necessary.

We will show, that  $\text{CaCrO}_3$  is a real 3D metal. We measured the infrared reflectivity  $R(\omega)$  of a cold-pressed pellet between 7 meV and 0.9 eV ( $56 - 7260 \text{ cm}^{-1}$ ). The reference measurement was done with *in-situ* Au evaporation. Determining the optical reflectance involves some problems, due to the polycrystalline nature of the sample: If the wavelength is much smaller than the typical grain size ( $\sim 20 \mu\text{m}$ ) of the sample, we see an averaged admixture of different directions  $R_a$  (parallel to the **a** direction),  $R_b$  (parallel to the **b** direction), and  $R_c$  (parallel to the **c** direction). For the opposite case, we have to take the insulating grain boundaries into account and use an effective medium theory to describe the sample. Initially, we assume an isotropic sample and analyze the optical reflectance  $R(\omega)$ . In a second step, we consider the problems mentioned above.

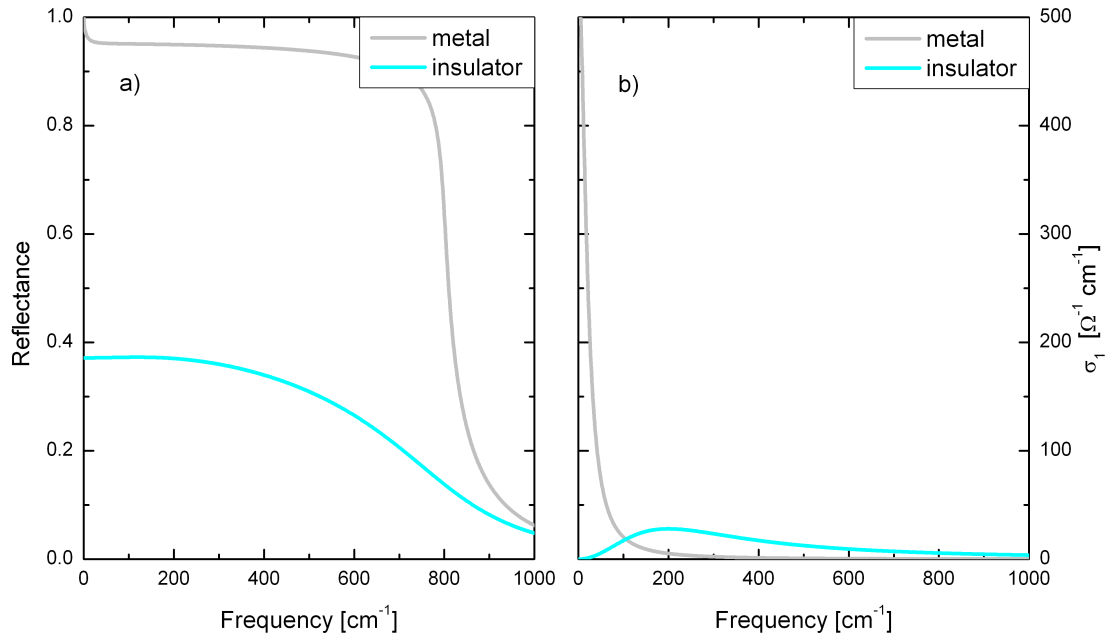


Figure 4.72: A sketch of a) the optical reflectance  $R(\omega)$  and b) the real part of the optical conductivity  $\sigma_1(\omega)$  of a metal (grey color,  $\omega_0 = 0 \text{ cm}^{-1}$ ,  $\omega_p = 800 \text{ cm}^{-1}$ ,  $\gamma = 20.0 \text{ cm}^{-1}$ ) and an insulator (cyan color,  $\omega_0 = 200 \text{ cm}^{-1}$ ,  $\omega_p = 800 \text{ cm}^{-1}$ ,  $\gamma = 380.0 \text{ cm}^{-1}$ ). Here, the Drude-Lorentz model parameters ( $\omega_0$ ,  $\omega_p$ ,  $\gamma$ ) represent the eigenfrequency, the plasma frequency  $\omega_p$  and the damping, respectively.

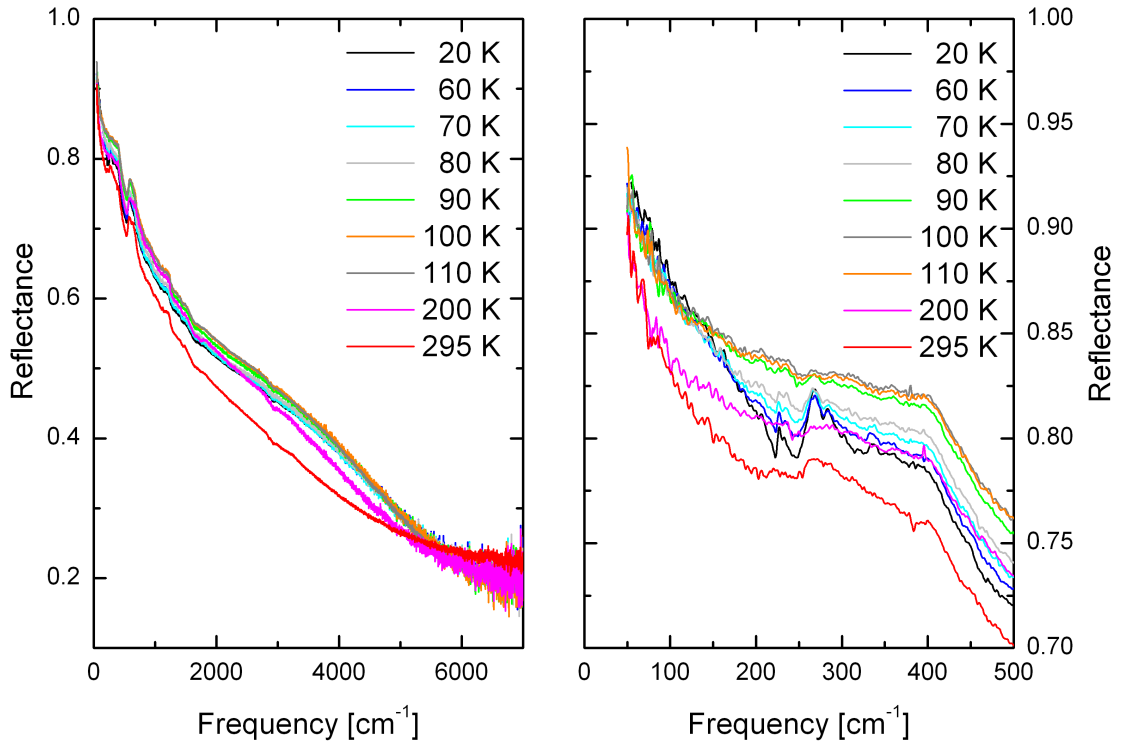


Figure 4.73: The infrared reflectance  $R(\omega)$  of polycrystalline  $\text{CaCrO}_3$  at different temperatures.

As shown in Fig. 4.73, the infrared reflectivity  $R(\omega)$  of  $\text{CaCrO}_3$  extrapolates to 1 for  $\omega \rightarrow 0$ . The reflectance of a metal converges to 1 for  $\omega \rightarrow 0$ , whereas an insulator shows a constant reflectance smaller than one for low frequencies, see Fig. 4.72. We will describe this point in more detail later.

We will divide the analysis of the optical reflectance into three parts: In the first part, we assume an isotropic behavior and wavelengths  $\lambda$  much smaller than the typical grain size and use the conventional Drude-Lorentz model to describe the optical reflectance and apply the Kramers-Kronig transformation to determine the optical conductivity. In this case,  $\sigma(\omega)$  is dominated by a strong peak at  $\sim 2300 \text{ cm}^{-1}$  (0.35 eV). We attribute this peak to a transition from the lower (LHB) to the upper (UHB) Hubbard band, similar to  $\text{Sr}_2\text{CrO}_4$  [263]. This implies that correlations are important in  $\text{CaCrO}_3$ . In the second part, we still assume that the wavelength is smaller than the typical grain size, but consider anisotropic behavior using a model discussed by Orenstein *et al.* [280]. This analysis shows, that  $\text{CaCrO}_3$  is a real 3D metal. In the third part, we assume that the wavelength is much larger than the grain size, and use an effective medium theory to describe the behavior of the sample. We will show, that the effective medium theory cannot describe the peak at  $\sim 0.35 \text{ eV}$ . In addition, we show that for

a stack of metallic grains and insulating boundaries [278] with a length ratio of 1000:1 or larger, the deviation of  $R(\omega)$  from the bulk value is significant only below the lower limit of the experiment,  $56 \text{ cm}^{-1}$  (7 meV).

### Isotropic case

In order to analyze the reflectivity  $R(\omega)$ , we first assume that the real part of the optical conductivity  $\sigma_1(\omega)$  is isotropic, and that the wavelength is much smaller than the typical grain size. In this case, we can derive  $\sigma_1(\omega)$  via a Kramers-Kronig analysis of  $R(\omega)$ , which starts with an extrapolation of the reflectance data to lower and higher frequencies. We use the Drude-Lorentz model to fit the reflectance between  $56.5 \text{ cm}^{-1}$  and  $7260 \text{ cm}^{-1}$  ( $\sim 7 - 900 \text{ meV}$ ). The fit is rather sensitive to high-energy contributions. However, the roughness of the polycrystalline sample prevents measurements at higher frequencies, where the wavelength becomes comparable to the length scale of the surface roughness. In order to estimate the sensitivity to the high-energy extrapolation, we consider two different cases (see Fig. 4.74). In the first case, we estimated the high-energy contributions by using the data of insulating layered  $\text{Sr}_2\text{CrO}_4$ , also with  $\text{Cr}^{4+}$  in a  $d^2$  configuration and a Hubbard band at  $\sim 8000 \text{ cm}^{-1}$  (1 eV), as reported by Matsuno *et al.* [263]. As shown in Fig. 4.74, we reduce the oscillator strength of the Hubbard band at  $\sim 8000 \text{ cm}^{-1}$  (1 eV) because we assume that the Hubbard band in  $\text{CaCrO}_3$  is shifted to  $\sim 2800 \text{ cm}^{-1}$  (0.35 eV).

In the second fit, we estimate the high-energy contribution by  $\varepsilon_\infty$ . In both cases, we use four electronic peaks (at  $0 \text{ cm}^{-1}$ ,  $148 \text{ cm}^{-1}$ ,  $1174 \text{ cm}^{-1}$ , and  $3538 \text{ cm}^{-1}$  for  $T = 20 \text{ K}$ ) and four phonon peaks to describe the data in the measured frequency range. The fit parameters are shown in Tab. 4.30 for several temperatures.

Figs. 4.75 - 4.77 show the four electronic peaks used in the Drude-Lorentz fit at 20 K, 110 K, and 295 K. The oscillator strength of the peak at  $148 \text{ cm}^{-1}$  increases between 20 K and 110 K with increasing temperature and decreases from 110 K to 295 K. This is caused by the enhanced optical reflectance around  $T_N$ , see below.

The phonon modes used in the fits represent an effective description of the phonons because, as shown in Fig. 4.73, the phonons are strongly screened by the itinerant charge carriers and we cannot determine the eigenfrequencies and the oscillator strengths of the phonon modes exactly.

Using the fits, we can extrapolate the optical reflectance and apply the Kramers-Kronig transformation to determine the optical conductivity  $\sigma(\omega)$ . The results of the Kramers-Kronig transformation are shown in Fig. 4.78 for different temperatures. Fig. 4.73 and Fig. 4.78 clearly demonstrate that  $\text{CaCrO}_3$  is a metal with a moderate conductivity  $\sigma_1(\omega)$  of the order of a few hundred to  $1000 (\Omega\text{cm})^{-1}$ . The frequency dependence deviates strongly from a typical Drude behavior, as the spectral weight is dominated by the peak<sup>37</sup> at  $\sim 2800 \text{ cm}^{-1}$  (0.35 eV). In the fits, this behavior is described

<sup>37</sup>Comparing the results of the Kramers-Kronig transformation of the reflectance data with the optical conductivity determined by the fit shown in Fig. 4.75 b), we see that the peak at  $\sim 2800 \text{ cm}^{-1}$

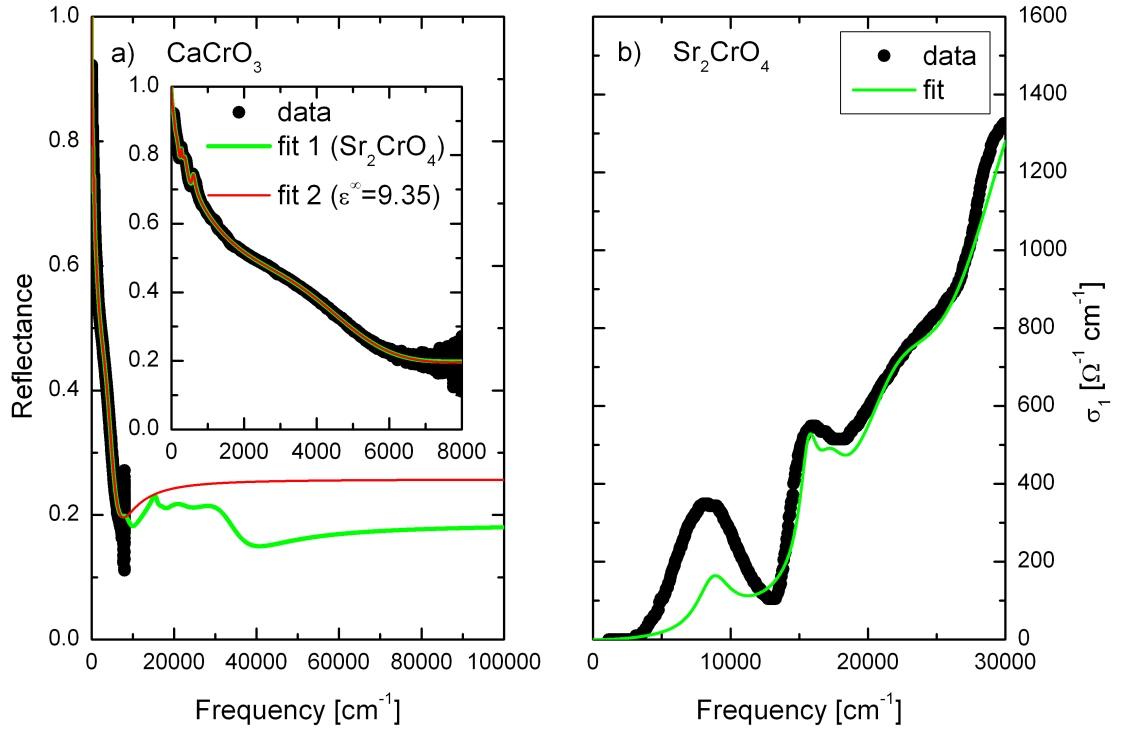


Figure 4.74: a) The optical reflectance  $R(\omega)$  at  $T = 20$  K (black), fit1 using  $\epsilon_\infty = 9.35$  (red) and fit2 (green) using five peaks at 8800, 15687, 17170, 22200, and 32600  $\text{cm}^{-1}$  describing the behavior of  $\text{Sr}_2\text{CrO}_4$  [263] at high frequencies ( $\omega > 8000$   $\text{cm}^{-1}$ ). b) Optical conductivity of  $\text{Sr}_2\text{CrO}_4$  reported by Matsuno *et al.* [263] and fit (used in a)), where the oscillator strength of the Hubbard band at  $\sim 8000$   $\text{cm}^{-1}$  (1 eV) was reduced because of the shift of the Hubbard band in  $\text{CaCrO}_3$  to  $\sim 2800$   $\text{cm}^{-1}$  (0.35 eV).

predominantly by the last electronic peak, see Figs. 4.76 - 4.77, whereas at  $T = 20$  K we need two peaks to describe the peak, see Fig. 4.75.

As shown in Fig. 4.79, the reflectance as well as the optical conductivity show a maximum around  $T_N$ , where the maximum in the optical conductivity is more pronounced than in the reflectance. Comparing the values of the optical conductivity at 200  $\text{cm}^{-1}$  for different temperatures, we find a difference of 433  $(\Omega\text{cm})^{-1}$  between 100 K and 295 K, whereas the difference at 3450  $\text{cm}^{-1}$  is only 164  $(\Omega\text{cm})^{-1}$ . In contrast to that, the differences in the reflectance between the maximum and the minimum stay nearly the same for all frequencies.

---

(0.35 eV) is not an artefact of the Kramers-Kronig analysis, because the peak is observed in both data and shows a temperature dependence.

$\omega_0$ [ $\text{cm}^{-1}$ ]	$\omega_p$ [ $\text{cm}^{-1}$ ]	$\gamma$ [ $\text{cm}^{-1}$ ]	S
T = 20 K			
0	2251	82.3	-
148	1596	162.7	117.000
227	135	3.8	0.355
269	929	44.9	12.000
350	1209	95.8	11.900
585	1084	82.4	3.430
1174	14579	5609.1	154.000
3538	8309	4409.6	5.5200
T = 110 K			
0	1691	32.8	-
195	4745	469.9	590.000
224	533	59.0	5.690
298	1109	88.1	13.900
371	894	68.4	5.800
585	1104	77.9	3.570
991	6613	1705.5	44.500
3114	14494	5359.6	21.700
T = 295 K			
0	1279	36.1	-
204	4100	651.0	403.000
271	1185	104.2	19.200
339	658	76.2	3.780
394	699	78.0	3.140
590	1126	100.2	3.640
845	1869	696.3	4.890
2617	16646	8347.1	40.500

Table 4.30: Drude-Lorentz model parameters for  $\text{CaCrO}_3$  at several temperatures. Here,  $S$  denotes the oscillator strength  $S = \omega_p^2/\omega_0^2$ . The high-frequency dielectric constant is  $\epsilon_\infty = 9.35$  for all temperatures.

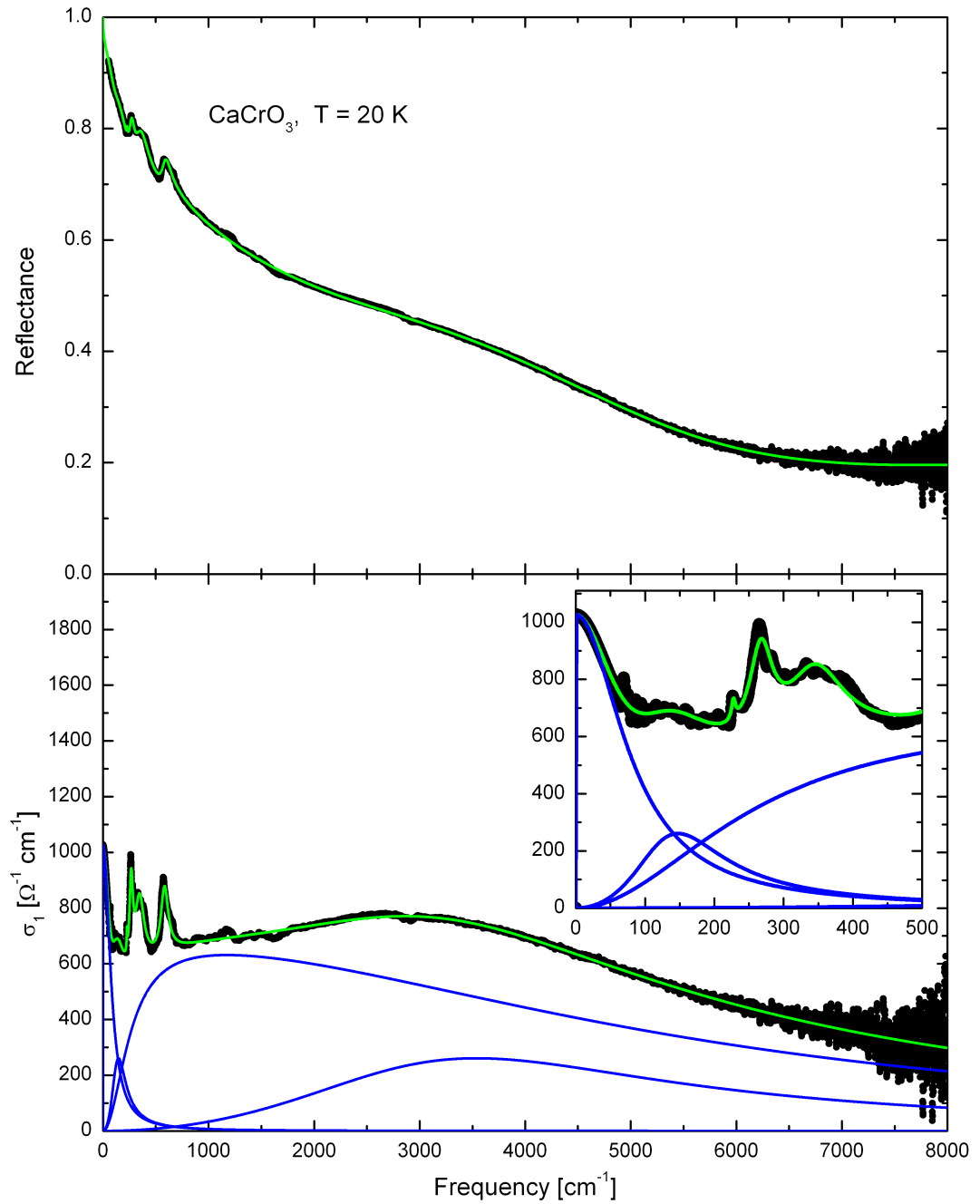


Figure 4.75: The four electronic peaks (blue) of the Drude-Lorentz fit (fit2, green) compared with a) the experimental reflectivity data (black) and b) the Kramers-Kronig analysis (black) at 20 K. Note, that individual contributions are additive in  $\sigma_1(\omega)$ , but not in  $R(\omega)$ .

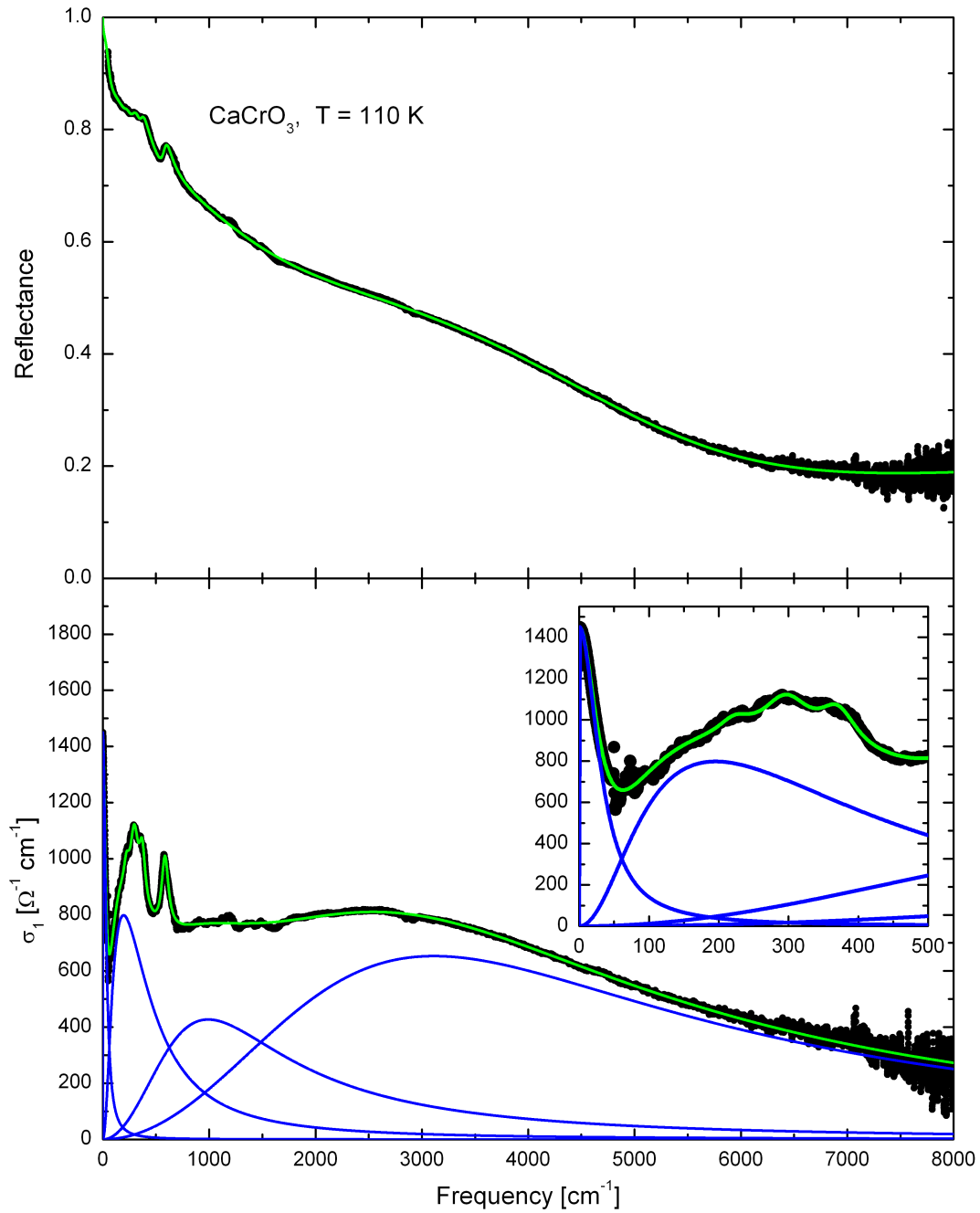


Figure 4.76: The four electronic peaks (blue) of the Drude-Lorentz fit (fit2, green) compared with a) the experimental reflectivity data (black) and b) the Kramers-Kronig analysis (black) at 110 K.

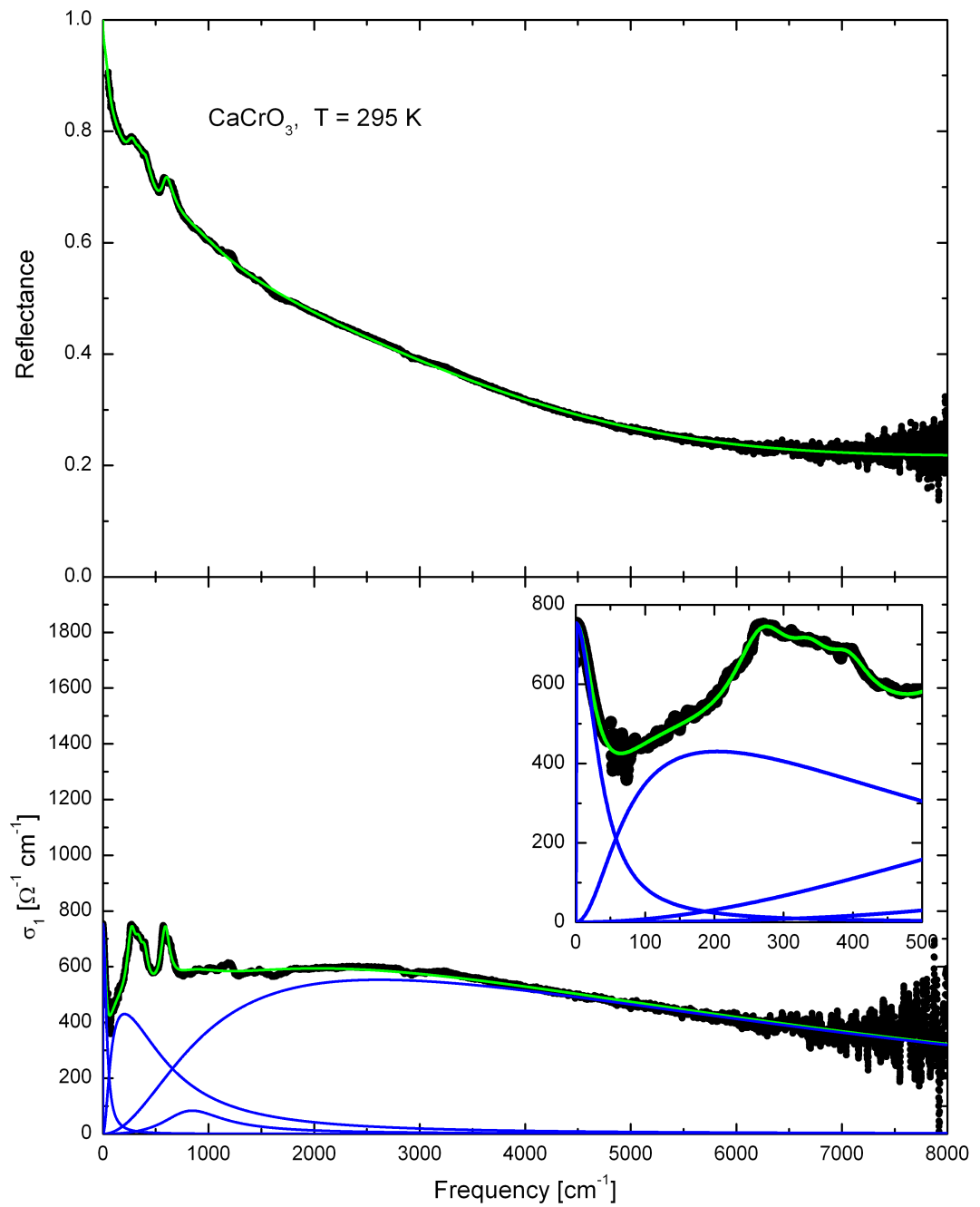


Figure 4.77: The four electronic peaks (blue) of the Drude-Lorentz fit (fit2, green) compared with a) the experimental reflectivity data (black) and b) the Kramers-Kronig analysis (black) at 295 K.

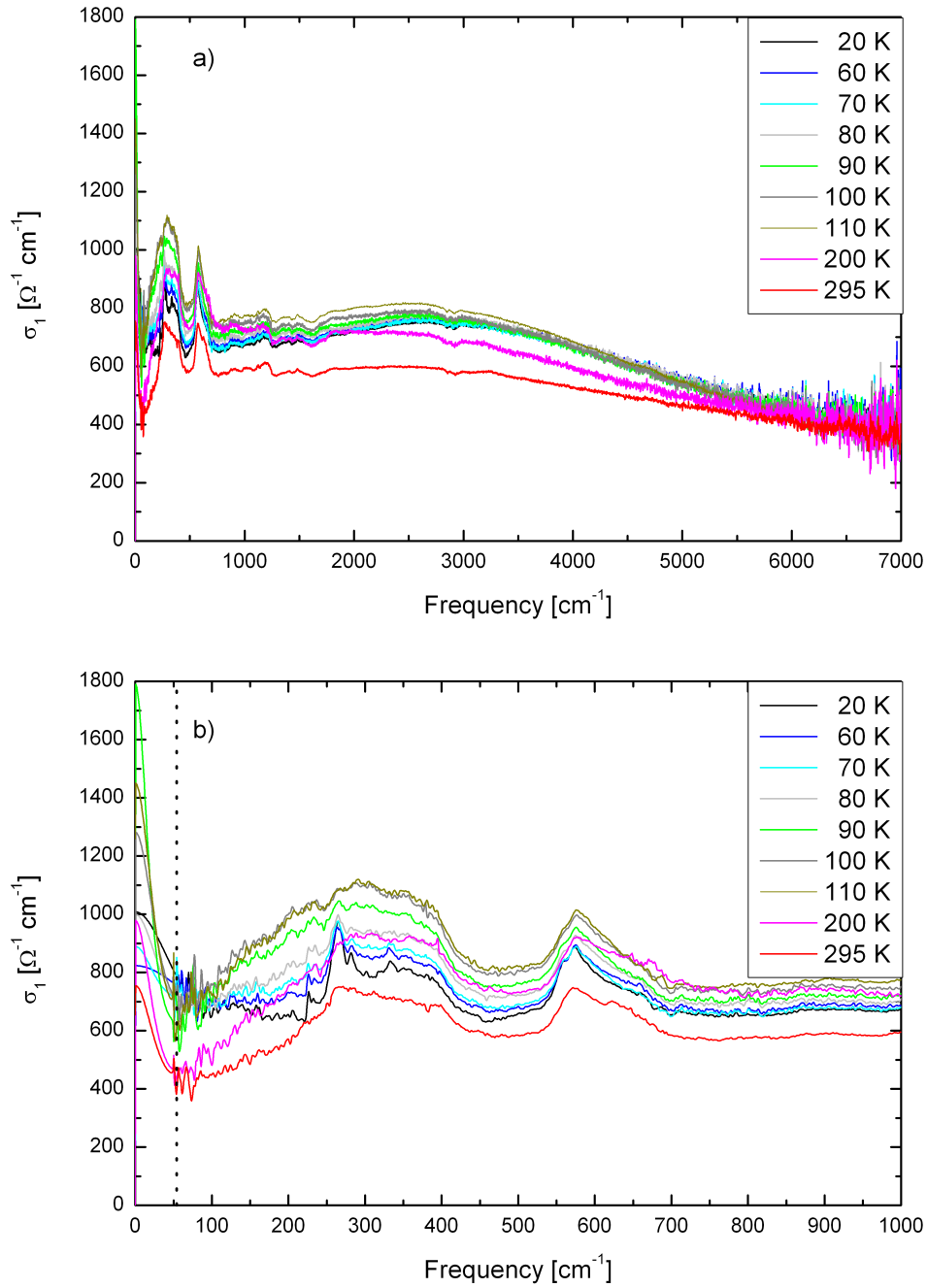


Figure 4.78: The optical conductivity  $\sigma_1(\omega)$  as derived from a Kramers-Kronig analysis of  $R(\omega)$  for a) the entire measured frequency range and b) the phonon range. The data on the left side of the dashed line are extrapolated.

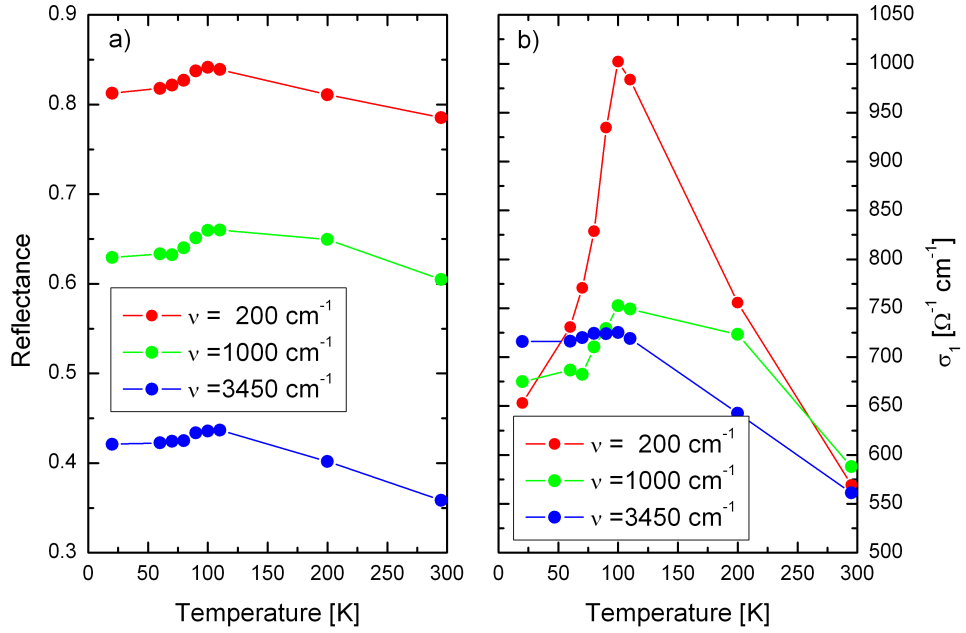


Figure 4.79: a) Reflectance and b) optical conductivity  $\sigma_1(\omega)$  of  $\text{CaCrO}_3$  at  $200 \text{ cm}^{-1}$ ,  $1000 \text{ cm}^{-1}$ , and  $3450 \text{ cm}^{-1}$  as a function of temperature.

Although  $\sigma_1(\omega)$  seems to be dominated by excitations with finite frequency, the infrared reflectance  $R(\omega)$  clearly demonstrates the presence of free carriers. This agrees with the magnetic susceptibility, which is very small above  $T_N$  and shows only a small temperature dependence indicating itinerant magnetism, see Fig. 4.70 a).<sup>38</sup> In our samples of  $\text{CaCrO}_3$ , the typical grain size is of the order of  $20 \mu\text{m}$ . Since a wavelength of  $\lambda = 20 \mu\text{m}$  is equivalent to a photon energy of  $\sim 500 \text{ cm}^{-1}$  (0.06 eV), grain-size effects can become important only much below  $\sim 2800 \text{ cm}^{-1}$  (0.35 eV) [278]. We assume, that the peak at  $\sim 2800 \text{ cm}^{-1}$  (0.35 eV) is caused by excitations from the lower (LHB) to the upper (UHB) Hubbard band, similar to insulating  $\text{Sr}_2\text{CrO}_4$  with  $\text{Cr}^{4+}$  where this excitation is observed at  $\sim 8000 \text{ cm}^{-1}$  (1.0 eV) [263]. Due to the high valence of  $\text{Cr}^{4+}$ , the Cr Hubbard bands shift down towards the fully occupied O-2p band, whereas the  $pd$  hybridization between Cr and O bands pushes the LHB back upwards, reducing the effective Coulomb repulsion  $U_{\text{eff}}$  and admixing O-2p states to the LHB and the UHB in the same way as it was demonstrated for  $\text{CrO}_2$  [262]. The reduction of the spectral weight of the LHB-UHB transition below  $T_N$  at low frequencies (see Fig. 4.79) can tentatively be explained by the fact, that the band width is smaller within the antiferromagnetic phase, which reduces the peak width and decreases the spectral weight at low frequencies.

<sup>38</sup>As discussed below, the presence of insulating grain boundaries cannot explain the peak observed at  $\sim 2800 \text{ cm}^{-1}$  (0.35 eV).

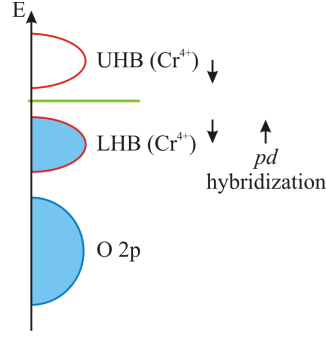


Figure 4.80: A sketch of the Cr Hubbard bands of  $\text{CaCrO}_3$ . The high valence of  $\text{Cr}^{4+}$ , shifts the Cr Hubbard bands down towards the fully occupied O-2p band. In contrast to that the  $pd$  hybridization between Cr and O bands pushes the LHB back upwards.

Applying the f-sum rule

$$\int_0^{\infty} \sigma_1(\omega) d\omega = \frac{\omega_{pl}^2}{8} \quad (4.5.1)$$

and integrating from  $0 \text{ cm}^{-1}$  to  $8000 \text{ cm}^{-1}$ , we get the plasma frequency  $\omega_{pl}$  for different temperatures. Using the expression

$$N_{\text{eff}} = \omega_{pl}^2 \frac{\epsilon_0 m V}{e^2}, \quad (4.5.2)$$

in which  $m$  represents the free electron mass,  $e$  the elementary electronic charge, and  $V$  the volume per Cr ion, we can determine the effective number of charge carriers  $N_{\text{eff}}$  per Cr ion, as shown in Fig. 4.81 a). Repeating this procedure for  $\text{Sr}_2\text{CrO}_4$ , we determine the spectral weight of the LHB-UHB peak observed at 1.0 eV in  $\text{Sr}_2\text{CrO}_4$  [263] at 290 K: Integrating the optical conductivity from  $0 \text{ cm}^{-1}$  to  $13000 \text{ cm}^{-1}$ , we find  $\omega_{pl} = 8865 \text{ cm}^{-1}$ . Using equation (4.5.2) we can determine the effective number of charge carriers  $N_{\text{eff}}$  per Cr ion in  $\text{Sr}_2\text{CrO}_4$ :  $N_{\text{eff}} = 7.9 \%$ . Comparing both results, we find a good agreement between our data and the result for  $\text{Sr}_2\text{CrO}_4$ , giving strong support to our interpretation of the peak at  $\sim 2800 \text{ cm}^{-1}$  (0.35 eV) as the transition from the LHB to the UHB. The metallic behavior of  $\text{CaCrO}_3$  compared to insulating  $\text{Sr}_2\text{CrO}_4$  should be a consequence of the three-dimensional crystal structure inducing larger band widths and thus smaller  $U_{\text{eff}}$ .

Additionally, we can estimate the free-carrier Drude contribution. But, at low temperatures, we cannot determine  $\omega_{pl}$  directly from the fit, due to the electronic oscillator at  $148 \text{ cm}^{-1}$ , which falsifies the Drude contribution. Therefore we carry out a Drude-Lorentz fit with one Drude peak and two electronic peaks in the mid-infrared range, but the error of this procedure is roughly more than 50 % at 20 K. The free-carrier Drude contribution is shown in Fig. 4.81 b). The Drude contribution first decreases with increasing temperature and has its minimum in the vicinity of  $T_N$ . Above the Néel temperature the Drude contribution increases.

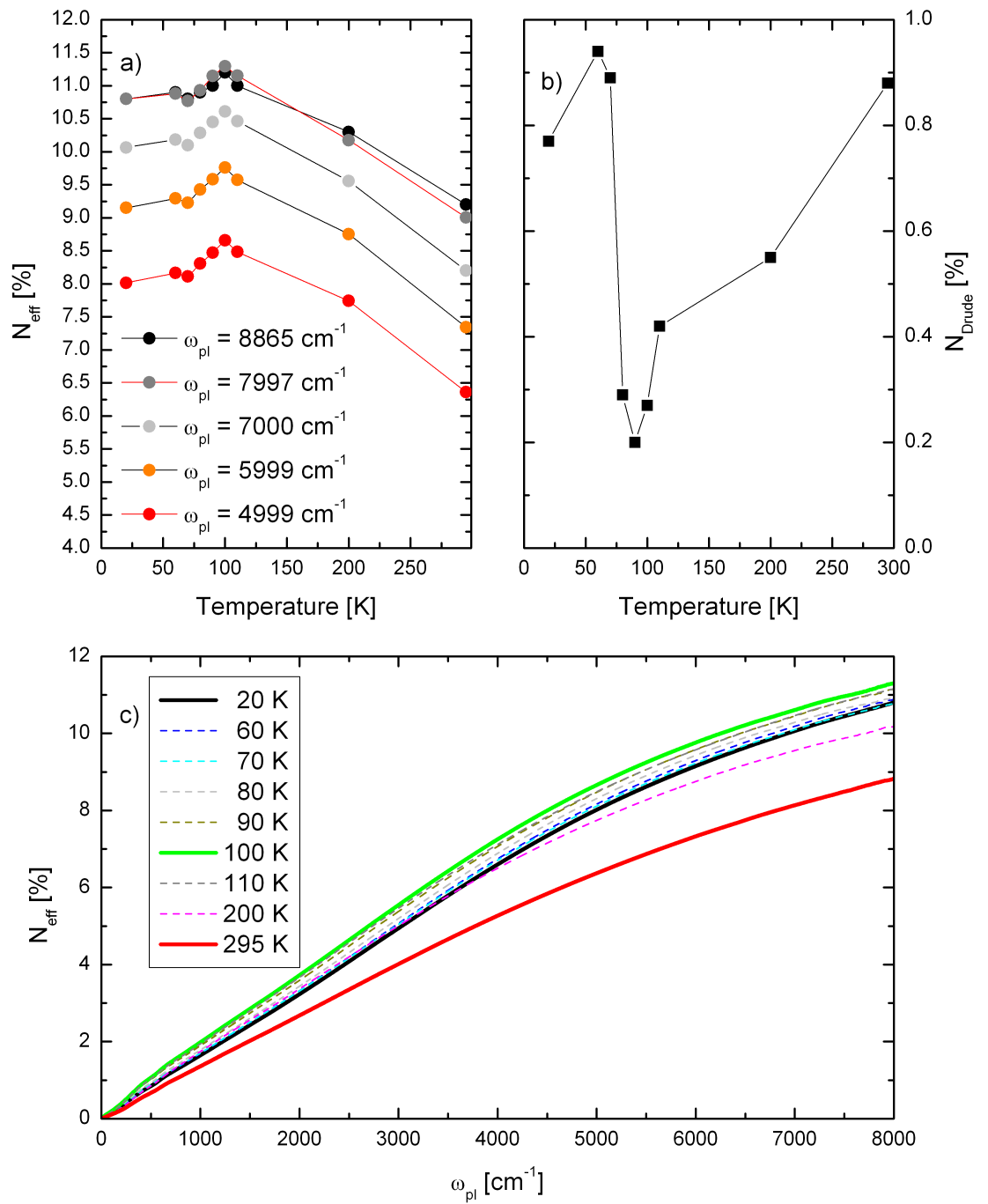


Figure 4.81: a) Effective number of charge carriers  $N_{\text{eff}}$  per Cr ion for integration from 0 to different values of the plasma frequency  $\omega_{\text{pl}}$ . b) Effective number  $N_{\text{Drude}}$  of the Drude contribution.

$\epsilon_{\perp}$				$\epsilon_{\parallel}$			
$\sigma^{ab}$	$\epsilon_{\infty}^{ab}$	$\omega_p^{ab} [cm^{-1}]$	$\gamma^{ab} [cm^{-1}]$	$\sigma^c$	$\epsilon_{\infty}^c$	$\omega_p^c [cm^{-1}]$	$\gamma^c [cm^{-1}]$
545.3	2.4	8848	2393	0.2	16.7	0	0
0.2	25.4	0	0	689.7	5.1	14944	5398
100.3	9.0	4437	3280	1253.4	9.0	17961	4290
266.2	10.3	12454	9729	1327.1	9.4	18401	4253

Table 4.31: Parameters of the Orenstein model at  $T = 20$  K for several values of the optical conductivity within the **ab** plane and parallel to the **c** axis ( $\sigma \equiv \sigma(\omega = 0)$ ).

### Anisotropic case

If  $\sigma_1(\omega)$  is strongly anisotropic,  $R(\omega)$  of a polycrystal represents an average over the different orientations of the grains [280], and the Kramers-Kronig analysis may produce a peak at finite frequencies although the individual components show conventional Drude behavior. In order to demonstrate that  $\text{CaCrO}_3$  is not a 2D metal, we study a model discussed by Orenstein *et al.* for the layered cuprates [280], i.e. for an optically uniaxial material with principal components of the dielectric tensor  $\epsilon_{\parallel}$  and  $\epsilon_{\perp}$ , representing the **c** axis and **ab** plane, respectively. When the direction of propagation, in this case parallel to the surface normal, **n**, is not parallel to **c**, there are two distinct modes of propagation: the ordinary, *o*, and extraordinary, *e*, modes. The component of the incident electric field  $\mathbf{E}_i$  perpendicular to the **nc** plane couples to the *o* mode, while the in-plane component launches the *e* mode. The effective dielectric functions are  $\epsilon_0 = \epsilon_{\perp}$  for the ordinary mode *o* and

$$\epsilon_e = \frac{\epsilon_{\perp} \epsilon_{\parallel}}{\epsilon_{\parallel} \cos^2 \theta + \epsilon_{\perp} \sin^2 \theta} \quad (4.5.3)$$

for the extraordinary mode *e*. Here  $\theta$  represents the angle between **n** and **c**.

We can model the optical conductivity  $\sigma(\omega)$  of a quasi-2D metallic crystal with  $\epsilon_{\parallel} = \epsilon_{\infty}^{ab} - (\omega_p^{ab})^2 / \omega(\omega + i\gamma^{ab})$  and  $\epsilon_{\perp} = \epsilon_{\infty}^c - (\omega_p^c)^2 / \omega(\omega + i\gamma^c)$ , where  $\epsilon_{\infty}^{ab,c}$ ,  $\omega_p^{ab,c}$ , and  $\gamma^{ab,c}$  are used as fit parameters. For the ordinary mode *o*,  $\sigma(\omega)$  has the Drude form. The extraordinary mode also has the Drude form for  $\theta = 0^\circ$  or  $90^\circ$ . We calculate an averaged reflectance [280]

$$\langle R \rangle = \frac{1}{2} \left[ R_o + \int_0^{\pi/2} R_e(\theta) \sin \theta d\theta \right] \quad (4.5.4)$$

with  $R_e$  and  $R_o$  representing the reflectivities of the *e* and *o* modes, respectively, and apply the Kramers-Kronig transformation to  $\langle R \rangle$ . Different parameter sets used in the Orenstein model are shown in Tab. 4.31, whereas the fit results for different values of the optical conductivity within the **ab** plane are given in Fig. 4.82.

As shown in Fig. 4.82, we compare different parameter sets of the Orenstein model. In the first model we assume a 2D metal, where  $\epsilon_{\parallel}$  shows insulating and  $\epsilon_{\perp}$  metallic

behavior. Using these assumptions we can describe the reflectance above  $3000 \text{ cm}^{-1}$  but fail in describing the low-energy range. In the second model we describe a 1D metal by assuming metallic conductivity only parallel to the **c** axis and insulating behavior within the **ab** plane. Within this model, we can describe the reflectance only above  $2000 \text{ cm}^{-1}$ .

In order to achieve a better description we have to estimate the anisotropy of the optical conductivity between both directions. As mentioned in the last section, we can model the reflectance within an isotropic model. As shown in Fig. 4.82, we need  $\sigma_1^{ab}(\omega = 0) \approx 200 (\Omega\text{cm})^{-1}$  within the **ab** plane and an enhanced optical conductivity parallel to the **c** axis. If we exchange both directions, we cannot describe the reflectance.

Therefore, we require a strong metallic behavior parallel to the **c** axis and a moderate conductivity within the **ab** plane to obtain a reasonable description of  $R(\omega)$ . This demonstrates, that  $\text{CaCrO}_3$  is a real 3D metal even in this anisotropic model.

As shown in Fig. 4.82 we achieve for the green fit ( $\sigma_1^{ab} = 266 (\Omega\text{cm})^{-1}$ ) a good description of the optical data for all frequencies. Especially, the excitation at  $\sim 2800 \text{ cm}^{-1}$  (0.35 eV) is described without an additional mid-infrared excitation. But this scenario requires a strong anisotropy ( $\sigma_1^{ab} = 266 (\Omega\text{cm})^{-1}$ ,  $\sigma_1^c = 1327 (\Omega\text{cm})^{-1}$ ) which is contrary to the results of the Wannier function projection procedure within the LDA calculation. This procedure predicts that the nearest-neighbor hopping matrix elements differ only by  $\sim 10 \%$  between the **c** axis and the **ab** plane, which renders a pronounced anisotropy of  $\sigma_1(\omega)$  very unlikely. Hence we tentatively attribute the peak at  $\sim 2800 \text{ cm}^{-1}$  (0.35 eV) to excitations from the lower to the upper Hubbard band. In addition, the strong temperature dependence of this excitation prevents the interpretation that this peak is an artefact of the anisotropic model.

Nevertheless, the results of the Orenstein model show that we cannot determine the spectral weight of this excitation without measuring on a single crystal. Furthermore, the LHB - UHB excitation should be anisotropic as well, because this peak represents a transition between two different Cr sites: For the energetically lowest transition the spins are aligned parallel to each other resulting in a stronger transition probability along the **c** axis than within the **ab** plane, see [116].

### Effective medium theory for large wavelengths

At the end of the section, we will try to describe the behavior of the sample within an effective medium theory. Our aim is to model metallic grains which are separated by insulating grain boundaries. For the sake of simplicity, we discuss a stack of alternating layers in the form  $ABAB\dots$ , where the layer  $A$  corresponds to the metallic grains of  $\text{CaCrO}_3$  and layer  $B$  to their insulating grain boundaries. We will still treat the individual layers and the fields therein as homogeneous, but assume different local dielectric functions  $\tilde{\epsilon}_A(\omega) = \epsilon_A + \epsilon_h$  and  $\tilde{\epsilon}_B(\omega) = \epsilon_B + \epsilon_h$  within the layers. We are only interested in the electromagnetic response along the stacking direction. The averaged

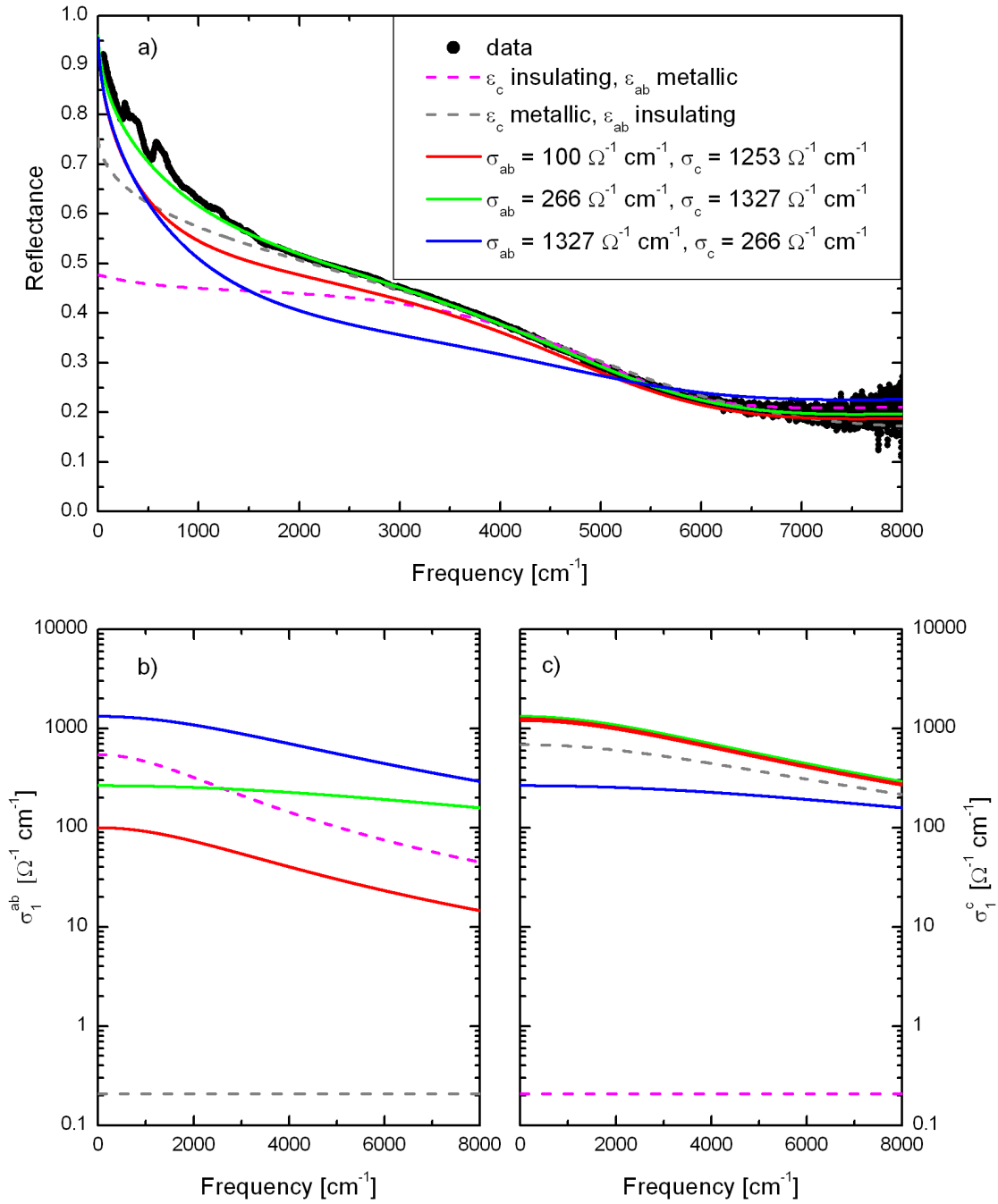


Figure 4.82: Comparison of a) the reflectance and the optical conductivity b) within the **ab** plane and c) parallel to the **c** axis for different parameters sets for the Orenstein model.

electric field  $E$  for the whole stack is given by [284]

$$E = \frac{1}{\epsilon} D = \sum_j \frac{x_j}{\epsilon_j} D, \quad j \in \{A, B\}, \quad (4.5.5)$$

where  $D$  represents the displacement field, which is the same in both layers, and  $x_j = d_j/d$  denotes the relative volume fraction. Here  $d_j$  is the thickness of layer  $j$  and  $d_A + d_B = d$ . Starting from this equation we can derive<sup>39</sup> the following expressions

$$\begin{aligned} \frac{1}{\epsilon(\omega)} &= \frac{x_A}{\epsilon_A(\omega) + \epsilon_h(\omega)} + \frac{x_B}{\epsilon_B(\omega) + \epsilon_h(\omega)}, & \epsilon_h(\omega) &= \epsilon_\infty + \sum_i \frac{\omega_{p,i}^2}{\omega_{0,i}^2 - \omega^2 - i\gamma_i\omega}, \\ \Rightarrow \epsilon(\omega) &= \frac{(\epsilon_A(\omega) + \epsilon_h(\omega)) \cdot (\epsilon_B(\omega) + \epsilon_h(\omega))}{\epsilon_h(\omega) + x_A \cdot \epsilon_B(\omega) + x_B \cdot \epsilon_A(\omega)}, \end{aligned} \quad (4.5.6)$$

assuming that the phonons and  $\epsilon_\infty$  are homogeneous, thus they are combined in  $\epsilon_h$ . But this homogeneous contribution “feels” the inhomogeneous local fields. The model recovers the conventional Drude-Lorentz form if we either choose  $\epsilon_A = \epsilon_B$  or  $x_A = 1 - x_B = 0$ .

This model implies some difficulties: We do not know the dielectric functions  $\epsilon_A(\omega)$  and  $\epsilon_B(\omega)$  exactly. We assume that the  $\text{CaCrO}_3$  crystallites in layer  $A$  are metallic and that we can describe  $\epsilon_A(\omega)$  by a Drude peak (plus the homogeneous phonon contribution  $\epsilon_h$ ). The  $B$  layers correspond to the insulating grain boundaries and we approximate the related dielectric function  $\epsilon_B$  by a single constant for all frequencies (plus the homogeneous phonon contribution  $\epsilon_h$ ). Additionally, we assume that the homogenous phonons are described by the Drude-Lorentz fit described above, see Tab. 4.30. Furthermore, we assume that the grain boundaries are thin compared to the grains  $x_B \ll x_A$ . In the fit, we use a relative volume fraction of 99.9 % to 0.1 %. For a typical grain size of 20  $\mu\text{m}$ , this corresponds to a grain boundary of 20 nm. The fit parameters are shown in Tab. 4.32, and the corresponding fit is presented in Fig. 4.83.

As shown in Fig. 4.83, we achieve a good description of the reflectance, but find a clear disagreement for low frequencies. In contrast to the isotropic analysis, the reflectance extrapolates to a value smaller than one for  $\omega \rightarrow 0$ , since  $\sigma_{DC}$  along the stack equals 0. Furthermore, we achieve a better description of the reflectance below 100  $\text{cm}^{-1}$  within the isotropic analysis. The thin insulating layer  $B$  prevents a metallic behavior of the whole sample, although we assume metallic conductivity within the  $\text{CaCrO}_3$  grains, see inset of Fig. 4.83 b). For a grain size of  $L = 20 \mu\text{m}$  the insulating layer should be relevant for wavelength less than 500  $\text{cm}^{-1}$ , but the suppression in  $R(\omega)$  only below 100  $\text{cm}^{-1}$  and in  $\sigma_1(\omega)$  only far below the limits of our experiment ( $\sim 56 \text{ cm}^{-1}$ ).

<sup>39</sup>For details of the derivation see [284].

$\omega_0$ [cm <sup>-1</sup> ]	$\omega_p$ [cm <sup>-1</sup> ]	$\gamma$ [cm <sup>-1</sup> ]	S
$\epsilon_A(\omega)$			
0	20736	10696.1	-
$\epsilon_h(\omega)$			
226	483	677.1	4.57
260	672	31.4	6.66
343	1155	109.6	11.31
577	1361	161.6	5.57

Table 4.32: Parameters of the effective medium model for CaCrO<sub>3</sub> at T = 20 K. Here,  $S$  denotes the oscillator strength  $S = \omega_p^2/\omega_0^2$ . The high-frequency dielectric constant is:  $\epsilon_\infty = 5.61$ . The dielectric constant describing layer  $B$  is  $\epsilon_B(\omega) = 3.00$ .

Furthermore, we see that the effective medium theory describe the reflectance  $R(\omega)$  very well without a peak in  $\sigma_1(\omega)$  at 0.35 eV. But, the premises of the theory are no longer fulfilled: At this frequencies the wavelengths are much shorter than the typical grain size.

Summarizing our investigation, we have shown that if we assume that the real part of the optical conductivity is isotropic, and that the wavelength is much smaller than the typical grain size, we can describe the optical properties for all measured frequencies. Within this isotropic model, we attribute the peak at 350 meV to excitations from the lower to the upper Hubbard band, similar to insulating Sr<sub>2</sub>CrO<sub>4</sub> where this excitation is observed at 1 eV. This implies that correlation effects are important in this compound. In a second scenario, we describe the optical data by using a model presented by Orenstein *et al.* [280] where the optical conductivity within the **ab** plane is much smaller than parallel to the **c** axis. We can describe the reflectance as well for all measured frequencies but we obtain a reasonable description of  $R(\omega)$  only for  $\sigma_1(\omega = 0) \geq 200$  ( $\Omega\text{cm}$ )<sup>-1</sup> for each direction which clearly demonstrates the 3D metallic behavior of CaCrO<sub>3</sub>. Furthermore, we achieve a good description even of the mid-infrared excitation at  $\sim 2800$  cm<sup>-1</sup> (0.35 eV) for  $\sigma_1^{ab} = 266$  ( $\Omega\text{cm}$ )<sup>-1</sup>,  $\sigma_1^c = 1327$  ( $\Omega\text{cm}$ )<sup>-1</sup>. But this is contrary to the results of the Wannier function projection procedure within the LDA calculation, which predicts a much smaller difference between the optical conductivity parallel the **c** axis and within the **ab** plane.

In addition, we have used an effective medium theory to describe the behavior of the sample at low frequencies. We model metallic grains which are separated by insulating grain boundaries and assume that the wavelength is much larger than the grain size. We find significant differences between the effective medium theory and the isotropic analysis only below 100 cm<sup>-1</sup>: Within the effective medium theory, the reflectance extrapolates to a value smaller than one for  $\omega \rightarrow 0$  whereas the reflectance extrapolates to one within the isotropic model.

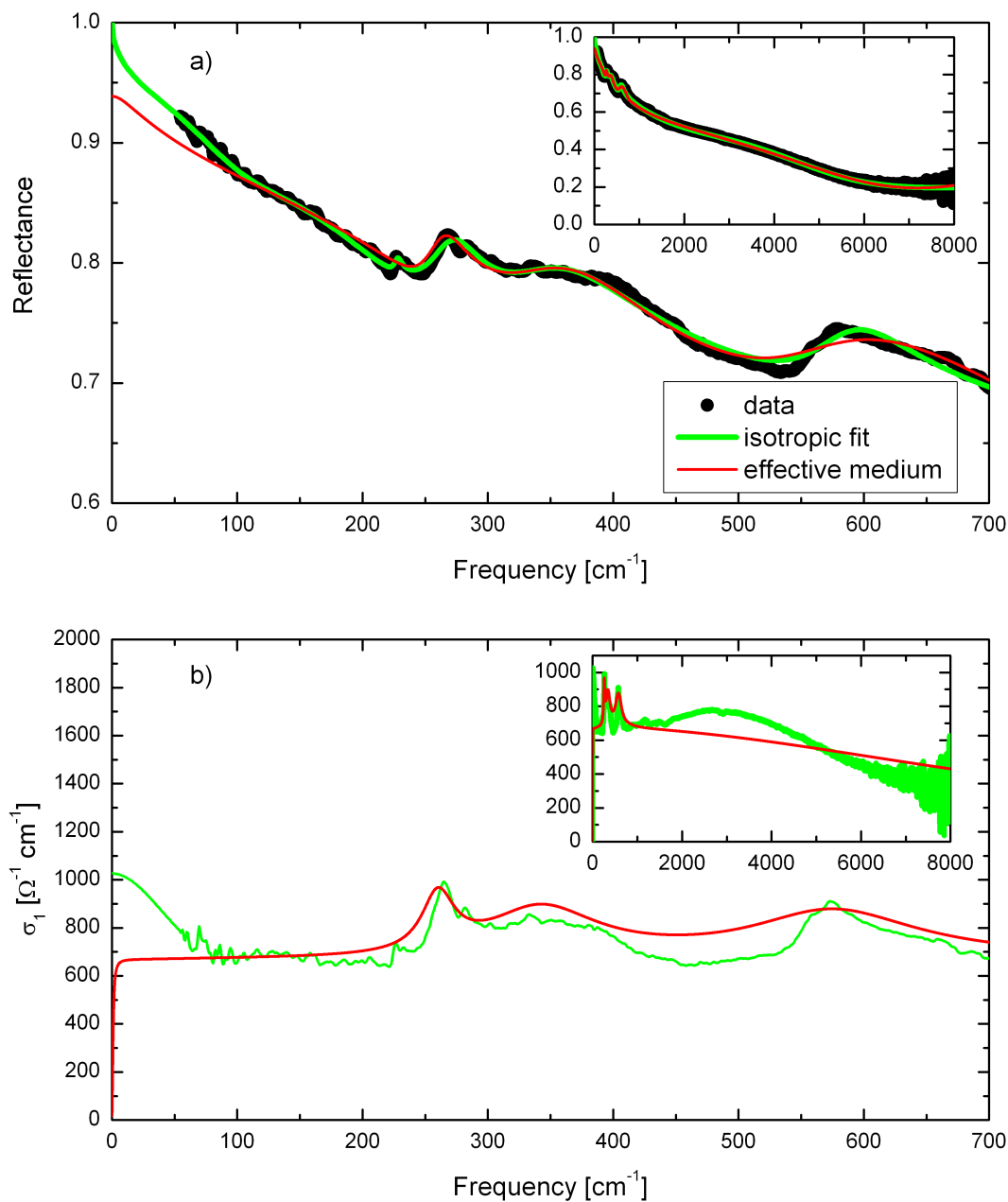


Figure 4.83: Comparison between the effective medium model (red) and the results of the isotropic analysis (green). The upper panel shows the reflectance, whereas the optical conductivity is shown in the bottom panel. The optical conductivity of the effective medium model (red) is determined by applying equation (2.11.8) to (4.5.6).

In conclusion  $\text{CaCrO}_3$  is an antiferromagnetic transition-metal oxide showing 3D metallic behavior. The anisotropic C-type magnetic structure is explained by frustrating  $nnn$  (diagonal) interactions. The magnetic interactions are caused by the strong  $pd$  hybridization, which is a consequence of the high oxidation state associated with a small or negative charge-transfer gap. The peak at 0.35 eV in  $\sigma_1(\omega)$  suggests that electronic correlations are relevant in  $\text{CaCrO}_3$ . A quantitative determination of the spectral weight of this peak requires measurements on a single crystal.



## 5 Conclusion

In this thesis we have investigated the low-energetic excitations in different highly correlated transition-metal oxides by means of optical spectroscopy. Additionally, we have analyzed the electronic structure and the optical spectra of some transition-metal oxides by using a cluster-model configuration-interaction calculation.

In the first part we gave a detailed description of the cluster-model calculation, which was developed in the framework of this thesis. In many cases a cluster-model calculation with full ionic multiplet structure, including crystal-field effects and covalency within a local cluster-model, provides a reasonable description of the experimental results. We have presented a general expression for the matrix elements of the crystal-field operator using the Racah-Wigner algebra, where the wave functions are expressed as coupled multiplet wave functions within a given angular momentum coupling scheme. The knowledge of all possible Slater determinants is not necessary and the matrix elements can be written as compact expressions computable with arbitrary accuracy. Furthermore, we gave a general expression for the matrix elements of the tight-binding operator within the Slater-Koster approximation. This expression was derived within Sobel'man's parentage scheme.

The second part describes the investigation of low-energetic excitations in several transition-metal compounds. We have started with the analysis of crystal-field excitations in  $\text{VOCl}$  by using group-theoretical considerations as well as cluster-model calculations.  $\text{VOCl}$  is used as a reference system for  $\text{YVO}_3$  [116] where orbital excitations were observed. In  $\text{YVO}_3$ , orbitals on different sites interact with each other [117, 118] via the collective Jahn-Teller effect, i.e. the coupling to the lattice, and via exchange interactions. We have performed transmittance measurements at 20 K and 295 K and identified the crystal-field excitations by using the cluster-model calculation.

In the following we investigated two compounds being part of the class of multiferroic materials which have attracted increasing attention because of the coexistence of ferroelectric and magnetic order. In order to study the spin-lattice interaction in the hexagonal multiferroic compounds  $\text{YMnO}_3$  and  $\text{YMn}_{0.7}\text{Ga}_{0.3}\text{O}_3$  and their probable contribution to the occurrence of ferroelectricity in these compounds, we have performed a detailed temperature-dependent analysis of the phonon spectra between 20 K and 295 K including a factor-group analysis. By analyzing the lattice dynamics and the dependence of the phonon spectra on Ga doping we investigated the influence of the magnetization on the dynamical polarization and achieved a better understanding of the origin of ferroelectricity. In case of  $\text{YMnO}_3$  we found all phonon modes predicted by the factor-group analysis but required a further mode for each polarization direction

to describe the phonon spectrum properly. The additional mode is probably caused by the multi-phonon background. Furthermore we quantified the change of the fit parameters with increasing temperature. Thereby we have found no change in the phonon spectra around the antiferromagnetic ordering temperature  $T_N$ . In addition, we identified the lowest phonon mode as a soft mode. In case of the Ga doped system we have found for  $\mathbf{E} \parallel \mathbf{c}$  more than the expected number of phonon modes, because the system represents a mixture of  $\text{YMnO}_3$  and  $\text{YGaO}_3$  and we found additional Mn-Ga vibrations. In contrast to pure Mn-Mn or Ga-Ga vibrations, the Mn-Ga vibrations have a dipole moment and are infrared active. In case of  $\mathbf{E} \perp \mathbf{c}$  we find most of the phonon modes predicted by the factor-group analysis and quantified the change of the fit parameters with increasing temperature. We found no change in the fit parameters around  $T_N$ . Following Iliev *et al.* [152] we associated the lowest phonon mode with displacements of the Y ions along the  $\mathbf{c}$  axis which indicated the important role of the Y ions for the occurrence of ferroelectricity in  $\text{YMnO}_3$ , whereas the  $\text{Mn}^{3+}$  ions have no influence due to the  $d^0$ -ness rule. By comparing the behavior of the lowest phonon mode in the doped and the undoped system we confirmed the results of Adem *et al.* [169] concerning the elongation of the  $\text{YO}_6$  antiprisms and the reduction of the local dipole moments associated with the Y ions.

In addition we have analyzed the spin-lattice interaction of a further multiferroic, monoclinic compound  $\text{MnWO}_4$ . The spin-lattice interaction plays an important role in the coupling between the antiferromagnetic and the ferroelectric order parameters.  $\text{MnWO}_4$  is one of the multiferroic materials in which the cycloidal spin structure induces ferroelectricity [190]. According to Lautenschläger *et al.* [195] the compound undergoes successive magnetic phase transitions at  $T_{N_3} \sim 13.5$  K,  $T_{N_2} \sim 12.7$  K, and  $T_{N_1} \sim 7.5$  K which are related to three magnetic ordering states, AF3, AF2, and AF1 where only the AF2 phase shows ferroelectricity. Here, the magnetic phase transitions are not related with structural phase transitions. In order to achieve a better understanding of the coupling between the antiferromagnetic and the ferroelectric order parameters we have performed a detailed analysis of the phonon spectra for different temperatures between 10 K and 295 K including a factor-group analysis. The monoclinic symmetry of this compound requires for  $\mathbf{E} \parallel \mathbf{ac}$  the application of a generalized Drude-Lorentz model developed by Kuz'menko *et al.* [188]. (For  $\mathbf{E} \parallel \mathbf{b}$  we used the conventional Drude-Lorentz model.) Within the  $\mathbf{ac}$  plane we need an additional fit parameter to describe the angle between the dipole moment associated with the phonon mode and the  $\mathbf{x}$  axis. In order to apply the generalized Drude-Lorentz model we developed in collaboration with Alexander Gössling a new fit program for performing the fit procedure where we have to fit at least three different polarization directions (with  $\mathbf{E} \parallel \mathbf{ac}$  plane) to determine the orientation of each phonon mode within the  $\mathbf{ac}$  plane. We achieved a good description of the reflectance for  $\mathbf{E} \parallel \mathbf{ac}$  except between 600 and 800  $\text{cm}^{-1}$ , which is caused probably by a large multi-phonon background like in  $\text{YMnO}_3$ . Additionally, the reflectance is pretty high in this energy range and weak features may have a significant influence on the reflectivity. We have found all infrared-active phonon modes predicted by the factor-group analysis but require for

---

**E** || **ac** a further mode to describe the optical data properly. In addition we described the change of the fit parameters with increasing temperature. We have found no qualitative change in the phonon spectra between the AF2, AF3, and the paramagnetic phase. (The determination of the phonon modes within the AF1 phase could not be realized.) The spin-lattice interaction within this compound is too weak to change the phonon spectra remarkably. Additionally, we investigated the infrared excitations below the band gap by performing transmittance measurements at 30 K and 295 K and analyzed the spectra by using the cluster-model calculation presented in the first part of this thesis. We achieved an excellent description of the optical data and identified all excitations. Furthermore we described the dependence of the results of the cluster-model calculation on several calculation parameters.

In the following we have analyzed the phonon spectra of  $\text{BiB}_3\text{O}_6$ . The exceptional optical nonlinearities of this compound have been attributed to the bonds of the  $[\text{BO}_3]$  units and to a lone-pair electron at the Bi ion [238]. In order to investigate the lattice dynamics which are essential for a quantitative description of these bonds we performed reflectance measurements at 20 K and 295 K. By using the generalized Drude-Lorentz model and comparing our data with room-temperature Raman data [236, 242, 243], neutron data [248], and first-principle calculations [248, 249] we identified the fundamental phonon modes and achieved a good agreement with the results of a factor-group analysis. Furthermore, we gave a possible explanation for the unusual shift of the phonon mode at  $168\text{ cm}^{-1}$ ,  $645\text{ cm}^{-1}$ , and  $647\text{ cm}^{-1}$  with increasing temperature: The temperature dependence of the displacement of the Bi ions and the complex interplay of the different  $[\text{BiO}_4]^{5-}$ ,  $[\text{BO}_3]^{3-}$ , and  $[\text{BO}_4]^{5-}$  units may cause the unusual phonon shift.

At the end of the thesis, optical studies of the anomalous antiferromagnetic metallic oxide  $\text{CaCrO}_3$  were presented. This metallic oxide shows an exception from the rule, that in transition-metal oxides ferromagnetism typically coexists with metallic conductivity, whereas insulators usually exhibit antiferromagnetism. Observations of antiferromagnetic order in transition-metal oxides with metallic conductivity are of great interest. In collaboration with the groups of M. Braden, D.I. Khomskii, and V.I. Anisimov we have shown that the perovskite  $\text{CaCrO}_3$  with orthorhombic space group  $Pbnm$  is a three-dimensional transition-metal oxide with metallic conductivity, antiferromagnetic exchange interactions, and C-type antiferromagnetic order. In addition, we associated the excitation at 0.35 eV with excitations from the lower to the upper Hubbard band, similar to insulating  $\text{Sr}_2\text{CrO}_4$ . This implies that electronic correlations are important in this compound.



# A Wigner n-j symbols

The application of Racah's expressions for the matrix elements of tensor operators in section "2.4 Racah-Wigner Algebra" requires the recoupling of different angular momenta. The Wigner n-j symbols describe this recoupling process depending on the number of the angular momenta being involved.

## A.1 3-j symbol

The 3-j symbol is related to the well-known Clebsch-Gordan coefficients, which describe the coupling of two quantum mechanical angular momenta  $J_1$  and  $J_2$  to a total angular momentum  $J$ :

$$\begin{pmatrix} J_1 & J_2 & J \\ m_1 & m_2 & -M \end{pmatrix} \equiv \frac{(-1)^{J_1-J_2+M}}{\sqrt{2J+1}} \langle J_1 J_2 m_1 m_2 | J M \rangle. \quad (\text{A.1.1})$$

The resulting space has a  $(2J_1 + 1)(2J_2 + 1)$ -dimensional uncoupled basis

$$|J_1 m_1\rangle |J_2 m_2\rangle \equiv |J_1 m_1\rangle \otimes |J_2 m_2\rangle, \quad m_1 = -J_1, \dots, J_1, \quad m_2 = -J_2, \dots, J_2. \quad (\text{A.1.2})$$

The 3-j symbol is an algebraic function of six arguments that may be defined by the expression [7]

$$\begin{aligned} \begin{pmatrix} J_1 & J_2 & J_3 \\ m_1 & m_2 & m_3 \end{pmatrix} &\equiv \delta_{m_1+m_2+m_3,0} (-1)^{J_1-J_2-m_3} \\ &\times \left[ \frac{(J_1 + J_2 - J_3)! (J_1 - J_2 + J_3)! (-J_1 + J_2 + J_3)! (J_1 - m_1)! (J_1 + m_1)!}{(J_1 + J_2 + J_3 + 1)!} \right. \\ &\times \left. \frac{(J_2 - m_2)! (J_2 + m_2)! (J_3 - m_3)! (J_3 + m_3)!}{(J_1 + J_2 + J_3 + 1)!} \right]^{1/2} \\ &\times \sum_k \left[ \frac{(-1)^k}{k! (J_1 + J_2 - J_3 - k)! (J_1 - m_1 - k)! (J_2 + m_2 - k)!} \right. \\ &\times \left. \frac{(-1)^k}{(J_3 - J_2 + m_1 + k)! (J_3 - J_1 - m_2 + k)!} \right], \end{aligned} \quad (\text{A.1.3})$$

in which the summation is finite, being over those integer values of  $k$  that satisfy

$$\max(0, J_2 - J_3 - m_1, J_1 - J_3 + m_2) \leq k \leq \min(J_1 + J_2 - J_3, J_1 - m_1, J_2 + m_2). \quad (\text{A.1.4})$$

The function (A.1.3) is defined only for values of  $J_i$  and  $m_i$  such that the arguments of all factorials are non-negative integers. It follows that  $J_i$  and  $m_i$  must both be either

integer or half-integer, with  $J_i \geq |m_i| \geq 0$  (each  $i$ ), that  $J_1 + J_2 + J_3$  and  $m_1 + m_2 + m_3$  must be integer, and that  $J_1 - J_2 - m_3$  is integer, so that the 3-j symbol is real. Also the three  $J_i$  must satisfy the three inequalities

$$\begin{aligned} J_1 + J_2 &\geq J_3, \\ J_2 + J_3 &\geq J_1, \\ J_3 + J_1 &\geq J_2. \end{aligned} \tag{A.1.5}$$

These inequalities together with the integer-sum restriction are called the “triangle relations”. (The symbol  $\delta(J_1 J_2 J_3)$  is +1 if the triangle relations are satisfied and zero otherwise.)

## A.2 6-j symbol

Let  $J$  be the total angular momentum of a system formed of three separate component systems of angular momenta  $J_1$ ,  $J_2$ , and  $J_3$ , respectively:

$$J = J_1 + J_2 + J_3. \tag{A.2.1}$$

In the  $\prod_{i=1}^3 (2J_i + 1)$  dimensional space spanned by the vectors

$$|m_1 m_2 m_3\rangle = \prod_{i=1}^3 |J_i m_i\rangle \tag{A.2.2}$$

the following couplings lead to two different basis systems:

1.  $|(J_1 J_2) J_{12} J_3 J M\rangle : J_1 + J_2 = J_{12}, \quad J_{12} + J_3 = J.$
2.  $|(J_2 J_3) J_{23} J_1 J M\rangle : J_2 + J_3 = J_{23}, \quad J_{23} + J_1 = J.$

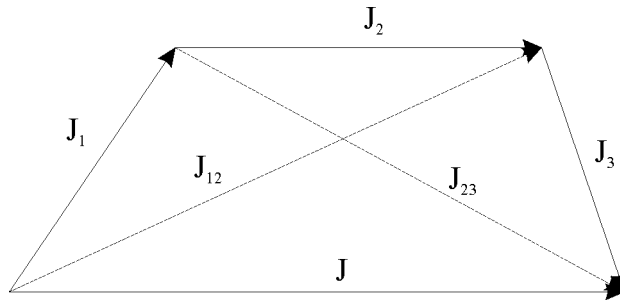


Figure A.2.1: Tetrahedron associated with the 6-j symbol.

We can pass from one system to the other by a certain unitary transformation. This transformation is described by a function of six arguments, the so-called 6-j symbol

that may be defined by the expression [53, 285]

$$\left\{ \begin{array}{ccc} J_1 & J_2 & J_{12} \\ J_3 & J & J_{23} \end{array} \right\} = \Delta(J_1, J_2, J_{12}) \Delta(J_1, J, J_{23}) \Delta(J_3, J, J_{12})$$

$$\times \sum_k \left[ \frac{(-1)^k (k+1)!}{(k-J_1-J_2-J_{12})! (k-J_1-J-J_{23})! (k-J_3-J_2-J_{23})! (k-J_3-J-J_{12})!} \right]$$

$$\times \frac{1}{(J_1+J_2+J_3+J-k)! (J_2+J_{12}+J+J_{23}-l)! (J_{12}+J_1+J_{23}+J_3-k)!}, \quad (\text{A.2.3})$$

in which

$$\Delta(a, b, c) = \left[ \frac{(a+b-c)!(a-b+c)!(-a+b+c)!}{(a+b+c+1)!} \right]^{1/2}. \quad (\text{A.2.4})$$

The 6-j symbol is related to Racah's  $W$  coefficient [54]

$$W(J_1 J_2 J J_3; J_{12} J_{23}) = (-1)^{J_1+J_2+J_3+J} \left\{ \begin{array}{ccc} J_1 & J_2 & J_{12} \\ J_3 & J & J_{23} \end{array} \right\}. \quad (\text{A.2.5})$$

The 6-j symbol is considered to be zero unless the argument of each factorial in (A.2.3) and (A.2.4) is a non-negative integer. This means that each of the arguments of the 6-j symbol must be a non-negative integer or half-integer, and that all four of the triangle relations

$$\delta(J_1 J_2 J_{12}), \quad \delta(J_1 J J_{23}), \quad \delta(J_3 J_2 J_{23}), \quad \delta(J_3 J J_{12}) \quad (\text{A.2.6})$$

must be satisfied. The summation in (A.2.3) is finite and covers integer values of  $k$  in the range

$$\max(J_1+J_2+J_{12}, J_1+J+J_{23}, J_3+J_2+J_{23}, J_3+J+J_{12})$$

$$\leq k \leq \min(J_1+J_2+J_3+J, J_2+J_{12}+J+J_{23}, J_{12}+J_1+J_{23}+J_3). \quad (\text{A.2.7})$$

The recoupling of even more than three angular momenta can be described by the 6-j symbol. But in the special case of four angular momenta, we use the 9-j symbol for simplification.

## A.3 9-j symbol

For a system with total angular momentum  $J$  which consists of four subsystems with respective angular momenta  $J_1, J_2, J_3,$  and  $J_4,$  we have

$$J = J_1 + J_2 + J_3 + J_4. \quad (\text{A.3.1})$$

In the  $\prod_{i=1}^4 (2J_i + 1)$  dimensional space spanned by the vectors

$$|m_1 m_2 m_3 m_4\rangle = \prod_{i=1}^4 |J_i m_i\rangle \quad (\text{A.3.2})$$

the following couplings lead to two different basis systems:

1.  $|(J_1 J_2) J_{12} (J_3 J_4) J_{34} J M\rangle : J_1 + J_2 = J_{12}, \quad J_3 + J_4 = J_{34}, \quad J_{12} + J_{34} = J.$
2.  $|(J_1 J_3) J_{13} (J_2 J_4) J_{24} J M\rangle : J_1 + J_3 = J_{13}, \quad J_2 + J_4 = J_{24}, \quad J_{13} + J_{24} = J.$

The transformation between these two different basis systems is described by the 9-j symbol, which is defined as [53, 285]

$$\begin{aligned} \left\{ \begin{array}{ccc} j_{11} & j_{12} & j_{13} \\ j_{21} & j_{22} & j_{23} \\ j_{31} & j_{32} & j_{33} \end{array} \right\} &= \sum_j (-1)^{2j} (2j + 1) \left\{ \begin{array}{ccc} j_{11} & j_{12} & j_{13} \\ j_{32} & j_{33} & j \end{array} \right\} \\ &\times \left\{ \begin{array}{ccc} j_{12} & j_{22} & j_{32} \\ j_{21} & j & j_{23} \end{array} \right\} \left\{ \begin{array}{ccc} j_{13} & j_{23} & j_{33} \\ j & j_{11} & j_{12} \end{array} \right\}, \end{aligned} \quad (\text{A.3.3})$$

in which the sum runs over all integer values of  $j$  with

$$\max(|j_{11} - j_{33}|, |j_{32} - j_{21}|, |j_{12} - j_{23}|) \leq j \leq \min(j_{11} + j_{33}, j_{32} - j_{21}, j_{12} - j_{23}). \quad (\text{A.3.4})$$

From the properties of the 6-j symbol it follows that the 9-j symbol is zero unless the arguments in each row and in each column satisfy the triangle relations.

The 9-j symbol is related to Fano's  $X$  coefficient [149]

$$\left\{ \begin{array}{ccc} j_{11} & j_{12} & j_{13} \\ j_{21} & j_{22} & j_{23} \\ j_{31} & j_{32} & j_{33} \end{array} \right\} = X(j_{11}j_{12}j_{13}, j_{21}j_{22}j_{23}, j_{31}j_{32}j_{33}). \quad (\text{A.3.5})$$

Higher-order  $3n$ -j symbols can be defined, though not uniquely – there being two essentially different 12-j symbols, five different 15-j symbols, and eighteen different 18-j symbols [286].

## B Expansion coefficients for tight-binding operator

The  $b_q^t(l_i, l_j, m'_1)$  expansion coefficients used in (2.8.36) are given in terms of the Eulerian angles

$$\alpha = \arctan [y/x] \quad (\text{B.0.1})$$

and

$$\beta = \arccos \left[ z / (\sqrt{x^2 + y^2 + z^2}) \right], \quad (\text{B.0.2})$$

where  $x$ ,  $y$ , and  $z$  indicate the components of the vector connecting the  $i$ th and the  $j$ th ion. Note, that within the angle representation the  $b_q^t$  coefficients for  $l_i > l_j$  are equal to the  $b_q^t$  coefficients for  $l_i < l_j$ .

$(l_1 l_2 m'_1)$	$t$	$q$	$b_q^t$
$ss\sigma$	0	0	1
$sp\sigma$	1	(-1)	$\sqrt{\frac{3}{2}} e^{i\alpha} \sin(\beta)$
	1	0	$\sqrt{3} \cos(\beta)$
	1	1	$-\sqrt{\frac{3}{2}} e^{-i\alpha} \sin(\beta)$
$sd\sigma$	2	(-2)	$\frac{1}{2} \sqrt{\frac{15}{2}} e^{2i\alpha} \sin^2(\beta)$
	2	(-1)	$\sqrt{\frac{15}{2}} e^{i\alpha} \cos(\beta) \sin(\beta)$
	2	0	$\frac{1}{4} \sqrt{5} (3 \cos(2\beta) + 1)$
	2	1	$-\sqrt{\frac{15}{2}} e^{-i\alpha} \cos(\beta) \sin(\beta)$
	2	2	$\frac{1}{2} \sqrt{\frac{15}{2}} e^{-2i\alpha} \sin^2(\beta)$
$sf\sigma$	3	(-3)	$\frac{1}{4} \sqrt{35} e^{3i\alpha} \sin^3(\beta)$
	3	(-2)	$\frac{1}{2} \sqrt{\frac{105}{2}} e^{2i\alpha} \cos(\beta) \sin^2(\beta)$
	3	(-1)	$\frac{1}{8} \sqrt{21} e^{i\alpha} (5 \cos(2\beta) + 3) \sin(\beta)$
	3	0	$\frac{1}{8} \sqrt{7} (3 \cos(\beta) + 5 \cos(3\beta))$
	3	1	$-\frac{1}{8} \sqrt{21} e^{-i\alpha} (5 \cos(2\beta) + 3) \sin(\beta)$
	3	2	$\frac{1}{2} \sqrt{\frac{105}{2}} e^{-2i\alpha} \cos(\beta) \sin^2(\beta)$
	3	3	$-\frac{1}{4} \sqrt{35} e^{-3i\alpha} \sin^3(\beta)$

Table B.1: PART I

$(l_1 l_2 m'_1)$	$t$	$q$	$b_q^t$
$sg\sigma$	4	(-4)	$\frac{3}{8}\sqrt{\frac{35}{2}}e^{4i\alpha}\sin^4(\beta)$
	4	(-3)	$\frac{3}{4}\sqrt{35}e^{3i\alpha}\cos(\beta)\sin^3(\beta)$
	4	(-2)	$\frac{3}{8}\sqrt{\frac{5}{2}}e^{2i\alpha}(7\cos(2\beta)+5)\sin^2(\beta)$
	4	(-1)	$\frac{3}{16}\sqrt{5}e^{i\alpha}(7\cos(2\beta)+1)\sin(2\beta)$
	4	0	$\frac{3}{64}(20\cos(2\beta)+35\cos(4\beta)+9)$
	4	1	$-\frac{3}{16}\sqrt{5}e^{-i\alpha}(7\cos(2\beta)+1)\sin(2\beta)$
	4	2	$\frac{3}{8}\sqrt{\frac{5}{2}}e^{-2i\alpha}(7\cos(2\beta)+5)\sin^2(\beta)$
	4	3	$-\frac{3}{4}\sqrt{35}e^{-3i\alpha}\cos(\beta)\sin^3(\beta)$
	4	4	$\frac{3}{8}\sqrt{\frac{35}{2}}e^{-4i\alpha}\sin^4(\beta)$
$sh\sigma$	5	(-5)	$\frac{3}{16}\sqrt{77}e^{5i\alpha}\sin^5(\beta)$
	5	(-4)	$\frac{3}{8}\sqrt{\frac{385}{2}}e^{4i\alpha}\cos(\beta)\sin^4(\beta)$
	5	(-3)	$\frac{1}{32}\sqrt{385}e^{3i\alpha}(9\cos(2\beta)+7)\sin^3(\beta)$
	5	(-2)	$\frac{1}{8}\sqrt{\frac{1155}{2}}e^{2i\alpha}\cos(\beta)(3\cos(2\beta)+1)\sin^2(\beta)$
	5	(-1)	$\frac{1}{8}\sqrt{\frac{165}{2}}e^{i\alpha}(21\cos^4(\beta)-14\cos^2(\beta)+1)\sin(\beta)$
	5	0	$\frac{1}{8}\sqrt{11}\cos(\beta)(63\cos^4(\beta)-70\cos^2(\beta)+15)$
	5	1	$-\frac{1}{8}\sqrt{\frac{165}{2}}e^{-i\alpha}(21\cos^4(\beta)-14\cos^2(\beta)+1)\sin(\beta)$
	5	2	$\frac{1}{8}\sqrt{\frac{1155}{2}}e^{-2i\alpha}\cos(\beta)(3\cos(2\beta)+1)\sin^2(\beta)$
	5	3	$-\frac{1}{32}\sqrt{385}e^{-3i\alpha}(9\cos(2\beta)+7)\sin^3(\beta)$
	5	4	$\frac{3}{8}\sqrt{\frac{385}{2}}e^{-4i\alpha}\cos(\beta)\sin^4(\beta)$
5	5	$-\frac{3}{16}\sqrt{77}e^{-5i\alpha}\sin^5(\beta)$	
$pp\sigma$	0	0	$\frac{1}{3}$
	2	(-2)	$\frac{5e^{2i\alpha}\sin^2(\beta)}{2\sqrt{6}}$
	2	(-1)	$\frac{5e^{i\alpha}\cos(\beta)\sin(\beta)}{\sqrt{6}}$
	2	0	$\frac{5}{12}(3\cos(2\beta)+1)$
	2	1	$-\frac{5e^{-i\alpha}\cos(\beta)\sin(\beta)}{\sqrt{6}}$
	2	2	$\frac{5e^{-2i\alpha}\sin^2(\beta)}{2\sqrt{6}}$
$pp\pi$	0	0	$\frac{2}{3}$
	2	(-2)	$-\frac{5e^{2i\alpha}\sin^2(\beta)}{2\sqrt{6}}$
	2	(-1)	$-\frac{5e^{i\alpha}\cos(\beta)\sin(\beta)}{\sqrt{6}}$
	2	0	$\frac{5}{6}-\frac{5\cos^2(\beta)}{2}$
	2	1	$\frac{5e^{-i\alpha}\cos(\beta)\sin(\beta)}{\sqrt{6}}$
	2	2	$-\frac{5e^{-2i\alpha}\sin^2(\beta)}{2\sqrt{6}}$

Table B.2: PART II

$(l_1 l_2 m'_1)$	$t$	$q$	$b_q^t$	
$pd\sigma$	1	(-1)	$\sqrt{\frac{3}{10}} e^{i\alpha} \sin(\beta)$	
	1	0	$\sqrt{\frac{3}{5}} \cos(\beta)$	
	1	1	$-\sqrt{\frac{3}{10}} e^{-i\alpha} \sin(\beta)$	
	3	(-3)	$\frac{7e^{3i\alpha} \sin^3(\beta)}{4\sqrt{3}}$	
	3	(-2)	$\frac{7e^{2i\alpha} \cos(\beta) \sin^2(\beta)}{2\sqrt{2}}$	
	3	(-1)	$\frac{7e^{i\alpha} (5 \cos(2\beta) + 3) \sin(\beta)}{8\sqrt{5}}$	
	3	0	$\frac{7(3 \cos(\beta) + 5 \cos(3\beta))}{8\sqrt{15}}$	
	3	1	$-\frac{7e^{-i\alpha} (5 \cos(2\beta) + 3) \sin(\beta)}{8\sqrt{5}}$	
	3	2	$\frac{7e^{-2i\alpha} \cos(\beta) \sin^2(\beta)}{2\sqrt{2}}$	
	3	3	$-\frac{7e^{-3i\alpha} \sin^3(\beta)}{4\sqrt{3}}$	
	$pd\pi$	1	(-1)	$\frac{3e^{i\alpha} \sin(\beta)}{\sqrt{10}}$
		1	0	$\frac{3 \cos(\beta)}{\sqrt{5}}$
		1	1	$-\frac{3e^{-i\alpha} \sin(\beta)}{\sqrt{10}}$
3		(-3)	$-\frac{7}{6} e^{3i\alpha} \sin^3(\beta)$	
3		(-2)	$-\frac{7e^{2i\alpha} \cos(\beta) \sin^2(\beta)}{\sqrt{6}}$	
3		(-1)	$-\frac{7e^{i\alpha} (5 \cos(2\beta) + 3) \sin(\beta)}{4\sqrt{15}}$	
3		0	$\frac{7 \cos(\beta) (3 - 5 \cos^2(\beta))}{3\sqrt{5}}$	
3		1	$\frac{7e^{-i\alpha} (5 \cos(2\beta) + 3) \sin(\beta)}{4\sqrt{15}}$	
3		2	$-\frac{7e^{-2i\alpha} \cos(\beta) \sin^2(\beta)}{\sqrt{6}}$	
3		3	$\frac{7}{6} e^{-3i\alpha} \sin^3(\beta)$	
$pf\sigma$		2	(-2)	$\frac{5e^{2i\alpha} \sin^2(\beta)}{2\sqrt{14}}$
		2	(-1)	$\frac{5e^{i\alpha} \cos(\beta) \sin(\beta)}{\sqrt{14}}$
		2	0	$\frac{5(3 \cos(2\beta) + 1)}{4\sqrt{21}}$
	2	1	$-\frac{5e^{-i\alpha} \cos(\beta) \sin(\beta)}{\sqrt{14}}$	
	2	2	$\frac{5e^{-2i\alpha} \sin^2(\beta)}{2\sqrt{14}}$	
	4	(-4)	$\frac{3}{8} \sqrt{\frac{15}{2}} e^{4i\alpha} \sin^4(\beta)$	
	4	(-3)	$\frac{3}{4} \sqrt{15} e^{3i\alpha} \cos(\beta) \sin^3(\beta)$	
	4	(-2)	$\frac{3}{8} \sqrt{\frac{15}{14}} e^{2i\alpha} (7 \cos(2\beta) + 5) \sin^2(\beta)$	
	4	(-1)	$\frac{3}{16} \sqrt{\frac{15}{7}} e^{i\alpha} (7 \cos(2\beta) + 1) \sin(2\beta)$	
	4	0	$\frac{3}{64} \sqrt{\frac{3}{7}} (20 \cos(2\beta) + 35 \cos(4\beta) + 9)$	

Table B.3: PART III

$(l_1 l_2 m'_1)$	$t$	$q$	$b_q^t$
	4	1	$-\frac{3}{16}\sqrt{\frac{15}{7}}e^{-i\alpha}(7\cos(2\beta)+1)\sin(2\beta)$
	4	2	$\frac{3}{8}\sqrt{\frac{15}{14}}e^{-2i\alpha}(7\cos(2\beta)+5)\sin^2(\beta)$
	4	3	$-\frac{3}{4}\sqrt{15}e^{-3i\alpha}\cos(\beta)\sin^3(\beta)$
	4	4	$\frac{3}{8}\sqrt{\frac{15}{2}}e^{-4i\alpha}\sin^4(\beta)$
$pf\pi$	2	(-2)	$\frac{5e^{2i\alpha}\sin^2(\beta)}{\sqrt{21}}$
	2	(-1)	$\frac{5e^{i\alpha}\sin(2\beta)}{\sqrt{21}}$
	2	0	$\frac{5(3\cos(2\beta)+1)}{3\sqrt{14}}$
	2	1	$-\frac{5e^{-i\alpha}\sin(2\beta)}{\sqrt{21}}$
	2	2	$\frac{5e^{-2i\alpha}\sin^2(\beta)}{\sqrt{21}}$
	4	(-4)	$-\frac{9}{16}\sqrt{5}e^{4i\alpha}\sin^4(\beta)$
	4	(-3)	$-\frac{9}{4}\sqrt{\frac{5}{2}}e^{3i\alpha}\cos(\beta)\sin^3(\beta)$
	4	(-2)	$-\frac{9}{16}\sqrt{\frac{5}{7}}e^{2i\alpha}(7\cos(2\beta)+5)\sin^2(\beta)$
	4	(-1)	$-\frac{9}{16}\sqrt{\frac{5}{14}}e^{i\alpha}(7\cos(2\beta)+1)\sin(2\beta)$
	4	0	$-\frac{9(20\cos(2\beta)+35\cos(4\beta)+9)}{64\sqrt{14}}$
	4	1	$\frac{9}{16}\sqrt{\frac{5}{14}}e^{-i\alpha}(7\cos(2\beta)+1)\sin(2\beta)$
	4	2	$-\frac{9}{16}\sqrt{\frac{5}{7}}e^{-2i\alpha}(7\cos(2\beta)+5)\sin^2(\beta)$
	4	3	$\frac{9}{4}\sqrt{\frac{5}{2}}e^{-3i\alpha}\cos(\beta)\sin^3(\beta)$
	4	4	$-\frac{9}{16}\sqrt{5}e^{-4i\alpha}\sin^4(\beta)$
$pg\sigma$	3	(-3)	$\frac{7}{12}\sqrt{\frac{5}{3}}e^{3i\alpha}\sin^3(\beta)$
	3	(-2)	$\frac{7}{6}\sqrt{\frac{5}{2}}e^{2i\alpha}\cos(\beta)\sin^2(\beta)$
	3	(-1)	$\frac{7}{24}e^{i\alpha}(5\cos(2\beta)+3)\sin(\beta)$
	3	0	$\frac{7(3\cos(\beta)+5\cos(3\beta))}{24\sqrt{3}}$
	3	1	$-\frac{7}{24}e^{-i\alpha}(5\cos(2\beta)+3)\sin(\beta)$
	3	2	$\frac{7}{6}\sqrt{\frac{5}{2}}e^{-2i\alpha}\cos(\beta)\sin^2(\beta)$
	3	3	$-\frac{7}{12}\sqrt{\frac{5}{3}}e^{-3i\alpha}\sin^3(\beta)$
	5	(-5)	$\frac{11}{16}\sqrt{\frac{7}{3}}e^{5i\alpha}\sin^5(\beta)$
	5	(-4)	$\frac{11}{8}\sqrt{\frac{35}{6}}e^{4i\alpha}\cos(\beta)\sin^4(\beta)$
	5	(-3)	$\frac{11}{96}\sqrt{\frac{35}{3}}e^{3i\alpha}(9\cos(2\beta)+7)\sin^3(\beta)$
	5	(-2)	$\frac{11}{24}\sqrt{\frac{35}{2}}e^{2i\alpha}\cos(\beta)(3\cos(2\beta)+1)\sin^2(\beta)$

Table B.4: PART IV

$(l_1 l_2 m'_1)$	$t$	$q$	$b_q^t$
	5	(-1)	$\frac{11}{24} \sqrt{\frac{5}{2}} e^{i\alpha} (21 \cos^4(\beta) - 14 \cos^2(\beta) + 1) \sin(\beta)$
	5	0	$\frac{11 \cos(\beta) (63 \cos^4(\beta) - 70 \cos^2(\beta) + 15)}{24\sqrt{3}}$
	5	1	$-\frac{11}{24} \sqrt{\frac{5}{2}} e^{-i\alpha} (21 \cos^4(\beta) - 14 \cos^2(\beta) + 1) \sin(\beta)$
	5	2	$\frac{11}{24} \sqrt{\frac{35}{2}} e^{-2i\alpha} \cos(\beta) (3 \cos(2\beta) + 1) \sin^2(\beta)$
	5	3	$-\frac{11}{96} \sqrt{\frac{35}{3}} e^{-3i\alpha} (9 \cos(2\beta) + 7) \sin^3(\beta)$
	5	4	$\frac{11}{8} \sqrt{\frac{35}{6}} e^{-4i\alpha} \cos(\beta) \sin^4(\beta)$
	5	5	$-\frac{11}{16} \sqrt{\frac{7}{3}} e^{-5i\alpha} \sin^5(\beta)$
$pg\pi$	3	(-3)	$\frac{35e^{3i\alpha} \sin^3(\beta)}{12\sqrt{6}}$
	3	(-2)	$\frac{35}{12} e^{2i\alpha} \cos(\beta) \sin^2(\beta)$
	3	(-1)	$\frac{7}{24} \sqrt{\frac{5}{2}} e^{i\alpha} (5 \cos(2\beta) + 3) \sin(\beta)$
	3	0	$\frac{7}{24} \sqrt{\frac{5}{6}} (3 \cos(\beta) + 5 \cos(3\beta))$
	3	1	$-\frac{7}{24} \sqrt{\frac{5}{2}} e^{-i\alpha} (5 \cos(2\beta) + 3) \sin(\beta)$
	3	2	$\frac{35}{12} e^{-2i\alpha} \cos(\beta) \sin^2(\beta)$
	3	3	$-\frac{35e^{-3i\alpha} \sin^3(\beta)}{12\sqrt{6}}$
	5	(-5)	$-\frac{11}{4} \sqrt{\frac{7}{30}} e^{5i\alpha} \sin^5(\beta)$
	5	(-4)	$-\frac{11}{4} \sqrt{\frac{7}{3}} e^{4i\alpha} \cos(\beta) \sin^4(\beta)$
	5	(-3)	$-\frac{11}{24} \sqrt{\frac{7}{6}} e^{3i\alpha} (9 \cos(2\beta) + 7) \sin^3(\beta)$
	5	(-2)	$-\frac{11}{12} \sqrt{7} e^{2i\alpha} \cos(\beta) (3 \cos(2\beta) + 1) \sin^2(\beta)$
	5	(-1)	$-\frac{11}{96} e^{i\alpha} (28 \cos(2\beta) + 21 \cos(4\beta) + 15) \sin(\beta)$
	5	0	$-\frac{11(30 \cos(\beta) + 35 \cos(3\beta) + 63 \cos(5\beta))}{96\sqrt{30}}$
	5	1	$\frac{11}{96} e^{-i\alpha} (28 \cos(2\beta) + 21 \cos(4\beta) + 15) \sin(\beta)$
	5	2	$-\frac{11}{12} \sqrt{7} e^{-2i\alpha} \cos(\beta) (3 \cos(2\beta) + 1) \sin^2(\beta)$
	5	3	$\frac{11}{24} \sqrt{\frac{7}{6}} e^{-3i\alpha} (9 \cos(2\beta) + 7) \sin^3(\beta)$
	5	4	$-\frac{11}{4} \sqrt{\frac{7}{3}} e^{-4i\alpha} \cos(\beta) \sin^4(\beta)$
	5	5	$\frac{11}{4} \sqrt{\frac{7}{30}} e^{-5i\alpha} \sin^5(\beta)$
$ph\sigma$	4	(-4)	$\frac{3}{8} \sqrt{\frac{105}{22}} e^{4i\alpha} \sin^4(\beta)$
	4	(-3)	$\frac{3}{4} \sqrt{\frac{105}{11}} e^{3i\alpha} \cos(\beta) \sin^3(\beta)$
	4	(-2)	$\frac{3}{8} \sqrt{\frac{15}{22}} e^{2i\alpha} (7 \cos(2\beta) + 5) \sin^2(\beta)$
	4	(-1)	$\frac{3}{16} \sqrt{\frac{15}{11}} e^{i\alpha} (7 \cos(2\beta) + 1) \sin(2\beta)$

Table B.5: PART V

$(l_1 l_2 m'_1)$	$t$	$q$	$b_q^t$
	4	0	$\frac{3}{64} \sqrt{\frac{3}{11}} (20 \cos(2\beta) + 35 \cos(4\beta) + 9)$
	4	1	$-\frac{3}{16} \sqrt{\frac{15}{11}} e^{-i\alpha} (7 \cos(2\beta) + 1) \sin(2\beta)$
	4	2	$\frac{3}{8} \sqrt{\frac{15}{22}} e^{-2i\alpha} (7 \cos(2\beta) + 5) \sin^2(\beta)$
	4	3	$-\frac{3}{4} \sqrt{\frac{105}{11}} e^{-3i\alpha} \cos(\beta) \sin^3(\beta)$
	4	4	$\frac{3}{8} \sqrt{\frac{105}{22}} e^{-4i\alpha} \sin^4(\beta)$
	6	(-6)	$\frac{13}{32} \sqrt{7} e^{6i\alpha} \sin^6(\beta)$
	6	(-5)	$\frac{13}{16} \sqrt{21} e^{5i\alpha} \cos(\beta) \sin^5(\beta)$
	6	(-4)	$\frac{13}{32} \sqrt{\frac{21}{22}} e^{4i\alpha} (11 \cos(2\beta) + 9) \sin^4(\beta)$
	6	(-3)	$\frac{13}{32} \sqrt{\frac{35}{11}} e^{3i\alpha} \cos(\beta) (11 \cos(2\beta) + 5) \sin^3(\beta)$
	6	(-2)	$\frac{13}{32} \sqrt{\frac{35}{11}} e^{2i\alpha} (33 \cos^4(\beta) - 18 \cos^2(\beta) + 1) \sin^2(\beta)$
	6	(-1)	$\frac{13}{8} \sqrt{\frac{7}{22}} e^{i\alpha} \cos(\beta) (33 \cos^4(\beta) - 30 \cos^2(\beta) + 5) \sin(\beta)$
	6	0	$\frac{13(105 \cos(2\beta) + 126 \cos(4\beta) + 231 \cos(6\beta) + 50)}{512\sqrt{33}}$
	6	1	$-\frac{13}{8} \sqrt{\frac{7}{22}} e^{-i\alpha} \cos(\beta) (33 \cos^4(\beta) - 30 \cos^2(\beta) + 5) \sin(\beta)$
	6	2	$\frac{13}{32} \sqrt{\frac{35}{11}} e^{-2i\alpha} (33 \cos^4(\beta) - 18 \cos^2(\beta) + 1) \sin^2(\beta)$
	6	3	$-\frac{13}{32} \sqrt{\frac{35}{11}} e^{-3i\alpha} \cos(\beta) (11 \cos(2\beta) + 5) \sin^3(\beta)$
	6	4	$\frac{13}{32} \sqrt{\frac{21}{22}} e^{-4i\alpha} (11 \cos(2\beta) + 9) \sin^4(\beta)$
	6	5	$-\frac{13}{16} \sqrt{21} e^{-5i\alpha} \cos(\beta) \sin^5(\beta)$
	6	6	$\frac{13}{32} \sqrt{7} e^{-6i\alpha} \sin^6(\beta)$
$ph\pi$	4	(-4)	$\frac{9}{4} \sqrt{\frac{7}{22}} e^{4i\alpha} \sin^4(\beta)$
	4	(-3)	$\frac{9}{2} \sqrt{\frac{7}{11}} e^{3i\alpha} \cos(\beta) \sin^3(\beta)$
	4	(-2)	$\frac{9e^{2i\alpha} (7 \cos(2\beta) + 5) \sin^2(\beta)}{4\sqrt{22}}$
	4	(-1)	$\frac{9e^{i\alpha} (7 \cos(2\beta) + 1) \sin(2\beta)}{8\sqrt{11}}$
	4	0	$\frac{9(20 \cos(2\beta) + 35 \cos(4\beta) + 9)}{32\sqrt{55}}$
	4	1	$-\frac{9e^{-i\alpha} (7 \cos(2\beta) + 1) \sin(2\beta)}{8\sqrt{11}}$
	4	2	$\frac{9e^{-2i\alpha} (7 \cos(2\beta) + 5) \sin^2(\beta)}{4\sqrt{22}}$
	4	3	$-\frac{9}{2} \sqrt{\frac{7}{11}} e^{-3i\alpha} \cos(\beta) \sin^3(\beta)$
	4	4	$\frac{9}{4} \sqrt{\frac{7}{22}} e^{-4i\alpha} \sin^4(\beta)$
	6	(-6)	$-\frac{13}{32} \sqrt{\frac{35}{3}} e^{6i\alpha} \sin^6(\beta)$
	6	(-5)	$-\frac{13}{16} \sqrt{35} e^{5i\alpha} \cos(\beta) \sin^5(\beta)$

Table B.6: PART VI

$(l_1 l_2 m'_1)$	$t$	$q$	$b_q^t$
	6	(-4)	$-\frac{13}{32} \sqrt{\frac{35}{22}} e^{4i\alpha} (11 \cos(2\beta) + 9) \sin^4(\beta)$
	6	(-3)	$-\frac{65}{32} \sqrt{\frac{7}{33}} e^{3i\alpha} \cos(\beta) (11 \cos(2\beta) + 5) \sin^3(\beta)$
	6	(-2)	$-\frac{65}{32} \sqrt{\frac{7}{33}} e^{2i\alpha} (33 \cos^4(\beta) - 18 \cos^2(\beta) + 1) \sin^2(\beta)$
	6	(-1)	$-\frac{13}{8} \sqrt{\frac{35}{66}} e^{i\alpha} \cos(\beta) (33 \cos^4(\beta) - 30 \cos^2(\beta) + 5) \sin(\beta)$
	6	0	$-\frac{13 \sqrt{\frac{5}{11}} (105 \cos(2\beta) + 126 \cos(4\beta) + 231 \cos(6\beta) + 50)}{1536}$
	6	1	$\frac{13}{8} \sqrt{\frac{35}{66}} e^{-i\alpha} \cos(\beta) (33 \cos^4(\beta) - 30 \cos^2(\beta) + 5) \sin(\beta)$
	6	2	$-\frac{65}{32} \sqrt{\frac{7}{33}} e^{-2i\alpha} (33 \cos^4(\beta) - 18 \cos^2(\beta) + 1) \sin^2(\beta)$
	6	3	$\frac{65}{32} \sqrt{\frac{7}{33}} e^{-3i\alpha} \cos(\beta) (11 \cos(2\beta) + 5) \sin^3(\beta)$
	6	4	$-\frac{13}{32} \sqrt{\frac{35}{22}} e^{-4i\alpha} (11 \cos(2\beta) + 9) \sin^4(\beta)$
	6	5	$\frac{13}{16} \sqrt{35} e^{-5i\alpha} \cos(\beta) \sin^5(\beta)$
	6	6	$-\frac{13}{32} \sqrt{\frac{35}{3}} e^{-6i\alpha} \sin^6(\beta)$
$dd\sigma$	0	0	$\frac{1}{5}$
	2	(-2)	$\frac{1}{2} \sqrt{\frac{3}{2}} e^{2i\alpha} \sin^2(\beta)$
	2	(-1)	$\sqrt{\frac{3}{2}} e^{i\alpha} \cos(\beta) \sin(\beta)$
	2	0	$\frac{1}{4} (3 \cos(2\beta) + 1)$
	2	1	$-\sqrt{\frac{3}{2}} e^{-i\alpha} \cos(\beta) \sin(\beta)$
	2	2	$\frac{1}{2} \sqrt{\frac{3}{2}} e^{-2i\alpha} \sin^2(\beta)$
	4	(-4)	$\frac{9}{8} \sqrt{\frac{7}{10}} e^{4i\alpha} \sin^4(\beta)$
	4	(-3)	$\frac{9}{4} \sqrt{\frac{7}{5}} e^{3i\alpha} \cos(\beta) \sin^3(\beta)$
	4	(-2)	$\frac{9e^{2i\alpha} (7 \cos(2\beta) + 5) \sin^2(\beta)}{8\sqrt{10}}$
	4	(-1)	$\frac{9e^{i\alpha} (7 \cos(2\beta) + 1) \sin(2\beta)}{16\sqrt{5}}$
	4	0	$\frac{9}{320} (20 \cos(2\beta) + 35 \cos(4\beta) + 9)$
	4	1	$-\frac{9e^{-i\alpha} (7 \cos(2\beta) + 1) \sin(2\beta)}{16\sqrt{5}}$
	4	2	$\frac{9e^{-2i\alpha} (7 \cos(2\beta) + 5) \sin^2(\beta)}{8\sqrt{10}}$
	4	3	$-\frac{9}{4} \sqrt{\frac{7}{5}} e^{-3i\alpha} \cos(\beta) \sin^3(\beta)$
	4	4	$\frac{9}{8} \sqrt{\frac{7}{10}} e^{-4i\alpha} \sin^4(\beta)$
$dd\pi$	0	0	$\frac{2}{5}$
	2	(-2)	$\frac{1}{2} \sqrt{\frac{3}{2}} e^{2i\alpha} \sin^2(\beta)$
	2	(-1)	$\sqrt{\frac{3}{2}} e^{i\alpha} \cos(\beta) \sin(\beta)$

Table B.7: PART VII

$(l_1 l_2 m'_1)$	$t$	$q$	$b_q^t$
	2	0	$\frac{1}{4}(3 \cos(2\beta) + 1)$
	2	1	$-\sqrt{\frac{3}{2}}e^{-i\alpha} \cos(\beta) \sin(\beta)$
	2	2	$\frac{1}{2}\sqrt{\frac{3}{2}}e^{-2i\alpha} \sin^2(\beta)$
	4	(-4)	$-\frac{3}{2}\sqrt{\frac{7}{10}}e^{4i\alpha} \sin^4(\beta)$
	4	(-3)	$-3\sqrt{\frac{7}{5}}e^{3i\alpha} \cos(\beta) \sin^3(\beta)$
	4	(-2)	$-\frac{3e^{2i\alpha}(7 \cos^2(\beta)-1) \sin^2(\beta)}{\sqrt{10}}$
	4	(-1)	$-\frac{3e^{i\alpha} \cos(\beta)(7 \cos^2(\beta)-3) \sin(\beta)}{\sqrt{5}}$
	4	0	$-\frac{3}{80}(20 \cos(2\beta) + 35 \cos(4\beta) + 9)$
	4	1	$\frac{3e^{-i\alpha} \cos(\beta)(7 \cos^2(\beta)-3) \sin(\beta)}{\sqrt{5}}$
	4	2	$-\frac{3e^{-2i\alpha}(7 \cos^2(\beta)-1) \sin^2(\beta)}{\sqrt{10}}$
	4	3	$3\sqrt{\frac{7}{5}}e^{-3i\alpha} \cos(\beta) \sin^3(\beta)$
	4	4	$-\frac{3}{2}\sqrt{\frac{7}{10}}e^{-4i\alpha} \sin^4(\beta)$
$dd\delta$	0	0	$\frac{2}{5}$
	2	(-2)	$-\sqrt{\frac{3}{2}}e^{2i\alpha} \sin^2(\beta)$
	2	(-1)	$-\sqrt{6}e^{i\alpha} \cos(\beta) \sin(\beta)$
	2	0	$1 - 3 \cos^2(\beta)$
	2	1	$\sqrt{6}e^{-i\alpha} \cos(\beta) \sin(\beta)$
	2	2	$-\sqrt{\frac{3}{2}}e^{-2i\alpha} \sin^2(\beta)$
	4	(-4)	$\frac{3}{8}\sqrt{\frac{7}{10}}e^{4i\alpha} \sin^4(\beta)$
	4	(-3)	$\frac{3}{4}\sqrt{\frac{7}{5}}e^{3i\alpha} \cos(\beta) \sin^3(\beta)$
	4	(-2)	$\frac{3e^{2i\alpha}(7 \cos(2\beta)+5) \sin^2(\beta)}{8\sqrt{10}}$
	4	(-1)	$\frac{3e^{i\alpha}(7 \cos(2\beta)+1) \sin(2\beta)}{16\sqrt{5}}$
	4	0	$\frac{3}{320}(20 \cos(2\beta) + 35 \cos(4\beta) + 9)$
	4	1	$-\frac{3e^{-i\alpha}(7 \cos(2\beta)+1) \sin(2\beta)}{16\sqrt{5}}$
	4	2	$\frac{3e^{-2i\alpha}(7 \cos(2\beta)+5) \sin^2(\beta)}{8\sqrt{10}}$
	4	3	$-\frac{3}{4}\sqrt{\frac{7}{5}}e^{-3i\alpha} \cos(\beta) \sin^3(\beta)$
	4	4	$\frac{3}{8}\sqrt{\frac{7}{10}}e^{-4i\alpha} \sin^4(\beta)$
$df\sigma$	1	(-1)	$\frac{3e^{i\alpha} \sin(\beta)}{\sqrt{70}}$
	1	0	$\frac{3 \cos(\beta)}{\sqrt{35}}$
	1	1	$-\frac{3e^{-i\alpha} \sin(\beta)}{\sqrt{70}}$

Table B.8: PART VIII

$(l_1 l_2 m_1')$	$t$	$q$	$b_q^t$
	3	(-3)	$\frac{1}{4}\sqrt{7}e^{3i\alpha}\sin^3(\beta)$
	3	(-2)	$\frac{1}{2}\sqrt{\frac{21}{2}}e^{2i\alpha}\cos(\beta)\sin^2(\beta)$
	3	(-1)	$\frac{1}{8}\sqrt{\frac{21}{5}}e^{i\alpha}(5\cos(2\beta)+3)\sin(\beta)$
	3	0	$\frac{1}{8}\sqrt{\frac{7}{5}}(3\cos(\beta)+5\cos(3\beta))$
	3	1	$-\frac{1}{8}\sqrt{\frac{21}{5}}e^{-i\alpha}(5\cos(2\beta)+3)\sin(\beta)$
	3	2	$\frac{1}{2}\sqrt{\frac{21}{2}}e^{-2i\alpha}\cos(\beta)\sin^2(\beta)$
	3	3	$-\frac{1}{4}\sqrt{7}e^{-3i\alpha}\sin^3(\beta)$
	5	(-5)	$\frac{33e^{5i\alpha}\sin^5(\beta)}{16\sqrt{5}}$
	5	(-4)	$\frac{33e^{4i\alpha}\cos(\beta)\sin^4(\beta)}{8\sqrt{2}}$
	5	(-3)	$\frac{11}{32}e^{3i\alpha}(9\cos(2\beta)+7)\sin^3(\beta)$
	5	(-2)	$\frac{11}{8}\sqrt{\frac{3}{2}}e^{2i\alpha}\cos(\beta)(3\cos(2\beta)+1)\sin^2(\beta)$
	5	(-1)	$\frac{11}{8}\sqrt{\frac{3}{14}}e^{i\alpha}(21\cos^4(\beta)-14\cos^2(\beta)+1)\sin(\beta)$
	5	0	$\frac{11(30\cos(\beta)+35\cos(3\beta)+63\cos(5\beta))}{128\sqrt{35}}$
	5	1	$-\frac{11}{8}\sqrt{\frac{3}{14}}e^{-i\alpha}(21\cos^4(\beta)-14\cos^2(\beta)+1)\sin(\beta)$
	5	2	$\frac{11}{8}\sqrt{\frac{3}{2}}e^{-2i\alpha}\cos(\beta)(3\cos(2\beta)+1)\sin^2(\beta)$
	5	3	$-\frac{11}{32}e^{-3i\alpha}(9\cos(2\beta)+7)\sin^3(\beta)$
	5	4	$\frac{33e^{-4i\alpha}\cos(\beta)\sin^4(\beta)}{8\sqrt{2}}$
	5	5	$-\frac{33e^{-5i\alpha}\sin^5(\beta)}{16\sqrt{5}}$
$df\pi$	1	(-1)	$\frac{4e^{i\alpha}\sin(\beta)}{\sqrt{35}}$
	1	0	$4\sqrt{\frac{2}{35}}\cos(\beta)$
	1	1	$-\frac{4e^{-i\alpha}\sin(\beta)}{\sqrt{35}}$
	3	(-3)	$\frac{1}{4}\sqrt{\frac{7}{2}}e^{3i\alpha}\sin^3(\beta)$
	3	(-2)	$\frac{1}{4}\sqrt{21}e^{2i\alpha}\cos(\beta)\sin^2(\beta)$
	3	(-1)	$\frac{1}{8}\sqrt{\frac{21}{10}}e^{i\alpha}(5\cos(2\beta)+3)\sin(\beta)$
	3	0	$\frac{1}{8}\sqrt{\frac{7}{10}}(3\cos(\beta)+5\cos(3\beta))$
	3	1	$-\frac{1}{8}\sqrt{\frac{21}{10}}e^{-i\alpha}(5\cos(2\beta)+3)\sin(\beta)$
	3	2	$\frac{1}{4}\sqrt{21}e^{-2i\alpha}\cos(\beta)\sin^2(\beta)$
	3	3	$-\frac{1}{4}\sqrt{\frac{7}{2}}e^{-3i\alpha}\sin^3(\beta)$
	5	(-5)	$-\frac{33e^{5i\alpha}\sin^5(\beta)}{8\sqrt{10}}$
	5	(-4)	$-\frac{33}{8}e^{4i\alpha}\cos(\beta)\sin^4(\beta)$

Table B.9: PART IX

$(l_1 l_2 m'_1)$	$t$	$q$	$b_q^t$
	5	(-3)	$-\frac{11e^{3i\alpha}(9\cos(2\beta)+7)\sin^3(\beta)}{16\sqrt{2}}$
	5	(-2)	$-\frac{11}{8}\sqrt{3}e^{2i\alpha}\cos(\beta)(3\cos(2\beta)+1)\sin^2(\beta)$
	5	(-1)	$-\frac{11}{8}\sqrt{\frac{3}{7}}e^{i\alpha}(21\cos^4(\beta)-14\cos^2(\beta)+1)\sin(\beta)$
	5	0	$-\frac{11(30\cos(\beta)+35\cos(3\beta)+63\cos(5\beta))}{64\sqrt{70}}$
	5	1	$\frac{11}{8}\sqrt{\frac{3}{7}}e^{-i\alpha}(21\cos^4(\beta)-14\cos^2(\beta)+1)\sin(\beta)$
	5	2	$-\frac{11}{8}\sqrt{3}e^{-2i\alpha}\cos(\beta)(3\cos(2\beta)+1)\sin^2(\beta)$
	5	3	$\frac{11e^{-3i\alpha}(9\cos(2\beta)+7)\sin^3(\beta)}{16\sqrt{2}}$
	5	4	$-\frac{33}{8}e^{-4i\alpha}\cos(\beta)\sin^4(\beta)$
	5	5	$\frac{33e^{-5i\alpha}\sin^5(\beta)}{8\sqrt{10}}$
$df\delta$	1	(-1)	$\sqrt{\frac{2}{7}}e^{i\alpha}\sin(\beta)$
	1	0	$\frac{2\cos(\beta)}{\sqrt{7}}$
	1	1	$-\sqrt{\frac{2}{7}}e^{-i\alpha}\sin(\beta)$
	3	(-3)	$-\frac{1}{4}\sqrt{35}e^{3i\alpha}\sin^3(\beta)$
	3	(-2)	$-\frac{1}{2}\sqrt{\frac{105}{2}}e^{2i\alpha}\cos(\beta)\sin^2(\beta)$
	3	(-1)	$-\frac{1}{8}\sqrt{21}e^{i\alpha}(5\cos(2\beta)+3)\sin(\beta)$
	3	0	$-\frac{1}{8}\sqrt{7}(3\cos(\beta)+5\cos(3\beta))$
	3	1	$\frac{1}{8}\sqrt{21}e^{-i\alpha}(5\cos(2\beta)+3)\sin(\beta)$
	3	2	$-\frac{1}{2}\sqrt{\frac{105}{2}}e^{-2i\alpha}\cos(\beta)\sin^2(\beta)$
	3	3	$\frac{1}{4}\sqrt{35}e^{-3i\alpha}\sin^3(\beta)$
	5	(-5)	$\frac{33}{80}e^{5i\alpha}\sin^5(\beta)$
	5	(-4)	$\frac{33e^{4i\alpha}\cos(\beta)\sin^4(\beta)}{8\sqrt{10}}$
	5	(-3)	$\frac{11e^{3i\alpha}(9\cos(2\beta)+7)\sin^3(\beta)}{32\sqrt{5}}$
	5	(-2)	$\frac{11}{8}\sqrt{\frac{3}{10}}e^{2i\alpha}\cos(\beta)(3\cos(2\beta)+1)\sin^2(\beta)$
	5	(-1)	$\frac{11}{8}\sqrt{\frac{3}{70}}e^{i\alpha}(21\cos^4(\beta)-14\cos^2(\beta)+1)\sin(\beta)$
	5	0	$\frac{11(30\cos(\beta)+35\cos(3\beta)+63\cos(5\beta))}{640\sqrt{7}}$
	5	1	$-\frac{11}{8}\sqrt{\frac{3}{70}}e^{-i\alpha}(21\cos^4(\beta)-14\cos^2(\beta)+1)\sin(\beta)$
	5	2	$\frac{11}{8}\sqrt{\frac{3}{10}}e^{-2i\alpha}\cos(\beta)(3\cos(2\beta)+1)\sin^2(\beta)$
	5	3	$-\frac{11e^{-3i\alpha}(9\cos(2\beta)+7)\sin^3(\beta)}{32\sqrt{5}}$
	5	4	$\frac{33e^{-4i\alpha}\cos(\beta)\sin^4(\beta)}{8\sqrt{10}}$
	5	5	$-\frac{33}{80}e^{-5i\alpha}\sin^5(\beta)$
$dg\sigma$	2	(-2)	$\frac{1}{2}\sqrt{\frac{5}{6}}e^{2i\alpha}\sin^2(\beta)$
	2	(-1)	$\sqrt{\frac{5}{6}}e^{i\alpha}\cos(\beta)\sin(\beta)$

Table B.10: PART X

$(l_1 l_2 m'_1)$	$t$	$q$	$b_q^t$
	2	0	$\frac{1}{12}\sqrt{5}(3\cos(2\beta)+1)$
	2	1	$-\sqrt{\frac{5}{6}}e^{-i\alpha}\cos(\beta)\sin(\beta)$
	2	2	$\frac{1}{2}\sqrt{\frac{5}{6}}e^{-2i\alpha}\sin^2(\beta)$
	4	(-4)	$\frac{3}{8}\sqrt{\frac{7}{2}}e^{4i\alpha}\sin^4(\beta)$
	4	(-3)	$\frac{3}{4}\sqrt{7}e^{3i\alpha}\cos(\beta)\sin^3(\beta)$
	4	(-2)	$\frac{3e^{2i\alpha}(7\cos(2\beta)+5)\sin^2(\beta)}{8\sqrt{2}}$
	4	(-1)	$\frac{3}{16}e^{i\alpha}(7\cos(2\beta)+1)\sin(2\beta)$
	4	0	$\frac{3(20\cos(2\beta)+35\cos(4\beta)+9)}{64\sqrt{5}}$
	4	1	$-\frac{3}{16}e^{-i\alpha}(7\cos(2\beta)+1)\sin(2\beta)$
	4	2	$\frac{3e^{-2i\alpha}(7\cos(2\beta)+5)\sin^2(\beta)}{8\sqrt{2}}$
	4	3	$-\frac{3}{4}\sqrt{7}e^{-3i\alpha}\cos(\beta)\sin^3(\beta)$
	4	4	$\frac{3}{8}\sqrt{\frac{7}{2}}e^{-4i\alpha}\sin^4(\beta)$
	6	(-6)	$\frac{13}{32}\sqrt{\frac{77}{15}}e^{6i\alpha}\sin^6(\beta)$
	6	(-5)	$\frac{13}{16}\sqrt{\frac{77}{5}}e^{5i\alpha}\cos(\beta)\sin^5(\beta)$
	6	(-4)	$\frac{13}{32}\sqrt{\frac{7}{10}}e^{4i\alpha}(11\cos(2\beta)+9)\sin^4(\beta)$
	6	(-3)	$\frac{13}{32}\sqrt{\frac{7}{3}}e^{3i\alpha}\cos(\beta)(11\cos(2\beta)+5)\sin^3(\beta)$
	6	(-2)	$\frac{13}{32}\sqrt{\frac{7}{3}}e^{2i\alpha}(33\cos^4(\beta)-18\cos^2(\beta)+1)\sin^2(\beta)$
	6	(-1)	$\frac{13}{8}\sqrt{\frac{7}{30}}e^{i\alpha}\cos(\beta)(33\cos^4(\beta)-30\cos^2(\beta)+5)\sin(\beta)$
	6	0	$\frac{13(105\cos(2\beta)+126\cos(4\beta)+231\cos(6\beta)+50)}{1536\sqrt{5}}$
	6	1	$-\frac{13}{8}\sqrt{\frac{7}{30}}e^{-i\alpha}\cos(\beta)(33\cos^4(\beta)-30\cos^2(\beta)+5)\sin(\beta)$
	6	2	$\frac{13}{32}\sqrt{\frac{7}{3}}e^{-2i\alpha}(33\cos^4(\beta)-18\cos^2(\beta)+1)\sin^2(\beta)$
	6	3	$-\frac{13}{32}\sqrt{\frac{7}{3}}e^{-3i\alpha}\cos(\beta)(11\cos(2\beta)+5)\sin^3(\beta)$
	6	4	$\frac{13}{32}\sqrt{\frac{7}{10}}e^{-4i\alpha}(11\cos(2\beta)+9)\sin^4(\beta)$
	6	5	$-\frac{13}{16}\sqrt{\frac{77}{5}}e^{-5i\alpha}\cos(\beta)\sin^5(\beta)$
	6	6	$\frac{13}{32}\sqrt{\frac{77}{15}}e^{-6i\alpha}\sin^6(\beta)$
$dg\pi$	2	(-2)	$\frac{5}{6}e^{2i\alpha}\sin^2(\beta)$
	2	(-1)	$\frac{5}{3}e^{i\alpha}\cos(\beta)\sin(\beta)$
	2	0	$\frac{5(3\cos(2\beta)+1)}{6\sqrt{6}}$
	2	1	$-\frac{5}{3}e^{-i\alpha}\cos(\beta)\sin(\beta)$
	2	2	$\frac{5}{6}e^{-2i\alpha}\sin^2(\beta)$
	4	(-4)	$\frac{3}{16}\sqrt{\frac{21}{5}}e^{4i\alpha}\sin^4(\beta)$

Table B.11: PART XI

$(l_1 l_2 m'_1)$	$t$	$q$	$b_q^t$
	4	(-3)	$\frac{3}{4}\sqrt{\frac{21}{10}}e^{3i\alpha}\cos(\beta)\sin^3(\beta)$
	4	(-2)	$\frac{3}{16}\sqrt{\frac{3}{5}}e^{2i\alpha}(7\cos(2\beta)+5)\sin^2(\beta)$
	4	(-1)	$\frac{3}{16}\sqrt{\frac{3}{10}}e^{i\alpha}(7\cos(2\beta)+1)\sin(2\beta)$
	4	0	$\frac{3}{320}\sqrt{\frac{3}{2}}(20\cos(2\beta)+35\cos(4\beta)+9)$
	4	1	$-\frac{3}{16}\sqrt{\frac{3}{10}}e^{-i\alpha}(7\cos(2\beta)+1)\sin(2\beta)$
	4	2	$\frac{3}{16}\sqrt{\frac{3}{5}}e^{-2i\alpha}(7\cos(2\beta)+5)\sin^2(\beta)$
	4	3	$-\frac{3}{4}\sqrt{\frac{21}{10}}e^{-3i\alpha}\cos(\beta)\sin^3(\beta)$
	4	4	$\frac{3}{16}\sqrt{\frac{21}{5}}e^{-4i\alpha}\sin^4(\beta)$
	6	(-6)	$-\frac{13}{60}\sqrt{\frac{77}{2}}e^{6i\alpha}\sin^6(\beta)$
	6	(-5)	$-\frac{13}{10}\sqrt{\frac{77}{6}}e^{5i\alpha}\cos(\beta)\sin^5(\beta)$
	6	(-4)	$-\frac{13}{40}\sqrt{\frac{7}{3}}e^{4i\alpha}(11\cos(2\beta)+9)\sin^4(\beta)$
	6	(-3)	$-\frac{13}{12}\sqrt{\frac{7}{10}}e^{3i\alpha}\cos(\beta)(11\cos(2\beta)+5)\sin^3(\beta)$
	6	(-2)	$-\frac{13}{96}\sqrt{\frac{7}{10}}e^{2i\alpha}(60\cos(2\beta)+33\cos(4\beta)+35)\sin^2(\beta)$
	6	(-1)	$-\frac{13}{30}\sqrt{7}e^{i\alpha}\cos(\beta)(33\cos^4(\beta)-30\cos^2(\beta)+5)\sin(\beta)$
	6	0	$-\frac{13(105\cos(2\beta)+126\cos(4\beta)+231\cos(6\beta)+50)}{960\sqrt{6}}$
	6	1	$\frac{13}{30}\sqrt{7}e^{-i\alpha}\cos(\beta)(33\cos^4(\beta)-30\cos^2(\beta)+5)\sin(\beta)$
	6	2	$-\frac{13}{96}\sqrt{\frac{7}{10}}e^{-2i\alpha}(60\cos(2\beta)+33\cos(4\beta)+35)\sin^2(\beta)$
	6	3	$\frac{13}{12}\sqrt{\frac{7}{10}}e^{-3i\alpha}\cos(\beta)(11\cos(2\beta)+5)\sin^3(\beta)$
	6	4	$-\frac{13}{40}\sqrt{\frac{7}{3}}e^{-4i\alpha}(11\cos(2\beta)+9)\sin^4(\beta)$
	6	5	$\frac{13}{10}\sqrt{\frac{77}{6}}e^{-5i\alpha}\cos(\beta)\sin^5(\beta)$
	6	6	$-\frac{13}{60}\sqrt{\frac{77}{2}}e^{-6i\alpha}\sin^6(\beta)$
$dg\delta$	2	(-2)	$\frac{5e^{2i\alpha}\sin^2(\beta)}{6\sqrt{2}}$
	2	(-1)	$\frac{5e^{i\alpha}\cos(\beta)\sin(\beta)}{3\sqrt{2}}$
	2	0	$\frac{5(3\cos(2\beta)+1)}{12\sqrt{3}}$
	2	1	$-\frac{5e^{-i\alpha}\cos(\beta)\sin(\beta)}{3\sqrt{2}}$
	2	2	$\frac{5e^{-2i\alpha}\sin^2(\beta)}{6\sqrt{2}}$
	4	(-4)	$-\frac{9}{8}\sqrt{\frac{21}{10}}e^{4i\alpha}\sin^4(\beta)$
	4	(-3)	$-\frac{9}{4}\sqrt{\frac{21}{5}}e^{3i\alpha}\cos(\beta)\sin^3(\beta)$
	4	(-2)	$-\frac{9}{8}\sqrt{\frac{3}{10}}e^{2i\alpha}(7\cos(2\beta)+5)\sin^2(\beta)$

Table B.12: PART XII

$(l_1 l_2 m'_1)$	$t$	$q$	$b_q^t$
	4	(-1)	$-\frac{9}{16}\sqrt{\frac{3}{5}}e^{i\alpha}(7\cos(2\beta)+1)\sin(2\beta)$
	4	0	$-\frac{9}{320}\sqrt{3}(20\cos(2\beta)+35\cos(4\beta)+9)$
	4	1	$\frac{9}{16}\sqrt{\frac{3}{5}}e^{-i\alpha}(7\cos(2\beta)+1)\sin(2\beta)$
	4	2	$-\frac{9}{8}\sqrt{\frac{3}{10}}e^{-2i\alpha}(7\cos(2\beta)+5)\sin^2(\beta)$
	4	3	$\frac{9}{4}\sqrt{\frac{21}{5}}e^{-3i\alpha}\cos(\beta)\sin^3(\beta)$
	4	4	$-\frac{9}{8}\sqrt{\frac{21}{10}}e^{-4i\alpha}\sin^4(\beta)$
	6	(-6)	$\frac{13}{240}\sqrt{77}e^{6i\alpha}\sin^6(\beta)$
	6	(-5)	$\frac{13}{40}\sqrt{\frac{77}{3}}e^{5i\alpha}\cos(\beta)\sin^5(\beta)$
	6	(-4)	$\frac{13}{80}\sqrt{\frac{7}{6}}e^{4i\alpha}(11\cos(2\beta)+9)\sin^4(\beta)$
	6	(-3)	$\frac{13}{48}\sqrt{\frac{7}{5}}e^{3i\alpha}\cos(\beta)(11\cos(2\beta)+5)\sin^3(\beta)$
	6	(-2)	$\frac{13}{48}\sqrt{\frac{7}{5}}e^{2i\alpha}(33\cos^4(\beta)-18\cos^2(\beta)+1)\sin^2(\beta)$
	6	(-1)	$\frac{13}{60}\sqrt{\frac{7}{2}}e^{i\alpha}\cos(\beta)(33\cos^4(\beta)-30\cos^2(\beta)+5)\sin(\beta)$
	6	0	$\frac{13(105\cos(2\beta)+126\cos(4\beta)+231\cos(6\beta)+50)}{3840\sqrt{3}}$
	6	1	$-\frac{13}{60}\sqrt{\frac{7}{2}}e^{-i\alpha}\cos(\beta)(33\cos^4(\beta)-30\cos^2(\beta)+5)\sin(\beta)$
	6	2	$\frac{13}{48}\sqrt{\frac{7}{5}}e^{-2i\alpha}(33\cos^4(\beta)-18\cos^2(\beta)+1)\sin^2(\beta)$
	6	3	$-\frac{13}{48}\sqrt{\frac{7}{5}}e^{-3i\alpha}\cos(\beta)(11\cos(2\beta)+5)\sin^3(\beta)$
	6	4	$\frac{13}{80}\sqrt{\frac{7}{6}}e^{-4i\alpha}(11\cos(2\beta)+9)\sin^4(\beta)$
	6	5	$-\frac{13}{40}\sqrt{\frac{77}{3}}e^{-5i\alpha}\cos(\beta)\sin^5(\beta)$
	6	6	$\frac{13}{240}\sqrt{77}e^{-6i\alpha}\sin^6(\beta)$
$dh\sigma$	3	(-3)	$\frac{7e^{3i\alpha}\sin^3(\beta)}{4\sqrt{11}}$
	3	(-2)	$\frac{7}{2}\sqrt{\frac{3}{22}}e^{2i\alpha}\cos(\beta)\sin^2(\beta)$
	3	(-1)	$\frac{7}{8}\sqrt{\frac{3}{55}}e^{i\alpha}(5\cos(2\beta)+3)\sin(\beta)$
	3	0	$\frac{7(3\cos(\beta)+5\cos(3\beta))}{8\sqrt{55}}$
	3	1	$-\frac{7}{8}\sqrt{\frac{3}{55}}e^{-i\alpha}(5\cos(2\beta)+3)\sin(\beta)$
	3	2	$\frac{7}{2}\sqrt{\frac{3}{22}}e^{-2i\alpha}\cos(\beta)\sin^2(\beta)$
	3	3	$-\frac{7e^{-3i\alpha}\sin^3(\beta)}{4\sqrt{11}}$
	5	(-5)	$\frac{3}{16}\sqrt{\frac{77}{5}}e^{5i\alpha}\sin^5(\beta)$
	5	(-4)	$\frac{3}{8}\sqrt{\frac{77}{2}}e^{4i\alpha}\cos(\beta)\sin^4(\beta)$
	5	(-3)	$\frac{1}{32}\sqrt{77}e^{3i\alpha}(9\cos(2\beta)+7)\sin^3(\beta)$

Table B.13: PART XIII

$(l_1 l_2 m'_1)$	$t$	$q$	$b_q^t$
	5	(-2)	$\frac{1}{8}\sqrt{\frac{231}{2}}e^{2i\alpha}\cos(\beta)(3\cos(2\beta)+1)\sin^2(\beta)$
	5	(-1)	$\frac{1}{8}\sqrt{\frac{33}{2}}e^{i\alpha}(21\cos^4(\beta)-14\cos^2(\beta)+1)\sin(\beta)$
	5	0	$\frac{1}{128}\sqrt{\frac{11}{5}}(30\cos(\beta)+35\cos(3\beta)+63\cos(5\beta))$
	5	1	$-\frac{1}{8}\sqrt{\frac{33}{2}}e^{-i\alpha}(21\cos^4(\beta)-14\cos^2(\beta)+1)\sin(\beta)$
	5	2	$\frac{1}{8}\sqrt{\frac{231}{2}}e^{-2i\alpha}\cos(\beta)(3\cos(2\beta)+1)\sin^2(\beta)$
	5	3	$-\frac{1}{32}\sqrt{77}e^{-3i\alpha}(9\cos(2\beta)+7)\sin^3(\beta)$
	5	4	$\frac{3}{8}\sqrt{\frac{77}{2}}e^{-4i\alpha}\cos(\beta)\sin^4(\beta)$
	5	5	$-\frac{3}{16}\sqrt{\frac{77}{5}}e^{-5i\alpha}\sin^5(\beta)$
	7	(-7)	$\frac{3}{32}\sqrt{\frac{195}{2}}e^{7i\alpha}\sin^7(\beta)$
	7	(-6)	$\frac{3}{32}\sqrt{1365}e^{6i\alpha}\cos(\beta)\sin^6(\beta)$
	7	(-5)	$\frac{3}{64}\sqrt{\frac{105}{2}}e^{5i\alpha}(13\cos(2\beta)+11)\sin^5(\beta)$
	7	(-4)	$\frac{3}{32}\sqrt{\frac{105}{2}}e^{4i\alpha}\cos(\beta)(13\cos(2\beta)+7)\sin^4(\beta)$
	7	(-3)	$\frac{3}{32}\sqrt{\frac{105}{22}}e^{3i\alpha}(143\cos^4(\beta)-66\cos^2(\beta)+3)\sin^3(\beta)$
	7	(-2)	$\frac{3}{32}\sqrt{\frac{105}{11}}e^{2i\alpha}\cos(\beta)(143\cos^4(\beta)-110\cos^2(\beta)+15)\sin^2(\beta)$
	7	(-1)	$\frac{3}{32}\sqrt{\frac{35}{22}}e^{i\alpha}(429\cos^6(\beta)-495\cos^4(\beta)+135\cos^2(\beta)-5)\sin(\beta)$
	7	0	$\frac{3\sqrt{\frac{5}{11}}(175\cos(\beta)+189\cos(3\beta)+231\cos(5\beta)+429\cos(7\beta))}{1024}$
	7	1	$-\frac{3}{32}\sqrt{\frac{35}{22}}e^{-i\alpha}(429\cos^6(\beta)-495\cos^4(\beta)+135\cos^2(\beta)-5)\sin(\beta)$
	7	2	$\frac{3}{32}\sqrt{\frac{105}{11}}e^{-2i\alpha}\cos(\beta)(143\cos^4(\beta)-110\cos^2(\beta)+15)\sin^2(\beta)$
	7	3	$-\frac{3}{32}\sqrt{\frac{105}{22}}e^{-3i\alpha}(143\cos^4(\beta)-66\cos^2(\beta)+3)\sin^3(\beta)$
	7	4	$\frac{3}{32}\sqrt{\frac{105}{2}}e^{-4i\alpha}\cos(\beta)(13\cos(2\beta)+7)\sin^4(\beta)$
	7	5	$-\frac{3}{64}\sqrt{\frac{105}{2}}e^{-5i\alpha}(13\cos(2\beta)+11)\sin^5(\beta)$
	7	6	$\frac{3}{32}\sqrt{1365}e^{-6i\alpha}\cos(\beta)\sin^6(\beta)$
	7	7	$-\frac{3}{32}\sqrt{\frac{195}{2}}e^{-7i\alpha}\sin^7(\beta)$
$dh\pi$	3	(-3)	$\frac{7e^{3i\alpha}\sin^3(\beta)}{\sqrt{55}}$
	3	(-2)	$7\sqrt{\frac{6}{55}}e^{2i\alpha}\cos(\beta)\sin^2(\beta)$
	3	(-1)	$\frac{7}{10}\sqrt{\frac{3}{11}}e^{i\alpha}(5\cos(2\beta)+3)\sin(\beta)$
	3	0	$\frac{7(3\cos(\beta)+5\cos(3\beta))}{10\sqrt{11}}$
	3	1	$-\frac{7}{10}\sqrt{\frac{3}{11}}e^{-i\alpha}(5\cos(2\beta)+3)\sin(\beta)$

Table B.14: PART XIV

$(l_1 l_2 m'_1)$	$t$	$q$	$b_q^t$
	3	2	$7\sqrt{\frac{6}{55}}e^{-2i\alpha}\cos(\beta)\sin^2(\beta)$
	3	3	$-\frac{7e^{-3i\alpha}\sin^3(\beta)}{\sqrt{55}}$
	5	(-5)	$\frac{3}{80}\sqrt{77}e^{5i\alpha}\sin^5(\beta)$
	5	(-4)	$\frac{3}{8}\sqrt{\frac{77}{10}}e^{4i\alpha}\cos(\beta)\sin^4(\beta)$
	5	(-3)	$\frac{1}{32}\sqrt{\frac{77}{5}}e^{3i\alpha}(9\cos(2\beta)+7)\sin^3(\beta)$
	5	(-2)	$\frac{1}{8}\sqrt{\frac{231}{10}}e^{2i\alpha}\cos(\beta)(3\cos(2\beta)+1)\sin^2(\beta)$
	5	(-1)	$\frac{1}{8}\sqrt{\frac{33}{10}}e^{i\alpha}(21\cos^4(\beta)-14\cos^2(\beta)+1)\sin(\beta)$
	5	0	$\frac{1}{640}\sqrt{11}(30\cos(\beta)+35\cos(3\beta)+63\cos(5\beta))$
	5	1	$-\frac{1}{8}\sqrt{\frac{33}{10}}e^{-i\alpha}(21\cos^4(\beta)-14\cos^2(\beta)+1)\sin(\beta)$
	5	2	$\frac{1}{8}\sqrt{\frac{231}{10}}e^{-2i\alpha}\cos(\beta)(3\cos(2\beta)+1)\sin^2(\beta)$
	5	3	$-\frac{1}{32}\sqrt{\frac{77}{5}}e^{-3i\alpha}(9\cos(2\beta)+7)\sin^3(\beta)$
	5	4	$\frac{3}{8}\sqrt{\frac{77}{10}}e^{-4i\alpha}\cos(\beta)\sin^4(\beta)$
	5	5	$-\frac{3}{80}\sqrt{77}e^{-5i\alpha}\sin^5(\beta)$
	7	(-7)	$-\frac{5}{16}\sqrt{\frac{39}{2}}e^{7i\alpha}\sin^7(\beta)$
	7	(-6)	$-\frac{5}{16}\sqrt{273}e^{6i\alpha}\cos(\beta)\sin^6(\beta)$
	7	(-5)	$-\frac{5}{32}\sqrt{\frac{21}{2}}e^{5i\alpha}(13\cos(2\beta)+11)\sin^5(\beta)$
	7	(-4)	$-\frac{5}{16}\sqrt{\frac{21}{2}}e^{4i\alpha}\cos(\beta)(13\cos(2\beta)+7)\sin^4(\beta)$
	7	(-3)	$-\frac{5}{16}\sqrt{\frac{21}{22}}e^{3i\alpha}(143\cos^4(\beta)-66\cos^2(\beta)+3)\sin^3(\beta)$
	7	(-2)	$-\frac{5}{16}\sqrt{\frac{21}{11}}e^{2i\alpha}\cos(\beta)(143\cos^4(\beta)-110\cos^2(\beta)+15)\sin^2(\beta)$
	7	(-1)	$-\frac{5}{16}\sqrt{\frac{7}{22}}e^{i\alpha}(429\cos^6(\beta)-495\cos^4(\beta)+135\cos^2(\beta)-5)\sin(\beta)$
	7	0	$-\frac{5(175\cos(\beta)+189\cos(3\beta)+231\cos(5\beta)+429\cos(7\beta))}{512\sqrt{11}}$
	7	1	$\frac{5}{16}\sqrt{\frac{7}{22}}e^{-i\alpha}(429\cos^6(\beta)-495\cos^4(\beta)+135\cos^2(\beta)-5)\sin(\beta)$
	7	2	$-\frac{5}{16}\sqrt{\frac{21}{11}}e^{-2i\alpha}\cos(\beta)(143\cos^4(\beta)-110\cos^2(\beta)+15)\sin^2(\beta)$
	7	3	$\frac{5}{16}\sqrt{\frac{21}{22}}e^{-3i\alpha}(143\cos^4(\beta)-66\cos^2(\beta)+3)\sin^3(\beta)$
	7	4	$-\frac{5}{16}\sqrt{\frac{21}{2}}e^{-4i\alpha}\cos(\beta)(13\cos(2\beta)+7)\sin^4(\beta)$
	7	5	$\frac{5}{32}\sqrt{\frac{21}{2}}e^{-5i\alpha}(13\cos(2\beta)+11)\sin^5(\beta)$
	7	6	$-\frac{5}{16}\sqrt{273}e^{-6i\alpha}\cos(\beta)\sin^6(\beta)$
	7	7	$\frac{5}{16}\sqrt{\frac{39}{2}}e^{-7i\alpha}\sin^7(\beta)$
$dh\delta$	3	(-3)	$\frac{7}{4}\sqrt{\frac{7}{55}}e^{3i\alpha}\sin^3(\beta)$

Table B.15: PART XV

$(l_1 l_2 m_1')$	$t$	$q$	$b_q^t$
	3	(-2)	$\frac{7}{2}\sqrt{\frac{21}{110}}e^{2i\alpha}\cos(\beta)\sin^2(\beta)$
	3	(-1)	$\frac{7}{40}\sqrt{\frac{21}{11}}e^{i\alpha}(5\cos(2\beta)+3)\sin(\beta)$
	3	0	$\frac{7}{40}\sqrt{\frac{7}{11}}(3\cos(\beta)+5\cos(3\beta))$
	3	1	$-\frac{7}{40}\sqrt{\frac{21}{11}}e^{-i\alpha}(5\cos(2\beta)+3)\sin(\beta)$
	3	2	$\frac{7}{2}\sqrt{\frac{21}{110}}e^{-2i\alpha}\cos(\beta)\sin^2(\beta)$
	3	3	$-\frac{7}{4}\sqrt{\frac{7}{55}}e^{-3i\alpha}\sin^3(\beta)$
	5	(-5)	$-\frac{21}{40}\sqrt{11}e^{5i\alpha}\sin^5(\beta)$
	5	(-4)	$-\frac{21}{4}\sqrt{\frac{11}{10}}e^{4i\alpha}\cos(\beta)\sin^4(\beta)$
	5	(-3)	$-\frac{7}{16}\sqrt{\frac{11}{5}}e^{3i\alpha}(9\cos(2\beta)+7)\sin^3(\beta)$
	5	(-2)	$-\frac{7}{4}\sqrt{\frac{33}{10}}e^{2i\alpha}\cos(\beta)(3\cos(2\beta)+1)\sin^2(\beta)$
	5	(-1)	$-\frac{1}{4}\sqrt{\frac{231}{10}}e^{i\alpha}(21\cos^4(\beta)-14\cos^2(\beta)+1)\sin(\beta)$
	5	0	$-\frac{1}{320}\sqrt{77}(30\cos(\beta)+35\cos(3\beta)+63\cos(5\beta))$
	5	1	$\frac{1}{4}\sqrt{\frac{231}{10}}e^{-i\alpha}(21\cos^4(\beta)-14\cos^2(\beta)+1)\sin(\beta)$
	5	2	$-\frac{7}{4}\sqrt{\frac{33}{10}}e^{-2i\alpha}\cos(\beta)(3\cos(2\beta)+1)\sin^2(\beta)$
	5	3	$\frac{7}{16}\sqrt{\frac{11}{5}}e^{-3i\alpha}(9\cos(2\beta)+7)\sin^3(\beta)$
	5	4	$-\frac{21}{4}\sqrt{\frac{11}{10}}e^{-4i\alpha}\cos(\beta)\sin^4(\beta)$
	5	5	$\frac{21}{40}\sqrt{11}e^{-5i\alpha}\sin^5(\beta)$
	7	(-7)	$\frac{5}{16}\sqrt{\frac{39}{14}}e^{7i\alpha}\sin^7(\beta)$
	7	(-6)	$\frac{5}{16}\sqrt{39}e^{6i\alpha}\cos(\beta)\sin^6(\beta)$
	7	(-5)	$\frac{5}{32}\sqrt{\frac{3}{2}}e^{5i\alpha}(13\cos(2\beta)+11)\sin^5(\beta)$
	7	(-4)	$\frac{5}{16}\sqrt{\frac{3}{2}}e^{4i\alpha}\cos(\beta)(13\cos(2\beta)+7)\sin^4(\beta)$
	7	(-3)	$\frac{5}{16}\sqrt{\frac{3}{22}}e^{3i\alpha}(143\cos^4(\beta)-66\cos^2(\beta)+3)\sin^3(\beta)$
	7	(-2)	$\frac{5}{16}\sqrt{\frac{3}{11}}e^{2i\alpha}\cos(\beta)(143\cos^4(\beta)-110\cos^2(\beta)+15)\sin^2(\beta)$
	7	(-1)	$\frac{5e^{i\alpha}(429\cos^6(\beta)-495\cos^4(\beta)+135\cos^2(\beta)-5)\sin(\beta)}{16\sqrt{22}}$
	7	0	$\frac{5(175\cos(\beta)+189\cos(3\beta)+231\cos(5\beta)+429\cos(7\beta))}{512\sqrt{77}}$
	7	1	$-\frac{5e^{-i\alpha}(429\cos^6(\beta)-495\cos^4(\beta)+135\cos^2(\beta)-5)\sin(\beta)}{16\sqrt{22}}$
	7	2	$\frac{5}{16}\sqrt{\frac{3}{11}}e^{-2i\alpha}\cos(\beta)(143\cos^4(\beta)-110\cos^2(\beta)+15)\sin^2(\beta)$
	7	3	$-\frac{5}{16}\sqrt{\frac{3}{22}}e^{-3i\alpha}(143\cos^4(\beta)-66\cos^2(\beta)+3)\sin^3(\beta)$
	7	4	$\frac{5}{16}\sqrt{\frac{3}{2}}e^{-4i\alpha}\cos(\beta)(13\cos(2\beta)+7)\sin^4(\beta)$

Table B.16: PART XVI

$(l_1 l_2 m'_1)$	$t$	$q$	$b_q^t$
	7	5	$-\frac{5}{32}\sqrt{\frac{3}{2}}e^{-5i\alpha}(13\cos(2\beta)+11)\sin^5(\beta)$
	7	6	$\frac{5}{16}\sqrt{39}e^{-6i\alpha}\cos(\beta)\sin^6(\beta)$
	7	7	$-\frac{5}{16}\sqrt{\frac{39}{14}}e^{-7i\alpha}\sin^7(\beta)$
$ff\sigma$	0	0	$\frac{1}{7}$
	2	(-2)	$\frac{5}{14}\sqrt{\frac{3}{2}}e^{2i\alpha}\sin^2(\beta)$
	2	(-1)	$\frac{5}{7}\sqrt{\frac{3}{2}}e^{i\alpha}\cos(\beta)\sin(\beta)$
	2	0	$\frac{5}{28}(3\cos(2\beta)+1)$
	2	1	$-\frac{5}{7}\sqrt{\frac{3}{2}}e^{-i\alpha}\cos(\beta)\sin(\beta)$
	2	2	$\frac{5}{14}\sqrt{\frac{3}{2}}e^{-2i\alpha}\sin^2(\beta)$
	4	(-4)	$\frac{9}{8}\sqrt{\frac{5}{14}}e^{4i\alpha}\sin^4(\beta)$
	4	(-3)	$\frac{9}{4}\sqrt{\frac{5}{7}}e^{3i\alpha}\cos(\beta)\sin^3(\beta)$
	4	(-2)	$\frac{9}{56}\sqrt{\frac{5}{2}}e^{2i\alpha}(7\cos(2\beta)+5)\sin^2(\beta)$
	4	(-1)	$\frac{9}{112}\sqrt{5}e^{i\alpha}(7\cos(2\beta)+1)\sin(2\beta)$
	4	0	$\frac{9}{448}(20\cos(2\beta)+35\cos(4\beta)+9)$
	4	1	$-\frac{9}{112}\sqrt{5}e^{-i\alpha}(7\cos(2\beta)+1)\sin(2\beta)$
	4	2	$\frac{9}{56}\sqrt{\frac{5}{2}}e^{-2i\alpha}(7\cos(2\beta)+5)\sin^2(\beta)$
	4	3	$-\frac{9}{4}\sqrt{\frac{5}{7}}e^{-3i\alpha}\cos(\beta)\sin^3(\beta)$
	4	4	$\frac{9}{8}\sqrt{\frac{5}{14}}e^{-4i\alpha}\sin^4(\beta)$
	6	(-6)	$\frac{13}{32}\sqrt{\frac{33}{7}}e^{6i\alpha}\sin^6(\beta)$
	6	(-5)	$\frac{39}{16}\sqrt{\frac{11}{7}}e^{5i\alpha}\cos(\beta)\sin^5(\beta)$
	6	(-4)	$\frac{39e^{4i\alpha}(11\cos(2\beta)+9)\sin^4(\beta)}{32\sqrt{14}}$
	6	(-3)	$\frac{13}{32}\sqrt{\frac{15}{7}}e^{3i\alpha}\cos(\beta)(11\cos(2\beta)+5)\sin^3(\beta)$
	6	(-2)	$\frac{13}{32}\sqrt{\frac{15}{7}}e^{2i\alpha}(33\cos^4(\beta)-18\cos^2(\beta)+1)\sin^2(\beta)$
	6	(-1)	$\frac{13}{8}\sqrt{\frac{3}{14}}e^{i\alpha}\cos(\beta)(33\cos^4(\beta)-30\cos^2(\beta)+5)\sin(\beta)$
	6	0	$\frac{13(105\cos(2\beta)+126\cos(4\beta)+231\cos(6\beta)+50)}{3584}$
	6	1	$-\frac{13}{8}\sqrt{\frac{3}{14}}e^{-i\alpha}\cos(\beta)(33\cos^4(\beta)-30\cos^2(\beta)+5)\sin(\beta)$
	6	2	$\frac{13}{32}\sqrt{\frac{15}{7}}e^{-2i\alpha}(33\cos^4(\beta)-18\cos^2(\beta)+1)\sin^2(\beta)$
	6	3	$-\frac{13}{32}\sqrt{\frac{15}{7}}e^{-3i\alpha}\cos(\beta)(11\cos(2\beta)+5)\sin^3(\beta)$
	6	4	$\frac{39e^{-4i\alpha}(11\cos(2\beta)+9)\sin^4(\beta)}{32\sqrt{14}}$
	6	5	$-\frac{39}{16}\sqrt{\frac{11}{7}}e^{-5i\alpha}\cos(\beta)\sin^5(\beta)$

Table B.17: PART XVII

$(l_1 l_2 m'_1)$	$t$	$q$	$b_q^t$
	6	6	$\frac{13}{32} \sqrt{\frac{33}{7}} e^{-6i\alpha} \sin^6(\beta)$
$ff\pi$	0	0	$\frac{2}{7}$
	2	(-2)	$\frac{15}{28} \sqrt{\frac{3}{2}} e^{2i\alpha} \sin^2(\beta)$
	2	(-1)	$\frac{15}{14} \sqrt{\frac{3}{2}} e^{i\alpha} \cos(\beta) \sin(\beta)$
	2	0	$\frac{15}{56} (3 \cos(2\beta) + 1)$
	2	1	$-\frac{15}{14} \sqrt{\frac{3}{2}} e^{-i\alpha} \cos(\beta) \sin(\beta)$
	2	2	$\frac{15}{28} \sqrt{\frac{3}{2}} e^{-2i\alpha} \sin^2(\beta)$
	4	(-4)	$\frac{3}{8} \sqrt{\frac{5}{14}} e^{4i\alpha} \sin^4(\beta)$
	4	(-3)	$\frac{3}{4} \sqrt{\frac{5}{7}} e^{3i\alpha} \cos(\beta) \sin^3(\beta)$
	4	(-2)	$\frac{3}{56} \sqrt{\frac{5}{2}} e^{2i\alpha} (7 \cos(2\beta) + 5) \sin^2(\beta)$
	4	(-1)	$\frac{3}{112} \sqrt{5} e^{i\alpha} (7 \cos(2\beta) + 1) \sin(2\beta)$
	4	0	$\frac{3}{448} (20 \cos(2\beta) + 35 \cos(4\beta) + 9)$
	4	1	$-\frac{3}{112} \sqrt{5} e^{-i\alpha} (7 \cos(2\beta) + 1) \sin(2\beta)$
	4	2	$\frac{3}{56} \sqrt{\frac{5}{2}} e^{-2i\alpha} (7 \cos(2\beta) + 5) \sin^2(\beta)$
	4	3	$-\frac{3}{4} \sqrt{\frac{5}{7}} e^{-3i\alpha} \cos(\beta) \sin^3(\beta)$
	4	4	$\frac{3}{8} \sqrt{\frac{5}{14}} e^{-4i\alpha} \sin^4(\beta)$
	6	(-6)	$-\frac{39}{64} \sqrt{\frac{33}{7}} e^{6i\alpha} \sin^6(\beta)$
	6	(-5)	$-\frac{117}{32} \sqrt{\frac{11}{7}} e^{5i\alpha} \cos(\beta) \sin^5(\beta)$
	6	(-4)	$-\frac{117 e^{4i\alpha} (11 \cos(2\beta) + 9) \sin^4(\beta)}{64 \sqrt{14}}$
	6	(-3)	$-\frac{39}{64} \sqrt{\frac{15}{7}} e^{3i\alpha} \cos(\beta) (11 \cos(2\beta) + 5) \sin^3(\beta)$
	6	(-2)	$-\frac{39}{64} \sqrt{\frac{15}{7}} e^{2i\alpha} (33 \cos^4(\beta) - 18 \cos^2(\beta) + 1) \sin^2(\beta)$
	6	(-1)	$-\frac{39}{16} \sqrt{\frac{3}{14}} e^{i\alpha} \cos(\beta) (33 \cos^4(\beta) - 30 \cos^2(\beta) + 5) \sin(\beta)$
	6	0	$-\frac{39(105 \cos(2\beta) + 126 \cos(4\beta) + 231 \cos(6\beta) + 50)}{7168}$
	6	1	$\frac{39}{16} \sqrt{\frac{3}{14}} e^{-i\alpha} \cos(\beta) (33 \cos^4(\beta) - 30 \cos^2(\beta) + 5) \sin(\beta)$
	6	2	$-\frac{39}{64} \sqrt{\frac{15}{7}} e^{-2i\alpha} (33 \cos^4(\beta) - 18 \cos^2(\beta) + 1) \sin^2(\beta)$
	6	3	$\frac{39}{64} \sqrt{\frac{15}{7}} e^{-3i\alpha} \cos(\beta) (11 \cos(2\beta) + 5) \sin^3(\beta)$
	6	4	$-\frac{117 e^{-4i\alpha} (11 \cos(2\beta) + 9) \sin^4(\beta)}{64 \sqrt{14}}$
	6	5	$\frac{117}{32} \sqrt{\frac{11}{7}} e^{-5i\alpha} \cos(\beta) \sin^5(\beta)$
	6	6	$-\frac{39}{64} \sqrt{\frac{33}{7}} e^{-6i\alpha} \sin^6(\beta)$
$ff\delta$	0	0	$\frac{2}{7}$

Table B.18: PART XVIII

$(l_1 l_2 m'_1)$	$t$	$q$	$b_q^t$
	2	(-2)	0
	2	(-1)	0
	2	0	0
	2	1	0
	2	2	0
	4	(-4)	$-\frac{3}{8}\sqrt{\frac{35}{2}}e^{4i\alpha}\sin^4(\beta)$
	4	(-3)	$-\frac{3}{4}\sqrt{35}e^{3i\alpha}\cos(\beta)\sin^3(\beta)$
	4	(-2)	$-\frac{3}{8}\sqrt{\frac{5}{2}}e^{2i\alpha}(7\cos(2\beta)+5)\sin^2(\beta)$
	4	(-1)	$-\frac{3}{16}\sqrt{5}e^{i\alpha}(7\cos(2\beta)+1)\sin(2\beta)$
	4	0	$-\frac{3}{64}(20\cos(2\beta)+35\cos(4\beta)+9)$
	4	1	$\frac{3}{16}\sqrt{5}e^{-i\alpha}(7\cos(2\beta)+1)\sin(2\beta)$
	4	2	$-\frac{3}{8}\sqrt{\frac{5}{2}}e^{-2i\alpha}(7\cos(2\beta)+5)\sin^2(\beta)$
	4	3	$\frac{3}{4}\sqrt{35}e^{-3i\alpha}\cos(\beta)\sin^3(\beta)$
	4	4	$-\frac{3}{8}\sqrt{\frac{35}{2}}e^{-4i\alpha}\sin^4(\beta)$
	6	(-6)	$\frac{39}{160}\sqrt{\frac{33}{7}}e^{6i\alpha}\sin^6(\beta)$
	6	(-5)	$\frac{117}{80}\sqrt{\frac{11}{7}}e^{5i\alpha}\cos(\beta)\sin^5(\beta)$
	6	(-4)	$\frac{117e^{4i\alpha}(11\cos(2\beta)+9)\sin^4(\beta)}{160\sqrt{14}}$
	6	(-3)	$\frac{39}{32}\sqrt{\frac{3}{35}}e^{3i\alpha}\cos(\beta)(11\cos(2\beta)+5)\sin^3(\beta)$
	6	(-2)	$\frac{39}{32}\sqrt{\frac{3}{35}}e^{2i\alpha}(33\cos^4(\beta)-18\cos^2(\beta)+1)\sin^2(\beta)$
	6	(-1)	$\frac{39}{40}\sqrt{\frac{3}{14}}e^{i\alpha}\cos(\beta)(33\cos^4(\beta)-30\cos^2(\beta)+5)\sin(\beta)$
	6	0	$\frac{39}{560}(231\cos^6(\beta)-315\cos^4(\beta)+105\cos^2(\beta)-5)$
	6	1	$-\frac{39}{40}\sqrt{\frac{3}{14}}e^{-i\alpha}\cos(\beta)(33\cos^4(\beta)-30\cos^2(\beta)+5)\sin(\beta)$
	6	2	$\frac{39}{32}\sqrt{\frac{3}{35}}e^{-2i\alpha}(33\cos^4(\beta)-18\cos^2(\beta)+1)\sin^2(\beta)$
	6	3	$-\frac{39}{32}\sqrt{\frac{3}{35}}e^{-3i\alpha}\cos(\beta)(11\cos(2\beta)+5)\sin^3(\beta)$
	6	4	$\frac{117e^{-4i\alpha}(11\cos(2\beta)+9)\sin^4(\beta)}{160\sqrt{14}}$
	6	5	$-\frac{117}{80}\sqrt{\frac{11}{7}}e^{-5i\alpha}\cos(\beta)\sin^5(\beta)$
	6	6	$\frac{39}{160}\sqrt{\frac{33}{7}}e^{-6i\alpha}\sin^6(\beta)$
$ff\phi$	0	0	$\frac{2}{7}$
	2	(-2)	$-\frac{25}{28}\sqrt{\frac{3}{2}}e^{2i\alpha}\sin^2(\beta)$
	2	(-1)	$-\frac{25}{14}\sqrt{\frac{3}{2}}e^{i\alpha}\cos(\beta)\sin(\beta)$
	2	0	$-\frac{25}{56}(3\cos(2\beta)+1)$
	2	1	$\frac{25}{14}\sqrt{\frac{3}{2}}e^{-i\alpha}\cos(\beta)\sin(\beta)$

Table B.19: PART XIX

$(l_1 l_2 m'_1)$	$t$	$q$	$b_q^t$
	2	2	$-\frac{25}{28}\sqrt{\frac{3}{2}}e^{-2i\alpha}\sin^2(\beta)$
	4	(-4)	$\frac{9}{8}\sqrt{\frac{5}{14}}e^{4i\alpha}\sin^4(\beta)$
	4	(-3)	$\frac{9}{4}\sqrt{\frac{5}{7}}e^{3i\alpha}\cos(\beta)\sin^3(\beta)$
	4	(-2)	$\frac{9}{56}\sqrt{\frac{5}{2}}e^{2i\alpha}(7\cos(2\beta)+5)\sin^2(\beta)$
	4	(-1)	$\frac{9}{112}\sqrt{5}e^{i\alpha}(7\cos(2\beta)+1)\sin(2\beta)$
	4	0	$\frac{9}{448}(20\cos(2\beta)+35\cos(4\beta)+9)$
	4	1	$-\frac{9}{112}\sqrt{5}e^{-i\alpha}(7\cos(2\beta)+1)\sin(2\beta)$
	4	2	$\frac{9}{56}\sqrt{\frac{5}{2}}e^{-2i\alpha}(7\cos(2\beta)+5)\sin^2(\beta)$
	4	3	$-\frac{9}{4}\sqrt{\frac{5}{7}}e^{-3i\alpha}\cos(\beta)\sin^3(\beta)$
	4	4	$\frac{9}{8}\sqrt{\frac{5}{14}}e^{-4i\alpha}\sin^4(\beta)$
	6	(-6)	$-\frac{13}{320}\sqrt{\frac{33}{7}}e^{6i\alpha}\sin^6(\beta)$
	6	(-5)	$-\frac{39}{160}\sqrt{\frac{11}{7}}e^{5i\alpha}\cos(\beta)\sin^5(\beta)$
	6	(-4)	$-\frac{39e^{4i\alpha}(11\cos(2\beta)+9)\sin^4(\beta)}{320\sqrt{14}}$
	6	(-3)	$-\frac{13}{64}\sqrt{\frac{3}{35}}e^{3i\alpha}\cos(\beta)(11\cos(2\beta)+5)\sin^3(\beta)$
	6	(-2)	$-\frac{13}{64}\sqrt{\frac{3}{35}}e^{2i\alpha}(33\cos^4(\beta)-18\cos^2(\beta)+1)\sin^2(\beta)$
	6	(-1)	$-\frac{13}{80}\sqrt{\frac{3}{14}}e^{i\alpha}\cos(\beta)(33\cos^4(\beta)-30\cos^2(\beta)+5)\sin(\beta)$
	6	0	$-\frac{13(105\cos(2\beta)+126\cos(4\beta)+231\cos(6\beta)+50)}{35840}$
	6	1	$\frac{13}{80}\sqrt{\frac{3}{14}}e^{-i\alpha}\cos(\beta)(33\cos^4(\beta)-30\cos^2(\beta)+5)\sin(\beta)$
	6	2	$-\frac{13}{64}\sqrt{\frac{3}{35}}e^{-2i\alpha}(33\cos^4(\beta)-18\cos^2(\beta)+1)\sin^2(\beta)$
	6	3	$\frac{13}{64}\sqrt{\frac{3}{35}}e^{-3i\alpha}\cos(\beta)(11\cos(2\beta)+5)\sin^3(\beta)$
	6	4	$-\frac{39e^{-4i\alpha}(11\cos(2\beta)+9)\sin^4(\beta)}{320\sqrt{14}}$
	6	5	$\frac{39}{160}\sqrt{\frac{11}{7}}e^{-5i\alpha}\cos(\beta)\sin^5(\beta)$
	6	6	$-\frac{13}{320}\sqrt{\frac{33}{7}}e^{-6i\alpha}\sin^6(\beta)$
$fg\sigma$	1	(-1)	$\frac{e^{i\alpha}\sin(\beta)}{\sqrt{14}}$
	1	0	$\frac{\cos(\beta)}{\sqrt{7}}$
	1	1	$-\frac{e^{-i\alpha}\sin(\beta)}{\sqrt{14}}$
	3	(-3)	$\frac{1}{12}\sqrt{35}e^{3i\alpha}\sin^3(\beta)$
	3	(-2)	$\frac{1}{2}\sqrt{\frac{35}{6}}e^{2i\alpha}\cos(\beta)\sin^2(\beta)$
	3	(-1)	$\frac{1}{8}\sqrt{\frac{7}{3}}e^{i\alpha}(5\cos(2\beta)+3)\sin(\beta)$
	3	0	$\frac{1}{24}\sqrt{7}(3\cos(\beta)+5\cos(3\beta))$

Table B.20: PART XX

$(l_1 l_2 m'_1)$	$t$	$q$	$b_q^t$
	3	1	$-\frac{1}{8}\sqrt{\frac{7}{3}}e^{-i\alpha}(5\cos(2\beta)+3)\sin(\beta)$
	3	2	$\frac{1}{2}\sqrt{\frac{35}{6}}e^{-2i\alpha}\cos(\beta)\sin^2(\beta)$
	3	3	$-\frac{1}{12}\sqrt{35}e^{-3i\alpha}\sin^3(\beta)$
	5	(-5)	$\frac{11}{16}e^{5i\alpha}\sin^5(\beta)$
	5	(-4)	$\frac{11}{8}\sqrt{\frac{5}{2}}e^{4i\alpha}\cos(\beta)\sin^4(\beta)$
	5	(-3)	$\frac{11}{96}\sqrt{5}e^{3i\alpha}(9\cos(2\beta)+7)\sin^3(\beta)$
	5	(-2)	$\frac{11}{8}\sqrt{\frac{5}{6}}e^{2i\alpha}\cos(\beta)(3\cos(2\beta)+1)\sin^2(\beta)$
	5	(-1)	$\frac{11}{8}\sqrt{\frac{5}{42}}e^{i\alpha}(21\cos^4(\beta)-14\cos^2(\beta)+1)\sin(\beta)$
	5	0	$\frac{11(30\cos(\beta)+35\cos(3\beta)+63\cos(5\beta))}{384\sqrt{7}}$
	5	1	$-\frac{11}{8}\sqrt{\frac{5}{42}}e^{-i\alpha}(21\cos^4(\beta)-14\cos^2(\beta)+1)\sin(\beta)$
	5	2	$\frac{11}{8}\sqrt{\frac{5}{6}}e^{-2i\alpha}\cos(\beta)(3\cos(2\beta)+1)\sin^2(\beta)$
	5	3	$-\frac{11}{96}\sqrt{5}e^{-3i\alpha}(9\cos(2\beta)+7)\sin^3(\beta)$
	5	4	$\frac{11}{8}\sqrt{\frac{5}{2}}e^{-4i\alpha}\cos(\beta)\sin^4(\beta)$
	5	5	$-\frac{11}{16}e^{-5i\alpha}\sin^5(\beta)$
	7	(-7)	$\frac{5}{32}\sqrt{\frac{429}{14}}e^{7i\alpha}\sin^7(\beta)$
	7	(-6)	$\frac{5}{32}\sqrt{429}e^{6i\alpha}\cos(\beta)\sin^6(\beta)$
	7	(-5)	$\frac{5}{64}\sqrt{\frac{33}{2}}e^{5i\alpha}(13\cos(2\beta)+11)\sin^5(\beta)$
	7	(-4)	$\frac{5}{32}\sqrt{\frac{33}{2}}e^{4i\alpha}\cos(\beta)(13\cos(2\beta)+7)\sin^4(\beta)$
	7	(-3)	$\frac{5}{32}\sqrt{\frac{3}{2}}e^{3i\alpha}(143\cos^4(\beta)-66\cos^2(\beta)+3)\sin^3(\beta)$
	7	(-2)	$\frac{5}{32}\sqrt{3}e^{2i\alpha}\cos(\beta)(143\cos^4(\beta)-110\cos^2(\beta)+15)\sin^2(\beta)$
	7	(-1)	$\frac{5e^{i\alpha}(429\cos^6(\beta)-495\cos^4(\beta)+135\cos^2(\beta)-5)\sin(\beta)}{32\sqrt{2}}$
	7	0	$\frac{5\cos(\beta)(429\cos^6(\beta)-693\cos^4(\beta)+315\cos^2(\beta)-35)}{16\sqrt{7}}$
	7	1	$-\frac{5e^{-i\alpha}(429\cos^6(\beta)-495\cos^4(\beta)+135\cos^2(\beta)-5)\sin(\beta)}{32\sqrt{2}}$
	7	2	$\frac{5}{32}\sqrt{3}e^{-2i\alpha}\cos(\beta)(143\cos^4(\beta)-110\cos^2(\beta)+15)\sin^2(\beta)$
	7	3	$-\frac{5}{32}\sqrt{\frac{3}{2}}e^{-3i\alpha}(143\cos^4(\beta)-66\cos^2(\beta)+3)\sin^3(\beta)$
	7	4	$\frac{5}{32}\sqrt{\frac{33}{2}}e^{-4i\alpha}\cos(\beta)(13\cos(2\beta)+7)\sin^4(\beta)$
	7	5	$-\frac{5}{64}\sqrt{\frac{33}{2}}e^{-5i\alpha}(13\cos(2\beta)+11)\sin^5(\beta)$
	7	6	$\frac{5}{32}\sqrt{429}e^{-6i\alpha}\cos(\beta)\sin^6(\beta)$
	7	7	$-\frac{5}{32}\sqrt{\frac{429}{14}}e^{-7i\alpha}\sin^7(\beta)$
$fg\pi$	1	(-1)	$\frac{1}{2}\sqrt{\frac{15}{14}}e^{i\alpha}\sin(\beta)$

Table B.21: PART XXI

$(l_1 l_2 m'_1)$	$t$	$q$	$b_q^t$
	1	0	$\frac{1}{2}\sqrt{\frac{15}{7}}\cos(\beta)$
	1	1	$-\frac{1}{2}\sqrt{\frac{15}{14}}e^{-i\alpha}\sin(\beta)$
	3	(-3)	$\frac{5}{12}\sqrt{\frac{7}{3}}e^{3i\alpha}\sin^3(\beta)$
	3	(-2)	$\frac{5}{6}\sqrt{\frac{7}{2}}e^{2i\alpha}\cos(\beta)\sin^2(\beta)$
	3	(-1)	$\frac{1}{24}\sqrt{35}e^{i\alpha}(5\cos(2\beta)+3)\sin(\beta)$
	3	0	$\frac{1}{24}\sqrt{\frac{35}{3}}(3\cos(\beta)+5\cos(3\beta))$
	3	1	$-\frac{1}{24}\sqrt{35}e^{-i\alpha}(5\cos(2\beta)+3)\sin(\beta)$
	3	2	$\frac{5}{6}\sqrt{\frac{7}{2}}e^{-2i\alpha}\cos(\beta)\sin^2(\beta)$
	3	3	$-\frac{5}{12}\sqrt{\frac{7}{3}}e^{-3i\alpha}\sin^3(\beta)$
	5	(-5)	$\frac{11e^{5i\alpha}\sin^5(\beta)}{32\sqrt{15}}$
	5	(-4)	$\frac{11e^{4i\alpha}\cos(\beta)\sin^4(\beta)}{16\sqrt{6}}$
	5	(-3)	$\frac{11e^{3i\alpha}(9\cos(2\beta)+7)\sin^3(\beta)}{192\sqrt{3}}$
	5	(-2)	$\frac{11e^{2i\alpha}\cos(\beta)(3\cos(2\beta)+1)\sin^2(\beta)}{48\sqrt{2}}$
	5	(-1)	$\frac{11e^{i\alpha}(21\cos^4(\beta)-14\cos^2(\beta)+1)\sin(\beta)}{48\sqrt{14}}$
	5	0	$\frac{11(30\cos(\beta)+35\cos(3\beta)+63\cos(5\beta))}{768\sqrt{105}}$
	5	1	$-\frac{11e^{-i\alpha}(21\cos^4(\beta)-14\cos^2(\beta)+1)\sin(\beta)}{48\sqrt{14}}$
	5	2	$\frac{11e^{-2i\alpha}\cos(\beta)(3\cos(2\beta)+1)\sin^2(\beta)}{48\sqrt{2}}$
	5	3	$-\frac{11e^{-3i\alpha}(9\cos(2\beta)+7)\sin^3(\beta)}{192\sqrt{3}}$
	5	4	$\frac{11e^{-4i\alpha}\cos(\beta)\sin^4(\beta)}{16\sqrt{6}}$
	5	5	$-\frac{11e^{-5i\alpha}\sin^5(\beta)}{32\sqrt{15}}$
	7	(-7)	$-\frac{3}{16}\sqrt{\frac{715}{14}}e^{7i\alpha}\sin^7(\beta)$
	7	(-6)	$-\frac{3}{16}\sqrt{715}e^{6i\alpha}\cos(\beta)\sin^6(\beta)$
	7	(-5)	$-\frac{3}{32}\sqrt{\frac{55}{2}}e^{5i\alpha}(13\cos(2\beta)+11)\sin^5(\beta)$
	7	(-4)	$-\frac{3}{16}\sqrt{\frac{55}{2}}e^{4i\alpha}\cos(\beta)(13\cos(2\beta)+7)\sin^4(\beta)$
	7	(-3)	$-\frac{3}{16}\sqrt{\frac{5}{2}}e^{3i\alpha}(143\cos^4(\beta)-66\cos^2(\beta)+3)\sin^3(\beta)$
	7	(-2)	$-\frac{3}{16}\sqrt{5}e^{2i\alpha}\cos(\beta)(143\cos^4(\beta)-110\cos^2(\beta)+15)\sin^2(\beta)$
	7	(-1)	$-\frac{1}{16}\sqrt{\frac{15}{2}}e^{i\alpha}(429\cos^6(\beta)-495\cos^4(\beta)+135\cos^2(\beta)-5)\sin(\beta)$
	7	0	$-\frac{1}{8}\sqrt{\frac{15}{7}}\cos(\beta)(429\cos^6(\beta)-693\cos^4(\beta)+315\cos^2(\beta)-35)$
	7	1	$\frac{1}{16}\sqrt{\frac{15}{2}}e^{-i\alpha}(429\cos^6(\beta)-495\cos^4(\beta)+135\cos^2(\beta)-5)\sin(\beta)$
	7	2	$-\frac{3}{16}\sqrt{5}e^{-2i\alpha}\cos(\beta)(143\cos^4(\beta)-110\cos^2(\beta)+15)\sin^2(\beta)$

Table B.22: PART XXII

$(l_1 l_2 m_1')$	$t$	$q$	$b_q^t$
	7	3	$\frac{3}{16} \sqrt{\frac{5}{2}} e^{-3i\alpha} (143 \cos^4(\beta) - 66 \cos^2(\beta) + 3) \sin^3(\beta)$
	7	4	$-\frac{3}{16} \sqrt{\frac{55}{2}} e^{-4i\alpha} \cos(\beta) (13 \cos(2\beta) + 7) \sin^4(\beta)$
	7	5	$\frac{3}{32} \sqrt{\frac{55}{2}} e^{-5i\alpha} (13 \cos(2\beta) + 11) \sin^5(\beta)$
	7	6	$-\frac{3}{16} \sqrt{715} e^{-6i\alpha} \cos(\beta) \sin^6(\beta)$
	7	7	$\frac{3}{16} \sqrt{\frac{715}{14}} e^{-7i\alpha} \sin^7(\beta)$
$fg\delta$	1	(-1)	$\sqrt{\frac{3}{14}} e^{i\alpha} \sin(\beta)$
	1	0	$\sqrt{\frac{3}{7}} \cos(\beta)$
	1	1	$-\sqrt{\frac{3}{14}} e^{-i\alpha} \sin(\beta)$
	3	(-3)	$-\frac{1}{12} \sqrt{\frac{35}{3}} e^{3i\alpha} \sin^3(\beta)$
	3	(-2)	$-\frac{1}{6} \sqrt{\frac{35}{2}} e^{2i\alpha} \cos(\beta) \sin^2(\beta)$
	3	(-1)	$-\frac{1}{24} \sqrt{7} e^{i\alpha} (5 \cos(2\beta) + 3) \sin(\beta)$
	3	0	$-\frac{1}{24} \sqrt{\frac{7}{3}} (3 \cos(\beta) + 5 \cos(3\beta))$
	3	1	$\frac{1}{24} \sqrt{7} e^{-i\alpha} (5 \cos(2\beta) + 3) \sin(\beta)$
	3	2	$-\frac{1}{6} \sqrt{\frac{35}{2}} e^{-2i\alpha} \cos(\beta) \sin^2(\beta)$
	3	3	$\frac{1}{12} \sqrt{\frac{35}{3}} e^{-3i\alpha} \sin^3(\beta)$
	5	(-5)	$-\frac{11e^{5i\alpha} \sin^5(\beta)}{4\sqrt{3}}$
	5	(-4)	$-\frac{11}{2} \sqrt{\frac{5}{6}} e^{4i\alpha} \cos(\beta) \sin^4(\beta)$
	5	(-3)	$-\frac{11}{24} \sqrt{\frac{5}{3}} e^{3i\alpha} (9 \cos(2\beta) + 7) \sin^3(\beta)$
	5	(-2)	$-\frac{11}{6} \sqrt{\frac{5}{2}} e^{2i\alpha} \cos(\beta) (3 \cos(2\beta) + 1) \sin^2(\beta)$
	5	(-1)	$-\frac{11}{6} \sqrt{\frac{5}{14}} e^{i\alpha} (21 \cos^4(\beta) - 14 \cos^2(\beta) + 1) \sin(\beta)$
	5	0	$-\frac{11(30 \cos(\beta) + 35 \cos(3\beta) + 63 \cos(5\beta))}{96\sqrt{21}}$
	5	1	$\frac{11}{6} \sqrt{\frac{5}{14}} e^{-i\alpha} (21 \cos^4(\beta) - 14 \cos^2(\beta) + 1) \sin(\beta)$
	5	2	$-\frac{11}{6} \sqrt{\frac{5}{2}} e^{-2i\alpha} \cos(\beta) (3 \cos(2\beta) + 1) \sin^2(\beta)$
	5	3	$\frac{11}{24} \sqrt{\frac{5}{3}} e^{-3i\alpha} (9 \cos(2\beta) + 7) \sin^3(\beta)$
	5	4	$-\frac{11}{2} \sqrt{\frac{5}{6}} e^{-4i\alpha} \cos(\beta) \sin^4(\beta)$
	5	5	$\frac{11e^{-5i\alpha} \sin^5(\beta)}{4\sqrt{3}}$
	7	(-7)	$\frac{3}{16} \sqrt{\frac{143}{14}} e^{7i\alpha} \sin^7(\beta)$
	7	(-6)	$\frac{3}{16} \sqrt{143} e^{6i\alpha} \cos(\beta) \sin^6(\beta)$
	7	(-5)	$\frac{3}{32} \sqrt{\frac{11}{2}} e^{5i\alpha} (13 \cos(2\beta) + 11) \sin^5(\beta)$

Table B.23: PART XXIII

B Expansion coefficients for tight-binding operator

$(l_1 l_2 m'_1)$	$t$	$q$	$b_q^t$
	7	(-4)	$\frac{3}{16} \sqrt{\frac{11}{2}} e^{4i\alpha} \cos(\beta) (13 \cos(2\beta) + 7) \sin^4(\beta)$
	7	(-3)	$\frac{3e^{3i\alpha} (143 \cos^4(\beta) - 66 \cos^2(\beta) + 3) \sin^3(\beta)}{16\sqrt{2}}$
	7	(-2)	$\frac{3}{16} e^{2i\alpha} \cos(\beta) (143 \cos^4(\beta) - 110 \cos^2(\beta) + 15) \sin^2(\beta)$
	7	(-1)	$\frac{1}{16} \sqrt{\frac{3}{2}} e^{i\alpha} (429 \cos^6(\beta) - 495 \cos^4(\beta) + 135 \cos^2(\beta) - 5) \sin(\beta)$
	7	0	$\frac{1}{8} \sqrt{\frac{3}{7}} \cos(\beta) (429 \cos^6(\beta) - 693 \cos^4(\beta) + 315 \cos^2(\beta) - 35)$
	7	1	$-\frac{1}{16} \sqrt{\frac{3}{2}} e^{-i\alpha} (429 \cos^6(\beta) - 495 \cos^4(\beta) + 135 \cos^2(\beta) - 5) \sin(\beta)$
	7	2	$\frac{3}{16} e^{-2i\alpha} \cos(\beta) (143 \cos^4(\beta) - 110 \cos^2(\beta) + 15) \sin^2(\beta)$
	7	3	$-\frac{3e^{-3i\alpha} (143 \cos^4(\beta) - 66 \cos^2(\beta) + 3) \sin^3(\beta)}{16\sqrt{2}}$
	7	4	$\frac{3}{16} \sqrt{\frac{11}{2}} e^{-4i\alpha} \cos(\beta) (13 \cos(2\beta) + 7) \sin^4(\beta)$
	7	5	$-\frac{3}{32} \sqrt{\frac{11}{2}} e^{-5i\alpha} (13 \cos(2\beta) + 11) \sin^5(\beta)$
	7	6	$\frac{3}{16} \sqrt{143} e^{-6i\alpha} \cos(\beta) \sin^6(\beta)$
	7	7	$-\frac{3}{16} \sqrt{\frac{143}{14}} e^{-7i\alpha} \sin^7(\beta)$
$fg\phi$	1	(-1)	$\frac{e^{i\alpha} \sin(\beta)}{2\sqrt{2}}$
	1	0	$\frac{\cos(\beta)}{2}$
	1	1	$-\frac{e^{-i\alpha} \sin(\beta)}{2\sqrt{2}}$
	3	(-3)	$-\frac{7}{12} \sqrt{5} e^{3i\alpha} \sin^3(\beta)$
	3	(-2)	$-\frac{7}{2} \sqrt{\frac{5}{6}} e^{2i\alpha} \cos(\beta) \sin^2(\beta)$
	3	(-1)	$-\frac{7e^{i\alpha} (5 \cos(2\beta) + 3) \sin(\beta)}{8\sqrt{3}}$
	3	0	$-\frac{7}{24} (3 \cos(\beta) + 5 \cos(3\beta))$
	3	1	$\frac{7e^{-i\alpha} (5 \cos(2\beta) + 3) \sin(\beta)}{8\sqrt{3}}$
	3	2	$-\frac{7}{2} \sqrt{\frac{5}{6}} e^{-2i\alpha} \cos(\beta) \sin^2(\beta)$
	3	3	$\frac{7}{12} \sqrt{5} e^{-3i\alpha} \sin^3(\beta)$
	5	(-5)	$\frac{11}{32} \sqrt{7} e^{5i\alpha} \sin^5(\beta)$
	5	(-4)	$\frac{11}{16} \sqrt{\frac{35}{2}} e^{4i\alpha} \cos(\beta) \sin^4(\beta)$
	5	(-3)	$\frac{11}{192} \sqrt{35} e^{3i\alpha} (9 \cos(2\beta) + 7) \sin^3(\beta)$
	5	(-2)	$\frac{11}{16} \sqrt{\frac{35}{6}} e^{2i\alpha} \cos(\beta) (3 \cos(2\beta) + 1) \sin^2(\beta)$
	5	(-1)	$\frac{11}{16} \sqrt{\frac{5}{6}} e^{i\alpha} (21 \cos^4(\beta) - 14 \cos^2(\beta) + 1) \sin(\beta)$
	5	0	$\frac{11}{768} (30 \cos(\beta) + 35 \cos(3\beta) + 63 \cos(5\beta))$
	5	1	$-\frac{11}{16} \sqrt{\frac{5}{6}} e^{-i\alpha} (21 \cos^4(\beta) - 14 \cos^2(\beta) + 1) \sin(\beta)$
	5	2	$\frac{11}{16} \sqrt{\frac{35}{6}} e^{-2i\alpha} \cos(\beta) (3 \cos(2\beta) + 1) \sin^2(\beta)$
	5	3	$-\frac{11}{192} \sqrt{35} e^{-3i\alpha} (9 \cos(2\beta) + 7) \sin^3(\beta)$

Table B.24: PART XXIV

$(l_1 l_2 m'_1)$	$t$	$q$	$b_q^t$
	5	4	$\frac{11}{16} \sqrt{\frac{35}{2}} e^{-4i\alpha} \cos(\beta) \sin^4(\beta)$
	5	5	$-\frac{11}{32} \sqrt{7} e^{-5i\alpha} \sin^5(\beta)$
	7	(-7)	$-\frac{1}{112} \sqrt{\frac{429}{2}} e^{7i\alpha} \sin^7(\beta)$
	7	(-6)	$-\frac{1}{16} \sqrt{\frac{429}{7}} e^{6i\alpha} \cos(\beta) \sin^6(\beta)$
	7	(-5)	$-\frac{1}{32} \sqrt{\frac{33}{14}} e^{5i\alpha} (13 \cos(2\beta) + 11) \sin^5(\beta)$
	7	(-4)	$-\frac{1}{16} \sqrt{\frac{33}{14}} e^{4i\alpha} \cos(\beta) (13 \cos(2\beta) + 7) \sin^4(\beta)$
	7	(-3)	$-\frac{1}{16} \sqrt{\frac{3}{14}} e^{3i\alpha} (143 \cos^4(\beta) - 66 \cos^2(\beta) + 3) \sin^3(\beta)$
	7	(-2)	$-\frac{1}{16} \sqrt{\frac{3}{7}} e^{2i\alpha} \cos(\beta) (143 \cos^4(\beta) - 110 \cos^2(\beta) + 15) \sin^2(\beta)$
	7	(-1)	$-\frac{e^{i\alpha} (429 \cos^6(\beta) - 495 \cos^4(\beta) + 135 \cos^2(\beta) - 5) \sin(\beta)}{16\sqrt{14}}$
	7	0	$\frac{1}{56} (-429 \cos^7(\beta) + 693 \cos^5(\beta) - 315 \cos^3(\beta) + 35 \cos(\beta))$
	7	1	$\frac{e^{-i\alpha} (429 \cos^6(\beta) - 495 \cos^4(\beta) + 135 \cos^2(\beta) - 5) \sin(\beta)}{16\sqrt{14}}$
	7	2	$-\frac{1}{16} \sqrt{\frac{3}{7}} e^{-2i\alpha} \cos(\beta) (143 \cos^4(\beta) - 110 \cos^2(\beta) + 15) \sin^2(\beta)$
	7	3	$\frac{1}{16} \sqrt{\frac{3}{14}} e^{-3i\alpha} (143 \cos^4(\beta) - 66 \cos^2(\beta) + 3) \sin^3(\beta)$
	7	4	$-\frac{1}{16} \sqrt{\frac{33}{14}} e^{-4i\alpha} \cos(\beta) (13 \cos(2\beta) + 7) \sin^4(\beta)$
	7	5	$\frac{1}{32} \sqrt{\frac{33}{14}} e^{-5i\alpha} (13 \cos(2\beta) + 11) \sin^5(\beta)$
	7	6	$-\frac{1}{16} \sqrt{\frac{429}{7}} e^{-6i\alpha} \cos(\beta) \sin^6(\beta)$
	7	7	$\frac{1}{112} \sqrt{\frac{429}{2}} e^{-7i\alpha} \sin^7(\beta)$
$gg\sigma$	0	0	$\frac{1}{9}$
	2	(-2)	$\frac{5e^{2i\alpha} \sin^2(\beta)}{6\sqrt{6}}$
	2	(-1)	$\frac{5e^{i\alpha} \sin(2\beta)}{6\sqrt{6}}$
	2	0	$\frac{5}{36} (3 \cos(2\beta) + 1)$
	2	1	$-\frac{5e^{-i\alpha} \sin(2\beta)}{6\sqrt{6}}$
	2	2	$\frac{5e^{-2i\alpha} \sin^2(\beta)}{6\sqrt{6}}$
	4	(-4)	$\frac{1}{8} \sqrt{\frac{35}{2}} e^{4i\alpha} \sin^4(\beta)$
	4	(-3)	$\frac{1}{4} \sqrt{35} e^{3i\alpha} \sin^3(\beta) \cos(\beta)$
	4	(-2)	$\frac{1}{8} \sqrt{\frac{5}{2}} e^{2i\alpha} \sin^2(\beta) (7 \cos(2\beta) + 5)$
	4	(-1)	$\frac{1}{16} \sqrt{5} e^{i\alpha} \sin(2\beta) (7 \cos(2\beta) + 1)$
	4	0	$\frac{1}{64} (20 \cos(2\beta) + 35 \cos(4\beta) + 9)$
	4	1	$-\frac{1}{16} \sqrt{5} e^{-i\alpha} \sin(2\beta) (7 \cos(2\beta) + 1)$
	4	2	$\frac{1}{8} \sqrt{\frac{5}{2}} e^{-2i\alpha} \sin^2(\beta) (7 \cos(2\beta) + 5)$

Table B.25: PART XXV

$(l_1 l_2 m'_1)$	$t$	$q$	$b_q^t$
	4	3	$-\frac{1}{4}\sqrt{35}e^{-3i\alpha}\sin^3(\beta)\cos(\beta)$
	4	4	$\frac{1}{8}\sqrt{\frac{35}{2}}e^{-4i\alpha}\sin^4(\beta)$
	6	(-6)	$\frac{13}{96}\sqrt{\frac{77}{3}}e^{6i\alpha}\sin^6(\beta)$
	6	(-5)	$\frac{13}{48}\sqrt{77}e^{5i\alpha}\sin^5(\beta)\cos(\beta)$
	6	(-4)	$\frac{13}{96}\sqrt{\frac{7}{2}}e^{4i\alpha}\sin^4(\beta)(11\cos(2\beta)+9)$
	6	(-3)	$\frac{13}{96}\sqrt{\frac{35}{3}}e^{3i\alpha}\sin^3(\beta)\cos(\beta)(11\cos(2\beta)+5)$
	6	(-2)	$\frac{13}{96}\sqrt{\frac{35}{3}}e^{2i\alpha}\sin^2(\beta)(33\cos^4(\beta)-18\cos^2(\beta)+1)$
	6	(-1)	$\frac{13}{24}\sqrt{\frac{7}{6}}e^{i\alpha}\sin(\beta)\cos(\beta)(33\cos^4(\beta)-30\cos^2(\beta)+5)$
	6	0	$\frac{13(105\cos(2\beta)+126\cos(4\beta)+231\cos(6\beta)+50)}{4608}$
	6	1	$-\frac{13}{24}\sqrt{\frac{7}{6}}e^{-i\alpha}\sin(\beta)\cos(\beta)(33\cos^4(\beta)-30\cos^2(\beta)+5)$
	6	2	$\frac{13}{96}\sqrt{\frac{35}{3}}e^{-2i\alpha}\sin^2(\beta)(33\cos^4(\beta)-18\cos^2(\beta)+1)$
	6	3	$-\frac{13}{96}\sqrt{\frac{35}{3}}e^{-3i\alpha}\sin^3(\beta)\cos(\beta)(11\cos(2\beta)+5)$
	6	4	$\frac{13}{96}\sqrt{\frac{7}{2}}e^{-4i\alpha}\sin^4(\beta)(11\cos(2\beta)+9)$
	6	5	$-\frac{13}{48}\sqrt{77}e^{-5i\alpha}\sin^5(\beta)\cos(\beta)$
	6	6	$\frac{13}{96}\sqrt{\frac{77}{3}}e^{-6i\alpha}\sin^6(\beta)$
	8	(-8)	$\frac{17}{384}\sqrt{\frac{715}{2}}e^{8i\alpha}\sin^8(\beta)$
	8	(-7)	$\frac{17}{96}\sqrt{\frac{715}{2}}e^{7i\alpha}\sin^7(\beta)\cos(\beta)$
	8	(-6)	$\frac{17}{384}\sqrt{\frac{143}{3}}e^{6i\alpha}\sin^6(\beta)(15\cos(2\beta)+13)$
	8	(-5)	$\frac{17}{192}\sqrt{\frac{1001}{2}}e^{5i\alpha}\sin^5(\beta)\cos(\beta)(5\cos(2\beta)+3)$
	8	(-4)	$\frac{17}{192}\sqrt{\frac{77}{2}}e^{4i\alpha}\sin^4(\beta)(65\cos^4(\beta)-26\cos^2(\beta)+1)$
	8	(-3)	$\frac{17}{96}\sqrt{\frac{385}{6}}e^{3i\alpha}\sin^3(\beta)\cos(\beta)(39\cos^4(\beta)-26\cos^2(\beta)+3)$
	8	(-2)	$\frac{17}{192}\sqrt{35}e^{2i\alpha}\sin^2(\beta)(143\cos^6(\beta)-143\cos^4(\beta)+33\cos^2(\beta)-1)$
	8	(-1)	$\frac{17e^{i\alpha}\sin(2\beta)(869\cos(2\beta)+286\cos(4\beta)+715\cos(6\beta)+178)}{6144\sqrt{2}}$
	8	0	$\frac{17(6435\cos^8(\beta)-12012\cos^6(\beta)+6930\cos^4(\beta)-1260\cos^2(\beta)+35)}{1152}$
	8	1	$-\frac{17e^{-i\alpha}\sin(2\beta)(869\cos(2\beta)+286\cos(4\beta)+715\cos(6\beta)+178)}{6144\sqrt{2}}$
	8	2	$\frac{17}{192}\sqrt{35}e^{-2i\alpha}\sin^2(\beta)(143\cos^6(\beta)-143\cos^4(\beta)+33\cos^2(\beta)-1)$

Table B.26: PART XXVI

$(l_1 l_2 m'_1)$	$t$	$q$	$b_q^t$
	8	3	$-\frac{17}{96} \sqrt{\frac{385}{6}} e^{-3i\alpha} \sin^3(\beta) \cos(\beta) (39 \cos^4(\beta) - 26 \cos^2(\beta) + 3)$
	8	4	$\frac{17}{192} \sqrt{\frac{77}{2}} e^{-4i\alpha} \sin^4(\beta) (65 \cos^4(\beta) - 26 \cos^2(\beta) + 1)$
	8	5	$-\frac{17}{192} \sqrt{\frac{1001}{2}} e^{-5i\alpha} \sin^5(\beta) \cos(\beta) (5 \cos(2\beta) + 3)$
	8	6	$\frac{17}{384} \sqrt{\frac{143}{3}} e^{-6i\alpha} \sin^6(\beta) (15 \cos(2\beta) + 13)$
	8	7	$-\frac{17}{96} \sqrt{\frac{715}{2}} e^{-7i\alpha} \sin^7(\beta) \cos(\beta)$
	8	8	$\frac{17}{384} \sqrt{\frac{715}{2}} e^{-8i\alpha} \sin^8(\beta)$
$gg\pi$	0	0	$\frac{2}{9}$
	2	(-2)	$\frac{17e^{2i\alpha} \sin^2(\beta)}{12\sqrt{6}}$
	2	(-1)	$\frac{17e^{i\alpha} \sin(\beta) \cos(\beta)}{6\sqrt{6}}$
	2	0	$\frac{17}{72} (3 \cos(2\beta) + 1)$
	2	1	$-\frac{17e^{-i\alpha} \sin(\beta) \cos(\beta)}{6\sqrt{6}}$
	2	2	$\frac{17e^{-2i\alpha} \sin^2(\beta)}{12\sqrt{6}}$
	4	(-4)	$\frac{1}{8} \sqrt{\frac{35}{2}} e^{4i\alpha} \sin^4(\beta)$
	4	(-3)	$\frac{1}{4} \sqrt{35} e^{3i\alpha} \sin^3(\beta) \cos(\beta)$
	4	(-2)	$\frac{1}{8} \sqrt{\frac{5}{2}} e^{2i\alpha} \sin^2(\beta) (7 \cos(2\beta) + 5)$
	4	(-1)	$\frac{1}{16} \sqrt{5} e^{i\alpha} \sin(2\beta) (7 \cos(2\beta) + 1)$
	4	0	$\frac{1}{64} (20 \cos(2\beta) + 35 \cos(4\beta) + 9)$
	4	1	$-\frac{1}{16} \sqrt{5} e^{-i\alpha} \sin(2\beta) (7 \cos(2\beta) + 1)$
	4	2	$\frac{1}{8} \sqrt{\frac{5}{2}} e^{-2i\alpha} \sin^2(\beta) (7 \cos(2\beta) + 5)$
	4	3	$-\frac{1}{4} \sqrt{35} e^{-3i\alpha} \sin^3(\beta) \cos(\beta)$
	4	4	$\frac{1}{8} \sqrt{\frac{35}{2}} e^{-4i\alpha} \sin^4(\beta)$
	6	(-6)	$-\frac{13}{960} \sqrt{\frac{77}{3}} e^{6i\alpha} \sin^6(\beta)$
	6	(-5)	$-\frac{13}{480} \sqrt{77} e^{5i\alpha} \sin^5(\beta) \cos(\beta)$
	6	(-4)	$-\frac{13}{960} \sqrt{\frac{7}{2}} e^{4i\alpha} \sin^4(\beta) (11 \cos(2\beta) + 9)$
	6	(-3)	$-\frac{13}{192} \sqrt{\frac{7}{15}} e^{3i\alpha} \sin^3(\beta) \cos(\beta) (11 \cos(2\beta) + 5)$
	6	(-2)	$-\frac{13}{192} \sqrt{\frac{7}{15}} e^{2i\alpha} \sin^2(\beta) (33 \cos^4(\beta) - 18 \cos^2(\beta) + 1)$
	6	(-1)	$-\frac{13}{240} \sqrt{\frac{7}{6}} e^{i\alpha} \sin(\beta) \cos(\beta) (33 \cos^4(\beta) - 30 \cos^2(\beta) + 5)$
	6	0	$-\frac{13(105 \cos(2\beta) + 126 \cos(4\beta) + 231 \cos(6\beta) + 50)}{46080}$
	6	1	$\frac{13}{240} \sqrt{\frac{7}{6}} e^{-i\alpha} \sin(\beta) \cos(\beta) (33 \cos^4(\beta) - 30 \cos^2(\beta) + 5)$

Table B.27: PART XXVII

$(l_1 l_2 m_1')$	$t$	$q$	$b_q^t$
	6	2	$-\frac{13}{192} \sqrt{\frac{7}{15}} e^{-2i\alpha} \sin^2(\beta) (33 \cos^4(\beta) - 18 \cos^2(\beta) + 1)$
	6	3	$\frac{13}{192} \sqrt{\frac{7}{15}} e^{-3i\alpha} \sin^3(\beta) \cos(\beta) (11 \cos(2\beta) + 5)$
	6	4	$-\frac{13}{960} \sqrt{\frac{7}{2}} e^{-4i\alpha} \sin^4(\beta) (11 \cos(2\beta) + 9)$
	6	5	$\frac{13}{480} \sqrt{77} e^{-5i\alpha} \sin^5(\beta) \cos(\beta)$
	6	6	$-\frac{13}{960} \sqrt{\frac{77}{3}} e^{-6i\alpha} \sin^6(\beta)$
	8	(-8)	$-\frac{17}{48} \sqrt{\frac{143}{10}} e^{8i\alpha} \sin^8(\beta)$
	8	(-7)	$-\frac{17}{12} \sqrt{\frac{143}{10}} e^{7i\alpha} \sin^7(\beta) \cos(\beta)$
	8	(-6)	$-\frac{17}{240} \sqrt{\frac{143}{3}} e^{6i\alpha} \sin^6(\beta) (15 \cos(2\beta) + 13)$
	8	(-5)	$-\frac{17}{120} \sqrt{\frac{1001}{2}} e^{5i\alpha} \sin^5(\beta) \cos(\beta) (5 \cos(2\beta) + 3)$
	8	(-4)	$-\frac{17}{120} \sqrt{\frac{77}{2}} e^{4i\alpha} \sin^4(\beta) (65 \cos^4(\beta) - 26 \cos^2(\beta) + 1)$
	8	(-3)	$-\frac{17}{96} \sqrt{\frac{77}{30}} e^{3i\alpha} \sin^3(\beta) \cos(\beta) (52 \cos(2\beta) + 39 \cos(4\beta) + 37)$
	8	(-2)	$-\frac{17}{24} \sqrt{\frac{7}{5}} e^{2i\alpha} \sin^2(\beta) (143 \cos^6(\beta) - 143 \cos^4(\beta) + 33 \cos^2(\beta) - 1)$
	8	(-1)	$-\frac{17e^{i\alpha} \sin(2\beta) (869 \cos(2\beta) + 286 \cos(4\beta) + 715 \cos(6\beta) + 178)}{3840\sqrt{2}}$
	8	0	$-\frac{17}{720} (6435 \cos^8(\beta) - 12012 \cos^6(\beta) + 6930 \cos^4(\beta) - 1260 \cos^2(\beta) + 35)$
	8	1	$\frac{17e^{-i\alpha} \sin(2\beta) (869 \cos(2\beta) + 286 \cos(4\beta) + 715 \cos(6\beta) + 178)}{3840\sqrt{2}}$
	8	2	$-\frac{17}{24} \sqrt{\frac{7}{5}} e^{-2i\alpha} \sin^2(\beta) (143 \cos^6(\beta) - 143 \cos^4(\beta) + 33 \cos^2(\beta) - 1)$
	8	3	$\frac{17}{96} \sqrt{\frac{77}{30}} e^{-3i\alpha} \sin^3(\beta) \cos(\beta) (52 \cos(2\beta) + 39 \cos(4\beta) + 37)$
	8	4	$-\frac{17}{120} \sqrt{\frac{77}{2}} e^{-4i\alpha} \sin^4(\beta) (65 \cos^4(\beta) - 26 \cos^2(\beta) + 1)$
	8	5	$\frac{17}{120} \sqrt{\frac{1001}{2}} e^{-5i\alpha} \sin^5(\beta) \cos(\beta) (5 \cos(2\beta) + 3)$
	8	6	$-\frac{17}{240} \sqrt{\frac{143}{3}} e^{-6i\alpha} \sin^6(\beta) (15 \cos(2\beta) + 13)$
	8	7	$\frac{17}{12} \sqrt{\frac{143}{10}} e^{-7i\alpha} \sin^7(\beta) \cos(\beta)$
	8	8	$-\frac{17}{48} \sqrt{\frac{143}{10}} e^{-8i\alpha} \sin^8(\beta)$
$gg\delta$	0	0	$\frac{2}{9}$
	2	(-2)	$\frac{1}{3} \sqrt{\frac{2}{3}} e^{2i\alpha} \sin^2(\beta)$
	2	(-1)	$\frac{1}{3} \sqrt{\frac{2}{3}} e^{i\alpha} \sin(2\beta)$
	2	0	$\frac{1}{9} (3 \cos(2\beta) + 1)$

Table B.28: PART XXVIII

$(l_1 l_2 m'_1)$	$t$	$q$	$b_q^t$
	2	1	$-\frac{1}{3}\sqrt{\frac{2}{3}}e^{-i\alpha}\sin(2\beta)$
	2	2	$\frac{1}{3}\sqrt{\frac{2}{3}}e^{-2i\alpha}\sin^2(\beta)$
	4	(-4)	$-\frac{11}{72}\sqrt{\frac{35}{2}}e^{4i\alpha}\sin^4(\beta)$
	4	(-3)	$-\frac{11}{36}\sqrt{35}e^{3i\alpha}\sin^3(\beta)\cos(\beta)$
	4	(-2)	$-\frac{11}{72}\sqrt{\frac{5}{2}}e^{2i\alpha}\sin^2(\beta)(7\cos(2\beta)+5)$
	4	(-1)	$-\frac{11}{144}\sqrt{5}e^{i\alpha}\sin(2\beta)(7\cos(2\beta)+1)$
	4	0	$-\frac{11}{576}(20\cos(2\beta)+35\cos(4\beta)+9)$
	4	1	$\frac{11}{144}\sqrt{5}e^{-i\alpha}\sin(2\beta)(7\cos(2\beta)+1)$
	4	2	$-\frac{11}{72}\sqrt{\frac{5}{2}}e^{-2i\alpha}\sin^2(\beta)(7\cos(2\beta)+5)$
	4	3	$\frac{11}{36}\sqrt{35}e^{-3i\alpha}\sin^3(\beta)\cos(\beta)$
	4	4	$-\frac{11}{72}\sqrt{\frac{35}{2}}e^{-4i\alpha}\sin^4(\beta)$
	6	(-6)	$-\frac{143}{480}\sqrt{\frac{77}{3}}e^{6i\alpha}\sin^6(\beta)$
	6	(-5)	$-\frac{143}{240}\sqrt{77}e^{5i\alpha}\sin^5(\beta)\cos(\beta)$
	6	(-4)	$-\frac{143}{480}\sqrt{\frac{7}{2}}e^{4i\alpha}\sin^4(\beta)(11\cos(2\beta)+9)$
	6	(-3)	$-\frac{143}{96}\sqrt{\frac{7}{15}}e^{3i\alpha}\sin^3(\beta)\cos(\beta)(11\cos(2\beta)+5)$
	6	(-2)	$-\frac{143}{96}\sqrt{\frac{7}{15}}e^{2i\alpha}\sin^2(\beta)(33\cos^4(\beta)-18\cos^2(\beta)+1)$
	6	(-1)	$-\frac{143}{120}\sqrt{\frac{7}{6}}e^{i\alpha}\sin(\beta)\cos(\beta)(33\cos^4(\beta)-30\cos^2(\beta)+5)$
	6	0	$-\frac{143}{720}(231\cos^6(\beta)-315\cos^4(\beta)+105\cos^2(\beta)-5)$
	6	1	$\frac{143}{120}\sqrt{\frac{7}{6}}e^{-i\alpha}\sin(\beta)\cos(\beta)(33\cos^4(\beta)-30\cos^2(\beta)+5)$
	6	2	$-\frac{143}{96}\sqrt{\frac{7}{15}}e^{-2i\alpha}\sin^2(\beta)(33\cos^4(\beta)-18\cos^2(\beta)+1)$
	6	3	$\frac{143}{96}\sqrt{\frac{7}{15}}e^{-3i\alpha}\sin^3(\beta)\cos(\beta)(11\cos(2\beta)+5)$
	6	4	$-\frac{143}{480}\sqrt{\frac{7}{2}}e^{-4i\alpha}\sin^4(\beta)(11\cos(2\beta)+9)$
	6	5	$\frac{143}{240}\sqrt{77}e^{-5i\alpha}\sin^5(\beta)\cos(\beta)$
	6	6	$-\frac{143}{480}\sqrt{\frac{77}{3}}e^{-6i\alpha}\sin^6(\beta)$
	8	(-8)	$\frac{17}{96}\sqrt{\frac{143}{10}}e^{8i\alpha}\sin^8(\beta)$
	8	(-7)	$\frac{17}{24}\sqrt{\frac{143}{10}}e^{7i\alpha}\sin^7(\beta)\cos(\beta)$
	8	(-6)	$\frac{17}{480}\sqrt{\frac{143}{3}}e^{6i\alpha}\sin^6(\beta)(15\cos(2\beta)+13)$
	8	(-5)	$\frac{17}{240}\sqrt{\frac{1001}{2}}e^{5i\alpha}\sin^5(\beta)\cos(\beta)(5\cos(2\beta)+3)$

Table B.29: PART XXIX

B Expansion coefficients for tight-binding operator

$(l_1 l_2 m_1')$	$t$	$q$	$b_q^t$
	8	(-4)	$\frac{17}{240} \sqrt{\frac{77}{2}} e^{4i\alpha} \sin^4(\beta) (65 \cos^4(\beta) - 26 \cos^2(\beta) + 1)$
	8	(-3)	$\frac{17}{24} \sqrt{\frac{77}{30}} e^{3i\alpha} \sin^3(\beta) \cos(\beta) (39 \cos^4(\beta) - 26 \cos^2(\beta) + 3)$
	8	(-2)	$\frac{17}{48} \sqrt{\frac{7}{5}} e^{2i\alpha} \sin^2(\beta) (143 \cos^6(\beta) - 143 \cos^4(\beta) + 33 \cos^2(\beta) - 1)$
	8	(-1)	$\frac{17e^{i\alpha} \sin(2\beta)(869 \cos(2\beta)+286 \cos(4\beta)+715 \cos(6\beta)+178)}{7680\sqrt{2}}$
	8	0	$\frac{17(6435 \cos^8(\beta)-12012 \cos^6(\beta)+6930 \cos^4(\beta)-1260 \cos^2(\beta)+35)}{1440}$
	8	1	$-\frac{17e^{-i\alpha} \sin(2\beta)(869 \cos(2\beta)+286 \cos(4\beta)+715 \cos(6\beta)+178)}{7680\sqrt{2}}$
	8	2	$\frac{17}{48} \sqrt{\frac{7}{5}} e^{-2i\alpha} \sin^2(\beta) (143 \cos^6(\beta) - 143 \cos^4(\beta) + 33 \cos^2(\beta) - 1)$
	8	3	$-\frac{17}{24} \sqrt{\frac{77}{30}} e^{-3i\alpha} \sin^3(\beta) \cos(\beta) (39 \cos^4(\beta) - 26 \cos^2(\beta) + 3)$
	8	4	$\frac{17}{240} \sqrt{\frac{77}{2}} e^{-4i\alpha} \sin^4(\beta) (65 \cos^4(\beta) - 26 \cos^2(\beta) + 1)$
	8	5	$-\frac{17}{240} \sqrt{\frac{1001}{2}} e^{-5i\alpha} \sin^5(\beta) \cos(\beta) (5 \cos(2\beta) + 3)$
	8	6	$\frac{17}{480} \sqrt{\frac{143}{3}} e^{-6i\alpha} \sin^6(\beta) (15 \cos(2\beta) + 13)$
	8	7	$-\frac{17}{24} \sqrt{\frac{143}{10}} e^{-7i\alpha} \sin^7(\beta) \cos(\beta)$
	8	8	$\frac{17}{96} \sqrt{\frac{143}{10}} e^{-8i\alpha} \sin^8(\beta)$
$gg\phi$	0	0	$\frac{2}{9}$
	2	(-2)	$-\frac{7e^{2i\alpha} \sin^2(\beta)}{12\sqrt{6}}$
	2	(-1)	$-\frac{7e^{i\alpha} \sin(\beta) \cos(\beta)}{6\sqrt{6}}$
	2	0	$-\frac{7}{72} (3 \cos(2\beta) + 1)$
	2	1	$\frac{7e^{-i\alpha} \sin(\beta) \cos(\beta)}{6\sqrt{6}}$
	2	2	$-\frac{7e^{-2i\alpha} \sin^2(\beta)}{12\sqrt{6}}$
	4	(-4)	$-\frac{7}{24} \sqrt{\frac{35}{2}} e^{4i\alpha} \sin^4(\beta)$
	4	(-3)	$-\frac{7}{12} \sqrt{35} e^{3i\alpha} \sin^3(\beta) \cos(\beta)$
	4	(-2)	$-\frac{7}{24} \sqrt{\frac{5}{2}} e^{2i\alpha} \sin^2(\beta) (7 \cos(2\beta) + 5)$
	4	(-1)	$-\frac{7}{48} \sqrt{5} e^{i\alpha} \sin(2\beta) (7 \cos(2\beta) + 1)$
	4	0	$-\frac{7}{192} (20 \cos(2\beta) + 35 \cos(4\beta) + 9)$
	4	1	$\frac{7}{48} \sqrt{5} e^{-i\alpha} \sin(2\beta) (7 \cos(2\beta) + 1)$
	4	2	$-\frac{7}{24} \sqrt{\frac{5}{2}} e^{-2i\alpha} \sin^2(\beta) (7 \cos(2\beta) + 5)$
	4	3	$\frac{7}{12} \sqrt{35} e^{-3i\alpha} \sin^3(\beta) \cos(\beta)$
	4	4	$-\frac{7}{24} \sqrt{\frac{35}{2}} e^{-4i\alpha} \sin^4(\beta)$
	6	(-6)	$\frac{221}{960} \sqrt{\frac{77}{3}} e^{6i\alpha} \sin^6(\beta)$

Table B.30: PART XXX

$(l_1 l_2 m'_1)$	$t$	$q$	$b_q^t$
6	(-5)		$\frac{221}{480} \sqrt{77} e^{5i\alpha} \sin^5(\beta) \cos(\beta)$
6	(-4)		$\frac{221}{960} \sqrt{\frac{7}{2}} e^{4i\alpha} \sin^4(\beta) (11 \cos(2\beta) + 9)$
6	(-3)		$\frac{221}{192} \sqrt{\frac{7}{15}} e^{3i\alpha} \sin^3(\beta) \cos(\beta) (11 \cos(2\beta) + 5)$
6	(-2)		$\frac{221}{192} \sqrt{\frac{7}{15}} e^{2i\alpha} \sin^2(\beta) (33 \cos^4(\beta) - 18 \cos^2(\beta) + 1)$
6	(-1)		$\frac{221}{240} \sqrt{\frac{7}{6}} e^{i\alpha} \sin(\beta) \cos(\beta) (33 \cos^4(\beta) - 30 \cos^2(\beta) + 5)$
6	0		$\frac{221(105 \cos(2\beta) + 126 \cos(4\beta) + 231 \cos(6\beta) + 50)}{46080}$
6	1		$-\frac{221}{240} \sqrt{\frac{7}{6}} e^{-i\alpha} \sin(\beta) \cos(\beta) (33 \cos^4(\beta) - 30 \cos^2(\beta) + 5)$
6	2		$\frac{221}{192} \sqrt{\frac{7}{15}} e^{-2i\alpha} \sin^2(\beta) (33 \cos^4(\beta) - 18 \cos^2(\beta) + 1)$
6	3		$-\frac{221}{192} \sqrt{\frac{7}{15}} e^{-3i\alpha} \sin^3(\beta) \cos(\beta) (11 \cos(2\beta) + 5)$
6	4		$\frac{221}{960} \sqrt{\frac{7}{2}} e^{-4i\alpha} \sin^4(\beta) (11 \cos(2\beta) + 9)$
6	5		$-\frac{221}{480} \sqrt{77} e^{-5i\alpha} \sin^5(\beta) \cos(\beta)$
6	6		$\frac{221}{960} \sqrt{\frac{77}{3}} e^{-6i\alpha} \sin^6(\beta)$
8	(-8)		$-\frac{17}{336} \sqrt{\frac{143}{10}} e^{8i\alpha} \sin^8(\beta)$
8	(-7)		$-\frac{17}{84} \sqrt{\frac{143}{10}} e^{7i\alpha} \sin^7(\beta) \cos(\beta)$
8	(-6)		$-\frac{17}{840} \sqrt{\frac{143}{3}} e^{6i\alpha} \sin^6(\beta) (15 \cos^2(\beta) - 1)$
8	(-5)		$-\frac{17}{120} \sqrt{\frac{143}{14}} e^{5i\alpha} \sin^5(\beta) \cos(\beta) (5 \cos(2\beta) + 3)$
8	(-4)		$-\frac{17}{120} \sqrt{\frac{11}{14}} e^{4i\alpha} \sin^4(\beta) (65 \cos^4(\beta) - 26 \cos^2(\beta) + 1)$
8	(-3)		$-\frac{17}{96} \sqrt{\frac{11}{210}} e^{3i\alpha} \sin^3(\beta) \cos(\beta) (52 \cos(2\beta) + 39 \cos(4\beta) + 37)$
8	(-2)		$-\frac{17e^{2i\alpha} \sin^2(\beta) (143 \cos^6(\beta) - 143 \cos^4(\beta) + 33 \cos^2(\beta) - 1)}{24\sqrt{35}}$
8	(-1)		$-\frac{17e^{i\alpha} \sin(2\beta) (869 \cos(2\beta) + 286 \cos(4\beta) + 715 \cos(6\beta) + 178)}{26880\sqrt{2}}$
8	0		$-\frac{17(6435 \cos^8(\beta) - 12012 \cos^6(\beta) + 6930 \cos^4(\beta) - 1260 \cos^2(\beta) + 35)}{5040}$
8	1		$\frac{17e^{-i\alpha} \sin(2\beta) (869 \cos(2\beta) + 286 \cos(4\beta) + 715 \cos(6\beta) + 178)}{26880\sqrt{2}}$
8	2		$\frac{17e^{-2i\alpha} \sin^2(\beta) (143 \cos^6(\beta) - 143 \cos^4(\beta) + 33 \cos^2(\beta) - 1)}{24\sqrt{35}}$
8	3		$\frac{17}{96} \sqrt{\frac{11}{210}} e^{-3i\alpha} \sin^3(\beta) \cos(\beta) (52 \cos(2\beta) + 39 \cos(4\beta) + 37)$
8	4		$-\frac{17}{120} \sqrt{\frac{11}{14}} e^{-4i\alpha} \sin^4(\beta) (65 \cos^4(\beta) - 26 \cos^2(\beta) + 1)$
8	5		$\frac{17}{120} \sqrt{\frac{143}{14}} e^{-5i\alpha} \sin^5(\beta) \cos(\beta) (5 \cos(2\beta) + 3)$
8	6		$-\frac{17}{840} \sqrt{\frac{143}{3}} e^{-6i\alpha} \sin^6(\beta) (15 \cos^2(\beta) - 1)$
8	7		$\frac{17}{84} \sqrt{\frac{143}{10}} e^{-7i\alpha} \sin^7(\beta) \cos(\beta)$

Table B.31: PART XXXI

$(l_1 l_2 m_1')$	$t$	$q$	$b_q^t$
	8	8	$-\frac{17}{336} \sqrt{\frac{143}{10}} e^{-8i\alpha} \sin^8(\beta)$
$gg\gamma$	0	0	$\frac{2}{9}$
	2	(-2)	$-\frac{7e^{2i\alpha} \sin^2(\beta)}{3\sqrt{6}}$
	2	(-1)	$-\frac{7e^{i\alpha} \sin(2\beta)}{3\sqrt{6}}$
	2	0	$\frac{7}{9} - \frac{7\cos^2(\beta)}{3}$
	2	1	$\frac{7e^{-i\alpha} \sin(2\beta)}{3\sqrt{6}}$
	2	2	$-\frac{7e^{-2i\alpha} \sin^2(\beta)}{3\sqrt{6}}$
	4	(-4)	$\frac{7}{36} \sqrt{\frac{35}{2}} e^{4i\alpha} \sin^4(\beta)$
	4	(-3)	$\frac{7}{18} \sqrt{35} e^{3i\alpha} \sin^3(\beta) \cos(\beta)$
	4	(-2)	$\frac{7}{36} \sqrt{\frac{5}{2}} e^{2i\alpha} \sin^2(\beta) (7 \cos(2\beta) + 5)$
	4	(-1)	$\frac{7}{72} \sqrt{5} e^{i\alpha} \sin(2\beta) (7 \cos(2\beta) + 1)$
	4	0	$\frac{7}{288} (20 \cos(2\beta) + 35 \cos(4\beta) + 9)$
	4	1	$-\frac{7}{72} \sqrt{5} e^{-i\alpha} \sin(2\beta) (7 \cos(2\beta) + 1)$
	4	2	$\frac{7}{36} \sqrt{\frac{5}{2}} e^{-2i\alpha} \sin^2(\beta) (7 \cos(2\beta) + 5)$
	4	3	$-\frac{7}{18} \sqrt{35} e^{-3i\alpha} \sin^3(\beta) \cos(\beta)$
	4	4	$\frac{7}{36} \sqrt{\frac{35}{2}} e^{-4i\alpha} \sin^4(\beta)$
	6	(-6)	$-\frac{13}{240} \sqrt{\frac{77}{3}} e^{6i\alpha} \sin^6(\beta)$
	6	(-5)	$-\frac{13}{120} \sqrt{77} e^{5i\alpha} \sin^5(\beta) \cos(\beta)$
	6	(-4)	$-\frac{13}{240} \sqrt{\frac{7}{2}} e^{4i\alpha} \sin^4(\beta) (11 \cos(2\beta) + 9)$
	6	(-3)	$-\frac{13}{48} \sqrt{\frac{7}{15}} e^{3i\alpha} \sin^3(\beta) \cos(\beta) (11 \cos(2\beta) + 5)$
	6	(-2)	$-\frac{13}{48} \sqrt{\frac{7}{15}} e^{2i\alpha} \sin^2(\beta) (33 \cos^4(\beta) - 18 \cos^2(\beta) + 1)$
	6	(-1)	$-\frac{13}{60} \sqrt{\frac{7}{6}} e^{i\alpha} \sin(\beta) \cos(\beta) (33 \cos^4(\beta) - 30 \cos^2(\beta) + 5)$
	6	0	$-\frac{13}{360} (231 \cos^6(\beta) - 315 \cos^4(\beta) + 105 \cos^2(\beta) - 5)$
	6	1	$\frac{13}{60} \sqrt{\frac{7}{6}} e^{-i\alpha} \sin(\beta) \cos(\beta) (33 \cos^4(\beta) - 30 \cos^2(\beta) + 5)$
	6	2	$-\frac{13}{48} \sqrt{\frac{7}{15}} e^{-2i\alpha} \sin^2(\beta) (33 \cos^4(\beta) - 18 \cos^2(\beta) + 1)$
	6	3	$\frac{13}{48} \sqrt{\frac{7}{15}} e^{-3i\alpha} \sin^3(\beta) \cos(\beta) (11 \cos(2\beta) + 5)$
	6	4	$-\frac{13}{240} \sqrt{\frac{7}{2}} e^{-4i\alpha} \sin^4(\beta) (11 \cos(2\beta) + 9)$
	6	5	$\frac{13}{120} \sqrt{77} e^{-5i\alpha} \sin^5(\beta) \cos(\beta)$
	6	6	$-\frac{13}{240} \sqrt{\frac{77}{3}} e^{-6i\alpha} \sin^6(\beta)$
	8	(-8)	$\frac{17 \sqrt{\frac{143}{10}} e^{8i\alpha} \sin^8(\beta)}{2688}$
	8	(-7)	$\frac{17}{672} \sqrt{\frac{143}{10}} e^{7i\alpha} \sin^7(\beta) \cos(\beta)$

Table B.32: PART XXXII

$(l_1 l_2 m_1')$	$t$	$q$	$b_q^t$
	8	(-6)	$\frac{17\sqrt{\frac{143}{3}}e^{6i\alpha}\sin^6(\beta)(15\cos^2(\beta)-1)}{6720}$
	8	(-5)	$\frac{17}{960}\sqrt{\frac{143}{14}}e^{5i\alpha}\sin^5(\beta)\cos(\beta)(5\cos(2\beta)+3)$
	8	(-4)	$\frac{17}{960}\sqrt{\frac{11}{14}}e^{4i\alpha}\sin^4(\beta)(65\cos^4(\beta)-26\cos^2(\beta)+1)$
	8	(-3)	$\frac{17}{96}\sqrt{\frac{11}{210}}e^{3i\alpha}\sin^3(\beta)\cos(\beta)(39\cos^4(\beta)-26\cos^2(\beta)+3)$
	8	(-2)	$\frac{17e^{2i\alpha}\sin^2(\beta)(143\cos^6(\beta)-143\cos^4(\beta)+33\cos^2(\beta)-1)}{192\sqrt{35}}$
	8	(-1)	$\frac{17e^{i\alpha}\sin(2\beta)(869\cos(2\beta)+286\cos(4\beta)+715\cos(6\beta)+178)}{215040\sqrt{2}}$
	8	0	$\frac{17(6435\cos^8(\beta)-12012\cos^6(\beta)+6930\cos^4(\beta)-1260\cos^2(\beta)+35)}{40320}$
	8	1	$-\frac{17e^{-i\alpha}\sin(2\beta)(869\cos(2\beta)+286\cos(4\beta)+715\cos(6\beta)+178)}{215040\sqrt{2}}$
	8	2	$\frac{17e^{-2i\alpha}\sin^2(\beta)(143\cos^6(\beta)-143\cos^4(\beta)+33\cos^2(\beta)-1)}{192\sqrt{35}}$
	8	3	$-\frac{17}{96}\sqrt{\frac{11}{210}}e^{-3i\alpha}\sin^3(\beta)\cos(\beta)(39\cos^4(\beta)-26\cos^2(\beta)+3)$
	8	4	$\frac{17}{960}\sqrt{\frac{11}{14}}e^{-4i\alpha}\sin^4(\beta)(65\cos^4(\beta)-26\cos^2(\beta)+1)$
	8	5	$-\frac{17}{960}\sqrt{\frac{143}{14}}e^{-5i\alpha}\sin^5(\beta)\cos(\beta)(5\cos(2\beta)+3)$
	8	6	$\frac{17\sqrt{\frac{143}{3}}e^{-6i\alpha}\sin^6(\beta)(15\cos^2(\beta)-1)}{6720}$
	8	7	$-\frac{17}{672}\sqrt{\frac{143}{10}}e^{-7i\alpha}\sin^7(\beta)\cos(\beta)$
	8	8	$\frac{17\sqrt{\frac{143}{10}}e^{-8i\alpha}\sin^8(\beta)}{2688}$
$gh\sigma$	1	(-1)	$\frac{e^{i\alpha}\sin(\beta)}{\sqrt{22}}$
	1	0	$\frac{\cos(\beta)}{\sqrt{11}}$
	1	1	$-\frac{e^{-i\alpha}\sin(\beta)}{\sqrt{22}}$
	3	(-3)	$\frac{7}{12}\sqrt{\frac{5}{11}}e^{3i\alpha}\sin^3(\beta)$
	3	(-2)	$\frac{7}{2}\sqrt{\frac{5}{66}}e^{2i\alpha}\sin^2(\beta)\cos(\beta)$
	3	(-1)	$\frac{7e^{i\alpha}\sin(\beta)(5\cos(2\beta)+3)}{8\sqrt{33}}$
	3	0	$\frac{7(3\cos(\beta)+5\cos(3\beta))}{24\sqrt{11}}$
	3	1	$-\frac{7e^{-i\alpha}\sin(\beta)(5\cos(2\beta)+3)}{8\sqrt{33}}$
	3	2	$\frac{7}{2}\sqrt{\frac{5}{66}}e^{-2i\alpha}\sin^2(\beta)\cos(\beta)$
	3	3	$-\frac{7}{12}\sqrt{\frac{5}{11}}e^{-3i\alpha}\sin^3(\beta)$
	5	(-5)	$\frac{1}{16}\sqrt{77}e^{5i\alpha}\sin^5(\beta)$
	5	(-4)	$\frac{1}{8}\sqrt{\frac{385}{2}}e^{4i\alpha}\sin^4(\beta)\cos(\beta)$
	5	(-3)	$\frac{1}{96}\sqrt{385}e^{3i\alpha}\sin^3(\beta)(9\cos(2\beta)+7)$
	5	(-2)	$\frac{1}{8}\sqrt{\frac{385}{6}}e^{2i\alpha}\sin^2(\beta)\cos(\beta)(3\cos(2\beta)+1)$

Table B.33: PART XXXIII

$(l_1 l_2 m_1')$	$t$	$q$	$b_q^t$
	5	(-1)	$\frac{1}{8}\sqrt{\frac{55}{6}}e^{i\alpha}\sin(\beta)(21\cos^4(\beta)-14\cos^2(\beta)+1)$
	5	0	$\frac{1}{384}\sqrt{11}(30\cos(\beta)+35\cos(3\beta)+63\cos(5\beta))$
	5	1	$-\frac{1}{8}\sqrt{\frac{55}{6}}e^{-i\alpha}\sin(\beta)(21\cos^4(\beta)-14\cos^2(\beta)+1)$
	5	2	$\frac{1}{8}\sqrt{\frac{385}{6}}e^{-2i\alpha}\sin^2(\beta)\cos(\beta)(3\cos(2\beta)+1)$
	5	3	$-\frac{1}{96}\sqrt{385}e^{-3i\alpha}\sin^3(\beta)(9\cos(2\beta)+7)$
	5	4	$\frac{1}{8}\sqrt{\frac{385}{2}}e^{-4i\alpha}\sin^4(\beta)\cos(\beta)$
	5	5	$-\frac{1}{16}\sqrt{77}e^{-5i\alpha}\sin^5(\beta)$
	7	(-7)	$\frac{5}{32}\sqrt{\frac{39}{2}}e^{7i\alpha}\sin^7(\beta)$
	7	(-6)	$\frac{5}{32}\sqrt{273}e^{6i\alpha}\sin^6(\beta)\cos(\beta)$
	7	(-5)	$\frac{5}{64}\sqrt{\frac{21}{2}}e^{5i\alpha}\sin^5(\beta)(13\cos(2\beta)+11)$
	7	(-4)	$\frac{5}{32}\sqrt{\frac{21}{2}}e^{4i\alpha}\sin^4(\beta)\cos(\beta)(13\cos(2\beta)+7)$
	7	(-3)	$\frac{5}{32}\sqrt{\frac{21}{22}}e^{3i\alpha}\sin^3(\beta)(143\cos^4(\beta)-66\cos^2(\beta)+3)$
	7	(-2)	$\frac{5}{32}\sqrt{\frac{21}{11}}e^{2i\alpha}\sin^2(\beta)\cos(\beta)(143\cos^4(\beta)-110\cos^2(\beta)+15)$
	7	(-1)	$\frac{5}{32}\sqrt{\frac{7}{22}}e^{i\alpha}\sin(\beta)(429\cos^6(\beta)-495\cos^4(\beta)+135\cos^2(\beta)-5)$
	7	0	$\frac{5(175\cos(\beta)+189\cos(3\beta)+231\cos(5\beta)+429\cos(7\beta))}{1024\sqrt{11}}$
	7	1	$-\frac{5}{32}\sqrt{\frac{7}{22}}e^{-i\alpha}\sin(\beta)(429\cos^6(\beta)-495\cos^4(\beta)+135\cos^2(\beta)-5)$
	7	2	$\frac{5}{32}\sqrt{\frac{21}{11}}e^{-2i\alpha}\sin^2(\beta)\cos(\beta)(143\cos^4(\beta)-110\cos^2(\beta)+15)$
	7	3	$-\frac{5}{32}\sqrt{\frac{21}{22}}e^{-3i\alpha}\sin^3(\beta)(143\cos^4(\beta)-66\cos^2(\beta)+3)$
	7	4	$\frac{5}{32}\sqrt{\frac{21}{2}}e^{-4i\alpha}\sin^4(\beta)\cos(\beta)(13\cos(2\beta)+7)$
	7	5	$-\frac{5}{64}\sqrt{\frac{21}{2}}e^{-5i\alpha}\sin^5(\beta)(13\cos(2\beta)+11)$
	7	6	$\frac{5}{32}\sqrt{273}e^{-6i\alpha}\sin^6(\beta)\cos(\beta)$
	7	7	$-\frac{5}{32}\sqrt{\frac{39}{2}}e^{-7i\alpha}\sin^7(\beta)$
	9	(-9)	$\frac{19}{768}\sqrt{1105}e^{9i\alpha}\sin^9(\beta)$
	9	(-8)	$\frac{19}{128}\sqrt{\frac{1105}{2}}e^{8i\alpha}\sin^8(\beta)\cos(\beta)$
	9	(-7)	$\frac{19}{512}\sqrt{65}e^{7i\alpha}\sin^7(\beta)(17\cos(2\beta)+15)$
	9	(-6)	$\frac{19}{64}\sqrt{\frac{65}{3}}e^{6i\alpha}\sin^6(\beta)\cos(\beta)(17\cos^2(\beta)-3)$
	9	(-5)	$\frac{19}{128}\sqrt{13}e^{5i\alpha}\sin^5(\beta)(85\cos^4(\beta)-30\cos^2(\beta)+1)$
	9	(-4)	$\frac{19}{64}\sqrt{\frac{455}{2}}e^{4i\alpha}\sin^4(\beta)\cos(\beta)(17\cos^4(\beta)-10\cos^2(\beta)+1)$
	9	(-3)	$\frac{19}{128}\sqrt{\frac{35}{3}}e^{3i\alpha}\sin^3(\beta)(221\cos^6(\beta)-195\cos^4(\beta)+39\cos^2(\beta)-1)$

Table B.34: PART XXXIV

$(l_1 l_2 m_1')$	$t$	$q$	$b_q^t$
	9	(-2)	$\frac{19}{64}\sqrt{5}e^{2i\alpha}\sin^2(\beta)\cos(\beta)(221\cos^6(\beta)-273\cos^4(\beta)+91\cos^2(\beta)-7)$
	9	(-1)	$\frac{19}{128}\sqrt{\frac{5}{22}}e^{i\alpha}\sin(\beta)(2431\cos^8(\beta)-4004\cos^6(\beta)+2002\cos^4(\beta)-308\cos^2(\beta)+7)$
	9	0	$\frac{19(4410\cos(\beta)+11(420\cos(3\beta)+13(36\cos(5\beta)+45\cos(7\beta)+85\cos(9\beta))))}{98304\sqrt{11}}$
	9	1	$-\frac{19}{128}\sqrt{\frac{5}{22}}e^{-i\alpha}\sin(\beta)(2431\cos^8(\beta)-4004\cos^6(\beta)+2002\cos^4(\beta)-308\cos^2(\beta)+7)$
	9	2	$\frac{19}{64}\sqrt{5}e^{-2i\alpha}\sin^2(\beta)\cos(\beta)(221\cos^6(\beta)-273\cos^4(\beta)+91\cos^2(\beta)-7)$
	9	3	$-\frac{19}{128}\sqrt{\frac{35}{3}}e^{-3i\alpha}\sin^3(\beta)(221\cos^6(\beta)-195\cos^4(\beta)+39\cos^2(\beta)-1)$
	9	4	$\frac{19}{64}\sqrt{\frac{455}{2}}e^{-4i\alpha}\sin^4(\beta)\cos(\beta)(17\cos^4(\beta)-10\cos^2(\beta)+1)$
	9	5	$-\frac{19}{128}\sqrt{13}e^{-5i\alpha}\sin^5(\beta)(85\cos^4(\beta)-30\cos^2(\beta)+1)$
	9	6	$\frac{19}{64}\sqrt{\frac{65}{3}}e^{-6i\alpha}\sin^6(\beta)\cos(\beta)(17\cos^2(\beta)-3)$
	9	7	$-\frac{19}{512}\sqrt{65}e^{-7i\alpha}\sin^7(\beta)(17\cos(2\beta)+15)$
	9	8	$\frac{19}{128}\sqrt{\frac{1105}{2}}e^{-8i\alpha}\sin^8(\beta)\cos(\beta)$
	9	9	$-\frac{19}{768}\sqrt{1105}e^{-9i\alpha}\sin^9(\beta)$
$gh\pi$	1	(-1)	$\frac{4}{5}\sqrt{\frac{3}{11}}e^{i\alpha}\sin(\beta)$
	1	0	$\frac{4}{5}\sqrt{\frac{6}{11}}\cos(\beta)$
	1	1	$-\frac{4}{5}\sqrt{\frac{3}{11}}e^{-i\alpha}\sin(\beta)$
	3	(-3)	$\frac{133e^{3i\alpha}\sin^3(\beta)}{12\sqrt{330}}$
	3	(-2)	$\frac{133e^{2i\alpha}\sin^2(\beta)\cos(\beta)}{12\sqrt{55}}$
	3	(-1)	$\frac{133e^{i\alpha}\sin(\beta)(5\cos(2\beta)+3)}{120\sqrt{22}}$
	3	0	$\frac{133(3\cos(\beta)+5\cos(3\beta))}{120\sqrt{66}}$
	3	1	$-\frac{133e^{-i\alpha}\sin(\beta)(5\cos(2\beta)+3)}{120\sqrt{22}}$
	3	2	$\frac{133e^{-2i\alpha}\sin^2(\beta)\cos(\beta)}{12\sqrt{55}}$
	3	3	$-\frac{133e^{-3i\alpha}\sin^3(\beta)}{12\sqrt{330}}$
	5	(-5)	$\frac{1}{8}\sqrt{\frac{77}{6}}e^{5i\alpha}\sin^5(\beta)$
	5	(-4)	$\frac{1}{8}\sqrt{\frac{385}{3}}e^{4i\alpha}\sin^4(\beta)\cos(\beta)$
	5	(-3)	$\frac{1}{48}\sqrt{\frac{385}{6}}e^{3i\alpha}\sin^3(\beta)(9\cos(2\beta)+7)$
	5	(-2)	$\frac{1}{24}\sqrt{385}e^{2i\alpha}\sin^2(\beta)\cos(\beta)(3\cos(2\beta)+1)$
	5	(-1)	$\frac{1}{24}\sqrt{55}e^{i\alpha}\sin(\beta)(21\cos^4(\beta)-14\cos^2(\beta)+1)$

Table B.35: PART XXXV

$(l_1 l_2 m_1')$	$t$	$q$	$b_q^t$
	5	0	$\frac{1}{192} \sqrt{\frac{11}{6}} (30 \cos(\beta) + 35 \cos(3\beta) + 63 \cos(5\beta))$
	5	1	$-\frac{1}{24} \sqrt{55} e^{-i\alpha} \sin(\beta) (21 \cos^4(\beta) - 14 \cos^2(\beta) + 1)$
	5	2	$\frac{1}{24} \sqrt{385} e^{-2i\alpha} \sin^2(\beta) \cos(\beta) (3 \cos(2\beta) + 1)$
	5	3	$-\frac{1}{48} \sqrt{\frac{385}{6}} e^{-3i\alpha} \sin^3(\beta) (9 \cos(2\beta) + 7)$
	5	4	$\frac{1}{8} \sqrt{\frac{385}{3}} e^{-4i\alpha} \sin^4(\beta) \cos(\beta)$
	5	5	$-\frac{1}{8} \sqrt{\frac{77}{6}} e^{-5i\alpha} \sin^5(\beta)$
	7	(-7)	$-\frac{3}{64} \sqrt{13} e^{7i\alpha} \sin^7(\beta)$
	7	(-6)	$-\frac{3}{32} \sqrt{\frac{91}{2}} e^{6i\alpha} \sin^6(\beta) \cos(\beta)$
	7	(-5)	$-\frac{3}{64} \sqrt{7} e^{5i\alpha} \sin^5(\beta) (13 \cos^2(\beta) - 1)$
	7	(-4)	$-\frac{3}{64} \sqrt{7} e^{4i\alpha} \sin^4(\beta) \cos(\beta) (13 \cos(2\beta) + 7)$
	7	(-3)	$-\frac{3}{64} \sqrt{\frac{7}{11}} e^{3i\alpha} \sin^3(\beta) (143 \cos^4(\beta) - 66 \cos^2(\beta) + 3)$
	7	(-2)	$-\frac{3}{32} \sqrt{\frac{7}{22}} e^{2i\alpha} \sin^2(\beta) \cos(\beta) (143 \cos^4(\beta) - 110 \cos^2(\beta) + 15)$
	7	(-1)	$-\frac{1}{64} \sqrt{\frac{21}{11}} e^{i\alpha} \sin(\beta) (429 \cos^6(\beta) - 495 \cos^4(\beta) + 135 \cos^2(\beta) - 5)$
	7	0	$-\frac{\sqrt{\frac{3}{22}} (175 \cos(\beta) + 189 \cos(3\beta) + 231 \cos(5\beta) + 429 \cos(7\beta))}{1024}$
	7	1	$\frac{1}{64} \sqrt{\frac{21}{11}} e^{-i\alpha} \sin(\beta) (429 \cos^6(\beta) - 495 \cos^4(\beta) + 135 \cos^2(\beta) - 5)$
	7	2	$-\frac{3}{32} \sqrt{\frac{7}{22}} e^{-2i\alpha} \sin^2(\beta) \cos(\beta) (143 \cos^4(\beta) - 110 \cos^2(\beta) + 15)$
	7	3	$\frac{3}{64} \sqrt{\frac{7}{11}} e^{-3i\alpha} \sin^3(\beta) (143 \cos^4(\beta) - 66 \cos^2(\beta) + 3)$
	7	4	$-\frac{3}{64} \sqrt{7} e^{-4i\alpha} \sin^4(\beta) \cos(\beta) (13 \cos(2\beta) + 7)$
	7	5	$\frac{3}{64} \sqrt{7} e^{-5i\alpha} \sin^5(\beta) (13 \cos^2(\beta) - 1)$
	7	6	$-\frac{3}{32} \sqrt{\frac{91}{2}} e^{-6i\alpha} \sin^6(\beta) \cos(\beta)$
	7	7	$\frac{3}{64} \sqrt{13} e^{-7i\alpha} \sin^7(\beta)$
	9	(-9)	$-\frac{19}{192} \sqrt{\frac{1105}{6}} e^{9i\alpha} \sin^9(\beta)$
	9	(-8)	$-\frac{19}{64} \sqrt{\frac{1105}{3}} e^{8i\alpha} \sin^8(\beta) \cos(\beta)$
	9	(-7)	$-\frac{19}{64} \sqrt{\frac{65}{6}} e^{7i\alpha} \sin^7(\beta) (17 \cos^2(\beta) - 1)$
	9	(-6)	$-\frac{19}{96} \sqrt{\frac{65}{2}} e^{6i\alpha} \sin^6(\beta) \cos(\beta) (17 \cos(2\beta) + 11)$
	9	(-5)	$-\frac{19}{32} \sqrt{\frac{13}{6}} e^{5i\alpha} \sin^5(\beta) (85 \cos^4(\beta) - 30 \cos^2(\beta) + 1)$
	9	(-4)	$-\frac{19}{32} \sqrt{\frac{455}{3}} e^{4i\alpha} \sin^4(\beta) \cos(\beta) (17 \cos^4(\beta) - 10 \cos^2(\beta) + 1)$

Table B.36: PART XXXVI

$(l_1 l_2 m'_1)$	$t$	$q$	$b_q^t$
	9	(-3)	$-\frac{19}{96}\sqrt{\frac{35}{2}}e^{3i\alpha}\sin^3(\beta)(221\cos^6(\beta)-195\cos^4(\beta)+39\cos^2(\beta)-1)$
	9	(-2)	$-\frac{19}{16}\sqrt{\frac{5}{6}}e^{2i\alpha}\sin^2(\beta)\cos(\beta)(221\cos^6(\beta)-273\cos^4(\beta)+91\cos^2(\beta)-7)$
	9	(-1)	$-\frac{19}{64}\sqrt{\frac{5}{33}}e^{i\alpha}\sin(\beta)(2431\cos^8(\beta)-4004\cos^6(\beta)+2002\cos^4(\beta)-308\cos^2(\beta)+7)$
	9	0	$-\frac{19(4410\cos(\beta)+11(420\cos(3\beta)+13(36\cos(5\beta)+45\cos(7\beta)+85\cos(9\beta))))}{24576\sqrt{66}}$
	9	1	$\frac{19}{64}\sqrt{\frac{5}{33}}e^{-i\alpha}\sin(\beta)(2431\cos^8(\beta)-4004\cos^6(\beta)+2002\cos^4(\beta)-308\cos^2(\beta)+7)$
	9	2	$-\frac{19}{16}\sqrt{\frac{5}{6}}e^{-2i\alpha}\sin^2(\beta)\cos(\beta)(221\cos^6(\beta)-273\cos^4(\beta)+91\cos^2(\beta)-7)$
	9	3	$\frac{19}{96}\sqrt{\frac{35}{2}}e^{-3i\alpha}\sin^3(\beta)(221\cos^6(\beta)-195\cos^4(\beta)+39\cos^2(\beta)-1)$
	9	4	$-\frac{19}{32}\sqrt{\frac{455}{3}}e^{-4i\alpha}\sin^4(\beta)\cos(\beta)(17\cos^4(\beta)-10\cos^2(\beta)+1)$
	9	5	$\frac{19}{32}\sqrt{\frac{13}{6}}e^{-5i\alpha}\sin^5(\beta)(85\cos^4(\beta)-30\cos^2(\beta)+1)$
	9	6	$-\frac{19}{96}\sqrt{\frac{65}{2}}e^{-6i\alpha}\sin^6(\beta)\cos(\beta)(17\cos(2\beta)+11)$
	9	7	$\frac{19}{64}\sqrt{\frac{65}{6}}e^{-7i\alpha}\sin^7(\beta)(17\cos^2(\beta)-1)$
	9	8	$-\frac{19}{64}\sqrt{\frac{1105}{3}}e^{-8i\alpha}\sin^8(\beta)\cos(\beta)$
	9	9	$\frac{19}{192}\sqrt{\frac{1105}{6}}e^{-9i\alpha}\sin^9(\beta)$
$gh\delta$	1	(-1)	$\frac{1}{5}\sqrt{\frac{42}{11}}e^{i\alpha}\sin(\beta)$
	1	0	$\frac{2}{5}\sqrt{\frac{21}{11}}\cos(\beta)$
	1	1	$-\frac{1}{5}\sqrt{\frac{42}{11}}e^{-i\alpha}\sin(\beta)$
	3	(-3)	$\frac{7}{12}\sqrt{\frac{7}{165}}e^{3i\alpha}\sin^3(\beta)$
	3	(-2)	$\frac{7}{6}\sqrt{\frac{7}{110}}e^{2i\alpha}\sin^2(\beta)\cos(\beta)$
	3	(-1)	$\frac{7}{120}\sqrt{\frac{7}{11}}e^{i\alpha}\sin(\beta)(5\cos(2\beta)+3)$
	3	0	$\frac{7}{120}\sqrt{\frac{7}{33}}(3\cos(\beta)+5\cos(3\beta))$
	3	1	$-\frac{7}{120}\sqrt{\frac{7}{11}}e^{-i\alpha}\sin(\beta)(5\cos(2\beta)+3)$
	3	2	$\frac{7}{6}\sqrt{\frac{7}{110}}e^{-2i\alpha}\sin^2(\beta)\cos(\beta)$
	3	3	$-\frac{7}{12}\sqrt{\frac{7}{165}}e^{-3i\alpha}\sin^3(\beta)$

Table B.37: PART XXXVII

$(l_1 l_2 m'_1)$	$t$	$q$	$b_q^t$
	5	(-5)	$-\frac{7}{16}\sqrt{\frac{11}{3}}e^{5i\alpha}\sin^5(\beta)$
	5	(-4)	$-\frac{7}{8}\sqrt{\frac{55}{6}}e^{4i\alpha}\sin^4(\beta)\cos(\beta)$
	5	(-3)	$-\frac{7}{96}\sqrt{\frac{55}{3}}e^{3i\alpha}\sin^3(\beta)(9\cos(2\beta)+7)$
	5	(-2)	$-\frac{7}{24}\sqrt{\frac{55}{2}}e^{2i\alpha}\sin^2(\beta)\cos(\beta)(3\cos(2\beta)+1)$
	5	(-1)	$-\frac{1}{24}\sqrt{\frac{385}{2}}e^{i\alpha}\sin(\beta)(21\cos^4(\beta)-14\cos^2(\beta)+1)$
	5	0	$-\frac{1}{384}\sqrt{\frac{77}{3}}(30\cos(\beta)+35\cos(3\beta)+63\cos(5\beta))$
	5	1	$\frac{1}{24}\sqrt{\frac{385}{2}}e^{-i\alpha}\sin(\beta)(21\cos^4(\beta)-14\cos^2(\beta)+1)$
	5	2	$-\frac{7}{24}\sqrt{\frac{55}{2}}e^{-2i\alpha}\sin^2(\beta)\cos(\beta)(3\cos(2\beta)+1)$
	5	3	$\frac{7}{96}\sqrt{\frac{55}{3}}e^{-3i\alpha}\sin^3(\beta)(9\cos(2\beta)+7)$
	5	4	$-\frac{7}{8}\sqrt{\frac{55}{6}}e^{-4i\alpha}\sin^4(\beta)\cos(\beta)$
	5	5	$\frac{7}{16}\sqrt{\frac{11}{3}}e^{-5i\alpha}\sin^5(\beta)$
	7	(-7)	$-\frac{3}{2}\sqrt{\frac{13}{14}}e^{7i\alpha}\sin^7(\beta)$
	7	(-6)	$-\frac{3}{2}\sqrt{13}e^{6i\alpha}\sin^6(\beta)\cos(\beta)$
	7	(-5)	$-\frac{3e^{5i\alpha}\sin^5(\beta)(13\cos(2\beta)+11)}{4\sqrt{2}}$
	7	(-4)	$-\frac{3e^{4i\alpha}\sin^4(\beta)\cos(\beta)(13\cos^2(\beta)-3)}{\sqrt{2}}$
	7	(-3)	$-\frac{3e^{3i\alpha}\sin^3(\beta)(143\cos^4(\beta)-66\cos^2(\beta)+3)}{2\sqrt{22}}$
	7	(-2)	$-\frac{3e^{2i\alpha}\sin^2(\beta)\cos(\beta)(143\cos^4(\beta)-110\cos^2(\beta)+15)}{2\sqrt{11}}$
	7	(-1)	$-\frac{1}{2}\sqrt{\frac{3}{22}}e^{i\alpha}\sin(\beta)(429\cos^6(\beta)-495\cos^4(\beta)+135\cos^2(\beta)-5)$
	7	0	$\sqrt{\frac{3}{77}}\cos(\beta)(-429\cos^6(\beta)+693\cos^4(\beta)-315\cos^2(\beta)+35)$
	7	1	$\frac{1}{2}\sqrt{\frac{3}{22}}e^{-i\alpha}\sin(\beta)(429\cos^6(\beta)-495\cos^4(\beta)+135\cos^2(\beta)-5)$
	7	2	$-\frac{3e^{-2i\alpha}\sin^2(\beta)\cos(\beta)(143\cos^4(\beta)-110\cos^2(\beta)+15)}{2\sqrt{11}}$
	7	3	$\frac{3e^{-3i\alpha}\sin^3(\beta)(143\cos^4(\beta)-66\cos^2(\beta)+3)}{2\sqrt{22}}$
	7	4	$-\frac{3e^{-4i\alpha}\sin^4(\beta)\cos(\beta)(13\cos^2(\beta)-3)}{\sqrt{2}}$
	7	5	$\frac{3e^{-5i\alpha}\sin^5(\beta)(13\cos(2\beta)+11)}{4\sqrt{2}}$
	7	6	$-\frac{3}{2}\sqrt{13}e^{-6i\alpha}\sin^6(\beta)\cos(\beta)$
	7	7	$\frac{3}{2}\sqrt{\frac{13}{14}}e^{-7i\alpha}\sin^7(\beta)$
	9	(-9)	$\frac{19}{192}\sqrt{\frac{1105}{21}}e^{9i\alpha}\sin^9(\beta)$

Table B.38: PART XXXVIII

$(l_1 l_2 m_1')$	$t$	$q$	$b_q^t$
	9	(-8)	$\frac{19}{32} \sqrt{\frac{1105}{42}} e^{8i\alpha} \sin^8(\beta) \cos(\beta)$
	9	(-7)	$\frac{19}{64} \sqrt{\frac{65}{21}} e^{7i\alpha} \sin^7(\beta) (17 \cos^2(\beta) - 1)$
	9	(-6)	$\frac{19}{96} \sqrt{\frac{65}{7}} e^{6i\alpha} \sin^6(\beta) \cos(\beta) (17 \cos(2\beta) + 11)$
	9	(-5)	$\frac{19}{32} \sqrt{\frac{13}{21}} e^{5i\alpha} \sin^5(\beta) (85 \cos^4(\beta) - 30 \cos^2(\beta) + 1)$
	9	(-4)	$\frac{19}{16} \sqrt{\frac{65}{6}} e^{4i\alpha} \sin^4(\beta) \cos(\beta) (17 \cos^4(\beta) - 10 \cos^2(\beta) + 1)$
	9	(-3)	$\frac{19}{96} \sqrt{5} e^{3i\alpha} \sin^3(\beta) (221 \cos^6(\beta) - 195 \cos^4(\beta) + 39 \cos^2(\beta) - 1)$
	9	(-2)	$\frac{19}{16} \sqrt{\frac{5}{21}} e^{2i\alpha} \sin^2(\beta) \cos(\beta) (221 \cos^6(\beta) - 273 \cos^4(\beta) + 91 \cos^2(\beta) - 7)$
	9	(-1)	$\frac{19}{32} \sqrt{\frac{5}{462}} e^{i\alpha} \sin(\beta) (2431 \cos^8(\beta) - 4004 \cos^6(\beta) + 2002 \cos^4(\beta) - 308 \cos^2(\beta) + 7)$
	9	0	$\frac{19(4410 \cos(\beta) + 11(420 \cos(3\beta) + 13(36 \cos(5\beta) + 45 \cos(7\beta) + 85 \cos(9\beta))))}{24576\sqrt{231}}$
	9	1	$-\frac{19}{32} \sqrt{\frac{5}{462}} e^{-i\alpha} \sin(\beta) (2431 \cos^8(\beta) - 4004 \cos^6(\beta) + 2002 \cos^4(\beta) - 308 \cos^2(\beta) + 7)$
	9	2	$\frac{19}{16} \sqrt{\frac{5}{21}} e^{-2i\alpha} \sin^2(\beta) \cos(\beta) (221 \cos^6(\beta) - 273 \cos^4(\beta) + 91 \cos^2(\beta) - 7)$
	9	3	$-\frac{19}{96} \sqrt{5} e^{-3i\alpha} \sin^3(\beta) (221 \cos^6(\beta) - 195 \cos^4(\beta) + 39 \cos^2(\beta) - 1)$
	9	4	$\frac{19}{16} \sqrt{\frac{65}{6}} e^{-4i\alpha} \sin^4(\beta) \cos(\beta) (17 \cos^4(\beta) - 10 \cos^2(\beta) + 1)$
	9	5	$-\frac{19}{32} \sqrt{\frac{13}{21}} e^{-5i\alpha} \sin^5(\beta) (85 \cos^4(\beta) - 30 \cos^2(\beta) + 1)$
	9	6	$\frac{19}{96} \sqrt{\frac{65}{7}} e^{-6i\alpha} \sin^6(\beta) \cos(\beta) (17 \cos(2\beta) + 11)$
	9	7	$-\frac{19}{64} \sqrt{\frac{65}{21}} e^{-7i\alpha} \sin^7(\beta) (17 \cos^2(\beta) - 1)$
	9	8	$\frac{19}{32} \sqrt{\frac{1105}{42}} e^{-8i\alpha} \sin^8(\beta) \cos(\beta)$
	9	9	$-\frac{19}{192} \sqrt{\frac{1105}{21}} e^{-9i\alpha} \sin^9(\beta)$
$gh\phi$	1	(-1)	$\frac{4}{5} \sqrt{\frac{2}{11}} e^{i\alpha} \sin(\beta)$
	1	0	$\frac{8 \cos(\beta)}{5\sqrt{11}}$
	1	1	$-\frac{4}{5} \sqrt{\frac{2}{11}} e^{-i\alpha} \sin(\beta)$
	3	(-3)	$-\frac{49e^{3i\alpha} \sin^3(\beta)}{12\sqrt{55}}$
	3	(-2)	$-\frac{49e^{2i\alpha} \sin^2(\beta) \cos(\beta)}{2\sqrt{330}}$
	3	(-1)	$-\frac{49e^{i\alpha} \sin(\beta) (5 \cos(2\beta) + 3)}{40\sqrt{33}}$
	3	0	$-\frac{49(3 \cos(\beta) + 5 \cos(3\beta))}{120\sqrt{11}}$
	3	1	$\frac{49e^{-i\alpha} \sin(\beta) (5 \cos(2\beta) + 3)}{40\sqrt{33}}$

Table B.39: PART XXXIX

$(l_1 l_2 m'_1)$	$t$	$q$	$b_q^t$
	3	2	$-\frac{49e^{-2i\alpha} \sin^2(\beta) \cos(\beta)}{2\sqrt{330}}$
	3	3	$\frac{49e^{-3i\alpha} \sin^3(\beta)}{12\sqrt{55}}$
	5	(-5)	$-\frac{1}{8}\sqrt{77}e^{5i\alpha} \sin^5(\beta)$
	5	(-4)	$-\frac{1}{4}\sqrt{\frac{385}{2}}e^{4i\alpha} \sin^4(\beta) \cos(\beta)$
	5	(-3)	$-\frac{1}{48}\sqrt{385}e^{3i\alpha} \sin^3(\beta)(9 \cos(2\beta) + 7)$
	5	(-2)	$-\frac{1}{4}\sqrt{\frac{385}{6}}e^{2i\alpha} \sin^2(\beta) \cos(\beta)(3 \cos(2\beta) + 1)$
	5	(-1)	$-\frac{1}{4}\sqrt{\frac{55}{6}}e^{i\alpha} \sin(\beta) (21 \cos^4(\beta) - 14 \cos^2(\beta) + 1)$
	5	0	$-\frac{1}{192}\sqrt{11}(30 \cos(\beta) + 35 \cos(3\beta) + 63 \cos(5\beta))$
	5	1	$\frac{1}{4}\sqrt{\frac{55}{6}}e^{-i\alpha} \sin(\beta) (21 \cos^4(\beta) - 14 \cos^2(\beta) + 1)$
	5	2	$-\frac{1}{4}\sqrt{\frac{385}{6}}e^{-2i\alpha} \sin^2(\beta) \cos(\beta)(3 \cos(2\beta) + 1)$
	5	3	$\frac{1}{48}\sqrt{385}e^{-3i\alpha} \sin^3(\beta)(9 \cos(2\beta) + 7)$
	5	4	$-\frac{1}{4}\sqrt{\frac{385}{2}}e^{-4i\alpha} \sin^4(\beta) \cos(\beta)$
	5	5	$\frac{1}{8}\sqrt{77}e^{-5i\alpha} \sin^5(\beta)$
	7	(-7)	$\frac{19}{64}\sqrt{\frac{39}{2}}e^{7i\alpha} \sin^7(\beta)$
	7	(-6)	$\frac{19}{64}\sqrt{273}e^{6i\alpha} \sin^6(\beta) \cos(\beta)$
	7	(-5)	$\frac{19}{64}\sqrt{\frac{21}{2}}e^{5i\alpha} \sin^5(\beta) (13 \cos^2(\beta) - 1)$
	7	(-4)	$\frac{19}{64}\sqrt{\frac{21}{2}}e^{4i\alpha} \sin^4(\beta) \cos(\beta)(13 \cos(2\beta) + 7)$
	7	(-3)	$\frac{19}{64}\sqrt{\frac{21}{22}}e^{3i\alpha} \sin^3(\beta) (143 \cos^4(\beta) - 66 \cos^2(\beta) + 3)$
	7	(-2)	$\frac{19}{64}\sqrt{\frac{21}{11}}e^{2i\alpha} \sin^2(\beta) \cos(\beta) (143 \cos^4(\beta) - 110 \cos^2(\beta) + 15)$
	7	(-1)	$\frac{19}{64}\sqrt{\frac{7}{22}}e^{i\alpha} \sin(\beta) (429 \cos^6(\beta) - 495 \cos^4(\beta) + 135 \cos^2(\beta) - 5)$
	7	0	$\frac{19(175 \cos(\beta) + 189 \cos(3\beta) + 231 \cos(5\beta) + 429 \cos(7\beta))}{2048\sqrt{11}}$
	7	1	$-\frac{19}{64}\sqrt{\frac{7}{22}}e^{-i\alpha} \sin(\beta) (429 \cos^6(\beta) - 495 \cos^4(\beta) + 135 \cos^2(\beta) - 5)$
	7	2	$\frac{19}{64}\sqrt{\frac{21}{11}}e^{-2i\alpha} \sin^2(\beta) \cos(\beta) (143 \cos^4(\beta) - 110 \cos^2(\beta) + 15)$
	7	3	$-\frac{19}{64}\sqrt{\frac{21}{22}}e^{-3i\alpha} \sin^3(\beta) (143 \cos^4(\beta) - 66 \cos^2(\beta) + 3)$
	7	4	$\frac{19}{64}\sqrt{\frac{21}{2}}e^{-4i\alpha} \sin^4(\beta) \cos(\beta)(13 \cos(2\beta) + 7)$
	7	5	$-\frac{19}{64}\sqrt{\frac{21}{2}}e^{-5i\alpha} \sin^5(\beta) (13 \cos^2(\beta) - 1)$
	7	6	$\frac{19}{64}\sqrt{273}e^{-6i\alpha} \sin^6(\beta) \cos(\beta)$
	7	7	$-\frac{19}{64}\sqrt{\frac{39}{2}}e^{-7i\alpha} \sin^7(\beta)$
	9	(-9)	$-\frac{19\sqrt{1105}e^{9i\alpha} \sin^9(\beta)}{2688}$

Table B.40: PART XL

$(l_1 l_2 m'_1)$	$t$	$q$	$b_q^t$
	9	(-8)	$-\frac{19}{448}\sqrt{\frac{1105}{2}}e^{8i\alpha}\sin^8(\beta)\cos(\beta)$
	9	(-7)	$-\frac{19}{896}\sqrt{65}e^{7i\alpha}\sin^7(\beta)(17\cos^2(\beta)-1)$
	9	(-6)	$-\frac{19}{448}\sqrt{\frac{65}{3}}e^{6i\alpha}\sin^6(\beta)\cos(\beta)(17\cos(2\beta)+11)$
	9	(-5)	$-\frac{19}{448}\sqrt{13}e^{5i\alpha}\sin^5(\beta)(85\cos^4(\beta)-30\cos^2(\beta)+1)$
	9	(-4)	$-\frac{19}{32}\sqrt{\frac{65}{14}}e^{4i\alpha}\sin^4(\beta)\cos(\beta)(17\cos^4(\beta)-10\cos^2(\beta)+1)$
	9	(-3)	$-\frac{19}{64}\sqrt{\frac{5}{21}}e^{3i\alpha}\sin^3(\beta)(221\cos^6(\beta)-195\cos^4(\beta)+39\cos^2(\beta)-1)$
	9	(-2)	$-\frac{19}{224}\sqrt{5}e^{2i\alpha}\sin^2(\beta)\cos(\beta)(221\cos^6(\beta)-273\cos^4(\beta)+91\cos^2(\beta)-7)$
	9	(-1)	$-\frac{19}{448}\sqrt{\frac{5}{22}}e^{i\alpha}\sin(\beta)(2431\cos^8(\beta)-4004\cos^6(\beta)+2002\cos^4(\beta)-308\cos^2(\beta)+7)$
	9	0	$-\frac{19(4410\cos(\beta)+11(420\cos(3\beta)+13(36\cos(5\beta)+45\cos(7\beta)+85\cos(9\beta))))}{344064\sqrt{11}}$
	9	1	$\frac{19}{448}\sqrt{\frac{5}{22}}e^{-i\alpha}\sin(\beta)(2431\cos^8(\beta)-4004\cos^6(\beta)+2002\cos^4(\beta)-308\cos^2(\beta)+7)$
	9	2	$-\frac{19}{224}\sqrt{5}e^{-2i\alpha}\sin^2(\beta)\cos(\beta)(221\cos^6(\beta)-273\cos^4(\beta)+91\cos^2(\beta)-7)$
	9	3	$\frac{19}{64}\sqrt{\frac{5}{21}}e^{-3i\alpha}\sin^3(\beta)(221\cos^6(\beta)-195\cos^4(\beta)+39\cos^2(\beta)-1)$
	9	4	$-\frac{19}{32}\sqrt{\frac{65}{14}}e^{-4i\alpha}\sin^4(\beta)\cos(\beta)(17\cos^4(\beta)-10\cos^2(\beta)+1)$
	9	5	$\frac{19}{448}\sqrt{13}e^{-5i\alpha}\sin^5(\beta)(85\cos^4(\beta)-30\cos^2(\beta)+1)$
	9	6	$-\frac{19}{448}\sqrt{\frac{65}{3}}e^{-6i\alpha}\sin^6(\beta)\cos(\beta)(17\cos(2\beta)+11)$
	9	7	$\frac{19}{896}\sqrt{65}e^{-7i\alpha}\sin^7(\beta)(17\cos^2(\beta)-1)$
	9	8	$-\frac{19}{448}\sqrt{\frac{1105}{2}}e^{-8i\alpha}\sin^8(\beta)\cos(\beta)$
	9	9	$\frac{19\sqrt{1105}e^{-9i\alpha}\sin^9(\beta)}{2688}$
$gh\gamma$	1	(-1)	$\frac{3}{5}\sqrt{\frac{2}{11}}e^{i\alpha}\sin(\beta)$
	1	0	$\frac{6\cos(\beta)}{5\sqrt{11}}$
	1	1	$-\frac{3}{5}\sqrt{\frac{2}{11}}e^{-i\alpha}\sin(\beta)$
	3	(-3)	$-\frac{49e^{3i\alpha}\sin^3(\beta)}{6\sqrt{55}}$
	3	(-2)	$-\frac{49e^{2i\alpha}\sin^2(\beta)\cos(\beta)}{\sqrt{330}}$
	3	(-1)	$-\frac{49e^{i\alpha}\sin(\beta)(5\cos(2\beta)+3)}{20\sqrt{33}}$
	3	0	$\frac{49\cos(\beta)(3-5\cos^2(\beta))}{15\sqrt{11}}$
	3	1	$\frac{49e^{-i\alpha}\sin(\beta)(5\cos(2\beta)+3)}{20\sqrt{33}}$
	3	2	$-\frac{49e^{-2i\alpha}\sin^2(\beta)\cos(\beta)}{\sqrt{330}}$

Table B.41: PART XLI

$(l_1 l_2 m_1')$	$t$	$q$	$b_q^t$
	3	3	$\frac{49e^{-3i\alpha} \sin^3(\beta)}{6\sqrt{55}}$
	5	(-5)	$\frac{1}{8}\sqrt{77}e^{5i\alpha} \sin^5(\beta)$
	5	(-4)	$\frac{1}{4}\sqrt{\frac{385}{2}}e^{4i\alpha} \sin^4(\beta) \cos(\beta)$
	5	(-3)	$\frac{1}{48}\sqrt{385}e^{3i\alpha} \sin^3(\beta)(9 \cos(2\beta) + 7)$
	5	(-2)	$\frac{1}{4}\sqrt{\frac{385}{6}}e^{2i\alpha} \sin^2(\beta) \cos(\beta)(3 \cos(2\beta) + 1)$
	5	(-1)	$\frac{1}{4}\sqrt{\frac{55}{6}}e^{i\alpha} \sin(\beta) (21 \cos^4(\beta) - 14 \cos^2(\beta) + 1)$
	5	0	$\frac{1}{192}\sqrt{11}(30 \cos(\beta) + 35 \cos(3\beta) + 63 \cos(5\beta))$
	5	1	$-\frac{1}{4}\sqrt{\frac{55}{6}}e^{-i\alpha} \sin(\beta) (21 \cos^4(\beta) - 14 \cos^2(\beta) + 1)$
	5	2	$\frac{1}{4}\sqrt{\frac{385}{6}}e^{-2i\alpha} \sin^2(\beta) \cos(\beta)(3 \cos(2\beta) + 1)$
	5	3	$-\frac{1}{48}\sqrt{385}e^{-3i\alpha} \sin^3(\beta)(9 \cos(2\beta) + 7)$
	5	4	$\frac{1}{4}\sqrt{\frac{385}{2}}e^{-4i\alpha} \sin^4(\beta) \cos(\beta)$
	5	5	$-\frac{1}{8}\sqrt{77}e^{-5i\alpha} \sin^5(\beta)$
	7	(-7)	$-\frac{3}{32}\sqrt{\frac{39}{2}}e^{7i\alpha} \sin^7(\beta)$
	7	(-6)	$-\frac{3}{32}\sqrt{273}e^{6i\alpha} \sin^6(\beta) \cos(\beta)$
	7	(-5)	$-\frac{3}{64}\sqrt{\frac{21}{2}}e^{5i\alpha} \sin^5(\beta)(13 \cos(2\beta) + 11)$
	7	(-4)	$-\frac{3}{32}\sqrt{\frac{21}{2}}e^{4i\alpha} \sin^4(\beta) \cos(\beta)(13 \cos(2\beta) + 7)$
	7	(-3)	$-\frac{3}{32}\sqrt{\frac{21}{22}}e^{3i\alpha} \sin^3(\beta) (143 \cos^4(\beta) - 66 \cos^2(\beta) + 3)$
	7	(-2)	$-\frac{3}{32}\sqrt{\frac{21}{11}}e^{2i\alpha} \sin^2(\beta) \cos(\beta) (143 \cos^4(\beta) - 110 \cos^2(\beta) + 15)$
	7	(-1)	$-\frac{3}{32}\sqrt{\frac{7}{22}}e^{i\alpha} \sin(\beta) (429 \cos^6(\beta) - 495 \cos^4(\beta) + 135 \cos^2(\beta) - 5)$
	7	0	$-\frac{3(175 \cos(\beta) + 189 \cos(3\beta) + 231 \cos(5\beta) + 429 \cos(7\beta))}{1024\sqrt{11}}$
	7	1	$\frac{3}{32}\sqrt{\frac{7}{22}}e^{-i\alpha} \sin(\beta) (429 \cos^6(\beta) - 495 \cos^4(\beta) + 135 \cos^2(\beta) - 5)$
	7	2	$-\frac{3}{32}\sqrt{\frac{21}{11}}e^{-2i\alpha} \sin^2(\beta) \cos(\beta) (143 \cos^4(\beta) - 110 \cos^2(\beta) + 15)$
	7	3	$\frac{3}{32}\sqrt{\frac{21}{22}}e^{-3i\alpha} \sin^3(\beta) (143 \cos^4(\beta) - 66 \cos^2(\beta) + 3)$
	7	4	$-\frac{3}{32}\sqrt{\frac{21}{2}}e^{-4i\alpha} \sin^4(\beta) \cos(\beta)(13 \cos(2\beta) + 7)$
	7	5	$\frac{3}{64}\sqrt{\frac{21}{2}}e^{-5i\alpha} \sin^5(\beta)(13 \cos(2\beta) + 11)$
	7	6	$-\frac{3}{32}\sqrt{273}e^{-6i\alpha} \sin^6(\beta) \cos(\beta)$
	7	7	$\frac{3}{32}\sqrt{\frac{39}{2}}e^{-7i\alpha} \sin^7(\beta)$
	9	(-9)	$\frac{19\sqrt{1105}e^{9i\alpha} \sin^9(\beta)}{16128}$
	9	(-8)	$\frac{19\sqrt{\frac{1105}{2}}e^{8i\alpha} \sin^8(\beta) \cos(\beta)}{2688}$

Table B.42: PART XLII

$(l_1 l_2 m'_1)$	$t$	$q$	$b_q^t$
	9	(-7)	$\frac{19\sqrt{65}e^{7i\alpha}\sin^7(\beta)(17\cos^2(\beta)-1)}{5376}$
	9	(-6)	$\frac{19\sqrt{\frac{65}{3}}e^{6i\alpha}\sin^6(\beta)\cos(\beta)(17\cos(2\beta)+11)}{2688}$
	9	(-5)	$\frac{19\sqrt{13}e^{5i\alpha}\sin^5(\beta)(85\cos^4(\beta)-30\cos^2(\beta)+1)}{2688}$
	9	(-4)	$\frac{19}{192}\sqrt{\frac{65}{14}}e^{4i\alpha}\sin^4(\beta)\cos(\beta)(17\cos^4(\beta)-10\cos^2(\beta)+1)$
	9	(-3)	$\frac{19}{384}\sqrt{\frac{5}{21}}e^{3i\alpha}\sin^3(\beta)(221\cos^6(\beta)-195\cos^4(\beta)+39\cos^2(\beta)-1)$
	9	(-2)	$\frac{19\sqrt{5}e^{2i\alpha}\sin^2(\beta)\cos(\beta)(221\cos^6(\beta)-273\cos^4(\beta)+91\cos^2(\beta)-7)}{1344}$
	9	(-1)	$\frac{19\sqrt{\frac{5}{22}}e^{i\alpha}\sin(\beta)(2431\cos^8(\beta)-4004\cos^6(\beta)+2002\cos^4(\beta)-308\cos^2(\beta)+7)}{2688}$
	9	0	$\frac{19(4410\cos(\beta)+11(420\cos(3\beta)+13(36\cos(5\beta)+45\cos(7\beta)+85\cos(9\beta))))}{2064384\sqrt{11}}$
	9	1	$-\frac{19\sqrt{\frac{5}{22}}e^{-i\alpha}\sin(\beta)(2431\cos^8(\beta)-4004\cos^6(\beta)+2002\cos^4(\beta)-308\cos^2(\beta)+7)}{2688}$
	9	2	$\frac{19\sqrt{5}e^{-2i\alpha}\sin^2(\beta)\cos(\beta)(221\cos^6(\beta)-273\cos^4(\beta)+91\cos^2(\beta)-7)}{1344}$
	9	3	$-\frac{19}{384}\sqrt{\frac{5}{21}}e^{-3i\alpha}\sin^3(\beta)(221\cos^6(\beta)-195\cos^4(\beta)+39\cos^2(\beta)-1)$
	9	4	$\frac{19}{192}\sqrt{\frac{65}{14}}e^{-4i\alpha}\sin^4(\beta)\cos(\beta)(17\cos^4(\beta)-10\cos^2(\beta)+1)$
	9	5	$-\frac{19\sqrt{13}e^{-5i\alpha}\sin^5(\beta)(85\cos^4(\beta)-30\cos^2(\beta)+1)}{2688}$
	9	6	$\frac{19\sqrt{\frac{65}{3}}e^{-6i\alpha}\sin^6(\beta)\cos(\beta)(17\cos(2\beta)+11)}{2688}$
	9	7	$-\frac{19\sqrt{65}e^{-7i\alpha}\sin^7(\beta)(17\cos^2(\beta)-1)}{5376}$
	9	8	$\frac{19\sqrt{\frac{1105}{2}}e^{-8i\alpha}\sin^8(\beta)\cos(\beta)}{2688}$
	9	9	$-\frac{19\sqrt{1105}e^{-9i\alpha}\sin^9(\beta)}{16128}$
$hh\sigma$	0	0	$\frac{1}{11}$
	2	(-2)	$\frac{5}{22}\sqrt{\frac{3}{2}}e^{2i\alpha}\sin^2(\beta)$
	2	(-1)	$\frac{5}{22}\sqrt{\frac{3}{2}}e^{i\alpha}\sin(2\beta)$
	2	0	$\frac{5}{44}(3\cos(2\beta)+1)$
	2	1	$-\frac{5}{22}\sqrt{\frac{3}{2}}e^{-i\alpha}\sin(2\beta)$
	2	2	$\frac{5}{22}\sqrt{\frac{3}{2}}e^{-2i\alpha}\sin^2(\beta)$
	4	(-4)	$\frac{9}{88}\sqrt{\frac{35}{2}}e^{4i\alpha}\sin^4(\beta)$
	4	(-3)	$\frac{9}{44}\sqrt{35}e^{3i\alpha}\sin^3(\beta)\cos(\beta)$
	4	(-2)	$\frac{9}{88}\sqrt{\frac{5}{2}}e^{2i\alpha}\sin^2(\beta)(7\cos(2\beta)+5)$
	4	(-1)	$\frac{9}{176}\sqrt{5}e^{i\alpha}\sin(2\beta)(7\cos(2\beta)+1)$
	4	0	$\frac{9}{704}(20\cos(2\beta)+35\cos(4\beta)+9)$
	4	1	$-\frac{9}{176}\sqrt{5}e^{-i\alpha}\sin(2\beta)(7\cos(2\beta)+1)$

Table B.43: PART XLIII

$(l_1 l_2 m'_1)$	$t$	$q$	$b_q^t$
	4	2	$\frac{9}{88} \sqrt{\frac{5}{2}} e^{-2i\alpha} \sin^2(\beta) (7 \cos(2\beta) + 5)$
	4	3	$-\frac{9}{44} \sqrt{35} e^{-3i\alpha} \sin^3(\beta) \cos(\beta)$
	4	4	$\frac{9}{88} \sqrt{\frac{35}{2}} e^{-4i\alpha} \sin^4(\beta)$
	6	(-6)	$\frac{13}{32} \sqrt{\frac{21}{11}} e^{6i\alpha} \sin^6(\beta)$
	6	(-5)	$\frac{39}{16} \sqrt{\frac{7}{11}} e^{5i\alpha} \sin^5(\beta) \cos(\beta)$
	6	(-4)	$\frac{39}{352} \sqrt{\frac{7}{2}} e^{4i\alpha} \sin^4(\beta) (11 \cos(2\beta) + 9)$
	6	(-3)	$\frac{13}{352} \sqrt{105} e^{3i\alpha} \sin^3(\beta) \cos(\beta) (11 \cos(2\beta) + 5)$
	6	(-2)	$\frac{13}{352} \sqrt{105} e^{2i\alpha} \sin^2(\beta) (33 \cos^4(\beta) - 18 \cos^2(\beta) + 1)$
	6	(-1)	$\frac{13}{88} \sqrt{\frac{21}{2}} e^{i\alpha} \sin(\beta) \cos(\beta) (33 \cos^4(\beta) - 30 \cos^2(\beta) + 5)$
	6	0	$\frac{13(105 \cos(2\beta) + 126 \cos(4\beta) + 231 \cos(6\beta) + 50)}{5632}$
	6	1	$-\frac{13}{88} \sqrt{\frac{21}{2}} e^{-i\alpha} \sin(\beta) \cos(\beta) (33 \cos^4(\beta) - 30 \cos^2(\beta) + 5)$
	6	2	$\frac{13}{352} \sqrt{105} e^{-2i\alpha} \sin^2(\beta) (33 \cos^4(\beta) - 18 \cos^2(\beta) + 1)$
	6	3	$-\frac{13}{352} \sqrt{105} e^{-3i\alpha} \sin^3(\beta) \cos(\beta) (11 \cos(2\beta) + 5)$
	6	4	$\frac{39}{352} \sqrt{\frac{7}{2}} e^{-4i\alpha} \sin^4(\beta) (11 \cos(2\beta) + 9)$
	6	5	$-\frac{39}{16} \sqrt{\frac{7}{11}} e^{-5i\alpha} \sin^5(\beta) \cos(\beta)$
	6	6	$\frac{13}{32} \sqrt{\frac{21}{11}} e^{-6i\alpha} \sin^6(\beta)$
	8	(-8)	$\frac{51}{128} \sqrt{\frac{65}{22}} e^{8i\alpha} \sin^8(\beta)$
	8	(-7)	$\frac{51}{32} \sqrt{\frac{65}{22}} e^{7i\alpha} \sin^7(\beta) \cos(\beta)$
	8	(-6)	$\frac{17}{64} \sqrt{\frac{39}{11}} e^{6i\alpha} \sin^6(\beta) (15 \cos^2(\beta) - 1)$
	8	(-5)	$\frac{51}{64} \sqrt{\frac{91}{22}} e^{5i\alpha} \sin^5(\beta) \cos(\beta) (5 \cos(2\beta) + 3)$
	8	(-4)	$\frac{51}{64} \sqrt{\frac{7}{22}} e^{4i\alpha} \sin^4(\beta) (65 \cos^4(\beta) - 26 \cos^2(\beta) + 1)$
	8	(-3)	$\frac{17}{32} \sqrt{\frac{105}{22}} e^{3i\alpha} \sin^3(\beta) \cos(\beta) (39 \cos^4(\beta) - 26 \cos^2(\beta) + 3)$
	8	(-2)	$\frac{51}{704} \sqrt{35} e^{2i\alpha} \sin^2(\beta) (143 \cos^6(\beta) - 143 \cos^4(\beta) + 33 \cos^2(\beta) - 1)$
	8	(-1)	$\frac{51 e^{i\alpha} \sin(2\beta) (869 \cos(2\beta) + 286 \cos(4\beta) + 715 \cos(6\beta) + 178)}{22528 \sqrt{2}}$
	8	0	$\frac{17(6435 \cos^8(\beta) - 12012 \cos^6(\beta) + 6930 \cos^4(\beta) - 1260 \cos^2(\beta) + 35)}{1408}$
	8	1	$-\frac{51 e^{-i\alpha} \sin(2\beta) (869 \cos(2\beta) + 286 \cos(4\beta) + 715 \cos(6\beta) + 178)}{22528 \sqrt{2}}$
	8	2	$\frac{51}{704} \sqrt{35} e^{-2i\alpha} \sin^2(\beta) (143 \cos^6(\beta) - 143 \cos^4(\beta) + 33 \cos^2(\beta) - 1)$
	8	3	$-\frac{17}{32} \sqrt{\frac{105}{22}} e^{-3i\alpha} \sin^3(\beta) \cos(\beta) (39 \cos^4(\beta) - 26 \cos^2(\beta) + 3)$
	8	4	$\frac{51}{64} \sqrt{\frac{7}{22}} e^{-4i\alpha} \sin^4(\beta) (65 \cos^4(\beta) - 26 \cos^2(\beta) + 1)$

Table B.44: PART XLIV

$(l_1 l_2 m_1')$	$t$	$q$	$b_q^t$
	8	5	$-\frac{51}{64} \sqrt{\frac{91}{22}} e^{-5i\alpha} \sin^5(\beta) \cos(\beta) (5 \cos(2\beta) + 3)$
	8	6	$\frac{17}{64} \sqrt{\frac{39}{11}} e^{-6i\alpha} \sin^6(\beta) (15 \cos^2(\beta) - 1)$
	8	7	$-\frac{51}{32} \sqrt{\frac{65}{22}} e^{-7i\alpha} \sin^7(\beta) \cos(\beta)$
	8	8	$\frac{51}{128} \sqrt{\frac{65}{22}} e^{-8i\alpha} \sin^8(\beta)$
10	(-10)		$\frac{21}{512} \sqrt{\frac{4199}{11}} e^{10i\alpha} \sin^{10}(\beta)$
10	(-9)		$\frac{21}{256} \sqrt{\frac{20995}{11}} e^{9i\alpha} \sin^9(\beta) \cos(\beta)$
10	(-8)		$\frac{21}{512} \sqrt{\frac{1105}{22}} e^{8i\alpha} \sin^8(\beta) (19 \cos(2\beta) + 17)$
10	(-7)		$\frac{21}{512} \sqrt{\frac{3315}{11}} e^{7i\alpha} \sin^7(\beta) \cos(\beta) (19 \cos(2\beta) + 13)$
10	(-6)		$\frac{21}{512} \sqrt{\frac{195}{11}} e^{6i\alpha} \sin^6(\beta) (323 \cos^4(\beta) - 102 \cos^2(\beta) + 3)$
10	(-5)		$\frac{21}{128} \sqrt{\frac{39}{11}} e^{5i\alpha} \sin^5(\beta) \cos(\beta) (323 \cos^4(\beta) - 170 \cos^2(\beta) + 15)$
10	(-4)		$\frac{21}{128} \sqrt{\frac{195}{22}} e^{4i\alpha} \sin^4(\beta) (323 \cos^6(\beta) - 255 \cos^4(\beta) + 45 \cos^2(\beta) - 1)$
10	(-3)		$\frac{21}{128} \sqrt{\frac{195}{11}} e^{3i\alpha} \sin^3(\beta) \cos(\beta) (323 \cos^6(\beta) - 357 \cos^4(\beta) + 105 \cos^2(\beta) - 7)$
10	(-2)		$\frac{21}{256} \sqrt{\frac{15}{22}} e^{2i\alpha} \sin^2(\beta) (4199 \cos^8(\beta) - 6188 \cos^6(\beta) + 2730 \cos^4(\beta) - 364 \cos^2(\beta) + 7)$
10	(-1)		$\frac{21}{128} \sqrt{\frac{5}{22}} e^{i\alpha} \sin(\beta) \cos(\beta) (4199 \cos^8(\beta) - 7956 \cos^6(\beta) + 4914 \cos^4(\beta) - 1092 \cos^2(\beta) + 63)$
10	0		$\frac{21(46189 \cos^{10}(\beta) - 109395 \cos^8(\beta) + 90090 \cos^6(\beta) - 30030 \cos^4(\beta) + 3465 \cos^2(\beta))}{2816}$
			$-\frac{1323}{2816}$
10	1		$-\frac{21}{128} \sqrt{\frac{5}{22}} e^{-i\alpha} \sin(\beta) \cos(\beta) (4199 \cos^8(\beta) - 7956 \cos^6(\beta) + 4914 \cos^4(\beta) - 1092 \cos^2(\beta) + 63)$
10	2		$\frac{21}{256} \sqrt{\frac{15}{22}} e^{-2i\alpha} \sin^2(\beta) (4199 \cos^8(\beta) - 6188 \cos^6(\beta) + 2730 \cos^4(\beta) - 364 \cos^2(\beta) + 7)$
10	3		$-\frac{21}{128} \sqrt{\frac{195}{11}} e^{-3i\alpha} \sin^3(\beta) \cos(\beta) (323 \cos^6(\beta) - 357 \cos^4(\beta) + 105 \cos^2(\beta) - 7)$
10	4		$\frac{21}{128} \sqrt{\frac{195}{22}} e^{-4i\alpha} \sin^4(\beta) (323 \cos^6(\beta) - 255 \cos^4(\beta) + 45 \cos^2(\beta) - 1)$
10	5		$-\frac{21}{128} \sqrt{\frac{39}{11}} e^{-5i\alpha} \sin^5(\beta) \cos(\beta) (323 \cos^4(\beta) - 170 \cos^2(\beta) + 15)$
10	6		$\frac{21}{512} \sqrt{\frac{195}{11}} e^{-6i\alpha} \sin^6(\beta) (323 \cos^4(\beta) - 102 \cos^2(\beta) + 3)$
10	7		$-\frac{21}{512} \sqrt{\frac{3315}{11}} e^{-7i\alpha} \sin^7(\beta) \cos(\beta) (19 \cos(2\beta) + 13)$

Table B.45: PART XLV

B Expansion coefficients for tight-binding operator

$(l_1 l_2 m'_1)$	$t$	$q$	$b_q^t$
	10	8	$\frac{21}{512} \sqrt{\frac{1105}{22}} e^{-8i\alpha} \sin^8(\beta) (19 \cos(2\beta) + 17)$
	10	9	$-\frac{21}{256} \sqrt{\frac{20995}{11}} e^{-9i\alpha} \sin^9(\beta) \cos(\beta)$
	10	10	$\frac{21}{512} \sqrt{\frac{4199}{11}} e^{-10i\alpha} \sin^{10}(\beta)$
$hh\pi$	0	0	$\frac{2}{11}$
	2	(-2)	$\frac{9}{22} \sqrt{\frac{3}{2}} e^{2i\alpha} \sin^2(\beta)$
	2	(-1)	$\frac{9}{22} \sqrt{\frac{3}{2}} e^{i\alpha} \sin(2\beta)$
	2	0	$\frac{9}{44} (3 \cos(2\beta) + 1)$
	2	1	$-\frac{9}{22} \sqrt{\frac{3}{2}} e^{-i\alpha} \sin(2\beta)$
	2	2	$\frac{9}{22} \sqrt{\frac{3}{2}} e^{-2i\alpha} \sin^2(\beta)$
	4	(-4)	$\frac{3}{22} \sqrt{\frac{35}{2}} e^{4i\alpha} \sin^4(\beta)$
	4	(-3)	$\frac{3}{11} \sqrt{35} e^{3i\alpha} \sin^3(\beta) \cos(\beta)$
	4	(-2)	$\frac{3}{22} \sqrt{\frac{5}{2}} e^{2i\alpha} \sin^2(\beta) (7 \cos(2\beta) + 5)$
	4	(-1)	$\frac{3}{44} \sqrt{5} e^{i\alpha} \sin(2\beta) (7 \cos(2\beta) + 1)$
	4	0	$\frac{3}{176} (20 \cos(2\beta) + 35 \cos(4\beta) + 9)$
	4	1	$-\frac{3}{44} \sqrt{5} e^{-i\alpha} \sin(2\beta) (7 \cos(2\beta) + 1)$
	4	2	$\frac{3}{22} \sqrt{\frac{5}{2}} e^{-2i\alpha} \sin^2(\beta) (7 \cos(2\beta) + 5)$
	4	3	$-\frac{3}{11} \sqrt{35} e^{-3i\alpha} \sin^3(\beta) \cos(\beta)$
	4	4	$\frac{3}{22} \sqrt{\frac{35}{2}} e^{-4i\alpha} \sin^4(\beta)$
	6	(-6)	$\frac{39}{160} \sqrt{\frac{21}{11}} e^{6i\alpha} \sin^6(\beta)$
	6	(-5)	$\frac{117}{80} \sqrt{\frac{7}{11}} e^{5i\alpha} \sin^5(\beta) \cos(\beta)$
	6	(-4)	$\frac{117 \sqrt{\frac{7}{2}} e^{4i\alpha} \sin^4(\beta) (11 \cos(2\beta) + 9)}{1760}$
	6	(-3)	$\frac{39}{352} \sqrt{\frac{21}{5}} e^{3i\alpha} \sin^3(\beta) \cos(\beta) (11 \cos(2\beta) + 5)$
	6	(-2)	$\frac{39}{352} \sqrt{\frac{21}{5}} e^{2i\alpha} \sin^2(\beta) (33 \cos^4(\beta) - 18 \cos^2(\beta) + 1)$
	6	(-1)	$\frac{39}{440} \sqrt{\frac{21}{2}} e^{i\alpha} \sin(\beta) \cos(\beta) (33 \cos^4(\beta) - 30 \cos^2(\beta) + 5)$
	6	0	$\frac{39}{880} (231 \cos^6(\beta) - 315 \cos^4(\beta) + 105 \cos^2(\beta) - 5)$
	6	1	$-\frac{39}{440} \sqrt{\frac{21}{2}} e^{-i\alpha} \sin(\beta) \cos(\beta) (33 \cos^4(\beta) - 30 \cos^2(\beta) + 5)$
	6	2	$\frac{39}{352} \sqrt{\frac{21}{5}} e^{-2i\alpha} \sin^2(\beta) (33 \cos^4(\beta) - 18 \cos^2(\beta) + 1)$
	6	3	$-\frac{39}{352} \sqrt{\frac{21}{5}} e^{-3i\alpha} \sin^3(\beta) \cos(\beta) (11 \cos(2\beta) + 5)$
	6	4	$\frac{117 \sqrt{\frac{7}{2}} e^{-4i\alpha} \sin^4(\beta) (11 \cos(2\beta) + 9)}{1760}$
	6	5	$-\frac{117}{80} \sqrt{\frac{7}{11}} e^{-5i\alpha} \sin^5(\beta) \cos(\beta)$

Table B.46: PART XLVI

$(l_1 l_2 m'_1)$	$t$	$q$	$b_q^t$
	6	6	$\frac{39}{160} \sqrt{\frac{21}{11}} e^{-6i\alpha} \sin^6(\beta)$
	8	(-8)	$-\frac{51}{64} \sqrt{\frac{13}{110}} e^{8i\alpha} \sin^8(\beta)$
	8	(-7)	$-\frac{51}{16} \sqrt{\frac{13}{110}} e^{7i\alpha} \sin^7(\beta) \cos(\beta)$
	8	(-6)	$-\frac{17}{320} \sqrt{\frac{39}{11}} e^{6i\alpha} \sin^6(\beta) (15 \cos(2\beta) + 13)$
	8	(-5)	$-\frac{51}{160} \sqrt{\frac{91}{22}} e^{5i\alpha} \sin^5(\beta) \cos(\beta) (5 \cos(2\beta) + 3)$
	8	(-4)	$-\frac{51}{160} \sqrt{\frac{7}{22}} e^{4i\alpha} \sin^4(\beta) (65 \cos^4(\beta) - 26 \cos^2(\beta) + 1)$
	8	(-3)	$-\frac{17}{16} \sqrt{\frac{21}{110}} e^{3i\alpha} \sin^3(\beta) \cos(\beta) (39 \cos^4(\beta) - 26 \cos^2(\beta) + 3)$
	8	(-2)	$-\frac{51}{352} \sqrt{\frac{7}{5}} e^{2i\alpha} \sin^2(\beta) (143 \cos^6(\beta) - 143 \cos^4(\beta) + 33 \cos^2(\beta) - 1)$
	8	(-1)	$-\frac{51e^{i\alpha} \sin(2\beta)(869 \cos(2\beta) + 286 \cos(4\beta) + 715 \cos(6\beta) + 178)}{56320\sqrt{2}}$
	8	0	$-\frac{17(6435 \cos^8(\beta) - 12012 \cos^6(\beta) + 6930 \cos^4(\beta) - 1260 \cos^2(\beta) + 35)}{3520}$
	8	1	$\frac{51e^{-i\alpha} \sin(2\beta)(869 \cos(2\beta) + 286 \cos(4\beta) + 715 \cos(6\beta) + 178)}{56320\sqrt{2}}$
	8	2	$-\frac{51}{352} \sqrt{\frac{7}{5}} e^{-2i\alpha} \sin^2(\beta) (143 \cos^6(\beta) - 143 \cos^4(\beta) + 33 \cos^2(\beta) - 1)$
	8	3	$\frac{17}{16} \sqrt{\frac{21}{110}} e^{-3i\alpha} \sin^3(\beta) \cos(\beta) (39 \cos^4(\beta) - 26 \cos^2(\beta) + 3)$
	8	4	$-\frac{51}{160} \sqrt{\frac{7}{22}} e^{-4i\alpha} \sin^4(\beta) (65 \cos^4(\beta) - 26 \cos^2(\beta) + 1)$
	8	5	$\frac{51}{160} \sqrt{\frac{91}{22}} e^{-5i\alpha} \sin^5(\beta) \cos(\beta) (5 \cos(2\beta) + 3)$
	8	6	$-\frac{17}{320} \sqrt{\frac{39}{11}} e^{-6i\alpha} \sin^6(\beta) (15 \cos(2\beta) + 13)$
	8	7	$\frac{51}{16} \sqrt{\frac{13}{110}} e^{-7i\alpha} \sin^7(\beta) \cos(\beta)$
	8	8	$-\frac{51}{64} \sqrt{\frac{13}{110}} e^{-8i\alpha} \sin^8(\beta)$
10	(-10)		$-\frac{35}{512} \sqrt{\frac{4199}{11}} e^{10i\alpha} \sin^{10}(\beta)$
10	(-9)		$-\frac{35}{256} \sqrt{\frac{20995}{11}} e^{9i\alpha} \sin^9(\beta) \cos(\beta)$
10	(-8)		$-\frac{35}{512} \sqrt{\frac{1105}{22}} e^{8i\alpha} \sin^8(\beta) (19 \cos(2\beta) + 17)$
10	(-7)		$-\frac{35}{512} \sqrt{\frac{3315}{11}} e^{7i\alpha} \sin^7(\beta) \cos(\beta) (19 \cos(2\beta) + 13)$
10	(-6)		$-\frac{35}{512} \sqrt{\frac{195}{11}} e^{6i\alpha} \sin^6(\beta) (323 \cos^4(\beta) - 102 \cos^2(\beta) + 3)$
10	(-5)		$-\frac{35}{128} \sqrt{\frac{39}{11}} e^{5i\alpha} \sin^5(\beta) \cos(\beta) (323 \cos^4(\beta) - 170 \cos^2(\beta) + 15)$
10	(-4)		$-\frac{35}{128} \sqrt{\frac{195}{22}} e^{4i\alpha} \sin^4(\beta) (323 \cos^6(\beta) - 255 \cos^4(\beta) + 45 \cos^2(\beta) - 1)$

Table B.47: PART XLVII

B Expansion coefficients for tight-binding operator

$(l_1 l_2 m'_1)$	$t$	$q$	$b_q^t$
	10	(-3)	$-\frac{35}{128} \sqrt{\frac{195}{11}} e^{3i\alpha} \sin^3(\beta) \cos(\beta) (323 \cos^6(\beta) - 357 \cos^4(\beta) + 105 \cos^2(\beta) - 7)$
	10	(-2)	$-\frac{35}{256} \sqrt{\frac{15}{22}} e^{2i\alpha} \sin^2(\beta) (4199 \cos^8(\beta) - 6188 \cos^6(\beta) + 2730 \cos^4(\beta) - 364 \cos^2(\beta) + 7)$
	10	(-1)	$-\frac{35}{128} \sqrt{\frac{5}{22}} e^{i\alpha} \sin(\beta) \cos(\beta) (4199 \cos^8(\beta) - 7956 \cos^6(\beta) + 4914 \cos^4(\beta) - 1092 \cos^2(\beta) + 63)$
	10	0	$\frac{35(46189 \cos^{10}(\beta) - 109395 \cos^8(\beta) + 90090 \cos^6(\beta) - 30030 \cos^4(\beta) + 3465 \cos^2(\beta))}{2816} + \frac{2205}{2816}$
	10	1	$\frac{35}{128} \sqrt{\frac{5}{22}} e^{-i\alpha} \sin(\beta) \cos(\beta) (4199 \cos^8(\beta) - 7956 \cos^6(\beta) + 4914 \cos^4(\beta) - 1092 \cos^2(\beta) + 63)$
	10	2	$-\frac{35}{256} \sqrt{\frac{15}{22}} e^{-2i\alpha} \sin^2(\beta) (4199 \cos^8(\beta) - 6188 \cos^6(\beta) + 2730 \cos^4(\beta) - 364 \cos^2(\beta) + 7)$
	10	3	$\frac{35}{128} \sqrt{\frac{195}{11}} e^{-3i\alpha} \sin^3(\beta) \cos(\beta) (323 \cos^6(\beta) - 357 \cos^4(\beta) + 105 \cos^2(\beta) - 7)$
	10	4	$-\frac{35}{128} \sqrt{\frac{195}{22}} e^{-4i\alpha} \sin^4(\beta) (323 \cos^6(\beta) - 255 \cos^4(\beta) + 45 \cos^2(\beta) - 1)$
	10	5	$\frac{35}{128} \sqrt{\frac{39}{11}} e^{-5i\alpha} \sin^5(\beta) \cos(\beta) (323 \cos^4(\beta) - 170 \cos^2(\beta) + 15)$
	10	6	$-\frac{35}{512} \sqrt{\frac{195}{11}} e^{-6i\alpha} \sin^6(\beta) (323 \cos^4(\beta) - 102 \cos^2(\beta) + 3)$
	10	7	$\frac{35}{512} \sqrt{\frac{3315}{11}} e^{-7i\alpha} \sin^7(\beta) \cos(\beta) (19 \cos(2\beta) + 13)$
	10	8	$-\frac{35}{512} \sqrt{\frac{1105}{22}} e^{-8i\alpha} \sin^8(\beta) (19 \cos(2\beta) + 17)$
	10	9	$\frac{35}{256} \sqrt{\frac{20995}{11}} e^{-9i\alpha} \sin^9(\beta) \cos(\beta)$
	10	10	$-\frac{35}{512} \sqrt{\frac{4199}{11}} e^{-10i\alpha} \sin^{10}(\beta)$
$hh\delta$	0	0	$\frac{2}{11}$
	2	(-2)	$\frac{3}{11} \sqrt{\frac{3}{2}} e^{2i\alpha} \sin^2(\beta)$
	2	(-1)	$\frac{3}{11} \sqrt{6} e^{i\alpha} \sin(\beta) \cos(\beta)$
	2	0	$\frac{3}{22} (3 \cos(2\beta) + 1)$
	2	1	$-\frac{3}{11} \sqrt{6} e^{-i\alpha} \sin(\beta) \cos(\beta)$
	2	2	$\frac{3}{11} \sqrt{\frac{3}{2}} e^{-2i\alpha} \sin^2(\beta)$
	4	(-4)	$-\frac{3}{88} \sqrt{\frac{35}{2}} e^{4i\alpha} \sin^4(\beta)$
	4	(-3)	$-\frac{3}{44} \sqrt{35} e^{3i\alpha} \sin^3(\beta) \cos(\beta)$
	4	(-2)	$-\frac{3}{88} \sqrt{\frac{5}{2}} e^{2i\alpha} \sin^2(\beta) (7 \cos(2\beta) + 5)$
	4	(-1)	$-\frac{3}{176} \sqrt{5} e^{i\alpha} \sin(2\beta) (7 \cos(2\beta) + 1)$

Table B.48: PART XLVIII

$(l_1 l_2 m'_1)$	$t$	$q$	$b_q^t$
	4	0	$-\frac{3}{704}(20 \cos(2\beta) + 35 \cos(4\beta) + 9)$
	4	1	$\frac{3}{176}\sqrt{5}e^{-i\alpha} \sin(2\beta)(7 \cos(2\beta) + 1)$
	4	2	$-\frac{3}{88}\sqrt{\frac{5}{2}}e^{-2i\alpha} \sin^2(\beta)(7 \cos(2\beta) + 5)$
	4	3	$\frac{3}{44}\sqrt{35}e^{-3i\alpha} \sin^3(\beta) \cos(\beta)$
	4	4	$-\frac{3}{88}\sqrt{\frac{35}{2}}e^{-4i\alpha} \sin^4(\beta)$
	6	(-6)	$-\frac{117}{160}\sqrt{\frac{21}{11}}e^{6i\alpha} \sin^6(\beta)$
	6	(-5)	$-\frac{351}{80}\sqrt{\frac{7}{11}}e^{5i\alpha} \sin^5(\beta) \cos(\beta)$
	6	(-4)	$-\frac{351\sqrt{\frac{7}{2}}e^{4i\alpha} \sin^4(\beta)(11 \cos(2\beta)+9)}{1760}$
	6	(-3)	$-\frac{117}{352}\sqrt{\frac{21}{5}}e^{3i\alpha} \sin^3(\beta) \cos(\beta)(11 \cos(2\beta) + 5)$
	6	(-2)	$-\frac{117}{352}\sqrt{\frac{21}{5}}e^{2i\alpha} \sin^2(\beta) (33 \cos^4(\beta) - 18 \cos^2(\beta) + 1)$
	6	(-1)	$-\frac{117}{440}\sqrt{\frac{21}{2}}e^{i\alpha} \sin(\beta) \cos(\beta) (33 \cos^4(\beta) - 30 \cos^2(\beta) + 5)$
	6	0	$-\frac{117}{880}(231 \cos^6(\beta) - 315 \cos^4(\beta) + 105 \cos^2(\beta) - 5)$
	6	1	$\frac{117}{440}\sqrt{\frac{21}{2}}e^{-i\alpha} \sin(\beta) \cos(\beta) (33 \cos^4(\beta) - 30 \cos^2(\beta) + 5)$
	6	2	$-\frac{117}{352}\sqrt{\frac{21}{5}}e^{-2i\alpha} \sin^2(\beta) (33 \cos^4(\beta) - 18 \cos^2(\beta) + 1)$
	6	3	$\frac{117}{352}\sqrt{\frac{21}{5}}e^{-3i\alpha} \sin^3(\beta) \cos(\beta)(11 \cos(2\beta) + 5)$
	6	4	$-\frac{351\sqrt{\frac{7}{2}}e^{-4i\alpha} \sin^4(\beta)(11 \cos(2\beta)+9)}{1760}$
	6	5	$\frac{351}{80}\sqrt{\frac{7}{11}}e^{-5i\alpha} \sin^5(\beta) \cos(\beta)$
	6	6	$-\frac{117}{160}\sqrt{\frac{21}{11}}e^{-6i\alpha} \sin^6(\beta)$
	8	(-8)	$-\frac{867}{224}\sqrt{\frac{13}{110}}e^{8i\alpha} \sin^8(\beta)$
	8	(-7)	$-\frac{867}{56}\sqrt{\frac{13}{110}}e^{7i\alpha} \sin^7(\beta) \cos(\beta)$
	8	(-6)	$-\frac{289}{560}\sqrt{\frac{39}{11}}e^{6i\alpha} \sin^6(\beta) (15 \cos^2(\beta) - 1)$
	8	(-5)	$-\frac{867}{80}\sqrt{\frac{13}{154}}e^{5i\alpha} \sin^5(\beta) \cos(\beta)(5 \cos(2\beta) + 3)$
	8	(-4)	$-\frac{867e^{4i\alpha} \sin^4(\beta)(65 \cos^4(\beta)-26 \cos^2(\beta)+1)}{80\sqrt{154}}$
	8	(-3)	$-\frac{289}{8}\sqrt{\frac{3}{770}}e^{3i\alpha} \sin^3(\beta) \cos(\beta) (39 \cos^4(\beta) - 26 \cos^2(\beta) + 3)$
	8	(-2)	$-\frac{867e^{2i\alpha} \sin^2(\beta)(143 \cos^6(\beta)-143 \cos^4(\beta)+33 \cos^2(\beta)-1)}{176\sqrt{35}}$
	8	(-1)	$-\frac{867e^{i\alpha} \sin(\beta)(869 \cos(2\beta)+286 \cos(4\beta)+715 \cos(6\beta)+178)}{197120\sqrt{2}}$
	8	0	$-\frac{289(6435 \cos^8(\beta)-12012 \cos^6(\beta)+6930 \cos^4(\beta)-1260 \cos^2(\beta)+35)}{12320}$
	8	1	$\frac{867e^{-i\alpha} \sin(\beta)(869 \cos(2\beta)+286 \cos(4\beta)+715 \cos(6\beta)+178)}{197120\sqrt{2}}$
	8	2	$-\frac{867e^{-2i\alpha} \sin^2(\beta)(143 \cos^6(\beta)-143 \cos^4(\beta)+33 \cos^2(\beta)-1)}{176\sqrt{35}}$

Table B.49: PART XLIX

$(l_1 l_2 m'_1)$	$t$	$q$	$b_q^t$
	8	3	$\frac{289}{8} \sqrt{\frac{3}{770}} e^{-3i\alpha} \sin^3(\beta) \cos(\beta) (39 \cos^4(\beta) - 26 \cos^2(\beta) + 3)$
	8	4	$-\frac{867 e^{-4i\alpha} \sin^4(\beta) (65 \cos^4(\beta) - 26 \cos^2(\beta) + 1)}{80\sqrt{154}}$
	8	5	$\frac{867}{80} \sqrt{\frac{13}{154}} e^{-5i\alpha} \sin^5(\beta) \cos(\beta) (5 \cos(2\beta) + 3)$
	8	6	$-\frac{289}{560} \sqrt{\frac{39}{11}} e^{-6i\alpha} \sin^6(\beta) (15 \cos^2(\beta) - 1)$
	8	7	$\frac{867}{56} \sqrt{\frac{13}{110}} e^{-7i\alpha} \sin^7(\beta) \cos(\beta)$
	8	8	$-\frac{867}{224} \sqrt{\frac{13}{110}} e^{-8i\alpha} \sin^8(\beta)$
10	(-10)		$\frac{5}{128} \sqrt{\frac{4199}{11}} e^{10i\alpha} \sin^{10}(\beta)$
10	(-9)		$\frac{5}{64} \sqrt{\frac{20995}{11}} e^{9i\alpha} \sin^9(\beta) \cos(\beta)$
10	(-8)		$\frac{5}{64} \sqrt{\frac{1105}{22}} e^{8i\alpha} \sin^8(\beta) (19 \cos^2(\beta) - 1)$
10	(-7)		$\frac{5}{64} \sqrt{\frac{3315}{11}} e^{7i\alpha} \sin^7(\beta) \cos(\beta) (19 \cos^2(\beta) - 3)$
10	(-6)		$\frac{5}{128} \sqrt{\frac{195}{11}} e^{6i\alpha} \sin^6(\beta) (323 \cos^4(\beta) - 102 \cos^2(\beta) + 3)$
10	(-5)		$\frac{5}{32} \sqrt{\frac{39}{11}} e^{5i\alpha} \sin^5(\beta) \cos(\beta) (323 \cos^4(\beta) - 170 \cos^2(\beta) + 15)$
10	(-4)		$\frac{5}{32} \sqrt{\frac{195}{22}} e^{4i\alpha} \sin^4(\beta) (323 \cos^6(\beta) - 255 \cos^4(\beta) + 45 \cos^2(\beta) - 1)$
10	(-3)		$\frac{5}{32} \sqrt{\frac{195}{11}} e^{3i\alpha} \sin^3(\beta) \cos(\beta) (323 \cos^6(\beta) - 357 \cos^4(\beta) + 105 \cos^2(\beta) - 7)$
10	(-2)		$\frac{5}{64} \sqrt{\frac{15}{22}} e^{2i\alpha} \sin^2(\beta) (4199 \cos^8(\beta) - 6188 \cos^6(\beta) + 2730 \cos^4(\beta) - 364 \cos^2(\beta) + 7)$
10	(-1)		$\frac{5}{32} \sqrt{\frac{5}{22}} e^{i\alpha} \sin(\beta) \cos(\beta) (4199 \cos^8(\beta) - 7956 \cos^6(\beta) + 4914 \cos^4(\beta) - 1092 \cos^2(\beta) + 63)$
10	0		$\frac{5}{704} (46189 \cos^{10}(\beta) - 109395 \cos^8(\beta) + 90090 \cos^6(\beta) - 30030 \cos^4(\beta) + 3465 \cos^2(\beta) - 63)$
10	1		$-\frac{5}{32} \sqrt{\frac{5}{22}} e^{-i\alpha} \sin(\beta) \cos(\beta) (4199 \cos^8(\beta) - 7956 \cos^6(\beta) + 4914 \cos^4(\beta) - 1092 \cos^2(\beta) + 63)$
10	2		$\frac{5}{64} \sqrt{\frac{15}{22}} e^{-2i\alpha} \sin^2(\beta) (4199 \cos^8(\beta) - 6188 \cos^6(\beta) + 2730 \cos^4(\beta) - 364 \cos^2(\beta) + 7)$
10	3		$-\frac{5}{32} \sqrt{\frac{195}{11}} e^{-3i\alpha} \sin^3(\beta) \cos(\beta) (323 \cos^6(\beta) - 357 \cos^4(\beta) + 105 \cos^2(\beta) - 7)$
10	4		$\frac{5}{32} \sqrt{\frac{195}{22}} e^{-4i\alpha} \sin^4(\beta) (323 \cos^6(\beta) - 255 \cos^4(\beta) + 45 \cos^2(\beta) - 1)$

Table B.50: PART L

$(l_1 l_2 m'_1)$	$t$	$q$	$b_q^t$
	10	5	$-\frac{5}{32} \sqrt{\frac{39}{11}} e^{-5i\alpha} \sin^5(\beta) \cos(\beta) (323 \cos^4(\beta) - 170 \cos^2(\beta) + 15)$
	10	6	$\frac{5}{128} \sqrt{\frac{195}{11}} e^{-6i\alpha} \sin^6(\beta) (323 \cos^4(\beta) - 102 \cos^2(\beta) + 3)$
	10	7	$-\frac{5}{64} \sqrt{\frac{3315}{11}} e^{-7i\alpha} \sin^7(\beta) \cos(\beta) (19 \cos^2(\beta) - 3)$
	10	8	$\frac{5}{64} \sqrt{\frac{1105}{22}} e^{-8i\alpha} \sin^8(\beta) (19 \cos^2(\beta) - 1)$
	10	9	$-\frac{5}{64} \sqrt{\frac{20995}{11}} e^{-9i\alpha} \sin^9(\beta) \cos(\beta)$
	10	10	$\frac{5}{128} \sqrt{\frac{4199}{11}} e^{-10i\alpha} \sin^{10}(\beta)$
$hh\phi$	0	0	$\frac{2}{11}$
	2	(-2)	$\frac{1}{22} \sqrt{\frac{3}{2}} e^{2i\alpha} \sin^2(\beta)$
	2	(-1)	$\frac{1}{22} \sqrt{\frac{3}{2}} e^{i\alpha} \sin(2\beta)$
	2	0	$\frac{1}{44} (3 \cos(2\beta) + 1)$
	2	1	$-\frac{1}{22} \sqrt{\frac{3}{2}} e^{-i\alpha} \sin(2\beta)$
	2	2	$\frac{1}{22} \sqrt{\frac{3}{2}} e^{-2i\alpha} \sin^2(\beta)$
	4	(-4)	$-\frac{9}{44} \sqrt{\frac{35}{2}} e^{4i\alpha} \sin^4(\beta)$
	4	(-3)	$-\frac{9}{22} \sqrt{35} e^{3i\alpha} \sin^3(\beta) \cos(\beta)$
	4	(-2)	$-\frac{9}{44} \sqrt{\frac{5}{2}} e^{2i\alpha} \sin^2(\beta) (7 \cos(2\beta) + 5)$
	4	(-1)	$-\frac{9}{88} \sqrt{5} e^{i\alpha} \sin(2\beta) (7 \cos(2\beta) + 1)$
	4	0	$-\frac{9}{352} (20 \cos(2\beta) + 35 \cos(4\beta) + 9)$
	4	1	$\frac{9}{88} \sqrt{5} e^{-i\alpha} \sin(2\beta) (7 \cos(2\beta) + 1)$
	4	2	$-\frac{9}{44} \sqrt{\frac{5}{2}} e^{-2i\alpha} \sin^2(\beta) (7 \cos(2\beta) + 5)$
	4	3	$\frac{9}{22} \sqrt{35} e^{-3i\alpha} \sin^3(\beta) \cos(\beta)$
	4	4	$-\frac{9}{44} \sqrt{\frac{35}{2}} e^{-4i\alpha} \sin^4(\beta)$
	6	(-6)	$-\frac{377}{640} \sqrt{\frac{21}{11}} e^{6i\alpha} \sin^6(\beta)$
	6	(-5)	$-\frac{1131}{320} \sqrt{\frac{7}{11}} e^{5i\alpha} \sin^5(\beta) \cos(\beta)$
	6	(-4)	$-\frac{1131 \sqrt{\frac{7}{2}} e^{4i\alpha} \sin^4(\beta) (11 \cos(2\beta) + 9)}{7040}$
	6	(-3)	$-\frac{377 \sqrt{\frac{21}{5}} e^{3i\alpha} \sin^3(\beta) \cos(\beta) (11 \cos(2\beta) + 5)}{1408}$
	6	(-2)	$-\frac{377 \sqrt{\frac{21}{5}} e^{2i\alpha} \sin^2(\beta) (33 \cos^4(\beta) - 18 \cos^2(\beta) + 1)}{1408}$
	6	(-1)	$-\frac{377 \sqrt{\frac{21}{2}} e^{i\alpha} \sin(\beta) \cos(\beta) (33 \cos^4(\beta) - 30 \cos^2(\beta) + 5)}{1760}$
	6	0	$-\frac{377 (231 \cos^6(\beta) - 315 \cos^4(\beta) + 105 \cos^2(\beta) - 5)}{3520}$
	6	1	$\frac{377 \sqrt{\frac{21}{2}} e^{-i\alpha} \sin(\beta) \cos(\beta) (33 \cos^4(\beta) - 30 \cos^2(\beta) + 5)}{1760}$

Table B.51: PART LI

$(l_1 l_2 m'_1)$	$t$	$q$	$b_q^t$
	6	2	$-\frac{377\sqrt{\frac{21}{5}}e^{-2i\alpha}\sin^2(\beta)(33\cos^4(\beta)-18\cos^2(\beta)+1)}{1408}$
	6	3	$\frac{377\sqrt{\frac{21}{5}}e^{-3i\alpha}\sin^3(\beta)\cos(\beta)(11\cos(2\beta)+5)}{1408}$
	6	4	$-\frac{1131\sqrt{\frac{7}{2}}e^{-4i\alpha}\sin^4(\beta)(11\cos(2\beta)+9)}{7040}$
	6	5	$\frac{1131}{320}\sqrt{\frac{7}{11}}e^{-5i\alpha}\sin^5(\beta)\cos(\beta)$
	6	6	$-\frac{377}{640}\sqrt{\frac{21}{11}}e^{-6i\alpha}\sin^6(\beta)$
	8	(-8)	$\frac{3723}{896}\sqrt{\frac{13}{110}}e^{8i\alpha}\sin^8(\beta)$
	8	(-7)	$\frac{3723}{224}\sqrt{\frac{13}{110}}e^{7i\alpha}\sin^7(\beta)\cos(\beta)$
	8	(-6)	$\frac{1241\sqrt{\frac{39}{11}}e^{6i\alpha}\sin^6(\beta)(15\cos(2\beta)+13)}{4480}$
	8	(-5)	$\frac{3723}{320}\sqrt{\frac{13}{154}}e^{5i\alpha}\sin^5(\beta)\cos(\beta)(5\cos(2\beta)+3)$
	8	(-4)	$\frac{3723e^{4i\alpha}\sin^4(\beta)(65\cos^4(\beta)-26\cos^2(\beta)+1)}{320\sqrt{154}}$
	8	(-3)	$\frac{1241}{32}\sqrt{\frac{3}{770}}e^{3i\alpha}\sin^3(\beta)\cos(\beta)(39\cos^4(\beta)-26\cos^2(\beta)+3)$
	8	(-2)	$\frac{3723e^{2i\alpha}\sin^2(\beta)(143\cos^6(\beta)-143\cos^4(\beta)+33\cos^2(\beta)-1)}{704\sqrt{35}}$
	8	(-1)	$\frac{3723e^{i\alpha}\sin(2\beta)(869\cos(2\beta)+286\cos(4\beta)+715\cos(6\beta)+178)}{788480\sqrt{2}}$
	8	0	$\frac{1241(6435\cos^8(\beta)-12012\cos^6(\beta)+6930\cos^4(\beta)-1260\cos^2(\beta)+35)}{49280}$
	8	1	$-\frac{3723e^{-i\alpha}\sin(2\beta)(869\cos(2\beta)+286\cos(4\beta)+715\cos(6\beta)+178)}{788480\sqrt{2}}$
	8	2	$\frac{3723e^{-2i\alpha}\sin^2(\beta)(143\cos^6(\beta)-143\cos^4(\beta)+33\cos^2(\beta)-1)}{704\sqrt{35}}$
	8	3	$-\frac{1241}{32}\sqrt{\frac{3}{770}}e^{-3i\alpha}\sin^3(\beta)\cos(\beta)(39\cos^4(\beta)-26\cos^2(\beta)+3)$
	8	4	$\frac{3723e^{-4i\alpha}\sin^4(\beta)(65\cos^4(\beta)-26\cos^2(\beta)+1)}{320\sqrt{154}}$
	8	5	$-\frac{3723}{320}\sqrt{\frac{13}{154}}e^{-5i\alpha}\sin^5(\beta)\cos(\beta)(5\cos(2\beta)+3)$
	8	6	$\frac{1241\sqrt{\frac{39}{11}}e^{-6i\alpha}\sin^6(\beta)(15\cos(2\beta)+13)}{4480}$
	8	7	$-\frac{3723}{224}\sqrt{\frac{13}{110}}e^{-7i\alpha}\sin^7(\beta)\cos(\beta)$
	8	8	$\frac{3723}{896}\sqrt{\frac{13}{110}}e^{-8i\alpha}\sin^8(\beta)$
	10	(-10)	$-\frac{15\sqrt{\frac{4199}{11}}e^{10i\alpha}\sin^{10}(\beta)}{1024}$
	10	(-9)	$-\frac{15}{512}\sqrt{\frac{20995}{11}}e^{9i\alpha}\sin^9(\beta)\cos(\beta)$
	10	(-8)	$-\frac{15}{512}\sqrt{\frac{1105}{22}}e^{8i\alpha}\sin^8(\beta)(19\cos^2(\beta)-1)$
	10	(-7)	$-\frac{15}{512}\sqrt{\frac{3315}{11}}e^{7i\alpha}\sin^7(\beta)\cos(\beta)(19\cos^2(\beta)-3)$
	10	(-6)	$-\frac{15\sqrt{\frac{195}{11}}e^{6i\alpha}\sin^6(\beta)(323\cos^4(\beta)-102\cos^2(\beta)+3)}{1024}$

Table B.52: PART LII

$(l_1 l_2 m'_1)$	$t$	$q$	$b_q^t$
	10	(-5)	$-\frac{15}{256} \sqrt{\frac{39}{11}} e^{5i\alpha} \sin^5(\beta) \cos(\beta) (323 \cos^4(\beta) - 170 \cos^2(\beta) + 15)$
	10	(-4)	$-\frac{15}{256} \sqrt{\frac{195}{22}} e^{4i\alpha} \sin^4(\beta) (323 \cos^6(\beta) - 255 \cos^4(\beta) + 45 \cos^2(\beta) - 1)$
	10	(-3)	$-\frac{15}{256} \sqrt{\frac{195}{11}} e^{3i\alpha} \sin^3(\beta) \cos(\beta) (323 \cos^6(\beta) - 357 \cos^4(\beta) + 105 \cos^2(\beta) - 7)$
	10	(-2)	$-\frac{15}{512} \sqrt{\frac{15}{22}} e^{2i\alpha} \sin^2(\beta) (4199 \cos^8(\beta) - 6188 \cos^6(\beta) + 2730 \cos^4(\beta) - 364 \cos^2(\beta) + 7)$
	10	(-1)	$-\frac{15}{256} \sqrt{\frac{5}{22}} e^{i\alpha} \sin(\beta) \cos(\beta) (4199 \cos^8(\beta) - 7956 \cos^6(\beta) + 4914 \cos^4(\beta) - 1092 \cos^2(\beta) + 63)$
	10	0	$-\frac{15(46189 \cos^{10}(\beta) - 109395 \cos^8(\beta) + 90090 \cos^6(\beta) - 30030 \cos^4(\beta) + 3465 \cos^2(\beta))}{5632} + \frac{945}{5632}$
	10	1	$\frac{15}{256} \sqrt{\frac{5}{22}} e^{-i\alpha} \sin(\beta) \cos(\beta) (4199 \cos^8(\beta) - 7956 \cos^6(\beta) + 4914 \cos^4(\beta) - 1092 \cos^2(\beta) + 63)$
	10	2	$-\frac{15}{512} \sqrt{\frac{15}{22}} e^{-2i\alpha} \sin^2(\beta) (4199 \cos^8(\beta) - 6188 \cos^6(\beta) + 2730 \cos^4(\beta) - 364 \cos^2(\beta) + 7)$
	10	3	$\frac{15}{256} \sqrt{\frac{195}{11}} e^{-3i\alpha} \sin^3(\beta) \cos(\beta) (323 \cos^6(\beta) - 357 \cos^4(\beta) + 105 \cos^2(\beta) - 7)$
	10	4	$-\frac{15}{256} \sqrt{\frac{195}{22}} e^{-4i\alpha} \sin^4(\beta) (323 \cos^6(\beta) - 255 \cos^4(\beta) + 45 \cos^2(\beta) - 1)$
	10	5	$\frac{15}{256} \sqrt{\frac{39}{11}} e^{-5i\alpha} \sin^5(\beta) \cos(\beta) (323 \cos^4(\beta) - 170 \cos^2(\beta) + 15)$
	10	6	$-\frac{15 \sqrt{\frac{195}{11}} e^{-6i\alpha} \sin^6(\beta) (323 \cos^4(\beta) - 102 \cos^2(\beta) + 3)}{1024}$
	10	7	$\frac{15}{512} \sqrt{\frac{3315}{11}} e^{-7i\alpha} \sin^7(\beta) \cos(\beta) (19 \cos^2(\beta) - 3)$
	10	8	$-\frac{15}{512} \sqrt{\frac{1105}{22}} e^{-8i\alpha} \sin^8(\beta) (19 \cos^2(\beta) - 1)$
	10	9	$\frac{15}{512} \sqrt{\frac{20995}{11}} e^{-9i\alpha} \sin^9(\beta) \cos(\beta)$
	10	10	$-\frac{15 \sqrt{\frac{4199}{11}} e^{-10i\alpha} \sin^{10}(\beta)}{1024}$
$hh\gamma$	0	0	$\frac{2}{11}$
	2	(-2)	$-\frac{3}{11} \sqrt{\frac{3}{2}} e^{2i\alpha} \sin^2(\beta)$
	2	(-1)	$-\frac{3}{11} \sqrt{6} e^{i\alpha} \sin(\beta) \cos(\beta)$
	2	0	$-\frac{3}{22} (3 \cos(2\beta) + 1)$
	2	1	$\frac{3}{11} \sqrt{6} e^{-i\alpha} \sin(\beta) \cos(\beta)$
	2	2	$-\frac{3}{11} \sqrt{\frac{3}{2}} e^{-2i\alpha} \sin^2(\beta)$

Table B.53: PART LIII

$(l_1 l_2 m'_1)$	$t$	$q$	$b_q^t$
	4	(-4)	$-\frac{9}{44}\sqrt{\frac{35}{2}}e^{4i\alpha}\sin^4(\beta)$
	4	(-3)	$-\frac{9}{22}\sqrt{35}e^{3i\alpha}\sin^3(\beta)\cos(\beta)$
	4	(-2)	$-\frac{9}{44}\sqrt{\frac{5}{2}}e^{2i\alpha}\sin^2(\beta)(7\cos(2\beta)+5)$
	4	(-1)	$-\frac{9}{88}\sqrt{5}e^{i\alpha}\sin(2\beta)(7\cos(2\beta)+1)$
	4	0	$-\frac{9}{352}(20\cos(2\beta)+35\cos(4\beta)+9)$
	4	1	$\frac{9}{88}\sqrt{5}e^{-i\alpha}\sin(2\beta)(7\cos(2\beta)+1)$
	4	2	$-\frac{9}{44}\sqrt{\frac{5}{2}}e^{-2i\alpha}\sin^2(\beta)(7\cos(2\beta)+5)$
	4	3	$\frac{9}{22}\sqrt{35}e^{-3i\alpha}\sin^3(\beta)\cos(\beta)$
	4	4	$-\frac{9}{44}\sqrt{\frac{35}{2}}e^{-4i\alpha}\sin^4(\beta)$
	6	(-6)	$\frac{39}{40}\sqrt{\frac{21}{11}}e^{6i\alpha}\sin^6(\beta)$
	6	(-5)	$\frac{117}{20}\sqrt{\frac{7}{11}}e^{5i\alpha}\sin^5(\beta)\cos(\beta)$
	6	(-4)	$\frac{117}{440}\sqrt{\frac{7}{2}}e^{4i\alpha}\sin^4(\beta)(11\cos(2\beta)+9)$
	6	(-3)	$\frac{39}{88}\sqrt{\frac{21}{5}}e^{3i\alpha}\sin^3(\beta)\cos(\beta)(11\cos(2\beta)+5)$
	6	(-2)	$\frac{39}{88}\sqrt{\frac{21}{5}}e^{2i\alpha}\sin^2(\beta)(33\cos^4(\beta)-18\cos^2(\beta)+1)$
	6	(-1)	$\frac{39}{110}\sqrt{\frac{21}{2}}e^{i\alpha}\sin(\beta)\cos(\beta)(33\cos^4(\beta)-30\cos^2(\beta)+5)$
	6	0	$\frac{39(105\cos(2\beta)+126\cos(4\beta)+231\cos(6\beta)+50)}{7040}$
	6	1	$-\frac{39}{110}\sqrt{\frac{21}{2}}e^{-i\alpha}\sin(\beta)\cos(\beta)(33\cos^4(\beta)-30\cos^2(\beta)+5)$
	6	2	$\frac{39}{88}\sqrt{\frac{21}{5}}e^{-2i\alpha}\sin^2(\beta)(33\cos^4(\beta)-18\cos^2(\beta)+1)$
	6	3	$-\frac{39}{88}\sqrt{\frac{21}{5}}e^{-3i\alpha}\sin^3(\beta)\cos(\beta)(11\cos(2\beta)+5)$
	6	4	$\frac{117}{440}\sqrt{\frac{7}{2}}e^{-4i\alpha}\sin^4(\beta)(11\cos(2\beta)+9)$
	6	5	$-\frac{117}{20}\sqrt{\frac{7}{11}}e^{-5i\alpha}\sin^5(\beta)\cos(\beta)$
	6	6	$\frac{39}{40}\sqrt{\frac{21}{11}}e^{-6i\alpha}\sin^6(\beta)$
	8	(-8)	$-\frac{1581}{896}\sqrt{\frac{13}{110}}e^{8i\alpha}\sin^8(\beta)$
	8	(-7)	$-\frac{1581}{224}\sqrt{\frac{13}{110}}e^{7i\alpha}\sin^7(\beta)\cos(\beta)$
	8	(-6)	$-\frac{527\sqrt{\frac{39}{11}}e^{6i\alpha}\sin^6(\beta)(15\cos(2\beta)+13)}{4480}$
	8	(-5)	$-\frac{1581}{320}\sqrt{\frac{13}{154}}e^{5i\alpha}\sin^5(\beta)\cos(\beta)(5\cos(2\beta)+3)$
	8	(-4)	$-\frac{1581e^{4i\alpha}\sin^4(\beta)(65\cos^4(\beta)-26\cos^2(\beta)+1)}{320\sqrt{154}}$
	8	(-3)	$-\frac{527}{32}\sqrt{\frac{3}{770}}e^{3i\alpha}\sin^3(\beta)\cos(\beta)(39\cos^4(\beta)-26\cos^2(\beta)+3)$
	8	(-2)	$-\frac{1581e^{2i\alpha}\sin^2(\beta)(143\cos^6(\beta)-143\cos^4(\beta)+33\cos^2(\beta)-1)}{704\sqrt{35}}$

Table B.54: PART LIV

$(l_1 l_2 m'_1)$	$t$	$q$	$b_q^t$
	8	(-1)	$-\frac{1581e^{i\alpha} \sin(2\beta)(869 \cos(2\beta)+286 \cos(4\beta)+715 \cos(6\beta)+178)}{788480\sqrt{2}}$
	8	0	$-\frac{527(6435 \cos^8(\beta)-12012 \cos^6(\beta)+6930 \cos^4(\beta)-1260 \cos^2(\beta)+35)}{49280}$
	8	1	$\frac{1581e^{-i\alpha} \sin(2\beta)(869 \cos(2\beta)+286 \cos(4\beta)+715 \cos(6\beta)+178)}{788480\sqrt{2}}$
	8	2	$-\frac{1581e^{-2i\alpha} \sin^2(\beta)(143 \cos^6(\beta)-143 \cos^4(\beta)+33 \cos^2(\beta)-1)}{704\sqrt{35}}$
	8	3	$\frac{527}{32} \sqrt{\frac{3}{770}} e^{-3i\alpha} \sin^3(\beta) \cos(\beta) (39 \cos^4(\beta) - 26 \cos^2(\beta) + 3)$
	8	4	$-\frac{1581e^{-4i\alpha} \sin^4(\beta)(65 \cos^4(\beta)-26 \cos^2(\beta)+1)}{320\sqrt{154}}$
	8	5	$\frac{1581}{320} \sqrt{\frac{13}{154}} e^{-5i\alpha} \sin^5(\beta) \cos(\beta) (5 \cos(2\beta) + 3)$
	8	6	$-\frac{527\sqrt{\frac{39}{11}} e^{-6i\alpha} \sin^6(\beta)(15 \cos(2\beta)+13)}{4480}$
	8	7	$\frac{1581}{224} \sqrt{\frac{13}{110}} e^{-7i\alpha} \sin^7(\beta) \cos(\beta)$
	8	8	$-\frac{1581}{896} \sqrt{\frac{13}{110}} e^{-8i\alpha} \sin^8(\beta)$
10	(-10)		$\frac{5\sqrt{\frac{4199}{11}} e^{10i\alpha} \sin^{10}(\beta)}{1536}$
10	(-9)		$\frac{5}{768} \sqrt{\frac{20995}{11}} e^{9i\alpha} \sin^9(\beta) \cos(\beta)$
10	(-8)		$\frac{5}{768} \sqrt{\frac{1105}{22}} e^{8i\alpha} \sin^8(\beta) (19 \cos^2(\beta) - 1)$
10	(-7)		$\frac{5}{512} \sqrt{\frac{1105}{33}} e^{7i\alpha} \sin^7(\beta) \cos(\beta) (19 \cos(2\beta) + 13)$
10	(-6)		$\frac{5}{512} \sqrt{\frac{65}{33}} e^{6i\alpha} \sin^6(\beta) (323 \cos^4(\beta) - 102 \cos^2(\beta) + 3)$
10	(-5)		$\frac{5}{128} \sqrt{\frac{13}{33}} e^{5i\alpha} \sin^5(\beta) \cos(\beta) (323 \cos^4(\beta) - 170 \cos^2(\beta) + 15)$
10	(-4)		$\frac{5}{128} \sqrt{\frac{65}{66}} e^{4i\alpha} \sin^4(\beta) (323 \cos^6(\beta) - 255 \cos^4(\beta) + 45 \cos^2(\beta) - 1)$
10	(-3)		$\frac{5}{128} \sqrt{\frac{65}{33}} e^{3i\alpha} \sin^3(\beta) \cos(\beta) (323 \cos^6(\beta) - 357 \cos^4(\beta) + 105 \cos^2(\beta) - 7)$
10	(-2)		$\frac{5}{256} \sqrt{\frac{5}{66}} e^{2i\alpha} \sin^2(\beta) (4199 \cos^8(\beta) - 6188 \cos^6(\beta) + 2730 \cos^4(\beta) - 364 \cos^2(\beta) + 7)$
10	(-1)		$\frac{5}{384} \sqrt{\frac{5}{22}} e^{i\alpha} \sin(\beta) \cos(\beta) (4199 \cos^8(\beta) - 7956 \cos^6(\beta) + 4914 \cos^4(\beta) - 1092 \cos^2(\beta) + 63)$
10	0		$\frac{5(46189 \cos^{10}(\beta)-109395 \cos^8(\beta)+90090 \cos^6(\beta)-30030 \cos^4(\beta)+3465 \cos^2(\beta)-63)}{8448}$
10	1		$-\frac{5}{384} \sqrt{\frac{5}{22}} e^{-i\alpha} \sin(\beta) \cos(\beta) (4199 \cos^8(\beta) - 7956 \cos^6(\beta) + 4914 \cos^4(\beta) - 1092 \cos^2(\beta) + 63)$
10	2		$\frac{5}{256} \sqrt{\frac{5}{66}} e^{-2i\alpha} \sin^2(\beta) (4199 \cos^8(\beta) - 6188 \cos^6(\beta) + 2730 \cos^4(\beta) - 364 \cos^2(\beta) + 7)$

Table B.55: PART LV

B Expansion coefficients for tight-binding operator

$(l_1 l_2 m'_1)$	$t$	$q$	$b_q^t$
	10	3	$-\frac{5}{128} \sqrt{\frac{65}{33}} e^{-3i\alpha} \sin^3(\beta) \cos(\beta) (323 \cos^6(\beta) - 357 \cos^4(\beta) + 105 \cos^2(\beta) - 7)$
	10	4	$\frac{5}{128} \sqrt{\frac{65}{66}} e^{-4i\alpha} \sin^4(\beta) (323 \cos^6(\beta) - 255 \cos^4(\beta) + 45 \cos^2(\beta) - 1)$
	10	5	$-\frac{5}{128} \sqrt{\frac{13}{33}} e^{-5i\alpha} \sin^5(\beta) \cos(\beta) (323 \cos^4(\beta) - 170 \cos^2(\beta) + 15)$
	10	6	$\frac{5}{512} \sqrt{\frac{65}{33}} e^{-6i\alpha} \sin^6(\beta) (323 \cos^4(\beta) - 102 \cos^2(\beta) + 3)$
	10	7	$-\frac{5}{512} \sqrt{\frac{1105}{33}} e^{-7i\alpha} \sin^7(\beta) \cos(\beta) (19 \cos(2\beta) + 13)$
	10	8	$\frac{5}{768} \sqrt{\frac{1105}{22}} e^{-8i\alpha} \sin^8(\beta) (19 \cos^2(\beta) - 1)$
	10	9	$-\frac{5}{768} \sqrt{\frac{20995}{11}} e^{-9i\alpha} \sin^9(\beta) \cos(\beta)$
	10	10	$\frac{5 \sqrt{\frac{4199}{11}} e^{-10i\alpha} \sin^{10}(\beta)}{1536}$
$hh\eta$	0	0	$\frac{2}{11}$
	2	(-2)	$-\frac{15}{22} \sqrt{\frac{3}{2}} e^{2i\alpha} \sin^2(\beta)$
	2	(-1)	$-\frac{15}{22} \sqrt{\frac{3}{2}} e^{i\alpha} \sin(2\beta)$
	2	0	$-\frac{15}{44} (3 \cos(2\beta) + 1)$
	2	1	$\frac{15}{22} \sqrt{\frac{3}{2}} e^{-i\alpha} \sin(2\beta)$
	2	2	$-\frac{15}{22} \sqrt{\frac{3}{2}} e^{-2i\alpha} \sin^2(\beta)$
	4	(-4)	$\frac{9}{44} \sqrt{\frac{35}{2}} e^{4i\alpha} \sin^4(\beta)$
	4	(-3)	$\frac{9}{22} \sqrt{35} e^{3i\alpha} \sin^3(\beta) \cos(\beta)$
	4	(-2)	$\frac{9}{44} \sqrt{\frac{5}{2}} e^{2i\alpha} \sin^2(\beta) (7 \cos(2\beta) + 5)$
	4	(-1)	$\frac{9}{88} \sqrt{5} e^{i\alpha} \sin(2\beta) (7 \cos(2\beta) + 1)$
	4	0	$\frac{9}{352} (20 \cos(2\beta) + 35 \cos(4\beta) + 9)$
	4	1	$-\frac{9}{88} \sqrt{5} e^{-i\alpha} \sin(2\beta) (7 \cos(2\beta) + 1)$
	4	2	$\frac{9}{44} \sqrt{\frac{5}{2}} e^{-2i\alpha} \sin^2(\beta) (7 \cos(2\beta) + 5)$
	4	3	$-\frac{9}{22} \sqrt{35} e^{-3i\alpha} \sin^3(\beta) \cos(\beta)$
	4	4	$\frac{9}{44} \sqrt{\frac{35}{2}} e^{-4i\alpha} \sin^4(\beta)$
	6	(-6)	$-\frac{39}{128} \sqrt{\frac{21}{11}} e^{6i\alpha} \sin^6(\beta)$
	6	(-5)	$-\frac{117}{64} \sqrt{\frac{7}{11}} e^{5i\alpha} \sin^5(\beta) \cos(\beta)$
	6	(-4)	$-\frac{117 \sqrt{\frac{7}{2}} e^{4i\alpha} \sin^4(\beta) (11 \cos(2\beta) + 9)}{1408}$
	6	(-3)	$-\frac{39 \sqrt{105} e^{3i\alpha} \sin^3(\beta) \cos(\beta) (11 \cos(2\beta) + 5)}{1408}$
	6	(-2)	$-\frac{39 \sqrt{105} e^{2i\alpha} \sin^2(\beta) (33 \cos^4(\beta) - 18 \cos^2(\beta) + 1)}{1408}$

Table B.56: PART LVI

$(l_1 l_2 m_1')$	$t$	$q$	$b_q^t$
	6	(-1)	$-\frac{39}{352} \sqrt{\frac{21}{2}} e^{i\alpha} \sin(\beta) \cos(\beta) (33 \cos^4(\beta) - 30 \cos^2(\beta) + 5)$
	6	0	$-\frac{39}{704} (231 \cos^6(\beta) - 315 \cos^4(\beta) + 105 \cos^2(\beta) - 5)$
	6	1	$\frac{39}{352} \sqrt{\frac{21}{2}} e^{-i\alpha} \sin(\beta) \cos(\beta) (33 \cos^4(\beta) - 30 \cos^2(\beta) + 5)$
	6	2	$-\frac{39\sqrt{105}e^{-2i\alpha} \sin^2(\beta)(33 \cos^4(\beta) - 18 \cos^2(\beta) + 1)}{1408}$
	6	3	$\frac{39\sqrt{105}e^{-3i\alpha} \sin^3(\beta) \cos(\beta)(11 \cos(2\beta) + 5)}{1408}$
	6	4	$-\frac{117\sqrt{\frac{7}{2}}e^{-4i\alpha} \sin^4(\beta)(11 \cos(2\beta) + 9)}{1408}$
	6	5	$\frac{117}{64} \sqrt{\frac{7}{11}} e^{-5i\alpha} \sin^5(\beta) \cos(\beta)$
	6	6	$-\frac{39}{128} \sqrt{\frac{21}{11}} e^{-6i\alpha} \sin^6(\beta)$
	8	(-8)	$\frac{51}{896} \sqrt{\frac{65}{22}} e^{8i\alpha} \sin^8(\beta)$
	8	(-7)	$\frac{51}{224} \sqrt{\frac{65}{22}} e^{7i\alpha} \sin^7(\beta) \cos(\beta)$
	8	(-6)	$\frac{17}{896} \sqrt{\frac{39}{11}} e^{6i\alpha} \sin^6(\beta) (15 \cos(2\beta) + 13)$
	8	(-5)	$\frac{51}{64} \sqrt{\frac{13}{154}} e^{5i\alpha} \sin^5(\beta) \cos(\beta) (5 \cos(2\beta) + 3)$
	8	(-4)	$\frac{51e^{4i\alpha} \sin^4(\beta)(65 \cos^4(\beta) - 26 \cos^2(\beta) + 1)}{64\sqrt{154}}$
	8	(-3)	$\frac{17}{32} \sqrt{\frac{15}{154}} e^{3i\alpha} \sin^3(\beta) \cos(\beta) (39 \cos^4(\beta) - 26 \cos^2(\beta) + 3)$
	8	(-2)	$\frac{51}{704} \sqrt{\frac{5}{7}} e^{2i\alpha} \sin^2(\beta) (143 \cos^6(\beta) - 143 \cos^4(\beta) + 33 \cos^2(\beta) - 1)$
	8	(-1)	$\frac{51e^{i\alpha} \sin(2\beta)(869 \cos(2\beta) + 286 \cos(4\beta) + 715 \cos(6\beta) + 178)}{157696\sqrt{2}}$
	8	0	$\frac{17(6435 \cos^8(\beta) - 12012 \cos^6(\beta) + 6930 \cos^4(\beta) - 1260 \cos^2(\beta) + 35)}{9856}$
	8	1	$-\frac{51e^{-i\alpha} \sin(2\beta)(869 \cos(2\beta) + 286 \cos(4\beta) + 715 \cos(6\beta) + 178)}{157696\sqrt{2}}$
	8	2	$\frac{51}{704} \sqrt{\frac{5}{7}} e^{-2i\alpha} \sin^2(\beta) (143 \cos^6(\beta) - 143 \cos^4(\beta) + 33 \cos^2(\beta) - 1)$
	8	3	$-\frac{17}{32} \sqrt{\frac{15}{154}} e^{-3i\alpha} \sin^3(\beta) \cos(\beta) (39 \cos^4(\beta) - 26 \cos^2(\beta) + 3)$
	8	4	$\frac{51e^{-4i\alpha} \sin^4(\beta)(65 \cos^4(\beta) - 26 \cos^2(\beta) + 1)}{64\sqrt{154}}$
	8	5	$-\frac{51}{64} \sqrt{\frac{13}{154}} e^{-5i\alpha} \sin^5(\beta) \cos(\beta) (5 \cos(2\beta) + 3)$
	8	6	$\frac{17}{896} \sqrt{\frac{39}{11}} e^{-6i\alpha} \sin^6(\beta) (15 \cos(2\beta) + 13)$
	8	7	$-\frac{51}{224} \sqrt{\frac{65}{22}} e^{-7i\alpha} \sin^7(\beta) \cos(\beta)$
	8	8	$\frac{51}{896} \sqrt{\frac{65}{22}} e^{-8i\alpha} \sin^8(\beta)$
10	(-10)		$-\frac{\sqrt{\frac{4199}{11}} e^{10i\alpha} \sin^{10}(\beta)}{3072}$
10	(-9)		$-\frac{\sqrt{\frac{20995}{11}} e^{9i\alpha} \sin^9(\beta) \cos(\beta)}{1536}$

Table B.57: PART LVII

B Expansion coefficients for tight-binding operator

$(l_1 l_2 m'_1)$	$t$	$q$	$b_q^t$
	10	(-8)	$-\frac{\sqrt{\frac{1105}{22}} e^{8i\alpha} \sin^8(\beta)(19 \cos(2\beta)+17)}{3072}$
	10	(-7)	$-\frac{1}{512} \sqrt{\frac{1105}{33}} e^{7i\alpha} \sin^7(\beta) \cos(\beta) (19 \cos^2(\beta) - 3)$
	10	(-6)	$-\frac{\sqrt{\frac{65}{33}} e^{6i\alpha} \sin^6(\beta)(323 \cos^4(\beta)-102 \cos^2(\beta)+3)}{1024}$
	10	(-5)	$-\frac{1}{256} \sqrt{\frac{13}{33}} e^{5i\alpha} \sin^5(\beta) \cos(\beta) (323 \cos^4(\beta) - 170 \cos^2(\beta) + 15)$
	10	(-4)	$-\frac{1}{256} \sqrt{\frac{65}{66}} e^{4i\alpha} \sin^4(\beta) (323 \cos^6(\beta) - 255 \cos^4(\beta) + 45 \cos^2(\beta) - 1)$
	10	(-3)	$-\frac{1}{256} \sqrt{\frac{65}{33}} e^{3i\alpha} \sin^3(\beta) \cos(\beta) (323 \cos^6(\beta) - 357 \cos^4(\beta) + 105 \cos^2(\beta) - 7)$
	10	(-2)	$-\frac{1}{512} \sqrt{\frac{5}{66}} e^{2i\alpha} \sin^2(\beta) (4199 \cos^8(\beta) - 6188 \cos^6(\beta) + 2730 \cos^4(\beta) - 364 \cos^2(\beta) + 7)$
	10	(-1)	$-\frac{1}{768} \sqrt{\frac{5}{22}} e^{i\alpha} \sin(\beta) \cos(\beta) (4199 \cos^8(\beta) - 7956 \cos^6(\beta) + 4914 \cos^4(\beta) - 1092 \cos^2(\beta) + 63)$
	10	0	$\frac{-46189 \cos^{10}(\beta)+109395 \cos^8(\beta)-90090 \cos^6(\beta)+30030 \cos^4(\beta)-3465 \cos^2(\beta)+63}{16896}$
	10	1	$\frac{1}{768} \sqrt{\frac{5}{22}} e^{-i\alpha} \sin(\beta) \cos(\beta) (4199 \cos^8(\beta) - 7956 \cos^6(\beta) + 4914 \cos^4(\beta) - 1092 \cos^2(\beta) + 63)$
	10	2	$-\frac{1}{512} \sqrt{\frac{5}{66}} e^{-2i\alpha} \sin^2(\beta) (4199 \cos^8(\beta) - 6188 \cos^6(\beta) + 2730 \cos^4(\beta) - 364 \cos^2(\beta) + 7)$
	10	3	$\frac{1}{256} \sqrt{\frac{65}{33}} e^{-3i\alpha} \sin^3(\beta) \cos(\beta) (323 \cos^6(\beta) - 357 \cos^4(\beta) + 105 \cos^2(\beta) - 7)$
	10	4	$-\frac{1}{256} \sqrt{\frac{65}{66}} e^{-4i\alpha} \sin^4(\beta) (323 \cos^6(\beta) - 255 \cos^4(\beta) + 45 \cos^2(\beta) - 1)$
	10	5	$\frac{1}{256} \sqrt{\frac{13}{33}} e^{-5i\alpha} \sin^5(\beta) \cos(\beta) (323 \cos^4(\beta) - 170 \cos^2(\beta) + 15)$
	10	6	$-\frac{\sqrt{\frac{65}{33}} e^{-6i\alpha} \sin^6(\beta)(323 \cos^4(\beta)-102 \cos^2(\beta)+3)}{1024}$
	10	7	$\frac{1}{512} \sqrt{\frac{1105}{33}} e^{-7i\alpha} \sin^7(\beta) \cos(\beta) (19 \cos^2(\beta) - 3)$
	10	8	$-\frac{\sqrt{\frac{1105}{22}} e^{-8i\alpha} \sin^8(\beta)(19 \cos(2\beta)+17)}{3072}$
	10	9	$\frac{\sqrt{\frac{20995}{11}} e^{-9i\alpha} \sin^9(\beta) \cos(\beta)}{1536}$
	10	10	$-\frac{\sqrt{\frac{4199}{11}} e^{-10i\alpha} \sin^{10}(\beta)}{3072}$

Table B.58: PART LVIII

# List of Figures

2.1	Zaanen-Sawatzky-Allen scheme . . . . .	6
2.2	Orientation of Sharma system . . . . .	48
3.1	Bruker IFS 66v/S Fourier-transform spectrometer . . . . .	74
3.2	The interferogram of a monochromatic light source . . . . .	74
3.3	Interferogram of a polychromatic light source . . . . .	75
3.4	Dependence of the Kramers-Kronig analysis on $\omega_1$ . . . . .	82
4.1	Crystal structure of VOCl . . . . .	87
4.2	$-\ln(T(\omega))/d$ of VOCl . . . . .	89
4.3	Franck-Condon principle . . . . .	94
4.4	Tanabe-Sugano diagram for a $d^2$ configuration . . . . .	95
4.5	Increasing crystal-field splitting of VOCl . . . . .	96
4.6	Crystal-field splitting of VOCl . . . . .	97
4.7	Line shape and Franck-Condon principle . . . . .	100
4.8	Dependence of the excitation energies on $\Delta_{V-Cl}$ and $\Delta_{V-O}$ . . . . .	104
4.9	Dependence of $\sigma_1(\omega)$ on $\Delta_{V-O}$ for $\Delta_{V-Cl} = 2$ eV . . . . .	105
4.10	Dependence of $\sigma_1(\omega)$ on $\Delta_{V-O}$ for $\Delta_{V-Cl} = 3$ eV . . . . .	106
4.11	Dependence of $\sigma_1(\omega)$ on $\Delta_{V-O}$ for $\Delta_{V-Cl} = 4$ eV . . . . .	107
4.12	Dependence of $\sigma_1(\omega)$ on $\Delta_{V-O}$ for $\Delta_{V-Cl} = 5$ eV . . . . .	108
4.13	Dependence of $\sigma_1(\omega)$ on $\Delta_{V-O}$ for $\Delta_{V-Cl} = 6$ eV . . . . .	109
4.14	Dependence of $\sigma_1(\omega)$ on $\Delta_{V-O}$ for $\Delta_{V-Cl} = 7$ eV . . . . .	110
4.15	Dependence of $\sigma_1(\omega)$ on $\Delta_{V-O}$ for $\Delta_{V-Cl} = 8$ eV . . . . .	111
4.16	Dependence of $\sigma_1(\omega)$ on the Hubbard $U_V$ . . . . .	113
4.17	Dependence of $\sigma_1(\omega)$ on the screening factor . . . . .	114
4.18	Dependence of $\sigma_1(\omega)$ on $r_{Cl}$ . . . . .	115
4.19	Calculated optical conductivity of VOCl . . . . .	116
4.20	Results of the cluster-model calculation for TiOCl . . . . .	123
4.21	Crystal structure of YMnO <sub>3</sub> . . . . .	126
4.22	Reflectance of YMnO <sub>3</sub> and fit at T = 20 K . . . . .	133
4.23	Reflectance of YMnO <sub>3</sub> and fit at T = 295 K . . . . .	134
4.24	Reflectance of YMnO <sub>3</sub> . . . . .	136
4.25	Optical conductivity of YMnO <sub>3</sub> . . . . .	137
4.26	Relative eigenfrequency $\omega_0(T)/\omega_0(T=20$ K) of YMnO <sub>3</sub> . . . . .	138
4.27	Relative plasma frequency $\omega_p(T)/\omega_p(T=20$ K) of YMnO <sub>3</sub> . . . . .	139
4.28	Relative damping $\gamma(T)/\gamma(T=20$ K) of YMnO <sub>3</sub> . . . . .	140
4.29	Optical properties of YMnO <sub>3</sub> around $T_N$ . . . . .	141
4.30	Relative eigenfrequency of YMnO <sub>3</sub> at 168 cm <sup>-1</sup> extrapolated . . . . .	142

4.31	Absorption spectrum of $\text{YMnO}_3$ at $T = 295 \text{ K}$ . . . . .	144
4.32	Reflectance of $\text{YMn}_{0.7}\text{Ga}_{0.3}\text{O}_3$ and fit at $T = 20 \text{ K}$ . . . . .	146
4.33	Reflectance of $\text{YMn}_{0.7}\text{Ga}_{0.3}\text{O}_3$ and fit at $T = 295 \text{ K}$ . . . . .	147
4.34	Reflectance of $\text{YMn}_{0.7}\text{Ga}_{0.3}\text{O}_3$ . . . . .	149
4.35	Optical conductivity of $\text{YMn}_{0.7}\text{Ga}_{0.3}\text{O}_3$ . . . . .	150
4.36	Relative eigenfrequency $\omega_0(T)/\omega_0(T=20 \text{ K})$ of $\text{YMn}_{0.7}\text{Ga}_{0.3}\text{O}_3$ . . . . .	151
4.37	Relative plasma frequency $\omega_p(T)/\omega_p(T=20 \text{ K})$ of $\text{YMn}_{0.7}\text{Ga}_{0.3}\text{O}_3$ . . . . .	152
4.38	Relative damping $\gamma(T)/\gamma(T=20 \text{ K})$ of $\text{YMn}_{0.7}\text{Ga}_{0.3}\text{O}_3$ . . . . .	153
4.39	Comparison of $\text{YMnO}_3$ and $\text{YMn}_{0.7}\text{Ga}_{0.3}\text{O}_3$ for $\mathbf{E} \parallel \mathbf{c}$ . . . . .	154
4.40	Comparison of $\text{YMnO}_3$ and $\text{YMn}_{0.7}\text{Ga}_{0.3}\text{O}_3$ for $\mathbf{E} \perp \mathbf{c}$ . . . . .	155
4.41	Lowest phonon mode of $\text{YMnO}_3$ and $\text{YMn}_{0.7}\text{Ga}_{0.3}\text{O}_3$ . . . . .	156
4.42	Crystal and magnetic structure of $\text{MnWO}_4$ . . . . .	160
4.43	Magnetic structure of $\text{MnWO}_4$ . . . . .	162
4.44	Magnetic phase diagram of $\text{MnWO}_4$ . . . . .	164
4.45	Reflectance of $\text{MnWO}_4$ for different angles at $T = 10 \text{ K}$ . . . . .	166
4.46	Orientation of axes in monoclinic $\text{MnWO}_4$ . . . . .	167
4.47	Rotation angles of the tensor of the dielectric function in $\text{MnWO}_4$ . . . . .	168
4.48	Reflectance of $\text{MnWO}_4$ and fit at $T = 10 \text{ K}$ . . . . .	170
4.49	Reflectance of $\text{MnWO}_4$ and fit at $T = 295 \text{ K}$ . . . . .	171
4.50	Reflectance of $\text{MnWO}_4$ ( $\mathbf{E} \parallel \mathbf{b}$ ) . . . . .	173
4.51	Reflectance of $\text{MnWO}_4$ ( $\mathbf{E} \parallel \mathbf{ac}$ ) at $\chi = 0^\circ$ and $\chi = 30^\circ$ . . . . .	174
4.52	Reflectance of $\text{MnWO}_4$ ( $\mathbf{E} \parallel \mathbf{ac}$ ) at $\chi = 60^\circ$ and $\chi = 90^\circ$ . . . . .	175
4.53	Optical conductivity of $\text{MnWO}_4$ and at $T = 10 \text{ K}$ . . . . .	176
4.54	Reflectance of $\text{MnWO}_4$ below $50 \text{ K}$ . . . . .	177
4.55	Relative eigenfrequencies $\omega_0(T)/\omega_0(T=10 \text{ K})$ of $\text{MnWO}_4$ . . . . .	178
4.56	Relative plasma frequencies $\omega_p(T)/\omega_p(T=10 \text{ K})$ of $\text{MnWO}_4$ . . . . .	179
4.57	Relative damping $\gamma(T)/\gamma(T=10 \text{ K})$ of $\text{MnWO}_4$ . . . . .	180
4.58	Absolute change of the angle $\theta_i$ of $\text{MnWO}_4$ . . . . .	181
4.59	Orientation of axes in monoclinic $\text{MnWO}_4$ . . . . .	182
4.60	$-\ln(T(\omega))/d$ of $\text{MnWO}_4$ . . . . .	183
4.61	Crystal-field splitting in $\text{MnWO}_4$ . . . . .	185
4.62	Results of cluster-model calculation for $\text{MnWO}_4$ . . . . .	190
4.63	Crystal structure of $\text{BiB}_3\text{O}_6$ . . . . .	196
4.64	Reflectivity spectra of $\text{BiB}_3\text{O}_6$ at $T = 300 \text{ K}$ for 14 angles . . . . .	198
4.65	Reflectivity spectra of $\text{BiB}_3\text{O}_6$ at $T = 300 \text{ K}$ . . . . .	199
4.66	Reflectivity spectra of $\text{BiB}_3\text{O}_6$ at $T = 20 \text{ K}$ . . . . .	200
4.67	Reflectivity spectra of $\text{BiB}_3\text{O}_6$ within the FIR range . . . . .	201
4.68	Crystal and magnetic structure of $\text{CaCrO}_3$ . . . . .	207
4.69	Lattice Parameters of $\text{CaCrO}_3$ . . . . .	209
4.70	Magnetic susceptibility of $\text{CaCrO}_3$ . . . . .	210
4.71	Electrical resistivity of $\text{CaCrO}_3$ . . . . .	212
4.72	A sketch of optical properties of a metal and an insulator . . . . .	213
4.73	Infrared reflectivity of $\text{CaCrO}_3$ . . . . .	214
4.74	High-energy contributions in fit of $\text{CaCrO}_3$ at $T = 20 \text{ K}$ . . . . .	216

4.75	Drude-Lorentz fit $\text{CaCrO}_3$ at $T = 020$ K . . . . .	218
4.76	Drude-Lorentz fit $\text{CaCrO}_3$ at $T = 110$ K . . . . .	219
4.77	Drude-Lorentz fit $\text{CaCrO}_3$ at $T = 295$ K . . . . .	220
4.78	Optical conductivity of $\text{CaCrO}_3$ . . . . .	221
4.79	Reflectance and optical conductivity of $\text{CaCrO}_3$ at $200 \text{ cm}^{-1}$ . . . . .	222
4.80	Sketch of the Cr Hubbard bands of $\text{CaCrO}_3$ . . . . .	223
4.81	$N_{\text{eff}}$ of $\text{CaCrO}_3$ . . . . .	224
4.82	Comparison $\text{CaCrO}_3$ and Orenstein . . . . .	227
4.83	Effective medium model for $\text{CaCrO}_3$ . . . . .	230
A.2.1	Tetrahedron associated with the 6-j symbol . . . . .	238



# List of Publications

1. **CaCrO<sub>3</sub>: an anomalous antiferromagnetic metallic oxide**  
A. C. Komarek, S. V. Streltsov, M. Isobe, T. Möller, M. Hoelzel, A. Senyshyn, D. Trots, M. T. Fernández-Díaz, T. Hansen, H. Gotou, T. Yagi, Y. Ueda, V. I. Anisimov, M. Grüninger, D. I. Khomskii and M. Braden  
Phys. Rev. Lett. **101**, 167204 (2008)
2. **Collective orbital excitations in orbitally ordered YVO<sub>3</sub> and HoVO<sub>3</sub>**  
E. Benckiser, R. Rückamp, T. Möller, T. Taetz, A. Möller, A. A. Nugrohok, T. T. M. Palstra, G.S. Uhrig and M. Grüninger  
New Journal of Physics **10**, 053027 (2008)
3. **Phonon modes of monoclinic BiB<sub>3</sub>O<sub>6</sub>**  
A. Gössling, T. Möller, W.-D. Stein, P. Becker, L. Bohatý, and M. Grüninger  
phys. stat. sol. (b) **242**, R85 (2005)
4. **Conference contributions**
  - Spring meeting of the German Physical Society (DPG), division condensed matter, Berlin, 2005, Dresden, 2006, Berlin, 2008
  - International Workshop on Highly Correlated Transition Metal Compounds II of SFB 608, Cologne, 2006



# Danksagung

Ich möchte mich wirklich bedanken bei ...

- meinem Doktorvater Prof. Dr. M. Grüninger für die Betreuung dieser Arbeit und die vielen konstruktiven Diskussionen und wertvollen Korrekturvorschlägen.
- Herrn Priv.-Doz. Dr. R. Bulla, dem Zweitgutachter dieser Arbeit, für sein Engagement.
- Herrn Prof. Dr. A. Freimuth, der mir die Möglichkeit gegeben hat, meine Promotion in Köln durchzuführen.
- den Optikern Dr. Eva Benckiser, Christina Hilgers, Dr. Alexander Gössling und Dr. Reinhard Rückamp für die gute und nette Zusammenarbeit, die mir sehr viel Spaß gemacht hat.
- Prof. Dr. L. Bohatý für die Übernahme des Vorsitzes der Prüfungskommission.
- Dr. Wolf Dieter Stein, Dr. Alexander Gössling, Frau Dr. P. Becker-Bohatý und Prof. Dr. L. Bohatý für die Zusammenarbeit im BiBO-Projekt. Prof. Dr. L. Bohatý und Prof. Dr. P. Becker-Bohatý ein zusätzlicher Dank für die Bereitstellung des  $\text{MnWO}_4$  Kristalls.
- Alexander Komarek für die Zusammenarbeit im  $\text{CaCrO}_3$ -Projekt.
- den Mitarbeitern der Werkstätten unter Leitung von Herrn Külzer (Feinmechanik) und Herrn Menz (Elektronik), für die ständige Hilfsbereitschaft.
- den Mitarbeitern im Rechenzentrum, allen voran Dr. Stefan Borowski und Dr. Daniel Tiggemann für Eure Hilfe, auch wenn ihr mich manchmal zur Verzweiflung gebracht habt.
- Frau Dorothea Hochscheid, für die stets freundlich Beschaffung jeglicher Literatur und warmherzige Atmosphäre und die schnelle und engagierte
- Frau Claudia Hermann – Doris wird sie vermissen.
- den technischen Mitarbeiterinnen Lucie Hamdan, Inge Simons und Susanne Heiligen für ihre Hilfsbereitschaft.
- Dr. Thomas Lorentz für seine Hilfe bei Fragen aller Art.
- Dr. Harald Kierspel für seine Hilfe bei allen organisatorischen Fragestellungen.

- Herrn Dommel für das flüssige Helium und für den flüssigen Stickstoff, auch wenn es mal ganz schnell gehen muß.
- Dr. Ralf Müller für seine verlässliche Beschaffung von Kaffee, Wasser und anderen Chemikalien.
- meinen ehemaligen und aktuellen Zimmerkollegen Dr. Alexander Gössling, Dr. Markus Kriener, Dr. Kostas Kordonis, Dr. Alexandr Sologubenko, Kerstin Dönecke und Marco Reuther für die nette Arbeitsatmosphäre
- Olaf Schumann für die Hilfe bei Problemen mit Hard- und Software.
- Carmen Handels für ein freundliches Lächeln.
- allen Mitgliedern des Institutes für eine angenehme Atmosphäre und ihre Hilfsbereitschaft.
- der Deutschen Forschungsgemeinschaft (DFG) für die Finanzierung meiner Doktorandenstelle durch den SFB 608.
- Herrn Meltzer für die Hilfe mit der englischen Sprache.
- Sir Olli für den nötigen Ausgleich.
- meinen Schwiegereltern.
- meinen Eltern.
- meiner Frau Melanie für ihre unglaubliche Unterstützung, dass sie so viel Rücksicht auf mich genommen und mir so viel Rückhalt gegeben hat. Danke für alles.

## Abstract

The thesis is divided into two parts. The first part describes the development of a new program for doing cluster-model configuration-interaction calculations within the Racah-Wigner algebra, which enables a highly accurate analysis of the optical spectra of transition-metal oxides. The application of the Racah-Wigner algebra and the related Wigner-Eckart theorem reduces the computational effort compared with the creation/annihilation algebra and makes the knowledge of the Slater determinants no longer necessary. The advantages of the Racah-Wigner algebra becomes becomes important, if the size of the calculated cluster is more and more increased, e.g. for double-cluster calculations because the number of Slater determinants scales drastically with increasing cluster size. Furthermore we can analyze the dependence of the results of the cluster model calculation on the ionic multiplets. In order to use the Racah-Wigner algebra one has to represent the contributions to the Hamiltonian as spherical tensor operators. A general expression for the matrix elements of the crystal-field operator within the Racah-Wigner algebra was derived, which is valid for arbitrary configurations. In addition to the crystal-field operator we give a general expression for the matrix elements of the covalency operator within the widely-used Slater-Koster tight-binding approximation using Sobel'man's parentage scheme. Although this description is not as fast and elegant as the Racah-Wigner algebra, we do not need to know the Slater determinants and conserve the ionic multiplet dependence as well. Furthermore, the program enables the investigation of the  $4s$  shell and the ligand crystal-field splitting contribution to the optical spectra. The optical conductivity is calculated within the Kubo-Greenwood model.

The second part includes the investigation of energetically low-lying excitations in several transition-metal compounds. We start with the analysis of crystal-field excitations in the transition-metal oxyhalide  $\text{VOCl}$  and perform a detailed group-theoretical analysis combined with a full multiplet cluster-model configuration-interaction. In the following a detailed temperature-dependent analysis of the phonon spectra of the hexagonal multiferroic compounds  $\text{YMnO}_3$  and  $\text{YMn}_{0.7}\text{Ga}_{0.3}\text{O}_3$  was done in order to investigate the spin-lattice interaction and their probable contribution to the occurrence of ferroelectricity in combination with antiferromagnetism in these compounds. Furthermore, the spin-lattice interaction in the monoclinic multiferroic  $\text{MnWO}_4$  was analyzed, by means of a generalized Drude-LLorentz model. Subsequently, a detailed phonon analysis of the monoclinic  $\text{BiB}_3\text{O}_6$  was done, due to the outstanding nonlinear optical properties of this compound. At the end of the thesis optical studies of the anomalous antiferromagnetic metallic oxide  $\text{CaCrO}_3$  were presented. This metallic oxide shows an exception from the rule, that in transition-metal oxides ferromagnetism typically coexists with metallic conductivity, whereas insulators usually exhibit antiferromagnetism.



## Zusammenfassung

Die vorliegende Doktorarbeit ist in zwei Teil gegliedert. Im ersten Teil wird die Entwicklung eines neuen Programmes zur Cluster-Rechnung im Rahmen der Racah-Wigner Algebra beschrieben, welches eine sehr genaue Analyse der optischen Spektren von Übergangsmetalloxiden erlaubt. Die Verwendung der Racah-Wigner Algebra und dem damit verbundenen Wigner-Eckart Theorem reduziert – im Vergleich mit der Anwendung der Erzeuger/Vernichter Algebra – den erforderlichen Rechenaufwand. Die Abhängigkeit der Ergebnisse von den ionischen Multipletts wird dabei ersichtlich. Des weiteren ist die Kenntnis der einzelnen Slater Determinanten nicht mehr länger erforderlich, welches umso wichtiger wird, je größer der berechnete Cluster ist, z.B. bei Doppel-Cluster Rechnungen, da hierbei die Anzahl der Slater Determinanten sehr ungünstig mit der Größe des Cluster skaliert. Um nun die Racah-Wigner Algebra anwenden zu können, muß man jeden Beitrag des Hamilton Operators als sphärischen Tensor Operator ausdrücken. Im Rahmen der Doktorarbeit wurde ein allgemeiner Ausdruck für die Matrixelemente des Kristallfeld-Operators innerhalb der Racah-Wigner Algebra hergeleitet, welcher für beliebige Konfigurationen gültig ist. Des weiteren wurde ein Ausdruck für den Kovalenz-Operator innerhalb der weit verbreiteten Slater-Koster Näherung erarbeitet, wobei Sobel'mans Parentage-Scheme benutzt wurde. Obwohl diese Beschreibung nicht so schnell und elegant wie die Racah-Wigner Algebra ist, erfordert sie keine Slater Determinanten und erhält die Abhängigkeit der Ergebnisse von den ionischen Multipletts. Der zweite Teil der Arbeit behandelt die Untersuchung von energetisch tiefliegenden Anregungen verschiedener Übergangsmetall-Verbindungen. Hierbei findet das im Rahmen dieser Arbeit entwickelte Programm Verwendung, da es die Untersuchung der Einflüsse der  $4s$  Schale und der Liganden-Kristallfeld-Aufspaltung auf die optischen Spektren erlaubt. Die optische Leitfähigkeit wird hierbei im Rahmen des Kubo-Greenwood Modells berechnet. Es wird mit der Analyse von Kristallfeld-Anregungen in VOCl begonnen, im Zuge derer eine detaillierte gruppentheoretische Analyse verbunden mit einer Cluster-Rechnung durchgeführt wurde. Daran anschließend folgt eine Vorstellung der temperaturabhängigen Analyse der Phononenspektren von hexagonalem  $\text{YMnO}_3$  und  $\text{YMn}_{0.7}\text{Ga}_{0.3}\text{O}_3$ , um die Spin-Gitter Wechselwirkung und ihre mögliche Beteiligung an dem Auftreten von Ferroelektrizität und Antiferromagnetismus in diesen Substanzen zu untersuchen. Des weiteren wird die Spin-Gitter Wechselwirkung in der monoklinischen, multiferroischen Substanz  $\text{MnWO}_4$  mit Hilfe eines verallgemeinerten Drude-Lorentz Modells analysiert. Daran anschließend wird, aufgrund der besonderen optischen Eigenschaften, eine Analyse der Phononen von monoklinischem  $\text{BiB}_3\text{O}_6$  vorgestellt. Abschließend folgt die Untersuchung des anormalen, antiferromagnetischen Metalloxids  $\text{CaCrO}_3$ , welches eine Ausnahme der Regel darstellt, nach der in Übergangsmetalloxiden Ferromagnetismus mit metallischer Leitfähigkeit und Antiferromagnetismus mit isolierendem Verhalten korreliert.



## Bibliography

- [1] E. Wigner, *Einige Folgerungen aus der Schrödingerschen Theorie für die Termstrukturen*, Z. Physik **43**, 624 (1927)
- [2] C. Eckart, *The Application of Group theory to the Quantum Dynamics of Monatomic Systems*, Rev. Mod. Phys. **2**, 305 (1930)
- [3] G. Racah, *Theory of Complex Spectra I*, Phys. Rev. **61**, 186 (1942)
- [4] G. Racah, *Theory of Complex Spectra II*, Phys. Rev. **62**, 438 (1942)
- [5] G. Racah, *Theory of Complex Spectra III*, Phys. Rev. **63**, 367 (1943)
- [6] G. Racah, *Theory of Complex Spectra VI*, Phys. Rev. **76**, 1352 (1949)
- [7] R. D. Cowan, *The Theory of Atomic Structure and Spectra*, University of California Press, Berkeley (1981)
- [8] R. P. Gupta, S. K. Sen, *Crystal Field Theory and Calculations of the Inner Shell Vacancy Levels*, in W. Dekeyser, L. Fiermans, G. Vanderkelen, J. Vennik, *Electron Emission Spectroscopy*, D. Reidel Publishing Company, Dordrecht-Holland (1972)
- [9] G. Grenet *et al.*, *Interpretation of  $3d^N$ -ion photoemission spectra. II. A general formalism for the core levels*, Phys. Rev. B **24**, 2349 (1981)
- [10] P. P. Ewald, *Die Berechnung optischer und elektrostatischer Gitterpotentiale*, Ann. Phys. **64**, 253 (1921)
- [11] J. C. Slater, G. F. Koster, *Simplified LCAO Method for the Periodic Potential Problem*, Phys. Rev. B **94**, 1498 (1954)
- [12] I. I. Sobel'man, *Introduction to the Theory of Atomic Spectra*, Pergamon Press, Oxford (Englische Version 1969)
- [13] J. Zaanen, G. A. Sawatzky, J. W. Allen, Phys. Rev. Lett. **55**, 418 (1985)
- [14] N. F. Hubbard, Proc. Phys. Soc., London, Sect. A **62**, 416 (1949)
- [15] D. R. Hartree, *The Calculation of Atomic Structures*, John Wiley, New York, (1957)
- [16] M. Born, R. Oppenheimer, *Zur Quantentheorie der Molekülen*, Ann. d. Physik **84**, 457 (1927)

- [17] W. A. Fock, *Näherungsmethode zur Lösung des quantenmechanischen Mehrkörperproblems*, Z. Phys. **61**, 126 (1930)
- [18] W. A. Fock, “*Selfconsistent field*” mit Austausch für Natrium, Z. Phys. **62**, 795 (1930)
- [19] W. A. Fock, M. J. Petrashen, Physik. Z. Sowjetunion **6**, 368 (1934)
- [20] C. C. J. Roothaan, *New Developments in Molecular Orbital Theory*, Rev. Mod. Phys. **23**, 69 (1951)
- [21] G. G. Hall, *The molecular orbital theory of chemical valency. VIII - A Method of calculating ionization potentials*, Proc. Roy. Soc. [London] **A205**, 541 (1951)
- [22] T. Koopmans, *Über die Zuordnung von Wellenfunktionen und Eigenwerten zu den Einzelnen Elektronen Eines Atoms*, Physica **1**, 104 (1934)
- [23] D. R. Hartree, Proc. Cambridge Phil. Soc. **24**, 111 (1928)
- [24] B. Numerov, Publ. Observ. Central Astrophys. Russ. **2**, 188 (1933)
- [25] R. D. Cowan, *Atomic Self-Consistent-Field Calculations Using Statistical Approximations for Exchange and Correlation*, Phys. Rev. **163**, 54 (1967)
- [26] J. C. Slater, *A Simplification of the Hartree-Fock Method*, Phys. Rev. **81**, 385 (1951)
- [27] F. Herman, S. Skillman, *Atomic Structure Calculations*, Prentice-Hall, Englewood Cliffs, N. J. (1963)
- [28] “<http://vergil.chemistry.gatech.edu/notes/ci/node5.html>”, call February 22<sup>nd</sup> (2009)
- [29] “<http://vergil.chemistry.gatech.edu/notes/ci/node20.html>”, call February 22<sup>nd</sup> (2009)
- [30] “<http://vergil.chemistry.gatech.edu/notes/ci/node17.html>”, call February 24<sup>th</sup> (2009)
- [31] W. Heisenberg, *Über quantentheoretische Umdeutung kinematischer und mechanischer Beziehungen*, Z. Phys. **33**, 879 (1925)
- [32] E. Schrödinger, *Über das Verhältnis der Heisenberg-Born-Jordanschen Quantenmechanik zu der meinen*, Ann. d. Phys. **79**, 734 (1926)
- [33] C. Eckart, *Operator Calculus and the Solution of the Equations of Quantum Dynamics*, Phys. Rev. **28**, 711 (1926)
- [34] A. Szabo, N. S. Ostlund, *Modern Quantum Chemistry: Introduction to Advanced Electronic Structure Theory*, McGraw-Hill, New York, (1989)

- 
- [35] J. Paldus, *Group theoretical approach to the configuration interaction and perturbation theory calculations for atomic and molecular systems*, J. Chem. Phys. **61**, 5321 (1974)
- [36] P. E. M. Siegbahn, *The direct CI method*, in *Methods in Computational Molecular Physics*, edited by G. H. F. Diercksen and S. Wilson, pages 189-207, D. Reidel, Dordrecht, (1983)
- [37] J. K. L. MacDonald, *Successive Approximations by the Rayleigh-Ritz Variation Method*, Phys. Rev. **43**, 830 (1933)
- [38] E. A. Hylleraas, B. Undheim, *Numerische Berechnung der 2S-Terme von Ortho- und Par-Helium*, Z. Phys. **65**, 759 (1930)
- [39] L. Brillouin, J. Phys. **3**, 373 (1932)
- [40] W. Duch, G. H. F. Diercksen, *Size-extensivity corrections in configuration interaction methods*, J. Chem. Phys. **101**, 3018 (1994)
- [41] S. R. Langhoff, E. R. Davidson, *Configuration interaction calculations on the nitrogen molecule*, Int. J. Quantum Chem. **8**, 61 (1974)
- [42] “<http://faculty.ccbcmd.edu/~bhoffm30/instructional/ci/node12.htm>”, call February 22<sup>nd</sup> (2009)
- [43] H. N. Russell, F. A. Saunders, *New Regularities in the Spectra of the Alkaline Earths*, Astrophys. J. **61**, 38 (1925)
- [44] L. Armstrong, Jr., *Matrix Elements Between Configurations Having Several Open Shells. II*, Phys. Rev. **172**, 18 (1968)
- [45] C. W. Nielson, G. F. Koster, *Spectroscopic Coefficients for the  $p^n$ ,  $d^n$  and  $f^n$  Configurations*, The M.I.T. Press, Cambridge (1963)
- [46] R. D. Cowan, *Theoretical Calculation of Atomic Spectra Using Digital Computers*, J. Opt. Soc. Am. **58**, 808 (1968)
- [47] J. C. Slater, *The Theory of Complex Spectra*, Phys. Rev. **34**, 1293 (1929)
- [48] E. U. Condon, *The Theory of Complex Spectra*, Phys. Rev. **36**, 1121 (1930)
- [49] U. Fano, *Interaction between Configurations with Several Open Shells*, Phys. Rev. **140**, A67 (1965)
- [50] E. U. Condon, G. H. Shortley, *The Theory of Atomic Spectra*, Cambridge at the University Press (1967)
- [51] J. C. Slater, *Quantum Theory of Atomic Structure Volume II*, McGraw-Hill Book Company, Inc., New York (1960)

- [52] U. Fano, G. Racah, *Irreducible Tensorial Sets*, Academic Press, Inc., New York (1959)
- [53] A. R. Edmonds, *Drehimpulse in der Quantenmechanik*, B.I-Hochschultaschenbücherverlag (1960)
- [54] A. Messiah, *Quantum Mechanics Volume II*, North-Holland Publishing Company, Amsterdam, 8th Printing (1976)
- [55] J. A. Gaunt, *The Triplets of Helium*, Phil. Trans. Roy. Soc. London **A228**, 192 (1929)
- [56] K. Rajnak, B. G. Wybourne, *Configuration Interaction Effects in  $l^N$  Configurations*, Phys. Rev **132**, 280 (1963)
- [57] K. Rajnak, B. G. Wybourne, *Electrostatically Correlated Spin-Orbit Interactions in  $l^N$ -Type Configurations*, Phys. Rev **134**, A596 (1964)
- [58] B. G. Wybourne, *Generalization of the "Linear Theory" of Configuration Interaction*, Phys. Rev **137**, A364 (1965)
- [59] G. Racah, J. Stein, *Effective Electrostatic Interactions in  $l^N$  Configurations*, Phys. Rev. **156**, 58 (1967)
- [60] B. G. Wybourne, *Spectroscopic Properties of the Rare Earths*, Interscience, New York, (1965)
- [61] S. Sugano, Y. Tanabe, and H. Kamimura, *Multiplets of Transition-Metal Ions in Crystals* (Academic Press, INC., New York and London, 1970)
- [62] M. W. Haverkort, *Spin and orbital degrees of freedom in transition metal oxides and oxide thin films studied by soft x-ray absorption spectroscopy*, Universität zu Köln (2005)
- [63] E. Müller-Hartmann, *Theoretische Festkörperphysik I*, (1998)
- [64] P. R. Wallace, *Mathematical Analysis of Physical Problems*, Dover, New York, (1984)
- [65] J. Huang, *Integral representations of harmonic lattice sums*, J. Math. Phys. **40**, 5240 (1999)
- [66] T. Mayer-Kuckuk, *Atomphysik*, Teubner Verlag, (1997)
- [67] L. H. Thomas, *The motion of the spinning electron*, Nature **117**, 514 (1926)
- [68] "[http://www.ece.ucsb.edu/faculty/Kroemer/pubs/13\\_04Thomas.pdf](http://www.ece.ucsb.edu/faculty/Kroemer/pubs/13_04Thomas.pdf)", call February 22<sup>nd</sup> (2009)

- 
- [69] F. Bloch, *Über die Quantenmechanik der Elektronen in Kristallgittern.*, Z. Phys. **52**, 555 (1928)
- [70] W. M. C. Foulkes, R. Haydock, *Tight-binding models and density-functional theory*, Phys.Rev. B **39**, 12520 (1989)
- [71] P. O. Löwdin, *On the Non-Orthogonality Problem Connected with the Use of Atomic Wave Functions in the Theory of Molecules and Crystals*, J. Chem. Phys. **18**, 365 (1950)
- [72] P. Hohenberg, W. Kohn *Inhomogeneous Electron Gas*, Phys. Rev. **136**, B864 (1964)
- [73] W. Kohn, L. J. Sham *Self-Consistent Equations Including Exchange and Correlation Effects*, Phys. Rev. **140**, A1133 (1965)
- [74] D. A. Papaconstantopoulos *Handbook of Electronic Structure of Elemental Solids*, New York: Plenum (1986)
- [75] J. L. Jr. Mercer, M. Y. Chou, *Tight-binding model with intra-atomic matrix elements*, Phys. Rev. B **49**, 8506 (1994)
- [76] R. E. Cohen, L. Stixrude, E. Wasserman, *Tight-binding computations of elastic anisotropy of Fe, Xe, and Si under compression*, Phys. Rev. B **56**, 8575 (1997)
- [77] L. F. Mattheiss, *Electronic Structure of the 3d Transition-Metal Monoxides. I. Energy-Band Results*, Phys. Rev. B **5**, 290 (1972)
- [78] R. R. Sharma, *General expressions for reducing the Slater-Koster linear combination of atomic orbitals integrals to the two-center approximation*, Phys. Rev. B **19**, 2813 (1978)
- [79] W. A. Harrison, *Elementary Electronic Structure*, World Scientific, Singapore (1999)
- [80] J. M. Willis, W. A. Harrison, *Interionic interactions in transition metals*, Phys. Rev. B **28**, 4363 (1983)
- [81] I. I. Sobel'man, *Atomic Spectra and Radiative Transitions*, Springer Verlag, Berlin (1979)
- [82] M.-A. Arrio *et al.*, *Calculation of multipole transitions at the Fe K pre-edge through  $p - d$  hybridization in the Ligand Field Multiplet model*, Europhys. Lett. **51**, 4 (2000)
- [83] P. M. Levy, *Anisotropy in Two-Center Exchange Interactions*, Phys. Rev. **177**, 509 (1968)

- [84] H. J. Silverstone, *Expansion about an Arbitrary Point of Three-Dimensional Functions Involving Spherical Harmonics by the Fourier-Transform Convolution Theorem*, J. Chem. Phys. **47**, 537 (1967)
- [85] J. Stark, Sitzber. preuss. Akad. Wiss. Berlin, 932 (1913), Ann. Physik **43**, 965 (1914)
- [86] P. Zeeman, Versl. Akad. Wet. Amsterdam 5, 242 (1896), Phil. Mag. **43**, 226 (1897)
- [87] C. M. Fowler, *Megagauss Physics*, Science **180**, 261 (1973)
- [88] M. Dressel, G. Grüner *Electrodynamics of Solids*, Cambridge University Press, Cambridge (2002)
- [89] H. A. Kramers, Nature **117**, 775 (1926); H. A. Kramers *Estratto dagli Atti del Confr. Int. Fis.*, Vol. 2 (Zanichelli, Bologna, 1927), p. 545; *Collected Scientific Papers* (North Holland, Amsterdam, 1956)
- [90] R. de L. Kronig, *The theory of dispersion of x-rays*, J. Opt. Soc. Am. **12**, 547 (1926); *Ned. Tijdschr. Natuurk.* **9**, 402 (1942)
- [91] R. Kubo, *Statistical-Mechanical Theory of Irreversible Processes*, J. Phys. Soc. Jpn. **12**, 570 (1957)
- [92] D. A. Greenwood, *The Boltzmann Equation in the Theory of Electrical Conduction in Metals*, Proc. Phys. Soc. London **71**, 585 (1958)
- [93] I. Paul, G. Kotliar, *Thermal transport for many-body tight-binding models*, Phys. Rev. B **67**, 115131 (2003)
- [94] S. Kumar, P. Majumdar, *Anti-localisation to strong localisation: The interplay of magnetic scattering and structural disorder*, Europhys. Lett. **65**, 75 (2004)
- [95] E. Dagotto, *Correlated electrons in high-temperature superconductors*, Rev. Mod. Phys. **66**, 763 (1994)
- [96] E. Müller-Hartmann, *Theoretische Festkörperphysik II*, (2006)
- [97] M. Born, K. Huang, *Dynamical Theory of Crystal Lattices*, Oxford University Press Oxford, (1954)
- [98] R. M. Martin, *Electronic Structure*, Cambridge University Press (2004)
- [99] W. H. Press, S. A. Teukolsky, W. T. Vetterling, B. P. Flannery, *Numerical Recipes in Fortran 77* Cambridge University Press, Cambridge (2001)
- [100] N. Greif, H. Schrepf, *Richtlinie für die Programmierung in Fortran*, Physikalisch-Technische Bundesanstalt, (2002)
- [101] “<http://das101.isan.troitsk.ru/cowan.htm>”, call September 6<sup>th</sup>, (2007)

- 
- [102] C. Lanczos, *An iterative method for the solution of the eigenvalue problem of linear differential and integral operators*, J. Res. Nat. Bur. Stand. **45**, 255 (1950)
- [103] “[http://en.wikipedia.org/wiki/Lanczos\\_algorithm](http://en.wikipedia.org/wiki/Lanczos_algorithm)”, call February 22<sup>nd</sup>, (2009)
- [104] R. B. Lehoucq, D. C. Sorensen, C. Yang, *ARPACK Users’ Guide: Solution of Large-Scale Eigenvalue Problems with Implicitly Restarted Arnoldi Methods*, “<http://www.caam.rice.edu/software/ARPACK/UG/ug.html#ARPACK%20Users%20Guide>”, call September 6<sup>th</sup>, (2007)
- [105] D. Calvetti, L. Reichel, D. C. Sorensen *An Implicitly Restarted Lanczos Method for Large Symmetric Eigenvalue Problems*, Electronic Transactions on Numerical Analysis. **2**, 1 (1994)
- [106] “<http://www.caam.rice.edu/software/ARPACK/>”, call September 6<sup>th</sup>, (2007)
- [107] “<http://www.netlib.org/lapack/>”, call February 22<sup>nd</sup> (2009)
- [108] “<http://www.netlib.org/blas/>”, call February 22<sup>nd</sup> (2009)
- [109] P. B. Fellgett, PhD thesis, University of Cambridge (1949)
- [110] A. A. Michelson, *Studies In Optics*, University of Chicago Press: Chicago (1927)
- [111] R. Bracewell, *The Fourier Transform and Its Applications*, 3rd ed. New York: McGraw-Hill, pp. 108-112, (1999)
- [112] “[http://en.wikipedia.org/wiki/Nyquist%E2%80%93Shannon\\_sampling\\_theorem](http://en.wikipedia.org/wiki/Nyquist%E2%80%93Shannon_sampling_theorem)”, “[http://en.wikipedia.org/wiki/Sampling\\_rate](http://en.wikipedia.org/wiki/Sampling_rate)”, call February 22<sup>nd</sup> (2009)
- [113] L. Mertz, *Auxiliary computation for Fourier spectrometry*, Infrared Phys. **7**, 17 (1967)
- [114] F. Wooten, *Optical properties of solids*, Academic Press, New York, (1972)
- [115] A. B. Kuz’menko, R. Tediosi, private communication, (2007)
- [116] E. Benckiser *et al.*, *Collective orbital excitations in orbitally ordered YVO<sub>3</sub> and HoVO<sub>3</sub>*, New J. Phys. **10**, 053027 (2008)
- [117] K. I. Kugel and D. I. Khomskii, Sov. Phys.–JETP **37**, 725 (1973)
- [118] H. A. Jahn and E. Teller, *Stability of Polyatomic Molecules in Degenerate Electronic States*, Proc. R. Soc. A **161**, 220 (1937)
- [119] C. F. Ballhausen, *Introduction to Ligand Field Theory*, (New York:McGraw-Hill) (1962)
- [120] R. Rückamp *et al.*, *Optical study of orbital excitations in transition-metal oxides*, New J. Phys. **7**, 144 (2005)

- [121] S. Ishihara and S. Maekawa, *Theory of orbital excitation and resonant inelastic x-ray scattering in manganites*, Phys. Rev. B **62**, 2338 (2000)
- [122] R. Rückamp *et al.*, *Zero-Field Incommensurate Spin-Peierls Phase with Inter-chain Frustration in TiOCl*, Phys. Rev. Lett. **95**, 097203 (2005)
- [123] A. Komarek, private communication, (2008); A. Komarek *et al.*, *Strong magnetoelastic coupling in VOCl: Neutron and synchrotron powder x-ray diffraction study*, Phys. Rev. B **79**, 104425 (2009)
- [124] E. Benckiser, *Optical Spectroscopy of Orbital and Magnetic Excitations in Vanadates and Cuprates*, Ph.D. thesis, University of Cologne, Germany (2007).
- [125] P. Ehrlich, H.-J. Seifert, *Über Vanadinchloride*, Z. Allg. Anorg. Chem. **301**, 282 (1959)
- [126] A. Haase, G. Brauer, *Vanadium Oxychloride*, Acta. Cryst. B **31**, 2521 (1975)
- [127] D. Fausti *et al.*, *Symmetry disquisition on the TiOX phase diagram (X = Br, Cl)*, Phys. Rev. B **75**, 245114 (2007)
- [128] A. Wiedenmann *et al.*, *Two-dimensional behavior and magnetic ordering in the layered compound VOCl*, J. Magn. Magn. Mater. **45**, 275 (1984)
- [129] J. P. Venien *et al.*, *Vanadium (III) oxychloride: magnetic, optical and electrical properties; lithium and molecular intercalations*, Mat. Res. Bull. **14**, 891 (1979)
- [130] “<http://mathworld.wolfram.com/SymmetryOperation.html>”, call February 19<sup>th</sup>, (2009)
- [131] “<http://ww1.iucr.org/comm/cteach/pamphlets/22/node22.html>”, call February 19<sup>th</sup>, (2009)
- [132] “<http://www.gps.caltech.edu/~gab/ch21b/lectures/lecture08.pdf>”, call July 18<sup>th</sup>, (2008)
- [133] A. Wiedenmann *et al.*, *Magnetic ordering of the quasi-two-dimensional system*, J. Phys. C: Solid State Phys. **16**, 5339 (1983)
- [134] R. J. Beynon and J. A. Wilson, *TiOCl, TiOBr-are these RVB  $d^1$ ,  $S = \frac{1}{2}$  materials? The results of scandium substitution set in the context of other  $S = \frac{1}{2}$  systems of current interest for high-temperature superconductivity and the metal-insulator transition*, J. Phys.: Condens. Matter **5**, 1983 (1993)
- [135] R. Rückamp, *Orbital excitations of transition-metal oxides in optical spectroscopy*, PhD thesis, University of Cologne, (2006)
- [136] M. Grüninger *et al.*, *Magnetic excitations in two-leg spin 1/2 ladders: experiment and theory*, J. Phys. Chem. Sol. **63**, 2167 (2002)

- 
- [137] T. Hahn, *International Tables for Crystallography, Volume A: Space Group Symmetry*, Springer Netherlands (2002)
- [138] R. L. Greene *et al.*, *Observation of a spin-wave sideband in the optical spectrum of MnF<sub>2</sub>*, Phys. Rev. Lett. **15**, 656 (1965)
- [139] J. Woods Halley, I. Silvera, *Odd-Exciton Magnon Interaction and Explanation of Anomalous Far-Infrared Absorption in Antiferromagnetic FeF<sub>2</sub>*, Phys. Rev. Lett. **15**, 654 (1965)
- [140] R. Bhandari, L. M. Falicov, *Theory of the magnon sidebands in optical transitions of antiferromagnetic insulators*, J. Phys. C: Sol. State Phys. **5**, 1445 (1972)
- [141] M. Gerloch, E. C. Constable, *Transition Metal Chemistry*, (VCH Weinheim, 1994)
- [142] D. R. Wood, K. L. Andrew, *Zeeman Effect and Intensity Anomalies in PbI*, J. Opt. Soc. Am. **58**, 818 (1968)
- [143] J. Franck, *Elementary Processes of Photochemical Reactions*, Trans. Faraday Soc. **21**, 536 (1926)
- [144] E. Condon, *A Theory of Intensity Distribution in Band Systems*, Phys. Rev. **28**, 1182 (1926)
- [145] E. Condon, *Nuclear Motions Associated with Electron Transitions in Diatomic Molecules*, Phys. Rev. **32**, 858 (1928)
- [146] A. S. Coolidge *et al.*, *A Study of the Franck-Condon Principle*, The J. Chem. Phys. **3**, 193 (1936)
- [147] Y. Tanabe, S. Sugano, *On the Absorption Spectra of Complex Ions. I*, J. Phys. Soc. Japan **9**, 753 (1954)
- [148] R. J. Lancashire, "<http://wwwchem.uwimona.edu.jm:1104/courses/Tanabe-Sugano/TSSpread.html>", call July 17<sup>th</sup>, (2008)
- [149] D. M. Brink, G. R. Satchler, *Angular Momentum in Quantum Mechanics Third Edition*, Clarendon Press, Oxford (1993)
- [150] M. Fiebig, *Revival of the magnetoelectric effect*, J. Phys. D **38**, R123 (2005)
- [151] W. Prellier *et al.*, *The single-phase multiferroic oxides: from bulk to thin film*, J. Phys.: Condens. Matter **17**, R803 (2005)
- [152] M. N. Iliev *et al.*, *Raman- and infrared-active phonons in hexagonal YMnO<sub>3</sub>: Experiment and lattice-dynamical calculations*, Phys. Rev. B **56**, 2488 (1997)
- [153] D. Fröhlich *et al.*, *Nonlinear Optical Spectroscopy of the Two-Order-Parameter Compound YMnO<sub>3</sub>*, Phys. Rev. Lett. **81**, 3239 (1998)

- [154] M. Fiebig *et al.*, *Observation of coupled magnetic and electric domains*, Nature (London) **419**, 818 (2002)
- [155] T. Katsufuji *et al.*, *Dielectric and magnetic anomalies and spin frustration in hexagonal RMnO<sub>3</sub> (R=Y, Yb, and Lu)*, Phys. Rev. B **64**, 104419 (2001)
- [156] P. A. Sharma *et al.*, *Thermal Conductivity of Geometrically Frustrated, Ferroelectric YMnO<sub>3</sub>: Extraordinary Spin-Phonon Interactions*, Phys. Rev. Lett. **93**, 177202 (2004)
- [157] T. Kimura *et al.*, *Magnetic control of ferroelectric polarization*, Nature (London) **426**, 55 (2003)
- [158] T. Goto *et al.*, *Ferroelectricity and Giant Magnetocapacitance in Perovskite Rare-Earth Manganites*, Phys. Rev. Lett. **92**, 257201 (2004)
- [159] H. L. Yakel, *On the Structures of some Compounds of the Perovskite Type*, Acta Cryst. **8**, 394 (1955)
- [160] A. P. Ramirez, *Colossal magnetoresistance*, J. Phys. Condens. Matter **9**, 8171 (1997)
- [161] M. Mostovoy, *Helicoidal Ordering in Iron Perovskites*, Phys. Rev. Lett. **94**, 137205 (2005)
- [162] H. Katsura *et al.*, *Spin Current and Magnetoelectric Effect in Noncollinear Magnets*, Phys. Rev. Lett. **95**, 057205 (2005)
- [163] I. A. Sergienko, E. Dagotto, *Role of the Dzyaloshinskii-Moriya interaction in multiferroic perovskites*, Phys. Rev. B **73**, 094434 (2006)
- [164] J. A. S. Barker, *Temperature Dependence of the Transverse and Longitudinal Optic Mode Frequencies and Charges in SrTiO<sub>3</sub> and BaTiO<sub>3</sub>*, Phys. Rev. **145**, 391 (1966)
- [165] H. L. Yakel *et al.*, *On the Crystal Structure of the Manganese (III) Trioxides of the Heavy Lanthanides and Yttrium\**, Acta Cryst. **16**, 957 (1963)
- [166] T. Katsufuji *et al.*, *Crystal structure and magnetic properties of hexagonal RMnO<sub>3</sub> (R = Y, Lu, and Sc) and the effect of doping*, Phys. Rev. B **66**, 134434 (2002)
- [167] J-C. Peuzin, C. R. Acad. Sc. Paris **261**, 2195 (1965)
- [168] A. A. Nugroho *et al.*, *Enhancing the magnetoelectric coupling in YMnO<sub>3</sub> by Ga doping*, Phys. Rev. B **75**, 174435 (2007)
- [169] U. Adem *et al.*, *Ferroelectric displacements in multiferroic Y(Mn,Ga)O<sub>3</sub>*, Phys. Rev. B **75**, 014108 (2007)

- 
- [170] E. F. Bertraut *et al.*, *Compt. Rend.* **256**, 1958 (1963)
- [171] B. B. van Aken *et al.*, *The origin of ferroelectricity in magnetoelectric YMnO<sub>3</sub>*, *Nat. Mater.* **3**, 164 (2004)
- [172] C. J. Fennie, K. M. Rabe, *Ferroelectric transition in YMnO<sub>3</sub> from first principles*, *Phys. Rev. B* **72**, 100103(R) (2005)
- [173] N. A. Hill, A. Filippetti, *Why are there any magnetic ferroelectrics?*, *J. Magn. Magn. Mater.* **242-245**, 976 (2002)
- [174] N. A. Spandin, W. E. Pickett, *Computational design of multifunctional materials*, *J. Solid State Chem.* **176**, 615 (2003)
- [175] G. Nénert *et al.*, *Experimental evidence for an intermediate phase in the multiferroic YMnO<sub>3</sub>*, cond-mat/0601547 (2005)
- [176] K. Lukaszewicz, J. Karut-Kalicińska, *X-ray investigations of the crystal structure and phase transitions of YMnO<sub>3</sub>*, *Ferroelectrics* **7**, 81 (1974)
- [177] T. Lonkai *et al.* *Development of the high-temperature phase of hexagonal manganites*, *Phys. Rev. B* **69**, 134108 (2004)
- [178] S. Geller *et al.*, *The Crystal Structure of a New High-Temperature Modification of YGaO<sub>3</sub>*, *Acta Crystallogr., Sect. B: Struct. Crystallogr. Cryst. Chem.* **B31**, 2770 (1975)
- [179] H. D. Zhou *et al.*, *Effect of Ga doping on the multiferroic properties of RMn<sub>1-x</sub>Ga<sub>x</sub>O<sub>3</sub> (R = Ho, Y)*, *Phys. Rev. B* **72**, 224401 (2005)
- [180] S. C. Abrahams, *Ferroelectricity and structure in the YMnO<sub>3</sub> family*, *Acta Crystallogr., Sect. B: Struct. Sci.* **B57**, 485 (2001)
- [181] S. Bhagavantum, T. Venkatarayudu, *Proc. Indian Acad. Sci. Sect A* **9**, 224 (1939)
- [182] S. Bhagavantum, *Proc. Indian Acad. Sci. Sect A* **13**, 543 (1941)
- [183] S. Bhagavantum, T. Venkatarayudu, *Theory of Groups and Its Application to Physical Problems*, Audhra University, Waltair, India (1962)
- [184] D. L. Rousseau *et al.*, *Normal Mode Determination in Crystals*, *J. Raman Spectrosc.* **10**, 253 (1981)
- [185] A. M. Schönflies, *Krystallsysteme und Krystallstruktur*, Leipzig (B. G. Teubner), 1891
- [186] Hermann, C. (Hrsg.), *Internationale Tabellen zur Bestimmung von Kristallstrukturen*, Berlin (Gebr. Borntraeger), (1935)

- [187] E.B. Wilson, Jr., J.C. Decius, and P.C. Cross, *Molecular Vibrations*, (McGraw-Hill, New York, 1955)
- [188] A. B. Kuz'menko *et al.*, *Infrared spectroscopic study of CuO: Signatures of strong spin-phonon interaction and structural distortion*, Phys. Rev. B **63**, 094303 (2001);  
A. B. Kuz'menko *et al.*, *Transverse optic modes in monoclinic  $\alpha$ -Bi<sub>2</sub>O<sub>3</sub>*, J. Phys.: Condens. Matter **8**, 6199 (1996)
- [189] D. Senff, private communication, (2008)
- [190] K. Taniguchi *et al.*, *Ferroelectric Polarization Flop in a Frustrated Magnet MnWO<sub>4</sub> Induced by a Magnetic Field*, Phys. Rev. Lett. **97**, 097203 (2006)
- [191] K. Taniguchi *et al.*, *Magnetic-field dependence of the ferroelectric polarization and spin-lattice coupling in multiferroic MnWO<sub>4</sub>*, Phys. Rev. B **77**, 064408 (2008)
- [192] A. W. Sleight, *Accurate cell dimensions for ABO<sub>4</sub> molybdates and tungstates*, Acta Cryst. B **28**, 2899 (1972).
- [193] H. Weitzel, *Two antiferromagnetic phases in mixed crystals (Mn<sub>1-x</sub>, Fe<sub>x</sub>) WO<sub>4</sub>*, Solid State Commun. **7**, 1249 (1969)
- [194] H. Kuzmany, *Solid-State Spectroscopy*, Springer, (1998)
- [195] G. Lautenschläger *et al.*, *Magnetic phase transitions of MnWO<sub>4</sub> studied by the use of neutron diffraction*, Phys. Rev. B **48**, 6087 (1993)
- [196] P. Becker-Bohatý, private communication, (2008)
- [197] C. Landee *et al.*, *Thermophysical measurements on transition-metal tungstates, III. Heat capacity of antiferromagnetic manganese tungstate*, J. Chem. Thermodynamics **8**, 663 (1976)
- [198] H. Dachs, *Zur Deutung der magnetischen Struktur des Hübernits, MnWO<sub>4</sub>*, Solid State Commun. **7**, 1015 (1969)
- [199] A. H. Arkenbout *et al.*, *Ferroelectricity in the cycloidal spiral magnetic phase of MnWO<sub>4</sub>*, Phys. Rev. B **74**, 184431 (2006)
- [200] M. Mostovoy, *Ferroelectricity in Spiral Magnets*, Phys. Rev. Lett. **96**, 067601 (2006)
- [201] O. Heyer *et al.*, *A new multiferroic material: MnWO<sub>4</sub>*, J. Phys.: Condens. Matter **18**, L471 (2006)
- [202] H. Katsura *et al.*, *Spin Current and Magnetoelectric Effect in Noncollinear Magnets*, Phys. Rev. Lett. **95**, 057205 (2005)
- [203] Y. Aharonov, A. Casher, *Topological Quantum Effects for Neutral Particles*, Phys. Rev. Lett. **53**, 319 (1984)

- 
- [204] I. A. Sergienko, E. Dagotto, *Role of the Dzyaloshinskii-Moriya interaction in multiferroic perovskites*, Phys. Rev. B **73**, 094434 (2006)
- [205] I. Dzyaloshinsky, *A thermodynamic theory of “weak” ferromagnetism of antiferromagnetics*, J. Phys. Chem. Solids **4**, 241 (1958)
- [206] T. Moriya, *Anisotropic Superexchange Interaction and Weak Ferromagnetism*, Phys. Rev. **120**, 91 (1960)
- [207] A. Gössling, *Electronic structure of Titanates and layered Manganites probed by optical spectroscopy*, PhD thesis, University of Cologne, (2007)
- [208] T. Ejima *et al.*, *Microscopic optical and photoelectron measurements of  $MWO_4$  ( $M = Mn, Fe, \text{ and } Ni$ )*, J. Luminescence **119-120**, 59 (2006)
- [209] A. Nogami *et al.*, *Second Harmonic Generation from Multiferroic  $MnWO_4$* , J. Phys. Soc. Jpn. **77**, 115001 (2008)
- [210] J. van Elp *et al.*, *Electronic structure of  $MnO$* , Phys. Rev. B **44**, 1530 (1991)
- [211] L. E. Orgel, J. Chem. Phys. **23**, 1004 (1955)
- [212] B. Fromme *et al.*,  *$d - d$  excitations and interband transitions in  $MnO$ : A spin-polarized electron-energy-loss study*, Phys. Rev. B **58**, 9783 (1998)
- [213] R. N. Iskenderov *et al.*, Sov. Phys. Solid State **10**, 2031 (1969)
- [214] G. W. Pratt, Jr., R. Coelho, *Optical Absorption of  $CoO$  and  $MnO$  above and below the Néel Temperature*, Phys. Rev. **116**, 281 (1959)
- [215] D. R. Huffman *et al.*, *Optical Absorption Spectra of Crystal-Field Transitions in  $MnO$* , J. Chem. Phys. **50**, 4092 (1969)
- [216] J. P. Kemp *et al.*, *High-resolution electron energy loss studies of some transition metal oxides*, J. Phys.: Condens. Matter **1**, 5313 (1989)
- [217] S.-P. Jeng, V. E. Henrich, *interference between  $3d \rightarrow 3d$  electron-exchange transitions and interband excitations in  $MnO$  (100)*, Solid State Commun. **82**, 879 (1992)
- [218] W. L. Roth, *Magnetic Structures of  $MnO$ ,  $FeO$ ,  $CoO$ , and  $NiO$* , Phys. Rev. **110**, 1333 (1958).
- [219] B. Morosin, *Exchange Striction Effects in  $MnO$  and  $MnS$* , Phys. Rev. B **1**, 236 (1970)
- [220] D. M. Sherman, Am. Mineral. **69**, 788 (1984)
- [221] L. Messick *et al.*, *Direct and Temperature-Modulated Reflectance Spectra of  $MnO$ ,  $CoO$ , and  $NiO$* , Phys. Rev. B **6**, 3941 (1972)

- [222] J. Hugel, C. Carabatos, *Band structure and optical properties of MnO*, Solid State Commun. **60**, 369 (1986)
- [223] L. F. Mattheiss, *Electronic Structure of the 3d Transition-Metal Monoxides. II. Interpretation*, Phys. Rev. B **5**, 306 (1972)
- [224] J. van Elp *et al.*, *Electronic structure of CoO, Li-doped CoO, and LiCoO<sub>2</sub>*, Phys. Rev. B **44**, 6090 (1991)
- [225] Ghiringhelli *et al.*, *Resonant inelastic x-ray scattering of MnO: L<sub>2,3</sub> edge measurements and assessment of their interpretation*, Phys. Rev. B **73**, 035111 (2006)
- [226] F. Müller, S. Hufner, *Angle-resolved electron energy-loss spectroscopy investigation of crystal-field transitions on MnO and NiO surfaces: Exchange scattering versus direct scattering*, Phys. Rev. B **78**, 085438 (2008)
- [227] R. C. Powell *et al.*, *Optical spectroscopy of Mn<sub>2</sub>SiO<sub>4</sub> crystals*, J. Chem. Phys. **84**, 657 (1986)
- [228] H.-L. Park *et al.*, *Transition Behavior of Mn<sup>2+</sup> - and Ni<sup>2+</sup>-Doped ZnGa<sub>2</sub>S<sub>4</sub> Crystals*, phys. stat. sol. (b) **180**, K69 (1993)
- [229] J. W. Stout, *Absorption Spectrum of Manganous Fluoride*, J. Chem. Phys. **31**, 709 (1959)
- [230] T. Tsuboi, P. Ahmet, *Temperature dependence of the optical exciton-magnon absorption lines in MnF<sub>2</sub> crystals*, Phys. Rev. B **45** 468 (1991)
- [231] D. D. Sell *et al.*, *Optical Exciton-Magnon Absorption in MnF<sub>2</sub>*, Phys. Rev. **158**, 489 (1966)
- [232] I. Pollini *et al.*, *Vibrational structure of crystal-field spectra in layered 3d-metal dihalides*, Phys. Rev. B **22**, 6369 (1979)
- [233] H. Hellwig *et al.*, *Exceptional large nonlinear optical coefficients in the monoclinic bismuth borate BiB<sub>3</sub>O<sub>6</sub> (BIBO)*, Solid State Commun. **109**, 249 (1999)
- [234] H. Hellwig *et al.*, *Linear optical properties of the monoclinic bismuth borate BiB<sub>3</sub>O<sub>6</sub>*, J. Appl. Phys. **88**, 240 (200)
- [235] M. Peltz *et al.*, *Bismuth triborate (BiB<sub>3</sub>O<sub>6</sub>) optical parametric oscillators*, Appl. Phys. B **80**, 55 (2005)
- [236] A. A. Kaminskii *et al.*, *Monoclinic bismuth triborate BiB<sub>3</sub>O<sub>6</sub> – a new efficient  $\chi(2)+\chi(3)$ -nonlinear crystal: multiple stimulated Raman scattering and self-sum-frequency lasing effects*, Opt. Commun. **206**, 179 (2002)
- [237] A. Gössling *et al.*, *Phonon modes of monoclinic BiB<sub>3</sub>O<sub>6</sub>*, phys. stat. sol. b **242**, R85 (2005)

- 
- [238] D. Xue *et al.*, *Origin of the Large Nonlinear Optical Coefficients in Bismuth Borate  $\text{BiB}_3\text{O}_6$* , *phys. stat. sol. a*, **176**, R1 (1999)
- [239] D. Xue *et al.*, *Nonlinear optical properties of borate crystals*, *Solid State Commun.* **114**, 21 (2000)
- [240] Z. Lin *et al.*, *Mechanism for linear and nonlinear optical effects in monoclinic bismuth borate ( $\text{BiB}_3\text{O}_6$ ) crystal*, *J. Appl. Phys.* **90**, 5585 (2001)
- [241] H. R. Xia *et al.*, *Raman scattering from bismuth triborate*, *J. Raman Spectrosc.* **33**, 278 (2002)
- [242] X. Hu *et al.*, *Raman study of phonons in bismuth triborate  $\text{BiB}_3\text{O}_6$  crystal*, *J. Appl. Phys.* **97**, 033501 (2005)
- [243] D. Kasprowicz *et al.*, *Characterization of bismuth triborate single crystal using Brillouin and Raman spectroscopy*, *Cryst. Res. Technol.* **40**, 459 (2005)
- [244] P. Becker *et al.*, *Crystal Growth and Spectroscopic Characterisation of  $\text{BiB}_3\text{O}_6:\text{RE}^{3+}$  ( $\text{RE}^{3+} = \text{Pr}^{3+}, \text{Nd}^{3+}, \text{Gd}^{3+}, \text{Er}^{3+}, \text{Tm}^{3+}$ )*, *Cryst. Res. Technol.* **36**, 27 (2001)
- [245] P. Becker *et al.*, *Top-seeded growth of bismuth triborate,  $\text{BiB}_3\text{O}_6$* , *J. Cryst. Growth* **203**, 149 (1999)
- [246] R. Fröhlich *et al.*, *Die Kristallstruktur von Wismutborat,  $\text{BiB}_3\text{O}_6$* , *Acta Cryst. C* **40**, 343 (1984)
- [247] W.-D. Stein *et al.*, *Temperature-dependent X-ray and neutron diffraction study of  $\text{BiB}_3\text{O}_6$* , *Z. Kristallogr.* **222**, 680 (2007)
- [248] W.-D. Stein, *Struktur und Gitterdynamik in azentrischen Boraten*, PhD thesis, University of Cologne, 2007
- [249] J. Yang, M. Dolg, *First-Principles Electronic Structure Study of the Monoclinic Crystal Bismuth Triborate  $\text{BiB}_3\text{O}_6$* , *J. Phys. Chem. B* **110**, 19254 (2006)
- [250] J. Yang, *Quantum Chemical Investigation of Electronic and Structural Properties of Crystalline Bismuth and Lanthanide Triborates*, PhD thesis, University of Cologne, 2007
- [251] J. B. Goodenough, *Magnetism and the Chemical Bond*, (Interscience publishers, New York-London. 1963)
- [252] J.-S. Zhou *et al.*, *Anomalous Electronic State in  $\text{CaCrO}_3$  and  $\text{SrCrO}_3$* , *Phys. Rev. Lett.* **96**, 046408 (2006)
- [253] A. J. Williams *et al.*, *Charge transfer and antiferromagnetic insulator phase in  $\text{SrRu}_{1-x}\text{Cr}_x\text{O}_3$  perovskites: Solid solutions between two itinerant electron oxides*, *Phys. Rev. B* **73**, 104409 (2006)

- [254] B. L. Chamberland, *Preparation and properties of SrCrO<sub>3</sub>*, Solid State Commun. **5**, 663 (1967)
- [255] J. B. Goodenough *et al.*, *Band antiferromagnetism and the new perovskite CaCrO<sub>3</sub>*, Mater. Res. Bull. **3**, 471 (1968)
- [256] J. F. Weiher *et al.*, *Magnetic and electrical transport properties of CaCrO<sub>3</sub>*, J. Solid State Chem. **3**, 529 (1971)
- [257] L. Ortega-San-Martin *et al.*, *Microstrain Sensitivity of Orbital and Electronic Phase Separation in SrCrO<sub>3</sub>*, Phys. Rev. Lett. **99**, 255701 (2007)
- [258] Y. Ren *et al.*, *Temperature-induced magnetization reversal in a YVO<sub>3</sub> single crystal*, Nature **396**, 441 (1998)
- [259] G. Cao *et al.*, *Thermal, magnetic, and transport properties of single-crystal Sr<sub>1-x</sub>Ca<sub>x</sub>RuO<sub>3</sub> (0 < x < 1.0)*, Phys. Rev. B **56**, 321 (1997)
- [260] J. Zaanen *et al.*, *Band gaps and electronic structure of transition-metal compounds*, Phys. Rev. Lett. **55**, 418 (1985)
- [261] D. I. Khomskii, *Unusual valence, negative charge-transfer gaps and self-doping in transition-metal compounds*, Lithuanian Journal of Physics **37**, 65 (1997); see also cond-mat/0101164
- [262] M. A. Korotin *et al.*, *CrO<sub>2</sub>: A Self-Doped Double Exchange Ferromagnet*, Phys. Rev. Lett. **80**, 4305 (1998)
- [263] J. Matsuno *et al.*, *Variation of the Electronic Structure in Systematically Synthesized Sr<sub>2</sub>MO<sub>4</sub> (M = Ti, V, Cr, Mn, and Co)*, Phys. Rev. Lett. **95**, 176404 (2005)
- [264] A. C. Komarek *et al.*, *CaCrO<sub>3</sub>: an anomalous antiferromagnetic metallic oxide*, accepted by Phys. Rev. Lett. (2008)
- [265] A. C. Komarek *et al.*, *Magnetoelastic coupling in RTiO<sub>3</sub> (R = La, Nd, Sm, Gd, Y) investigated with diffraction techniques and thermal expansion measurements*, Phys. Rev. B **75**, 224402 (2007)
- [266] A. C. Komarek, PhD thesis, University of Cologne, (2009)
- [267] M. Braden *et al.*, *Crystal and magnetic structure of Ca<sub>2</sub>RuO<sub>4</sub>: Magnetoelastic coupling and the metal-insulator transition*, Phys. Rev. B **58**, 847 (1998)
- [268] O. Friedt *et al.*, *Structural and magnetic aspects of the metal-insulator transition in Ca<sub>2-x</sub>Sr<sub>x</sub>RuO<sub>4</sub>*, Phys. Rev. B **63**, 174432 (2001)
- [269] A. Liebsch, H. Ishida, *Subband Filling and Mott Transition in Ca<sub>2-x</sub>Sr<sub>x</sub>RuO<sub>4</sub>*, Phys. Rev. Lett. **98**, 216403 (2007)

- [270] E. F. Bertaut, *Representation analysis of magnetic structures*, Acta. Cryst. A **24**, 217 (1968)
- [271] S. V. Streltsov *et al.*, *Band versus localized electron magnetism in CaCrO<sub>3</sub>*, Phys. Rev. B **78**, 054425 (2008)
- [272] O. K. Andersen, O. Jepsen, *Explicit, First-Principles Tight-Binding Theory*, Phys. Rev. Lett. **53**, 2571 (1984)
- [273] V. I. Anisimov *et al.*, *Band theory and Mott insulators: Hubbard U instead of Stoner I*, Phys. Rev. B **44**, 943 (1991)
- [274] J. B. Goodenough, *Theory of the Role of Covalence in the Perovskite-Type Manganites [La, M(II)]MnO<sub>3</sub>*, Phys. Rev. **100**, 564 (1955)
- [275] J. Kanamori, *Superexchange interaction and symmetry properties of electron orbitals*, J. Phys. Chem. Solids **10**, 87 (1959)
- [276] P. W. Anderson, *Theory of magnetic exchange interactions: exchange in insulators and semiconductors*, Solid State Phys. **14**, 99 (1963)
- [277] G. R. Blake *et al.*, *Transition between Orbital Orderings in YVO<sub>3</sub>*, Phys. Rev. Lett. **87**, 245501 (2001)
- [278] M. Grüninger *et al.*, *Observation of Out-of-Phase Bilayer Plasmons in YBa<sub>2</sub>Cu<sub>3</sub>O<sub>7- $\delta$</sub>* , Phys. Rev. Lett. **84**, 1575 (2000)
- [279] A. Gössling *et al.*, *Mott-Hubbard versus charge-transfer behavior in LaSrMnO<sub>4</sub> studied via optical conductivity*, Phys. Rev. B **77**, 035109 (2008)
- [280] J. Orenstein, D. H. Rapkine, *Comment on "Excitonic absorption and superconductivity in YBa<sub>2</sub>Cu<sub>3</sub>O<sub>7-y</sub>"*, Phys. Rev. Lett. **60**, 968 (1988)
- [281] M. Born, E. Wolf, *Principles of Optics* (Pergamon, New York, 1970), 4th ed.
- [282] L. N. Bulaevskii, Y. A. Kukharenskiy, *Fiz. Tverd. Tela (Leningrad)* **14**, 2401 (1972) [Sov. Phys. Solid State **14**, 2076 (1973)]
- [283] A. J. Glick, G. W. Bryant, *Effect of anisotropy on the optical-absorption spectrum of polyacetylene*, Phys. Rev. B **28**, 4295 (1983)
- [284] M. Grüninger, PhD thesis, Rijksuniversiteit Groningen, (1999)
- [285] M. Rotenberg, R. Bivins, N. Metropolis and J. Wooten, Jr., *The 3-j and 6-j Symbols*, The Technology Press, Massachusetts Institute of Technology, Cambridge (1959)
- [286] E. El-Baz, B. Castel, *Graphical Methods of Spin Algebras in Atomic, Nuclear, and Particle Physics*, Marcel Dekker, New York (1972)



# Supplement

## Offizielle Erklärung

Ich versichere, daß ich die von mir vorgelegte Dissertation selbständig angefertigt, die benutzten Quellen und Hilfsmittel vollständig angegeben und die Stellen der Arbeit - einschließlich Tabellen, Karten und Abbildungen -, die anderen Werken im Wortlaut oder dem Sinn nach entnommen sind, in jedem Einzelfall als Entlehnung kenntlich gemacht habe; daß diese Dissertation noch keiner anderen Fakultät oder Universität zur Prüfung vorgelegen hat; daß sie - abgesehen von unten angegebenen Teilpublikationen - noch nicht veröffentlicht worden ist sowie, daß ich eine solche Veröffentlichung vor Abschluß des Promotionsverfahrens nicht vornehmen werde. Die Bestimmungen dieser Promotionsordnung sind mir bekannt. Die von mir vorgelegte Dissertation ist von Prof. Dr. M. Grüninger betreut worden.

Köln, den 25. Februar 2009

Thomas Möller